: DEPARTMENT OF CHEMICAL ENGINEERING
: FACULTY OF SCIENCES AND TECHNOLOGY
: UNIVERSITY OF COIMBRA

CATALYTIC STUDIES AND TRICKLE-BED REACTOR BEHAVIOUR FOR WET OXIDATION OF PHENOLIC WASTEWATERS

CFD AND EXPERIMENTAL ANALYSIS

RODRIGO JOSÉ GÓIS LOPES

DEQ – FCTUC

Coimbra, 2009

: DEPARTMENT OF CHEMICAL ENGINEERING
: FACULTY OF SCIENCES AND TECHNOLOGY
: UNIVERSITY OF COIMBRA

CATALYTIC STUDIES AND TRICKLE-BED REACTOR BEHAVIOUR FOR WET OXIDATION OF PHENOLIC WASTEWATERS

CFD AND EXPERIMENTAL ANALYSIS

Dissertation by

RODRIGO JOSÉ GÓIS LOPES

to be presented with due permission for the public examination in the Sala dos Capelos at University of Coimbra, Portugal, to obtain the degree of Doctor in Chemical Engineering.

DEQ – FCTUC

Coimbra, 2009

"*In an age when man has forgotten his origins and is blind even to his most essential needs for survival, water along with other resources has become the victim of his indifference*"

Rachel Carson

Acknowledgements

I would like to express my acknowledgments in Portuguese since I am a native speaker and those persons who are hearing me would like to know these feelings in our mother tongue.

À orientadora Professora Doutora Rosa M. Quinta-Ferreira responsável pelo interesse que despertou em mim pela investigação científica, agradeço todo o apoio, motivação e enorme disponibilidade demonstrada ao longo destes anos em que trabalhamos juntos. Agradeço todas as sugestões, críticas, os elogios e o incentivo que sempre estiveram presentes no caminho que percorri.

À Fundação para a Ciência e Tecnologia do Ministério da Ciência e do Ensino Superior no âmbito do POCI 2010 Formação Avançada para a Ciência, POPH - QREN - Tipologia 4.1 - Formação Avançada, comparticipado pelo Fundo Social Europeu e por fundos nacionais do MCTES pela bolsa de doutoramento SFRH/BD/19933/2004 e pelo Projecto POCI/QUE/59895/2004.

À Fundação Calouste Gulbenkian pelo apoio à participação no Congresso Internacional GLS8 sob o processo nº 89205.

Ao Projecto Europeu REMOVALS: Reduction, modification and valorisation of sludge (http://www.etseq.urv.es/removals/), financiado pelo "Sixth framework programme, priority 1.1.6.3, Global change and ecosystems, FP6-018525".

Aos colaboradores e membros do GERSE, Grupo de Investigação em Reacção Química, Separação e Ambiente, liderado pela Professora Doutora Rosa M. Quinta-Ferreira, pelo Professor Doutor Licínio M. Gando-Ferreira e pela Professora Doutora Margarida J. Quina, agradeço todas as facilidades concedidas para a realização deste trabalho.

Ao Departamento de Engenharia Química da Faculdade de Ciências e Tecnologia da Universidade de Coimbra pela disponibilização dos respectivos serviços e laboratórios. Em particular agradeço à D. Mafalda Fernandes, D. Regina Seguro, D. Adamo Caetano, D. Maria João Bastos, D. Teresa Tavares, D. Cecília Paulino, Sr. António Amado, Srª. Dulce Pancas e Sr. José Santos.

Aos colegas do Departamento de Engenharia Química que contribuíram directa ou indirectamente no trabalho de laboratório. Em particular, agradeço ao Doutor Adrián Silva pela partilha de conhecimentos de oxidação catalítica húmida e aprendizagem de várias técnicas analíticas disponíveis no Laboratório de Reactores Químicos e que catalisou o meu trabalho e acima de tudo para uma verdadeira transferência de conhecimento. Aos colegas Rui, Fernando, Ângela, Fátima, Beatriz, Teresa, Vera e Nuno pelo espírito de entreajuda e camaradagem.

E porque há vida para além do doutoramento, agradeço a todos os meus amigos por estarem de um outra forma sempre disponíveis a ajudar.

À minha família pela eterna gratidão por tudo o que fizeram de e por mim, não poderia deixar de citar o meu Pai, a minha Mãe e a minha irmã que certamente se orgulham de me verem finalizar mais uma etapa da vida. Vem aí mais uma etapa …

RESUMO

Os recursos hídricos nunca estiveram tão em foco como nos anos mais recentes. Sendo vastas as aplicações da água, desde o seu uso na agricultura, e indústria até às actividades domésticas e recreativas, a educação e a responsabilidade da sua gestão têm vindo a ser introduzidas progressivamente como factores importantes sob o ponto de vista da valorização dos recursos aquíferos. As entidades regulamentares, seriamente preocupadas com a escalada da poluição ambiental e degradação dos recursos naturais, têm legislado, por seu turno, de forma cada vez mais rigorosa sobre a sustentabilidade da água. Em particular, a eliminação de águas residuais produzidas nos processos industriais, contendo poluentes nocivos com elevado poder tóxico, tem emergido com especial ênfase como objecto de estudo na comunidade universitária e industrial.

Na extensa classe de poluentes líquidos, os fenóis assumem um papel de relevo devido à descarga em larga escala no ambiente e à sua toxicidade para a fauna e flora aquáticas. Com o objectivo de cumprir os requisitos estabelecidos pelas rigorosas directivas ambientais, a oxidação húmida é um método de tratamento que se tem revelado atractivo para efluentes que são demasiadamente diluídos para a incineração e ainda predominantemente tóxicos para o tratamento biológico. A produção de azeite é uma das actividades agro-industriais mais remotas na bacia Mediterrânea que produz volumes consideráveis de águas residuais, sendo actualmente o seu tratamento um grande desafio para esta indústria. O principal problema associado a esta classe de efluentes reside na composição de cor escura com elevado conteúdo de matéria orgânica de carácter tóxico devido maioritariamente à presença de ácidos fenólicos. Deste modo, com o intuito de progredir no âmbito do desenvolvimento de reactores catalíticos multifásicos para operar em condições de temperatura e pressão elevada, o tratamento de águas residuais provenientes da extracção de azeite por oxidação catalítica húmida foi um factor chave de motivação para o estudo aprofundado ao longo da presente tese.

Neste âmbito, os efluentes agro-industriais produzidos na extracção de azeite foram seleccionados devido ao seu carácter sazonal, não-biodegradável e fitotóxico. Os compostos polifenólicos de base ácida, especificamente, os ácidos siríngico (*4*-hidróxi-*3,5*-dimetóxibenzoico), vanílico (*4*-hidróxi-*3*-metóxibenzoico), *3,4,5*-trimetóxibenzoico, verátrico (*3,4*-dimetóxibenzoico), protocateutico (*3,4*-dihidróxibenzoico) e *trans*-cinâmico, mereceram especial atenção no que diz respeito ao desempenho do processo de oxidação catalítica húmida a diferentes níveis: remoção do carbono orgânico total, formação de compostos intermediários, estabilidade do catalisador e modelização cinética, tendo sido testados vários catalisadores laboratoriais e comerciais. Os metais activos dos catalisadores estudados foram o manganésio, cobre, zinco, ferro e prata suportados em cério e alumina. Os catalisadores de

óxidos de manganésio e cério revelaram as melhores propriedades de remoção do carbono orgânico total exibindo bons parâmetros de estabilidade quantificados em adsorção de carbono e lixiviação dos metais activos. Um dos principais objectivos do presente trabalho englobou o desenvolvimento e estudo de modelos computacionais baseados nos códigos de Dinâmica de Fluidos Computacional com aplicações nos tratamentos ambientais de descontaminação de águas residuais por oxidação catalítica húmida em reactores trifásicos do tipo *trickle-bed*. Deste modo, após a selecção de catalisadores, foram realizados estudos com recurso ao modelo cinético generalizado, de forma a obter as expressões cinéticas necessárias ao projecto de reactores *trickle-bed*, através de técnicas de simulação avançadas.

Ao nível da simulação computacional, foram estudados dois modelos com uma malha tridimensional com o objectivo de previsão de parâmetros hidrodinâmicos como a fracção volumétrica de líquido e a queda de pressão no regime *trickling*. Os modelos *Euler-Euler* e *Volume-of-Fluid* foram optimizados com diferentes densidades de malha, passos temporais, critérios de convergência, métodos de discretização e modelos de turbulência do tipo *Reynolds Averaged Navier-Stokes*. O efeito dos caudais de líquido e gás assim como a influência da temperatura e pressão foram quantificados através dos parâmetros de fracção volumétrica de líquido e queda de pressão. O modelo *Euler-Euler* foi utilizado nos estudos de distribuição espacial do escoamento multifásico com diferentes distribuidores gás-líquido, enquanto o fenómeno de histerese na operação hidrodinâmica e a eficiência de molhagem foram estudados com o modelo *Volume-of-Fluid*.

Os parâmetros cinéticos foram posteriormente integrados nos modelos multifásicos *Euler-Euler* e *Volume-Fluid* nos quais foram contabilizados os fenómenos de transporte térmico e mássico no reactor *trickle-bed* a operar a pressões elevadas. Os perfis axiais e radiais dos parâmetros hidrodinâmicos e reaccionais foram avaliados em diferentes condições de operação e validados experimentalmente. A influência dos caudais de gás e líquido assim como o efeito da temperatura e pressão foram quantificados através da conversão de carbono orgânico total. A eficiência de descontaminação depende consideravelmente da temperatura em detrimento do efeito da pressão de operação. A influência do caudal de líquido foi atribuída maioritariamente ao tempo de reacção dos poluentes orgânicos ao passo que foi determinado um valor óptimo para o caudal de gás. O aumento da concentração do carbono orgânico total na corrente a tratar conduziu a eficiências de remoção mais rápidas. De um ponto de vista geral, as simulações computacionais do modelo *Euler-Euler* conferiram melhores previsões para diferentes parâmetros hidrodinâmicos e reaccionais em comparação com o modelo *Volume-of-Fluid*. Em suma, o modelo multifásico *Euler-Euler* permitirá ciclos de desenvolvimento de produto e/ou processo mais eficientes auxiliando na optimização e integração da relação mútua energia/ambiente em reactores multifásicos *trickle-bed*.

ABSTRACT

Water resources have never been so indulged as in recent years. Uses of water include agricultural, industrial, household and recreational activities. Therefore, education and awareness in the area of water management is increasingly important from a global perspective of resource valorization. Regulatory entities concerned about the unprecedented scale and speed of environmental pollution and degradation, and the depletion of natural resources have been legislating for the water sustainability. In particular, the disposal of wastewater streams containing highly toxic and hazardous organic pollutants generated by industrial processes has emerged as a topic of mounting concern in academia and industry.

Among the numerous classes of liquid pollutants, phenols are of particular importance due to their widespread discharge in the environment and toxicity to many water living organisms. In order to meet the requirements established by stringent environmental regulations, wet air oxidation is an attractive method for the treatment of waste streams which are too dilute to incinerate and yet too toxic to treat biologically. Indeed, olive oil production is one of the oldest agricultural industries in the Mediterranean basin that generates a considerable amount of olive oil wastewater heavily contaminated. The depuration of liquid wastes produced from olive oil production is still a major challenge facing this industry. The main problems are attributed to their dark color, high organic content and toxicity levels which are due to the presence of phenolic compounds. Therefore, aiming to advance the development of catalytic multiphase reactors to operate at high values of temperature and pressure, olive oil wastewaters remediation by catalytic wet oxidation was the key motivation factor to be fulfilled among this thesis.

In this regard, agro-food olive oil processing wastewaters were selected as an example of non-biodegradable and phytotoxic effluents. Specifically, major polyphenolic compounds: syringic (*4*-hydroxy-*3,5*-dimethoxybenzoic), vanillic (*4*-hydroxy-*3*-methoxybenzoic),*3,4,5* trimethoxybenzoic, veratric (*3,4*-dimethoxybenzoic), protocatechuic (*3,4*-dihydroxybenzoic) and *trans*-cinnamic acids typically found in olive oil mill wastewaters deserved particular attention. The process performance was evaluated at different levels including total organic carbon reduction, intermediate compounds formation, catalyst stability and kinetic modelling. Several commercial and laboratory-made catalysts were investigated addressing both the catalytic activity and stability. Regarding the selected catalysts, some were prepared in laboratory and others were commercially

obtained. The tested active materials were manganese, copper, zinc, iron and silver, while the catalysts supports were ceria and alumina. A major importance was given to cerium based catalysts and manganese catalysts. With the present contribution, our purpose was to integrate and couple state of the art CFD codes with environmental reaction applications in the wastewater remediation by catalytic wet oxidation in trickle-bed reactors. Therefore, after the catalyst screening, kinetic studies were performed taking into account the generalized kinetic model to bring up lumped kinetic parameters necessary for the design and scale-up of pilot and industrial trickle-bed reactors making use of advanced simulation techniques.

Two Computational Fluid Dynamics (CFD) frameworks were developed for the hydrodynamic analysis aiming to predict the liquid holdup and pressure drop in the trickling flow regime with a three-dimensional computational grid. Euler-Euler and Volume-of-Fluid multiphase models were optimized in terms of mesh density, time step, convergence criteria, discretization schemes and Reynolds Averaged Navier-Stokes turbulence models. Several computational runs were performed querying the effect of gas and liquid flow rates, operating pressure and temperature on liquid holdup and two-phase frictional pressure drop. Multiphase flow distribution was investigated with different gas-liquid distributors using the Eulerian framework, whereas hysteresis phenomena and wetting efficiency in trickle beds were evaluated with the Volume-of-Fluid model.

The kinetic parameters were further integrated within the Euler-Euler and Volume-of-Fluid models where the reaction aspects as well as the transport mechanisms were accounted for in a high-pressure trickle-bed reactor so that both multiphase CFD frameworks were evaluated for either cold flow or reacting flow conditions. Axial and radial profiles of hydrodynamic and reaction parameters were evaluated at different operating conditions for the sake of experimental validation. The influence of gas and liquid flow rates as well as the effect of temperature and pressure were investigated in terms of total organic carbon (TOC) conversions. TOC removal efficiency depends heavily on the bed temperature while the operating pressure has minor influence in final conversion. Whereas the effect of liquid flow rate was mainly related with the reaction time, the influence of gas flow rate led to a maximum on TOC conversion. Moreover, higher values of inlet pollutant concentration led also to higher conversions. The multiphase Eulerian predictions handled agreeably better the effect of different numerical solution parameters either supported at non- and reacting flow conditions with respect to Volume-of-Fluid model. In a nutshell, CFD can be useful to obtain shorter product/process development cycles and optimize energy/environment requirements in multiphase trickle-bed reactors.

LIST OF CONTENTS

Pag.

PART B. CWO CATALYST SCREENING

PART C. TRICKLE-BED REACTOR HYDRODYNAMICS: CFD STUDIES

PART D. TBR REACTION OPERATION: CFD AND EXPERIMENTAL STUDIES

Appendix A. FLUENT Solver 331

LIST OF FIGURES

Pag.

VI. Turbulence Modelling of Multiphase Flow in High-Pressure TBR 125

VII. CFD Modelling of Multiphase Flow Distribution in TBR 159

VIII. VOF Based Model for Multiphase Flow in High-Pressure TBR: Optimization of Numerical Parameters 185

IX. Numerical Simulation of TBR Hydrodynamics with RANS-Based Models Using a VOF Technique 213

XIII. Assessment of CFD VOF Method for CWO Modelling in TBR 287

XIV. Evaluation of Multiphase CFD Models in TBR for Pollution Abatement 307

LIST OF TABLES

PART A. THESIS SCOPE AND OUTLINE

The first part of this thesis identifies the major environmental issues of hydric resources. Special emphasis is given to the water consumption and wastewater generation in agro-food processing industries. Advanced environmental technologies for wastewater remediation are described in the context of advanced oxidation processes. Aiming to accelerate the industrial implementation of modern water depuration techniques, new tools for designing process equipment are probed including Computational Fluid Dynamics frameworks. A synopsis of computational flow models is structured for single- and multiphase flows. Finally, the motivation, scope and the outline of the thesis is presented at the end of the first chapter.

The second chapter schematizes the background work collected along the development of this thesis. Firstly, non- and catalyzed wet oxidation literature is reviewed for the representative pollutants encountered in agro-industrial wastewaters. Secondly, industrial non-catalytic and homogeneous/heterogeneous catalytic wet oxidations processes are briefly described. Afterwards, the multiphase trickle-bed reactor literature is addressed by presenting the fluid dynamics characterization as well as the transport properties. Finally, the theoretical methodologies adopted for the hydrodynamic prediction of trickle beds are presented with special focus on modern computational fluid dynamic codes.

I. Introduction

The current chapter provides a general overview of the core objectives of the present work. This chapter encompasses an introduction on advanced environmental technologies for wastewater remediation. Catalytic wet oxidation is briefly described in the context of gas-liquid-solid multiphase technology in which hazardous compounds are oxidized by molecular oxygen at elevated temperatures and pressures. Afterwards, modern tools in computational flow modelling are depicted with particular attention being given to Computational Fluid Dynamics. Current limitations and expectations in single- and multiphase flows are focused in terms of chemical and environmental industry applications. The motivation, scope and structure of the thesis are finally addressed.

I.1. Advanced Environmental Technologies for Wastewater Remediation

Water is becoming an increasingly commodity due to the massive amount reduction of potable water affected by long periods of drought and growing water demands in our *Blue Planet*. Several regional and planetary policies have been implemented for the safeguard and the economical exploitation of hydric resources. Recycling processes of industrial process waters and wastewaters were always a routing solution for the management of toxic and hazardous wastewaters streams. The compulsory regulations in manufacturing industries have been fruitful in the minimization of organic and inorganic compounds motivated by the development of highly efficient technologies capable of destroying hazardous pollutants.

Recently, agro-industrial processing waters received an increasing awareness due to its impact on aquatic and soil environment. Despite the nutrient levels, non-biodegradable and phytotoxic chemicals also characterize agro-food wastewaters. These compounds exhibit biocide behaviour and reduce significantly the efficiency of biodegradation treatments. Mediterranean countries are an example of the negative impact on water and soil quality endorsed by the presence of polyphenolic compounds in olive oil mills wastewater (OOMW) or in other water emissions from the agro-food sector, such as those deriving from the production of citrus juices and wineries. Olive oil industries generate around 30 million m^3 of wastewater characterized by a very high Biochemical Oxygen Demand (BOD) 12-60 kg O_2/m^3, Chemical Oxygen Demand (COD) in the 40-200 kg O_2/m^3 range and a high concentration of phenolic compounds (Niaounakis and Halvadakis *et al.*, 2004). The huge organic content load and the seasonal character of olive oil production impose the development of pre-treatments to increase biodegradability needed to

enhance the methanation rate and make the process economically feasible or ultimately to remove completely the organic compounds.

These environmental concerns had been responsible by the notorious research on advanced processes for wastewaters remediation. Among several separation and reaction based technologies, advanced oxidation processes such as wet air oxidation (WAO), supercritical water oxidation, ozonation, Fenton oxidation, photocatalytic oxidation, sonochemical degradation and microwave irradiation were the ones that received careful respectfulness (Collin *et al.*, 2009; Rivas *et al*., 2008; Zhou *et al.*, 2007; Cañizares *et al.*, 2007; Mandal *et al.*, 2004; Pera-Titus *et al*., 2004). Given the mineralization ability of organics to harmless final products using appropriate catalysts, catalytic wet air oxidation (CWAO) has been used in the treatment of wastewaters containing either moderately concentrated non-toxic or bio-toxic organic pollutants. Toxic and recalcitrant molecules are degraded leading to remarkable Total Organic Carbon (TOC) decontamination rates. Lumped parameters have been preferred to express the conversion level such as TOC, COD, BOD and TPh (total polyphenolic content assessed by Folin-Ciocalteau reagent) instead of specific conversions for a single compound. Carbon dioxide and water are final end products if complete oxidation is achieved. The biological refractory pollutants are oxidised by dissolved molecular oxygen at elevated temperatures (180-315ºC) and pressures (20-150 bar) (Luck, 1999). The wet oxidation can be further accelerated with a homogeneous or heterogeneous catalysts leading to more amenable operating temperatures and pressures (130-250ºC; 10-50 bar) by increasing the oxidation rate. High solubility of oxygen is promoted at those operating conditions increasing the oxidizing power and high temperatures are able to increase the reaction rates and the production of free radicals (Kolaczkowski *et al.*, 1999). According to the literature and our previous work, low molecular weight carboxylic acids have been found as refractory intermediates species during wet oxidation (Bhargava *et al.*, 2006; Silva, 2005, Luck, 1999). In fact, non- and catalytic wet oxidation have been a participate subject of extensive literature studies over the last three decades as researchers continue to investigate the aptitude of these processes to remove different types of organic compounds from a wide variety of simple and complex industrial and simulated wastewaters.

Taking into account the huge multiplicity of liquid pollutants that can be treated by wet oxidation, one should expect the industrial massification and dissemination of CWAO. However, the industrial application has been controlled by the scarce development of catalysts that are stable at high operating values of temperature and pressure. Additionally, high operating temperatures and pressures are often pointed out as noteworthy drawbacks of wet oxidation technology. Therefore, aiming to give some contribution to the technical know-how needed to clean up the environment

specifically the condition of the hydric resources, olive oil wastewaters remediation by catalytic wet oxidation will be a motivation factor to be fulfilled among this work/thesis.

Catalytic wet oxidation has been investigated in four different levels: reaction chemistry; reactors suitable for kinetic, mass and heat transport studies; catalyst screening, characterization and stability; and scale-up procedures for industrial implementation. Key features of CWO catalysts, catalyst preparation, catalyst stability and deactivation, and catalyst reuse and regeneration are well-known criteria on the CWO technology assessment (Bhargava *et al.*, 2006). The economic and environmental viability of a CWO system motivated a great interest in Academia and industry personnel who have been conducted several endeavours on the selection of optimum catalysts. While the first three aspects are purely experimental, the last one is deeply concerned with the engineering issues that arise in the design of industrial reactors. Numerous literature works attempted to demonstrate how CWO technology can be applied on an industrial scale and how reactor design is critical to the successful application of either non- or catalytic wet oxidation. In this ambit, exhaustive theoretical studies appeared on phenomena such as kinetics and mass transfer help in the design and selection of industrial reactors. Advantages and disadvantages were also systematized from the comparison of different reactor types.

I.2. Sensing New Tools for Designing Process Equipment: Computational Fluid Dynamics

Catalysis and chemical kinetic science are two major areas that can bring important advances for the chemical industries. The industrial profit has to encompass the proper design of chemical process equipment that ensure the delivery of materials and energy at the right places and at the right times in industrial units. The manipulation and optimization of underlying fluid dynamics is a top priority on the minimization of the capital and costs leading to competitive solutions. The main purposes dictate that tomorrow's processes should consume less energy and raw materials, cost less to build and operate, have no or minimum waste, be safer, and provide lower risk to the environment. In order to fulfil those objectives, existing plants need reengineering activities and careful analysis to improve their overall effectiveness and to become *environmentally friendly*. In this regard, Computational Fluid Dynamics (CFD) is one of the essential *technologies* that enable process engineers to predict, manipulate, and realize the desired fluid dynamics in wastewater process equipment. CFD is nothing more than an alternative body of knowledge and techniques to solve mathematical models of fluid dynamics on digital computers in comparison to traditional techniques, which are based overly in empirical correlations. Notable reviews identified CFD as one of the potential technologies to move forward the chemical, environmental, aerospace and

automotive industries (Norton and Sun, 2006; Ghidossi *et al.*, 2006; Oberkampf and Trucano, 2002; Dudukovic *et al.*, 2002). CFD allows shortening the efficient design of new products and processes, the optimization of existing processes to improve energy efficiency and the intensification of product-process development cycles. The contemporary status of computational flow modelling encourage strongly the application of modern CFD codes on the design and investigation of process equipment and aims to accomplish novel and stringent environmental regulations on the decontamination of high strength wastewaters.

The specification of operating protocols and hardware configuration in the design of process equipment provide suitable background to complete the desired process without compromising safety, environment, and most of all economics. The application of CFD is envisaged as a prevailing tool to gain more control in the delivery of reactants or energy and in the removal of products since any chemical or physical transformation process requires the addition or removal of different materials and energy. Therefore, the distribution of materials as well as the energy within the process vessel is improved noticeably if one has the capability to predict and control fluid dynamics by means of CFD. The overall methodology can be divided in four main stages: identification of process requirements to categorize the desired fluid dynamic characteristics; evaluation of possible hardware configurations and operating protocols to achieve the desired fluid dynamic characteristics; development of quantitative relationships between the hardware configuration and performance; and optimization and fine-tuning of the final design.

Although the importance of fluid dynamics in the whole process is understandable in CFD methodology, until the development of modern CFD codes attended by sophisticated computer architectures, process engineers had to manipulate fluid dynamics either by harnessing pressure, gravity, or surface forces or by employing rotating/moving elements in pilot plants. Laboratory, pilot and meso-scale equipment for heat and mass transfer allowed the development of several empirical correlations, which account for different characteristics of films/boundary layers and transport rates over different shapes. Instead of extensive and costly experimentation, CFD models allow the optimization of process equipment to maximize industrial benefit following rigorous environmental regulations. CFD enable the establishment of quantitative relationships between the throughput and operating flow regime avoiding a massive number of empirical parameters. Transport parameters such as heat- mass-transfer coefficients and several hydrodynamic parameters including film structures and thicknesses, boundary layer geometries, pressure drop, wetted area or even the residence time distribution are investigated and optimized for multiple process configurations. Consequently, CFD aids in the identification of most appropriate process configurations from the large selection of alternatives.

Multiphase systems characterize extensively the chemical industry, e.g. slurry reactors, packed and fluidized beds, bubble, spray and extraction columns so that a wide assortment of operating regimes could exist depending on the desired flow regime (Dudukovic *et al.*, 1999). To mention a few parameters, operating flow rates, phasic physical properties, hardware configuration, distributors design, size distribution of dispersed-phase particles, and flow regime are typical and relevant factors that play a major role in the scale-up approach. As a rule of thumb, the performance and process operability may be improved by means of CFD codes that intend to advance the technical expertise of environmental processes.

I.3. Synopsis of Computational Flow Models

CFD models can be divided in two main classes: *design* models that attempt to provide a quantitative relationship between the hardware and performance, and *learning* models, which provide a basic understanding of different underlying processes. Equipment design can thereby steered to different process arrangements and project concepts, which overcome usually the lack of experimental, time and funding resources. From a concise literature survey, the current status of CFD on flow simulation are summarized into two distinct categories: single-phase and multiphase flows.

I.3.1. Single-Phase Flows

Laminar flow and mixing of Newtonian fluids have been simulated in complex industrial process equipment accounting for temperature and composition dependent physical properties. Local hot or cold spots, complex geometries and scale-up were addressed satisfactorily for single-phase flows. The quantification of viscous drag, form drag, and losses due to directional changes in the overall pressure drop provide the efficient design of industrial process equipment according to several literature works (Dudukovic *et al.*, 2002). Recent developments on free surface flow allow a deep mathematical understanding of surface characteristics and surface phenomena (surface tension, contact angle, wall adhesion) involving contact of a gas, liquid and solid. During the last decade, the boost and enlargement of computational resources allowed the flow simulation of rheologically complex fluids with viscoelastic characteristics and the quantitative prediction of the flow regime transition (Ge and Fan, 2006).

The predictive capabilities of CFD codes have been always a discussion centre on the turbulence modelling. Turbulence models may be classified in three categories: direct numerical simulations (DNS), large eddy simulations (LES), and Reynolds-averaged Navier-Stokes equations (RANS) (Ranade, 2002). If one moves from DNS to RANS, more and more of the turbulent motions are

estimated and, therefore, less computational resources are required. DNS models simulate all of the dynamically important scales of turbulent flows directly being the specification of the initial and boundary conditions one of the imperative step. DNS provides valuable information about the interaction of small-scale and large-scale motions requiring huge computational resources. Therefore, applications of DNS for equipment design are not likely to be cost-effective for the near future unless one has a straightforward flow configuration with very low Reynolds numbers. In LES, the large-scale motions are resolved while the small-scale motions are modelled using the *subgrid scale* (SGS) models. Until recently, few theoretical studies have been accomplished with SGS models that exhibited low satisfactory levels. LES models are expected to be reformulated in the forthcoming decades with practical applications. Alternatively, RANS-based turbulence models are a ubiquitous approach that enables a good compromise between the width of application and computational economy. The quality of RANS simulations are strongly affected by the numerical issues, e.g. grid quality and/or density, discretization schemes, wall functions and unsteady flow features. It should be pointed out that RANS-base models contain more adjustable constants that need to be determined by fitting the experimental data in comparison with DNS and LES models. Hence, careful verification and validation should be performed through a meticulous error analysis to avoid dangerous extrapolations. Reacting flow simulations are one of the most intricate case-study since it requires the resolution of much finer scales and computational demands may increase significantly even with simple turbulent flow models. Adequate closure models for the estimation of turbulence characteristics that embody the interactions of chemical reactions with turbulence are needed either in single-phase or multiphase flows.

I.3.2. Multiphase Flows

Despite the advancement of CFD models in single-phase flow modelling, quantitative predictions of multiphase flows in industrial process equipment without adjustable parameters are still beyond the scope of CFD codes. However, CFD methodology provides valuable insights on multiphase flows, yet partially, in the improvement of process equipment design. DNS models for multiphase flows are foreseen as a breakthrough point to contribute with useful proficiency on several key issues from a singular investigation of phase distributors and characteristics of generated dispersed-phase particles to the extrapolation of cold flow data to higher temperature and pressures or even the entrainment of the continuous phase due to bubble or drop collapse at the free surface. There is also a lack of appropriate closure models for Eulerian-Eulerian frameworks and whenever DNS fails to simulate most likely denser multiphase flows, Eulerian-Lagrangian approach is a common practice. According to the literature, multiphase flow modelling began routinely applied for the design of cyclones, coal-fired burners, mist eliminators and electrostatic precipitators (Ranade, 2002). Notwithstanding, widespread modelling efforts have to be accomplished on the

development of reliable closure models in Eulerian-Eulerian mathematical approaches for dense and dispersed-phase flows. Mainly due to the scarce availability of high-quality experimental data to obtain different model parameters, the simulation of complex multiphase flows have been retained from further progress and, therefore, state-of-art multiphase CFD models are not feasible to generate quantitative predictions of interphase transport rates.

An outstanding effort has been made to understand single-phase or multiphase flow through a packed bed. It is well recognized that complexity of multiphase flows is further increased by odd geometry of packed beds. The simulation of packed bed flows encompass two major alternatives on the generation of bed geometry: the mapping of void space on a computational grid through visualization techniques (particle image velocimetry, laser dopler anemometry and magnetic resonance imaging); and statistical methods that rely on the porosity distribution. A large number of particles might be prohibitive since it becomes computationally intractable. CFD models can identify successfully how the presence of different particles arrangements affects reactor hydrodynamics. In fact, macroscopic CFD models based on closure models have done a reasonable job of simulating single-phase flows with adjustable parameters (Ranade, 2002). However, none simulation of gas-liquid flow through packed beds or trickle beds is reported in the literature. It is expected that CFD models will allow to understand the spreading of liquid over catalyst pellets, wetting phenomena and capillary forces in trickle-bed reactors. Furthermore, gas-liquid distribution or residence time distribution in trickle-bed reactors, wetting and mass transfer in a packed gas-liquid contactor are existing gaps to be satisfied in the near future. A lot of work remains also to be done in multiphase reaction engineering.

I.4. Motivation and Scope of the Thesis

Taking into account that computational flow models can assist the design and optimization of new and existing processes and products, reduce energy costs, increasing productivity and profit margins and, namely, improving environmental performance, the present work is driven by the great advantage that single-phase CFD models already demonstrated in the automotive, aerospace and chemical and power industries. The simulation of reacting and multiphase turbulent flows are rarely documented in the specialized literature and a broad segment of the chemical industry are anxiously waiting for its appliance. Numerous requirements have been identified on CFD tools so that they should be:

- Experimentally verified – simulations must be validated with experimental results.
- Computationally efficient – adaptable to multiprocessor workstations and clusters of processors, which provide expediently valuable results.

- Fundamentally based – containing more and better physics coupled with chemical reactions, rather than non-mechanistic correlations that are not scalable.
- Versatile – portable to various machines, usable by generalist rather than specialists, scalable, reliable, and compatible with current chemical industry databases.

The realization of maximum benefit from CFD modelling for design depends on how well CFD simulations can predict adequately an industrial unit either because of numerical inaccuracies or because of limitations in the physical models. Sophisticated numerical methods enable better control on discretization errors but grid-independent solutions are not straightforward even with the actual advancement in computing resources. Underlying physical models should be calibrated with high-quality experimental data aided by new tools based on modern visualization techniques (Oberkampf and Trucano, 2002). Electrical, radiation, optical and acoustic methods have already been developed to provide noninvasive, spatially, and temporally resolved measurements of single-phase and multiphase systems. The major drawback rely on the technical knowledge needed to examine experimental data on fluid-structure interactions, turbulence characterization, abrupt regime transitions/pulsing, and other important dynamic characteristics of multiphase flows. High-performance computing such as parallel machines/cluster computing allow fine-grid computations that will bring insightful interpretations on the mechanism of turbulent momentum transfer and provide insights into energy transfer and dissipation phenomena.

From the abovementioned forewords, catalytic wet oxidation is still a very fertile area of research in which there is room for significant improvement. The development of active, cost effective, robust catalysts for use in many different agro and food industries could lead to significant cleanup of hdyric resources by catalytic wet oxidation. With the present contribution, our main purpose is to integrate and couple state of the art CFD codes with environmental reaction applications in the wastewater remediation by catalytic wet oxidation in trickle-bed reactors. Commercial and laboratory-made catalyst will be investigated thoroughly in terms of oxidation efficiency and stability. After the catalyst screening, kinetic studies will be performed to bring up lumped kinetic parameters necessary for the design and scale-up of pilot and industrial trickle-bed reactors. Available CFD turbulence models will be integrated with different multiphase flow frameworks at non- and reacting flow conditions. Experimental verification and validation will be accomplished for either integral hydrodynamic parameters (two-phase frictional pressure drop and liquid holdup) or TOC removal efficiencies. With such methodology, one should expect a significant contribution to the performance enhancement of trickle-bed reactors in environmental applications.

I.5. Thesis Structure

Aiming to endorse and contextualize the reader with the present thesis, the current chapter has an introductory role on the CWO technology with environmental concerns and a relevant background, which probes the pertinent methodology on the investigation of single- and multiphase reactors. State of the art is outlined in Chapter II and is structured according to a concise survey of the scientific literature in non- and catalytic wet oxidation. Phenol and other aromatic alcohols were selected as they characterize agro-industrial wastewaters. Major polyphenolic pollutants typically found in olive oil mill wastewaters are then summarized and organized by research works with real and simulated effluents. An inventory of commercial non- and catalytic wet oxidation processes is presented including homogeneous and heterogeneous technologies. Multiphase reactors are reviewed in terms of fluid dynamics, catalyst wetting and gas-liquid-solid mass and heat transfer parameters. Macroscopic hydrodynamic models for trickle-bed reactors are presented as well as CFD simulation approaches that have been investigated for multiphase reactors. These two first chapters are joined together in Part A of this document.

The kernel of the thesis is divided into four main sections, the so-called Part B, C and D. It is worthwhile to mention that each chapter of these sections is mainly based upon the publication of peer-reviewed articles. Part B includes Chapters III and IV devoted to the investigation of active, stable and economical catalysts for the treatment of OMW, as well as the characterization of the reaction system through kinetic analysis, using various catalysts prepared in the laboratory or obtained commercially. Six major pollutants in OMW (syringic, vanillic, *3,4,5*-trimethoxybenzoic, veratric, protocatechuic and trans-cinnamic acids) are applied to mimic the polyphenolic content of agro effluents and kinetic expressions in terms of TOC are established aiming the successful design and operation of continuous CWO multiphasic chemical reactors in wastewaters treatment plants. Apart from the catalytic activity, active metal leaching and carbon adsorption on the catalyst surface are assessed from a catalytic stability point of view.

Part C is allocated to the hydrodynamic simulations of trickle-bed reactors by means of CFD codes: Euler-Euler and Volume-of-Fluid (VOF) multiphase models. The Eulerian framework is developed with momentum interphase exchange coefficients and the trickle-bed reactor under high-pressure operation is modelled through a three-dimensional mesh to bring up hydrodynamic studies in Chapter V. Aiming to examine laminar and different Reynolds Averaged Navier-Stokes (RANS) turbulence k-ε models (Standard, Realizable and Renormalization Group Theory (RNG) and Reynolds Stress Model (RSM)) for multiphase flow in trickle-bed reactors, in Chapter VI a multifluid Eulerian model is applied for the simulation of interstitial flow to describe the fluid phase scale interactions at the catalyst level in a regular packing. As long as the details of the flow

environment around the catalyst particles are essential, different mesh densities in the optimization of numerical solution parameters are performed under unsteady laminar and turbulent flow simulations in order to provide a more fundamental understanding of trickle-bed hydrodynamics. Phasic velocity maps and turbulent kinetic energy profiles are examined to provide insightful and realistic fluid flow conclusions. Several computational runs are performed for the purpose of hydrodynamic model validation either in terms of liquid holdup or two-phase pressure drop. Afterwards, in Chapter VII the quantitative understanding of flow maldistribution at the catalyst scale in the trickle bed is accomplished through the evaluation of time averaged axial and radial profiles for both hydrodynamic parameters. The influences of liquid distributor geometry as well as the effect of gas and liquid flow rates are investigated in the trickling flow regime.

Chapter VIII is dedicated to multiphase Volume-of-Fluid (VOF) model to simulate the wetting phenomena in high-pressure trickle-bed reactors providing a better understanding of its liquid distribution and hysteresis. The hydrodynamic validation is attained in terms of pressure drop and liquid holdup experimental data taken from the open literature and afterwards, computational predictions for the wetting efficiency are investigated at different liquid flow rates. Additionally, simulation activities on the gas-liquid-solid interface at different flow regimes are performed for the meaningful knowledge of interaction between TBR hydrodynamics and reaction parameters. High-pressure TBR simulation assisted with VOF model comprises the numerical validation in terms of well-known hydrodynamic parameters. Liquid holdup and two-phase pressure drop are selected for the parametric optimization of several models parameters including mesh aperture, time step and convergence criteria. The multiphase flow regime is presented with several RANS turbulent flow models as well as the laminar one in Chapter IX. The effect of gas and liquid flow rate on either frictional pressure drop or liquid holdup are also examined under trickling flow conditions with three-dimensional packed bed geometry.

Part D introduces the catalytic wet oxidation on Eulerian CFD simulations to investigate the behaviour of a pilot TBR unit considering the reaction aspects as well as the transport mechanisms involved in the treatment process of wastewaters from olive oil mills industries. The computational domains and modelling approach are firstly described and the hydrodynamics simulations are validated with single and two phase flow data reported in literature for experiments in TBR without chemical reaction. Regarding the simulation of the oxidation process in TBR, experimental studies involving the determination of reaction rates are accomplished for the TOC degradation of a single phenolic acid in Chapter X. Afterwards, in Chapter XI the catalytic wet oxidation of a phenolic acids mixture is simulated in a trickle-bed reactor by means of CFD at different temperatures and pressures as well as different gas and liquid flow rates. From the perspective of multiphase reactor engineering to gas-liquid-solid catalytic wet oxidation, scale-up

of chemical reactors as well as process optimization require detailed knowledge and information of concentration and thermal profiles. In Chapters XII and XIII, Euler-Euler and VOF model are used to gain insight and quantitative information about the axial and radial concentration and temperature profiles when a phenolic model solution is employed to simulate the CWAO in the multiphase reactor. Finally, in Chapter XIV, Eulerian framework is also compared against the VOF model in terms of hydrodynamic parameters and at reacting flow conditions to improve the current knowledge of interaction between hydrodynamics and chemical reaction in trickle beds.

The whole work presented along this thesis is resumed at last in Part E (Chapter XV) where the most relevant conclusions and further recommendations on future work are exposed. Finally, Appendix A describes the FLUENT CFD solver methodologies. Numerical details of algorithms are provided for the pressure-velocity coupling and discretization schemes for spatial and temporal derivatives are described along the evaluation methods of gradients and derivatives.

I.6. References

Bhargava, S. K., Tardio, J., Prasad, J., Foger, K., Akolekar, D. B. and Grocott, S. C. (2006). Wet Oxidation and Catalytic Wet Oxidation. *Ind. Eng. Chem. Res*. **45** (4), 1221-1258.

Cañizares, P., Lobato, J., Paz, R., Rodrigo, M.A., Sáez, C. (2007). Advanced oxidation processes for the treatment of olive-oil mills wastewater. *Chemosphere* **67** (4), 832-838.

Collin, J.G., Puma, G.L., Bono, A., Krishnaiah, D. (2009). Sonophotocatalysis in advanced oxidation process: a short review. *Ultrasonics Sonochemistry*, DOI: 10.1016/j.ultsonch.2009.02.002

Dudukovic, M. P., Larachi, F., Mills, P. L. (1999). Multiphase reactors – revisited. *Chemical Engineering Science* **54**, 13-14, 1975-1995.

Dudukovic, M.P., Larachi, F., Mills P.L. (2002). Multiphase catalytic reactors: A perspective on current knowledge and future trends. *Catalysis Reviews. Science and Engineering* **44** (1), 123-246.

Ge, Y., Fan, Liang-Shih. (2006). 3-D Direct Numerical Simulation of Gas-Liquid and Gas-Liquid-Solid Flow Systems Using the Level-Set and Immersed-Boundary Methods. *Advances in Chemical Engineering* **31**, 1-63.

Ghidossi, R., Veyret, D., Moulin, P. (2006). Computational fluid dynamics applied to membranes: State of the art and opportunities. *Chemical Engineering and Processing* **45** (6), 437-454.

Mandal, A., De, A.K., Bhattacharjee, S. (2004). Removal of catechol from aqueous solution by advanced photo-oxidation process. *Chemical Engineering Journal* **102** (2), 203-208.

Niaounakis, M., Halvadakis, C.P. (2004). Olive mill waste management, Literature Review and Patent Survey. *Typothito-George Dardanos Publications*, Athens, Greece.

Norton, T., Sun, Da-Wen. (2006). Computational fluid dynamics (CFD) – an effective and efficient design and analysis tool for the food industry: A review. *Trends in Food Science & Technology* **17** (11), 600-620.

Oberkampf, W.L., Trucano, T.G. (2002). Verification and validation in computational fluid dynamics. *Progress in Aerospace Sciences.* **38** (3), 209-272.

Pera-Titus, M., García-Molina, V., Baños, M.A., Giménez, J., Esplugas, S. (2004). Degradation of chlorophenols by means of advanced oxidation processes: a general review. *Applied Catalysis B: Environmental* **47** (4), 20 219-256.

Ranade, V.V. (2002). Computational Flow Modeling for Chemical Reactor Engineering. Academic Press, New York.

Rivas, F.J., Carbajo, M., Beltrán, F., Gimeno, O., Frades, J. (2008). Comparison of different advanced oxidation processes (AOPs) in the presence of perovskites. *Journal of Hazardous Materials* **155** (3), 407-414.

Silva, A.M.T., Treatment of Liquid Pollutants by Catalytic Wet Oxidation, PhD Dissertation, Coimbra, 2005.

Zhou, M., He, J. (2007). Degradation of azo dye by three clean advanced oxidation processes: Wet oxidation, electrochemical oxidation and wet electrochemical oxidation – A comparative study. *Electrochimica Acta* **53** (4), 1902-1910.

This page intentionally left blank

II. State of the Art

This chapter describes contemporary literature in non- and catalyzed wet oxidation. Literature is reviewed for phenol and other aromatic alcohols. Liquid pollutants in agro-food processing effluents are schematized in individual phenolic acids and raw olive oil mill wastewaters. Commercial processes are depicted for homogeneous and heterogeneous applications of wet oxidation. Afterwards, multiphase reactors are identified with special emphasis in trickle-bed reactors by presenting the major hydrodynamic parameters used in the characterization of fluid dynamics and transport phenomena. Finally, CFD simulation approaches are classified according to Eulerian, Lagrangian and Volume-of-Fluid frameworks.

II.1. Synopsis of the Literature in WO and CWO

The majority of wastewater streams originated in petrochemical and pharmaceutical plants are contaminated with toxic and hazardous organic compounds. Typical application and contributing areas include the manufacture of petroleum-based products and fuels, the production of commodity and specialty chemicals, pharmaceuticals, herbicides and pesticides, refining of ores, production of polymers and other materials. In order to gather the environmental regulations, these industrial wastewaters must be treated before they meet the specifications for discharge into a natural water body. Among the chemical oxidation technologies, wet oxidation (WO) process has proven its aptitude for the treatment of effluents containing a high content of organic matter, specifically, total organic carbon (TOC) concentration (20-85 g L^{-1}), chemical oxygen demand (COD) (40-200 g L^{-1}), biochemical oxygen demand (BOD) (12-60 g L^{-1}) in which direct biological purification is either aerobic or anaerobically unfeasible (Niaounakis and Halvadakis *et al.*, 2004).

WO is characterized by supporting the flameless pollutant oxidation in the aqueous phase with quite severe reaction conditions typically in the range of 473-573 K and 70-130 bar. A known disadvantage that adversely affects the cost-benefit of this process is related with such extreme conditions where most materials for construction are susceptible to stress corrosion cracking when chloride ions are present in the waste stream. Therefore, amenable technologies, such as catalytic wet oxidation (CWO), offer lower energy requirements and much higher oxidation efficiencies compared to conventional WO (Luck, 1996; Mishra *et al*., 1995; Wang *et al*., 1995; Wakakura *et al*., 1995). During CWO, organic pollutants are oxidized to innocuous inorganic compounds such

as CO_2, H_2O and hetero-atom dissolved ions at much lower temperatures and pressures than in unanalyzed thermal processes.

The vast variety of organic compounds and industrial processes and wastewaters that have been studied using the WO and CWO processes indicates the potential seen in these processes by numerous researchers. The WO oxidation process (or wet air oxidation, WAO), which was first patented by Zimmerman (1950) over 50 years ago, removes organic compounds in the liquid phase by oxidizing them completely to carbon dioxide and water using an oxidant such as oxygen or air. The process is extremely clean, because it does not involve the use of any harmful chemical reagents and the final products are carbon dioxide and water when the oxidation is complete. When sufficient temperatures and/or residence times are not used, partial oxidation occurs. In most cases, low molecular weight carboxylic acids, which are very difficult to oxidize, form from the partial oxidation of higher molecular weight compounds. This has led to a significant number of studies being conducted on the WO of low molecular weight carboxylic acids and the development of catalysts to reduce the reaction temperatures required to completely oxidize many organic compounds in a reasonable amount of time.

Mixtures of metal oxides of Cu, Zn, Co, Mn and Bi already exhibited good activity, but leaching of these catalysts was detected (Matatov-Meytal and Sheintuch, 1998; Collivignarelli *et al*., 1997; Zarzycki *et al*., 1997). On the contrary, heterogeneous catalysts based on precious metals deposited on stable supports are less prone to active ingredient leaching (Chen and Li, 1999; Luck, 1999; Tan *et al*., 1999; Sune and de Sores, 1999; Harada, 1999; Kolaczkowski *et al*., 1999; Imamura, 1999). Depending on the type and amount of organic compounds dissolved in the wastewater, the process can be designed either to reduce their concentration or ultimately destroy them. In the former case, the intermediate products formed during the oxidation must be biodegradable. For reactions necessitating a solid catalyst and involving both relatively volatile (oxygen) and nonvolatile reactants (pollutant in wastewater stream), three-phase reactors are required.

In the last three decades, several reviews on WO and CWO have been published with all of the reviews published prior to 1995 being summarized by Mishra *et al*. (1995). The reviews published after 1995 are listed in Table II.1. This list is based on the most recent review of WO/CWO (Bhargava *et al*., 2006) and other literature published up to and including 2009. Table II.1 focus predominantly on WO/CWO processes that use oxygen or air as an oxidant.

Table II.1. Reviews on Wet Oxidation (WO) and Catalytic Wet Oxidation (CWO) Published from 1995 to 2007.

Reference	Title	Main topics covered/comments
Levec and Pintar, 2007	Catalytic wet-air oxidation processes: A review	Heterogeneous CWAO, mechanisms, kinetics; CWAO commercialised processes of real industrial wastewaters in batch and continuous-flow oxidation reactors; presentation of novel titania-supported Ru catalysts to detoxify industrial effluents
Bhargava *et al*., 2006	Wet Oxidation and Catalytic Wet Oxidation	Fundamental chemistry of WO/CWO; important aspects of catalysts with regard to the CWO process; engineering aspects of the WO/CWO process; and industrial applications of CWO technology
Patria *et al*., 2004	Wet Air Oxidation Processes	Applications and commercial processes discussed in detail. Very brief discussion of uncatalyzed and catalyzed reaction mechanisms.
Cai *et al*., 2004	Progress of Wet Catalytic Air Oxidation Technology	CWAO advances in oxygen-containing organic compounds (phenol, carboxylic acids)
Oliviero *et al*., 2003	Wet Air Oxidation of Nitrogen-Containing Organic Compounds and Ammonia in Aqueous Media	CWAO of nitrogenous compounds produced in chemical and pharmaceutical industries towards several inorganic forms of nitrogen (NH_4^+, N_2, NO_2^-, NO_3^-) as well as phenolic compounds and carboxylic acids
Imamura, 2003	Catalytic Technology for Water Purification: I & II	Homogeneous and heterogeneous catalysts for water purification
Maugans *et al*., 2002	Wet Air Oxidation: A Review of Commercial Sub-critical Hydrothermal Treatment	Detailed discussion of commercial WAO processes
Yang *et al*., 2002	Catalytic Wet Air Oxidation	Air-based oxidant technology in catalytic wet oxidation
Zarzycki, 2001	Mechanism and Mathematical Modeling of Wet Oxidation Processes	Detailed discussion of reaction mechanisms and mathematical modelling of WO processes. Brief discussion of industrial applications of WO.
Debellefontaine and Foussard, 2000	Wet Air Oxidation for the Treatment of Industrial Wastes. Chemical Aspects, Reactor Design and Industrial Applications in Europe	Brief discussion of chemical aspects (mechanism and kinetics) of WAO and CWO. Detailed discussion of industrial aspects of WAO
Tan *et al*., 1999	Factors Affecting Wet Air Oxidation Treatment of Wastewater	Operating parameters, reactor design considerations and catalyst selection
Imamura, 1999	Catalytic and Noncatalytic Wet Oxidation	Discussed WO of compounds containing C, H, and O, amides, dyes, polymers. Discussed homogeneous copper salt catalysts and heterogeneous Co/Bi, Mn/Ce and Ru/Ce catalysts. Majority of studies reviewed were conducted by review author.
Kolaczkowski *et al*., 1999	Wet Air Oxidation: A Review of Process Technologies and Aspects in Reactor Design	Detailed discussion of kinetics and mass transfer and WO and CWO processes.
Sune and de Soares, 1999	Some Aspects of Total Catalytic Wet Oxidation of Organic Substances in an Aqueous Phase	Chemical reaction engineering issues in CWO of oxygen-containing organic compounds
Luck, 1999	Wet Air Oxidation: Past, Present and Future	WAO and CWAO processes discussed in detail. Limited discussion on chemistry of WAO and CWO.
Matatov-Meytal and Sheintuch, 1998	Catalytic Abatement of Water Pollutants	Detailed discussion of catalysts and catalytic processes (including hybrid processes) used to remove a range of organic and inorganic compounds.
Collivignarelli *et al*., 1997	Technical and Economic Feasibility of Wet Oxidation: Treatment in a Full-scale Plant. Part 1.	Economic evaluation of industrial wastewater treatment
Luck, 1996	A Review of Industrial Catalytic Wet Air Oxidation Processes	Description of commercialized reactor configurations and catalysts used in CWAO
Wang, 1995	Advances in Catalytic Wet Air Oxidation of Wastewater	Selection of suitable catalysts and chemical reaction engineering issues
Mishra *et al*., 1995	Wet Air Oxidation	Comprehensive review comparing aspects of WO and CWO. No detailed discussion about effect of pH.

Levec and Pintar (2007) have reviewed several catalysts and presented mechanistic speculations and kinetics that have been proposed for the catalytic wet air oxidation (CWAO) process. The process is discussed more in detail only in those cases where it is already commercialised or at least foreseen to be in the near future. Particular attention was given to the heterogeneously

catalyzed WAO of real industrial wastewaters such as Kraft bleach plant effluents in batch and continuous-flow oxidation reactors. Finally, they came up with some considerations about the biodegradability/toxicity of CWAO treated effluents whenever the detoxification is incomplete, reporting that WAO was found capable of improving the biodegradability of pesticide and acrylonitrile wastewaters (Mishra *et al*., 1995), olive mill wastewaters (Chakchouk *et al*., 1994), phenolic wastewaters (Lin *et al*., 1994), water-soluble polymer-containing wastewaters (Otal *et al*., 1997).

Bhargava *et al*. (2006) have discussed four main aspects of WO and CWO: the chemistry of WO and CWO, reactors suitable for WO and CWO, important aspects of CWO catalysts, and WO/CWO of industrial solutions. In that review, the chemistry of WO and CWO is discussed over a range of chemical reactions that may occur during WO/CWO in general and during the WO/CWO of specific compounds. The authors have presented some theoretical considerations into designing an industrial CWO reactor. Cost drivers in an industrial situation and the potential problems that must be considered for wet oxidative reactors are discussed. It is also shown how theoretical study on phenomena such as kinetics and mass transfer help in the design and selection of industrial reactors. The other reviews listed in Table II.1 are shortened referred through the main topics addressed in each work jointly with some brief comments. Noteworthy, the surprising number of reviews coming to the general literature, 20 in 13 years (from 1995 to 2008) attests the high level of interest for this remediation technology.

II.2. Wet Oxidation of Phenol and Other Aromatic Alcohols

Phenol and other aromatic alcohols is the investigation subject of election in the last three decades given the numerous studies that have been conducted on non-catalyzed wet oxidation. The major reason is related to the phenolic characteristics of several aqueous effluents produced by the petrochemical, coke, shale oil, pulp and paper and plastics industries.

The non-catalyzed phenol wet oxidation in terms of TOC/COD conversion is significantly influenced by reaction temperature, oxygen partial pressure, and solution pH. At 130 °C and P_{O2}=0.5 MPa, ≈5% TOC conversion occurs after 2 h (Hamoudi *et al.*, 1998), whereas at 220 °C and P_{O2}=3 MPa 88% TOC conversion occurs after 2 h (Imamura, 1999). According to Table II.2, phenol has received particular attention during the last decades. The maximum temperature tested was 320 ºC (Wilhelmi and Knopp, 1979) and the maximum pressure was 150 bar (Pruden and Le, 1976). At those severe operating conditions, the phenol conversion was almost complete: 99.77 and 99 % after 15 min, respectively. The removal efficiencies of phenol have been expressed in terms of TOC, COD and individual phenol conversion and, in general, the higher operating

temperature and/or pressure, the higher phenol conversion is attained. As it can be seen from Table II.2, the minimum temperature and oxygen pressure that enables satisfactory decontamination efficiencies after 1 h were 250 ºC and 50 bar. Table II.2 summarizes the relevant works on the wet oxidation of phenol and other aromatic alcohols where it can be seen that reasonably high TOC/COD conversions can be achieved for most of the compounds at lower reaction temperatures, compared to carboxylic acids/salts, which are not referred here once they are not within the scope of the work. It should be noted that the formation of acetic acid/sodium acetate as an intermediate significantly reduces the low-temperature complete WO of some aromatic alcohols. Despite the high number of investigations on non-catalyzed wet oxidation of phenol, few studies have been reported on benzene-substituted alcohols and other aromatic alcohols such as benzyl alcohol, benzenediol, butylphenol, cyclohexanol, dimethylphenol, nitrophenol, pentachlorophenol, chlorophenol, cresol and biological-based phenols (cellulose, glucose, cellobiose), compared to the number of studies conducted on the WO of carboxylic acids/salts reviewed by Imamura (2003) and Luck (1999). Therefore, no confident and universal conclusions can be made due to the lack of sufficient information on this class of compounds.

II.3. Catalytic Wet Oxidation Studies on Phenol

Table II.3 summarizes most relevant and cited studies on catalytic wet oxidation of phenol and other aromatic alcohols. It can be seen that one of the most active catalysts that have been developed for CWO of phenol, in terms of TOC removal, is a Pt_xAg_{1-x}-MnO_2/CeO_2 catalyst that was developed by Hamoudi *et al.* (2000). This catalyst achieved 80% TOC removal in 1 h at 80 °C, using an oxygen partial pressure of 0.5 MPa. In what concerns the catalyst stability, it has been observed the deposition of polymeric products on the catalyst surface and pores. Pintar and Levec (1992) also reported the deposition of polymeric products in their study on CWO of phenol using a catalyst comprised of ZnO, CuO and Al_2O_3. Chen *et al.* (2001) have developed a Mn-Ce-O catalyst for the efficient removal of phenol TOC. This catalyst was capable of removing 80%-90% of phenol TOC in 10 min at 110 °C, using an oxygen partial pressure of 0.5 MPa. The percentage TOC removal achieved using this catalyst was reported to be highly dependent on the Mn/Ce ratio. At a Ce/(Mn + Ce) ratio of 1 (i.e., no manganese), there is no TOC conversion, compared to the 80%-90% that is achieved using a Ce/(Mn + Ce) ratio of 4/6. According to Chen *et al.* (2001) the high activity of this Mn-Ce-O catalyst is presumably due to the following: (i) improved oxygen storage capacity, (ii) improved oxygen mobility on the surface of the catalyst, and (iii) an electron-rich surface, which may be very important in the activation of adsorbed oxygen. Chen *et al.* (2001) reported that the main oxidation products formed using the Mn-Ce-O catalyst are carbon dioxide, small amounts of water-dissolved oxidation intermediates and some carbonaceous deposits.

Table II.2. Wet Oxidation of phenol and other aromatic alcohols

Initial pH	P_{O_2} (bar)	T (ºC)	Results (% of removal)	Reference
			Phenol	
25 mol NaOH/kg H_2O	50	250	yield CO_2, 29.9% (2 h)	Furuya *et al.*, 1985
n.s.	$[O_2]$ = 2.4-3.8	150-225	compound, 80% (1 h, 200 °C)	Devlin and Harris, 1984
4.4-6.6	103	50-300	COD, 100% (1 h, 300 °C)	Lin and Chuang, 1994
n.s.		275	phenol, 99.8% (1 h)	Dietrich *et al.*, 1985
n.s.	51-102	170-220	phenol, 100% (10 min, 220 °C, 10MPa)	Vicente *et al.*, 2002
n.s.		150-200	TOC, 85% (80 min, 200 °C)	Wu *et al*., 2001
2.8 and 3.3	10	180-248	TOC, 93.4% (20 min, pH 2.8, 248 °C)	Imamura *et al.*,1982
n.s.	50-150	200-250	phenol, 99% (15 min, 250 °C, 15 MPa)	Pruden and Le, 1976
6.5 and >12	6.9	230	COD, 90% (pH 6.5 and >12, 30 min)	Vaidya and Mahajani, 2002
n.s.	34, *overpressure*	204-260	TOC, ≈ 85% (1 h, 204 °C)	Baillod *et al.*, 1982
5-7	9.3	155	COD, <2%	Birchmeier *et al.*, 2000
n.s.	5	130	TOC, ≈ 5% (2 h)	Hamoudi *et al.*, 1998
n.s.	34, *overpressure*	204-260	TOC, ≈ 85% (1 h, 204 °C)	Baillod *et al.*, 1982
n.s.	138 (air)	142-166	phenol, 100% (2.5 ks, 166 °C)	Willms *et al.*, 1987
n.s.	30	220	TOC, 88% (2 h); COD, 93% (2 h)	Imamura, 1999
n.s.		275, 320	phenol, 99.77 (275 °C)	Wilhelmi and Knopp, 1979
n.s.	32-39	170-230	phenol, 99% (1 h, 230 °C, 3.55 MPa)	Chang *et al.*, 1995
n.s.	7	150	phenol, ≈ 95% (5 h); TOC, ≈ 58% (5 h)	Arena *et al.*, 2003
			Benzyl Alcohol	
n.s.	30	220	TOC, 93% (2 h); COD, 92% (2 h)	Imamura, 1999
			***1,2*-Benzenediol**	
25 mol NaOH/kg H_2O	50	250	yield CO_2, 26.5% (2 h)	Furuya *et al.*, 1985
			***1,3*-Benzenediaol**	
"	"	"	yield CO_2, 31.5% (2 h)	"
			***1,4*-Benzenediaol**	
"	"	"	yield CO_2, 33.9% (2 h)	"
			***4-sec*-Butylphenol**	
"	"	"	yield CO_2, 42.6% (2 h)	"
			Cyclohexanol	
"	"	"	yield CO_2, 29.1% (2 h)	"
			***2,4*-Dimethylphenol**	
n.s.	n.s.	275	2,4-dimethylphenol, 99.99% (60 min)	Dietrich *et al.*, 1985
			4-Nitrophenol	
n.s.	n.s.	"	nitrophenol, 99.6% (60 min)	"
			Pentachlorophenol	
n.s.	n.s.	"	pentachlorophenol, 97.3% (60 min)	"
			***p*-Chlorophenol**	
2.40	26	180	TOC, 42.9% (1 h)	Qin *et al.*, 2001
			***2*-Chlorophenol**	
n.s.	35.5	210	2-chlorophenol, 99% (1 h)	Chang *et al.*, 1995
n.s.	34, *overpressure*	204-260	TOC, ≈ 80% (1 h, 260 °C)	Baillod *et al.*, 1982
n.s.	n.s.	275, 320	2-chlorophenol, 94.96% (275 °C)	Wilhelmi and Knopp, 1979
			Cellulose	
3.1	n.s.	260-320	TOC, 85% (30 min)	Robert *et al.*, 2002
			***o*-Cresol**	
n.s.	30	220	TOC, 78% (2 h); COD, 86% (2 h)	Imamura, 1999
			***p*-Cresol**	
2.47	6.9-13.4	150-225	COD, 54.95% (2 h, 225 °C)	Mishra *et al.*, 1993
			Veratryl Alcohol	
3	7	150-200	COD, <5% (2 h at 150 °C followed by 1 h at 200 °C)	Sonnen *et al.*, 1997
			Glucose	
3	7	150-200	COD, ≈ 60% (2 h at 150 °C followed by 1 h at 200 °C)	"
			Cellobiose	
5-7	9.3	155	COD, ≈ 5% (1 h)	Birchmeier *et al.*, 2000
			***4*-Nitrophenol**	
n.s.	n.s.	275, 320	4-nitrophenol, 99.6% (275 °C)	Wilhelmi and Knopp, 1979
			Pentachlorophenol	
n.s.	n.s.	275, 320	pentachlorophenol, 81.96% (275 °C)	Wilhelmi and Knopp 1979

According to Table II.3, whereas Pintar and Levec (1992) have claimed complete conversion of TOC with CuO-ZnO-Al_2O_3 at 130 ºC and 5.6 bar after 1h, Chen *et al.* (2001) achieved 90 % of TOC conversion catalyzed by Mn-Ce-O at 110 ºC and 5 bar after 10 min. With a noble catalyst,

Hamoudi *et al.* (2000) reported 80% of TOC conversion with $Pt_xAg_{1-x}MnO_2/CeO_2$ at 130 ºC and 5 bar of oxygen pressure.

Table II.3. Catalytic Wet Oxidation of phenol and other aromatic alcohols

Catalyst	pH_0	P_{O_2} (bar)	T (ºC)	Results (% of removal)	Reference
			Phenol		
$Na_5[PV_2Mo_{10}O_{40}]$	3-4.5	9.3	155	COD, 76%	Birchmeier *et al.*, 2000
CeO_2	NA	5-15	160-180	TOC, 80% (3 h, 1.0 MPa)	Lin *et al.*, 2003
Co/Bi	3.5-5.2	10	180-248	TOC, 95.8% (20 min, 248 ºC, pH 3.5)	Imamura *et al.*, 1982
CuO/C (Sofnocarb A21)	6.35	36	180	phenol, 95% (1 h)	Alvarez *et al.*, 2002
Cu/MCM-41	NA	34	150-200	TOC, 90% (80 min)	Wu *et al.*, 2001
Ru-Ce/C	~6	20	160	phenol, 100% (3 h)	Oliviero *et al.*, 2000
$Ru-CeO_2/C$	~6	20	160	phenol, 92% (3 h)	"
Ru/C	~6	20	160	phenol, 82% (3 h)	"
$CuSO_4$	NA	32	170	phenol, 98.8% (1 h)	Chang *et al.*, 1995
Co_2O_3	NA	32	170	phenol, 98.7% (1 h)	"
MnO_2	NA	32	170	phenol, 89% (1 h)	"
$CuO-ZnO-Al_2O_3$	NA	5.6	130	phenol, 100% (1 h)	Pintar and Levec, 1992
$Cu(NO_3)_2$	5-6	10	200	TOC, 93.5% (1 h)	Imamura *et al.*, 1988
Mn-Ce-O	NA	5	110	TOC, 80%-90% (10 min)	Chen *et al.*, 2001
Ru/Ce	5-6	10	200	TOC, 94.8% (1 h)	Imamura *et al.*, 1988
$FeSO_4$	6.5	6.9	175	COD, 78% (1 h)	Vaidya and Mahajani, 2002
$CuSO_4$	6.5	6.9	175	COD, 95% (1 h)	"
$CuO-ZnO-Al_2O_3$	NA	3	130	phenol, 100% (2 h)	Levec, 1990
Pt-graphite	2-8	0.1-8	120-180	phenol, 99% (150 ºC, 1.8 MPa)	Masende *et al.*, 2003
$ZnO-CuO-Al_2O_3$	5.5, 7.3	1.5-10	105-130	TOC, 95% (2 h, 130 ºC, 5.6 bar)	Pintar and Levec, 1992
$ZnO-CuO-C-Al_2O_3$	NA	5	130	phenol, 100% (40 min)	Akyurtlu *et al.*, 1998
$Pt_xAg_{1-x}MnO_2/CeO_2$	NA	5	80-130	TOC, 80% (1 h, 80 ºC)	Hamoudi *et al.*, 2000
CuO	2-7	1-17	96-120	no conversion data (reaction rates)	Sadana and Katzer, 1974
$CuO-CeO_2$	NA	7.3	150	TOC, 91% (5 h)	Hocevar *et al.*, 2000
$CeO_2/\gamma-Al_2O_3$	NA	15	180	phenol, >95% (2 h); COD, ~80% (2 h)	Chen *et al.*, 2004
Al-Fe PC	3.9-5.1	8-25	90-150	phenol, >95% (1 h, 150 ºC, pH 3.9)	Guo and Al-Dahhan, 2003
$Cu(NO_3)_2$		12-23	40-60	phenol, >95% (1 h, 60 ºC)	Wu *et al.*, 2003
			***p*-Chlorophenol**		
$CuSO_4$	NA	35.5	160-210	*p*-chlorophenol, >99% (1 h, 210 ºC)	Chang *et al.*, 1995
$CuO-ZnO-Al_2O_3$	NA	5.6	120	*p*-chlorophenol,100% (80 min)	Pintar and Levec, 1992
Pt/A.C.	5.01	26	180	TOC, 97.9% (1 h)	Qin *et al.*, 2001
Pt/Al_2O_3	2.37	"	"	TOC, 91.2% (1 h)	"
Pt/CeO_2	2.7	"	"	TOC, 50.4% (1 h)	"
Pd/A.C.	3.48	"	"	TOC, 97.5% (1 h)	"
Pd/Al_2O_3	2.25	"	"	TOC, 81.8% (1 h)	"
Pd/CeO_2	2.95	"	"	TOC, 45.4% (1 h)	"
Ru/A.C.	1.71	"	"	TOC, 91.8% (1 h)	"
Ru/Al_2O_3	1.88	"	"	TOC, 72.4% (1 h)	"
Ru/CeO_2	2.48	"	"	TOC, 65.7% (1 h)	"
$Pt/Pd/Al_2O_3$	2.17	"	"	TOC, 84.7% (1 h)	"
$Pt/Pd/Ce/Al_2O_3$	3.06	"	"	TOC, 68.6% (1 h)	"
Mn/Al_2O_3	5.46	"	"	TOC, 82.5% (1 h)	"
			Chlorophenol		
$CuO-ZnO-Al_2O_3$	NA	3	130	chlorophenol, 100% (100 min)	Levec, 1990
			Nitrophenol		
$CuO-ZnO-Al_2O_3$	NA	3	130	nitrophenol, 80% (2.5 h)	"
$CuO-ZnO-Al_2O_3$	NA	5.6	140	*p*-nitrophenol, 95% (2.5 h)	Pintar and Levec, 1992
Pt/TiO_2	NA		150, 200	TOC, 70% (0.5 h, 150 ºC)	Higashi *et al.*, 1992
Mn-Ce-Zr-Cu $[CuSO_4]$	NA	10	190	TOC, 71% (20 min); COD, 79% (20 min)	Yoon *et al.*, 2001
			***p*-Cresol**		
CuO	9, 13.5	20-30	190	COD, 69% (30 min, pH 9); 6.2% (30 min, pH 13.5)	Mishra *et al.*, 1993
$CuSO_4$	acidic	20-30	190	COD, 89% (2 h)	"
			Cellobiose		
$Na_5[PV_2Mo_{10}O_{40}]$	3.0-4.5	9.3	155	COD, 47% (1 h)	Birchmeier *et al.*, 2000

The CWO of other aromatic alcohols, such as chlorophenol and nitrophenol, has not been studied as extensively as phenol. However, some promising catalysts based on noble metals Pt and Ru (Qin *et al*., 2001) and Cu, Zn and Mn (Qin *et al*., 2001; Pintar and Levec, 1992) have been developed for the removal of these compounds. Reaction pathways for the CWO of phenol have been studied by several researchers over the last two or three decades. Evidentially, many different intermediates form from the CWO of phenol on various catalysts. These intermediates can have a significant effect on phenol TOC conversion. Acetic acid is formed as an intermediate during CWO of phenol using several different catalysts.

II.4. Research involving the pollutants studied in this work

The research conducted in this work was performed on the decontamination of agro-industrial wastewaters arising from the production of olive oil. Olive oil manufacturing is an important economic activity of many countries particularly throughout the Mediterranean Sea (the annual world olive oil production, estimated at about 1.5-1.7 Mt/year in the eighties, reached around 2.5 Mt/year in the recent seasons) (International Olive Oil Council, 2008). However, olive oil extraction is one of the most pollution intensive food-processing industries. It involves a high consumption of water and large volumes of strongly polluted wastewaters known as olive mill wastewater (OMW) are generated. The amount of olive oil mill wastewater depends on the milling process, ranging from about 0.6 m^3/t of olives processed for classical mills to about 1.7 m^3/t olives in centrifugal mills (Hamdi, 1993). Furthermore, OMW is characterized by a very high Chemical Oxygen Demand (COD up to 200 g l^{-1}), a high content in phenol-like substances (in the range 1–5 g l^{-1} measured as phenol) and acidity.

Mainly because of its highly phytotoxicity and strong antimicrobial properties (Perez *et al*., 1992; Capasso *et al*., 1995), the classical biological treatment cannot be applied. Alternative appropriate treatments have to be considered for the management of these wastewaters. Most physical and physicochemical methods, such as precipitation, flocculation/clarification, coagulation, filtration, evaporation in open ponds (Rozzi and Malpei, 1996) give only partial solution to the problem. Reverse osmosis or ultra-filtration is usually costly. Anaerobic biological digestion with production of biogas is increasingly being used, but is not yet completely satisfactory (Dalis *et al*., 1996; Beccari *et al*., 1996).

A possible solution would be the chemical oxidative degradation of OMW used as a pre-treatment process to decrease its toxicity prior to biological treatment. Ozone alone or combined with hydrogen peroxide or UV radiation (Beltran *et al*., 1999; Andreozzi *et al*., 1998; Benitez *et al*., 1997), photo-Fenton treatment (Gernjak *et al*., 2004; Rivas *et al*., 2001; Pulgarin *et al*., 1999),

Fenton's reagent (Rivas *et al*., 2001), oxidation with polymer supported $FeCl_3$ (Fiorentino *et al*., 2004), wet air oxidation (WAO) with the addition of H_2O_2 (Chakchouk *et al*., 1994) have been tested. CWAO is increasingly studied for the elimination of organic pollutants in a variety of wastewaters from different chemical plants since as mentioned before, CWAO operates at lower temperatures and pressures than WAO due to the presence of, e.g., noble or transition metal based catalysts (Bhargava *et al*., 2006; Luck, 1999; Kolaczkowski, 1999; Béziat *et al*., 1999; Matatov-Meytal and Sheintuch, 1998).

Typical OMW contains high concentrations of tyrosol, cinnamic and/or benzoic acid derivatives. The scope of this work was to investigate the use of CWAO to treat model molecules representative of OMW. In this regard, *p*-coumaric, *4*-hydroxybenzoic, ferulic, caffeic, gallic, hydroxytyrosol, tyrosol, *p*-hydroxyphenylacetic, syringic, vanillic, *3,4,5*-trimethoxybenzoic, veratric, protocatechuic and *trans*-cinnamic acids have been identified in the literature as a representative of the phenolic fraction. These are the main reasons that supported the selection of these pollutants for the research developed under the present work, namely, syringic (*4*-hydroxy-*3,5*-dimethoxybenzoic), vanillic (*4*-hydroxy-*3*-methoxybenzoic), *3,4,5*-trimethoxybenzoic, veratric (*3,4*-dimethoxybenzoic), protocatechuic (*3,4*-dihydroxybenzoic) and *trans*-cinnamic acids that are typically found in Olea europaea L.-based olive oil wastewaters (Mulinacci *et al.,* 2001).

Section II.4.1 presents the relevant works dedicated to the non- and catalyzed wet oxidation of individual phenolic acids and section II.4.2 brings up the wet oxidation studies of real olive oil wastewaters.

II.4.1. Individual Phenolic Acids

The reactivity of p-coumaric acid has been studied using ozone (Andreozzi *et al*., 1995), UV radiation and combination of ozone and UV radiation (Miranda *et al*., 2001), photo-assisted Fenton reaction (Herrera *et al*., 1998) or photocatalysis (Poulios and Kyriacou, 2002). Fe-ZSM5 catalysts and Fe-containing pillared clays in combination with hydrogen peroxide were found more active than the homogeneous Fe^{3+}-salt (Perhatoner and Centi, 2005). The wet air oxidation of p-coumaric acid has been investigated without catalyst (Mantzavinos *et al*., 1996a) and using various homogeneous (Fe^{2+}, Cu^{2+}, Zn^{2+}, Co^{2+}) and heterogeneous ($CuO\text{-}ZnO\text{-}Al_2O_3$) catalysts (Mantzavinos *et al*., 1996b). Some leaching of the heterogeneous catalyst was measured whose extention was strongly dependent on the operating conditions. Fe- and Zn-promoted ceria catalysts prepared by co-precipitation were also investigated in the wet air oxidation (Neri *et al*., 2002).

Table II.4 summarizes the works where the compounds studied in this thesis were used as simulated pollutants of OMW. From this table, it can be seen that mostly investigations with *p*-

coumaric, *4-h*ydroxybenzoic, ferulic, caffeic, hydroxytyrosol, tyrosol, *p-h*ydroxyphenylacetic, syringic and vanillic acids were performed with air using transition and noble metals supported on alumina and pillared clays. The operating reaction conditions, catalyst composition and the extent of degradation are reported. As it can be seen from Table II.4, *p*-coumaric acid was extensively studied during the last decade.

Table II.4. Catalytic Wet Oxidation of phenolic acids

Catalyst	pH_0	P_{O_2} (bar) / H_2O_2	T (ºC)	Results (% of removal)	Reference
			***p*-Coumaric Acid**		
Cu-PILC	n.s.	0.15-0.5 ml h^{-1} H_2O_2	60-90	TOC, 87% (4h)	Caudo *et al.*, 2008
Cu-Al_2O_3		"	"	"	"
Cu-bentonite		"	"	"	
Cu-Al_2O_3	~5	0.15 ml h^{-1} H_2O_2 (4 h)	60-90	TOC, 91% (4 h)	Caudo *et al.*, 2007a
Cu-bentonite		"	"	TOC, 70% (4 h)	"
Cu-ZrO_2		"	"	TOC, 73% (4 h)	"
Cu-ZSM-5		"	"	TOC, 78% (4 h)	"
Cu-PILC		"	"	TOC, 82% (4 h)	"
Fe-PILC		"	"	TOC, 75% (4 h)	"
Cu-PILC	n.s.	0.5 ml h^{-1} H_2O_2	70	TOC, 85% (4 h)	Caudo *et al.*, 2007b
Fe-PILC				TOC, 80% (4 h)	"
Cu-PILC	4.5-5.5	0.5 ml h^{-1} H_2O_2 (3 h)	80	TOC, 75% (3 h)	Najjar *et al.*, 2007
(Al-Fe)PILC	n.s.	0.02M H_2O_2 / UV	25	PolyPhOH, 28% (24 h)	Azabou *et al*., 2007
TiO_2 DT51	n.s.	50 (air)	140	TOC, (35)% (5 h)	Minh *et al*., 2006
TiO_2 P25		"	"	TOC, (30)% (5 h)	"
ZrO_2 MeL		"	"	TOC, (40)% (5 h)	"
ZrO_2 EP		"	"	TOC, (20)% (5 h)	"
Pt-TiO_2 P25		"	"	TOC, (75)% (5 h)	"
Pt-ZrO_2 MeL		"	"	TOC, (35)% (5 h)	"
Ru-TiO_2 P25		"	"	TOC, (65)% (5 h)	"
Ru-TiO_2 DT51		"	"	TOC, (70)% (5 h)	"
Ru-TiO_2 Eng		"	"	TOC, (75)% (5 h)	"
Ru-ZrO_2 MeL		"	"	TOC, (80)% (5 h)	"
Ru-ZrO_3 EP		"	"	TOC, (60)% (5 h)	"
CeO_2	n.s.	20	80	TOC, (80)% (5 h)	Milone *et al.*, 2006
Au-CeO_2		"	"	TOC, (85)% (5 h)	"
Pt-CeO_2		"	"	TOC, (90)% (5 h)	"
Pt-(TiO_2,ZrO_2)	n.s.	50 (air)	140	TOC, (95, 80)% (5 h)	Perkas *et al*., 2005
Ru-(TiO_2,ZrO_2)				TOC, (75, 80)% (5 h)	"
Fe-CeO_2	n.s.	20 (air)	80-130	TOC, 100% (30 min)	Neri *et al.*, 2002
Zn-CeO_2		"	"	Compound, 33% (1.5 h)	"
CeO_2		"	"	TOC, 80% (30 min)	"
Cu-Zn(Al_2O_3)	n.s.	27.3	130	TOC, 76% (1 h); Compound 100% (15 min)	Mantzavinos *et al.*, 1997 "
n.s.	n.s.	28	150	TOC, 36%; Compund 100% (2 h)	Mantzavinos *et al.*, 1996a
			***4*-Hydroxybenzoic Acid**		
(Al-Fe)PILC	n.s.	0.02M H_2O_2 / UV	25	PolyPhOH, 52% (24 h)	Azabou *et al*., 2007
Cu-PILC	n.s.	0.15-0.5 ml h^{-1} H_2O_2	60-90	TOC, 75% (4h)	Caudo *et al.*, 2008
Cu-Al_2O_3					
Cu-bentonite					
Pt-(TiO_2,ZrO_2)	n.s.	50 (air)	140	TOC, 62% (6 h)	Perkas *et al*., 2005
Ru-(TiO_2,ZrO_2)				TOC, 70% (6 h)	
			Ferulic Acid		
(Al-Fe)PILC	n.s.	0.02M H_2O_2 / UV	25	PolyPhOH, 58% (24 h)	Azabou *et al*., 2007
			Caffeic Acid		
(Al-Fe)PILC	n.s.	0.02M H_2O_2 / UV	25	PolyPhOH, 86% (24 h)	Azabou *et al*., 2007
			Hydroxytyrosol		
(Al-Fe)PILC	n.s.	0.02M H_2O_2 / UV	25	PolyPhOH, 70% (24 h)	Azabou *et al*., 2007
			Tyrosol		
(Al-Fe)PILC	n.s.	0.02M H_2O_2 / UV	25	PolyPhOH, 31% (24 h)	Azabou *et al*., 2007
			***p*-Hydroxyphenylacetic Acid**		
(Al-Fe)PILC	n.s.	0.02M H_2O_2 / UV	25	PolyPhOH, 32% (24 h)	Azabou *et al*., 2007
			Syringic Acid		
$Na_5[PV_2Mo_{10}O_{40}]$	3.2	9.3	155	COD, 40% (3 h)	Birchmeier *et al.,* 2000
			Vanillic Acid		
(Al-Fe)PILC	n.s.	0.02M H_2O_2 / UV	25	PolyPhOH, 50% (24 h)	Azabou *et al*., 2007

Transition metals such as Cu, Fe, Ti and Zr have been compared with noble metals e.g. Pt, Au and Ru as systematized by Minh *et al*. (2006). The TOC conversion of *p*-coumaric acid aqueous solutions was found to be strongly dependent on the oxidation temperature for reaction times up to 5h. Moreover, hydrogen peroxide was found to promote the TOC decontamination rates even at lower temperatures. Milone *et al.* (2006) and Neri *et al*. (2002) claimed that *p*-coumaric acid degradation can be further improved by ceria based catalysts with shorter residence times and lower temperatures and oxygen pressures. Apart from *p*-coumaric acid, the other phenolic acids were predominantly studied with aluminium and iron pillared clays and promoted by hydrogen peroxide irradiated by UV (Azabou *et al*., 2007). To the best of our knowledge, apart syringic and vannilic acids (Table II.4) there is no evidence in the literature up to date on the catalytic wet oxidation of the other phenolic compounds used in our work, namely, *3,4,5*-trimethoxybenzoic, veratric, protocatechuic, and *trans*-*c*innamic acids.

II.4.2. Olive Mill Wastewater

Table II.5 summarizes the works on the catalytic wet oxidation of olive mill wastewaters. It can be seen that only in the last couple of years the OMW decontamination was studied by means of CWO.

Table II.5. Oxidation of Olive Mill Wastewaters

Catalyst	pH_0	P_{O_2} (bar) / H_2O_2	T (ºC)	Results (% of removal)	Reference
			Olive Mill Wastewater		
Al-PILC $CuN_{1.7}$ $CuN_{2.8}$ $CuN_{5.6}$	n.s.	0.8-4% H_2O_2 (V/V)	25	TOC, 45% (2h)	Achma *et al*., 2008
Cu-PILC Cu-Al_2O_3 Cu-bentonite	4.6-5.1	30 ml h^{-1} H_2O_2	60-90	TOC, 29.8%; PolyPhOH, 38.8% (5h); COD, 20.8%	Caudo *et al.*, 2008
Pt/C (1 wt.% Pt) Ir/C (5 wt.% Ir)	4.3	6.9	100, 200	TOC, (41%, 100 ºC), (100%, 200 ºC) 8h TOC, (52%, 100 ºC), (85%, 200 ºC) 8h	Gomes *et al*., 2007
Cu-PILC Fe-PILC	4.8	0.5 ml h^{-1} H_2O_2	60-90	TOC, 16% (4 h); PolyPhOH, 46% TOC, 22% (4 h); PolyPhOH, 48%	Caudo *et al.*, 2007
Cu-PILC Cu-Silicalite	4.5-5.5	0.5 ml h^{-1} H_2O_2	50-80	TOC, 13% (6h); PolyPhOH, 45% COD, 78% (3 h); PolyPhOH, 97%	Najjar *et al.*, 2007
(Al-Fe)PILC		0.02M H_2O_2 / UV	25	TOC, 43%; PolyPhOH, 62% (24 h)	Azabou *et al*., 2007
Cu-BTC	3.6-4.2	113 mg L^{-1} H_2O_2	25	COD, 18%; PolyPhOH, 96% (3.5h)	de Rosa *et al*., 2005
Pt-Al_2O_3 (5% Pt) CuO-A.C. (5% CuO)	5.3	10 (air)	180	TOC, 30%; COD, 45% (6h) TOC, 45%; COD, 55% (6h)	Rivas *et al.*, 2001
NA (SCWO)	4.9	250 (total)/ 0.2M H_2O_2	380-500	TOC, 83%, COD, 86%; PolyPhOH, 99% (17s)	Rivas *et al.*, 2001

Achma *et al*. (2008) developed a novel method of preparing copper-exchanged aluminum-pillared montmorillonite. The catalysts containing different ratios of Cu/clay were prepared by solid-state reaction of the Al-pillared clay already synthesized with copper nitrate in controlled atmosphere.

The properties of copper-based catalysts were studied in the wet hydrogen peroxide photocatalytic previous oxidation (WHPPCO) (H_2O_2 with UV light) of real OMW.

Caudo *et al*. (2008) carried out a strict comparison of copper-based pillared clays (Cu-PILC) and the analogous iron-based clays (Fe-PILC) in the previous wet hydrogen peroxide catalytic oxidation (WHPCO) of model phenolic compounds (p-coumaric and p-hydroxybenzoic acids) and real OMW. Both catalysts show no leaching of the transition metal differently from other copper-based catalysts prepared by wetness impregnation on oxides (alumina, zirconia) or ion-exchange of clays (bentonite) or zeolite ZSM-5. Cu-PILC shows a comparable activity to dissolved Cu^{2+} ions, although the turnover number is lower assuming that all copper ions in Cu-PILC are active. Cu-PILC shows a high resistance to leaching and a good catalytic performance, which was attributed to the presence of copper essentially in the pillars of the clay.

Gomes *et al*. (2007) investigated the suitability of CWAO for the treatment of OMW in a high pressure reactor at 100 and 200 °C under an oxygen partial pressure of 6.9 bar, using carbon supported platinum (1 wt.% Pt) and iridium (5 wt.% Ir) catalysts prepared by incipient wetness impregnation. At 100 °C, refractory organic compounds persisted even after prolonged reaction time (8 h). At 200 °C, complete total organic carbon and colour removal was obtained with the Pt/C catalyst after 8 h of reaction. A kinetic model was developed taking into account catalytic and non-catalytic reactions, formation of refractory compounds and catalyst deactivation. The authors claimed a very good agreement between the proposed model and CWAO experimental data at 200 °C.

Caudo *et al*. (2007) performed several experiments on the WHPCO of model and real OMW with copper-pillared clays (Cu-PILC). The conversion results of model molecules (p-coumaric acid, p-hydroxybenzoic acid) were compared with the ones from real agro-industrial plants and showed that Cu-PILC layered materials might be used to treat real wastewater from agro-food production, and not only simple model chemicals as typically made in the literature. The authors have claimed that using a semi-batch slurry-type reactor with a continuous feed of H_2O_2, the behaviour both in TOC and in polyphenols abatement may be described by using pseudo-first-order reaction rates. Using real wastewater the rate constants are one or two orders of magnitude lower than using model molecules and a decrease in the ratio between rate constant of phenols conversion and rate constant of TOC abatement is observed. Scaling-up to a larger volume semi-continuous slurry-type reactor causes a further lowering of one order of magnitude in the rate constants of TOC and polyphenols depletion. The catalyst fouling has been identified as the preferential coupling of the organic radicals and deposition over the catalyst with respect to their further degradation by hydroxyl radicals generated from H_2O_2 activation on the copper ions of the catalyst.

Najjar *et al*. (2007) presented the OMW oxidation results obtained with WHPCO using Fenton-like type catalysts (Cu-Silicalite-1 and Cu-pillared clay). Both catalysts showed a high conversion in the oxidation of poly-phenols and were able to drastically reduce the chemical oxygen demand, the biochemical oxygen demand and the non-biodegradability of the OMW.

Azabou *et al*. (2007) studied WHPPCO catalyzed by aluminium–iron pillared montmorillonite (Al-Fe)PILC, of a mixture of eight model phenolic compounds present in OMW. 86% and 70% of phenol abatement have been achieved after 24 h of the o-diphenolic compounds caffeic acid and hydroxytyrosol, respectively. Monophenolic compounds tyrosol, p-hydroxyphenylacetic acid and p-coumaric acid were identified as the most resistant towards the WHPCO. The apparent rate constant of the phenolic molecule decreased with increasing initial pollutant concentration of organic molecule when the other parameters remained unchanged. Since the treatment was not complete, the toxicity of model and real OMW was also investigated for further process integration against the bioluminescent bacteria Vibrio fisheri being significantly decreased by 74% and 68%, respectively after the WHPCO. The subsequent biological treatment using a methanogenic consortium removed the remaining phenolic compounds by more than 70% even with the most recalcitrant compounds.

Rivas *et al*. (2001) have carried out the oxidation of OMW after diluting it with synthetic urban wastewater (1:10). Experiments conducted using air as the oxygen source showed a positive effect of the previous neutralization of the wastewater if compared to the oxidation conducted at the original pH of the effluent (pH=5.3). The COD depletion and final biodegradability characteristics of the effluent as well as the use of free radical promoters (H_2O_2) resulted in a significant enhancement of the process in the presence of two commercially available catalysts that were platinum supported on alumina and copper oxide supported on active carbon.

II.5. Commercial WO processes

II.5.1. Non-catalytic Techology

Only a few industrial processes are being practiced widely. Kolaczkowski *et al.* (1999) and Luck (1996) have published excellent reviews of various catalytic and non-catalytic reactor types, and the following section gives a short overview/summary of the processes. The major industrial noncatalytic wet oxidation processes are summarized in Table II.6.

Table II.6. Major Industrial Noncatalytic Wet Oxidation Processes

Process	Setup	Mixing	Application	T (ºC)	P (MPa)	Retention time (min)
Zimpro	co-current bubble column	axial and longitudinal	preliminary detoxification/COD reduction	~150-325	2-12	20-240
Wetox	compartmentalized horizontal reactor	stirrer and oxygen addition	preliminary to biological treatment or for complete conversion	~200-250	4	30-60
Vertech	subsurface vertical reactor	turbulent flow in downcomer	general industrial wastewater	~180-280	8.5-11	60
Kenox	two concentric shells	static mixer and ultrasonic probe	preliminary to biological treatment	200-240	4.1-4.7	40
Oxyjet	jet mixer feeding to tubular reactor	jet mixer	pharmaceutical, chemical, and wood waste	140-300		<5

II.5.2. Catalytic Technology

Homogeneous Catalysis

Homogeneous catalysts in WO systems have been reported to significantly enhance the destruction of organics, with copper salts showing high reaction rates (Kolaczkowski *et al.*, 1999; Mishra *et al*., 1995). Reactors chosen for a homogeneous catalytic system (two-phase regime) are similar to non-catalyzed WO. The major issue of the homogeneous catalytic system, however, is the need to recover/remove the catalyst from the effluent after treatment. This necessitates an additional processing step and increased capital cost of the system.

Homogeneous catalysis has been used with co-oxidation (where an easily oxidized material promotes the rate of oxidation of a more refractory material), as well as with radical promoters working in combination with transition metals. Examples are hydrogen peroxide with Fe^{2+} as a catalyst. Hydrogen peroxide has been associated with the generation of free radicals that are able to catalyze the reaction, especially when used with iron or copper salts. Often two or more metal salts act in a synergistic mode (Kolaczkowski *et al.*, 1999; Luck, 1996). Table II.7 summarizes the homogeneous CWO processes.

Table II.7. Homogeneous Catalytic Wet Oxidation Processes

Process	Reactor type	Application	T (°C)	P (MPa)	Catalyst/Oxidant
LOPROX	multistage bubble column	low reactive waste	<200	0.5-2	Fe^{2+}-acid/oxygen
Ciba-Geigy		chemical/pharma waste	~300		Cu^{2+}/air
ATHOS	completely stirred recirculation reactor	residual sludges	235-250	4.4-5.5	Cu^{2+}/oxygen
WPO		aquifer decontamination	90-130	0.1-0.5	Fe-Cu-Mn/H_2O_2
ORCAN		refractory waste pretreatment	120	0.3	Fe^{2+}/air + H_2O_2

Heterogeneous Catalysis

The major advantage of a heterogeneous over a homogeneous catalytic system is the ease of catalyst retrieval from the reaction media. However, the stability and durability of the catalyst under CWO operating conditions is severely tested. Catalyst deactivation occurs by sintering, poisoning of the active sites, or fouling of the catalyst surface by intermediate reaction products. Also, in hot acidic environments, the active component may be dissolved into the liquid phase. In fixed-bed catalytic reactors, the pressure drops across the reactor, because the catalyst is deactivated easily by fouling and plugging, interparticle and intraparticle mass transport limitations must be minimized (Kolaczkowski *et al.*, 1999). The pressure drop across the fixed-bed reactor is mainly determined by catalyst particle size. Increasing the diameter of catalyst particles reduces the pressure drop; however, in larger pellets, reaction rates become diffusion-limited. Sadana and Katzer (1974) have reported that reaction rates were lower with large catalyst particles ($dp>0.4$ mm) than with catalysts of smaller ($dp<0.06$ mm) pellet sizes, and they attributed this phenomenon to oxygen intraparticle diffusion limitations in the larger pellets.

In addition, as interfacial contact area between catalyst and solution is reduced with larger pellet size, a considerable proportion of the catalyst may not be utilized effectively (Kolaczkowski *et al.*, 1999). Suspended solid materials in the waste stream cause clogging of the reactor bed, eventually resulting in a large pressure drop. This can be prevented by the use of a two-stage reactor (Harada, 1999; Harada *et al*., 1987), where, in the first stage (noncatalytic), the solid matter is dissolved and then the waste is transferred to the second (catalytic) stage for oxidation. A monolith catalyst structure may be used as an alternative to a fixed bed. The monolith is comprised of several parallel channels, oriented in the direction of fluid flow. The catalyst is fixed onto the walls of these channels, so that intimate contact is established as the waste flows through the channels. The channel size, cell density, and wall thickness are fabricated to a designed cross-sectional area (Kolaczkowski *et al.*, 1999). Provided that this area is larger than the particulate size in the waste, there is little impediment to the flow of solution through the channel, minimizing pressure losses and plugging of the catalyst (Kolaczkowski *et al.*, 1999; Ishii *et al*., 1997). The shape of the channel cross-section can also be varied, with circular, rectangular, hexagonal, and sinusoidal forms being available. In addition, when operated in the slug flow regime (with gas and liquid plugs sandwiching each other), a recirculation pattern within each liquid plug is created, further improving mass transfer. This regime ensures formation of a thick liquid film between the channel wall and the gas, which promotes high mass-transfer rates and keeps the catalyst continuously wetted (Luck, 1999).

Heterogeneous catalytic processes include the Nippon Shokubai process and the Osaka Gas process. In the Nippon Shokubai process, heterogeneous catalysts are available in the form of pellets and honeycombs. Commonly, a gas-liquid vertical monolith reactor with a Pt-Pd/TiO_2/ZrO_2 supported catalyst is used (Kolaczkowski *et al*., 1999; Luck, 1996). Nippon Shokubai also developed a two-part catalyst: a component is comprised of iron oxide, combined with an oxide from at least one element from the group of titanium, silicon, and zirconium, whereas the other component is comprised of one or more elements from the group of cobalt, nickel, cerium, silver, gold, platinum, rhodium, ruthenium, and iridium. Compared to non-catalyzed wet oxidation processes, this process is able to oxidize the refractory materials, acetic acid, and ammonia and, thus, allows the treated wastewater to be discharged or reused as industrial water without further treatment. The company's patents cover a heterogeneous catalyst that is used for the conversion of organics and inorganics in wastewater to nitrogen, carbon dioxide, and water (Kolaczkowski *et al*., 1999). Titania or zirconia catalyst supports provide increased catalyst strength, when compared to alumina supports, but limit catalyst activity and durability. Catalysts from the lanthanide series have good catalytic activity but are not easily fabricated and, with time, decline unacceptably in strength. In the patented catalyst, a combination of titanium dioxide with oxides of the lanthanide series are used, resulting in a moldable, physically stable catalyst that shows only a slight loss in strength and catalytic activity with time (Kolaczkowski *et al*., 1999). The segmented gas-liquid flow in this process is highly beneficial. Each liquid plug is sandwiched between two gas plugs, which results in a recirculation pattern within each liquid plug that improves mass transfer dramatically and prevents the deposition of solids. In addition, mass-transfer rates are significantly enhanced by the thin liquid film that forms between the gas and the channel wall, which also acts to keep the catalyst continuously wetted (Luck, 1996). An operating temperature range of 160-270 °C, a pressure of 0.9-8 MPa, and a residence time of 1 h are typically used for the Nippon Shokubai process. Under these conditions, >99% conversion of pollutants such as phenol, formaldehyde, acetic acid, and glucose is achieved. Without a catalyst, the removal efficiencies would be 5%-50%. The catalyst is capable of treating organic wastes, including compounds that contain nitrogen, sulfur, or halogens, with lasting catalytic activity. Also, any nitrogen in the compound is decomposed to nitrogen gas. The use of this catalyst for the treatment of sulfur and halogen-containing organics is best performed under basic conditions, because acidic conditions shorten the life of the equipment that is used (Kolaczkowski *et al*., 1999).

The Osaka Gas process is similar to the non-catalytic Zimpro process, except for the use of an Fe-Co-Ni-Ru-Pd-Pt-Cu-Au-W catalyst supported on TiO_2 and ZrO_2 either as spherical particles or as honeycomb structures (Kolaczkowski *et al*., 1999; Luck, 1996). The process is used for the treatment of coal gasifier effluents, wastewater from coke ovens, concentrated cyanide wastewater

from the nitridation of steel, and sewage sludge and residential wastes. The operating conditions are tailored according to the type of waste and the required destruction efficiency. The catalyst exhibits optimal activity for long periods of time; e.g., in the treatment in the coke oven, wastewater at 250 °C and 6.9 MPa for more than 11 000 h showed no change in catalytic activity. A residence time of just 24 min allowed the waste COD to be reduced from 5870 mg/L to 10 mg/L. In the destruction of various nitrogen-containing compounds such as ammonia, ammonium salts, and nitrates, virtually complete conversion of the nitrogen content to nitrogen gas has been obtained (Kolaczkowski *et al*., 1999; Ishii *et al*., 1997, Harada *et al*., 1992ab).

II.6. Multiphase Reactors for CWO

The effectiveness and economical viability of the CWO processes to be applied to industrial problems is highly influenced by the choice of the reactor concept and its detailed design. This poses significant challenges to the chemical reactor engineering area. Iliuta and Larachi (2001) and Eftaxias *et al.* (2003) have identified the following inventory: (i) the multiphase nature of CWO reactions (two-phase for homogeneous reactions and three-phase for heterogeneous reactions), (ii) the temperatures and pressures of the reaction, and (iii) the radical reaction mechanism. In multiphase reactors, complex relationships between parameters such as chemical kinetics, thermodynamics, interphase, intraphase, intraparticle mass transport, flow patterns and hydrodynamics influence reactants mass transfer. Complex models have been developed to assess the influence of catalyst wetting, the interface mass transfer coefficients, the intraparticle effective diffusion coefficient, and the axial dispersion coefficient on CWO. Thus, multiphase reactions are greatly influenced by diffusion kinetics as the various interfaces in multiphase systems act as resistances, generally lowering the reaction rates.

Generally, three mechanistic steps are considered for a three-phase reaction: *(i)* mass transfer of the gaseous species to the gas/liquid interface, followed by *(ii)* mass transfer of the gaseous species from the gas/liquid interface to the bulk liquid, *(iii)* mass transfer of gaseous and liquid species to the catalyst surface, *(iv)* intraparticle diffusion of the reactant species to catalyst-active sites, *(v)* adsorption of species on active sites and surface reaction, and *(vi)* desorption and diffusion into the liquid phase. The homogeneous-heterogeneous radical reaction scheme, with its interplay of initiation, propagation, and termination reactions, can add further complexity. Common two-phase reactor types used in WO and homogeneous CWO include bubble columns, jet-agitated reactors, and mechanically stirred reactor vessels, and three-phase reactors used for heterogeneous CWO include trickle bed, bubble slurry column, and bubble fixed bed (monolith) or three-phase

fluidized bed reactors. The advantages and limitations of three-phase reactors as potential applications used in CWO are listed in Table II.8.

Table II.8. Multiphase Reactors Used in CWO

Reactor type	Advantages	Limitations
trickle bed reactor	high conversion as both gas and liquid flow regimes approach plug flow low liquid hold-up high catalyst loading low-pressure drop	poor liquid-phase distribution often only partial wetting of the catalyst high intraparticle resistance poor radial mixing low mass transfer coefficient temperature control can be difficult
slurry phase and three-phase fluidized bed reactor	high external mass transfer (G-L, L-S) low intraparticle resistance ease of catalyst addition and regeneration ease of thermal management	catalyst separation high axial mixing low catalyst load high liquid-to-solid ratio
bubble fixed-bed reactor	high G-L mass transfer (better G-L interaction) high liquid holdup well-wetted catalyst channeling eliminated good temperature control	high axial backmixing lower conversion compared to trickle-bed reactors high-pressure drop flooding problems

II.7. Synopsis of the Literature in Trickle-bed Reactors

Trickle-bed reactors (TBR) and bubble columns reactors (BCR) are the multiphase reactors most often used in the chemical industry. In contrast with BCR reactors, TBRs are generally fixed bed catalytic reactors in which gas and liquid flow in cocurrent downward mode. The traditional application of TBRs lies in the petroleum refining industry, more specifically in hydroprocessing. Recently, TBRs were envisaged as a new application technology for the pollutant removal in moderate contaminated wastewaters. The effective removal of reaction heat, as well as the intensive mass transfer, from gas to liquid and liquid to solid, is carried out by recycling gas compressed through the catalyst bed in a quantity that significantly exceeds its demand for the reaction purpose. Fixed-bed reactors have disadvantages coming from the comparatively big catalyst particles in comparison with slurry reactors. To enumerate a few number, the higher reaction pressure dictated by the low grade of catalyst utilisation because of intraparticle diffusion and low efficiency of gas-liquid-solid mass transfer; the complexity of temperature control in exothermic reactions and problems with so-called hot-spots that can lead to the uncontrolled reactor heating up, sometimes to the reactor destruction; and the necessity of liquid and gas distributors inside the reactor and complex equipment in the case of gas recycling are well reported in the literature.

In recent years, many works devoted to the numerous aspects of behaviour in fixed-bed reactors, such as hydrodynamics, chemical kinetics, mass and heat transfer have been published. Table II.9 lists by chronological order the papers on trickle-bed reactors which review various aspects of TBRs and summarizes the progress in a specific application area related to TBR performance.

However, only in the last decades particular attention has been given to the behaviour of pressurized TBRs (Saroha and Nigam, 1996; Martinez *et al.*, 1994; Larachi *et al*., 1993; Gianetto and Specchia, 1992) whereas all the others dealt with TBR research at atmospheric conditions. Recently, Boyer *et al.* (2007) established a large experimental database at "Institut Francais du Petrole" to measure simultaneously pressure drop and liquid holdup in packed bed reactor operated in trickle flow regime for a large range of operating conditions. The varying parameters are liquid viscosity and density, gas density, bed particle shape and size. This database has been first used to compare the prediction accuracy of the different models from the literature and the mechanistic model proposed by Attou *et al.* (1999) has been upgraded. This model has been validated over the whole data range and the accuracy has been checked with data external to the database. Experimental observations and modelling of high-pressure trickle-bed reactors was reviewed by Al-Dahhan *et al.* (1997) and Saroha and Nigam (1996) covering the following topics: flow regime transitions, pressure drop, liquid holdup, gas-liquid interfacial area and mass-transfer coefficient, catalyst wetting efficiency, catalyst dilution with inert fines, and evaluation of trickle-bed models for liquid-limited and gas-limited reactions. Saroha and Khera (2006) presented a hydrodynamic study of fixed beds with cocurrent upflow and downflow considering the effects of high-pressure operation, which is of industrial relevance, on the physicochemical and fluid dynamic parameters. Lange *et al.* (2004) described the experimental and mathematical formulation of TBRs under unsteady-operation, whereas Khadilkar *et al.* (1999) reviewed empirical and theoretical models developed to account for the effect of high pressure on the various parameters and transport phenomena for TBRs.

The current status in trickle-bed reactors with respect to hydrodynamics and its effect on process intensification has been also reviewed by Nigam and Larachi (2005). An integrated approach including catalyst selection, reactor design and process configuration have been recently presented from a process intensification point-of-view. It encompasses the investigation of different hydrodynamic, mass transfer and heat transfer parameters on the TBR performance. Catalyst wettability has been explained based on contact angle of the liquid on the surface of porous particle as alternating patches of saturated pore and solid surface (Baussaron *et al.*, 2007). The hysteresis behavior of hydrodynamics using this concept has also been explained. Recent studies have demonstrated reactor performance improvement over the optimal steady state under forced time-varying liquid flow rates. In this mode of operation, the bed is periodically flushed with liquid, while the gas phase is fed continuously.

Table II.9. Articles on TBRs that contain reviews of some aspects of trickle-bed operation

Authors	Year	Title
Aydin *et al.*	2008	Influence of temperature on fast-mode cyclic operation hydrodynamics in trickle-bed reactors
Baussaron *et al.*	2007	Effect of partial wetting on liquid/solid mass transfer in trickle bed reactors
Boyer *et al.*	2007	Hydrodynamics of trickle bed reactors at high pressure: Two-phase flow model for pressure drop and liquid holdup, formulation and experimental validation
Saroha and Khera	2006	Hydrodynamic study of fixed beds with cocurrent upflow and downflow
Nigam and Larachi	2005	Process intensification in trickle-bed reactors
Herk *et al.*	2005	Scaling down trickle bed reactors
Lange *et al.*	2004	Unsteady-state operation of trickle-bed reactors
Silveston and Hudgins	2004	Periodic temperature forcing of catalytic reactions
Dudukovic *et al.*	1999	Multiphase reactors – revisited
Khadilkar *et al.*	1999	Trickle-bed reactor models for systems with a volatile liquid phase
Al-Dahhan *et al.*	1997	High-Pressure Trickle-Bed Reactors: A Review
Saroha and Nigam	1996	Trickle-Bed Reactors
Martinez *et al.*	1994	Three-Phase Fixed Bed Catalytic Reactors: Application to Hydrotreatment Processes
Gianetto and Specchia	1992	Trickle-Bed Reactors: State of Art and Perspectives
Wild *et al.*	1992	Heat and Mass Transfer in Gas-Liquid-Solid Fixed Bed Reactors
Levec and Lakota	1992	Liquid-Solid Mass Transfer in Packed Beds with Cocurrent Downward Two-Phase Flow
Zhukova *et al.*	1990	Modeling and Design of Industrial Reactors with a Stationary Bed of Catalyst and Two-Phase Gas-Liquid Flows A Review
Lemcoff *et al.*	1988	Effectiveness Factor of Partially Wetted Catalyst Particles: Evaluation and Application to the Modeling of Trickle Bed Reactors
Ng and Chu	1987	Trickle-Bed Reactors
Ramachandran *et al.*	1987	Recent Advances in the Analysis and Design of Trickle-Bed Reactors
Gianetto and Berruti	1986	Modelling of Trickle-Bed Reactors
Charpentier	1986	Mass Transfer in Fixed Bed Reactors
Dudukovic and Mills	1986	Contacting and Hydrodynamics in Trickle-Bed Reactors
Hanika and Stanek	1986	Operation and Design of Trickle-Bed Reactors
Rao and Drinkenburg	1985	Solid-Liquid Mass Transfer in Packed Beds with Cocurrent Gas-Liquid Downflow
Gupta	1985	Handbook of Fluids in Motion
Mills and Dudukovic	1984	A Comparison of Current Models for Isothermal Trickle-Bed Reactors. Application of a Model Reaction System
Tarhan	1983	Catalytic Reactor Design
Hofmann	1983	Fluid Dynamics, Mass Transfer and Chemical Reaction in Multiphase Catalytic Fixed Bed Reactors
Germain	1983	Industrial Applications of Three-Phase Catalytic Fixed Bed Reactors
Crine and L'Homme	1983	Recent Trends in the Modelling of Catalytic Trickle-Bed Reactors
Ramachandran and Chaudhari	1983	Three-Phase Catalytic Reactors
Herskowitz and Smith	1983	Trickle-Bed Reactors: A Review
Tan and Smith	1982	A Dynamic Method for Liquid-Particle Mass Transfer in Trickle Beds
Morsi *et al.*	1982	Hydrodynamics and Interfacial Areas in Downward Cocurrent Gas-Liquid Flow through Fixed Beds. Influence of the Nature of the Liquid
Charpentier	1982	What's New in Absorption with Chemical Reaction
Morsi *et al.*	1981	Hydrodynamics and Gas-Liquid-Solid Interfacial Parameters of Cocurrent Downward Two-Phase Flow in Trickle-Bed Reactors
Turek and Lange	1981	Mass Transfer in Trickle-Bed Reactors at Low Reynolds Number
Koros	1981	Scale-up Considerations for Mixed Phase Catalytic Reactors
Baldi	1981a	Design and Scale-up of Trickle-Bed Reactors. Solid-Liquid Contacting Effectiveness
Baldi	1981b	Heat Transfer in Gas-Liquid-Solid Reactors
Baldi	1981c	Hydrodynamics of Multiphase Reactors
Van Landeghem	1980	Multiphase Reactors: Mass Transfer and Modeling
Shah	1979	Gas-Liquid-Solid Reactor Design
Charpentier	1979	Hydrodynamics of Two-Phase Flow Through Porous Media
Dirkx	1979a,b	De Trickle-Bed Reactor
Dudukovic and Mills	1978	Catalyst Effectiveness Factors in Trickle-Bed Reactors
Charpentier	1978	Gas-Liquid Reactors
Specchia *et al.*	1978	Solid-Liquid Mass Transfer in Cocurrent Two-Phase Flow through Packed Beds
Satterfield *et al.*	1978	Liquid-Solid Mass Transfer in Packed Bed with Downward Cocurrent Gas-Liquid Flow
Gianetto *et al.*	1978	Hydrodynamics and Solid-Liquid Contacting Effectiveness in Trickle-Bed Reactors
Dudukovic	1977	Catalyst Effectiveness Factor and Contacting Efficiency in Trickle-Bed Reactors
Goto *et al.*	1977	Trickle-Bed Oxidation Reactors
Charpentier	1976	Recent Progress in Two-Phase Gas-Liquid Mass Transfer in Packed Beds
Satterfield	1975	Trickle-Bed Reactors
Østergaard	1968	Gas-Liquid-Particle Operations in Chemical Reaction Engineering

Section II.7.1 discusses the relevant findings on the fluid dynamics of TBRs systematized by two major hydrodynamic parameters (pressure drop, liquid holdup as well as interphase parameters and catalyst wetting) and section II.7.2 presents a comparison of theoretical models for the prediction of hydrodynamics in TBRs.

II.7.1. Fluid Dynamics of TBRs

Trickle beds are operated in a multiplicity of cocurrent downflow regimes ranging from spray flow (liquid drops and continuous gas flow), trickle flow (continuous gas phase and one directional liquid rivulets and some discontinuous liquid films), pulse flow (intermittent passage of gas rich and liquid rich zones through the reactor), and downward bubble flow (continuous liquid and dispersed gas flow). Similarly, cocurrent upflow packed bubble columns can experience the so-called homogeneous and heterogeneous bubble flow, while the onset of flooding is of great importance in countercurrent flow operation.

The evaluation of available models and empirical correlations for prediction of the trickle to pulse flow transition boundary, which is of importance to numerous refining operations, was performed by Wild *et al.* (1991), Larachi *et al.* (1993) for high pressure operations, and by Burghardt and Bartelmus (1996) for organic systems. All of these studies reach the same conclusion that the use of available phenomenological and semi-theoretical models for prediction of flow transition leads to unacceptable errors at the time of proper scale-up.

Al-Dahhan *et al.* (1997) proposed general conclusions regarding the TBR flow regimes. The trickle-to-pulsing transition boundary, two-phase flow pressure drop and the liquid holdup can be experimentally replicated by different gases that differ in molecular weight when the pressures are set so as to achieve the same gas densities at the same gas and liquid superficial velocities. The trickle-to-pulse flow transition at a given liquid (or gas) superficial velocity shifts towards higher gas or liquid superficial velocities at higher-gas density, making the velocity range for trickle flow operation broader at elevated pressure. Moreover, at any pressure level, the transition from trickling to pulsing regime occurs at smaller fluid throughputs for viscous liquids than for less viscous liquids. The gas superficial velocity corresponding to the transition between foaming and foaming–pulsing decreases as pressure increases, whereas, regardless of pressure, the inception of the foaming-pulsing flow is delayed as the liquid throughput increases. In order to widen trickle flow region by delaying the inception of pulse flow to higher liquid flow rates for a given gas flow rate, a hydrophobic packing is preferred (Horowitz *et al.*, 1997). Conversely, the trickle-to-pulse flow changeover occurs earlier with non-Newtonian liquids compared with Newtonian liquids (Iliuta and Thyrion, 1997).

Pressure drop and Liquid holdup

Recent correlations and semi-theoretical models for prediction of two-phase pressure drop and liquid holdup at high-pressure operation have been summarized by Al-Dahhan *et al.* (1997). No correlation emerges as clearly superior to others, but those based on semi-theoretical and phenomenological models seem more reliable than strictly empirical correlations. In trickle flow regime, the slit (Holub *et al.*, 1993; Holub *et al.*, 1992), extended slit (Iliuta *et al.*, 1998) and double slit (Iliuta and Larachi, 1999) models, and the 1-D CFD model of Attou *et al.* (1999) are recommended for use to predict liquid holdup.

Generally, the following assertions can be inferred regarding the two major and integral hydrodynamic parameters. The two-phase pressure drop increases with gas and liquid mass fluxes, superficial velocities and liquid viscosity at a given density whereas liquid holdup increases with liquid mass flux and superficial velocity and liquid viscosity, but decreases with increasingly gas mass flux or superficial velocity. Nigam and Larachi (2005) and Saroha and Indraneel (2008) have reported that hydrodynamic hysteresis may occur at high pressure when the liquid is contaminated with impurities. Liquid holdup and two-phase pressure drop increase in beds where fines are mixed with the larger size catalyst particles. The impact of fines on the change in holdup and pressure drop strongly depends on the packing procedure that is used. At a given superficial velocity and as gas density is increased, the pressure drop increases while the liquid holdup decreases (Al-Dahhan *et al.*, 1997).

The interstitial nature of liquid flow in trickle beds has become available due to the increased use of non-invasive sophisticated measurement techniques such as capacitance tomography imaging to capture the transient pattern of liquid flow in a trickle bed (Schubert *et al*., 2008; Sederman and Gladden, 2005; Sederman and Gladden, 2001; Reinecke and Mewes, 1996; Reinecke and Mewes, 1997) and X-ray transmission tomography to capture two-phase flow distribution in trickle beds (Toye *et al.*, 1994). Non-invasive measurement techniques that can be utilized in multiphase flows have recently been summarized both in an extensive review article (Boyer *et al*., 2002; Dyakowski *et al*., 2000; Chaouki *et al.*, 1997).

Gas-Liquid Interfacial Areas and Interphase Mass Transfer Coefficients

Several correlations and models for predicting gas-liquid interfacial areas and volumetric gas-liquid and liquid-solid mass transfer coefficients in TBRs are summarized by Al-Dahhan *et al*. (1997) and Larachi *et al*. (1993). Among all these correlations, while there are plenty of correlations for the estimation of cold-flow low-pressure liquid-solid mass transfer coefficients, none are available for high pressure operation. Since elevated pressure operation has a profound

effect on both wetting efficiency and liquid holdup (Al-Dahhan and Dudukovic, 1995), it would be highly advisable to determine liquid-solid mass transfer coefficients at higher pressures. Mass transfer studies on catalytic structured packings are also scarce in the literature (van Baten and Krishna, 2002). The vast majority of gas-liquid mass transfer parameters in TBRs are derived using the so-called chemical methods. Two rules of thumb can be inferred about liquid-side volumetric mass transfer coefficients at elevated pressure: gas-liquid interfacial areas and volumetric liquid side mass transfer coefficients increase as liquid and gas mass fluxes or superficial velocities increase at a given gas density, and both mass transfer parameters improve in TBRs as the gas density increases for given gas and liquid superficial velocities.

Catalyst Wetting

Trickle flow regime has been found as a particular hydrodynamic state to promote partial wetting efficiencies, hence causing incomplete catalyst utilization, but enabling higher reaction residence times. One of the reasons advanced in the literature for poor catalyst wetting is due to reactor-scale liquid maldistribution that may leave certain portions of the bed poorly irrigated. Proper design of liquid distributors, operation with packing that gives the needed minimal pressure drop, and redistribution of the liquid in quench boxes and other devices can address this problem. Another cause of incomplete catalyst utilization is the particle-scale incomplete external wetting occurring at sufficiently low liquid mass velocity when the available liquid flow is insufficient to cover all the catalyst particles with a continuous liquid film. Several correlations and models developed for liquid-solid contacting efficiency, which is defined as the fraction of the external catalyst area covered by the flowing liquid film, have been reviewed by Al-Dahhan *et al.* (1997). The contacting efficiency has been found to improve noticeably with an increase in total pressure at a fixed liquid mass flux and at high gas velocities. Higher pressure drop and liquid mass velocity also lead to an increased contacting efficiency. Hence, both liquid and gas velocity increase the contacting efficiency at high pressures, which is the region where most reactors operate.

In order to address this fact, large-scale computational fluid dynamics (CFD) simulations can be helpful in establishing both the effect of the bed voidage variation and the presence of internals on gross liquid distribution. This approach is based on fundamental physical conservation laws and due to improved computational power, it is possible nowadays to solve the resulting complex flow models. In this field, there is also a parallel approach pursued by a limited number of authors to utilize the advances in computers and neural networks to train a neural net model based on a huge set of available data. In fact, over 28,000 data for the fluid dynamic parameters discussed above have been retrieved from the literature and used to make predictions based on such a model. Tarca *et al*. (2004), Larachi *et al.* (1998) and Bensetiti *et al.* (1997) illustrate the possibilities of this

approach. The weakness of neural network approach is that it is not mechanistically based to allow trustful extrapolations. Physical models, however, require in general more efforts to improve their capabilities. Another promising approach lies in the use of a hybrid methodology where neural networks can be combined to physical models. Such hybrid models combine the robustness advantage of physical models with the neural networks higher accuracy (Iliuta *et al.*, 1998).

II.7.2. Hydrodynamic Models for TBRs

Numerous theoretical attempts are being made to model the hydrodynamics of trickle-bed reactors. It ranges from merely empirical correlations (Ellman *et al.*, 1990; Larachi *et al.*, 1991; Iliuta and Larachi, 1999) to physically sound models (Nemec *et al*., 2005; Iliuta *et al*., 2000; Carbonell, 2000; Attou et al., 1999; Al-Dahhan *et al*., 1998; Holub *et al*., 1993; Sàez and Carbonell, 1985). No consensus has emerged as to whether general approaches yielding pressure drop and liquid holdup with acceptable accuracy can be recommended and this fact has been attributed to the complexity of the gas-liquid flow patterns prevailing in trickle beds, the lack of accurate descriptions of two phase flow interactions, the complex relationship between trickle bed hydrodynamic characteristics, fluids and bed properties and interfacial interactions, the restricted range of the experimental data, and the models/correlations derived thereof, usually reported for individual studies or system specific configurations.

Among the theoretical approaches that have been used for the prediction of hydrodynamics in TBRs, one can enumerate them as follows: the relative permeability model (Sàez and Carbonell, 1985), (ii) slit model (Holub et al., 1992, 1993; Al-Dahhan and Dudukovic, 1994; Al-Dahhan *et al*., 1998; Iliuta *et al*., 1999b), (iii) model based on fundamental force balance (Tung and Dhir, 1988; Narashiman *et al*., 2002), (iv) 1D-CFD model (Attou *et al*., 1999; Souadnia and Latifi, 2001) (v) F-function concept (Fourar *et al*., 2001), and (vi) CFD model (Jiang *et al*., 2002; Gunjal *et al*., 2003). Table II.10 summarizes the essential features of these theoretical models for the predictions of hydrodynamic parameters in trickle beds that have been developed along the years.

The relative permeability model is based on Ergun's equation and the relative permeability of each phase has been correlated as a function of liquid saturation of each phase depending on the experimental results. In this approach the gas-liquid interaction term has been neglected, hence, Holub *et al.* (1992) developed the slit model in which the complex geometry of the actual void space in the catalyst bed at the pore level has been represented by the multiphase flow inside a rectangular slit. It is also a modified form of Ergun's equation and, initially it was considered zero shear stress at the gas-liquid interface. Later Al-Dahhan *et al.* (1998) expressed the gas and liquid phase slip parameters as a function of gas and liquid phase Reynolds numbers. Guo and Al-

Dahhan (2005) presented a computational framework that accounts for the observed catalyst activities, combined with local transport and catalyst wetting effects. The authors claimed that a good agreement on the comparisons of simulated model predictions and lab scale experimental data demonstrated the importance of including the phase change effect in the reactor scale flow distribution. Recently, Atta *et al.* (2007) developed a CFD model based on porous media concept to model the hydrodynamics of two-phase flow in TBRs under cold-flow conditions. The two-phase Eulerian model describes the flow domain as a porous region to simulate the macroscale multiphase flow in trickle beds operating under trickle flow regime. The closure terms for phase interactions have been addressed by adopting the relative permeability concept (Saez and Carbonell, 1985). The discrete cell model has been used to simulate the steady-state behavior of packed-bed reactors for the catalytic wet oxidation of phenol with one-dimensional (1D) axial dispersion model for the liquid phase coupled with a cell stack model for the gas phase, providing considerable phase change under the selected operating conditions. Other CFD mathematical approaches will be reviewed in section II.8.

II.8. CFD simulation approaches for multiphase reactors

The precise knowledge of fluid dynamic and transport parameters is necessary for the development of appropriate models and scale-up rules given that is far from being complete due to the inherent complexity of multiphase flow processes. Therefore, a deep understanding and the development of predictive tools to simulate multiphase flow processes for better and economically viable reactor technologies is of paramount importance. In the past, knowledge of hydrodynamics and transport characteristics of multiphase reactors has been interpreted in the form of empirical correlations, which have numerous restrictions in terms of their validity for different operating conditions. CFD simulations, on the other hand, deal with the solution of fluid dynamic equations on digital computers, requiring conservation laws or fundamental principles and thus giving a complete description of the hydrodynamics of these reactors. This detailed predicted flow field gives an accurate insight to the fluid behaviour and can sometimes give information, which cannot be obtained from experiments.

Table II.10. Comparison of theoretical models for the prediction of hydrodynamics in TBR

Reference	Model	Characteristics of the model
Atta *et al.*, 2007	Euler – relative permeability model	1. CFD model based on porous media concept is presented to model the hydrodynamics of two-phase flow in trickle-bed reactors under cold-flow conditions. 2. The closure terms for phase interactions have been addressed by adopting the relative permeability concept.
Guo and Al-Dahhan, 2005	Discrete Cell model	1. Modeling of trickle-bed reactors under steady-state with exothermic reactions 2. Development of Cell network approach with multiphase mass transfer-reaction model and novel solution method.
Souadnia *et al.*, 2005	Statistical method for multimaterial non-equilibrium flow	1. The general multimaterial formulation of Kashiwa and Rauenzahn, (1994) is used to derive an hydrodynamic model for a trickle-bed reactor operating under trickling flow conditions with two equations: liquid volume fraction and pressure. 2. The equations exhibit elliptic (pressure) and hyperbolic (volume fraction) behaviours, which require the use of different numerical methods in order to correctly handle these different numerical behaviours.
Ortiz-Arroyo and Larachi, 2005	Lagrange-Euler-Euler	1. A Lagrange–Euler–Euler computational fluid dynamic approach was developed to represent the evolution of two-phase pressure gradients in trickle-bed reactors undergoing deposition of colloidal/non-colloidal fines under deep-bed filtration conditions. 2. The deep-bed filtration process was simulated in unsteady-state multidimensional code and the increase of pressure drop during plugging was explained by increasing local specific surface area and decreasing local porosity due to fines deposition.
Gunjal *et al.*, 2005	VOF	1. Computational study of liquid drop over flat and spherical surfaces based on the volume of fluid (VOF) method with inclusion of surface tension and wall adhesion phenomenon. 2. Drop spread and recoiling velocities were reconstructed from the experimental data in which micro-scale motion of liquid droplet was captured with a high-speed CCD camera.
van Baten and Krishna, 2002	2D-CFD model	1. Comparison of the radial and axial, liquid-phase dispersion dispersion characteristics of KATAPAK-S with a conventional packed bed. 2. The values of axial dispersion coefficient from CFD simulations are considerably lower than those measured experimentally whereas radial dispersion coefficient is in good agreement
Jiang *et al.*, 2002; Gunjal *et al.*, 2003	*k*-fluid model	1. The Eulerian CFD model, the flow equations are solved for the k^{th} fluid. 2. The drag exchange coefficients are obtained from the Holub model.
Fourar *et al.*, 2001	*F*-function concept	1. This model is based on Forchheimer's equation originally employed to explain the inertia deviations in Darcy's law for single phase flow. 2. Phasic F-function is multiplied with superficial velocity of each fluid.
Souadnia and Latifi, 2001; Propp *et al.*, 2000	1D-CFD model	1. Based on Eulerian approach consisting of volume averaged flow equations. 2. Drag force is evaluated using concept of relative permeability of each phase as proposed by Sàez and Carbonell (1985).
Attou *et al.*, 1999	1D-CFD model	1. These models are based on macroscopic mass and momentum conservation laws. 2. The liquid–solid and gas-solid interaction forces are formulated on the basis of Kozeny–Carman equation. 3. Model does not predict well at low *D/dp* ratio (<12–14) due to column wall effect. 4. The gas–liquid interfacial drag has been considered.
Mewes *et al.*, 1999	Packing is subdivided into elementary cells	1. Work review on models for two-phase flow in trickle-bed and monolithic reactors. 2. Flow regimes were solved based on entire porous media and the flow is evaluated concerning mass transfer performance as well as the velocity fields and phase distributions of vapor and liquid in packings and monoliths.
Tung and Dhir, 1988; Narasimhan *et al.*, 2002; Kundu *et al.*, 2003c	Model based on fundamental force	1. It involves force balance equations in liquid and gas phase in elemental reactor volume 2. The gas–liquid interfacial drag has been taken into account balance. 3. The tortuosity effect corrects the gravity term in the liquid phase and gas phase force balance equations.
Holub *et al.*, 1992, 1993; Al-Dahhan and Dudukovic, 1994; Al-Dahhan *et al.*, 1998; Iliuta *et al.*, 1999b	The slit model	1. The complex geometry of the actual void space in the catalyst bed at the pore level has been represented by the much simpler flow inside a rectangular slit. 2. It is modified form of Ergun equation. 3. Initially it is considered zero shear stress at the gas-liquid interface. Later Al-Dahhan *et al.* (1998) expressed the gas and liquid phase slip parameters as a function of gas and liquid phase Reynolds numbers.
Sàez and Carbonell, 1985	The relative permeability model	1. The model is based on Ergun's equation. 2. The relative permeability of each phase has been correlated as a function of liquid saturation of each phase depending on the experimental results. 3. The gas–liquid interaction term has been neglected.

Nowadays due to cheaper computational resources, CFD simulations are becoming economically reliable for modelling of multiphase processes. CFD simulation deals with the numerical solution of these equations in a flow geometry of interest using digital computers and is becoming a well-accepted and useful tool for hydrodynamic modeling of multiphase reactors. In recent years, CFD simulation for multiphase reactors has received much attention due to improved understanding of the flow phenomenon, rapid advances in available softwares (e.g., FLUENT, CFDLIB, CFX, PHOENICS, FLOW3D, and FIDAP) and availability of cheaper computational resources which is making it economically reliable for hydrodynamics studies of multiphase reactors. While it is now a standard tool for simulating single-phase flows, it is still at the development stage for multiphase systems, such as fixed and fluidized beds and three-phase bubble column slurry reactors, which has applications in "gas-to-liquid" processes, such as Fischer-Tropsch process for the production of synthesis gas. To make CFD suitable for modelling and scale-up of these complex multiphase reactors, experimental verification of multiphase flows, at least via cold flow models, is still needed (Dudukovic *et al*., 1999). Table II.11 summarizes the literature works on the CFD simulation of trickle-bed reactors.

Gunjal *et al.* (2005) developed a CFD model to predict two-phase pressure drop and liquid holdup and was evaluated by comparing numerical predictions with the experimental data. The CFD model was then extended to predict the fraction of liquid holdup suspended in the form of drops in the bed. Periodic operation was also investigated at atmospheric conditions. Jiang *et al*. (2002) presented an Eulerian *k*-fluid CFD model to simulate the macroscale multiphase flow in packed beds. The geometric complexity of the bed structure was resolved statistically by describing the porosity distribution. The multiphase interactions were computed using the Ergun type of formula developed based on bench-scale hydrodynamic experiments. The drag exchange coefficients were obtained from the model of Holub *et al*. (1992) for the particle-fluid interfaces and from the model of Attou *et al.* (1999) for the gas-liquid interface. The effect of particle external wetting on flow distribution was incorporated into the model through the capillary pressure evaluated by Attou and Ferschneider (1999). Both steady-state and unsteady-state (e.g., periodic operation) feed conditions were studied numerically and predictions of the *k*-fluid CFD model were compared with the experimental data in the literature for liquid upflow in a cylindrical packed bed. Attou and Ferschneider (1999) developed a physical model to predict the hydrodynamic parameters of steady-state cocurrent gas-liquid flow through trickle-bed reactors operating in the trickle flow regime. The trickle flow is described by an annular pattern in which the gas and liquid phases are completely separated by a smooth and stable interface. The formulation of the model involves balance equations deduced from the macroscopic mass and momentum conservation laws. The particle-liquid drag and the gas-liquid interactions, i.e. the gas-liquid drag due to the relative motion between the fluids and the force by which the gas pushes the liquid against the solid

particles were evaluated from theoretical considerations. Authors have claimed a reasonable agreement with existing experimental data obtained in a wide range of operating pressure (0.1-10 MPa) for various gas–liquid and packing systems for both liquid saturation and pressure gradient.

Table II.11. Summary of CFD models

Authors	Key features of model	Remarks
Gunjal *et al.*, 2005	Extension of their own previous model (Gunjal *et al.*, 2003) for simulating the spray flow regime and hysteresis on pressure drop Attempted to simulate the periodic flow	Though the simulation of periodic flow can be used to understand some key features, still development is essential in this field for better prediction
Gunjal *et al*., 2003	Two fluid approach using the closure of Attou *et al*. (1999) have been used in 2D as well as 3D geometry Liquid flow distribution and RTD were studied incorporating the effect of capillary pressure and porosity variation	The first effort to simulate the reactor in 3D Though the qualitative prediction of hysteresis was carried out but the development in quantitative comparison is required.
Jiang *et al*., 2002	Two fluid approach using CFDLIB (Los Alamos National Laboratory) Drag-exchange coefficients are calculated by the model of Attou *et al.* (1999) Capillary pressure is incorporated via *J*-function Bed structure implementation is resolved through statistical implementation of sectional porosities	Able to capture some of the key features of the hydrodynamics Bed structure implementation is involved
Souadnia and Latifi, 2001	One-dimensional computational model is used with the finite volume technique combined with Godunov's method. Drag forces are accounted for through the equations developed by Sàez and Carbonell, 1985 Porosity is assumed uniform and constant	Development in 2D model required for better prediction of parameters
Propp *et al.*, 2000	Flow is assumed to be governed by equations of flow in porous media Use of high-resolution finite-difference methods to discretize governing equations. Examined the effects of Ergun equation, capillary pressure and variable porosity	The code was tested with several test problems, no explicit validation with experimental results for different hydrodynamic parameters were presented
Attou and Ferschneider, 1999	Model developed on the basis of area-averaged mass and momentum balance equations of each fluid Capillary pressure gradient was deduced from a momentum balance analysis at the gas–liquid interface The liquid–solid and gas–liquid interaction forces are formulated on the basis of the Kozeny–Carman equation	As the model is one-dimensional, it cannot accommodate the variation of radial bed porosity distribution

The following sections encompass a review of different multiphase flow simulation approaches that has been published in the literature. The recent progress made in hydrodynamic modelling of multiphase reactors, their capabilities and limitations are briefly described for different simulation approaches including the Eulerian-Eulerian, Eulerian-Lagrangian and Volume-of-Fluid (VOF) models.

II.8.1. Eulerian-Eulerian Model

In Eulerian-Eulerian approach also called as two-fluid modelling, the different phases are treated mathematically as interpenetrating continua. Since the volume of a phase cannot be occupied by the other phases, the concept of phasic volume fraction is introduced. These volume fractions are assumed to be continuous functions of space and time and their sum is equal to one. Conservation equations for each phase are derived to obtain a set of equations, which have similar structure for all phases. Coupling is achieved through the pressure and interphase exchange co-effects. The manner in which this coupling is handled depends upon the type or phase involved. The individual interaction between the interpenetrating phases is accounted for using closure laws (Van Wachem and Almstedt, 2003).

The general governing equations are often presented in the form of volume-average for each individual phase and it can be found in Ranade (2002). The momentum equations can be expressed by the Navier-Stokes equations accounting for the gravity acceleration, hydrodynamic pressure, external body force, lift force and virtual mass force if any. The viscous stress tensor is formulated on the basis of Bousinessq hypothesis and it has the contribution of shear and bulk viscosity. A separate enthalpy equation is written for the description of energy conservation.

Eulerian-Eulerian approach is more suitable for modelling dispersed multiphase systems with a significant volume fraction of dispersed phase (>10%) and thus allows the computation of three-phase flow fields even with high solid and gas hold-ups. The accuracy of the Eulerian-Eulerian approach heavily relies on the empirical constitutive equations used. Although it requires significantly fewer computational resourses (which make it more effective for simulating the large individual reactions), it does not provide information about the hydrodynamics of individual bubbles and particles and thus has limitations in predicting certain discrete flow characteristics such as particle size effect, particle agglomeration or bubble coalescence and brake up (Ranade, 2002).

Lia and Salcudean (1987) simulated the bubble rise behaviour using Eulerian-Eulerian approach and obtained good agreement between experimental and predicted velocity field. Ranade (1992) used Eulerian approach to investigate the flow field in a bubble column reactor. This author (Ranade, 1997) reported later a new model based on Eulerian approach to include a radially varying slip velocity. Becker *et al*. (1994) simulated the dynamic behaviour of a relatively large laboratory column with a 2-D mesh. The Eulerian-Eulerian approach was applied for dynamic study of different characteristics of gas-liquid flow. The same case was the subject of study by Sokolichin and Eigenberger (1994). They used laminar flow conditions and concluded that unsteady-state simulations of gas liquid flow are essential in order to resolve the prevailing

oscillating structures. These authors in a later communication (Sokolichin and Eigenberger 1999), reported Eulerian simulation results with turbulent flow conditions in both 2D and 3D geometries. Mudde and Simonin (1999) reported two and three-dimensional simulations of a meandering bubble plume using the Eulerian-Eulerian method that included the k-ε turbulence model. They used the k-ε model to simulate the turbulent phenomena in the continuous phase. The dispersed phase was modelled using laminar flow conditions. A comparative study of different turbulence models for 2-D bubble column has also demonstrated the significance of k-ω model for quantitative prediction of the meandering behaviour of plume.

Gas-solid/gas-solid-liquid simulations with Eulerian-Eulerian approach is an emerging important research area in last decades. Gidaspow (1994) provides a comprehensive summary of the numerical models of gas-solid fluidized bed systems. Most of the effort was primarily focused on 2-D simulations. Becker *et al*. (1994) investigated gas-liquid flow in a flat bubble column with rectangular cross-section and two-dimensional flow structure. The bubble column was compared with an airlift loop reactor in terms of experimental techniques comprising visual observation of the flow structure and photographic documentation of the bubble distribution as well as detailed measurements of the two-phase flow characteristics at distinct levels over the column width. The experimental results were compared with numerical simulations based upon the dynamic laminar two-dimensional two-phase Euler-Euler model. The authors claimed that the steady state as well as the transient behaviour was well reproduced in the simulations and a good quantitative agreement could be obtained if the value of the laminar viscosity used was increased by a factor 100 to account for the influence of turbulent viscosity. Deen *et al*. (2001) presented large eddy simulations in numerical simulations of the gas-liquid flow in bubble columns. The Euler-Euler approach was used to describe the equations of motion of the two-phase flow. The authors have found that, when the drag, lift and virtual mass forces are used, the transient behaviour that was observed in experiments can be captured and a good quantitative agreement with experimental data is obtained both for the mean velocities and the fluctuating velocities. The large eddy simulations showed better agreement with the experimental data than simulations using the k-ε model. Taghipour *et al*. (2005) have recently applied multi-fluid Eulerian model to simulate gas-solid fluidized beds. Comparison of their model predictions and experimental measurements on the time averaged bed pressure drop, bed expansion, and qualitative gas-solid flow pattern has indicated reasonable agreement for different operating conditions. Recently, Dhotre *et al*. (2008) accomplished Euler-Euler simulations of the gas-liquid flow in a square cross-sectioned bubble column with large eddy simulation model (two sub-grid scale models) and the k-ε model. The sub-grid scale modeling was based on the Smagorinsky kernel in both its original form and the dynamic procedure of Germano. The attempt has been made to assess the performance of these

two sub-grid scale models. The sub-grid scale models were modified to account for bubble induced turbulence (Sato model) and it was observed that it did not change the results much. Predictions were also compared with the available experimental data. All the non-drag forces (turbulent dispersion force (only for Reynolds Averaged Navier-Stokes models), virtual mass force, lift force) and drag force were incorporated in the model. An extended k-ε turbulence model has been used with extra source terms introduced to account for the interaction between the bubbles and the liquid. As one can conclude, while there is an extensive literature on the two-phase flow model for bubble-column reactors, studies of three-phase flow hydrodynamics in trickle-beds are rather limited on the interstitial fluid flow simulation.

II.8.2. Eulerian-Lagrangian Model

The Lagrangian models have become a very useful and versatile tool to study the hydrodynamic behaviour of multiphase reactors with particulate flows. In this approach, the fluid phase is treated as a continuum by solving the time averaged Navier-Stokes equations in the same manner as for a single-phase system, while the dispersed phase is solved by tracking a large number of particles, bubbles or droplets through the calculated flow field using Newtonian equation of motion. Usually bubbles and particles are considered as having a fixed size and shape. The dispersed phase can exchange momentum, mass, and energy with the fluid phase (Lain et al., 2002).

In multiphase hydrodynamic modeling using Eulerian-Lagrangian approach, the particle models are combined with an Eulerian model for the continuous phase to simulate the disperse phase. The motion of fluid phase is calculated from the averaged fluid-phase governing equations, which are similar to Eulerian-Eulerian. The motion of the discrete phase particle (or droplet or bubble) is given by integrating the force balance on the particle, which is written in Lagrangian reference frame. This force balance equates the particle inertia with forces acting on the particle using Newton's second law. These forces acting on each particle, next to collisions, are gravity and the traction force of the fluid phase on the particle. Thus the momentum balance equation describing the acceleration of the particle is written as a function of mass, acceleration, velocity, volume fraction of solid particle, pressure and interphase momentum transfer coefficient (Van Wachem and Almstedt, 2003).

The advantage of Eulerian-Lagrangian approach is that the dynamics of the individual bubbles or particles can be assessed, however, in the case of turbulent flows, it is necessary to simulate a very large number of particle trajectories to obtain meaningful averages. With high concentrations of particles and for large size reactors, the tracking process becomes highly memory-intensive so that

this approach is, comprehensively, suitable for simulating multiphase flows containing a low (<10%) volume fraction of the dispersed phases (Ranade, 2002).

Regarding the Eulerian-Lagrangian simulations found in the literature, Grevet *et al.* (1982) were among the first researchers to theoretically investigate the bubble rise phenomenon. They used Eulerian-Lagrangian approach to simulate a bubble plume. Van Sint Annaland *et al*. (2005) used the same approach to simulate bubble trajectories in a bubble column reactor. Using 2D simulation, they obtained good agreement with the experimental observations of Becker *et al.* (1994). Delnoij et al. (1997) reported a CFD simulation of bubble rise in rectangular bubble column reactors. They studied the effect of aspect ratio of the bubble column reactor. As expected, they observed significantly complex flow patterns with numerical simulations. The Euler-Lagrange model was used to solve time dependent, two-dimensional motion of small, spherical gas bubbles in a liquid using the equation of motion. The model incorporated all relevant forces acting on a bubble as it rises through the liquid, and additionally accounts for direct bubble-bubble interactions. The liquid-phase hydrodynamics were described using the volume-averaged Navier-Stokes equations. The model was used to study the hydrodynamic behaviour of bubble columns with aspect ratios ranging from 1.0 to 11.4. The authors claimed that the computational results clearly showed the presence of vortical structures in the liquid phase at aspect ratios exceeding 2.0. These vortical structures in the liquid phase were studied experimentally using neutrally buoyant tracer particles and streak photography. The experimentally observed vortical structures were shown to resemble the computed structures. Later, Delnoij *et al*. (1999) discussed the development of a three-dimensional Euler-Lagrange CFD model for a gas-liquid bubble column. The model solved the time-dependent, three-dimensional motion of small, spherical gas bubbles in a liquid. The Euler-Lagrange incorporated all forces acting on a bubble rising in a liquid, and accounted for two-way momentum coupling between the gas and liquid phases. The liquid phase hydrodynamics were described using the volume-averaged Navier-Stokes equations for laminar flow. More recently, Darmana *et al*. (2005) developed a 3D discrete bubble model to investigate complex behavior involving hydrodynamics, mass transfer and chemical reactions in a gas-liquid bubble column reactor. A continuum description was adopted for the liquid phase and additionally each individual bubble was tracked in a Lagrangian framework, while accounting for bubble-bubble and bubble-wall interactions via an encounter model. The mass transfer rate was calculated for each individual bubble using a surface renewal model accounting for the instantaneous and local properties of the liquid phase in its vicinity. The distributions in space of chemical species residing in the liquid phase were computed from the coupled species balances considering the mass transfer from bubbles and reactions between the species. The model has been applied to simulate chemisorption of CO_2 bubbles in NaOH solutions. The authors claimed that Euler-Lagrange model

was able to predict the bubble size distribution as well as temporal and spatial variations of each chemical species involved. Zhang and Ahmadi (2005) have used similar approach to study the transient characteristics of three-phase flows. In addition to considering the interactions between particle-particle, bubble-bubble, and particle-bubble, bubble coalescence is also included and the effects of bubble size variation on flow pattern are very well demonstrated. From the above survey, it can be seen that this methodology has been found widespread application on bubble column reactors.

II.8.3. Volume-of-Fluid Model

The VOF model is a well-known method of interface tracking for multiphase flows. In this approach, the motion of all phases is modelled by solving a single set of transport equations using appropriate jump boundary conditions at the interface. The fluid location is recorded by employing a volume of fluid function which is defined as unity within the field regions and zero elsewhere. In practical numerical simulations employing a VOF algorithm, this function is unity in computational cells occupied completely by fluid of phase 1, zero in region occupied completely by phase 2, and a value between these limits in cells which contain a free surface (Van Wachem and Almstedt, 2003).

The tracking of the interface between the phases is accomplished by the solution of a continuity equation for the volume fraction of one (or more) of the phases. A single momentum equation is solved throughout the domain and shared by all the phases. The VOF model treats energy, E, and temperature, T, as mass-averaged variables. The major drawback of VOF method is the so-called artificial coalescence of gas bubbles which occurs when their mutual distances is less than the size of the computational cell, which also make this approach memory intensive for simulation of dispersed multiphase flows in large equipment (Ranade 2002). The first VOF type approach was suggested by Hirt and Nichols (1981). Although this scheme is still considered one of the simplest and well-known methods of interface tracking, it performs badly with low-order discretization schemes due to large amount of smearing of the interface violating the conservation of each one of the phases. The application of the so-called surface sharpening or reconstruction models, as present in some commercial CFD codes, can somewhat prevent the smearing of the interface. Table II.12 presents an overview of techniques for multiphase systems that have been used with VOF model.

Table II.12. Overview of techniques for multi-fluid flows with sharp interfaces

Method	Advantages	Disadvantages
Front tracking	Extremely accurate Robust Account for substantial topology changes in interface Merging and breakage of interfaces does not occur automatically	Mapping of interface mesh onto Eulerian mesh Dynamic remeshing required Merging and breakage of interfaces require sub-grid model
Level set	Conceptually simple Easy to implement	Limited accuracy Loss of mass (volume)
Shock capturing	Straightforward implementation Abundance of advection schemes are available	Numerical diffusion Fine grids required Limited to small discontinuities
Marker particle	Extremely accurate Robust Accounts for substantial topology changes in interface	Computationally expensive Re-distribution of marker particles required
SLIC VOF	Conceptually simple Straightforward extension to three dimensions	Numerical diffusion Limited accuracy Merging and breakage of interfaces occurs automatically
PLIC VOF	Relatively simple Accurate Accounts for substantial topology changes in interface	Difficult to implement in three dimensions Merging and breakage of interfaces occur automatically
Lattice Boltzmann	Accurate Accounts for substantial topology changes in interface	Difficult to implement Merging and breakage of interfaces occur automatically

Hydrodynamic modelling of fixed-bed reactors with VOF model is rarely documented in the open literature (Gunjal *et al*., 2005b). Bubble columns have received the foremost attention on the VOF simulation case studies. The motion of single bubbles is relatively well understood and extensive experimental data on shape and terminal velocity are available in the literature. Using available experimental data, simulation work for single bubble rising in stagnant fluid has been carried out by many researchers mostly in two-dimension (Krishna and van Baten, 1999; Essemiani *et al.*, 2001; Liu *et al.*, 2005) and few in three-dimension (Olmos et al., 2001; Van Sint Annaland *et al*., 2005). The rise trajectories of bubbles, their size, shape and rise velocity as well as the effect of fluid properties on bubble dynamics and gas hold-up were largely discussed. Chen and Fan (2004) have applied a level set formulation of VOF to simulate bubble motion for two and three-phase system. Bertola *et al.* (2004) predict the influence of bubble diameter and gas hold-up on the hydrodynamics of bubble column reactor using VOF approach.

Despite all of these significant efforts in predicting the characteristics of bubbly flows, there is still need to develop VOF model for three-phase reactors including trickle beds. Therefore, in the present work Euler-Euler and VOF models will be investigated for the hydrodynamic simulation of high-pressure trickle-bed reactors since the Euler-Lagrange is limited to those cases that are characterized by a highly diluted phase with a volumetric concentration lower than 10%.

II.9. Conclusions

As the abovementioned survey indicated, major improvements on active and stable heterogeneous catalyst are intended to be realized in the near future. This fact will allow substantial enhancements of catalytic wet oxidation technology to become economically and environmentally feasible in comparison to most of the conventional treatments. Catalytic wet oxidation should overcome common drawbacks associated with separation based as well as biological technologies as long as they cause non-depreciable secondary sources of environmental pollution. Foremost reviews on wet oxidation have identified refractory compounds to non-catalytic wet oxidation, which have a regular property of being low to moderate molecular weight oxygenated compounds.

In this ambit, agro-food processing wastewaters will be undertaken as an example of non-biodegradable and phytotoxic effluents. Specifically, major polyphenolic compounds: syringic (*4*-hydroxy-*3,5*-dimethoxybenzoic), vanillic (*4*-hydroxy-*3*-methoxybenzoic), *3,4,5*-trimethoxybenzoic, veratric (*3,4*-dimethoxybenzoic), protocatechuic (*3,4*-dihydroxybenzoic) and *trans*-cinnamic acids typically found in olive oil mill wastewaters deserve particular attention in what concerns the process performance at different levels as follows: total organic carbon reduction, intermediate compounds formation, catalyst stability and kinetic modelling. Several commercial and laboratory-made catalysts will be investigated addressing both the catalytic activity and stability. Regarding the selected catalysts some were prepared in laboratory and others were commercially obtained. The tested active materials were manganese, copper, zinc, iron and silver, while the catalysts supports were ceria and alumina. A major importance was given to cerium based catalysts and manganese catalysts. The kinetic parameters will be obtained taking into account the generalized kinetic model and this information will be further integrated into a hydrodynamic model developed by means of CFD where the reaction aspects as well as the transport mechanisms were accounted for a high-pressure trickle-bed reactor. Two multiphase CFD frameworks – Euler-Euler and Volume-of-Fluid – will be evaluated for either cold flow or reacting flow conditions. Axial and radial profiles of hydrodynamic and reaction parameters will be thoroughly evaluated at different operating conditions. The influence of gas and liquid flow rates as well as the effect of temperature and pressure will be investigated in terms of total organic carbon conversions.

II.10. References

Achma, R.B., Ghorbel, A., Sayadi, S., Dafinov, A., Medina, F. (2008). A novel method of copper-exchanged aluminum-pillared clay preparation for olive oil mill wastewater treatment. *Journal of Physics and Chemistry of Solids* **69**, 5-6, 1116-1120.

Akyurtlu, J. F. A., Akyurtlu, A., Kovenklioglu, S. (1998). Catalytic oxidation of phenol in aqueous solutions. *Cataysis Today*, **40**, 343.

Al-Dahhan, M.H., Larachi, F., Dudukovic, M.P., Laurent, A. (1997). High-Pressure Trickle-Bed Reactors: A Review. *Industrial and Engineering Chemistry Research* **36**, 8, 3292-3314.

Al-Dahhan, M.H.; Dudukovic, M.P. (1995). Catalyst wetting efficiency in trickle-bed reactors at high pressure. *Chemical Engineering Science* **50,** 2377-2389.

Al-Dahhan, M.H., Khadilkar, M.R., Wu, Y., Dudukovic, M.P. (1998). Prediction of pressure drop and liquid holdup in high pressure trickle bed reactors. *Industrial and Engineering Chemistry Research* **37** (3), 793-798.

Al-Dahhan, M.H., Dudukovic, M.P. (1994). Pressure drop and liquid holdup in high pressure trickle-bed reactors. *Chemical Engineering Science* **49**, 5681-5698.

Al-Dahhan, M.H., Khadilkar, M.R., Wu, Y., Dudukovic, M.P. (1998). Prediction of pressure drop and liquid holdup in high pressure trickle-bed reactors, *Industrial and Engineering Chemistry Research* **37**, 793-798.

Alvarez, P. M., McLurgh, D., Plucinski, P. (2002). Copper Oxide Mounted on Activated Carbon as Catalyst for Wet Air Oxidation of Aqueous Phenol. 2. Catalyst Stability. *Industrial and Engineering Chemistry Research* **41**, 2153.

Andreozzi, R., Longo, G., Majone, M., Modesti, G. (1998). Integrated treatment of olive oil mill effluents (OME): study of ozonation coupled with anaerobic digestion. *Water Research* **32**, 2357-2364.

Andreozzi, R., Caprio, V., D'Amore, M.G., Insola, A. (1995). p-Coumaric acid abatement by ozone in aqueous solution. *Water Research* **29**, 1-6.

Arena, F., Giovenco, R., Torre, T., Venuto, A., Parmaliana, A. (2003). Activity and resistance to leaching of Cu-based catalysts in the wet oxidation of phenol. *Applied Catalysis B: Environmental*, **45**, 51.

Atta, A, Roy, Shantanu, Nigam, K.D.P. (2007). Prediction of pressure drop and liquid holdup in trickle bed reactor using relative permeability concept in CFD. *Chemical Engineering Science* **62**, 21, 5870-5879.

Attou, A., Boyer, C., Ferschnider, G. (1999). Modelling of the hydrodynamics of the cocurrent gas-liquid trickle flow through a trickle-bed reactor. *Chemical Engineering Science* **54** (6), 785-802.

Attou, A., Ferschneider, G.A. (1999). Two-fluid model for flow regime transition in gas-liquid trickle-bed reactors. *Chemical Engineering Science* **54** (21), 5031-5037.

Aydin, B., Cassanello, M.C., Faiçal Larachi. (2008). Influence of temperature on fast-mode cyclic operation hydrodynamics in trickle-bed reactors. *Chemical Engineering Science* **63**, 1, 141-152.

Azabou, S., Najjar, W., Gargoubi, A., Ghorbel, A., Sayadi. S. (2007). Catalytic wet peroxide photo-oxidation of phenolic olive oil mill wastewater contaminants: Part II. Degradation and detoxification of low-molecular mass phenolic compounds in model and real effluent. *Applied Catalysis B: Environmental*, **77**, 1-2, 166-174.

Baillod, C. R., Faith, B. M., Masi, O. (1982). Fate of Specific Pollutants During Wet Oxidation and Ozonation. *Environmental Progress*, **1** (3), 217.

Baldi, G. (1981a). Design and Scale-up of Trickle-Bed Reactors. Solid-Liquid Contacting Effectiveness. In Multiphase Chemical Reactors, Rodrigues, A. E., Calo, J. M., Sweed, N. H., Eds., *NATO Advanced Study Institute Series E, Sitjhoff & Noordhoff: Aalphen aan den Rijn*, The Netherlands, **52**, 323.

Baldi, G. (1981b). Heat Transfer in Gas-Liquid-Solid Reactors. In Multiphase Chemical Reactors, Rodrigues, A. E., Calo, J. M., Sweed, N. H., Eds., *NATO Advanced Study Institute Series E, Sitjhoff & Noordhoff: Aalphen aan den Rijn*, The Netherlands, **52**, 307.

Baldi, G. (1981c). Hydrodynamics of Multiphase Reactors. In Multiphase Chemical Reactors, Rodrigues, A. E., Calo, J. M., Sweed, N. H., Eds., *NATO Adv. Study Inst. Series E, Sitjhoff & Noordhoff: Aalphen aan den Rijn*, The Netherlands, **52**, 271.

Baker, B., (1978). III. Determination of the Extent of Catalyst Utilization in a Trickle-Flow Reactor. *ACS Symp. Ser.* **65**, 425.

Baussaron, L., Julcour-Lebigue, C., Boyer, C., Wilhelm, A.M., Delmas, H. (2007). Effect of partial wetting on liquid/solid mass transfer in trickle bed reactors. *Chemical Engineering Science* **62**, 24, 7020-7025.

Beccari, M., Bonemazzi, F., Majone, M., Riccardi, C. (1996). Interaction between acidogenesis and methanogenesis in the anaerobic treatment of olive oil mill effluents. *Water Research* **30**, 183-189.

Becker, S., Sokolichin, A., Eigenberger, G. (1994). Gas-liquid flow in bubble columns and loop reactors: Part II. Comparison of detailed experiments and flow simulations, *Chemical Engineering Science* **49**, 24, 5747-5762.

Beltran, F.J., Garcia-Araya, J.F., Frades, J., Gimeno, O. (1999). Effects of single and combined ozonation with hydrogen peroxide or UV radiation on the chemical degradation and biodegradability of debittering table olive industrial wastewaters. *Water Research.* **33**, 723-732.

Benitez, F.J., Beltran-Heredia, J., Torregrosa, J., Acero, J.L. (1997). Treatments of wastewaters from olive oil mills by uv radiation and by combined ozone-UV radiation. *Toxicol. Environ. Chem.* **61**, 173-185.

Bensetiti, Z.; Larachi, F.; Grandjean, B.P.A.; Wild, G. (1997). Liquid saturation in cocurrent upflow fixed-bed reactors: a state-of-the-art correlation. *Chemical Engineering Science* **52**, 4239-4247.

Bertola, F., Baldi, G., Marchisio, D., Vanni, M. (2004). Momentum transfer in a swarm of bubbles: estimates from fluid-dynamic simulations. *Chemical Engineering Science* **59**, 22-23, 5209-5215.

Béziat, J.C., Besson, M., Gallezot, P., Durecu, S. (1999). Catalytic Wet Air Oxidation of Carboxylic Acids on TiO_2-Supported Ruthenium Catalysts. *Journal of Catalysis* **182**, 129-135.

Bhargava, S. K., Tardio, J., Prasad, J., Foger, K., Akolekar, D. B. and Grocott, S. C. (2006). Wet Oxidation and Catalytic Wet Oxidation. *Industrial and Engineering Chemistry Research* **45** (4), 1221-1258.

Birchmeier, M. J., Hill, C. G., Jr., Houtman, C. J., Atalla, R. H., Weinstock, I. (2000). Enhanced Wet Air Oxidation: Synergistic Rate Acceleration upon Effluent Recirculation. *Industrial and Engineering Chemistry Research* **39**, 55.

Boyer, C., Volpi, C., Ferschneider, G. (2007). Hydrodynamics of trickle bed reactors at high pressure: Two-phase flow model for pressure drop and liquid holdup, formulation and experimental validation. *Chemical Engineering Science* **62**, 24, 7026-7032.

Boyer, C., Duquenne, A.M., Wild, G. (2002). Measuring techniques in gas-liquid and gas-liquid-solid reactors. *Chemical Engineering Science* **57**, 16, 3185-3215.

Burghardt, A., Bartelmus, G. (1996). Hydrodynamics and mass transfer in three-phase cocurrent reactors. *Chemical Engineering Science* **51**, 2733-2738.

Cai, J., Li, A., Zhang, Q. (2004). Progress of wet catalytic air oxidation technology. *Hebei Daxue Xuebao, Ziran Kexueban*, **24** (3), 326.

Capasso, R., Evidente, A., Schivo, L., Orru, G., Marchialis, M., Cristinzio, G. (1995). Antibacterial polyphenols from olive oil mill waste waters. *J. Appl. Bacteriol.* **79**, 393-398.

Carbonell, R.G. (2000). Multiphase flow models in packed beds. *Oil & Gas Science and Technology* – Revue de l'IFP **55** (4), 417-425.

Caudo, S., Genovese, C., Perathoner, S., Centi, G. (2008). Copper-pillared clays (Cu-PILC) for agro-food wastewater purification with H_2O_2. *Microporous and Mesoporous Materials* **107**, 1-2, 46-57.

Caudo, S., Centi, G., Genovese, C., Perathoner, S. (2007a). Copper- and iron-pillared clay catalysts for the WHPCO of model and real wastewater streams from olive oil milling production. *Applied Catalysis B: Environmental*, **70**, 1-4, 437-446.

Caudo, S., Centi, G., Genovese, C., Giordano, G., Granato, T., Katovic, A., Perathoner. S. (2007b). Cu-MOF: a new highly active catalyst for WHPCO of waste water from agro-food production. *Studies in Surface Science and Catalysis*, **170**, 2054-2059.

Chakchouk, M., Hamdi, M., Foussard, J.N., Debellefontaine, H. (1994). Complete treatment of olive mill wastewaters by a wet air oxidation process coupled with a biological step. *Environmental Technology* **15**, 323-332.

Chang, C. J., Li, S. S., Ko, C. (1995). Catalytic wet oxidation of phenol and p-chlorophenol contaminated wastewaters. *Journal of Chemical Technology Biotechnology* **64** (3), 245.

Chaouki, J.; Larachi, F.; Dudukovic, M.P. (1997). Noninvasive Tomographic and Velocimetric Monitoring of Multiphase Flows. *Industrial and Engineering Chemistry Research* **36**, 4476-4503.

Charpentier, J. C. (1986). Mass Transfer in Fixed Bed Reactors. *In Multiphase Chemical Reactors Theory, Design, Scale-up*, Gianetto, A., Silveston, P. L., Eds., *Hemisphere Publ. Co.*: Washington, 289.

Charpentier, J. C. (1982). What's New in Absorption with Chemical eaction. *Trans. Inst. Chem. Eng*. **60**, 131.

Charpentier, J. C. (1979). Hydrodynamics of Two-Phase Flow Through Porous Media. *In Chemical Engineering of Gas-Liquid-Solid Catalyst Reactions*, L'Homme, G. A., Ed., CEBEDOC: Lie`ge, Belgium, 78.

Charpentier, J. C. (1978). Gas-Liquid Reactors. In Chemical Reaction Engineering Reviews, Luss, D., Weekman, V. W., Eds., ACS Symposium Series 72, *American Chemical Society*: Washington, DC, 223.

Charpentier, J. C. (1976). Recent Progress in Two-Phase Gas-Liquid Mass Transfer in Packed Beds. *Chemical Engineering Journal* **11**, 161.

Chen, Y., Li, Z. (1999). Technological progress of heterogeneous catalytic oxidation for treating wastewater. *Huagong Jinzhan*, **18** (5), 26.

Chen, H., Sayari, A., Adnot, A., Larachi, F.V. (2001). Composition activity effects of Mn-Ce-O composites on phenol catalytic wet oxidation. *Applied Catalysis B: Environmental* 32 (3), 195.

Chen, I.-P., Lin, S.-S., Wang, C.-H., Chang, L., Chang, J.-S. (2004). Preparing and characterizing an optimal supported ceria catalyst for the catalytic wet air oxidation of phenol. *Applied Catalysis B: Environmental* **50**, 49.

Chen, C., Fan, L.S. (2004). Discrete Simulation of Gas-Liquid Bubble Columns and Gas-Liquid-Solid Fluidized Beds. *AIChE Journal* **50**, 2, 288-300.

Collivignarelli, C., Baldi, M., Bertanza, G., Bissolotti, G., Calvi, R., Del Rio, M., Pergetti, M. (1997). Technical and economic feasibility of wet oxidation: treatment experience in a full-scale plant. *Part I. Ing. Ambientale*, **26** (3), 109.

Crine, M., L'Homme, G. (1983). Recent Trends in the Modelling of Catalytic Trickle-Bed Reactors. *In Mass Transfer with Chemical Reaction in Multiphase Systems: Three-Phase Systems, Alper, E., Ed., Martinus Nijhoff Publ.: The Hague*, The Netherlands, II, 99.

Dalis, D., Anagnostidis, K., Lopez, A., Letsiou, I., Hartmann, L. (1996). Anaerobic digestion of total raw olive-oil wastewater in a two-stage pilot-plant (up-flow and fixed-bed bioreactors). *Bioresource Technology* **57**, 237-243.

Darmana, D., Deen, N.G., Kuipers, J.A.M. (2005). Detailed modeling of hydrodynamics, mass transfer and chemical reactions in a bubble column using a discrete bubble model. *Chemical Engineering Science* **60**, 12, 3383-3404.

De Rosa, S., Giordano, G., Granato, T., Katovic, A., Siciliano, A., Tripicchio, F. (2005). Chemical Pretreatment of Olive Oil Mill Wastewater Using a Metal-Organic Framework Catalyst. *Journal of Agriculture and Food Chemistry* **53**, 21, 8306-8309.

Deen, N.G., Solberg, T., Hjertager, B.H. (2001). Large eddy simulation of the Gas–Liquid flow in a square cross-sectioned bubble column. *Chemical Engineering Science* **56**, 21-22, 6341-6349.

Debellefontaine, H., Foussard, J. N. (2000). Wet air oxidation for the treatment of industrial wastes. Chemical aspects, reactor design and industrial applications in Europe. *Waste Management* **20**, 15.

Delnoij, E., Kuipers, J.A.M., Van Swaaij, W.P.M. (1997). Dynamic simulation of gas–liquid two-phase flow: effect of column aspect ratio on the flow structure. *Chemical Engineering Science* **52**, 3759-3772.

Delnoij, E., Kuipers, J.A.M., Van Swaaij, W.P.M. (1999). Dynamic simulation of gas–liquid two-phase flow: effect of column aspect ratio on the flow structure. *Chemical Engineering Science* **54**, 13-14, 2217-2226.

Devlin, H. R., Harris, I. (1984). Mechanism of the Oxidation of Aqueous Phenol with Dissolved Oxygen. *Industrial and Engineering Chemistry Fundamentals* **23**, 387.

Dhotre, M.T., Niceno, B., Smith, B.L. (2008). Large eddy simulation of a bubble column using dynamic sub-grid scale model. *Chemical Engineering Journal* **136**, 2-3, 337-348.

Dietrich, M. J., Randall, T. L., Canney, P. J. (1985). Wet Air Oxidation of Hazardous Organics in Wastewater. *Environmental Progress*, **4** (3), 171.

Dirkx, J. M. H. De (1979a). Trickle-Bed Reactor Part I. *Polytech. Tijdschr.: Procestech*., **34**, 227.

Dirkx, J. M. H. De (1979b). Trickle-Bed Reactor Part II. *Polytech. Tijdschr. Procestech*., **34**, 316.

Dixon, A.G., Nijemeisland**,** M., Stitt, E.H. (2006)**.** Packed Tubular Reactor Modeling and Catalyst Design using Computational Fluid Dynamics. *Advances in Chemical Engineering* **31**, 307-389.

Dudukovic, M. P., Larachi, F., Mills, P. L. (1999). Multiphase reactors – revisited. *Chemical Engineering Science* **54**, 13-14, 1975-1995.

Dudukovic, M. P., Mills, P. L. (1978). Catalyst Effectiveness Factors in Trickle-Bed Reactors. *ACS Symp. Ser.* **65**, 387.

Dudukovic, M. P. (1977). Catalyst Effectiveness Factor and Contacting Efficiency in Trickle-Bed Reactors. *AIChE Journal* **23**, 940.

Dwivedi, P. N., Upadhyay, S. N. (1977). Particle-Fluid Mass Transfer in Fixed and Fluidized Beds. *Industrial and Engineering Chemistry Process Design and Development* **16**, 157.

Dyakowski, T., Jeanmeure, L.F.C., Jaworski, A.J. (2000). Applications of electrical tomography for gas-solids and liquid-solids flows – a review. *Powder Technology* **112**, 3, 174-192

Eftaxias, A., Larachi F., Stuber F. (2003). Modelling of trickle bed reactor for the catalytic wet air oxidation of phenol. *Canadian Journal of Chemical Engineering* **81** (3-4), 784.

Ellman, M.J., Midoux, N., Wild, G., Laurent, A., Charpentier, J.C. (1990). A new improved liquid holdup correlation for trickle bed reactors. *Chemical Engineering Science* **45** (7), 1677-1684.

Essemiani, K., Ducom, G., Cabassud, C., Line, A. (2001). Spherical cap bubbles in a flat sheet nanofiltration module: experiments and numerical simulation. *Chemical Engineering Science* **56**, 21-22, 6321-6327.

Fiorentino, A., Gentili, A., Isidori, M., Lavorgna, M., Parrella, A., Temussi, F. (2004). Olive Oil Mill Wastewater Treatment Using a Chemical and Biological Approach. *Journal of Agriculture and Food Chemistry* **52**, 5151-5154.

Fourar, M., Lenormand, R., Larachi, F. (2001). Extending the *F*-function concept to two-phase flow in trickle beds, *Chemical Engineering Science* **56** (21–22), 5987-5994.

Furuya, H., Uwabe, R., Sutoh, N., Okuwaki, A., Amano, A., Okabe, T. (1985). Oxidation of Coals in Liquid Phases. VII. Oxidation of Oxygen containing Model Compounds of Coal by Oxygen in Concentrated Sodium Hydroxide Solutions. *Bull. Chem. Soc. Jpn*., **58**, 3016.

Germain, A. (1983). Industrial Applications of Three-Phase Catalytic Fixed Bed Reactors. *In Mass Transfer with Chemical Reaction in Multiphase Systems: Three-Phase Systems, Alper, E., Ed., Martinus Nijhoff Publ.: The Hague*, The Netherlands, II, 19.

Gernjak, W., Maldonado, M.I., Malato, S., Caceres, J., Krutzler, T., Glaser, A., Bauer, R. (2004). Pilot-plant treatment of olive mill wastewater (OMW) by solar TiO_2 photocatalysis and solar photo-Fenton. *Solar Energy* 77, 567-572.

Gianetto, A., Specchia, V. (1992). Trickle-Bed Reactors: State of Art and Perspectives. *Chemical Engineering Science* **47**, 3197.

Gianetto, A., Berruti, F. (1986). Modelling of Trickle-Bed Reactors. *In Chemical Reactor Design and Technology*, DeLasa, H. I., Ed., Nijhoff: *The Hague*, The Netherlands, 631.

Gianetto, A., Baldi, G., Specchia, V., Sicardi, S. (1978). Hydrodynamics and Solid-Liquid Contacting Effectiveness in Trickle-Bed Reactors. *AIChE Journal* **24**, 1087.

Gidaspow, D., Bahary, M., Jayaswal, U.K. (1994). Hydrodynamic Models for Gas-Liquid-Solid Fluidization. Numerical Methods in Multiphase Flow. FED, ASME. New York, **185**, 117-124.

Gomes, H.T., Figueiredo, J.L., Faria, J.L. (2007). Catalytic wet air oxidation of olive mill wastewater. *Catalysis Today*, **124**, 3-4, 254-259.

Goto, S., Levec, J., Smith, J. M. (1977). Trickle-Bed Oxidation Reactors. *Catalysis Reviews: Science and Engineering* **15**, 187.

Grevet, J. H., Szekely, J., El-Kaddah, N. (1982). An Experimental and Theoretical Study of Gas Bubble Driven Circulation Systems. *International Journal of Heat and Mass Transfer* **25**, 487-497.

Gunjal, P.R., Ranade, V.V., Chaudhari, R.V. (2003). Liquid distribution and RTD in trickle-bed reactors: Experiments and CFD simulations, *Canadian Journal of Chemical Engineering* **81**, 821-830.

Gunjal, P.R., Kashid, M.N., Ranade, V.V., Chaudhari, R.V. (2005a). Hydrodynamics of Trickle-Bed Reactors: Experiments and CFD Modeling. *Industrial and Engineering Chemistry Research* **44**, 6278-6294.

Gunjal, P.R., Ranade, V.V., Chaudhari, R.V. (2005b). Dynamics of Drop Impact on Solid Surface: Experiments and VOF Simulations. *A.I.Ch.E. Journal* **51** (1), 59-78.

Guo, J., Al-Dahhan, M. (2003). Kinetics of Wet Air Oxidation of Phenol over a Novel Catalyst. *Industrial and Engineering Chemistry Research* **42**, 5473.

Guo, J., Al-Dahhan, M. (2005). Modeling Catalytic Trickle-Bed and Upflow Packed-Bed Reactors for Wet Air Oxidation of Phenol with Phase Change. *Industrial and Engineering Chemistry Research* **44** (17), 6634-6642.

Gupta, R. (1985). *In Handbook of Fluids in Motion, Cheremisinoff*, N. P., Gupta, R., Eds., Ann Arbor Science: Ann Arbor, MI.

Hamdi, M. (1993). Future prospects and constraints of olive mill wastewaters use and treatment: A review. *Bioprocess Engineering* **8**, 209-214

Hamoudi, S., Larachi, F., Cerrella, G., Cassanello, M. (1998). Wet Oxidation of Phenol Catalyzed by Unpromoted and Platinum-Promoted Manganese/Cerium Oxide. *Industrial and Engineering Chemistry Research* **37** (9), 3561.

Hamoudi, S., Sayari, A., Belkacemi, K., Bonneviot, L., Larachi, F. (2000). Catalytic wet oxidation of phenol over PtxAg1-xMnO2/CeO2 catalysts. *Catalysis Today* **62**, 379.

Hanika, J., Stanek, V. (1986). Operation and Design of Trickle-Bed Reactors. *In Handbook of Heat and Mass Transfer: Mass Transfer and Reactor Design, Cheremisinoff*, N. P., Ed., Gulf Publ. Corp.: Houston, TX, **2**, 1029.

Harada, Y. (1999). Industrial wastewater treatment by catalytic wet oxidation method. *Zosui Gijutsu*, **25** (3), 18.

Harada, Y., Fujiya, H., Hayashi, M. (1992a). Treatment of ammonium nitrate - containing wastewater. Jpn. Kokai Tokkyo Koho 1992, 12 pp. CODEN: JKXXAF JP 04200790 A2 19920721 Heisei. CAN 118: 11248 AN 1993: 11248 CAPLUS.

Harada, Y., Doi, Y., Miura, S. (1992b). Treatment of ammonium nitrate containing wastewater. Jpn. Kokai Tokkyo Koho 1992, 9 pp. CODEN: JKXXAF JP 04200692 A2 19920721 Heisei. CAN 118: 11249 AN 1993: 11249 CAPLUS.

Herk, D., Kreutzer, M.T., Makkee, M., Moulijn, J.A. (2005). Scaling down trickle bed reactors. *Catalysis Today* **106**, 1-4, 227-232.

Herrera, F., Pulgarin, C., Nadtochenko, V., Kiwi, J. (1998). Accelerated photo-oxidation of concentrated *p*-coumaric acid in homogeneous solution. Mechanistic studies, intermediates and precursors formed in the dark. *Applied Catalysis B: Environmental* **17**, 141-156.

Herskowitz, M., Smith, J. M. (1983). Trickle-Bed Reactors: A Review. *AIChE Journal* **29**, 1.

Higashi, K., Kawahara, A., Murakami, Y., Wakida, S., Yamane, M., Takeda, S. (1992). Decomposition of nitrophenol by wet oxidation in the presence of noble metal catalysts. *Kankyo Gijutsu*, **21** (11), 689.

Hirt, C.W., Nichols, B.D. (1981). Volume of Fluid (VOF) Method for the Dynamics of Free Boundaries. *Journal of Computational Physics* **39**, 201-225.

Hocevar, S., Krasovec, U. O., Orel, B., Arico, A. S., Kim, H. (2000). CWO of phenol on two differently prepared CuO-CeO2 catalysts. *Applied Catalysis B: Environmental* **28**, 113.

Hofmann, H. (1983). Fluid Dynamics, Mass Transfer and Chemical Reaction in Multiphase Catalytic Fixed Bed Reactors. *In Mass Transfer with Chemical Reaction in Multiphase Systems: Three-Phase Systems, Alper, E., Ed., Martinus Nijhoff Publ.: The Hague*, The Netherlands, Vol. II, 73.

Hofmann, H. (1978). Multiphase Catalytic Packed Bed Reactors. *Catalysis Reviews: Science and Engineering* **17**, 71.

Hofmann, H. (1977). Hydrodynamics, Transport Phenomena, and Mathematical Models in Trickle-Bed Reactors. *International Chemical Engineering* **17**, 19.

Holub, R.A., Dudukovic, M.P., Ramachandran, P.A. (1992). A phenomenological model for pressure drop, liquid holdup, and flow regime transition in gas-liquid trickle flow. *Chemical Engineering Science* **47**, 2343-2348.

Holub, R.A., Dudukovic, M.P., Ramachandran, P.A. (1993). Pressure drop, liquid holdup, and flow regime transition in trickle flow. *AIChE Journal* **39**, 302-321.

Horowitz, G.I., Cukierman, A.L., Cassanello, M.C. (1997). Flow regime transition in trickle beds packed with particles of different wetting characteristics – check-up on new tools *Chemical Engineering Science* **52**, 3747-3755.

Iliuta, I., Larachi, F. (2001). Wet air oxidation solid catalysis analysis of fixed and sparged three-phase reactors. *Chemical Engineering and Processing* **40**, 175.

Iliuta, I., Thyrion, F.C. (1997). Flow regimes, liquid holdups and two-phase pressure drop for two-phase cocurrent downflow and upflow through packed beds: air/Newtonian and non-Newtonian liquid systems. *Chemical Engineering Science* **52**, 4045-4053.

Iliuta, I., Larachi, F., Grandjean, B.P.A. (1998). Pressure Drop and Liquid Holdup in Trickle Flow Reactors: Improved Ergun Constants and Slip Correlations for the Slit Model. *Industrial and Engineering Chemistry Research* **37**, 4542-4550.

Iliuta, I., Larachi, F. (1999). The generalized slit model: Pressure gradient, liquid holdup & wetting efficiency in gas-liquid trickle flow. *Chemical Engineering Science* **54**, 5039-5045.

Iliuta, I., Larachi, F., Al-Dahhan, M.H. (2000). Double-slit model for partially wetted trickle flow hydrodynamics. *A.I.Ch.E. Journal* **46**, 597-609.

Imamura, S. (2003). Catalytic technology for water purification. (II). *Mizu Shori Gijutsu*, **44** (9), 417.

Imamura, S. (1999). Catalytic and Noncatalytic Wet Oxidation. *Industrial and Engineering Chemistry Research* **38** (5), 1743.

Imamura, S., Hirano, A., Kawabata, N. (1982). The wet oxidation of organic compounds catalyzed by Co-Bi complex oxide. *Bull. Chem. Soc. Jpn*., **55** (11), 3679.

Imamura, S., Hirano, A., Kawabata, N. (1982). Wet Oxidation of Acetic Acid Catalyzed by Co-Bi Complex Oxides. *Industrial and Engineering Chemistry Product Research and Development* **21** (4), 570.

Imamura, S., Fukuda, I., Ishida, S. (1988). Wet Oxidation Catalyzed by Ruthenium Supported on Cerium(IV) Oxides. *Industrial and Engineering Chemistry Research* **27** (4), 718.

Ishii, T., Mitsui, K., Sano, K., Shishida, K., Shiota, Y. (1997). Catalyst for treating wastewater, process for producing it, and process for treating wastewater with the catalyst. U. S. 1997, 22 pp., Cont.-in-part of U.S. 5,399,541. CODEN: USXXAM US 5620610 A 19970415 CAN 126: 333881 AN 1997: 276713 CAPLUS.

Jiang, Y., Khadilkar, M.R., Al-Dahhan, M.H., Dudukovic, M.P. (2002). CFD modeling of multiphase in packed bed reactors: results and applications. *A.I.Ch.E. Journal* **48**, 716-730.

Khadilkar, M. R., Mills, P.L., Dudukovic, M. P. (1999). Trickle-bed reactor models for systems with a volatile liquid phase. *Chemical Engineering Science* **54**, 13-14, 2421-2431.

Kolaczkowski, S. T., Plucinski, P., Beltran, F. J., Rivas, F. J., McLurgh, D. B. (1999). Wet air oxidation: a review of process technologies and aspects in reactor design. *Chemical Engineering Journal* **73** (2), 143.

Krishna, R., van Baten, J. M. (1999). Rise characteristics of gas bubbles in a 2D rectangular column: VOF simulations vs experiments. *International Communications in Heat and Mass Transfer* **26**, 7, 965-974.

Kundu, A., Nigam, K.D.P., Verma, R.P. (2003). Catalyst wetting characteristics in trickle-bed reactors. *A.I.Ch.E. Journal* **49** (9), 2253-2263.

Lain, S., Broder, D., Sommerfeld, M., Goz, M. F. (2002). Modelling hydrodynamics and turbulence in a bubble column using the Euler-Lagrange procedure. *International Journal of Multiphase Flow* **28**, 8, 1381-1407.

Lange, R., Schubert, M., Dietrich**,** W., Grünewald, M. (2004). Unsteady-state operation of trickle-bed reactors. *Chemical Engineering Science* **59**, 22-23, 5355-5361.

Larachi, F., Laurent, A., Wild, G., Midoux, N. (1993). Effet de la pression sur la transition ruisselant-pulsé dans les réacteurs catlytiques à lit fixe arose**.** *Canadian Journal of Chemical Engineering* **71**, 319-321.

Larachi, F.; Bensetiti, Z.; Grandjean, B.P.A.; Wild, G. (1998). Two-Phase Frictional Pressure Drop in Flooded-Bed Reactors: A State-of-the-art Correlation. *Chemical Engineering Technology* **21**, 887-893.

Larachi, F., Laurent, A., Midoux, N., Wild, G. (1991). Experimental study of a trickle bed reactor operating at high pressure: two-phase pressure drop and liquid saturation. *Chemical Engineering Science* **46** (5-6), 1233-1246.

Lemcoff, N. O., Cukierman, A. L., Martinez, O. M. (1988). Effectiveness Factor of Partially Wetted Catalyst Particles: Evaluation and Application to the Modeling of Trickle Bed Reactors. *Catalysis Reviews: Science and Engineering* **30**, 393.

Levec, J., Pintar, A. (2007). Catalytic wet-air oxidation processes: A review. *Catalysis Today* **124** (3-4), 172-184.

Levec, J. (1990). Catalytic Oxidation of Toxic Organics in Aqueous Solution. *Applied Catalysis B: Environmental* **63**, L1.

Levec, J., Lakota, A. (1992). Liquid-Solid Mass Transfer in Packed Beds with Cocurrent Downward Two-Phase Flow. *In Heat and Mass Transfer in Porous Media*, Quintard, M., Todorovic, M., Eds., Elsevier: Amsterdam, The Netherlands, 663.

Lia, K.Y., Salcudean, M. (1987). Computer Analysis of Multi-Dimensional, Turbulent, Buoyancy-Induced Two Phase Flows in Gas-Agitated Liquid Reactors. *Computers and Fluids*, 15, 281.

Lin, S.H., Chuang, T.S., Environ, J. (1994). Wet air oxidation and activated sludge treatment of phenolic wastewater. *Sci. Health Part A-Environ. Sci. Eng. Toxic Hazard. Sub. Control* **29**, 547- 564

Lin, S. H., Chuang, T. S. (1994). Combined Treatment of Phenolic Wastewater by Wet Air Oxidation and Activated Sludge. *Toxicol. Environ. Chem.,* **44**, 243.

Lin, S. S., Chang, D. J., Wang, C., Chen, C. C. (2003). Catalytic wet oxidation of phenol by CeO2 catalystseffect of reaction conditions. *Water Research* **37**, 793.

Liu, Z., Zheng, Y., Jia, L., Zhang, Q. (2005). Study of bubble induced flow structure using PIV. *Chemical Engineering Science* **60**, 13, 3537-3552.

Luck, F. (1999). Wet air oxidation: past, present and future. *Catalysis Today*, **53** (1), 81.

Luck, F. (1996). A review of industrial catalytic wet air oxidation processes. *Catalysis Today*, **27** (1-2), 195.

Mantzavinos, D., Hellenbrand, R., Metcalfe, I.S., Livingston, A.G. (1996a). Partial wet oxidation of *p*-coumaric acid: Oxidation intermediates, reaction pathways and implications for wastewater treatment. *Water Research* **30**, 2969-2976.

Mantzavinos, D., Hellenbrand, R., Livingston, A.G., Metcalfe, I. (1996b). Catalytic wet oxidation of *p*-coumaric acid: Partial oxidation intermediates, reaction pathways and catalyst leaching. *Applied Catalysis B: Environmental* **7**, 379-396.

Mantzavinos, D., Hellenbrand, R., Livingston, A.G., Metcalfe, I.S.. (1997). Reaction mechanisms and kinetics of chemical pretreatment of bioresistant organic molecules by wet air oxidation. *Water Science and Technology*, **35**, 4, 119-127.

Martinez, O. M., Cassanello, M. C., Cukierman, A. L. (1994). Three-Phase Fixed Bed Catalytic Reactors: Application to Hydrotreatment Processes. *Trends Chem. Eng.* **2**, 393.

Masende, Z. P. G., Kuster, B. F. M., Ptasinski, K. J., Janssen, F. J. J. G., Katima, J. H. Y., Schouten, J. C. (2003). Platinum catalysed wet oxidation of phenol in a stirred slurry reactor. The role of oxygen and phenol loads on reaction pathways. *Catalysis Today*, **79-80**, 357.

Matatov-Meytal, Y. I., Sheintuch, M. (1998). Catalytic Abatement of Water Pollutants. *Industrial and Engineering Chemistry Research* **37**, 309.

Maugans, C. B., Ellis, C. (2002). Wet air oxidation: a review of commercial sub-critical hydrothermal treatment. *In Proceedings of the Annual Conference on Incineration and Thermal Treatment Technologies*, New Orleans, LA, May, p 699.

Mewes, D., Loser, T., Millie, M. (1999). Modelling of two-phase flow in packings and monoliths. *Chemical Engineering Science* **54**, 21, 4729-4747.

Mills, P. L., Dudukovic, M. P. (1984). A Comparison of Current Models for Isothermal Trickle-Bed Reactors. *Application of a Model Reaction System*. ACS Symp. Ser., **234**, 37.

Milone, C., Fazio, M., Pistone, A., Galvagno, S. (2006). Catalytic wet air oxidation of p-coumaric acid on CeO_2, platinum and gold supported on CeO_2 catalysts. *Applied Catalysis B: Environmental* **68**, 1-2, 28-37.

Minh, D.P., Gallezot, P., Besson, M. (2006). Degradation of olive oil mill effluents by catalytic wet air oxidation: 1. Reactivity of p-coumaric acid over Pt and Ru supported catalysts. *Applied Catalysis B: Environmental* **63**, 1-2, 68-75.

Miranda, M.A., Amat, A.M., Arques, A.A. (2001). Abatement of the major contaminants present in olive oil industry wastewaters by different oxidation methods: Ozone and/or UV radiation versus solar light. *Water Science and Technology* **44**, 325-330**.**

Mishra, V. S., Mahajani, V. V., Joshi, J. B. (1995). Wet Air Oxidation. *Industrial and Engineering Chemistry Research* **34** (1), 2.

Mishra, V.S., Padiyar, V., Joshi, J.B., Mahajani, V.V., Desai, J.D. (1995). Treatment of acrylonitrile plant wastewater. *Process Safety Environ Prot.* **73**, 243.

Mishra, V. S., Joshi, J. B., Mahajani, V. V. (1993). Kinetics of p-Cresol Destruction via Wet Air Oxidation. *Indian Chem. Eng.*, **35** (4), 211.

Morsi, B. I., Midoux, N., Laurent, A., Charpentier, J. C. (1982). Hydrodynamics and Interfacial Areas in Downward Cocurrent Gas-Liquid Flow Through Fixed Beds. Influence of the Nature of the Liquid. *Int. Chem. Eng.*, **22**, 141.

Morsi, B. I., Laurent, A., Midoux, N., Barthole-Delauney, G., Storck, A., Charpentier, J. C. (1981). Hydrodynamics and Gas-Liquid-Solid Interfacial Parameters of Co-Current Downward Two-Phase Flow in Trickle-Bed Reactors. *AIChE Annual Meeting*, New Orleans, LA, Nov 8-12.

Mudde, R.F., Simonin, O. (1999). Two- and three-dimensional simulations of a bubble plume using a two-fluid model. *Chemical Engineering Science* **54**, 21, 5061-5069.

Mulinacci, N., Galardi, C., Pinelli, P., Vincieri, F.F. (2001). Polyphenolic Content in Olive Oil Waste Waters and Related Olive Samples. *Journal of Agriculture and Food Chemistry* **49** (8), 3509-3514.

Najjar, W., Perathoner, S., Centi, G., Ghorbel, A. (2007). Activity and stability of (Al-Fe) pillared montmorillonite catalysts for wet hydrogen peroxide oxidation of p-coumaric acid. *Studies in Surface Science and Catalysis*, **170**, 1425-1431.

Narashiman, C.S.L., Verma, R.P., Kundu, A., Nigam, K.D.P. (2002). Modeling hydrodynamics of trickle-bed reactors at high pressure, *A.I.Ch.E. Journal* **48** (11), 2459-2474.

Nemec, D., Levec, J. (2005). Flow through packed bed reactors: 2. Two phase concurrent downflow. *Chemical Engineering Science* **60** (24), 6958-6970.

Neri, G., Pistone, A., Milone, C., Galvagno, S. (2002). Wet air oxidation of *p*-coumaric acid over promoted ceria catalysts. *Applied Catalysis B: Environmental* **38**, 321-329.

Ng, K. M., Chu, C. F. (1987). Trickle-Bed Reactors. *Chemical Engineering Progress* Nov. 55.

Nigam, K.D.P., Larachi, F. (2005)**.** Process intensification in trickle-bed reactors. *Chemical Engineering Science* **60**, 22, 5880-5894.

Oliviero, L., Barbier, J., Duprez, D. (2003). Wet air oxidation of nitrogen containing organic compounds and ammonia in aqueous media. *Applied Catalysis B: Environmental* **40**, 163.

Olmos, E., Gentric, C., Vial, C., Wild, G., Midoux, N. (2001). Numerical simulation of multiphase flow in bubble column reactors. Influence of bubble coalescence and break-up. *Chemical Engineering Science* **56**, 21-22, 6359-6365.

Ortiz-Arroyo, A., Larachi, F. (2005). Lagrange–Euler–Euler CFD approach for modeling deep-bed filtration in trickle flow reactors. *Separation and Purification Technology*, **41**, 2, 155-172.

Østergaard, K. (1968). Gas-Liquid-Particle Operations in Chemical Reaction Engineering. *In Advances in Chemical Engineering*, Academic Press: Drew, T. B., Cokelet, G. R., Hoopes, J. W., Vermeulen, T., Eds., New York, **7**, 71.

Otal, E., Mantzavinos, D., Delgado, M.V., Hellenbrand, R., Lebrato, J., Metcalfe, I.S., Livingston, A.G. (1997). Integrated Wet Air Oxidation and Biological Treatment of Polyethylene Glycol-Containing Wastewaters. *Journal of Chemical Technology and Biotechnology* **70**, 147-156.

Patria, L., Maugans, C., Ellis, C., Belkhodja, M., Cretenot, D., Luck, F., Copa, B. (2004). Advanced Oxidation Processes for Water and Wastewater Treatment, *Parsons, S., Ed., IWA Publishing*: London, p 247.

Perez, J., De la Rubia, T., Moreno, E., Martinez, J. (1992). Phenolic content and antibacterial activity of olive oil waste waters. *Environ. Toxicol. Chem.* **11**, 489-495.

Perhatoner, S., Centi, G. (2005). Wet hydrogen peroxide catalytic oxidation (WHPCO) of organic waste in agro-food and industrial streams. *Top. Catal.* **33**, 207-224.

Perkas, N., Minh, D.P., Gallezot, P., Gedanken, A., Besson, M. (2005). Platinum and ruthenium catalysts on mesoporous titanium and zirconium oxides for the catalytic wet air oxidation of model compounds. *Applied Catalysis B: Environmental* **59**, 1-2, 121-130.

Pintar, A., Levec, J. (1992). Catalytic Oxidation of Organics in Aqueous Solutions 1. Kinetics of Phenol Oxidation. *J. Catal*., 135, 345.

Poulios, I., Kyriacou, G. (2002). Photocatalytic Degradation of p-Coumaric Acid over TiO_2 Suspensions. *Environmental Technology* **23**, 179-187.

Propp, R.M., Colella, P., Crutchfield, W.Y., Day, M.S. (2000). A numerical model for trickle bed reactors, *Journal of Computational Physics* **165**, 311-333.

Pruden, B. B., Le, H. (1976). Wet air oxidation of soluble components in wastewater. *Canadian Journal of Chemical Engineering* **54** (4), 319.

Pulgarin, C., Invernizzi, M., Parra, S., Sarria, V., Polania, R., Peringer, P. (1999). Strategy for the coupling of photochemical and biological flow reactors useful in mineralization of biorecalcitrant industrial pollutants. *Catalysis Today* **54**, 341-352.

Qin, J., Zhang, Q., Chuang, K. T. (2001). Catalytic Wet Oxidation of p-chlorophenol over supported noble metal catalysts. *Applied Catalysis B: Environmental* **29**, 115.

Ramachandran, P. A., Dudukovic, M. P., Mills, P. L. (1987). Recent Advances in the Analysis and Design of Trickle-Bed Reactors. *Sadhana*, **10**, 269.

Ramachandran, P. A., Chaudhari, R. V. (1983). Three-Phase Catalytic Reactors, *Gordon & Breach*: New York.

Ranade, V.V. (2002). Computational Flow Modeling for Chemical Reactor Engineering. *Academic Press,* New York.

Ranade, V.V. (1997). Modelling of Turbulent Flow in a Bubble Column Reactor, *Transactions of IChemE*, 75A, 14-23.

Rao, V. G., Drinkenburg, A. A. H. (1985). Solid-Liquid Mass Transfer in Packed Beds with Cocurrent Gas-Liquid Downflow. *AIChE Journal* **31**, 1059.

Reinecke, N.; Mewes, D. (1996). Tomographic imaging of trickle-bed reactors. *Chemical Engineering Science* **51**, 2131-2138.

Reinecke, N.; Mewes, D. (1997). Investigation of the two-phase flow in trickle-bed reactors using capacitance tomography. *Chemical Engineering Science* **52**, 2111-2127.

Rivas, F.J., Beltran, F.J., Gimeno, O., Frades, J. (2001). Treatment of Olive Oil Mill Wastewater by Fenton's Reagent. *Journal of Agriculture and Food Chemistry* **49**, 1873-1880.

Rivas, F. J., Gimeno, O., Portela, J. R., de la Ossa, E. M., Beltran, F. J. (2001). Supercritical Water Oxidation of Olive Oil Mill Wastewater. *Industrial and Engineering Chemistry Research* **40**, 16, 3670-3674.

Robert, R., Barbati, S., Ricq, N., Ambrosio, M. (2002). Intermediates in wet oxidation of cellulose: identification of hydroxyl radical and characterisation of hydrogen peroxide. *Water Research* **36**, 4821.

Rozzi, A., Malpei, F. (1996). Treatment and disposal of olive mill effluents. *Int. Biodeterior. Biodegr.* **38**, 135-144.

Sadana, A., Katzer, J. R. (1974). Involvement of Free Radicals in the Aqueous-Phase Catalytic Oxidation of Phenol Over Copper Oxide. *J. Catal.*, **35**, 140.

Saroha, A. K., Nigam, K. D. P. (1996). Trickle-Bed Reactors. *Reviews in Chemical Engineering* **12**, 3-4, 207.

Saroha, A.K., Khera, R. (2006). Hydrodynamic study of fixed beds with cocurrent upflow and downflow. *Chemical Engineering and Processing* **45**, 6, 455-460.

Saroha, A.K., Indraneel, N. (2008). Pressure drop hysteresis in trickle bed reactors. *Chemical Engineering Science* **63** (12), 3114-3119.

Satterfield, C. N. (1975). Trickle-Bed Reactors. *AIChE Journal* **21**, 209.

Satterfield, C. N., Van Eek, M. W., Bliss, G. S. (1978). Liquid-Solid Mass Transfer in Packed Bed with Downward Cocurrent Gas-Liquid Flow. *AIChE Journal* **24**, 709.

Schwartz, J. G., Weger, E., Dudukovic, M. P. (1976). A New Tracer Method for Determination of Solid-Liquid Contacting Efficiency in Trickle-Bed Reactors. *AIChE Journal* **22**, 894.

Schubert, M., Hessel, G., Zippe, C., Lange, R., Hampel, U. (2008). Liquid flow texture analysis in trickle bed reactors using high-resolution gamma ray tomography. *Chemical Engineering Journal* **140**, 332-340.

Sederman, A.J., Gladden, L.F. (2001). Magnetic resonance imaging as a quantitative probe of gas-liquid distribution and wetting efficiency in trickle-bed reactors. *Chemical Engineering Science* **56**, 2615-2628.

Sederman, A.J., Gladden, L.F. (2005). Transition to pulsing flow in trickle-bed reactors studied using MRI, *A.I.Ch.E. Journal* **51**, 615-621.

Shah, Y. T. (1979). Gas-Liquid-Solid Reactor Design, *McGraw-Hill*: New York.

Silva, A.M.T., Castelo-Branco, I., Quinta-Ferreira, R.M., Levec J. (2003a). Catalytic studies in wet oxidation of effluents from formaldehyde industry. *Chemical Engineering Science* **58** (3-6) 963-970.

Silva, A.M.T., Marques R.R.N., Quinta-Ferreira, R.M. (2004a). Catalysts based in cerium oxide for wet oxidation of acrylic acid in the prevention of environmental risks. *Applied Catalysis B: Environmental* **47** (4), 269-279.

Silva, A.M.T., Oliveira, A.C.M., Quinta-Ferreira, R.M. (2004b). Catalytic wet oxidation of ethylene glycol: kinetics of reaction on a Mn-Ce-O catalyst. *Chemical Engineering Science* **59** (22-23), 5291-5299.

Silva, A.M.T., Quinta-Ferreira, R.M., Levec J. (2003b). Catalytic and Noncatalytic Wet Oxidation of Formaldehyde. A Novel Kinetic Model. *Industrial and Engineering Chemistry Research* **42** (21), 5099-5108.

Silva, A.M.T., Treatment of Liquid Pollutants by Catalytic Wet Oxidation, PhD Dissertation, Coimbra, 2005.

Silveston, P.L., Hudgins, R.R. (2004). Periodic temperature forcing of catalytic reactions. *Chemical Engineering Science* **59**, 19, 4043-4053.

Sokolichin, A., Eigenberger, G. (1994). Gas-liquid flow in bubble columns and loop reactors: Part I. Detailed modelling and numerical simulation, *Chemical Engineering Science*, **49**, 24, 5735-5746.

Sokolichin, A., Eigenberger, G. (1999). Gas-Liquid Flow in Bubble Columns and Loop Reactors: Part 1. Detailed Modelling and Numerical Simulation. *Chemical Engineering Science*, **54**, 2273-2284.

Sonnen, D. M., Reiner, R. S., Atalla, R. H., Weinstock, I. A. (1997). Degradation of Pulp-Mill Effluent by Oxygen and $Na_5[PV_2Mo_{10}O_{40}]$, a Multipurpose Delignification and Wet Air Oxidation Catalyst. *Ind. Eng. Chem. Prod. Res. Dev.*, **36**, 4134.

Souadnia, A., Latifi, M.A. (2001). Analysis of two-phase flow distribution in trickle-bed reactors. *Chemical Engineering Science* **56**, 5977-5985.

Souadnia, A., Soltana, F., Lesage, F., Latifi. M.A. (2005). Some computational aspects in the simulation of hydrodynamics in a trickle-bed reactor. *Chemical Engineering and Processing*, **44**, 847-854

Specchia, V., Baldi, G., Gianetto, L. (1978). Solid-Liquid Mass Transfer in Cocurrent Two-Phase Flow Through Packed Beds. *Ind. Eng. Chem. Process Des. Dev.*, **17**, 362.

Sune, S., De Sores, V. (1999). Some aspects of total catalytic oxidation of organic substances in an aqueous phase. *An. Assoc. Bras. Quim.*, **48** (3), 163.

Taghipour, F., Ellis, N., Wong, C. (2005). Experimental and computational study of gas-solid fluidized bed hydrodynamics. *Chemical Engineering Science*. **60**, No. 24, 6857-6867.

Tan, Y., Jiang, Z., Yu, G. (1999). Wet air oxidation and catalytic wet air oxidation process for wastewater treatment. *Hunanjing Gongcheng*, **17** (4), 14.

Tan, C. S., Smith, J. M. (1982). A Dynamic Method for Liquid-Particle Mass Transfer in Trickle Beds. *AIChE J.*, **28**, 190.

Tarca, L.A., Grandjean, B.P.A., Larachi, F. (2004). Embedding monotonicity and concavity in the training of neural networks by means of genetic algorithms: Application to multiphase flow. *Computers and Chemical Engineering* **28**, 1701-1713.

Tarhan, M. O. (1983). Catalytic Reactor Design, *McGraw-Hill*: New York.

Toye, D.; Marchot, P.; Crine, M.; Homer, G.L. (1994). The use of large scale computer assisted tomography for the study of hydrodynamics in trickling filters. *Chemical Engineering Science* **49**, 5271-5280.

Tung, V.X., Dhir, V.K. (1988). A hydrodynamic model for two phase flow through porous media, *International Journal of Multiphase Flow* **14**, 47-65.

Turek, F., Lange, R. (1981). Mass Transfer in Trickle-Bed Reactors at Low Reynolds Number. *Chemical Engineering Science* **36**, 569-579.

Vaidya, P. D., Mahajani, V. V. (2002). Insight into sub-critical wet oxidation of phenol. *AdV. Environmental Research* **6**, 429.

Van Baten, J. M., Krishna, R. (2002). Gas and liquid phase mass transfer within KATAPAK-S® structures studied using CFD simulations. *Chemical Engineering Science* **57**, 9, 1531-1536.

Van de Vusse, J. G., Wesselingh, J. A. (1976). Multiphase Reactors. *Proceedings of the 4th International/6th European Symposium on Chemical Reaction Engineering*, VDI: Heidelberg, Germany.

Van Landeghem, H. (1980). Multiphase Reactors: Mass Transfer and Modeling. *Chemical Engineering Science* **35**, 1912-1949.

Van Sint Annaland, M., Deen, N. G., Kuipers, J. A. M. (2005). Numerical simulation of gas bubbles behaviour using a three-dimensional volume of fluid method. *Chemical Engineering Science* **60**, 11, 2999-3011.

Van Wachem, B. G. M., Almstedt, A. E. (2003). Methods for multiphase computational fluid dynamics. *Chemical Engineering Journal* **96**, 1-3, 81-98.

Vicente, J., Rosal, R., Diaz, M. (2002). Noncatalytic Oxidation of Phenol in Aqueous Solutions. *Industrial and Engineering Chemistry Research* **41**, 46.

Wang, Y., Yang., Z., Jiang, Z., Gu, X. (1995). Advances in catalytic wet air oxidation of wastewater. *Huanjing Kexue Jinzhan*, **3** (2), 35.

Weekman, V. W. (1976). Hydroprocessing Reaction Engineering. *In Proceedings of the 4th International/6th European Symposium on Chemical Reaction Engineering*, VDI: Heidelberg, Germany.

Wild, G., Larachi, F., Charpentier, J. C. (1992). Heat and Mass Transfer in Gas-Liquid-Solid Fixed Bed Reactors. *In Heat and Mass Transfer in Porous Medi*a, Quintard M., Todorovic, M., Eds., Elsevier: Amsterdam, The Netherlands, 616.

Wild, G., Larachi, F., Laurent, A. (1991). The Hydrodynamic Characteristics of Cocurrent Downflow and Cocurrent Upflow Gas-Liquid-Solid Catalytic Fixed Bed Reactors: the Effect of Pressure. *A. Rev. Inst. Franc. Pe´tr.*, 46, 467-490.

Wilhelmi, A. R., Knopp, P. V. (1979). Wet air oxidationsAn alternative to incineration. *Chemical Engineering Progress*, **75** (8), 46.

Willms, R. S., Balinsky, A. M., Reible, D. D., Wetzel, D. M., Harrison, D. P. (1987). Aqueous-Phase Oxidation: The Intrinsic Kinetics of Single Organic Compounds. *Industrial and Engineering Chemistry Research* **26** (1), 148.

Wu, Q., Hu, X., Yue, P. L., Zhao, X. S., Lu, G. Q. (2001). Copper/MCM-41 as catalyst for the wet oxidation of phenol. *Applied Catalysis B: Environmental* **32**, 151.

Wu, Q., Hu, X., Yue, P. (2003). Kinetics study on catalytic wet air oxidation of phenol. *Chemical Engineering Science* **58**, 923.

Yang, S., Feng, Y., Wan, J., Cai, W. (2002). Catalytic wet air oxidation. *Harbin Gongye Daxue Xuebao*, **34** (4), 540.

Yoon, C. H., Cho, S. H., Kim, S. H., Ha, S. R. (2001). Catalytic wet air oxidation of p-nitrophenol (PNP) aqueous solution using multicomponent heterogeneous catalysts. *Water Science and Technology* **43** (2), 229.

Zarzycki, R., Imbierowicz, M. (2001). Mechanism and mathematical modelling of wet oxidation processes. *Chem. Inz. Ekol*., **8** (12), 1205.

Zarzycki, R., Imbierowicz, M., Zawadzka, A. (1997). Wastewater treatment by wet oxidation. *Inz. Apar. Chem.*, **36** (4), 3.

Zhang, X., Ahmadi, G. (2005). Eulerian-Lagrangian simulations of liquid-gas-solid flows in three-phase slurry reactors. *Chemical Engineering Science*. **60**, 18, 5089-5104.

Zhukova, T., Pisarenko, B. V. N., Kafarov, V. V. (1990). Modeling and Design of Industrial Reactors with a Stationary Bed of Catalyst and Two-Phase Gas-Liquid Flows. A Review. *Int. Chem. Eng.*, **30**, 57.

Zimmerman, F. J. (1950). Wet air oxidation of hazardous organics in wastewater. U.S. Patent No. 2,665,249.

PART B. CATALYTIC WET OXIDATION: CATALYST SCREENING

The second part of the thesis belongs to the kernel of this work and starts with the experimental studies on catalyst screening for the CWO remediation of simulated phenolic wastewaters. Six model phenolic acids are undertaken to accomplish several oxidation experiments with commercial and laboratory-made catalysts prepared either by wetness impregnation or co-precipitation. Manganese, copper, zinc, iron, silver and ceria based catalysts are studied addressing both the catalytic activity in terms of Total Organic Carbon conversion and catalytic stability in terms of active metal leaching to the bulk liquid as well as in the deposition of carbonaceous material on the catalyst surface. Whereas Chapter III is concerned with the comparison of pollutant removal efficiencies between different commercial and laboratorial manganese/ceria catalyst formulations, Chapter IV is devoted to manganese and copper based catalysts. Different oxidation temperatures and air pressures are investigated and reaction intermediates are followed during experimental runs by HPLC. Special emphasis is given to the synergism behaviour of the multiphase reaction system for the CWO of a global phenolic mixture and for the individual parent compounds depletion. Kinetic parameters are determined with the Generalized Kinetic Model.

III. Commercial and Laboratorial Ceria Based Catalysts for CWO of Simulated Olive Mill Wastewaters[1]

Catalytic Wet Air Oxidation (CWO) of six model phenolic acids: syringic, vanillic, *3,4,5*-trimethoxybenzoic, veratric, protocatechuic and *trans*-cinnamic acid present in wastewaters from olive oil mills was studied at different temperatures. Experiments completed in the presence of four commercially available catalysts, CuO-MnO_x/Al_2O_3, CuO-ZnO/Al_2O_3, Fe_2O_3-MnO_x and CuO-MnO_x were compared with the ones related to various catalysts prepared in our laboratory, Ag-Ce-O, Mn-Ce-O, Mn-O and Ce-O. These catalysts showed a higher effective reduction of the total organic carbon (TOC) especially when the experiments were carried out with manganese oxide supported on ceria, an alternative and powerful catalyst to treat highly contaminated wastewaters containing phenolic compounds. Along the oxidation, acetic acid and phenol were detected and quantified by HPLC as the main intermediate species. Leaching, carbon adsorption as well as texture and morphology by SEM were analyzed and formation of whiskers at the catalyst surface was observed. Moreover, the kinetic parameters were obtained and co-oxidation of the phenolic compounds in the mixture was identified in our studies.

III.1. Introduction

Olive oil mill wastewaters (OMW) are characterized by high Chemical Oxygen Demand (COD) imposing serious problems at the time of proper management and disposal. COD of this type of effluents ranges between 25 to 300 g O_2 L^{-1} in the worst of the cases. The olive oil extraction industries in the Mediterranean countries generate each year an increasing volume of wastewaters with a great pollutant influence. It is mainly due to the high organic fraction including sugars, tannins, acids, pectins, lipids, and especially phenols and polyphenols which are not amenable to conventional biological oxidation (Balice *et al*., 1990; Hamdi, 1993). It is estimated that the production passes beyond 30 million m^3/year (Fiestas and Borja, 1992).

Among the different methods traditionally used to dispose OMW, the following have been mainly applied: a) Evaporation ponds: they are meant to remove water with the aid of solar energy avoiding anaerobic fermentation (low deep ponds); however, evaporation ponds are useful only for small factories and alternative solutions should be investigated; b) disposal in soil: wastewater from olive mills has been used as a fertilizer and in the irrigation of some kind of crops; c) incineration: given the high organic load of OMW, incineration may constitute an appealing

[1] *This Chapter is based upon the publication Lopes et al. (2007)*

method to treat these residues though inherent disadvantages of incinerators (fuel costs, gas emissions, etc.) have to be balanced; d) other uses: effluents of olive mills have been utilized as a source of fermentation products, such as fat and oils preservatives.

In recent times, most of the studies about OMW treatments are focused on aerobic (Hamdi, 1993; Velioglu *et al*., 1992) or anaerobic digestion (Gharsallah, 1994; Martin *et al*., 1994). However, many problems concerning the high toxicity and the biodegradability of the effluents have been encountered during these anaerobic treatments (Hamdi, 1993; González *et al*., 1990), and the experimental results are not satisfactory: they must be conducted on a highly dilute substrate once the aromatic and phenolic compounds are toxic for methanogenic bacteria (Boari *et al*., 1984; Hamdi, 1991).

Wet oxidation (WO) is a promising alternative that has been investigated in order to decrease the amount of phenolic compounds contained in the OMW (Mantzavinos *et al*., 1996). Although the uncatalyzed oxidation study provides us with a useful insight into the partial oxidation of each acid, a more promising process for industrial application is the use of a catalyst to promote the oxidation at shorter reaction times and milder operating conditions (Mantzavinos *et al*., 1997; Minh *et al*., 2006). In fact, different excellent reviews regarding WO and CWO processes have been published (Minh *et al*., 2006; Mishra *et al*., 1995; Matatov-Meytal and Sheintuch, 1998; Imamura, 1999; Luck, 1999; Kolaczkowski *et al*., 1999; Bhargava *et al*., 2006).

Homogeneous catalysts, particularly copper salts, are in general more effective than heterogeneous oxidation catalysts (Bhargava *et al*., 2006; Taghasira *et al*., 1975; Goto *et al*., 1977; Imamura *et al*., 1982) but their use needs a separation step such as precipitation or membrane separation to remove the toxic catalyst ions from the final effluent. In this context, heterogeneous catalysts have been mostly investigated. For instance, the catalytic oxidation of phenol and substituted phenols over mixed copper, zinc and cobalt oxide catalysts was studied (Pintar and Levec, 1992) and these catalysts were effective for the destruction of phenol and substituted phenols. Recently Bhargava *et al*. (2006) systematized the catalytic effect of noble metals on wet oxidation of phenols and other model pollutant compounds and found that Ru, Pt and Rh were also more active than a homogeneous copper catalyst. In particular, high performance has been attributed to activated carbon when used as catalyst support and impregnated with different noble metals (Pd, Pt, Ru, Rh, Ir, Au) or even with more economical species, such as metal oxides (Cu, Fe, Mo, Ce), during decontamination of synthetic and actual wastewaters (Santos *et al*., 2005; Stüber *et al*., 2005; Garcia *et al*., 2006). In fact, noble metals have shown to be effective for degradation of phenolics compounds contained in OMW such as *p*-coumaric acid (Minh *et al*., 2006). Nevertheless, the high cost of this kind of materials makes important to investigate more economical catalyst.

Cu, Zn and Mn have shown good catalytic properties when applied in the CWO technology (Matatov-Meytal and Sheintuch, 1998) and in particular, Mn-Ce-O has been active for degradation of different species appertaining to different chemical groups: phenols, aldehydes, carboxylic acids and alcohols (Imamura, 1999; Larachi, 2005; Silva *et al*., 2003a; Silva *et al*., 2004a; Silva *et al*., 2004b).

Therefore, the main objective of this work addresses the search for an active, stable and economical catalyst for the treatment of OMW, as well as the characterization of the reaction system through kinetic analysis, using various catalysts prepared in the laboratory or obtained commercially. The efficiency of the non-catalytic and catalytic wet air oxidation of OMW was studied for the selected acids, major pollutants in OMW (Balice and Cera, 1984), namely: syringic (4-hydroxy-3,5-dimethoxybenzoic), vanillic (4-hydroxy-3-methoxybenzoic), 3,4,5-trimethoxybenzoic, veratric (3,4-dimethoxybenzoic), protocatechuic (3,4-dihydroxybenzoic) and trans-cinnamic. The kinetic expressions in terms of TOC (total organic carbon) were established aiming the successful design and operation of continuous CWO multiphasic chemical reactors in wastewaters treatment plants.

III.2. Experimental

III.2.1. Material and catalysts

Syringic, vanillic, 3,4,5-trimethoxybenzoic, veratric, protocatechuic and trans-cinnamic acids were obtained from Sigma-Aldrich. Commercial catalysts were supplied by the Süd-Chemie Group, Munich: $CuO–ZnO/Al_2O_3$ (G66A: CuO-41%; ZnO-47%), $Fe_2O_3–MnO_x$ (N-150: Fe_2O_3-60%; MnO_x-30%), $CuO–MnO_x/Al_2O_3$ (SG2216: CuO>25%; MnO_x >25%) and $CuO–MnO_x$ (N-140: CuO-22%; MnO_x - 50%). Mn–Ce–O and Ag–Ce–O were prepared by co-precipitation, by mixing aqueous solutions of the respective metal salts using the corresponding metal nitrates as precursors (Riedel-de-Häen and Labsolve). For Ag–Ce–O, NaOH 3 M was added until pH was equal to 10; the precipitate formed was then filtrated, washed three times with ultra pure water and dried over night at 100 ºC, followed by calcination at 300 ºC. For Mn–Ce–O the mixture of aqueous solutions was poured into 200 mL of a 3 M NaOH solution, the precipitate was filtrated and washed five times with 500 mL of ultra pure water, dried over night at 100 ºC and finally calcinated at 300 ºC. Two different molar composition ratios were studied, 70 and 22% for the active metal (Mn) and, 30 and 78% for the support (Ce), respectively. Catalytic properties of individual oxides, Mn-O and Ce-O were also investigated. Before the experiments all the catalysts used in this work were crushed in a fine powder (125-250 μm particle size) with the aim to provide maximum specific surface area for reaction and to ensure the elimination of internal diffusion resistances.

III.2.2. Oxidation reactor and procedure

The experiments were performed in a high-pressure 1 L autoclave of 316-SS (4531M Parr model) described elsewhere (Silva *et al*., 2003b), equipped essentially with a two six-bladed mechanically-driven turbine agitator and a PID temperature controller (4842 Parr model). For the catalytic screening studies, the solution of phenolic acids (1200 mg/L, 200 mg/L for each phenolic acid: syringic, vanillic, 3,4,5-trimethoxybenzoic, veratric, protocatechuic and trans-cinnamic) was introduced in the system with the powder catalyst (6 $g.L^{-1}$) and preheated up to the operating temperature (160–220 ºC). For kinetic studies six solutions of each phenolic acid with a concentration about 200 mg/L were prepared. Pure air (99.999%) was introduced into the system up to the operating pressure (30 bar total pressure) and this instant was taken as the "zero" time for reaction. Samples were withdrawn periodically from the reactor and special attention was given to the liquid sampling procedure to avoid contamination of the samples and losses of the liquid phase and/or catalyst. Liquid samples were immediately filtered and then analyzed for total organic carbon (TOC).

III.2.3. Analytical techniques

TOC was measured with a *Shimadzu 5000 TOC Analyser*, which operates based on the combustion/ nondispersive infrared gas analysis method. Total carbon (TC) was first measured followed by the measurement of the inorganic carbon (IC). The TOC was then determined by subtracting IC from TC. pH was monitored along the reactions with a HANNA instrument-HI8711E.

Reaction intermediates were analyzed in a *Knauer HPLC system* equipped with a *WellChrom K-1001 pump*. The oven from *Jones Chromatography* (model 7971) was set at 75 ºC and a SS-Column 300×8 mm inside diameter was used (10 μm particle size of a sulfonated cross-linked styrene-divinylbenzene copolymer). 100% of 0.01 N H_2SO_4 at a flow rate of 1 mL/min was used as the mobile phase. The injection volume was 20 μl while detection was typically at 280 nm. Running external standards at various concentrations the linearity between absorbance and concentration (as described by the Beer-Lambert law) was observed over the whole range of concentrations under consideration, leading to the calibration curve. Blank samples were run between two consecutive HPLC runs to ensure that no residuals from the previous run were carried over to the next one. Both the standards and the samples were periodically run in duplicate to test the reproducibility of the measurements.

Elemental analysis was used to detect carbon adsorption in catalysts with a *Fisons Instruments EA 1108* CHNS-O equipped with a pre-packed ox/red quartz reactor, operating with a flash combustion and using a thermal conductivity detector (TCD); standard solutions of phenanthrene, sulfanilamide, and BBOT (2,5-bis(5-*tert*-butylbenzoxazol-2-yl)thiophen) were obtained from Fisons Instruments. *Atomic absorption* in a spectrometer *Perkin-Elmer 3300*, with hollow cathode lamps (Cathodeon) and standard solutions from BSB-Spectrol, was used to measure the leaching of manganese to the liquid phase.

The catalyst *Brunauer-Emmett-Teller (BET) surface area analysis* (S_{BET}) and respective isotherm were determined with an accelerated surface area and porosimetry analyzer (ASAP 2000) from Micrometrics using nitrogen at a constant temperature (-196ºC). *Scanning electron microscopy* (SEM) analysis at different scales/magnifications was performed in a JEOL JSM-5310 scanning microscope.

III.3. Results and discussion

III.3.1. Catalyst screening

A preliminary experiment was performed at 200 ºC in the absence of oxygen and no degradation was detected, highlighting the important role of oxygen in the oxidation process. Figure I.1a)-c) represent the TOC reduction for the non-catalytic WO and the catalytic process when using different commercial catalyst as well as laboratorial cerium-based catalysts with molar ratios of 70/30 and 22/78 for Mn-Ce-O and 70/30 for Ag-Ce-O. At 200 ºC and 15 bar of air partial pressure it is not possible to reduce efficiently the carbon content of the solution with the non-catalytic WO, leading only to 49.1% reduction after 2h (Fig. III.1a). When a catalyst is added to the system, significant increase in reaction rate is obtained and for the commercial catalysts supported on alumina, CuO-MnO_x/Al_2O_3 (98.9%) is more active than CuO-ZnO/Al_2O_3 (88.2%), with a high initial decrease followed by a slower degradation. The results of Fig. III.1b) point out that CuO-MnO_x is more active without the Al_2O_3 support. Moreover, Fe_2O_3-MnO_x and CuO-MnO_x showed different behaviours; these catalysts have as active metal manganese oxide in both cases but the latter has more significant activity along 60 min with respect to the TOC abatement. The cerium support (Ce-O) with two different active metals, manganese and silver, revealed strong catalytic properties leading practically to complete TOC reduction at 60 min. Nevertheless, Mn-Ce-O 70/30 was even more active than Ag-Ce-O 70/30 for shorter times, as for instance at 30 min, TOC reductions of 95.9 and 92.7% were respectively obtained Therefore, while phenolic solutions are not totally oxidized in terms of TOC without the use of catalyst, reaching an asymptotic value,

cerium-based catalysts showed significant activities with complete TOC removal and higher conversions than those detected for the commercial catalysts.

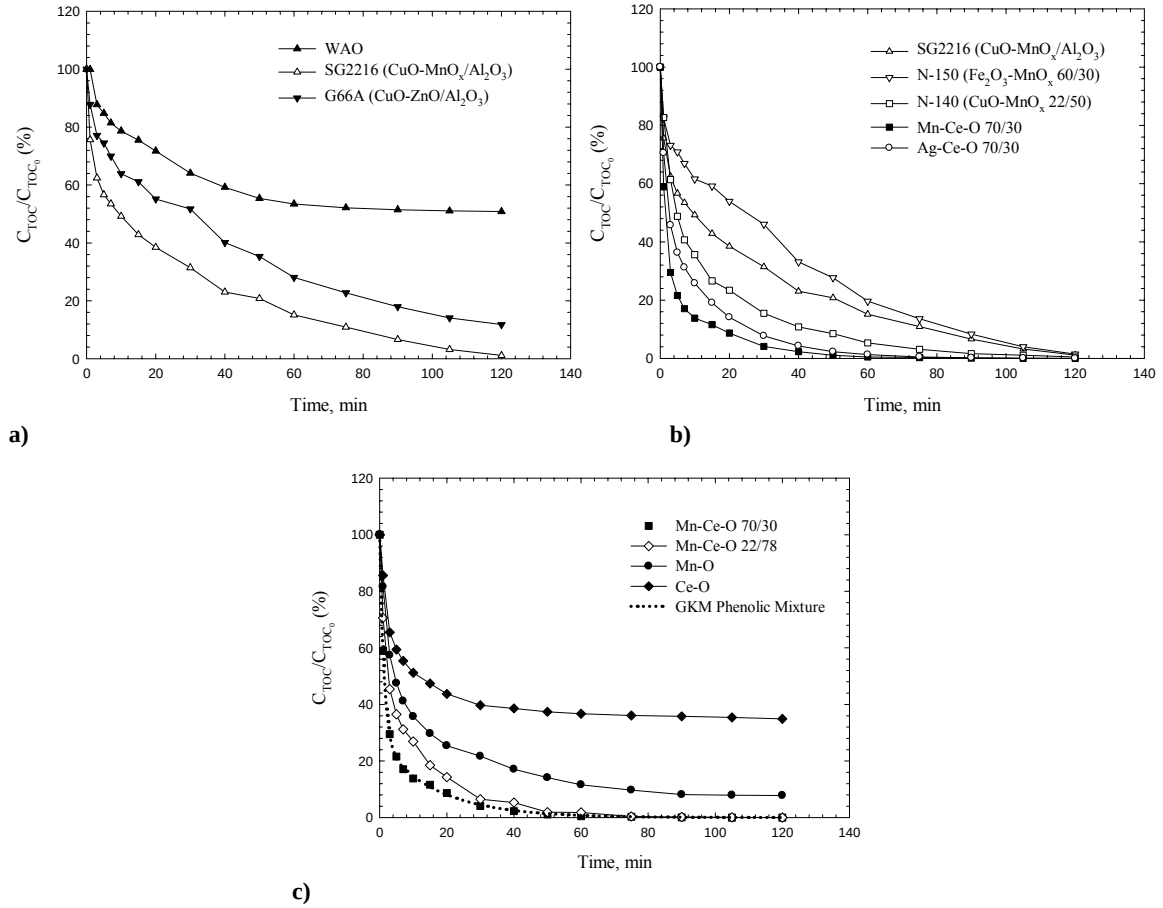

Figure III.1. Normalized TOC concentration reduction (%) as a function of time at 200ºC, 15 bar air and 3 g/L catalyst concentration for ***(a)*** non-catalytic wet oxidation and alumina supported catalysts, ***(b)*** different commercial and laboratorial catalysts, ***(c)*** cerium based laboratorial catalysts and respective oxides: Mn-O and Ce-O.

The activity of the Ce-O support is shown in Fig. III.1c) as well as for Mn-O. In previous CWO works Ce-O showed catalytic properties during the degradation of formaldehyde (Silva *et al.*, 2003a) and acrylic acid (Silva *et al.*, 2004a), while degradation was practically not observed when ethylene glycol was treated (Silva *et al.*, 2004b). Regarding the aromatic mixture used in this study, Ce-O alone present catalytic activity and probably play an important role in the catalytic activity of the Mn-Ce-O catalyst, due to the high ability of Ce-O as promoter of stored oxygen. In fact, the activity of Mn-O is increased when combined with Ce-O. Moreover, the molar ratio of Mn and Ce in the catalyst was also evaluated for 70/30 and 22/78 contents, and TOC reduction from 96.6% to 93.1% in 30 min was observed when the amount of Mn was decreased The efficiency of Mn-Ce-O 70/30 when compared to Ce-O and Mn-O has been explained in the literature as a consequence of different factors. When the cerium is mixed the manganese the concentration of Ce^{4+} increases in detriment of Ce^{3+} and the electrons of cerium seems to be

transferred to Mn, enhancing then efficient mobility of electrons and explaining the higher activity for bimetallic Mn-Ce-O catalysts. This efficiency is also related with the presence of more non-lattice oxygen (O_{II}) species in mixed oxides, which are more active than the lattice oxygen (O_I) (Silva, 2005; Chen *et al.*, 2001).

Therefore, Mn showed to be the best metal to be combined with Ce in terms of catalytic activity and, in particular, Mn-Ce-O 70/30 showed higher efficiency and higher TOC reductions in the first 30 min. When scaling-up a chemical reactor, time is a cost variable in continuous treatment, which emphasizes the great interest on the Mn-Ce-O catalyst for the CWO technology.

III.3.2. Intermediate compounds and pH

During the course of phenolic acids oxidation over Mn-Ce-O 70/30 various species were detected: (i) aromatic compounds, namely phenol and p-hydroxybenzoic acid; (ii) ring cleavage products, namely acetic acid. Fig. III.2 shows the molecular formula of the compounds used in this study and the two representative intermediates, phenol and acetic acid.

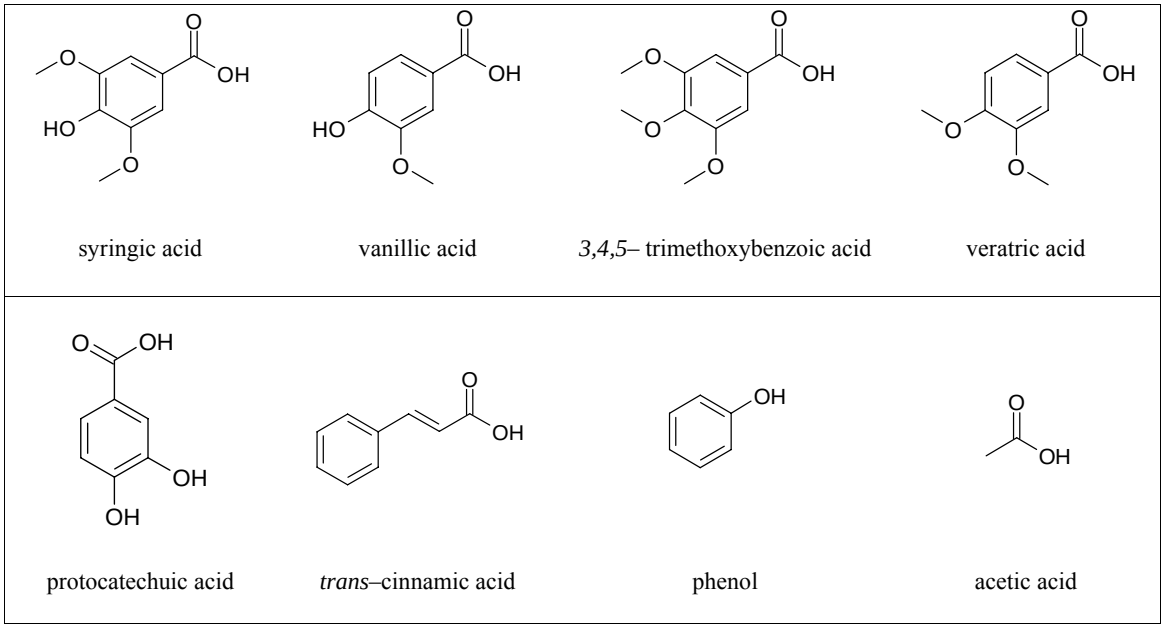

Figure III.2. The structure of phenolic acids and intermediate compounds

Fig. III.3a-b shows the concentration-time profiles for phenol and acetic acid at 200 ºC, respectively, whereas in Fig. III.3c-d it is presented the intermediates distribution as a function of TOC degradation where we can infer that during the first 10 min of oxidation the initial phenolic acids suffer a rapid conversion into intermediate compounds which are degraded slowly afterwards. Mn-Ce-O 70/30 proved once again to be the catalyst which gave faster oxidation.

Observation of intermediate compounds such as phenol and acetic acid allowed to conclude that the mechanism was followed through two routes: the decarboxylation reaction of aromatic end groups leading to phenol formation (Fig. III.3a) and an oxygen attack to the aromatic double bond to form open ring intermediate compounds such as acetic acid (Fig. III.3b).

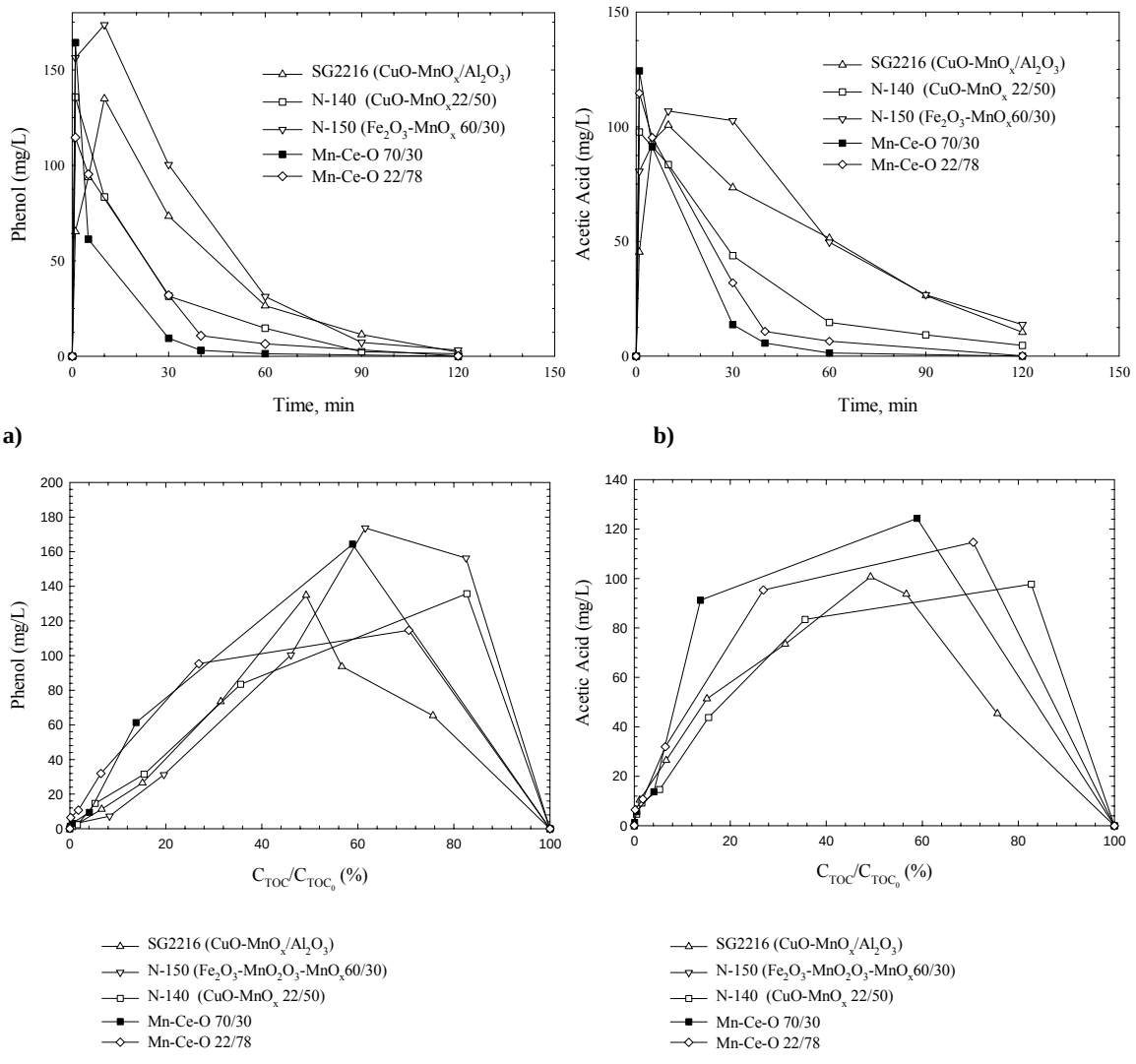

Figure III.3. Intermediate profiles of the reaction solution at 200 ºC, 15 bar air and 6 g/L catalyst catalyst as a function of time (a and b) and TOC degradation (c and d) for phenol and acetic acid.

Fig. III.4 shows a pH behaviour usually involving an initial slight decrease, probably due to formation of low weight carboxylic acids, followed by the pH growth tending to neutrality which may correspond to the high mineralization of TOC discussed early. This expected behaviour was observed for all catalysts showing, however, different rates to achieve a neutral pH.

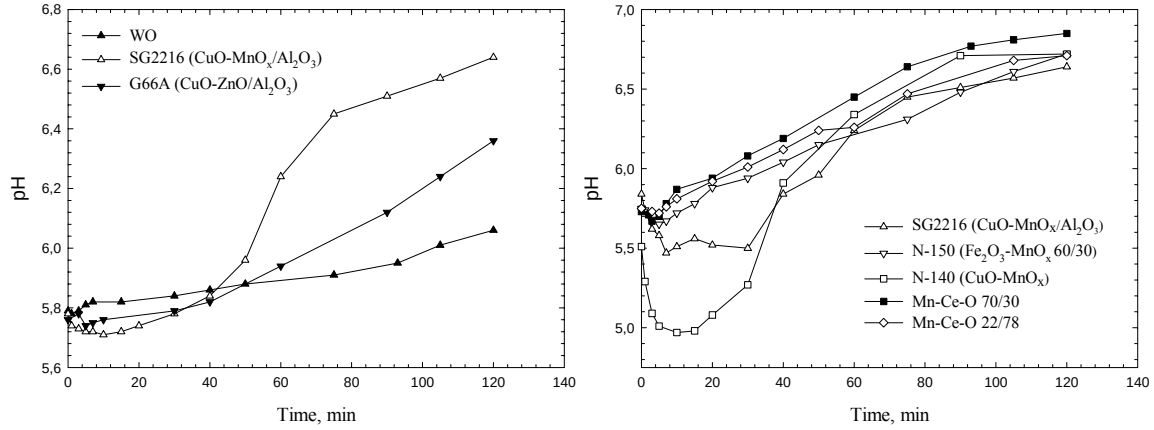

a) **b)**

Figure III.4. pH profiles of the reaction solution at 200 ºC, 15 bar air and 3 g/L catalyst concentration for ***(a)*** non-catalytic WO and alumina supported catalysts, ***(b)*** different commercial catalysts and cerium-based catalysts.

III.3.3. Catalyst characterization in terms of leaching & carbon adsorption

In order to evaluate the leaching of active species to the liquid phase that may become a second pollution source and an important catalytic deactivation factor that has to be avoided, the manganese metal was measured in terms of leaching for the experiments at 200ºC and 6 g/L of Mn-Ce-O initial concentration. After 2 hours, it was detected in the liquid phase more Mn for Mn–Ce–O 70/30 (2.67 mg/L) than for Mn–Ce–O 22/78 (1.51 mg/L). The value related to Mn–Ce–O 70/30 corresponds to 0.05% of the initial Mn concentration (2.87 g/L). Leaching of Mn with the phenolic mixture was higher than those observed in other works at the same conditions for ethylene glycol (Silva *et al*., 2004b), acrylic acid (Silva *et al*., 2004a) and formaldehyde (Silva *et al*., 2003a), respectively 0.318, 1.697 and 0.009 mg/L.

Moreover, the carbon adsorption for the Mn-Ce-O laboratorial catalyst was evaluated since deactivation has been also attributed to the formation of carbonaceous deposits on the catalyst surface irreversibly adsorbed on active sites (Santos *et al*., 2005). However, in our study low values of carbon were detected in the recovered Mn-Ce-O catalyst: 3.15% and 2.67% C (w/w) for Mn–Ce–O 70/30 and Mn–Ce–O 22/78, respectively, which corresponds to 94.5 and 80.1 mg/L of carbon in the 6.0 g/L of catalyst initially charged in the reactor and approximately 6.7% and 5.6% C (w/w) of adsorbed TOC. Therefore, practically 94% of the TOC was removed by oxidation and not by adsorption in the solid catalyst.

III.3.4. Catalyst characterization in terms of morphology

Morphology of Mn–Ce–O 70/30 was observed at different magnifications of SEM photographs for the fresh and used catalyst. For the ×200 magnification practically no differences were detected between both cases; however, with a ×3500 magnification one can observe the formation of whiskers in the used catalyst as seen in comparing fresh and used catalyst at Fig. III.5 (a) and (b), respectively. This magnification clearly shows that such filaments have different lengths up to approximately 10 μm and they can be better observed at a higher magnification (×15000). These whiskers have been identified as MnOOH and/or MnO_2 during the CWO of acrylic acid (Silva *et al*., 2004a) and ethylene glycol (Silva *et al*., 2004b).

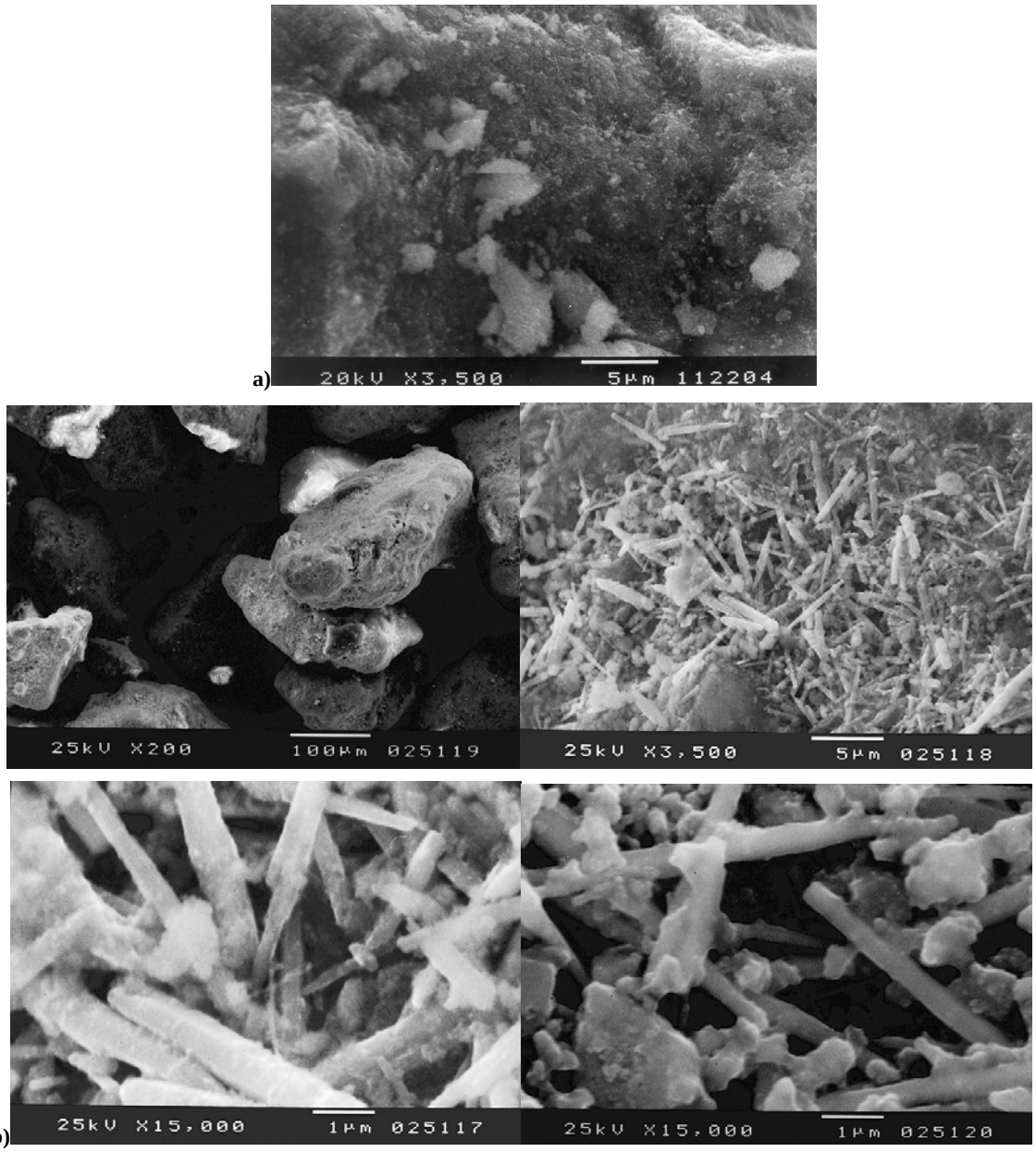

Figure III.5. SEM photographs showing different scales/magnifications for fresh (a) and used (b) Mn–Ce–O 70/30 catalyst.

The nitrogen adsorption isotherm, presented in Fig. III.6 for used Mn-Ce-O 70/30, shows a type IV isotherm with a hystersesis loop in the high range of relative pressure and suggests an intermediate behaviour between hysteresis type H1 and H3 (according to IUPAC classification). Therefore, for relative pressures higher than 0.8, condensation takes place giving a sharp adsorption volume increase, corresponding to mesoporous (20-500 Å pore diameter). The initial part of the type IV isotherm is attributed to monolayer-multilayer adsorption. The determined Brunauer-Emmett-Teller (BET) surface area (S_{BET}), 109.3 m^2/g, is similar to the one obtained for the fresh catalyst (102.5 m^2/g). Moreover, the average pore diameter was 151.4 Å which is in agreement with the range of mesoporous associated to the isotherm.

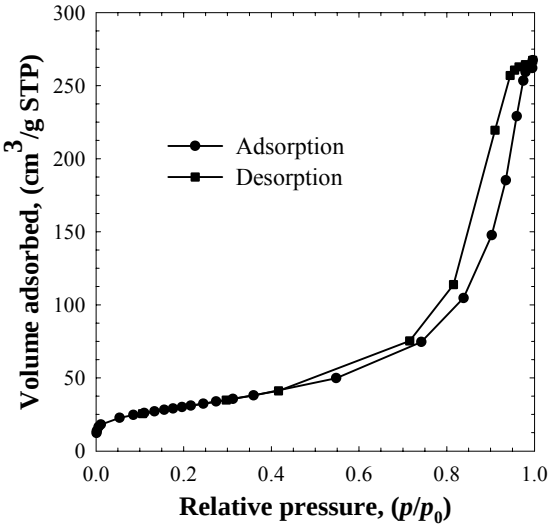

Figure III.6. Brunauer-Emmett-Teller (BET) isotherm plot for the used Mn-Ce-O 70/30 catalyst in the CWO of phenolic acids.

III.3.5. Kinetic studies of Phenolic Acids with the Mn-Ce-O 70/30 catalyst

In what concerns the kinetic studies of WO reactions, lumped kinetic models have been widely used in order to represent the experimental TOC results. The modified generalized kinetic model (MGKM, Fig. III.7a)) (Silva *et al.*, 2003b) is a global model that considers four types of compounds: easier degraded reactants (***A***); intermediates with difficult degradation (***B***); desired end products, namely carbon dioxide and water (***C***); and nonoxidizable matter (***D***). In the oxidation process of the phenolic solutions with Mn-Ce-O 70/30, phenol and acetic acid were formed as intermediate compounds, being totally degraded during the treatment and the overall TOC practically reduced to zero. In this context non-oxidizable matter (***D***) was not detected and the MGKM can be simplified to the generalized kinetic model (GKM) (Silva *et al.*, 2003). This model takes into account the degradation of ***A*** to ***C*** through a direct step (1st step), and a parallel

step (2nd step) for the degradation of ***A*** to ***B***, which is consequently degraded (by the 3rd step) in ***C***. In this model presented in Fig. III.7b, the reactions are considered as first order with respect to the TOC concentration of the reactant involved in each step *j* (m_j = 1; *j* = 1-3) and, in this context, the reaction rates of ***A*** and ***B*** are given by Equation (III.1), resulting its integration and arrangement in Equation (III.2).

$$-r_{TOC_A} = -\frac{d\,C_{TOC_A}}{dt} = \left(k_1' + k_2'\right) C_{TOC_A} \quad ; \quad -r_{TOC_B} = -\frac{d\,C_{TOC_B}}{dt} = k_3' C_{TOC_B} - k_2' C_{TOC_A} \qquad \text{(III.1)}$$

$$\frac{C_{TOC}}{C_{TOC_0}} = \frac{k_2'}{k_1'+k_2'-k_3'} e^{-k_3' t} + \frac{k_1'-k_3'}{k_1'+k_2'-k_3'} e^{-(k_1'+k_2')t} \qquad \text{(III.2)}$$

where k_j' is related to the apparent reaction rate constant. The apparent pre-exponential factor of each step *j* (A_j) and the activation energy (Ea_j) are given by the linearization of the Arrhenius equation.

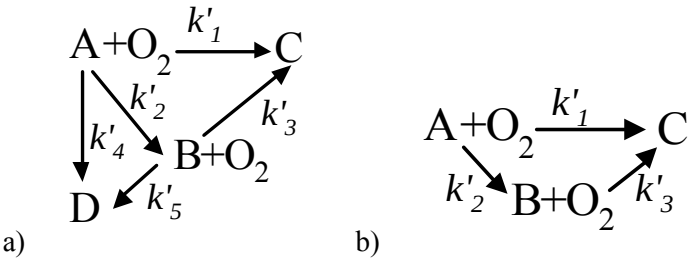

Figure III.7. Lumped reaction pathways diagram for *a)* MGKM and *b)* GKM

This model presupposes negligible mass-transfer resistance in the gas-liquid film, which was confirmed by the similar results of TOC reduction that were obtained under different agitation velocities from 50 to 350 *RPM*. Moreover, the solid was used in the original form obtained from the preparation procedure (particle size approximately up to 800 μm) and when using diameter equivalent particles in the range of 250-350 μm, similar TOC results were also obtained demonstrating the chemical regime. The good reproducibility of the experiments verified by performing different runs at the same conditions guaranteed the elimination of the experimental uncertainty transmission through kinetic calculations.

In Fig. III.8 one can observe the different oxidation rates in terms of TOC reduction for each one of the compounds present in the simulated solution when submitted separately to the CWO process. As can be inferred, these results show a crescent difficult on the degradation of those compounds by means of CWO over Mn-Ce-O by the following order: syringic acid < vanillic acid < *3,4,5*-trimethoxybenzoic acid < veratric acid < protocatechuic acid < *trans*-cinnamic acid. However, our results concerning the CWO of the global solution containing all the phenolic acids

simultaneously over the manganese oxide catalyst showed a complete reduction according to Fig. III.1c).

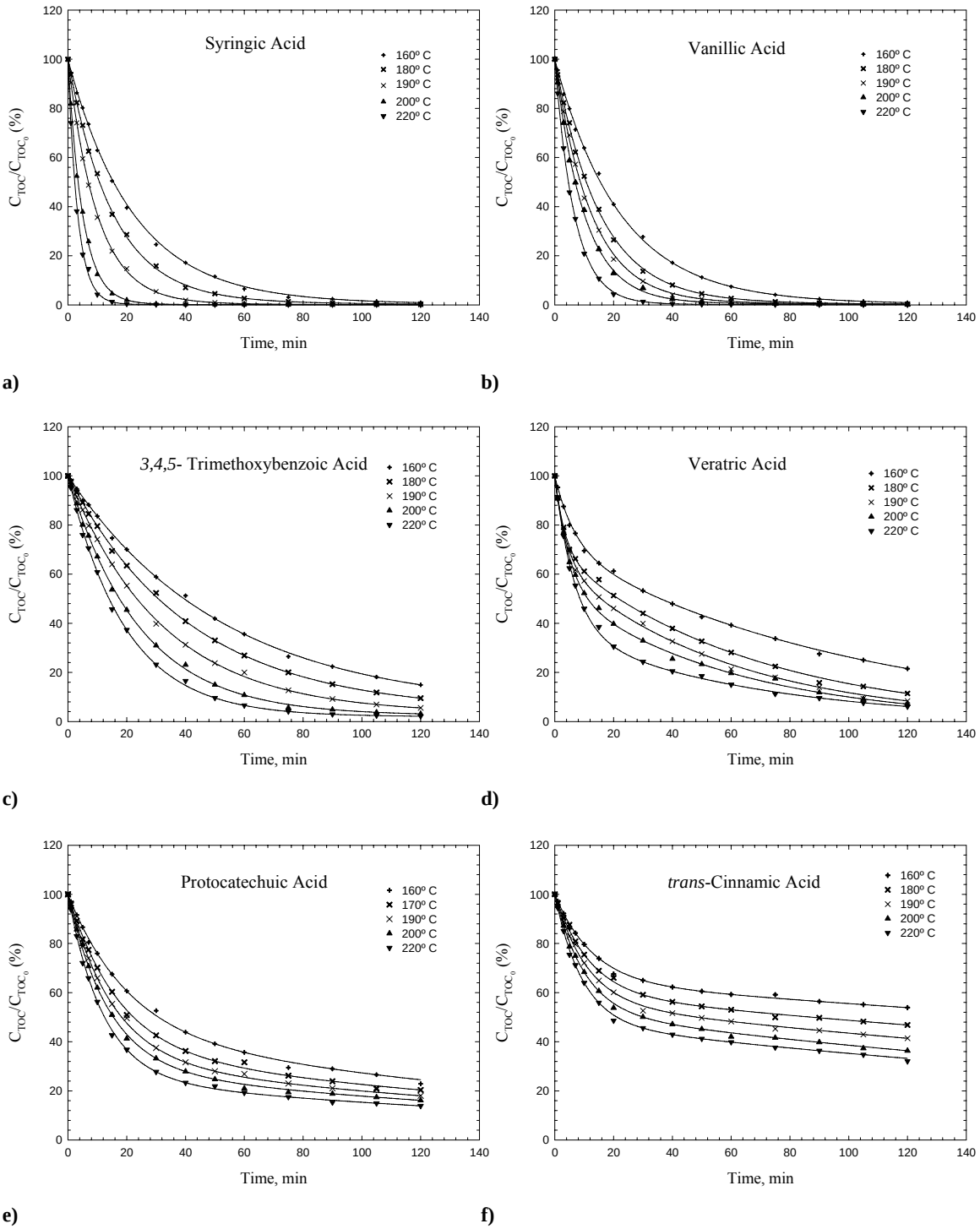

Figure III.8. Normalized TOC concentration (%) as a function of time at different temperatures, (3 g/L of Mn-Ce-O 70/30) and adjustment of the GKM, ***(a)*** syringic acid, ***(b)*** vanillic acid **,** ***(c)*** *3,4,5*-trimethoxybenzoic acid**,** ***(d)*** veratric acid**,** ***(e)*** protocatechuic acid**,** ***(f)*** *trans*-cinnamic acid.

Therefore, a different oxidation behaviour is observed when an isolated pollutant is treated and when is mixed with others. In fact, this behaviour has been also reported in some studies on CWO (Bhargava *et al*., 2006) and can be explained by a co-oxidation process. This phenomenon involves the enhancement of the degradation of a given organic compound through the free-radical intermediates produced from the oxidation of other organic compounds. As a consequence the observed rate of oxidation for a mixture of phenolic acids is much higher than the isolated compounds theoretical rate, which suggests that the oxidation reaction is free radical in nature with the active free-radical species produced from the mixture accelerating the reaction. This seems to point out that some of the results obtained in laboratorial studies with individual species can be improved in real situations due to the potential interactions with other compounds, which can favour the final treatment.

The adjustment of the kinetic model by fitting Equation (III.2) to the experimental points showed in Fig. III.8 at different temperatures gives the parameters, derived by means of *GKM* model, presented in Table III.1 for the six phenolic acids where the pre-exponential factor and the activation energy are also referred. The adjustments to the experimental points are quite good with high correlation coefficients (R^2 from 0.9954 up to 0.9998). Oxidation of phenolic acids can occur whether directly to ***C*** (1st step) or indirectly to intermediate products ***B*** and then to ***C***. In general k' values increase with temperature, and usually $k_1' > k_2' > k_3'$, what means that direct oxidation to carbon dioxide and water is more predominant than the parallel reaction to originate intermediate products, which are subsequently degraded to end products at lower reaction rate. Nevertheless, two deviations were observed: *i)* for syringic and vanillic acids $k_1' > k_3' > k_2'$, indicating that when the intermediates are produced by 2nd step, they are quickly degraded to carbon dioxide and water by the 3rd step; *ii)* for *trans*-cinnamic acid $k_2' > k_1' > k_3'$, pointing out that reaction proceeds preferentially by formation of intermediates which are difficult to be degraded (*B*) than by the 1st step. Therefore, intermediates generated by oxidation of *trans*-cinnamic acid will be present in higher amounts and further degradation will be more difficult than the one related to intermediates produced from other acids. The calculated activation energies confirm the order presented above concerning the difficulty to oxidize the TOC content related to each phenolic acid: values from 16.57 kJ/mol (for syringic acid) up to 157.74 kJ/mol (for trans-cinnamic acid) were obtained. Regarding the experiments with Mn-Ce-O 70/30 at 200ºC, Table III.2 resumes the k' values obtained with the *GKM* for the reaction of single phenolic components (Fig. III.8) as well as this table shows the k' values related to the phenolic mixture (obtained by fitting the model represented by dotted line to the experimental data in Fig. III.1c). By comparison, higher values from the kinetic determination are obtained with the phenolic mixture; this fact allows reinforcing that co-oxidation process occurs, leading to a faster oxidation due to the synergism between species.

Table III.1. Kinetic model parameters of the GKM for individual phenolic acids with Mn-Ce-O

	Syringic acid				**Vanillic acid**			
	$k_1'(min^{-1})$	$k_2'(min^{-1})$	$k_3'(min^{-1})$	R^2	$k_1'(min^{-1})$	$k_2'(min^{-1})$	$k_3'(min^{-1})$	R^2
160 ºC	0.0451	0.0448	0.0151	0.9997	0.0451	0.0012	0.0148	0.9995
170 ºC	0.0650	0.0012	0.0150	0.9998	0.0647	0.0011	0.0150	0.9984
190 ºC	0.1009	0.0048	0.0152	0.9985	0.0802	0.0013	0.0151	0.9987
200 ºC	0.2003	0.0004	0.0149	0.9988	0.1003	0.0012	0.0152	0.9994
220 ºC	0.2002	0.0005	0.0149	0.9998	0.1504	0.0005	0.0147	0.9996
Ea (kJ/mol)	16.57	19.85	53.71		18.33	24.18	67.94	
A (min^{-1})	0.61×10^{2}	2.46×10^{1}	7.93×10^{5}		0.68×10^{2}	3.17×10^{1}	5.85×10^{6}	
R^2	0.9563	0.9855	0.9628		0.9673	0.9678	0.9548	
	***3,4,5*-trimethoxybenzoic acid**				**Veratric acid**			
	$k_1'(min^{-1})$	$k_2'(min^{-1})$	$k_3'(min^{-1})$	R^2	$k_1'(min^{-1})$	$k_2'(min^{-1})$	$k_3'(min^{-1})$	R^2
160 ºC	0.0182	0.0009	0.0001	0.9998	0.0999	0.0506	0.0108	0.9985
170 ºC	0.0231	0.0010	0.0001	0.9994	0.1012	0.1901	0.0157	0.9994
190 ºC	0.0305	0.0013	0.0002	0.9996	0.1016	0.1503	0.0171	0.9983
200 ºC	0.0404	0.0010	0.0003	0.9957	0.1021	0.1016	0.0173	0.9997
220 ºC	0.0501	0.0017	0.0003	0.9978	0.1020	0.0506	0.0151	0.9997
Ea (kJ/mol)	53.65	30.91	83.64		47.03	58.43	96.31	
A (min^{-1})	1.07×10^{2}	6.37×10^{1}	7.13×10^{6}		3.58×10^{2}	2.87×10^{2}	4.15×10^{6}	
R^2	0.9563	0.9575	0.9461		0.9468	0.9857	0.9863	
	Protocatechuic acid				***trans*-Cinnamic acid**			
	$k_1'(min^{-1})$	$k_2'(min^{-1})$	$k_3'(min^{-1})$	R^2	$k_1'(min^{-1})$	$k_2'(min^{-1})$	$k_3'(min^{-1})$	R^2
160 ºC	0.0302	0.0211	0.0056	0.9992	0.0291	0.0504	0.0015	0.9974
170 ºC	0.0397	0.0216	0.0056	0.9968	0.0362	0.0505	0.0020	0.9998
190 ºC	0.0463	0.0202	0.0057	0.9997	0.0427	0.0505	0.0023	0.9996
200 ºC	0.0534	0.0208	0.0058	0.9965	0.0491	0.0506	0.0029	0.9954
220 ºC	0.0649	0.0207	0.0058	0.9985	0.0587	0.0505	0.0030	0.9991
Ea (kJ/mol)	63.76	67.72	106.04		67.62	81.56	157.74	
A (min^{-1})	1.38×10^{3}	6.17×10^{1}	4.52×10^{8}		1.46×10^{5}	0.48×10^{2}	6.15×10^{8}	
R^2	0.9869	0.9773	0.9578		0.9861	0.9728	0.9611	

Table III.2. Kinetic model parameters of the GKM at 200 ºC for phenolic mixture with Mn-Ce-O

	$k_1'(min^{-1})$	$k_2'(min^{-1})$	$k_3'(min^{-1})$
Syringic Acid	0.2003	0.0004	0.0149
Vanillic Acid	0.1003	0.0012	0.0152
3,4,5-Trimethoxybenzoic Acid	0.0404	0.0010	0.0003
Veratric Acid	0.1021	0.1016	0.0173
Protocatechuic Acid	0.0534	0.0208	0.0058
trans-Cinnamic Acid	0.0491	0.0506	0.0029
Phenolic Mixture	0.5797	0.1843	0.0588

III.4. Conclusions

Using non-catalytic WO at 200ºC and 15 bar of air it is not possible to oxidize phenolic acid more than 50% of the initial TOC. Among all the several commercial catalysts tested (G66A, SG2216, N140 and N150) as well as the ones prepared in our laboratory the Mn-Ce-O and Ag-Ce-O catalyst showed the higher activity in TOC reduction for total oxidation of polyphenols and complete abatement of the intermediate compounds formed in the reaction. The crescent order for the difficulty of degradation of the phenolic acids is syringic, vanillic, *3,4,5*-trimethoxybenzoic, veratric, protocatechuic and *trans*-cinnamic acid.

Manganese oxide supported in ceria showed to be a viable alternative of an heterogeneous catalyst to homogeneous catalysis in the total abatement of toxic organic load due to phenols, which are present in a significant amount in olive oil wastewaters. The carbon content in the solution was successfully removed by catalytic wet air oxidation at 200 ºC and 30 bar total pressure and two main intermediate compounds, phenol and acetic acid, were detected. Slight leaching of Mn was identified and the carbon content in the solution was removed by oxidation and not by adsorption on the solid catalyst.

The morphology of Mn–Ce–O 70/30 observed at different magnifications of SEM photographs revealed the formation of whiskers in the used catalyst. Therefore, in order to scale-up this technology more studies have to be done specifically related to catalytic stability of Mn-Ce-O to measure its life time in a continuous treatment. Finally, the kinetic parameters were obtained and this study highlighted a quite interesting phenomenon coming from the simultaneous treatment of various pollutants, clearly showing that the co-oxidation process is able to enhance the individual degradation of some compounds, which reinforces our strong belief on the success of this technology for real wastewaters.

III.5. References

Balice, V., Carrieri, C., Cera, O. (1990). Caratteristiche analitiche delle acque di vegetazione. *Riv. Ital. Sostanze Grasse* **67**, 9-16.

Balice, V., Cera, O. (1984). Acidic phenolic fraction of the olive vegetation water determined by a GC method. *Grasas Aceites* **35**,178-180.

Bhargava, S. K., Tardio, J., Prasad, J., Foger, K., Akolekar, D. B. and Grocott, S. C. (2006). Wet Oxidation and Catalytic Wet Oxidation. *Ind. Eng. Chem. Res.* **45** (4), 1221-1258.

Boari, G., Brunetti, A., Passino, R., Rozzi, A. (1984). Anaerobic digestion of olive oil mill wastewaters. *Agricultural Wastes* **10**, 161-175.

Chen, H., Sayari, A., Adnot, A., Larachi, F. (2001). Composition–activity effects of Mn-Ce-O composites on phenol catalytic wet oxidation. *Appl. Catal. B* **32** (3), 195-204.

Fiestas, J. A., Borja, R. (1992). Use and treatment of olive mill wastewater: current situation and prospects in Spain. *Grasas Aceites* **43**, 101-106.

Garcia, J., Gomes, H.T., Serp, Ph., Kalck, Ph., Figueiredo, J.L., Faria, J.L. (2006). Carbon nanotube supported ruthenium catalysts for the treatment of high strength wastewater with aniline using wet air oxidation. *Carbon* **44** (12), 2384-2391.

Gharsallah, N. (1994). Influence of dilution and phase separation on the anaerobic digestion of olive mill wastewaters. *Bioprocess Eng.* **10,** 29-34.

González, M.D., Moreno, E., Quevedo-Sarmiento, J., Ramos-Cormenzana, A. (1990). Studies on antibacterial activity of waste waters from olive oil mills: inhibitory activity of phenolic and fatty acids. *Chemosphere*, **20**, 423-432.

Goto, S., Levec, J., Smith, J.M. (1977). Trickle-Bed Oxidation Reactors. *Catal. Rev. Sci. Eng.* **15** (1), 187-247.

Hamdi, M. (1993). Future prospects and constraints of olive mill wastewaters use and treatment: A review. *Bioprocess Eng.* **8**, 209-214.

Hamdi, M. (1991). Effects of agitation and pretreatment on the batch anaerobic digestion of olive mil. *Bioresour. Technol.* **36** (2) 173-178.

Imamura, S. (1999). Catalytic and Noncatalytic Wet Oxidation. *Ind.Eng.Chem.Res.* **38** (5), 1743-1753.

Imamura, S., Hirano, A., Kawabata, N. (1982). Wet oxidation of acetic acid catalyzed by Co-Bi complex oxides. *Ind. Eng. Chem. Prod. Res. Dev.* **21** (4). 570-575.

Kolaczkowski, S.T., Plucinski, P., Beltran, F.J., Rivas, F.J., McLurgh, D.B. (1999). Wet air oxidation: a review of process technologies and aspects in reactor design. *Chem. Eng. J.* **73** (1999) 143-160.

Larachi, F. (2005). Catalytic wet oxidation: micro-meso-macro methodology from catalyst synthesis to reactor design. *Topics in Catalysis* **33** (1-4), 109-134.

Lopes, R., Silva, A., Quinta-Ferreira, R. (2007). Screening of catalysts and effect of temperature for kinetic degradation studies of aromatic compounds during wet oxidation. *Appl. Catal. B* **73**, 193-202.

Luck, F. (1999). Wet air oxidation: past, present and future. *Catal. Today* **53**, 81-91.

Mantzavinos, D., Hellenbrand, R., Metcalfe, I.S., Livingston, A.G. (1996). Partial wet oxidation of p-coumaric acid: Oxidation intermediates, reaction pathways and implications for wastewater treatment. *Water Res.* **30** (12) 2969-2976.

Mantzavinos, D., Hellenbrand, R., Livingston, A.G., Metcalfe, I.S. (1997). Kinetics of Wet Oxidation of *P*-Coumaric Acid over a CuO.ZnO-Al_2O_3 Catalyst. *IChemE.* **75**, 87-91.

Martin, A., Borja, R., Banks, C. J. (1994). Kinetic model for substrate utilization and methane production during the anaerobic digestion of olive mill wastewater and condensation water waste. *J. Chem. Technol. Biotechnol.* **60**, 7-16.

Matatov-Meytal, Y.I., Sheintuch, M. (1998). Catalytic Abatement of Water Pollutants. *Ind.Eng.Chem.Res.* **37** (2), 309-326.

Minh, D.P., Gallezot, P.; Besson, M. (2006). Degradation of olive oil mill effluents by catalytic wet air oxidation: 1. Reactivity of *p*-coumaric acid over Pt and Ru supported catalysts. *Appl. Catal. B* **63**, 68-75.

Mishra, V.S., Mahajani, V.V., Joshi, J.B. (1995). Wet Air Oxidation. *Ind.Eng.Chem.Res.* **34** (1), 2-48.

Pintar, A., Levec, J. (1992). Catalytic oxidation of organics in aqueous solutions: I. Kinetics of phenol oxidation. *J. Catal.* **135** (2) 345-357.

Santos, A., Yustos, P., Quintanilla, A., Ruiz, G., Garcia-Ochoa, F. (2005). Study of the copper leaching in the wet oxidation of phenol with CuO-based catalysts: Causes and effects., *Appl. Catal. B* **61** (3-4), 323-333.

Silva, A.M.T., Castelo-Branco, I., Quinta-Ferreira, R.M., Levec J. (2003a). Catalytic studies in wet oxidation of effluents from formaldehyde industry. *Chem. Eng. Sci.* **58** (3-6) 963-970.

Silva, A.M.T., Marques R.R.N., Quinta-Ferreira, R.M. (2004a). Catalysts based in cerium oxide for wet oxidation of acrylic acid in the prevention of environmental risks. *Appl. Catal. B* **47** (4), 269-279.

Silva, A.M.T., Oliveira, A.C.M., Quinta-Ferreira, R.M. (2004b). Catalytic wet oxidation of ethylene glycol: kinetics of reaction on a Mn-Ce-O catalyst. *Chem. Eng. Sci*. **59** (22-23), 5291-5299.

Silva, A.M.T., Quinta-Ferreira, R.M., Levec J. (2003b). Catalytic and Noncatalytic Wet Oxidation of Formaldehyde. A Novel Kinetic Model. *Ind. Eng. Chem. Res.* **42** (21), 5099-5108.

Silva, A.M.T., Treatment of Liquid Pollutants by Catalytic Wet Oxidation, PhD Dissertation, Coimbra, 2005.

Stüber, F., Fonta, J., Fortuny, A., Bengoa, C., Eftaxias, A., Fabregat, A. (2005). Carbon materials and catalytic wet air oxidation of organic pollutants in wastewater. *Topics in Catalysis*, **33** (1-4), 3-50.

Taghasira, Y., Takagi, H., Inagaki, K. (1975). *Chem. Abstr.* **84**, 79359.

Velioglu, S. G., Curi, K., Camlilar, S. R. (1992). Activated sludge treatability of olive oil-bearing wastewater. *Water Res.* **26**, 1415-1420.

This page intentionally left blank

IV. Manganese and Copper Based Catalysts for the Phenolic Wastewaters Remediation by CWO[1]

The catalytic wet air oxidation (CWAO) of a simulated phenolic wastewater was investigated at temperatures up to 200ºC and 15 bar of air partial pressure. Laboratorial (Mn-Ce-O 70/30 IMP, Mn-Ce-O 70/30 CP, MnCu 70/30, MnCu 50/50) and commercial catalysts (N140: CuO-MnOx 22/50) were used to evaluate the catalytic activity in terms of Total Organic Carbon (TOC). Among the manganese/cerium and manganese/copper catalysts tested with different molar ratios, Mn-Ce-O was the most active leading to the complete mineralization after 120 min of an aqueous solution containing six representative phenolic acids. The co-oxidation effect was identified when comparing the oxidation of global phenolic mixture and the individual parent compounds depletion. The catalyst preparation method had no significant differences in terms of catalytic activity. During the CWAO experiments, acetic acid and phenol were detected and measured by HPLC as the main reaction intermediate compounds. Concerning catalytic stability, manganese and copper catalyst revealed good properties in terms of active metal leaching to the bulk liquid as well as in the deposition of only 3 % (W/W) of carbonaceous material on the catalyst surface for the co-precipitated Mn-Ce-O 70/30 catalyst.

IV.1. Introduction

During the olive oil extraction and table olive production in the Mediterranean area, 30 million cubic meters per year of olive oil mill wastewaters (OOMW) are generated. The main producer countries are Spain, Italy, Greece, Tunisia, Turkey, Portugal and Syria. Alcohol distillation from different wine fractions also contributes to the huge volumetric rate of agro-industry wastewaters which became a serious environmental problem contaminating both land and aquatic ecosystems at the time of their disposal. OOMW are characterized by high levels of total organic carbon (TOC) concentration (20-85 g L^{-1}), chemical oxygen demand (COD) (40-200 g L^{-1}), biochemical oxygen demand (BOD) (12-60 g L^{-1}) and total solids content (40-150 g L^{-1}) with an acidic pH (<6) (Niaounakis and Halvadakis *et al.*, 2004) and are rich in dissolved and suspended organic substances such as sugars, phenols, nitrogenated compounds, organic acids, polyalcohols, and residual oil emulsion (DellaGreca *et al.,* 2004). These highly contaminant wastewaters exhibit a high organic and polyphenolic content which is responsible for the dark colour, phytotoxicity and antibacterial properties. Moreover, given that its main production arises in a short annual period of

[1] *This Chapter is based upon the publication Lopes and Quinta-Ferreira (2008)*

time from October to February, feasible and efficient treatment processes are needed for the OOMW remediation.

Treatment of OOMW, including physicochemical technologies (such as flocculation, ultrafiltration and reverse osmosis), biological processes (aerobic, anaerobic and combined systems) and chemical oxidation technologies have been employed for their proper disposal (Paraskeva and Diamadopoulos, 2006). In the past, OOMW have been regarded as a liquid amendment for the soil. The presence of a wide variety of organic matter and plant nutrients qualified these effluents as soil irrigation agents. OOMW is also collected in open-air lagoons and applied to soil without any further treatment. Nevertheless, these practices may cause several adverse effects on ecosystems due to the presence of unstable organic and insufficient mature matter consumable by fauna and flora. In fact, the transformation of fresh organic matter contained in OOMW into stabilized organic compounds exhibiting an humic-like behaviour that are biochemically similar to native soil humic substances, is also recommended in the literature (Sierra *et al*., 2001).

Alternative technologies have been developed to reduce these effluents based on chemical oxidations, namely, advanced oxidation processes in which the hydroxyl radicals are generated, and wet air oxidation (WAO) which uses oxygen as the oxidant at elevated temperature and pressure (Mantzavinos and Psillakis, 2004; Cañizares *et al.,* 2007). In order to reduce the refractory contaminants, chemical oxidations based on UV radiation are increasingly tested for the reduction of organic contaminants present in a variety of wastewaters from different industrial plants but this methodology is time consuming so that it has been necessary to develop more effective processes for the destruction of the contaminants. Taking into account the toxicity and non-biodegradability of OOMW, in the last decade wet air oxidation appears as one promising technology that has conquered an increasing interest as a suitable option for pollution abatement (Bhargava *et al.,* 2006). Indeed, with the application of a solid catalyst, the process can be conducted at milder operating conditions and it may be greatly improved towards the complete mineralization. Several heterogeneous catalysts have been investigated for the oxidation of various organic compounds being the majority characterized by mixed oxides mainly based on CuO, FeO, ZrO, RuO, ZnO, AgO, PdO, PtO or other noble metals on different supports) (Matatov-Meytal and Sheintuch, 1998; Bhargava *et al.,* 2006; Garcia *et al.,* 2006; Levec and Pintar, 2007; Cybulski, 2007). In spite of the high efficiency exhibited in the oxidation of various pollutants and industrial wastewaters, the ruthenium catalysts supported on titanium or zirconium oxides are expensive, so that this work is devoted for the evaluation of laboratorial and commercial catalysts based on less expensive manganese and copper oxides.

The main objective of this work addresses the catalytic activity (in terms of TOC) as well as catalytic stability (expressed as active metal leaching and carbon adsorption on the catalyst surface) for the treatment of simulated OOMW, after the optimization of the reaction system. Major pollutants in OOMW (Mulinacci *et al.,* 2001): syringic (*4*-hydroxy-*3,5*-dimethoxybenzoic), vanillic (*4*-hydroxy-*3*-methoxybenzoic), *3,4,5*-trimethoxybenzoic, veratric (*3,4*-dimethoxybenzoic), protocatechuic (*3,4*-dihydroxybenzoic) and *trans*-cinnamic are used to simulate the phenolic content of industrial wastewaters.

IV.2. Experimental

IV.2.1. Material and catalysts

Syringic, vanillic, 3,4,5-trimethoxybenzoic, veratric, protocatechuic and trans-cinnamic acids were obtained from Sigma-Aldrich. Mn-Ce-O and MnCu catalysts were prepared by co-precipitation (CP), by mixing aqueous solutions of the respective metal salts using the corresponding metal nitrates as precursors (Riedel-de-Häen and Labsolve). The solution was poured into 200 ml of a 3 M NaOH solution. The precipitate was filtrated and washed five times with 500 ml of ultra pure water and dried over night at 105ºC and finally calcinated at 300ºC. Mn-Ce-O was also prepared by wetness impregnation (IMP). This method consisted in putting in contact 40 g of the support with 200 mL of an aqueous solution of Mn metal precursor. The solution was mixed during 30 min and further dried at 105ºC. The dried catalyst was crushed in a fine powder (125-250 μm particle size) in order to provide with high specific surface area for reaction and calcination was carried out at 300ºC. Different molar composition ratios were studied, 70 and 30% for the manganese/cerium oxide, and 70, 50 and 30% for the manganese/copper oxides. Commercial catalyst was supplied by the Süd-Chemie Group, Munich: CuO–MnO_x (N-140: CuO-22%; MnO_x - 50%). Several catalyst loads were investigated in the range 1.5-6.0 g/L with the original and sieved catalyst diameter, d_p. Sieve analysis was carried out for measuring particle size distribution. The original size obtained from the preparation procedure was approximately 900 μm and after mechanical sieving, d_p was in the range of 250-350 μm.

Several Mn/Ce 70/30 samples were prepared by using different drying/calcinations temperatures aiming to analyse the influence on the BET areas of the drying and calcination temperatures. The BET results obtained through gaseous adsorption analysis for the drying/calcination pairs as follows: 100ºC/300ºC, 80ºC/500ºC, 100ºC/500ºC, indicate that the increase on the drying temperature, from 80ºC to 100ºC had no effect on the surface area (94 m^2/g). Conversely, when different calcination temperatures were used, namely 300ºC and 500ºC, a significant variation in the BET surface area was observed, from 102 to 94 m^2/g. Therefore, the catalyst samples will have

lower surface areas when higher temperatures are used. Regarding laboratory-made copper catalysts, the catalysts BET surface areas were: MnCu 50/50 – 145.98 m^2/g) and MnCu 70/30 – 138 m^2/g, whereas the commercial catalyst N140 had 161 m^2/g.

IV.2.2. Oxidation reactor and procedure

The oxidation experiments were carried out in a 316-SS high-pressure 1 L autoclave (Parr Instrument Company, model 4531M) equipped with two six-bladed mechanically driven turbine agitator and a PID temperature controller (4842 Parr model) described elsewhere (Silva *et al.*, 2003a). The thermocouple and liquid sample line are immersed in the solution and the system allows operating conditions up to 130 bar and 350ºC being air flow controlled by an electronic mass flow controller (Hastings). The solution of phenolic acids (1200 mg/L, 200 mg/L for each phenolic acid: syringic, vanillic, 3,4,5-trimethoxybenzoic, veratric, protocatechuic and trans-cinnamic) was introduced in the system with the powder catalyst (1.5-6 $g.L^{-1}$) and preheated up to the operating temperature (160-220 ºC) under different agitation velocities from 100 to 400 *RPM*. For the catalytic activity studies in terms of individual phenolic compounds depletion, six solutions of each phenolic acid with a concentration about 200 mg/L were prepared. Pure air (99.999%) was introduced into the system up to the operating pressure and preserving it at 15 or 30 bar total pressure during the catalytic runs. The "zero" time for reaction was taken at the first injection of oxidant. Samples were withdrawn periodically from the reactor and special attention was given to the liquid sampling procedure to avoid contamination of the samples and losses of the liquid phase and/or catalyst. Liquid samples were immediately filtered with a 316-SS filter with 0,5 μm pore sizes (Swagelok) to avoid catalyst particles in the samples withdrawn from the reactor and then analyzed for total organic carbon (TOC). The complete experimental setup on how air was sparged into the autoclave and how the total operating pressure was kept constant can be found in the work of Silva *et al.* (2003a).

IV.2.3. Analytical techniques

TOC was measured with a *Shimadzu 5000 TOC Analyser*, which operates based on the combustion/ nondispersive infrared gas analysis method. The parameter uncertainty in TOC measurement, quoted as the deviation of three separate measurements, was never larger than 2% for the range of the TOC concentrations. pH was monitored along the reactions with a HANNA instrument-HI8711E.

Intermediate compounds formed during the oxidation runs were analyzed in a *Knauer HPLC system* equipped with a *WellChrom K-1001 pump*. The oven from *Jones Chromatography* (model 7971) was set at 75 ºC and a SS-Column 300×8 mm inside diameter was used (10 μm particle size

of a sulfonated cross-linked styrene-divinylbenzene copolymer). 100% of 0.01 N H_2SO_4 at a flow rate of 1 mL/min was used as the mobile phase. The injection volume was 20 μl while detection was typically at 280 nm. Blank samples were run between two consecutive HPLC runs to ensure that no residuals from the previous run were carried over to the next one. Both the standards and the samples were periodically run in duplicate to test the reproducibility of the measurements.

Elemental analysis was used to detect carbon adsorption in catalysts with a *Fisons Instruments EA 1108* CHNS-O equipped with a pre-packed ox/red quartz reactor, operating with a flash combustion and using a thermal conductivity detector (TCD); standard solutions of phenanthrene, sulfanilamide, and BBOT (2,5-bis(5-*tert*-butylbenzoxazol-2-yl)thiophen) were obtained from Fisons Instruments. *Atomic absorption* in a spectrometer *Perkin-Elmer 3300*, with hollow cathode lamps (Cathodeon) and standard solutions from BSB-Spectrol, was used to measure the leaching of manganese to the liquid phase.

IV.3. Results and discussion

IV.3.1. Catalytic Activity in terms of TOC depletion

The catalytic activity of laboratorial and commercial manganese catalysts was investigated in terms of Total Organic Carbon depletion of the phenolic acids mixture. According to Fig. IV.1, catalytic wet air oxidation using Mn-Ce-O 70/30 was compared with non-catalytic (WO) and thermolysis treatments, the last one carried out in the absence of oxygen and catalyst.

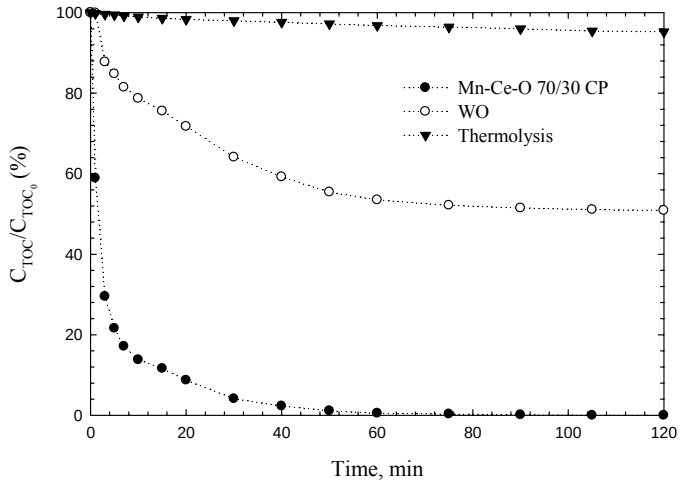

Figure IV.1. TOC reduction as a function of time for different non-catalytic (thermolysis, WO) and catalytic treatments (6 g/L Mn-Ce-O CP 70/30, 200ºC, 15 bar Air).

After 2 h, only 4.8% TOC reduction was achieved with thermolysis and 49.1 % for non-catalytic wet oxidation. Therefore, at 200 ºC and 15 bar of air, the non-catalytic treatments are not able to reduce efficiently the TOC content of the phenolic solution. However, when Mn-Ce-O catalyst (6 g/L) was added to the system, it was possible to obtain 95.9% TOC conversion after 1h being the complete TOC removal reached after 2h. Therefore, thermolysis or wet oxidation are not suitable for the phenolic solutions treatment without the use of an active catalyst.

The TOC profiles of the phenolic acids mixture achieved with laboratorial (Mn-Ce-O 70/30 IMP, Mn-Ce-O 70/30 CP, MnCu 70/30 and MnCu 50/50) and commercial (N140: CuO-MnO_x 22/50) catalysts were plotted in Fig. IV.2. According to these results, all the catalysts led to TOC reductions higher than those obtained in the experiments without catalyst (Fig. IV.1), which points out that the presence of a catalyst is of paramount significance for the oxidation of phenolic wastewaters. Moreover, after 120 min of reaction, almost complete mineralization was achieved for all catalysts either laboratorial or commercial so that the discussion is centred on intermediate times that are of particular interest in further pilot plant or industrial implementation of catalytic wet air oxidation. Specifically, after 15 min, the following decreasing order of catalytic activity can be established: Mn-Ce-O 70/30 IMP (91.6%) > Mn-Ce-O 70/30 CP (88.4%) > MnCu 70/30 (78.7%) > N140 (73.4%) > MnCu 50/50 (69.7%), where IMP and CP correspond to the Mn-Ce-O prepared via wetness impregnation and co-precipitation, respectively. Bearing in mind that catalytic activity can depend on the catalyst preparation method, the CWAO of phenolic solutions were carried out over manganese/cerium oxides either prepared by wetness impregnation or co-precipitation.

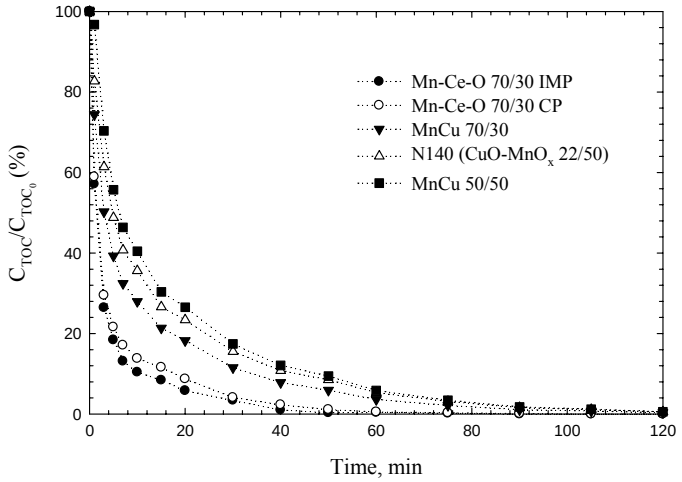

Figure IV.2. TOC reduction as a function of time for different laboratorial (Mn-Ce-O 70/30 IMP, Mn-Ce-O 70/30 CP, MnCu 70/30, MnCu 50/50) and a commercial one (N140: CuO-MnO_x 22/50) at 200ºC, 15 bar Air and 6 g/L of Mn-Ce-O CP 70/30.

According to Fig. IV.2, a minor dependence on the preparation method was observed leading roughly to the same TOC removal results. The higher difference in terms of TOC profiles for the two catalyst preparation methods, co-precipitation and wetness impregnation, was 3.2% TOC reduction observed at 15 min. Indeed, the manganese-based catalyst prepared by wetness impregnation shows better results with higher than 90% conversions for 15 min and 95% after 30 min, while the MnCu 70/30 exhibits a TOC conversion of 88%. For the same operating time, the commercial catalyst (N140) revealed a TOC conversion of 84.5%, a value between the MnCu laboratory-made catalysts with different molar compositions. The higher manganese content in the catalyst leads to the higher TOC conversion for the same residence time. The manganese metal revealed a major effect in the carbon content depletion in comparison with the copper metal. The effect of temperature and pressure on the CWAO using the Mn-Ce-O CP 70/30 catalyst is plotted in Fig. IV.3. The TOC degradation of the phenolic acids mixture obtained with different temperatures (160 and 200ºC) and different pressures (15 and 30 bar) demonstrated that temperature has more influence than the pressure. Fig. IV.1 illustrated the effect of the oxidant on the TOC removal so that when an experiment is accomplished in the absence of oxygen (thermolysis) the degradation of organic matter does not occur with relevant extension, which means that oxygen has an important role in the process. When carrying out an experiment at 160ºC and 30 bar, the TOC conversion was 64.2% whereas at 200ºC and 30 bar it was 88.4%, after 15 min. Therefore, a temperature increment of 40ºC resulted in a considerable acceleration of the reaction rate in the initial reaction times. However, maintaining the temperature at 200ºC and with an increase of 15 bar, the TOC removal changed from 83.8 to 88.4% showing that TOC depletion was scarcely affected by increasing air partial pressure. Nevertheless, the influence of temperature and pressure on the carbon content removal was reduced along the reaction time until both operating variables did not affect TOC conversion for residence times larger than 60 min.

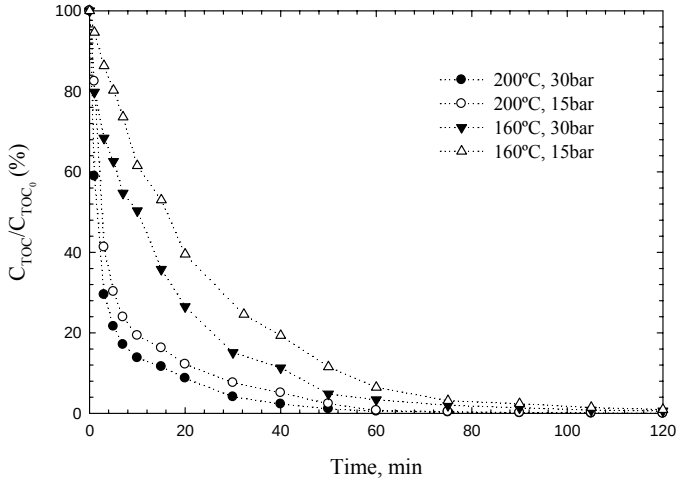

Figure IV.3. TOC reduction as a function of time for different temperatures (160-200ºC) and different air partial pressures (15–30 bar) and 6 g/L of Mn-Ce-O CP 70/30.

In order to evaluate the mass and heat transfer resistance in the gas–liquid film, several catalytic experiments were performed with the phenolic acids mixture varying the catalyst mass (1.5 – 6 g/L) and the agitation velocity in the range 100-400 RPM. The gas-side mass-transfer resistance was estimated to be negligible because of the very high diffusivity of oxygen in the gas phase and its low solubility in water. To check the liquid-phase mass-transfer resistance, the effect of impeller speed on TOC reduction of phenolic acids mixture was studied with Mn-Ce-O CP 70/30 at 200 ºC and 15 bar Air. However, the rate of oxidation was found to be independent of the impeller speed in a range of 350-400 *RPM*, indicating that there were no resistances associated with the oxygen transfer. The oxidation experiments were therefore carried out at 350 *RPM*. Fig. IV.4a) shows the effect of the mass of catalyst and differences were not detected. Moreover, practically the same TOC results were observed when the solid was used in the original form obtained from the preparation procedure (particle size approximately up to 900 μm) and when using particles in the range of 250-350 μm. According to Fig. IV.4b), the agitation velocity seems to have more effect on the TOC degradation with impeller speeds below 300 *RPM* so that the optimum velocity was fixed in 350 RPM to eliminate its effect on the external resistances of the reaction system.

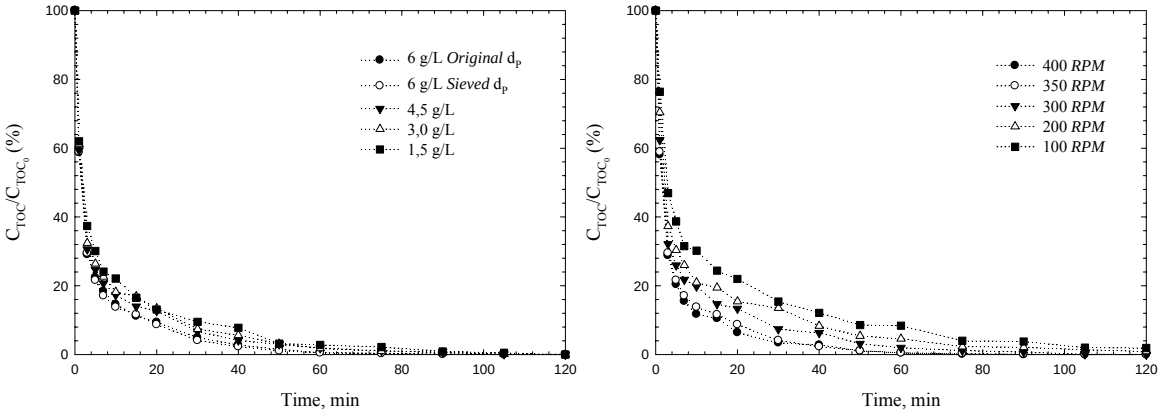

a) **b)**

Figure IV.4. Evolution of the TOC concentration: **a)** different mass of Mn-Ce-O CP 70/30 (200 ºC; 15 bar Air) and different catalyst particle sizes: original size (approximately up to 900 μm) and in the range of 250-350 μm; **b)** different agitation velocities

IV.3.2. Catalytic activity in terms of individual phenolic compounds depletion

The individual concentration of syringic, vanillic, *3,4,5*-trimethoxybenzoic, veratric, protocatechuic and *trans*-cinnamic acids were monitored by HPLC analysis along the catalytic oxidation of each individual phenolic acid. For this purpose, six solutions of each phenolic acid with a concentration about 200 mg/L were prepared and for each catalytic run a single phenolic acids solution was loaded into the batch reactor. In Fig. IV.5, the corresponding concentration

profiles are plotted for each one of the individual phenolic acids in various catalytic systems: a) Mn-Ce-O 70/30 IMP, b) Mn-Ce-O 70/30 CP, c) MnCu 70/30, d) N140 and e) MnCu 50/50.

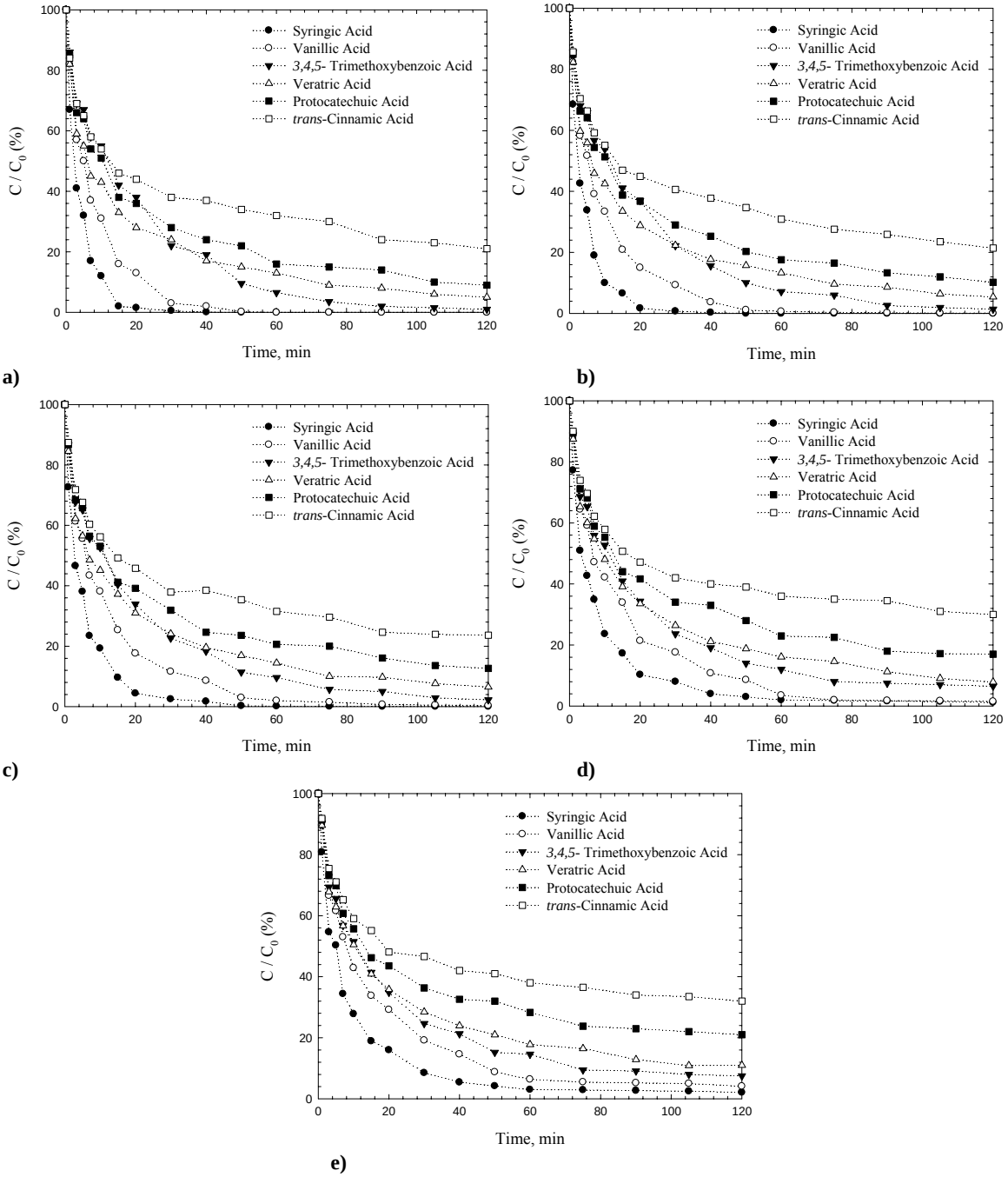

Figure IV.5. Individual phenolic acids oxidation for different catalytic systems(6 g/L, 200 ºC, 15 bar Air): **a)** Mn-Ce-O 70/30 IMP, **b)** Mn-Ce-O 70/30 CP**, c)** MnCu 70/30, **d)** N140 and **e)** MnCu 50/50

Among all catalysts, manganese/cerium oxides were the ones with higher degradation rates (Fig. IV.5a) and b)). Once more, their catalytic activity did not depend on the catalyst preparation method. After 30 min of oxidation performed with Mn-Ce-O 70/30 IMP catalyst, the conversions were 99.5%, 97.1%, 78.1%, 75.9%, 72% and 61% for syringic, vanillic, *3,4,5*-trimethoxybenzoic,

veratric, protocatechuic and *trans*-cinnamic acids, respectively, whereas with Mn-Ce-O 70/30 CP catalyst, 99.2%, 90.7%, 77.8%, 77.7%, 71% and 59.4% were detected. These minor differences were of the same order of those observed in Fig. IV.2. Moreover, the established decreasing order of catalytic activity in terms of TOC degradation is the same that are now evidenced in terms of individual phenolic acid depletion. In spite of this concordance, Fig. IV.5 a)-e) showed an interesting effect that is related with the overall conversion attained after 120 min. Concerning the CWAO of the six phenolic acids solution, whatever catalyst is used Fig. IV.2 showed that the mineralization is complete. Nevertheless, the individual catalytic oxidation of each phenolic acid revealed that the mineralization is incomplete for the same run time.

This fact has been reported in literature as a co-oxidation phenomenon and it has been also observed recently for manganese/cerium catalysts (Lopes *et al.,* 2007). Co-oxidation of the phenolic mixture involves the oxidation of a phenolic compound by free-radical intermediates produced from another phenolic compound. The interaction between organic compounds during WO of mixtures of organic compounds has a strong influence on the rates of removal comparing Figs. 1 and 5. It is clear from now on that this improvement does not depend on the catalyst used; indeed the catalytic activity seems to be more conditioned by the phenolic compound. Consequently, a mixture of aromatic or even other organic compounds may speed up the oxidation rate due to the synergism between pollutants as already shown by Shende and Levec (2000) on the subcritical aqueous-phase oxidation kinetics of unsaturated carboxylic acids: acrylic, maleic, fumaric, and muconic acids. These carboxylic acids have been observed as intermediate products in wet oxidation of phenols and a homogeneous radical mechanism is generally proposed as the reaction pathway. Additionally, there have been several studies that have provided indirect experimental evidence of co-oxidation (Mantzavinos *et al.*, 1996; Birchmeier *et al*., 2000). Imamura (1999) reported that the observed rate of oxidation for a mixture of high- and low-molecular-weight poly(ethylene glycol)s is much higher than the theoretical rate of oxidation and claimed that the oxidation reaction is free radical in nature and the active free-radical species produced from the more-fragile polymers attack low-molecular-weight and accelerate the reaction. Moreover, this phenomenon has been used as one method to indirectly determine if free-radical reactions are occurring during wet oxidation (Tardio *et al*., 2004).

Syringic acid was the most reactive phenolic pollutant being practically oxidized in the first 30 min with manganese/cerium catalysts and around 60 min for manganese/copper ones. In fact, it was in the initial reaction times that the higher oxidation rates were confirmed, and afterwards the conversion profile changed slowly corresponding to the formation and degradation of intermediate compounds with reasonable refractory power. Conversely, *trans*-cinnamic acid appeared as the one with the lower degradation rates for all catalysts. After 2h, the conversions were 79%, 78.5%,

76.4%, 69.8% and 67.9% for Mn-Ce-O 70/30 IMP, Mn-Ce-O 70/30 CP, MnCu 70/30, N140 and MnCu 50/50, respectively.

IV.3.3. pH and Intermediate Compounds

The pH of phenolic solutions was monitored along the oxidation treatment for all laboratorial and commercial catalysts. According to Fig. IV.6, all catalytic experiments exhibited the same trend with an initial pH decrease followed by a significant increase, namely for the manganese-copper catalysts. The minimum value of pH (4.9) was also observed for the MnCu catalysts whereas the maximum value (6.9) was detected for the manganese cerium oxides. For copper catalysts, either laboratorial or commercial, the considerable initial decrease of pH can be related with the slower TOC degradation rate observed in Fig. IV.2 for the same reaction time. For Mn-Ce-O catalyst the initial increase in TOC conversion was followed by a regular increase in pH that can be explained by the formation of end products: carbon dioxide and water, and after 1h, when the TOC conversion being almost complete reached a plateau, the corresponding pH increased slowly. Given that phenolic solution is initially acid, after 20 min it can be seen that Mn-Ce-O IMP catalyst is the one that revealed the higher value of pH. This fact seems to be related with the fastest TOC degradation rate observed for that catalyst (Fig. IV.2) that led to higher values of pH towards the solution mineralization, in terms of carbon content, and neutralization, in terms of pH. Slight pH differences were detected for both cerium catalysts either prepared by wetness impregnation or co-precipitation corresponding to the minor differences TOC conversions between both.

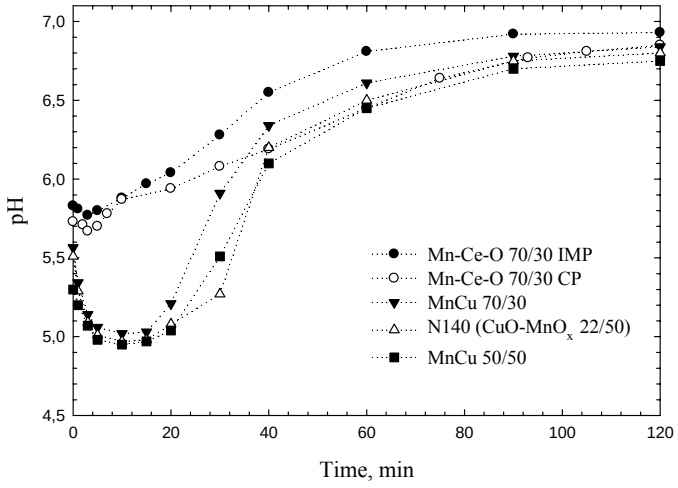

Figure IV.6. pH profiles of the reaction solution at 200 ºC, 15 bar Air and 6 g/L catalyst concentration for: Mn-Ce-O 70/30 IMP, Mn-Ce-O 70/30 CP**,** MnCu 70/30, N140 and MnCu 50/50

As the pH evolution is directly related with the reaction pathway, the intermediate compounds were also quantified by HPLC. During the oxidation course, phenol and acetic acid were detected

and its concentration profiles are shown in Fig. IV.7. The ring cleavage and low weight carboxylic acid products were found as major intermediaries in the CWAO treatment being possible to advance that the mechanism followed the decarboxylation reaction route of aromatic end groups leading to phenol formation, and an oxygen attack to the aromatic double bond resulting in the formation of intermediate compounds such as acetic acid.

For all the manganese catalysts tested (Fig. IV.6), the initial pH decrease can be related with the formation of low weight carboxylic acids such as acetic acid that may be potential intermediates products of the reaction. In fact, in the first 10 min of reaction the concentration profiles for acetic acid and phenol shown in Fig. IV.7 indicated the major production rates of these intermediate compounds. Following the initial pH decrease, a further increase more pronounced for manganese/copper catalysts should be due to the formation of carbon dioxide and water. After 1 h, pH did not change significantly most likely due to its slower TOC degradation rate in both copper and cerium catalysts. In what regards the Mn-Ce-O catalysts prepared by wetness impregnation and co-precipitation, minor variations were again observed for acetic acid and phenol concentration profiles being practically oxidized in the first hour of reaction time. Therefore, manganese/cerium catalyst revealed the highest catalytic activity towards the complete mineralization in shorter operating times.

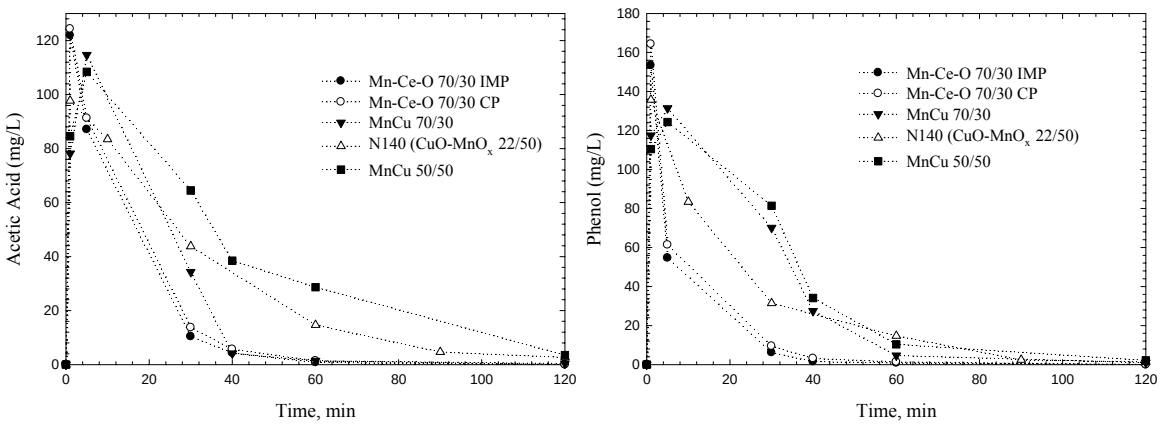

a) **b)**

Figure IV.7. **a)** Acetic acid and **b)** Phenol concentrations as a function of time for: Mn-Ce-O 70/30 IMP, Mn-Ce-O 70/30 CP**,** MnCu 70/30, N140 and MnCu 50/50

IV.3.4. Catalysts stability in terms of leaching and carbon adsorption

Concerning further industrial application of CWAO, the catalyst has not only to be active but it should be also stable in terms of premature deactivation. The most significant deactivation factors investigated in the literature are the active metal leaching from the catalytic structure to the liquid phase and the deposition of carbonaceous materials resulting in the irreversible loss of active sites through the poisoning of catalyst pores. It is well known that metal leaching to the bulk liquid can be relieved with the subsequent metal recovery step in order to purge this new pollution source, but its application implies a new industrial unit with relevant economical costs. In this study, the manganese leaching was quantified by atomic absorption and the adsorption of carbonyl species on the catalyst surface was measured by elemental analysis after the oxidation runs.

Table IV.1 reports the manganese concentration of the final aqueous solution after 120 min of oxidation catalyzed by Mn-Ce-O 70/30 IMP, Mn-Ce-O 70/30 CP**,** MnCu 70/30, N140 and MnCu 50/50. No differences were detected for both manganese/cerium oxides so that the preparation method had only a minor influence on the catalytic stability as previously concluded. In spite of their higher activity, Mn-Ce-O catalysts were the ones that exhibited the higher manganese solution concentrations in the treated effluent (2.67 mg Mn/L). Regarding the manganese/copper catalysts, the highest value of manganese leaching was obtained with laboratorial MnCu 70/30 catalyst, whereas the lowest values was attained with the commercial one N140 (CuO-MnO_x 22/50). Therefore, it seems that the higher catalytic activity verified for manganese/cerium oxides in comparison with the copper oxides is related with the higher manganese molar composition present in the first ones. In fact, among the manganese/copper catalysts, MnCu 70/30 was also responsible for the higher leaching levels due to its higher molar percentage in Mn metal.

Table IV.1. Mn leaching results to the liquid phase after 120 min for each Mn based catalyst (200ºC and 15 bar of Air, 6 g/L)

Catalyst	mg Mn/L
Mn-Ce-O 70/30 IMP	2.64
Mn-Ce-O 70/30 CP	2.67
MnCu 70/30	1.48
N140 (CuO-MnO_x 22/50)	0.11
MnCu 50/50	0.67

As the carbon deposition on the catalyst surface blocks the access of the reactants to active sites, elemental analysis was carried out after the recovery of the catalyst at the end of the experiments. The percentages of carbon weight found in the catalysts (%C w/w), hydrogen (%H w/w) and nitrogen (%N w/w) are shown in Table IV.2 as well as the TOC adsorbed relatively to the initial

TOC fed to the reactor and the TOC effectively oxidized after 120 min for each Mn based catalyst. According to these results, one may conclude that adsorbed carbon obtained is relatively low for both laboratorial and commercial catalysts. For instance, the maximum weight percentage of 3.152 % was obtained with the co-precipitated Mn-Ce-O 70/30 catalyst which corresponds to 6.65 % of adsorbed carbon being possible to conclude that the overall TOC conversion was not totally complete as Fig. IV.2 depicted. Effectively, 93.3 % of the initial TOC was converted to carbon dioxide and water. In terms of carbon adsorption, the preparation method was found to be responsible for the observed differences in the percentage of TOC obtained for both manganese/cerium oxides. Regarding the other analyzed elements (H and N), only hydrogen was detected both in the copper and cerium supported catalysts being the higher content obtained in the latter ones. In fact, according to the experimental results from literature (Silva *et al.,* 2003b; Lopes *et al.,* 2007), the hydrogen content on the catalyst particle may be regarded as the development of whiskers enriched in MnOOH.

Table IV.2. Carbon concentration adsorbed in the catalyst, initial TOC percentage adsorbed and effectively oxidized after 120 min for each Mn based catalyst (200ºC and 15 bar of Air, 6 g/L)

Catalyst	%C (w/w)	%H (w/w)	%N (w/w)	$\%TOC_{adsorbed}$	$\%TOC_{oxidized}$
Mn-Ce-O 70/30 IMP	1.543	4.187	< 0.01	3.26	96.7
Mn-Ce-O 70/30 CP	3.152	2.456	< 0.01	6.65	93.3
MnCu 70/30	2.973	0.191	< 0.01	6.27	93.4
N140 (CuO-MnO_x 22/50)	2.849	0.046	< 0.01	6.01	93.5
MnCu 50/50	2.911	0.104	< 0.01	6.14	93.3

IV.4. Conclusions

At 200ºC, with non-catalytic oxidation (15 bar Air) and thermolysis treatments it is only possible to achieve 49.1% and 4.8% of TOC degradation, respectively. Several manganese, ceria and copper based catalysts were tested for the catalytic wet air oxidation of a simulated wastewater involving phenolic acids with the following decreasing order of catalytic activity: Mn-Ce-O 70/30 IMP > Mn-Ce-O 70/30 CP > MnCu 70/30 > N140 (CuO-MnO_x 22/50) > MnCu 50/50. The catalytic results point out Mn-Ce-O 70/30 is an active catalyst for the complete TOC reduction in the phenolic wastewaters treatment after 120 min. The higher molar quantity of manganese in both co-precipitated and wetness impregnated catalyst led to the best TOC degradation results. The co-oxidation process was identified in the simultaneous treatment of a phenolic acids mixture clearly

showing the enhancement of carbon content depletion in comparison with the individual degradation of the same compounds.

The catalytic stability was addressed in terms of metal leaching and catalyst poisoning due to deposition of carbonaceous materials. Both manganese and copper catalysts exhibited low levels of carbon and hydrogen adsorption. Therefore, given the most active and stable behaviour, manganese/cerium catalyst was identified as an interesting formulation with further industrial implementation in CWAO of olive oil mill wastewaters.

IV.5. References

Bhargava, S. K., Tardio, J., Prasad, J., Foger, K., Akolekar, D. B. and Grocott, S. C. (2006). Wet Oxidation and Catalytic Wet Oxidation. *Ind. Eng. Chem. Res.* **45** (4), 1221-1258.

Birchmeier, M. J.; Hill, C. G., Jr.; Houtman, C. J.; Atalla, R. H.; Weinstock, I. (2000). Enhanced Wet Air Oxidation: Synergistic Rate Acceleration upon Effluent Recirculation. *Ind. Eng.Chem.Res.* **39** (1), 55-64.

Cañizares, P., Lobato, J., Paz, R., Rodrigo, M.A., Sáez, C. (2007). Advanced oxidation processes for the treatment of olive-oil mills wastewater. *Chemosphere* **67**, 832-838.

Cybulski. A. (2007). Catalytic Wet Air Oxidation: Are Monolithic Catalysts and Reactors Feasible? *Ind. Eng. Chem. Res.* **46** (12), 4007-4033.

DellaGreca, M., Previtera, F., Zarrelli, A. (2004). Low-molecular-weight Components of Olive Oil Mill Waste-waters. *Phytochem. Anal.* **15**, 184-188.

Garcia, J., Gomes, H.T., Serp, Ph., Kalck, Ph., Figueiredo, J.L., Faria, J.L. (2006). Carbon nanotube supported ruthenium catalysts for the treatment of high strength wastewater with aniline using wet air oxidation. *Carbon Vol.* **44**, 2384-2391.

Imamura, S. (1999). Catalytic and Noncatalytic Wet Oxidation. *Ind. Eng. Chem. Res.* **38** (5), 1743-1753.

Levec, J., Pintar, A. (2007). Catalytic wet-air oxidation processes: A review. *Catalysis Today* **124** (3-4), 172-184.

Shende, R., Levec, J. (2000). Subcritical Aqueous-Phase Oxidation Kinetics of Acrylic, Maleic, Fumaric, and Muconic Acids. *Ind. Eng. Chem. Res.* **39** (1), 40-47.

Lopes, R., Silva, A., Quinta-Ferreira, R. (2007). Screening of catalysts and effect of temperature for kinetic degradation studies of aromatic compounds during wet oxidation. *Appl. Catal. B* **73**, 193-202.

Lopes, R., Quinta-Ferreira, R.M. (2008). Manganese and Copper Catalysts for the Phenolic Wastewaters Remediation by Catalytic Wet Air Oxidation. International Journal of Chemical Reactor Engineering: Vol. 6: A116.

Mantzavinos, D.; Livingston, A. G.; Hellenbrand, R.; Metcalfe, I. S. (1996). Wet air oxidation mechanisms, intermediates and implications for integrated chemical-biological wastewater treatment. *Chem. Eng. Sci.* **51** (18), 4219-4235.

Mantzavinos, D., Psillakis, E. (2004). Enhancement of biodegradability of industrial wastewaters by chemical oxidation pre-treatment. *J. Chem. Technol. Biotechnol.* **79**, 431-454.

Matatov-Meytal, Y.I., Sheintuch, M. (1998). Catalytic Abatement of Water Pollutants. *Ind. Eng. Chem. Res.* **37**, 309-326.

Mulinacci, N., Galardi, C., Pinelli, P., Vincieri, F.F. (2001). Polyphenolic Content in Olive Oil Waste Waters and Related Olive Samples. *J. Agric. Food Chem.* **49** (8), 3509-3514.

Niaounakis, M., Halvadakis, C.P. (2004). Olive mill waste management, Literature Review and PatentSurvey. *Typothito-George Dardanos Publications*, Athens, Greece.

Paraskeva, P., Diamadopoulos, E. (2006). Technologies for olive mill wastewater (OMW) treatment: a review. *J. Chem. Technol. Biotechnol.* **81**, 1475-1485.

Silva, A., Castelo-Branco, I., Quinta-Ferreira, R., Levec, J. (2003a). Catalytic studies in wet oxidation of effluents from formaldehyde industry. *Chem. Eng. Sci.*, Vol. **58**, 963-970.

Silva, A., Marques, R., Quinta-Ferreira, R. (2003b). Catalytic wet oxidation of acrylic acid: studies with manganese-based oxides. *Int. J. Chem. React. Eng.* **1,** S4.

Sierra, J., Martí, E., Montserrat, G., Cruañas, R.; Garau, M.A. (2001). Characterisation and evolution of a soil affected by olive oil mill wastewater disposal. *Sci. Total Environ.* **279**, 207-214.

Tardio, J.; Bhargava, S.; Eyer, S.; Sumich, M.; Akolekar, D. B. (2004). Interactions between Specific Organic Compounds during Catalytic Wet Oxidation of Bayer Liquor. *Ind. Eng.Chem.Res.* **43** (4), 847-851.

PART C. TRICKLE-BED REACTOR HYDRODYNAMICS: CFD STUDIES

Trickle-bed reactors are envisaged for the oxidation of organic and hazardous chemical species from agro-industrial effluents. Traditionally, integral hydrodynamic parameters have been evaluated using empirical correlations for assessing whether its role is neutral or detrimental to the catalytic performance of trickle-bed reactors. This methodology often fails due to the high number of estimation parameters and also neglects the extent of catalyst wetting for different flow regimes since it depends on a multitude of effects including the physic-chemical properties of both gas, liquid and solid phases, the ratio of column diameter to particle diameter and most importantly the gas and liquid superficial velocities.

In this part of the work, two CFD frameworks are developed for the hydrodynamic studies aiming to predict the liquid holdup and pressure drop in the trickling flow regime with a 3D computational grid. Euler-Euler and Volume-of-Fluid multiphase models are optimized in terms of mesh density, time step, convergence criteria, discretization schemes and RANS turbulence models. Several computational runs are performed querying the effect of gas and liquid flow rates, operating pressure and temperature on liquid holdup and two-phase frictional pressure drop. Multiphase flow distribution studies are investigated with different gas-liquid distributors using the Eulerian framework, whereas hysteresis phenomena and wetting efficiency in trickle beds are evaluated with the Volume-of-Fluid model.

V. 3D Numerical Simulation of Pressure Drop and Liquid Holdup for High-Pressure TBR[1]

This study aims to investigate the hydrodynamic behaviour of a trickle-bed reactor (TBR) at high-pressure (30 bar) in terms of pressure drop and liquid holdup after the development of a multiphase model by means of computational fluid dynamics (CFD) codes. Taking into account transport phenomena expressed as interphase coupling terms in the momentum transfer between the gas, liquid and solid phases, an Euler-Euler model was developed resulting from the volume averaging of the continuity and momentum equations and solved for a 3D representation of the catalytic bed.

The CFD calculations were validated with experimental data from the literature and different mesh sizes were evaluated for a grid-independent CFD solution of multiphase flow in the packed bed. During grid optimization, coarse and fine physical mesh domains were applied in the hydrodynamic prediction of trickle-bed reactor. After the grid adjustment in terms of number of cells, several spherical particle diameters were tested to study its effect on hydrodynamics and it was found that pressure drop is strongly influenced by the packing size. The Eulerian mutiphase model was then used in the computation of pressure drop and liquid holdup and over a wide range for the calculated flow regime as a function of gas and liquid flow rates, the CFD theoretical predictions were in good agreement for both hydrodynamic parameters

V.1. Introduction

Major advances for the chemical industries will, no doubt, continue to emerge from catalysis, chemistry and systems engineering. However, maximizing the industrial benefit from these advances requires comparable advances in the design of chemical process equipment. Efficient and effective design of the industrial unities ensures the delivery of materials and energy at the right places and at the right times by manipulating underlying fluid dynamics. The existing plants also need careful analysis and reengineering for improving their effectiveness and the application of computational fluid dynamics (CFD) was expected to lead to shortened product-process development cycles, optimization of existing processes to improve energy efficiency, and the efficient design of new products and processes (Dudukovic *et al.*, 2002). An emerging area in lifecycle environmental applications involves multiphase flows in advanced processes for wastewater treatment, which represents a great challenge for aquatic flora and fauna preservation.

[1] *This Chapter is based upon the publication Lopes and Quinta-Ferreira (2008)*

In fact, bioremediation technologies have known limitations and alternative destruction methods such as catalytic wet air oxidation have been conducted successfully on a variety of organic compounds using numerous catalysts (Bhargava *et al.*, 2006).

Trickle-bed reactors (TBR) are widely used for heterogeneous catalyzed reactions between gas and liquid reactants, such as hydrotreatments, oxidation or partial oxidation and detoxification of liquid effluents. In these reactors, gas and liquid phase flow co-currently downward through a fixed bed of catalyst particles. The majority of the research studies on hydrodynamics have been performed at atmospheric pressure before 1990 (Sáez and Carbonell, 1985; Goto and Smith, 1975) while a few number of investigations was undertaken in pressurised trickle-bed reactors afterwards (Holub *et al.*, 1993; Al-Dahhan *et al.*, 1997; Carbonell, 2000; Gianetto and Specchia, 1992). Furthermore, some studies reported in the literature on the various hydrodynamic aspects of TBR was performed developing sophisticated empirical correlations (Lakota *et al.*, 2002) and using a neural network approach recently (Tarca *et al.*, 2004). Models for TBR simulation are extensively discriminated in the literature considering isothermal operation and using a pseudo-homogeneous approach or heterogeneous model with plug-flow for gas and liquid phase with some models accounting for liquid flow non-uniformity and maldistribution by using axial dispersion models (Sie and Krishna, 1998).

The difficulties in modelling flow in TBR are mainly due to the complex nature of the flow domain that is formed by channels around randomly packed particles. The structure of this interstitial space inside the packed bed is mainly determined by particle size, particle shape, ratio of column diameter and particle diameter and the packing method. Although the detailed 3D porosity information can be achieved through computer simulation of random packing, for flow simulation purposes the present case study employed the generation of a 3D uniform porosity distribution. Due to the inherent complexity of multiphase flows, from a physical as well as a numerical point of view, *general* applicable CFD codes are non-existent and the reasons for the lack of fundamental knowledge on multiphase flows are that multiphase flow is a very complex physical phenomenon where many flow types can occur (gas–solid, gas–liquid, liquid–liquid, etc.) and within each type several possible flow regimes can exist, especially in different hydrodynamic regimes that characterize the trickle-bed reactor operation (trickle flow, spray flow, pulse and bubbly flow). Also, the complex physical laws and mathematical treatment of phenomena occurring in the presence of the two phases are still largely undeveloped and the numerical algorithms for solving the governing equations and closure laws of multiphase flows are extremely complex due to its inherent oscillatory behaviour. Despite several notable works involving 2D computational studies on trickle-bed reactors (Jiang *et al.*, 2002; Farmer *et al.*, 2005), we still do

not have enough indication on predictive performance of Euler-Euler model at the catalyst level by means of 3D computations.

Recently, CFD activities have been introduced systematically in order to investigate multiphase reactors (Jiang *et al.*, 2002; Farmer *et al.*, 2005; Gunjal *et al.*, 2005). Most of Eulerian simulations have been carried out using a three-phase Eulerian model in where the drag-exchange coefficients are treated using the relative permeability concept or calculated by a mathematical formulation based on Ergun equation for a bidimensional computational domain. Advanced experimental studies have been also carried out based on MRI imaging studies wherein the flow features predicted at the particle and liquid-rivulet scale in the TBR can be anticipated with fidelity (Sederman and Gladden, 2005). Being aware that the design of TBR fluid dynamics controls the distribution of materials as well as the energy within the reactor vessel, a TBR was modelled at 3D to bring up hydrodynamic studies and concomitantly the assessment of mesh quality by means of CFD codes for a three-dimensional representation of packed bed flow under high-pressure operation (30 *bar*).

V.2. Computational Flow Domain

V.2.1. Mesh considerations

For successful computations of fluid flow in trickle-bed reactor operation some grid considerations during the mesh generation must be done since its intrinsic flow through the spatially varying effective viscosity plays a dominant role in the transport of mean momentum and other parameters, if high accuracy is required. In fact, the hydrodynamic well-known parameters, such as pressure drop and liquid holdup, and the strong interaction of the mean flow in catalytic bed simulations affect the numerical results for complex flows that tend to be more susceptible to grid dependency. All meshes representing catalytic bed grid generation for the trickle-bed reactor were created using the integrated solid modelling and meshing commercial program GAMBIT (GAMBIT 2, 2005). Unstructured tetrahedral meshes were used to represent the catalyst surface and void spaces whereas at the reactor wall hexahedral meshes were considered to be more appropriate for lower curvature domains. In this study, errors arising from the mesh style and quality were of interest and in order to isolate mesh related discretization errors, a common solution procedure based on the increase of mesh density has been selected and consistently applied to the different mesh considered.

The dimension of the pilot plant reactor is 1 m in length and 5 cm of internal diameter. In order to study the effect of different packing size on the hydrodynamic behaviour, several catalyst

diameters were used (*1, 2, 3, 4* mm diameter) and in all cases the spheres had no points of contact in order to improve the mesh quality. For all the catalyst diameters tested, the imposed gap (3% of diameter for 3 and 4 mm; 2% of diameter for 1 and 2 mm) was confirmed that had no effect in the overall solution for both hydrodynamic parameters remaining less that 1 % for the liquid holdup and 2 % for the pressure drop. To obtain grid-independent pressure drops under different operation conditions, the number of cells was increased from 2×10^5 to 10^6 per catalyst layer. The representative three-dimensional geometry for the tetrahedral mesh of trickle-bed reactor is shown in Fig. V.1a)-d) illustrating four cases for the number of cells from 2×10^5 to 10^6, respectively.

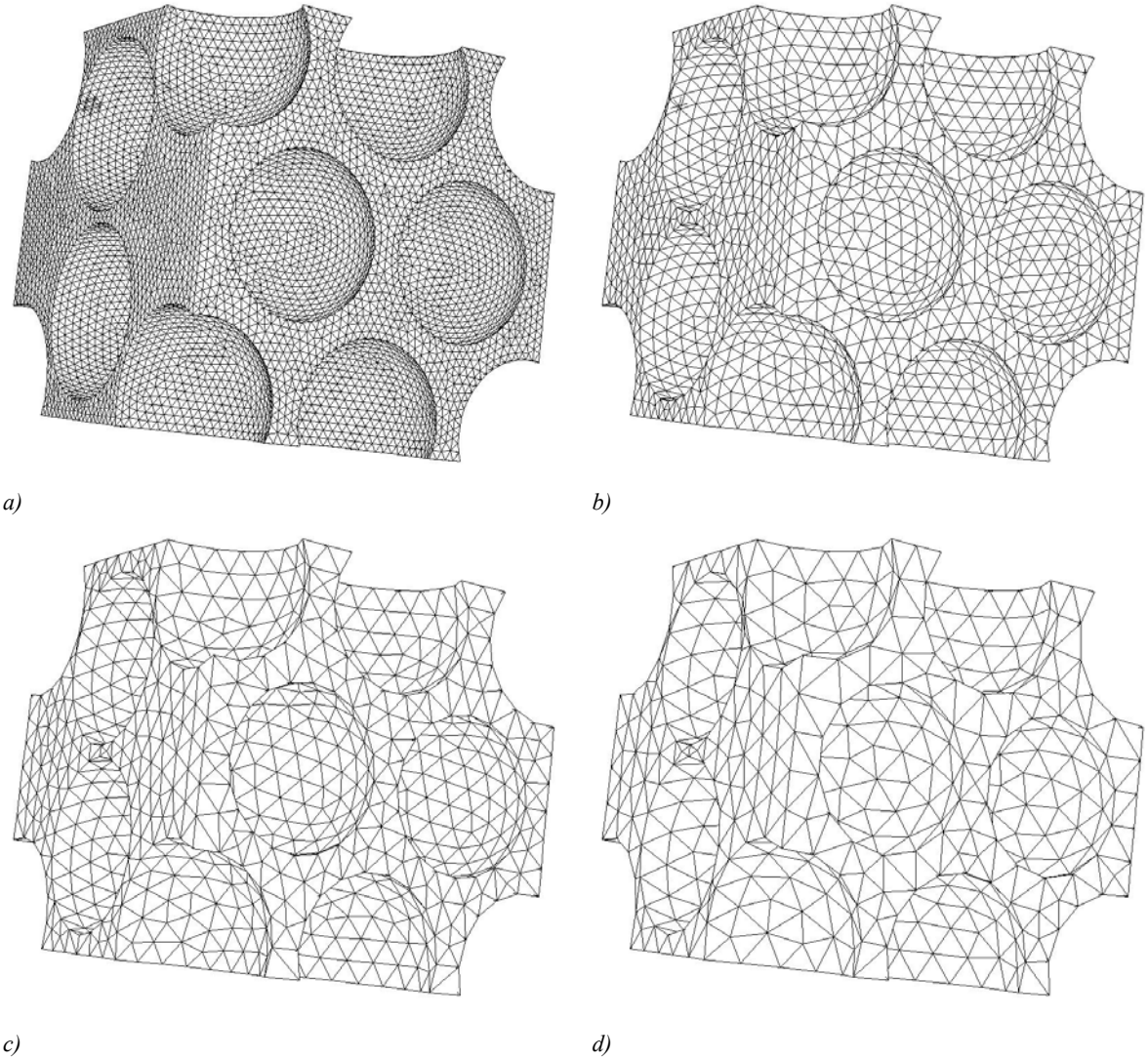

a) *b)* *c)* *d)*

Figure V.1. Representative three-dimensional geometry and mesh for trickle-bed: a) 10^6, b) 5×10^5, c) 4×10^5, d) 2×10^5 cells.

The computational domain is located in the axial and radial TBR centre so that it can be assumed that inlet flow effects can be neglected throughout the simulation activities. The spatial resolution or cell size in a fine mesh is less than d/20. These cell sizes are in line with the expected results

obtained for hydrodynamic data available in open literature so that the average of a cell is in the range 0.01–0.2 mm depending on the simulation and geometric conditions, for particles of 1-4 mm diameter. In the trickle-bed reactor, the cells sizes are also constrained by the need to fit in between the gaps and/or narrow spaces between particles, so they cannot be too large. This can result in the erroneous values taken for proper application of wall functions available in the commercial CFD solver FLUENT so that for turbulent flow standard wall functions were employed.

At 30 *bar* total operating pressure, the inflow gas (G = 0.1 – 0.7 kg/m^{2}s) and liquid (L = 1 – 15 kg/m^{2}s) are distributed uniformly with given superficial velocity simulating a uniform distributor at the top of trickle-bed reactor. The computational mesh of the catalytic bed was reduced in length given the high memory requirements so that the reactor was filled with 13 layers in which around 200 spherical particles of 2 *mm* diameter were necessary for each axial layer. To circumvent numerical difficulties associated with the mesh generation also reported in the literature (Nijemeisland and Dixon, 2001), the catalyst particles do not touch each other and the distance gap was fixed by 2-3 % percent of the sphere diameter. To assess the improved total efficiency in CFD solutions offered by grid density and types, comparison and validation studies are necessary. This is especially true for multifluid systems where the flow is not predominantly oriented in one single direction arising from geometric curvature of the catalytic bed in TBR.

V.2.2. Multiphase flow governing equations

In the present work, the flow in the trickle-bed reactor was modelled using a CFD multiphasic approach incorporated in the FLUENT (FLUENT 6.1, 2005) software that is the Euler-Euler multiphase model. In the Eulerian two-fluid approach, the different phases are treated mathematically as interpenetrating continua. The derivation of the conservation equations for mass, momentum and energy for each of the individual phases is done by ensemble averaging the local instantaneous balances for each of the phases. The current model formulation specifies that the probability of occurrence of any one phase in multiple realizations of the flow is given by the instantaneous volume fraction of that phase at that point where the total sum of all volume fractions at a point is identically unity. Fluids, gas and liquid, are treated as incompressible, and a single pressure field is shared by all phases. Turbulent flow conditions cause the fluid to behave as it has a very high momentum and thermal diffusivity, except near solid surfaces, where these transport mechanisms are reduced to laminar levels in relative short distances.

The description of multiphase flow as interpenetrating continua incorporates the concept of phasic volume fractions, denoted here by α_q. Volume fractions represent the space occupied by each

phase, and the laws of conservation of mass and momentum are satisfied by each phase individually.

The volume of phase q, V_q is defined by: $V_q = \int_V \alpha_q dV$ where $\sum_{q=1}^{n} \alpha_q = 1$. The effective density of phase q is: $\hat{\rho}_q = \alpha_q \rho_q$ where ρ_q is the physical density of phase q. The CFD model equations were solved in commercial software FLUENT (FLUENT 6.1, 2005). The general conservation equations are presented in this section, followed by the solving strategies. The continuity equation for phase q is:

$$\frac{\partial}{\partial t}(\alpha_q \rho_q) + \nabla \cdot (\alpha_q \rho_q \vec{u}_q) = \sum_{p=1}^{n} (\dot{m}_{pq} - \dot{m}_{qp}) + S_q \tag{V.1}$$

where $\vec{u}_q$ is the velocity of phase q and $\dot{m}_{pq}$ characterizes the mass transfer from the p^{th} to q^{th} phase, and $\dot{m}_{qp}$ characterizes the mass transfer from phase q to phase p, and it is possible to specify these mechanisms separately. By default, the source term S_q on the right-hand side of Equation (V.1) is zero, but it can specify a constant or user-defined mass source for each phase. A similar term appears in the momentum and enthalpy equations. The momentum balance for phase q yields:

$$\begin{aligned}&\frac{\partial}{\partial t}(\alpha_q \rho_q \vec{u}_q) + \nabla \cdot (\alpha_q \rho_q \vec{u}_q \vec{u}_q) = -\alpha_q \nabla p + \nabla \cdot \bar{\bar{\tau}}_q + \alpha_q \rho_q \vec{g} + \\ &\sum_{p=1}^{n} (\vec{R}_{pq} + \dot{m}_{pq} \vec{u}_{pq} - \dot{m}_{qp} \vec{u}_{qp}) + (\vec{F}_q + \vec{F}_{lift,q} + \vec{F}_{vm,q})\end{aligned} \tag{V.2}$$

where $\bar{\bar{\tau}}_q$ is the q^{th} phase viscous stress tensor:

$$\bar{\bar{\tau}}_q = \alpha_q \mu_q (\nabla \vec{u}_q + \nabla \vec{u}_q^T) + \alpha_q (\lambda_q - \frac{2}{3} \mu_q) \nabla \cdot \vec{u}_q \bar{\bar{I}} \tag{V.3}$$

Here μ_q ($\mu_q = \mu_{l,q} + \mu_{t,q}$) and λ_q are the shear and bulk viscosity of phase q, $\vec{R}_{pq}$ is an interaction force between phases, p is the pressure shared by all phases and $\vec{u}_{pq}, \vec{u}_{qp}$ are the interphase velocities. The last three terms on right-hand side of Equation (V.2) where $\vec{F}_q$ is an external body force, $\vec{F}_{lift,q}$ is a lift force and $\vec{F}_{vm,q}$ is a virtual mass force, have been neglected during trickling flow simulations. Equation (V.2) must account for suitable expressions for the interphase force $\vec{R}_{pq}$, which depends on the friction, pressure, cohesion, and other effects; it conforms to the conditions that $\vec{R}_{pq} = -\vec{R}_{qp}$ and $\vec{R}_{qq} = 0$ being possible to express a simple interaction term by:

$$\sum_{p=1}^{n} \vec{R}_{pq} = \sum_{p=1}^{n} K_{pq}(\vec{u}_p - \vec{u}_q) \tag{V.4}$$

where $K_{pq} = K_{qp}$ is the interphase momentum exchange coefficient. Interphase coupling terms, $\vec{R}_{pq}$, in the right side of Equation (V.2) were formulated based on similar equations to those that are typically used to express the pressure drop for packed beds by means of Ergun equation. Consequently, the model of Attou and Ferschneider (1999) was employed in the CFD model, which includes gas-liquid interaction forces and it was developed for the regime in which liquid flows in the form of film. The interphase coupling terms are expressed in terms of interstitial velocities and phase volume fractions for gas-liquid, gas-solid and liquid-solid momentum exchange forms:

$$K_{GL} = \alpha_G \left(\frac{E_1 \mu_G (1-\alpha_G)^2}{\alpha_G^2 d_p^2} \left[\frac{\alpha_S}{1-\alpha_G} \right]^{2/3} + \frac{E_2 \rho_G (u_G - u_L)(1-\alpha_G)}{\alpha_G d_p} \left[\frac{\alpha_S}{1-\alpha_G} \right]^{1/3} \right) \tag{V.5}$$

$$K_{GS} = \alpha_G \left(\frac{E_1 \mu_G (1-\alpha_G)^2}{\alpha_G^2 d_p^2} \left[\frac{\alpha_S}{1-\alpha_G} \right]^{2/3} + \frac{E_2 \rho_G u_G (1-\alpha_G)}{\alpha_G d_p} \left[\frac{\alpha_S}{1-\alpha_G} \right]^{1/3} \right) \tag{V.6}$$

$$K_{LS} = \alpha_L \left(\frac{E_1 \mu_L {\alpha_S}^2}{\alpha_L^2 d_p^2} + \frac{E_2 \rho_L u_G \alpha_S}{\alpha_L d_p} \right) \tag{V.7}$$

The turbulent viscosity $\mu_{t,q}$ is given in Equation (V.8).

$$\mu_{t,q} = \rho_q C_\mu \frac{k_q^2}{\varepsilon_q} \tag{V.8}$$

The turbulent viscosity is obtained from the prediction of the transport equations for the k_q, kinetic energy, and ε_q, dissipation energy, written for the continuous phase in Equations (V.9) and (V.10), respectively.

$$\begin{aligned} &\frac{\partial}{\partial t}(\rho_q \alpha_q k_q) + \nabla \cdot (\rho_q \alpha_q \vec{u}_q k_q) \\ &= \nabla \cdot \left(\alpha_q \frac{\mu_{t,q}}{\sigma_k} \nabla k_q \right) + \alpha_q G_{k,q} - \alpha_q \rho_q \varepsilon_q + \alpha_q \rho_q \Pi_{kq} \end{aligned} \tag{V.9}$$

$$\frac{\partial}{\partial t}(\rho_q \alpha_q \varepsilon_q) + \nabla \cdot (\rho_q \alpha_q \vec{u}_q \varepsilon_q) = \nabla \cdot \left(\alpha_q \frac{\mu_{t,q}}{\sigma_\varepsilon} \nabla \varepsilon_q \right) + \alpha_q \frac{\varepsilon_q}{k_q} \times (C_{1\varepsilon} G_{k,q} - C_{2\varepsilon} \rho_q \varepsilon_q) + \alpha_q \rho_q \Pi_{\varepsilon q} \quad \text{(V.10)}$$

In these equations, $G_{k,q}$ is the generation of turbulent kinetic energy, k_q, due to the mean velocity gradients (turbulent stress) as expressed in Equation (V.11).

$$G_{k,q} = \mu_{t,q} \left(\nabla \vec{u}_q + \left(\nabla \vec{u}_q \right)^T \right) : \nabla \vec{u}_q \quad \text{(V.11)}$$

$C_{1\varepsilon}$ and $C_{2\varepsilon}$ are the constants of k-ε dispersed model whereas σ_k and σ_ε are the turbulent Prandtl numbers for k and ε, respectively.

V.2.3. Numerical simulation, boundary conditions and wall functions

The solution method was control-volume-based for multiple tetrahedral mesh apertures. The numerical methodologies including the integration, discretization, linearization and algorithm followed by the CFD solver are described in Appendix A. A pressure-based segregated implicit solver (Appendix A, section A.2) was employed to evaluate the resulting linear system of equations using the Gauss-Seidel method in conjunction with an algebraic multigrid approach to solve the linearized equations. The governing equations were solved using the pressure-velocity SIMPLE coupling algorithm and the momentum equations were decoupled using the full elimination algorithm in which the variables for each phase are eliminated from the momentum equations for all other phases. The pressure correction equation was obtained by summing the continuity equations for each of the phases. The equations were then solved in a segregated, iterative fashion and were advanced in time (Appendix A, section A.3). Model equations were solved in a transient fashion with a time step of 0.001s for the Eulerian simulations. At each time step, with an initial guess for the pressure field, the primary- and secondary-phase velocities were computed. These were used in the pressure correction equation and based on the discrepancy between the guessed pressure field and the computed field, the velocities, L/G holdups and fluxes were suitably modified to obtain convergence in an iterative manner. The outer iteration procedure was stopped when the global mass residual had been reduced from its original value by five orders of magnitude and when the residual-reduction rates for both mass and momentum were sufficiently small and less than 10^{-6}. All calculations were performed in double precision to improve accuracy.

In the Eulerian multiphase calculations, phase coupled SIMPLE (PC-SIMPLE: Vasquez and Ivanov, 2000) algorithm was employed for the pressure-velocity coupling, which is an extension

of the SIMPLE algorithm (Patankar, 1980) to multiphase flows. The velocities are solved coupled by phases, but in a segregated fashion. The block algebraic multigrid scheme used by the density-based solver described is used to solve a vector equation formed by the velocity components of all phases simultaneously. Pressure and velocities are then corrected so as to satisfy the continuity constraint. For incompressible multiphase flow, the pressure-correction equation takes the form of Equations (V.12). (Appendix A, section A.3).

$$\sum_{q=1}^{n} \left\{ \frac{\partial}{\partial t} \alpha_q \rho_q + \nabla \cdot \alpha_q \rho_q \vec{u}_q^{'} + \nabla \cdot \alpha_q \rho_q \vec{u}_q^{*} - \left(\sum_{p=1}^{n} \left(\dot{m}_{pq} - \dot{m}_{qp} \right) \right) \right\} = 0 \qquad \text{(V.12)}$$

where ρ_{rq} is the phase reference density for the q^{th} phase (defined as the total volume average density of phase q), $\vec{u}_q^{'}$ is the velocity correction for the q^{th} phase, and $\vec{u}_q^{*}$ is the value of $\vec{u}_q$ at the current iteration. The velocity corrections are themselves expressed as functions of the pressure corrections. The volume fractions are obtained from the phase continuity equations. In discretized form, the q^{th} volume fraction is given by Equation (V.13).

$$a_{P,q} \alpha_q = \sum_{nb} \left(a_{nb,q} \alpha_{nb,q} \right) + b_q \qquad \text{(V.13)}$$

where the subscript *nb* refers to neighbor cells, and $a_{P,q}$ and a_{nb} are the linearized coefficients for α_q α_{nb} (Appendix A, section A.3). Experimentally, it is observed that trickle-bed reactors presents random directional flow fields imposing serious limitations in the convergence of tetrahedral meshes that could lead to an inefficient distribution of grid points in the final mesh. Therefore, the under-relaxation parameter for pressure was checked in the range between 0.2 and 0.6 whereas for velocity it was checked in the range 0.4-0.8. The common parameters used in the simulation are summarized in Table V.1. Inlet boundary conditions are assigned at the top distributor and outlet conditions at the free surface. The cell thickness (y^+) computed by the CFD solver was always below 200. At this point, it was possible to check the near-wall mesh in the post-processing treatment. The solution independency was then established after several assays with the definition of turbulence boundary conditions available in *k-ε* model. The boundary conditions at the walls are internally computed by FLUENT. The reactor wall and catalyst surfaces are treated as no slip boundaries with standard wall functions. It should be also pointed that inlet turbulence can significantly affect the downstream flow as observed in high pressure trickle-bed reactors. In the trickle-bed simulations performed, the fidelity of the results for turbulent flows was addressed by the turbulence model being used and in order to enhance the quality of turbulent flow simulations, the mesh generation accounts for wall-bounded flow on catalyst particles, since the wall is expected to significantly affect the flow.

Table V.1 – Parameters used in the CFD simulation

Grid	1000 mm (axial) × 50 mm (radial)
Cell size	0.01 - 0.20 mm (tetrahedral and hexahedral)
Particle diameter	1, 2, 3, 4 mm (spheres)
Time step	0.001s (Euler-Euler)
Iterations	≈ 50,000
Under-relaxation parameters	Euler-Euler: 0.2-0.6 (pressure), 0.4-0.8 (velocity)
Drag formulation	Attou and Ferschneider (1999)
Turbulence model	Laminar; standard k-ε model (Elghobashi & Abou-Arab, 1983)
Gas density (298 K, 30 bar)	35.670 kg/m^3
Gas viscosity (298 K, 30 bar)	1.845×10^{-5} Pa.s
Liquid density (298 K, 30 bar)	998.39 kg/m^3
Liquid viscosity (298 K, 30 bar)	8.925×10^{-4} Pa.s
Liquid surface tension (298 K, 30 bar)	7.284×10^{-2} N/m

In order to establish grid independence of the velocity field solutions, successive refinements of computational mesh have been considered. For each refinement, grid convergence was evaluated by using a relative error measure of velocity magnitude between the coarse and fine solutions. The conditions required for grid convergent results are based on a 1% relative error criterion and the simulations accuracy has been assessed by comparisons to experimental data available in the literature for the simulated velocity field (Nemec and Levec, 2005). The boundary conditions were specified based on FLUENT documentation. Inlet turbulent kinetic energy (k_q) was estimated from turbulence intensity as expressed in Equation (V.14).

$$k_q = \frac{3}{2}(u_q I_q)^2 \tag{V.14}$$

where I_q is the turbulence intensity being given by Equation (V.15).

$$I_q = 0.16\left(\mathrm{Re}_{q,d_H}\right)^{-1/8} \tag{V.15}$$

Inlet turbulent energy dissipation (ε_q) was estimated from the turbulent viscosity ratio as expressed by Equation (V.16).

$$\varepsilon_q = \rho_q C_\mu \frac{k_q^{\,2}}{\mu_q}\left(\frac{\mu_{t,q}}{\mu_q}\right)^{-1} \tag{V.16}$$

where C_μ is an empirical constant specified in the turbulence model (0.09). Table V.2 systematizes the initial and boundary conditions used during the CFD simulations convoyed with the reactor scheme. At 30 *bar* and 25^oC, the inlet turbulent kinetic energy and inlet turbulent energy dissipation for the gas and liquid phases are given in Table V.3. Computations are time dependent and were carried out until steady state conditions were reached. Standard wall functions available in the commercial CFD solver were employed during the simulations of turbulent multiphase flow. The calculations have been carried out on a Linux cluster based on AMD64 Dual-Core 2.2 GHz processor workstation.

Table V.2 – Initial and boundary conditions for the gas and liquid phases

	$t = 0$	$z = 0$
α_G	0.25	0.25
α_L	0.15	0.15
G / (kg/m^2s)	0.1-0.7	0.1-0.7
L / (kg/m^2s)	1-15	1-15
P / bar	10-40	10-40
k / (m^2/s^2)	*see Table V.3*	
ε / (m^2/s^3)		

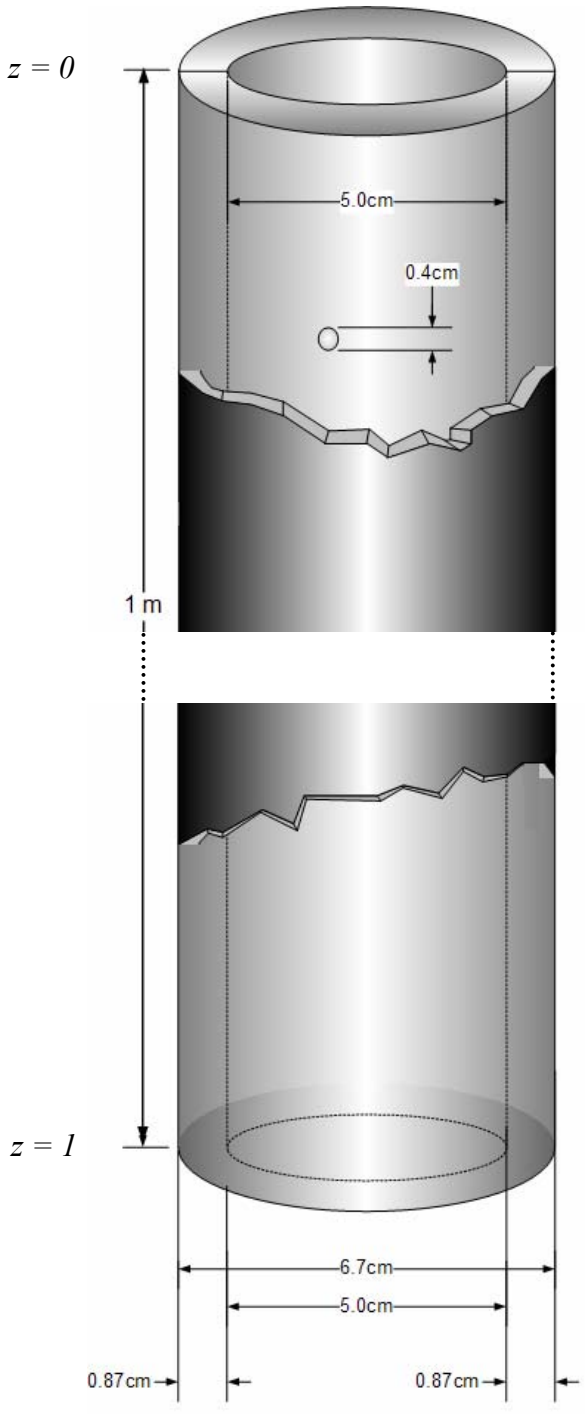

Table V.3 – Inlet boundary conditions for the gas and liquid phases: turbulent kinetic energy (k_q) and turbulent energy dissipation (ε_q) at T=25ºC and P=30 bar

G (kg/m^{2}s)	L (kg/m^{2}s)	k_G (mm^2/s^2)	k_L (mm^2/s^2)	ε_G (mm^2/s^3)	ε_L (mm^2/s^3)
0.1	1	0.2059	3.952×10^{-2}	3.690×10^{-3}	7.637×10^{-5}
0.4	1	2.330	3.952×10^{-2}	0.4723	7.637×10^{-5}
0.7	1	6.204	3.952×10^{-2}	3.349	7.637×10^{-5}
0.1	8	0.2059	1.504	3.690×10^{-3}	0.1106
0.4	8	2.330	1.504	0.4723	0.1106
0.7	8	6.204	1.504	3.349	0.1106
0.1	15	0.2059	4.518	3.690×10^{-3}	0.9982
0.4	15	2.330	4.518	0.4723	0.9982
0.7	15	6.204	4.518	3.349	0.9982

V.3. Results and Discussion

V.3.1. Mesh optimization and validation

Validation of CFD flow field calculations has generally taken one of two forms. In the first, non-invasive velocity measurements inside the packed bed have been made and compared to velocities computed from a model of either the entire experimental bed or a representative part of it. In the second form, computed pressure drops have been compared to either measured values or established correlations for pressure drop in fixed beds, such as the Ergun equation. The present case study makes use of the last method to assess the Eulerian model so that the numerical methodology is validated against experimental data available from literature related to the hydrodynamic information for TBR operation (Nemec and Levec, 2005). Different hydrodynamic regimes were simulated for the trickle-bed reactor either in laminar or turbulent flow. In both cases, the local refinement and coarsening of unstructured tetrahedral meshes in the case study required local grid modifications to efficiently resolve solution features for computing unsteady three-dimensional problems that arise in TBR simulation activities. In laminar flow, the mesh aperture was optimized near the catalyst and reactor walls. The higher level of numerical diffusion usually associated with tetrahedral meshes could not always be defeated increasing the number of cells since significant numerical diffusion errors and inaccuracies in near-wall particle interpolations may persist. The resulting liquid holdup and pressure drop along the catalytic bed were evaluated as a function of cells number as well as operating conditions.

The mesh strongly affects the accuracy of the simulation as shown by Fig. V.2. It has to be chosen with enough detail to describe the multiphase flow accurately and with a degree of coarseness that enables solution within an acceptable amount of time. We determined an appropriate mesh density

for CFD simulations by comparing computational results from several different meshes and then an optimal mesh density was established for hydrodynamic validation in trickle-bed operation. An edge length of the tetrahedral cell of 0.15 mm on a 3 mm diameter sphere corresponds to a number of about 3000 triangles in the surface mesh of the sphere, whereas an edge length of 0.2 mm corresponds to about 1000 triangles.

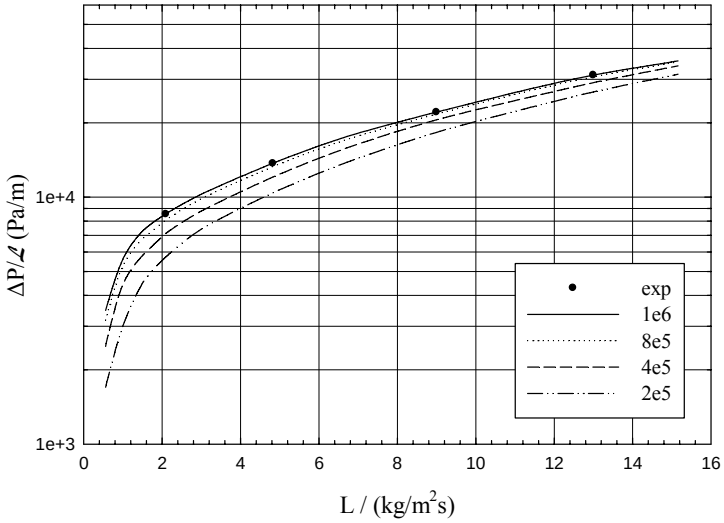

Figure V.2. Effect of numerical parameters on pressure drop versus liquid flow rate for different cells number: 10^6, 5×10^5, 4×10^5, 2×10^5 (P = 30 bar, G = 0.7 kg/m^{2}s, d = 2 mm, experimental data from Nemec and Levec, 2005).

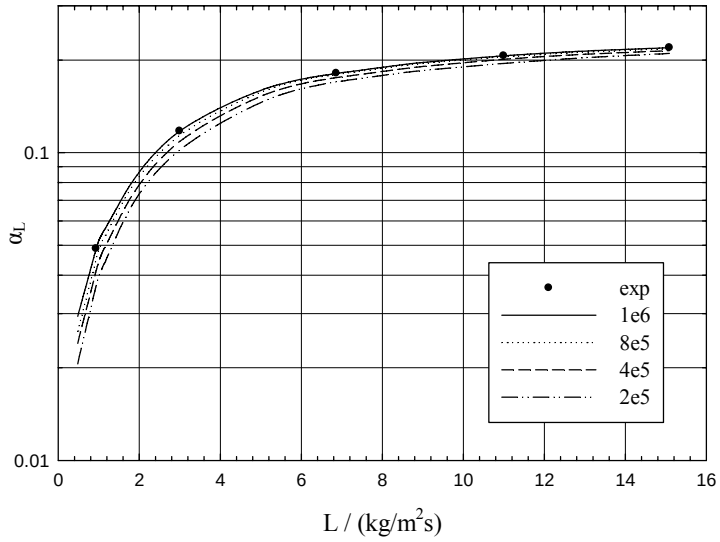

Figure V.3. Effect of numerical parameters on liquid holdup versus liquid flow rate for different cells number: 10^6, 5×10^5, 4×10^5, 2×10^5 (P = 30 bar, G = 0.7 kg/m^{2}s, d = 2 mm, experimental data from Nemec and Levec, 2005).

In accordance with Figs. V.2 and V.3 with G = 0.7 kg/m^{2}s, a total of about one million grid cells were needed when using a tetrahedral mesh edge length 0.15 mm. In terms of number of cells, the mesh dependency addressed in pressure drop (Fig. V.2) and liquid holdup (Fig. V.3) computations

are proportionally direct, as expected. In fact, if we increase the number of cells, the result is to enhance the grid detail accounting the void space in an appropriate manner. Numerically, this brings more iterations towards the convergence. In the current multiphase flow simulation, the grid independence of the solution was checked by varying the grid density. In Fig. V.2 the resulting pressure drops across the packed bed were plotted as a function of the cells number. This figure indicates that 10^6 cells are adequate to successfully predict pressure drop as well as the liquid holdup within 10% relative error, this one demonstrated in Fig. V.3. Comparing these two plots (Fig. V.2 and V.3), the TBR operation seems to be more sensible to pressure drop than to liquid holdup results when performing the same deviation scale in the cells number.

V.3.2. Influence of packing size on hydrodynamics

The catalytic bed was simulated with different packing made of spherical particles with diameters up to 4 mm. Indeed, the validation method was to compare simulation results in terms of pressure drop (Fig. V.4) and liquid holdup (Fig. V.5) evaluating the mesh sensitivity and discriminating the numerical results against the experimental data performed with equipment analogous to the system that is being replicated (Nemec and Levec, 2005). Geometrically, the trustworthiness of this modus operandi led to the final corroboration of CFD codes.

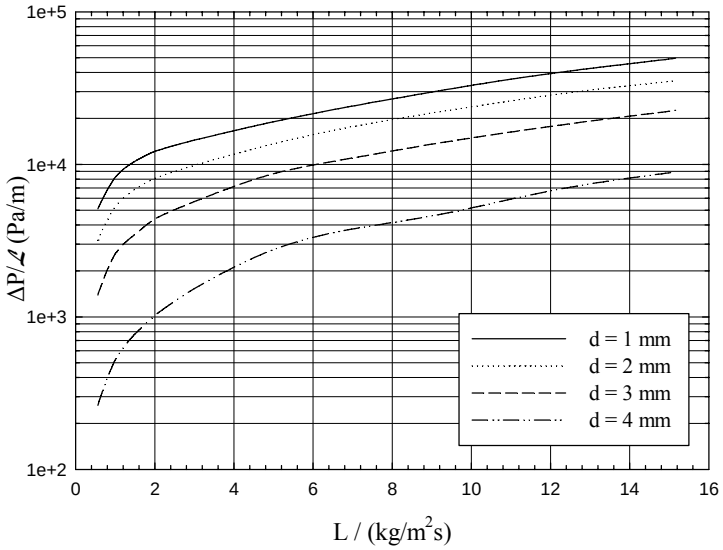

Figure V.4. Effect of packing size on pressure drop versus liquid flow rate for different packing particles: 1-4 mm (P = 30 bar, G = 0.7 kg/m^{2}s)

When the trickle-bed reactor is simulated with different spherical particle diameters, the overall effect of particles size is related to the specific surface area of the packing material for that particular bed. For instance, if the TBR is operated with spheres of *d = 1 mm*, the specific surface is higher than it is for spheres of *d = 4 mm* leading to the greater flow resistance.

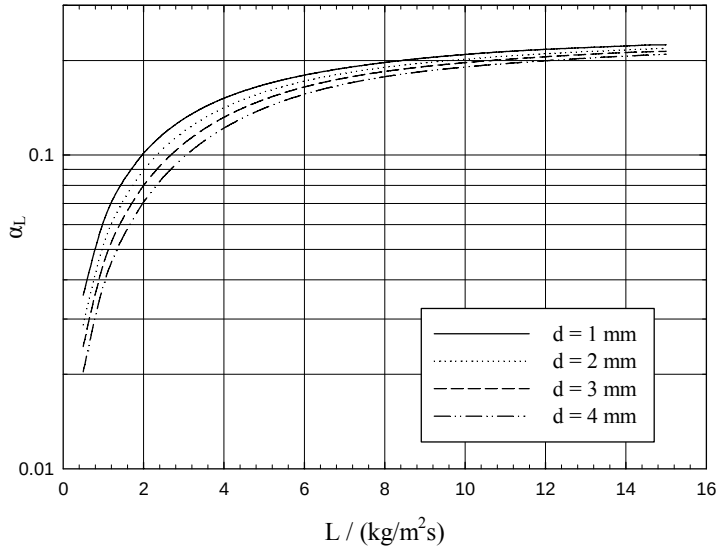

Figure V.5. Effect of packing size on liquid holdup versus liquid flow rate for different packing particles: 1-4 mm (P = 30 bar, G = 0.7 kg/m^{2}s)

Therefore, as the particle size decreases, the specific surface area of the bed increases and therefore the liquid holdup (Fig. V.5) also increases due to the fact that liquid phase finds it harder to flow downwards through the bed at a certain gas and liquid flow rate. According with Fig. V.4, one can observe that pressure drop also increases due to the increased bed specific surface area which gave lower bed porosities. The effect is more pronounced when the simulation is addressed in two-phase flow due to an additional increase in pressure drop than if one compares it to single-phase flow operation. This fact is associated with the enlargement of liquid holdup, which decreases the available void space for the flow of gas through the trickle-bed reactor.

V.3.3. Evaluation of Pressure drop and Liquid holdup predictions

After evaluating the mesh quality and its numerical independency for the TBR modelling, Eulerian model was used to predict pressure gradient and liquid holdup in scale-up activities to evaluate the effect of liquid and gas flow rates in the hydrodynamic parameters. The well established design of the TBR performance depends heavily in the accurate quantification of pressure drop because it affects the mechanical energy supply at the catalyst particle and it has been used to correlate the gas-liquid and solid-liquid mass transfer (van der Merwe and Nicol, 2005; Wammes and Westerterp, 1990). On the other side, the validation in terms of liquid fraction contained in the TBR column was referred with laboratory scale experiments. Therefore, whereas pressure drop is obviously connected with the dissipation power in the multiphase reactor that cannot be neglected when optimization is a subject matter, liquid holdup is particularly important when assessing the trickle flow encountered at low gas and liquid superficial velocities.

Two-phase pressure gradient results are plotted as a function of gas flow rate varying the liquid flow rate and vice versa in Figs. V.6 and V.7. The variation of the internal pressure per unit-reactor length is directly proportional to any phase flow rate. In fact, at the lowest liquid flow rate (1 kg/m^{2}s) if we decrease the operating gas flow rate from 0.7 to 0.1 kg/m^{2}s, the total pressure drop shifts from 8210 to 520 Pa/m, whereas the same relative change at the lowest gas flow rate (0.1 kg/m^{2}s) in liquid flow rate only produces a modification in terms of pressure drop from 4065 to 520 Pa/m. Therefore, 86% of reduction in the gas flow rate has a major effect for pressure drop (94%) rather than with the same reduction order for the liquid flow rate (87%). Moreover, the effect of gas flow rate on the pressure drop is enlarged at higher flow rates (G = 0.7 kg/m^{2}s) so that a shift from 15 to 1 kg/m^{2}s in liquid flow rate makes the pressure drop move from 50250 to 8210 Pa/m. Having the knowledge that pressure gradient is related to the mechanical energy dissipation due to the two-phase flow through the fixed bed of solid catalyst particles, comparing Figs. V.6 and V.7 illustrate that the effect at low gas flow rates is more meaningful for the pressure drop.

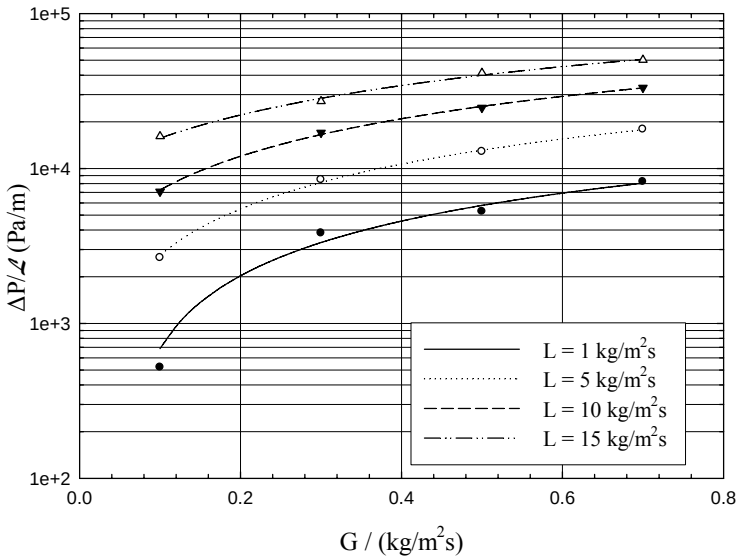

Figure V.6. Effect of liquid flow rate on pressure drop versus gas flow rate (P = 30 bar, d = 2 mm) (experimental data from Nemec and Levec, 2005).

Figure V.8a) shows an isocontour for the pressure field on the catalyst surface. As one can observe, the values of lower pressure were encountered in zones where the catalyst particles are closer to each other. As the flow is processed downwards, the higher pressure values were monitored at the top zone of the catalyst particle so that the fluid is compelled to navigate around the sphere and changing its flow direction.

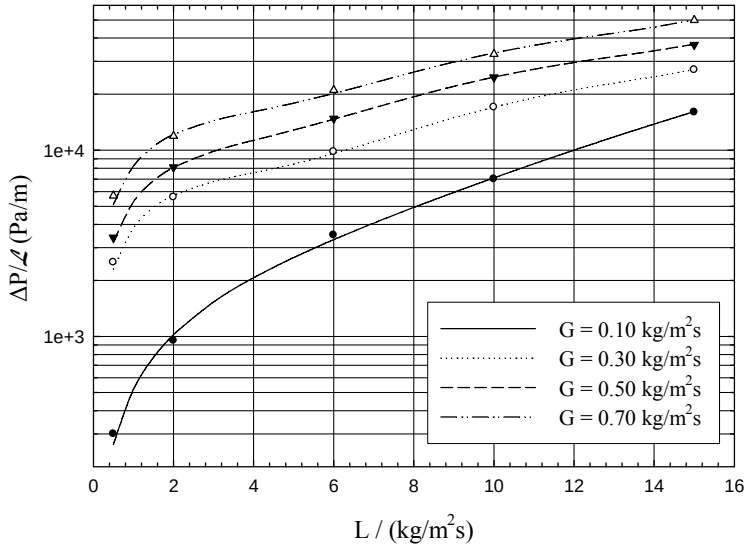

Figure V.7. Effect of gas flow rate on pressure drop versus liquid flow rate (P = 30 bar, d = 2 mm) (experimental data from Nemec and Levec, 2005).

In order to illustrate the flow direction adjustment around catalyst packing, Fig. V.8b) also sustains this fact so that the mean gas velocity is in accordance with the hydrodynamic regime simulated. Indeed, the maximum velocity attained for the gas phase is about 0.5 cm/s which enables the trickling flow operating conditions.

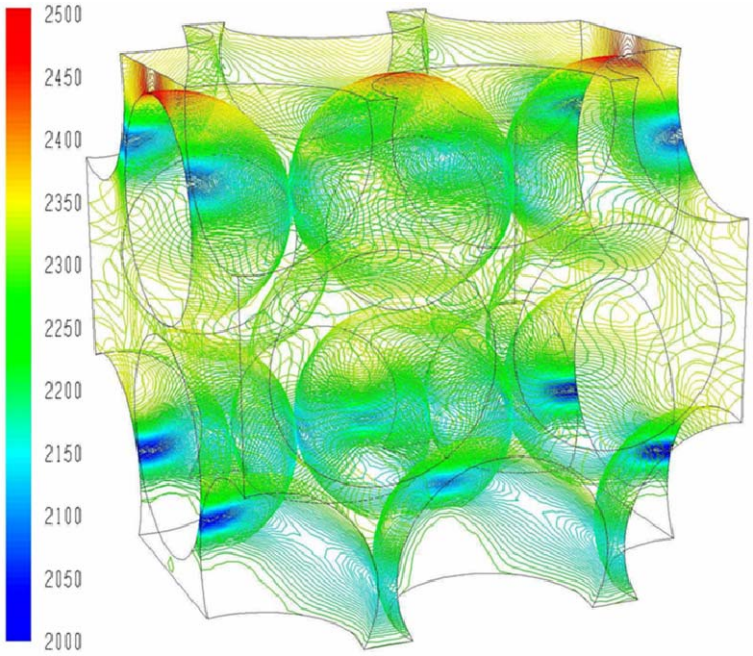

a)

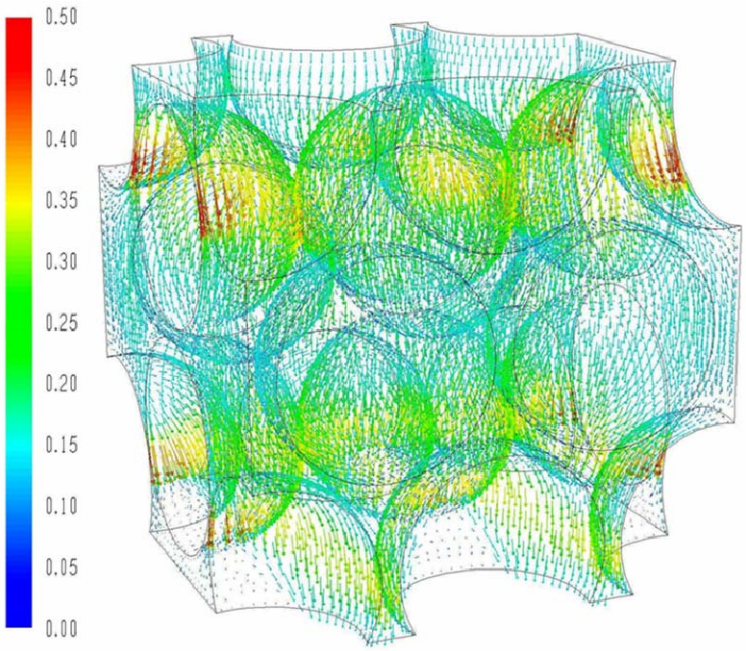

b)

Figure V.8. a) Isocontour of Pressure (Pa) field on the catalyst surface; **b)** flow pattern on the catalyst surface area showing instantaneous gas velocity vector (cm/s) (P = 30 bar, L = 5 kg/m^{2}s, G = 0.7 kg/m^{2}s, d = 2 mm)

According with Fig. V.8b), the computed vector field shows that phase velocity is not always fully developed around the catalyst particle and the higher values are observed in the sphere equatorial zone. The asymmetric gas velocities depicted in Fig. V.8b) between two or more catalyst particles as well as the pressure contours plotted in Fig. V.8a) demonstrate the existence of poor gas-liquid flow distribution in the packed bed as a consequence of rough stagnant zones.

In what concerns liquid holdup predictions, conversely to the effect advanced for the influence of the liquid flow rate in the computed global pressure drop, after the examination of Figs. V.9 and V.10, liquid holdup does not generate the same assertions. In fact, while the increasing of gas flow rate tends to reduce the volume of liquid contained in the bed per unit reactor volume, the opposite behaviour is observed when the liquid flow rate is charged. The influence of liquid holdup is also related to other important parameters, namely, pressure gradient, gas-liquid interfacial area, the mean residence time of the liquid phase, catalyst loading per unit volume, mass-transfer and heat-transfer coefficients. Notwithstanding, the Euler multiphase model takes into account the total liquid holdup resulting from the sum of static and dynamic liquid holdup and according to Fig. V.9, we could state that the semi-log plot reports this hydrodynamic parameter as a decreasing function of gas flow rate, as expected.

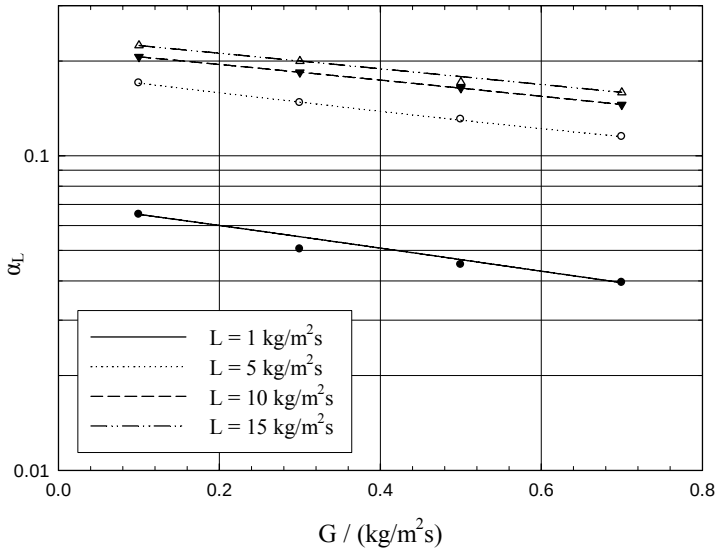

Figure V.9. Effect of liquid flow rate on liquid holdup drop versus gas flow rate (P = 30 bar, d = 2 mm) (experimental data from Nemec and Levec, 2005).

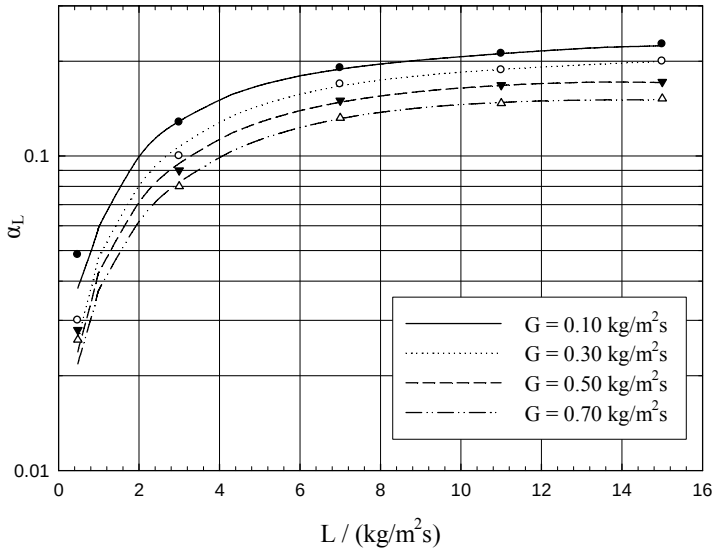

Figure V.10. Effect of gas flow rate on liquid holdup versus liquid flow rate (P = 30 bar, d = 2 mm) (experimental data from Nemec and Levec, 2005).

Taking into account that hydrodynamics is affected differently in each flow regime and the operating conditions that are of particular interest in the industry are the extensively used trickle flows encountered at low gas and liquid flow rates, the Eulerian model was employed in the following range for the Reynolds number: Re < 400. In Fig. V.11a), it is represented a snapshot of Reynolds number in a colour map for four vertical planes corresponding to the bulk space between the catalyst particles. The deviations of the local velocity near the solid surfaces observed in Fig. V.11a) indicate the existence of more or less stagnant zones near the points of approximation between spheres. In fact, for packed beds, large deviations of this nature might result in a variation of the boundary layer thickness values over the sphere surface. Indeed, according to Fig. V.11b) in

where it was also mapped the streamlines for the same planes coloured by the Reynolds number for the gas phase, the condition that the flow should be well developed in order for the standard wall model to be valid, might be fully met in the case of a trickle flow operation. Therefore, the good agreement achieved for the calculations performed with 10^6 of tetrahedral cells validated both the computed pressure drop and the liquid holdup.

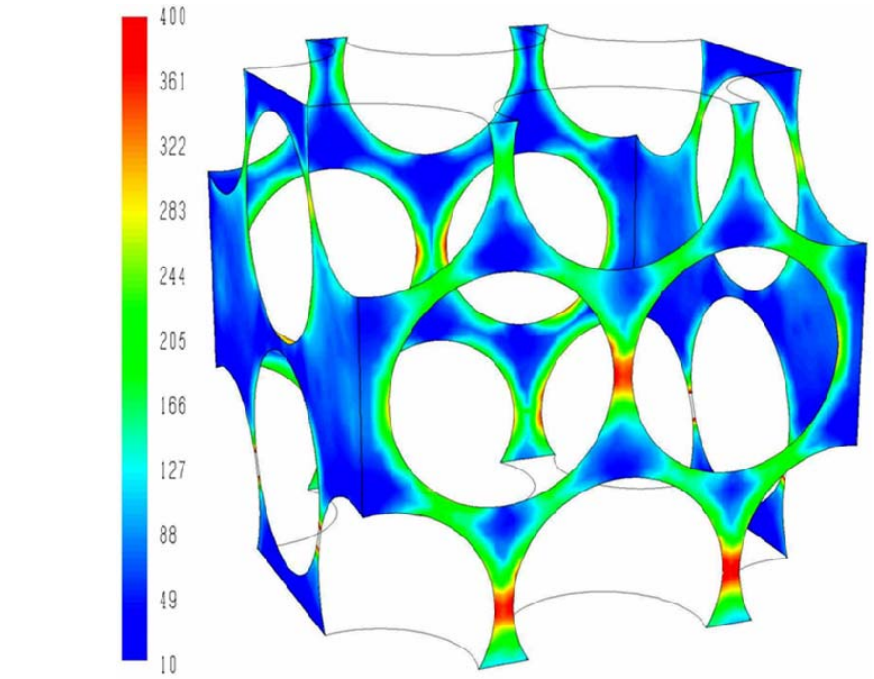

a)

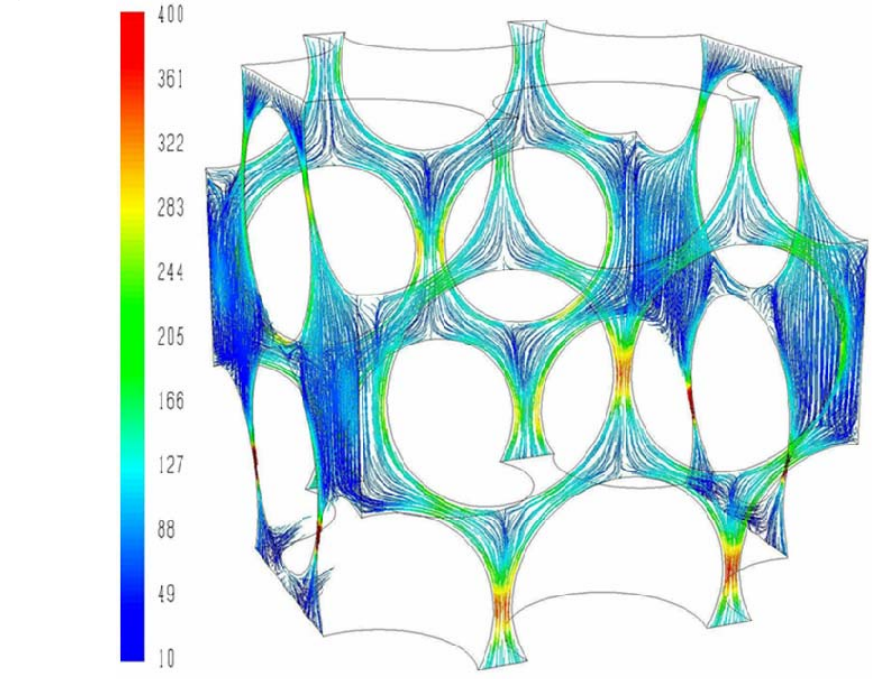

b

Figure V.11. a) Vertical colour maps of Reynolds number in laminar flow; **b)** Streamlines coloured by Reynolds number (P = 30 bar, L = 5 kg/m^{2}s, G = 0.7 kg/m^{2}s, d = 2 mm)

V.4. Conclusions

A unique physic-based three-dimensional model has been proposed to model trickle-bed reactors at elevated pressures for predicting the hydrodynamic parameters pressure drop and liquid holdup. The CFD unified approach allowed the complete fluid transport equations to be solved locally, to better understand the phenomena including the momentum balance and takes into account the interphase coupling terms in the momentum transfer between the gas, liquid and solid phases. The CFD calculations with different mesh sizes were checked against experiments and a good agreement was achieved.

The mesh generation technique and grid convergence were evaluated to establish grid independence using a relative error measure of hydrodynamic parameters magnitude between the coarse and fine solutions. Successive refinements of each mesh style have been considered to better resolve regions of significant velocity gradients encountered in the multiphase system. The coarse mesh affected considerably the accuracy of simulations so that an optimum number of cells was achieved with a fine mesh and used throughout the simulation activities.

The effect of packing size on the pressure drop and liquid holdup is ascribed by different specific surface area of the packing material for the trickle-bed reactor. It has been found that the packing characteristics affect the gas and liquid velocity with the effect of gas velocity being prominent at high superficial gas mass velocities. The theoretical predictions from the model correctly account for the strong influence of the gas flow on the hydrodynamic behaviour of the trickle-bed reactors, as shown by the several results examined in this work. The important influence of the gas flow is attributed to the interactions phenomena exerted by the gas phase on the liquid phase. These interactions clearly appear to be significant at high superficial gas mass velocities.

Finally, through the Reynolds numbers evaluation in flow colour maps, deviations of the local velocity near the solid surfaces were observed which indicated the existence of more or less stagnant zones near the points of approximation retained from the packing spheres which enables the unsteady state behaviour exhibited by TBR in tricking flow conditions.

V.5. Nomenclature

$C_{1\varepsilon}$, $C_{2\varepsilon}$	k-ε model parameters: 1.44, 1.92
d	Particle nominal diameter, m
d_H	Hydraulic diameter, m
E_1, E_2	Ergun's constants: 150, 1.75
$\vec{F}_{lift,q}$	Lift force of q^{th} phase
$\vec{F}_{vm,q}$	Virtual mass force of q^{th} phase
$\vec{F}_q$	External body force of q^{th} phase
$\vec{g}$	Gravitational acceleration, 9.81m/s^2
G	Gas mass flux, kg/m^{2}s
k	k-ε model kinetic energy
K_{qp}	Interphase momentum exchange coefficient
L	Liquid mass flux, kg/m^{2}s
$\mathcal{L}$	Reactor length, m
p	Pressure, bar
$\vec{R}_{pq}$	Interaction force between phases p and q
Re_q	Reynolds number of q^{th} phase, dimensionless
T	Temperature, K
$\vec{u}$	Superficial vector velocity, m/s

Greek symbols

α_q	volume fraction of q^{th} phase
ε	k-ε model dissipation energy
μ_q	viscosity of q^{th} phase, Pa.s
ρ_q	density of q^{th} phase, kg/m^3
Δp	total pressure drop, bar
Π_{kq} , $\Pi_{\varepsilon q}$	Influence of the dispersed phases k and ε on the continuous phase
σ_k , σ_ε	k-ε model parameters: 1.2, 1.0
$\overline{\overline{\tau}}_q$	Shear stress tensor of q^{th} phase, bar

Subscripts

G	gas phase
L	liquid phase
q	q^{th} phase

S solid phase

V.6. References

Al-Dahhan, M.H., Larachi, F., Dudukovic, M.P., Laurent, A. (1997). High pressure trickle-bed reactors: A Review. *Industrial and Engineering Chemistry Research* **36** (8), 3292-3314.

Attou, A., Ferschneider, G.A. (1999). Two-fluid model for flow regime transition in gas-liquid trickle-bed reactors. *Chemical Engineering Science* **54** (21), 5031-5037.

Bhargava, S.K., Tardio, J., Prasad, J., Foger, K., Akolekar, D.B., Grocott, S.C. (2006). Wet Oxidation and Catalytic Wet Oxidation. *Industrial and Engineering Chemistry Research.* **45** (4), 1221-1258.

Carbonell, R.G. (2000). Multiphase flow models in packed beds. *Oil & Gas Science and Technology – Revue de l'IFP* **55**, 417-425.

Dudukovic, M.P., Larachi, F., Mills P.L. (2002). Multiphase catalytic reactors: A perspective on current knowledge and future trends. *Catalysis Reviews. Science and Engineering* **44** (1), 123-246.

Farmer, R., Pike, R., Cheng, G. (2005). CFD analyses of complex flows. *Computers and Chemical Engineering* **29**, 2386-2403.

FLUENT 6.1. (2005). User's Manual to FLUENT 6.1. Fluent Inc. Centrera Resource Park, 10 Cavendish Court, Lebanon, USA.

GAMBIT 2. (2005). User's Manual to GAMBIT 2. Fluent Inc. Centrera Resource Park, 10 Cavendish Court, Lebanon, USA.

Gianetto, A., Specchia, V. (1992). Trickle-bed reactors: State of the art and perspectives. *Chemical Engineering Science* **47**, 3197-3213.

Goto, S., Smith, J.M. (1975). Trickle bed reactors performance: I hold-up and mass transfer effects. *A.I.Ch.E. Journal* **21**, 706-713.

Gunjal, P.R., Ranade, V.V., Chaudhari, R.V. (2005). Computational study of a single-phase flow in packed beds of spheres, *A.I.Ch.E. Journal* **51** (2), 365-378.

Holub, R.A., Dudukovic, M.P., Ramachandran, P.A. (1993). Pressure drop, liquid hold-up and flow regime transition in trickle flow. *A.I.Ch.E. Journal* **39** (2), 302-321.

Jiang, Y., Khadilkar, M.R., Al-Dahhan, M.H., Dudukovic, M.P. (2002). CFD modeling of multiphase in packed bed reactors: results and applications. *A.I.Ch.E. Journal* **48**, 716-730.

Lakota, A. Levec, J. Carbonell, R.G. (2002). Hydrodynamics of trickling flow in packed beds: relative permeability concept. *A.I.Ch.E. Journal* **48**, 731-738.

Lopes, R.J.G., Silva, A.M.T., Quinta-Ferreira, R.M. (2007a). Kinetic Modelling and Trickle-Bed CFD Studies in the Catalytic Wet Oxidation of Vanillic Acid. *Industrial and Engineering Chemistry Research* **46** (25), 8380-8387.

Lopes, R.J.G., Quinta-Ferreira, R.M. (2007b). Trickle-Bed CFD Studies in the Catalytic Wet Oxidation of Phenolic Acids. *Chemical Engineering Science* **62** (24), 7045-7052.

Lopes, R.J.G., Quinta-Ferreira, R.M. (2008). Three-Dimensional Numerical Simulation of Pressure Drop and Liquid Holdup for High-Pressure Trickle-Bed Reactor. *Chemical Engineering Journal* **145** (1), 112-120.

Nemec, D., Levec, J. (2005). Flow through packed bed reactors: 2. Two phase concurrent downflow. *Chemical Engineering Science* **60** (24), 6958-6970.

Nijemeisland, M., Dixon, A.G. (2001). Comparison of CFD simulations to experiment for convective heat transfer in a gas-solid fixed bed. *Chemical Engineering Science* **82**, 231-246.

Patankar, S. V. (1980). Numerical Heat Transfer and Fluid Flow. Hemisphere, Washington, DC

Sáez, A.E., Carbonell, R.G. (1985). Hydrodynamic parameters for gas liquid cocurrent flow in packed beds. *A.I.Ch.E. Journal* **31** (1), 52-62.

Sederman, A.J., Gladden, L.F. (2005). Transition to pulsing flow in trickle-bed reactors studied using MRI, *A.I.Ch.E. Journal* **51**, 615-621.

Sie, S.T., Krishna, R. (1998). Process development and scale up: III. Scale-up and scale-down of trickle bed processes. *Reviews in Chemical Engineering* **14**, 203-252.

Tarca, L.A., Grandjean, B.P.A., Larachi, F. (2004). Embedding monotonicity and concavity in the training of neural networks by means of genetic algorithms: Application to multiphase flow. *Computers and Chemical Engineering* **28**, 1701-1713.

van der Merwe, W., Nicol, W. (2005). Characterization of multiple flow morphologies within trickle flow regime. *Industrial and Engineering Chemistry Research* **44** (25), 9446-9450.

Vasquez, S. A., Ivanov, V. A. (2000). A Phase Coupled Method for Solving Multiphase Problems on Unstructured Meshes. *In Proceedings of ASME FEDSM'00: ASME 2000 Fluids Engineering Division Summer Meeting*, Boston, June.

Wammes, W.J.A., Westerterp, K.R. (1990). The influence of reactor pressure on the hydrodynamics in a cocurrent gas-liquid trickle-bed reactor. *Chemical Engineering Science* **45** (8), 2247-2254.

This page intentionally left blank

VI. Turbulence Modelling of Multiphase Flow in High-Pressure Trickle-Bed Reactor[1]

Computational fluid dynamics (CFD) has been used as a successful tool for single-phase reactors. However, fixed-bed reactors design depends overly in empirical correlations for the prediction of heat and mass transfer phenomena. Therefore, the aim of this work is to present the application of CFD to the simulation of three-dimensional interstitial flow in a multiphase reactor. A case study comprising a high-pressure trickle-bed reactor (30 bar) was modelled by means of an Euler-Euler CFD model. The numerical simulations were evaluated quantitatively by experimental data from the literature. During grid optimization and validation, the effects of mesh size, time step and convergence criteria were evaluated plotting the hydrodynamic predictions as a function of liquid flow rate. Among the discretization methods for the momentum equation, a monotonic upwind scheme for conservation laws was found to give better computed results for either liquid holdup or two-phase pressure drop since it reduces effectively the numerical dispersion in convective terms of transport equation.

After the parametric optimization of numerical solution parameters, four Reynolds Averaged Navier-Stokes (RANS) multiphase turbulence models were investigated in the whole range of simulated gas and liquid flow rates. During RANS turbulence modelling, standard k-ε dispersed turbulence model gave the better compromise between computer expense and numerical accuracy in comparison with both realizable, renormalization group and Reynolds stress based models. Finally, several computational runs were performed at different temperatures for the evaluation of either axial averaged velocity and turbulent kinetic energy profiles for gas and liquid phases. Flow disequilibrium and strong heterogeneities detected along the packed bed demonstrated liquid distribution issues with slighter impact at high temperatures.

VI.1. Introduction

Trickle-bed reactors (TBR) are fixed-bed vertical columns that are mostly operated in concurrent gas-liquid downflow hosting a variety of catalytic reactions mainly in hydrotreating processes (e.g. hydrocracking, hydrodesulfurization, hydrodemetallization) and fine chemicals processing industries and, more recently, in waste gas and wastewater treatment plants (Al-Dahhan *et al.*, 1997).

[1] *This Chapter is based upon the publication Lopes and Quinta-Ferreira (2009)*

The design of a TBR depends on the precise knowledge of hydrodynamic parameters as long as the conversion of reactants and selectivity depend not only on reaction kinetics, operating pressure and temperature but also on the hydrodynamics of the reactor. Atmospheric and pressurized TBR experimental studies on hydrodynamic parameters of TBR are reviewed extensively by Saroha and Nigam (1996) and Iliuta *et al.*, (1999) proposing state-of-the-art correlations. However, the experimental investigations and their fitting parameters are only confined in a particular range of operation. For this reason the exact mathematical description of two-phase downflow in TBRs based upon the knowledge of complete velocity and holdup field distributions of individual phases is accomplished by means of modern computational fluid dynamics (CFD) codes (Atta *et al.*, 2007; Gunjal *et al.*, 2005; Jiang *et al.*, 2002).

Initially, mathematical modelling was limited to a 2D geometry of a few particles for laminar single-phase flow. As soon as sufficient and increasing computing capabilities became available, 3D simulations were reported in the literature using CFD codes to simulate heat and mass transfers in packed bed (Romkes *et al.*, 2003; Magnico, 2003; Logtenberg *et al.*, 1999). Several computational studies have recently developed mathematical models for simulating single-phase flow in packed beds (Calis *et al.*, 2001; Freund *et al.*, 2003; Tobis, 2000; Zeiser *et al.*, 2002). Numerical simulations of multiphase flow in TBRs were also published ranging from the traditional homogeneous and heterogeneous models without solving the velocity field to the Eulerian and Lagrangian CFD codes. Stanek and Szekely (1974) formulated a diffusion model to solve the equations of flow and diffusion, but the effect of gas–liquid interactions is neglected. The relative permeability model was initially proposed by Saez and Carbonell (1985) where the drag force is calculated by using the concept of relative permeability of each phase. Holub *et al*. (1992) developed a single slit model for the local flow of liquid and gas around the catalyst particles by assuming flow in rectangular inclined slits of width related to void fraction of the medium. Later, Iliuta *et al.* (2000) extended the model to allow for a distribution of slits that are totally dry in addition to slits that have liquid flow along the wall. Attou and Ferschneider (1999) developed a fluid-fluid interfacial force model in which the drag force for each phase has contributions from the particle-fluid interaction as well as from the fluid-fluid interaction. Recently, drag exchange coefficients are obtained from the relative permeability concept developed by Saez and Carbonell (1985) to perform CFD simulations based on a porous media model (Anderson and Sapre, 1991; Souadnia and Latifi, 2001; Atta *et al.*, 2007). Alternatively, in the *k*-fluid model the drag exchange coefficients can be obtained from the fluid-fluid interfacial force model as reported by Jiang *et al.* (2002) and Gunjal *et al.* (2005).

VI.2. Previous work

In order to simulate three-dimensional interstitial flow in packed tubes, two CFD approaches have been used to simulate fluid flow in fixed-bed reactors. Firstly, the entire packed bed limited to very low number of particles arranged in either a regular fashion or a random fashion was investigated by Logtenberg *et al.* (1999) and Calis *et al.* (2001). Secondly, the so-called unit-cell approach was used to overcome the size of the bed and the number of particles and can be further subdivided as follows. Each particle is assumed to have a hypothetical sphere of influence around it (Dhole *et al.*, 2004) or a unit periodic cell consisting of only a few particles is repeated successively in order to represent the 3D packed bed as reported by (Martin *et al.*, 1951; Sørensen and Stewart, 1974) with different packing arrangements of particles.

Depending on the thermophysical properties of fluids, flow rates, and catalyst loading, several types of flow patterns were observed experimentally by several authors. Mickley *et al.* (1965) found that eddy shedding did not occur in the packing voids and that high local heat transfer coefficients in spherical packings must be due to turbulence intensity in the voids quantified as high as 50%. In regular packings, Van der Merwe and Gauvin (1971) observed no eddy shedding over the range 2,500 < Re < 27,000 except on the first bank of spheres and turbulence intensity values were about 25%. The transition from steady to unsteady flow in a dumped bed of spheres in the range 110 < Re < 150 was found by Jolls and Hanratty (1966) who observed a vigorous eddying motion that they took to indicate turbulence at Re = 300. Wegner *et al.* (1971) observed completely steady flow with nine regions of reverse flow on the surface of the sphere for Re = 82 in regular beds of spheres monitoring similar flow elements but with different sizes in an unsteady flow at Re = 200. Dybbs and Edwards (1984) used laser anemometry and flow visualization to study flow regimes of liquids in hexagonal packings of spheres and rods and concluded that there are four flow regimes for different ranges of Reynolds number, based on interstitial or pore velocity $Re_i = Re/\varepsilon$: for $Re_i < 1$, the creeping flow is dominated by viscous forces and pressure drop is linearly proportional to interstitial velocity; for $1 \leq Re_i \leq 150$, the steady laminar inertial flow in which pressure drop depends nonlinearly on interstitial velocity; for $150 \leq Re_i \leq 300$, the laminar inertial flow is unsteady; and for $Re_i > 300$, the flow is highly unsteady, chaotic and qualitatively resembling turbulent flow. Latifi *et al.* (1989) used microelectrodes as electrochemical sensors to get more precise regime transitions and later Rode et al., 1994 included the transfer function of the electrochemical probe and gave the transition to time-dependent chaotic flow as 110 < Re < 150. Seguin *et al.* (1998a) found extremely non-homogeneous at different spatial locations in a packed tube occurring at Re = 113 inside the bed and at Re = 135 at the wall. Seguin *et al.* (1998b) found that the transition to the turbulent regime is gradual and not at the same Re at all locations after

performing the stabilization of the fluctuation rate which corresponds to local turbulence at 90% of the electrodes for $Re > 600$.

Several computational studies have been also performed on the turbulence modeling of fluid flow in packed-beds. Hill *et al.* (2001ab) investigated the effects of inertia on flows in both ordered and random arrays of spheres for small and moderate *Re* by means of lattice-Boltzmann simulations. Stevenson (2003) indicated that the transition from laminar flow to turbulence may occur at much lower *Re* in a packed tube than an empty one, due to the reduced viscous damping of radial velocity components caused by flow instabilities. Logtenberg *et al.* (1999) used a finite element code to simulate two layers of four spheres in laminar and turbulent flow based on *k-ε* turbulence model ($9 < Re < 1450$). With a mesh composed of 30,747 tetrahedral cells, they found reasonable agreement for Nusselt number and effective thermal conductivity compared with experimental values. Romkes *et al.* (2003) used CFD simulations to predict mass and heat transfer in a packed bed of 32 spheres, both in laminar and turbulent flow. The transfer rates were obtained with an average error of 15% compared with experimental data for Reynolds number either based on interstitial velocity or hydraulic diameter from 10^{-1} to 10^{5}. Magnico (2003) presented a numerical sensitivity study of meshing and solving parameters in laminar fluid flow and mass transfer in a packed bed of several hundred of spheres. Guardo *et al.* (2005) compared the numerical prediction obtained with 5 turbulence models (Spalart-Almaras, standard *k-ε*, RNG *k-ε*, realizable *k-ε*, standard *k-w*) for a packed bed of 44 spheres. The best agreement with commonly used correlations was obtained with the Spalart-Almaras model which is less sensitive to the near-wall treatment. Gunjal *et al.* (2005) used a laminar model up to $Re_i = 204$ and turbulent models for $Re_i =$ 1,000-2,000. Merrikh and Lage (2005) used the CFD approach in the case of natural convection within up to 64 solid particles. They studied fluid flow and heat transfer in a differentially heated square enclosure with disconnected solids blocks.

VI.3. Present work

From the above survey, the detail of the fluid flow mechanical studies on particle arrays is not in accordance on which range for Reynolds number split the laminar flow from the turbulent flow. In the present work, we perform an evaluation of either laminar or different Reynolds Averaged Navier-Stokes (RANS) turbulence models (Standard (SKE), Realizable (RKE) and Renormalization Group Theory (RNG) *k-ε*, Reynolds Stress Model (RSM) for multiphase flow in trickle-bed reactors. A multifluid Eulerian model is presented with interphase coupling parameters in the momentum balance equation from the work developed by Attou and Ferschneider (1999). A trickle-bed reactor with regular packing is considered as the base geometry for the simulation of

the three-dimensional interstitial flow to describe the fluid phase scale interactions at the catalyst level. As long as the details of the flow environment around the catalyst particles are essential, different mesh densities in the optimization of numerical solution parameters (time step, convergence criteria and differencing scheme of governing equations) have to be performed under unsteady laminar and turbulent flow simulations in order to provide a more fundamental understanding of trickle-bed hydrodynamics. To the best of our knowledge, this investigation on multiphase flow turbulence is sought here in order to incorporate more realistic fluid flow and evaluate in detail three-dimensional velocity and turbulent kinetic energy profiles as well.

VI.4. CFD Modelling

VI.4.1. Euler-Euler framework and drag force formulation

Multiphase flow in the trickle-bed reactor was modelled using a CFD multiphasic approach incorporated in the FLUENT 6.1 software that is the Euler-Euler multiphase model. The Eulerian framework encompassing the continuity and momentum equations was presented in Equations (V.1) and (V.2) in Chapter V. The drag force formulation was expressed by the individual momentum exchange forms in terms of interstitial velocities and phase volume fraction as described in Equations (V.4)-(V.7) in Chapter V.

VI.4.2. RANS turbulence modelling

Aiming to describe the effects of turbulent fluctuations of velocities and scalar quantities for the multiphase flow in the present case study, three methods were investigated for modelling turbulence in the trickle-bed within the context of the k-ε models. SKE, RKE and RNG models have similar forms being the major difference between them the calculation of turbulent viscosity and turbulent Prandtl numbers. For this reason only the additional options for the standard k-ε turbulence model are described in Table VI.1, VI.2 and VI.3 that are mixture turbulence model, dispersed turbulence model (which is the default model used through the Eulerian simulations) and finally a turbulence model for each phase, respectively. In what concerns the RSM model (Table VI.4), two options were examined that are the mixture turbulence model and the dispersed turbulence model. For the RSM model, the tilde denotes phase-averaged variables while an overbar reflects time-averaged values.

Table VI.1. *k-ε* Mixture Turbulence Model

Transport Equations
$\frac{\partial}{\partial t}(\rho_m k)+\nabla\cdot(\rho_m \vec{u}_m k)=\nabla\cdot\left(\frac{\mu_{t,m}}{\sigma_k}\nabla k\right)+G_{k,m}-\rho_m\varepsilon$
$\frac{\partial}{\partial t}(\rho_m \varepsilon)+\nabla\cdot(\rho_m \vec{u}_m \varepsilon)=\nabla\cdot\left(\frac{\mu_{t,m}}{\sigma_\varepsilon}\nabla \varepsilon\right)+\frac{\varepsilon}{k}\times(C_{1\varepsilon}G_{k,m}-C_{2\varepsilon}\rho_m\varepsilon)$
$\rho_m=\sum_{i=1}^{N}\alpha_q\rho_q \qquad \vec{u}_m=\frac{\sum_{i=1}^{N}\alpha_q\rho_q\vec{u}_q}{\sum_{q=1}^{N}\alpha_q\rho_q} \qquad \mu_{t,m}=\rho_m C_\mu\frac{k^2}{\varepsilon}$
$G_{k,m}=\mu_{t,m}\left(\nabla\vec{u}_m+(\nabla\vec{u}_m)^T\right):\nabla\vec{u}_m$

Table VI.2. *k-ε* Dispersed Turbulence Model

Turbulence in the Continuous Phase
$\frac{\partial}{\partial t}(\alpha_q\rho_q k_q)+\nabla\cdot(\alpha_q\rho_q\vec{u}_q k_q)=\nabla\cdot\left(\alpha_q\frac{\mu_{t,q}}{\sigma_k}\nabla k_q\right)+\alpha_q G_{k,q}-\alpha_q\rho_q\varepsilon_q+\alpha_q\rho_q\Pi_{kq}$
$\frac{\partial}{\partial t}(\alpha_q\rho_q\varepsilon_q)+\nabla\cdot(\alpha_q\rho_q\vec{u}_q\varepsilon_q)=\nabla\cdot\left(\alpha_q\frac{\mu_{t,q}}{\sigma_\varepsilon}\nabla\varepsilon_q\right)+\alpha_q\frac{\varepsilon_q}{k_q}\times(C_{1\varepsilon}G_{k,q}-C_{2\varepsilon}\rho_q\varepsilon_q)+\alpha_q\rho_q\Pi_{\varepsilon q}$
$\overline{\overline{\tau}}_q=\alpha_q\mu_q(\nabla\vec{u}_q+\nabla\vec{u}_q^T)+\alpha_q(\lambda_q-\frac{2}{3}\mu_q)\nabla\cdot\vec{u}_q\overline{\overline{I}}$
$\mu_{t,q}=\rho_q C_\mu\frac{k_q^2}{\varepsilon_q} \qquad \tau_{t,q}=\frac{3}{2}C_\mu\frac{k_q}{\varepsilon_q} \qquad L_{t,q}=\sqrt{\frac{3}{2}}C_\mu\frac{k_q^{3/2}}{\varepsilon_q}$
$\Pi_{kq}=\sum_{p=1}^{M}\frac{K_{pq}}{\alpha_q\rho_q}\left(<\vec{u}_q''\cdot\vec{u}_p''>+(\vec{U}_p-\vec{U}_q)\cdot\vec{u}_{dr}\right) \qquad \Pi_{kq}=\sum_{p=1}^{M}\frac{K_{pq}}{\alpha_q\rho_q}\left(k_{pq}-2k_q+\vec{u}_{pq}\cdot\vec{u}_{dr}\right)$
$\Pi_{\varepsilon q}=C_{3\varepsilon}\frac{\varepsilon_q}{k_q}\Pi_{kq}$
Turbulence in the Dispersed Phase
$\tau_{F,pq}=\alpha_p\rho_q K_{pq}^{-1}\left(\frac{\rho_p}{\rho_q}+C_V\right) \qquad \tau_{t,pq}=\frac{\tau_{t,q}}{\sqrt{(1+C_\beta\xi^2)}} \qquad \xi=\frac{\lvert\vec{u}_{pq}\rvert\,\tau_{t,q}}{L_{t,q}}$
$C_\beta=1.8-1.35\cos^2\theta \qquad \eta_{pq}=\frac{\tau_{t,pq}}{\tau_{F,pq}} \qquad k_p=k_q\left(\frac{b^2+\eta_{pq}}{1+\eta_{pq}}\right)$
$k_{pq}=2k_q\left(\frac{b+\eta_{pq}}{1+\eta_{pq}}\right) \qquad D_{t,pq}=\frac{1}{3}k_{pq}\tau_{t,pq} \qquad D_p=D_{t,pq}+\left(\frac{2}{3}k_p-b\frac{1}{3}k_{pq}\right)\tau_{F,pq}$
$b=(1+C_V)\left(\frac{\rho_p}{\rho_q}+C_V\right)^{-1}$
Interphase Turbulent Momentum Transfer
$K_{pq}(\vec{u}_p-\vec{u}_q)=K_{pq}(\vec{U}_p-\vec{U}_q)-K_{pq}\vec{v}_{dr} \qquad \vec{u}_{dr}=-\left(\frac{D_p}{\sigma_{pq}\alpha_p}\nabla\alpha_p-\frac{D_q}{\sigma_{pq}\alpha_q}\nabla\alpha_q\right)$

Table VI.3. *k-ε* Turbulence Model for Each Phase

Transport Equations
$\frac{\partial}{\partial t}\left(\alpha_q \rho_q k_q\right)+\nabla\cdot\left(\alpha_q \rho_q \vec{U}_q k_q\right)=\nabla\cdot\left(\alpha_q \frac{\mu_{t,q}}{\sigma_k}\nabla k_q\right)+\left(\alpha_q G_{k,q}-\alpha_q \rho_q \varepsilon_q\right)+$
$\sum_{l=1}^{N} K_{lq}\left(C_{lq}k_l - C_{ql}k_q\right)-\sum_{l=1}^{N} K_{lq}\left(\vec{U}_l-\vec{U}_q\right)\cdot\frac{\mu_{t,l}}{\alpha_l\sigma_l}\nabla\alpha_l+\sum_{l=1}^{N} K_{lq}\left(\vec{U}_l-\vec{U}_q\right)\cdot\frac{\mu_{t,q}}{\alpha_q\sigma_q}\nabla\alpha_q$
$\frac{\partial}{\partial t}\left(\alpha_q \rho_q \varepsilon_q\right)+\nabla\cdot\left(\alpha_q \rho_q \vec{U}_q \varepsilon_q\right)=\nabla\cdot\left(\alpha_q \frac{\mu_{t,q}}{\sigma_\varepsilon}\nabla\varepsilon_q\right)+\frac{\varepsilon_q}{k_q}\left(C_{1\varepsilon}\alpha_q G_{k,q}+C_{2\varepsilon}\alpha_q\rho_q\varepsilon_q\right)+$
$C_{3\varepsilon}\frac{\varepsilon_q}{k_q}\left[\sum_{l=1}^{N} K_{lq}\left(C_{lq}k_l - C_{ql}k_q\right)-\sum_{l=1}^{N} K_{lq}\left(\vec{U}_l-\vec{U}_q\right)\cdot\frac{\mu_{t,l}}{\alpha_l\sigma_l}\nabla\alpha_l+\sum_{l=1}^{N} K_{lq}\left(\vec{U}_l-\vec{U}_q\right)\cdot\frac{\mu_{t,q}}{\alpha_q\sigma_q}\nabla\alpha_q\right]$
$C_{lq}=2\,,\quad C_{ql}=2\left(\frac{\eta_{lq}}{1+\eta_{lq}}\right)$
Interphase Turbulent Momentum Transfer
$\sum_{l=1}^{N} K_{lq}\left(\vec{v}_l-\vec{v}_q\right)=\sum_{l=1}^{N} K_{lq}\left(\vec{U}_l-\vec{U}_q\right)-\sum_{l=1}^{N} K_{lq}\vec{v}_{dr,lq}$

Table VI.4. RSM Turbulence Models

Transport Equations
$\frac{\partial}{\partial t}\left(\overline{\alpha_c}\rho_c\right)+\nabla\cdot\left(\overline{\alpha_c}\rho_c\widetilde{U}_c\right)=0$
$\frac{\partial}{\partial t}\left(\overline{\alpha_c}\rho_{rmc}\widetilde{U}_c\right)+\nabla\cdot\left(\overline{\alpha_c}\rho_{rmc}\widetilde{U}_c\otimes\widetilde{U}_c\right)=-\overline{\alpha_c}\nabla\tilde{p}+\nabla\cdot\tilde{\tau}_c^t+F_{Dc}$
$F_{Dc}=K_{dc}\left[\left(\widetilde{U}_d-\widetilde{U}_c\right)-\left(\frac{\overline{\alpha_d u_d^{'}}}{\overline{\alpha_d}}-\frac{\overline{\alpha_c u_c^{'}}}{\overline{\alpha_c}}\right)\right]$ $\qquad$ $\tilde{\tau}_k^t=-\overline{\alpha_k}\rho_k\widetilde{R}_{k,ij}$
RSM Dispersed Turbulence Model
$\frac{\partial}{\partial t}\left(\overline{\alpha}\rho\widetilde{R}_{ij}\right)+\frac{\partial}{\partial x_k}\left(\overline{\alpha}\rho\widetilde{U}_k\widetilde{R}_{ij}\right)=-\overline{\alpha}\rho\left(\widetilde{R}_{ik}\frac{\partial\widetilde{U}_j}{\partial x_k}+\widetilde{R}_{jk}\frac{\partial\widetilde{U}_i}{\partial x_k}\right)+\frac{\partial}{\partial x_k}\left[\overline{\alpha}\mu\frac{\partial}{\partial x_k}\left(\widetilde{R}_{ij}\right)\right]$ $\qquad$ $=\frac{\partial}{\partial x_k}\left[\overline{\alpha}\rho\overline{u_i^{'}u_j^{'}u_k^{'}}\right]+\overline{\alpha}\overline{p\left(\frac{\partial u_i^{'}}{\partial x_j}+\frac{\partial u_j^{'}}{\partial x_i}\right)}-\overline{\alpha}\rho\tilde{\varepsilon}_{ij}+\Pi_{R,ij}$
$\Pi_{R,ij}=K_{dc}C_{1,dc}\left(R_{dc,ij}-R_{c,ij}\right)+K_{dc}C_{2,dc}a_{dc,i}b_{dc,j}$ $\qquad$ $\Pi_{R,ij}=\frac{2}{3}\delta_{ij}\Pi_k$
$\Pi_{kc}=K_{dc}\left(\widetilde{k}_{dc}-2\widetilde{k}_c+\widetilde{U}_{rel}\cdot\widetilde{U}_{drift}\right)$
RSM Mixture Turbulence Model
$\widetilde{U}_m=\frac{\sum_{q=1}^{N}\overline{\alpha_q}\rho_q\widetilde{U}_q}{\sum_{q=1}^{N}\overline{\alpha_q}\rho_q}$ $\qquad$ $\rho_m=\sum_{q=1}^{N}\overline{\alpha_q}\rho_q$

VI.5. Numerical simulation

The present case-study encompasses a trickle-bed reactor that was designed using regular shape catalyst particles for multifluid Eulerian simulations. Gas-liquid flows through a catalytic bed comprised of monosized, spherical, solid particles arranged in a cylindrical container of a pilot TBR unit (50 mm internal diameter ×1.0 m length). The computational mesh of the catalytic bed was shortened in length given the high memory requirements so that the reactor was filled with 13 layers where approximately 200 non-overlapping spherical particles of 2 *mm* diameter were necessary for each axial layer as shown in Fig. VI.1.

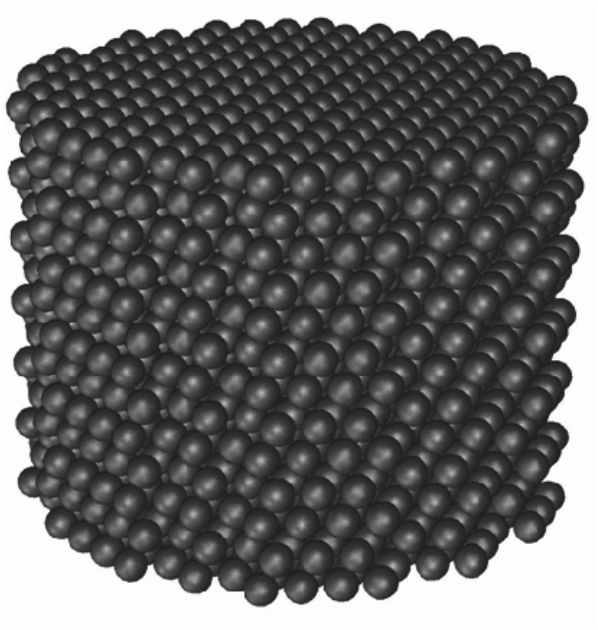

Figure VI.1. Schematic of the catalytic packing geometry for the trickle-bed reactor

In order to prevent numerical difficulties associated with the mesh generation also reported in the literature (Logtenberg *et al.*, 1999), the catalyst particles do not touch each other and the distance gap was fixed by 2-3 % percent of the sphere diameter. The grid of the catalytic bed was created using the integrated solid modelling and meshing commercial program GAMBIT. Geometrical errors arising from the mesh style and quality were evaluated according to different mesh densities and discretization parameters. Consecutively, the number of cells necessary to produce grid independent results for the hydrodynamic parameters was increased from 2×10^5 to 10^6, with other numerical solution parameters including operating conditions given by Table VI.5, where upwind differencing schemes are presented for discretization of convective terms for: *first-order upwind* (FOU), *second-order upwind*, (SOU), *Power-Law* (PL), *quadratic upwind interpolation for convective kinematics* (QUICK) and *monotonic upwind scheme for conservation laws* (MUSCL) (Appendix A, section A.4). Gas and liquid thermophysical properties used in the simulation are

summarized in Table VI.6. High-pressure operation was simulated at 30 *bar* total operating pressure with inflow gas (G = 0.1 – 0.7 kg/m^{2}s) and liquid (L = 1 – 15 kg/m^{2}s) being distributed uniformly with given superficial velocity replicating a uniform distributor at the top of trickle-bed reactor.

Table VI.5 – Numerical solution parameters used in the CFD simulation

Grid	1000 mm (axial) × 50 mm (radial)
Cell size	0.01 - 0.20 mm (tetrahedral and hexahedral)
Particle diameter	2 mm (spheres)
Time step	10^{-5} – 10^{-2} s
Convergence criteria	10^{-5} – 10^{-2}
Discretization	
Momentum	*FOU, SOU, Power-Law, QUICK, MUSCL*
Volume fraction	*FOU, QUICK*
Turbulent kinetic energy	*FOU, SOU, Power-Law, QUICK, MUSCL*
Turbulent energy dissipation	*FOU, SOU, Power-Law, QUICK, MUSCL*
Iterations	≈ 50,000
Under-relaxation parameters	Pressure: 0.2-0.6
	Velocity: 0.4-0.8
	Turbulent kinetic energy: 0.8
	Turbulent energy dissipation: 0.8
Drag formulation	Attou and Ferschneider (1999)
Turbulence model	SKE, RKE, RNG, RSM

Table VI.6 – Relevant thermophysical properties of gas and liquid phases

Properties	Value (P = 30bar)		Units
	T = 25ºC	T = 200ºC	
Liquid phase			
Viscosity	8.925×10^{-4}	1.340×10^{-4}	Pa.s
Density	998.4	866.9	kg/m^3
Surface tension	7.284×10^{-2}	3.770×10^{-2}	N.m
Thermal conductivity	6.063×10^{-1}	6.657×10^{-1}	W/mK
Gas phase			
Viscosity	1.845×10^{-5}	2.584×10^{-5}	Pa.s
Density	35.67	21.97	kg/m^3
Thermal conductivity	2.708×10^{-2}	3.839×10^{-2}	W/mK

To the inlet and boundary conditions requested for the solution of the Eulerian model given in Chapter V (Table V.2), turbulent kinetic energy, k, and turbulent energy dissipation, ε, at the reactor entrance at 200ºC must now be additionally supplied (Table VI.7), once computational runs at high temperatures were also carried out beyond the ambient temperature (25ºC) previously analysed.

Table VI.7 – Inlet boundary conditions for the gas and liquid phases: turbulent kinetic energy (k_q) and turbulent energy dissipation (ε_q) at T=200ºC and P=30 bar

G (kg/m^{2}s)	L (kg/m^{2}s)	k_G (mm^2/s^2)	k_L (mm^2/s^2)	ε_G (mm^2/s^3)	ε_L (mm^2/s^3)
0.1	1	0.5907	3.219×10^{-2}	1.335×10^{-2}	3.015×10^{-4}
0.4	1	6.683	3.219×10^{-2}	1.709	3.015×10^{-4}
0.7	1	17.79	3.219×10^{-2}	12.119	3.015×10^{-4}
0.1	8	0.5907	1.225	1.335×10^{-2}	0.4367
0.4	8	6.683	1.225	1.709	0.4367
0.7	8	17.79	1.225	12.119	0.4367
0.1	15	0.5907	3.680	1.335×10^{-2}	3.941
0.4	15	6.683	3.680	1.709	3.941
0.7	15	17.79	3.680	12.11	3.941

Aiming to assess the hydrodynamic scales of trickling flow, the Kolmogorov's theory was used to evaluate the turbulent microscales. The Kolmogorov's hypothesis of local isotropy for homogenous turbulence states that the turbulent kinetic energy is the same everywhere. The local isotropy means isotropy at small scales and large scale turbulence may still be anisotropic. Kolmogorov argued that the directional biases of the large scales are lost in the chaotic scale-reduction process as energy is transferred to successively smaller eddies. Hence Kolmogorov's hypothesis of local isotropy states that at sufficiently high Reynolds numbers, the small-scale turbulent motions are statistically isotropic. Given the two parameters ε (energy dissipation rate per unit mass with dimensions length^2/time^3) and ν (kinematic viscosity, length^2/time) we can form the following unique length and time scales $\eta_K = (\nu^3 / \varepsilon)^{1/4}$ and $\tau_K = (\nu / \varepsilon)^{1/2}$, respectively. These scales are indicative of the smallest eddies present in the flow that is the scale at which the kinetic energy is dissipated.

In this work, the hydrodynamic scales of length and time were computed to verify the adequacy of the computational grid and temporal discretization schemes. The Kolmogorov length (η_K) and time scales (τ_K) are calculated at different gas and liquid flow rates as well as at different pressures and temperatures as shown in Table VI.8. As it can be seen from the tabulated data, both Kolmogorov length and time scales attain continuously lower values as the gas and liquid flow rates are increased. Regarding the temperature influence, The range of microscale length and time scales varies between $1.028\text{-}7.574\times10^{-3}$ m and $0.018\text{-}20.51\times10^{-3}$ s for the gas phase, whereas for the liquid phase $0.175\text{-}10.59\times10^{-3}$ m and $0.198\text{-}113.7\times10^{-3}$ s, respectively. According to the Kolmogorov theory, acceptable accuracy in DNS is obtained if the grid spacing is four to six times lower than the Kolmogorov length scale. In our studies the time step range (10^{-2}-10^{-5}s) used in the temporal discretization, as well as the grid resolution (0.01-0.2mm) incorporates only partially the Kolmogorov criteria for DNS. Therefore, numerical results with various grid dimensions and time steps will be presented in order to guarantee appropriate CFD independent results in what concerns these numerical parameters.

Table VI.8 – Kolmogorov length (η_K) and time scales (τ_K) of gas and liquid phases

G / kg/m^{2}s	L / kg/m^{2}s	T / ºC	P / bar	$\eta_{K,G}$ ×10^3/ m	$\eta_{K,L}$ ×10^3/ m	$\tau_{K,G}$ ×10^3 / s	$\tau_{K,L}$ ×10^3/ s
0.1	1	25	30	5.6406	10.588	20.506	113.65
0.4	1	25	30	1.6770	10.588	1.8125	113.65
0.7	1	25	30	1.0277	10.588	0.6807	113.65
0.1	8	25	30	5.6406	1.7163	20.506	2.9865
0.4	8	25	30	1.6770	1.7163	1.8125	2.9865
0.7	8	25	30	1.0277	1.7163	0.6807	2.9865
0.1	15	25	30	5.6406	0.9902	20.506	0.9940
0.4	15	25	30	1.6770	0.9902	1.8125	0.9940
0.7	15	25	30	1.0277	0.9902	0.6807	0.9940
0.1	1	25	1	5.6406	10.070	0.6724	109.91
0.4	1	25	1	1.6770	10.070	0.0594	109.91
0.7	1	25	1	1.0277	10.070	0.0223	109.91
0.1	8	25	1	5.6406	1.6323	0.6724	2.8882
0.4	8	25	1	1.6770	1.6323	0.0594	2.8882
0.7	8	25	1	1.0277	1.6323	0.0223	2.8882
0.1	15	25	1	5.6406	0.9417	0.6724	0.9613
0.4	15	25	1	1.6770	0.9417	0.0594	0.9613
0.7	15	25	1	1.0277	0.9417	0.0223	0.9613
0.1	1	200	30	7.5738	1.9417	16.258	23.210
0.4	1	200	30	2.2517	1.9417	1.4370	23.210
0.7	1	200	30	1.3799	1.9417	0.5397	23.210
0.1	8	200	30	7.5738	0.3148	16.258	0.6099
0.4	8	200	30	2.2517	0.3148	1.4370	0.6099
0.7	8	200	30	1.3799	0.3148	0.5397	0.6099
0.1	15	200	30	7.5738	0.1816	16.258	0.2030
0.4	15	200	30	2.2517	0.1816	1.4370	0.2030
0.7	15	200	30	1.3799	0.1816	0.5397	0.2030
0.1	1	200	1	7.5738	1.8734	0.5447	22.663
0.4	1	200	1	2.2517	1.8734	0.0481	22.663
0.7	1	200	1	1.3799	1.8734	0.0181	22.663
0.1	8	200	1	7.5738	0.3037	0.5447	0.5955
0.4	8	200	1	2.2517	0.3037	0.0481	0.5955
0.7	8	200	1	1.3799	0.3037	0.0181	0.5955
0.1	15	200	1	7.5738	0.1752	0.5447	0.1982
0.4	15	200	1	2.2517	0.1752	0.0481	0.1982
0.7	15	200	1	1.3799	0.1752	0.0181	0.1982

VI.6. Results and discussion

VI.6.1. Parametric optimization of mesh size, time step and convergence criteria

The liquid holdup and pressure drop predicted by the CFD simulations are quantitatively compared with the literature experimental results (Nemec and Levec, 2005). We begin with a base case examining the influence of model solution parameters including different mesh apertures, time steps as well as convergence criteria. Concerning the mesh sensitivity analysis, several computational runs were performed changing the mesh density in order to properly capture the void space and catalyst particle surface.

In Fig. VI.2 it is plotted four simulation sets of liquid holdup as a function of liquid flow rate at P=30 bar and G=0.1 kg/m^{2}s with the coarsest mesh which corresponds to about 2×10^5 tetrahedral cells and the finest mesh with one million tetrahedral cells. The spatial resolution is about d/20

which gives an average cell size of 0.01-0.2 mm for the finer meshes depending on the packing geometry of the catalytic bed. As it can be seen from Fig. VI.2, low mesh density (2×10^5 of tetrahedral cells) at particle surface led to erroneous solutions due to an incorrect definition of interstitial space. As long as the mesh density increases, the theoretical predictions of liquid holdup improve considerably. The experimental data used for the parametric optimization were available from the work developed by Nemec and Levec (2005) in where it was decribed in detail the experimental setup. In that work, liquid holdup was measured by a gravimetric method that consists in weighting the column in two different ways to have good reproducibility.

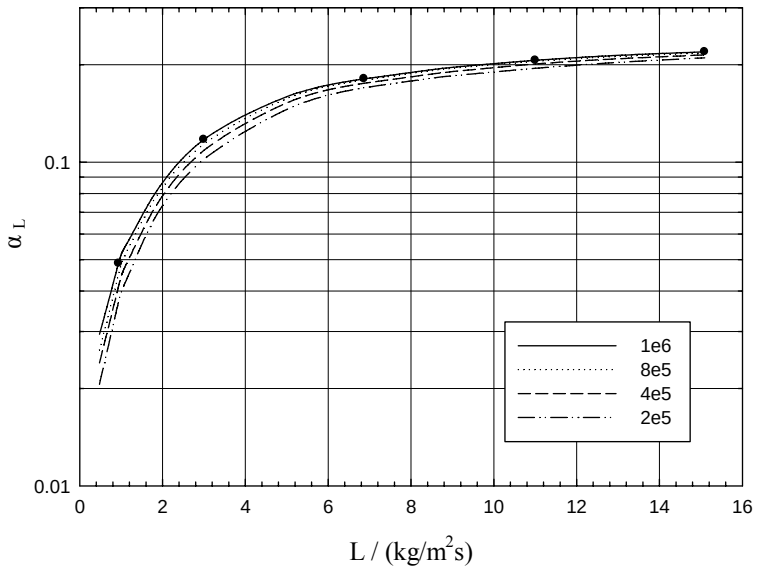

Figure VI.2. Comparison of liquid holdup predictions as a function of liquid flow rate for different mesh resolutions (G=0.1 kg/m^{2}s, P=30 bar, d=2 mm and experimental data represented by dots from Nemec and Levec, 2005)

After the bed was extensively prewetted, the reactor with dimensions similar to the ones described previously was operated first in a high interaction regime and then reduced to the desired level at which the pressure drop and liquid holdup were measured. According to Fig. VI.2 with G=0.1 kg/m^{2}s in where it was plotted the experimental data represented by dots from the work of Nemec and Levec (2005), the liquid holdup numerical simulations performed at L=1 kg/m^{2}s with the coarser meshes (2×10^5, 4×10^5) gave a relative error of 23.8 and 14.9%, while the finer meshes (8×10^5, 10^6) gave 7.1 and 1.5% of relative error, respectively. At L=15 kg/m^{2}s, the relative errors for the computed liquid holdup results were 4.1, 2.1, 1.7 and 1.0%. As a result, 10^6 tetrahedral cells correspond to the optimum number which gave mesh-independent results with respect to liquid holdup. Frictional pressure drop predictions as a function of liquid flow rate at high-pressure operation are plotted in Fig. VI.3 as well as the experimental data represented by dots from the work developed by Nemec and Levec (2005).

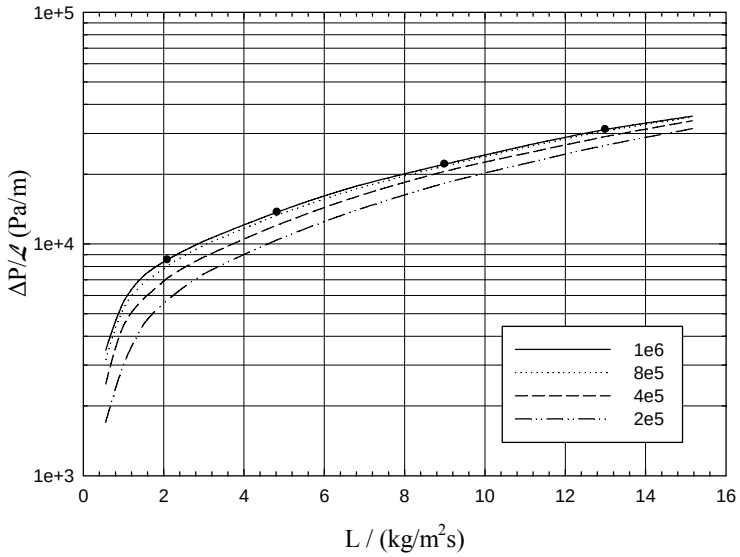

Figure VI.3. Comparison of two-phase pressure drop predictions as a function of liquid flow rate for different mesh resolutions (G=0.5 kg/m^{2}s, P=30 bar, d=2 mm and experimental data represented by dots from Nemec and Levec, 2005)

At P=30 bar and L=1 kg/m^{2}s, the relative errors obtained for the two-phase pressure drop were 32.7, 16.3, 5.2 and 1.6% from the coarse to the fine meshes, respectively. If the operation is simulated at the highest liquid flow rate (L=15 kg/m^{2}s), the relative errors became lesser 41.3, 6.6, 1.4 and 1.0% for 2×10^5, 4×10^5, 8×10^5 and 10^6 tetrahedral cells, respectively. Therefore, both hydrodynamic parameters are underpredicted if one uses a coarse mesh. The same value for the number of tetrahedral cells were achieved for mesh-independent results with respect to both liquid holdup and pressure drop with the finest mesh so that it was used as the base case setting for subsequent parametric investigation of other model solution parameters. These conclusions are in agreement with those achieved in the previous Chapter (Figs. V.2 and V.3), where a similar analysis was presented for a higher gas flow rate (G = 0.7 kg/m^{2}s).

Using as the base case the finest tetrahedral mesh with about one million cells, several computational runs were carried out with different time steps, whereas the precedent studies included in Chapter V were accomplished with a time step equal to 10^{-3} s (Lopes and Quinta-Ferreira, 2008). Taking into account that a nominal time step in the range 10^{-2}-10^{-3} s has often been used in the Eulerian simulations for gas-liquid flows (Gunjal *et al.*, 2003; Jiang *et al.*, 2002), this model parameter was selected in the parametric study with values of 10^{-5}, 10^{-4}, 10^{-3} and 10^{-2} s. In Fig. VI.4 it is plotted the computed liquid holdup as a function of liquid flow rate at P=30 bar and G=0.1 kg/m^{2}s with these time step values. As one can conclude, the decrease of time step from 10^{-2} to 10^{-3} and further to 10^{-4} s gave better agreement between the Eulerian model predictions and experimental data. However, a subsequent decrease to 10^{-5} s did not show any significant gain in numerical accuracy indicating that it reached an asymptotic solution. In fact, the numerical

predictions of liquid holdup at P=30 bar and G=0.1 kg/m^{2}s with the highest liquid flow rate exhibited a relative error of 17.4, 5.4, 1.9 and 1.0% for time steps of 10^{-2}, 10^{-3}, 10^{-4} and 10^{-5} s, respectively. In what concerns the predicted pressure field, in Fig. VI.5 it was plotted two-phase pressure drop as a function of liquid flow rate. The relative errors obtained at P=30 bar and L=15 kg/m^{2}s of 20.0, 7.9, 2.3 and 1.0% demonstrated that a time step of 10^{-4}s gave already a good compromise between computational power and the respective numerical accuracy achieved with both liquid holdup and pressure drop, whilst from now on 10^{-5} s was used for the numerical simulations.

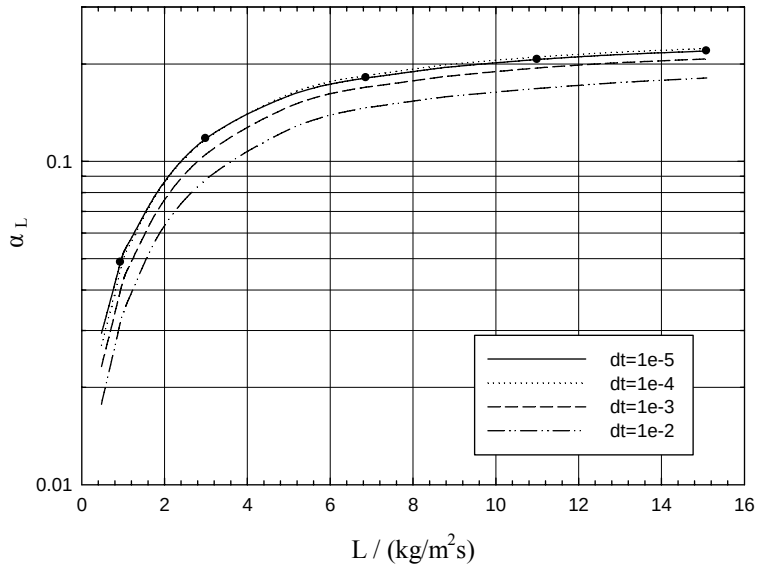

Figure VI.4. Effect of time step on liquid holdup predictions as a function of liquid flow rate with the finest mesh (10^6 of tetrahedral cells, G=0.1 kg/m^{2}s, P=30 bar, d=2 mm and experimental data represented by dots from Nemec and Levec, 2005)

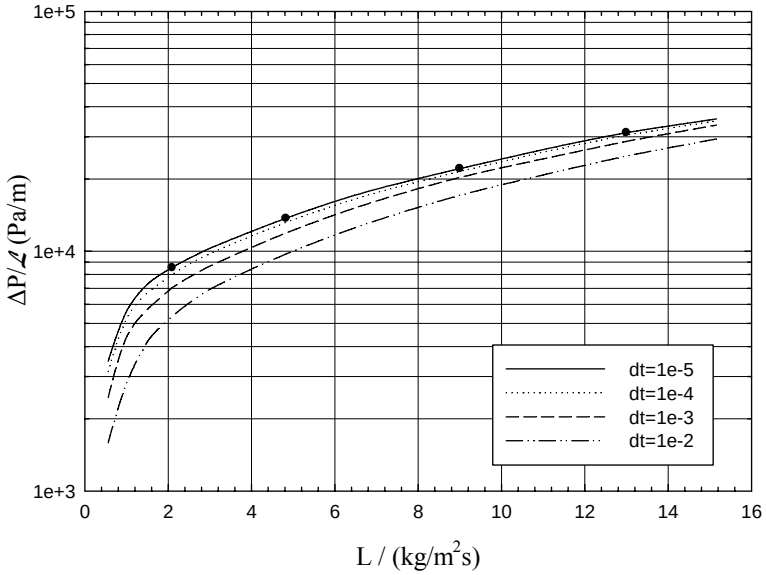

Figure VI.5. Effect of time step on two-phase pressure drop predictions as a function of liquid flow rate with the finest mesh (10^6 of tetrahedral cells, G=0.5 kg/m^{2}s, P=30 bar, d=2 mm and experimental data represented by dots from Nemec and Levec, 2005)

Aiming to examine the influence of different convergence criteria on the hydrodynamics predictions, different scaled residual components of volume fraction, *x, y, z*-velocity and turbulent kinetic energy and turbulent energy dissipation were investigated in the range 10^{-5}, 10^{-4}, 10^{-3} and 10^{-2}. Liquid holdup predictions as a function of liquid flow rate with different convergence criteria at P=30 bar and G=0.1 kg/m^{2}s are plotted in Fig. VI.6.

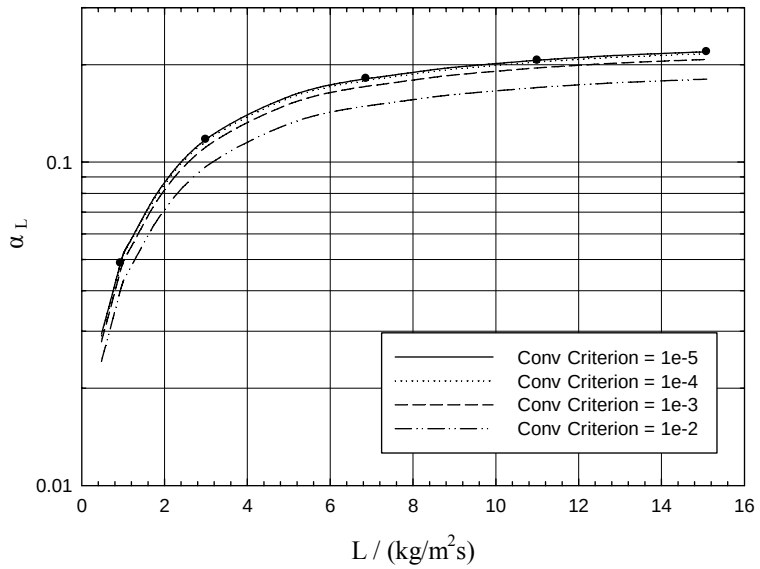

Figure VI.6. Effect of convergence criteria on liquid holdup predictions as a function of liquid flow rate (time step = 10^{-5} s, 10^6 of tetrahedral cells, G=0.1 kg/m^{2}s, P=30 bar, d=2 mm and experimental data represented by dots from Nemec and Levec, 2005)

According to this plot, it was found that changing the convergence criteria method produced almost the same effect as observed with different time steps. In fact, the relative errors between the computed results and experimental data were 17.6, 5.3, 1.2 and 1.0 at the highest liquid flow rate (L=15 kg/m^{2}s) with residual components of 10^{-2}, 10^{-3}, 10^{-4} and 10^{-5}, respectively. This computational behaviour was expected since a value decrease in the scaled residual component imply that the CFD calculation is performed with better accuracy. This fact was also observed in the pressure field computations as shown in Fig. VI.7, which established the following increasing order of relative error attained at L=15 kg/m^{2}s: 1.0, 3.1, 10.7 and 27.1% for 10^{-2}, 10^{-3}, 10^{-4} and 10^{-5}, respectively. Further studies were performed with this lower value, 10^{-5}.

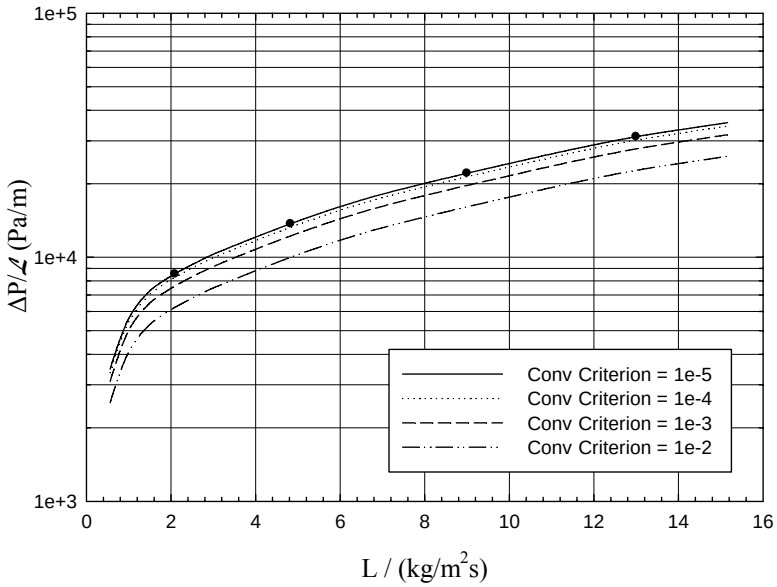

Figure VI.7. Effect of convergence criteria on two-phase pressure drop predictions as a function of liquid flow rate (time step = 10^{-5} s, 10^6 of tetrahedral cells, G=0.5 kg/m^{2}s, P=30 bar, d=2 mm and experimental data represented by dots from Nemec and Levec, 2005)

VI.6.2. Investigation of differencing scheme

After the base case definition and the achievement of grid size, time step and convergence criteria independent results with respect to both liquid holdup and two-phase pressure drop, five numerical upwind differencing schemes were evaluated for the discretization of momentum equation convective terms including FOU, SOU, PL, QUICK and MUSCL. Regarding the discretization of the convective terms of the volume fraction (for which only FOU and QUICK could be assessed in the FLUENT code), turbulent kinetic energy and energy dissipation equations, no differences were detected for different criteria, being thus used the scheme with lower order (FOU).

In Fig. VI.8 it is shown the liquid holdup predictions as a function of liquid flow rate with different discretization schemes at P=30 bar and G=0.1 kg/m^{2}s. Generally, as it can be seen from Fig. VI.8 second-order computations (SOU) agreed reasonably with liquid holdup experimental data (Nemec and Levec, 2005) for the whole range of simulated liquid flow rate. In fact, the simulation performed at the highest liquid flow rate (L=15 kg/m^{2}s) gave the following decreasing order of relative error: 25.6, 4.9, 4.9, 2.6, 1.0% for FOU, PL, SOU, QUICK and MUSCL, respectively. As one can conclude from these values, as long as the high-order of differencing scheme so do a better concordance was achieved for the liquid holdup simulations. The relative error obtained with PL and SOU was almost the same and their value decreased when the simulation is carried out with QUICK and further MUSCL schemes.

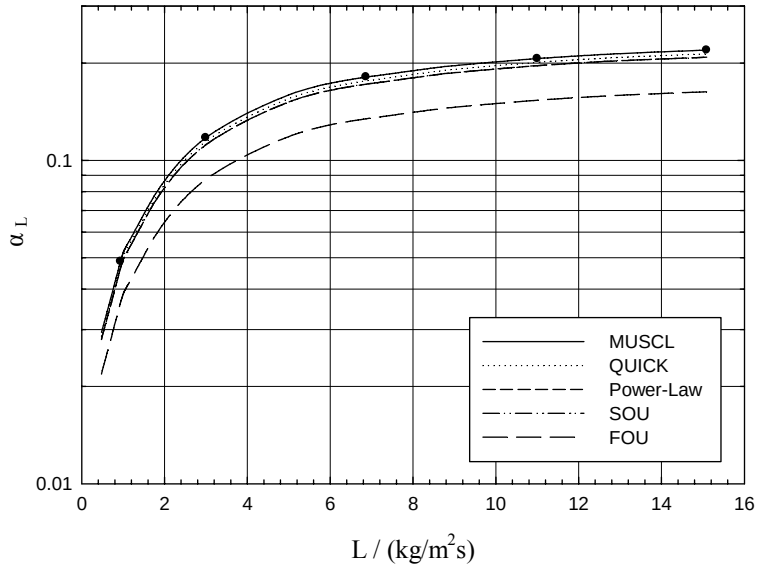

Figure VI.8. Effect of discretization scheme of volume fraction equation (MUSCL, QUICK, Power-Law, SOU and FOU) on liquid holdup predictions as a function of liquid flow rate (time step = 10^{-5} s, 10^6 of tetrahedral cells, G=0.1 kg/m^{2}s, P=30 bar, d=2 mm and experimental data represented by dots from Nemec and Levec, 2005)

The relative position of differencing schemes in respect to the obtained relative errors is more or less as expected since the third-order quadratic upwind scheme (QUICK) and SOU are generally better for complex flows than FOU providing a more realistic behaviour in terms of hydrodynamics predictions. Notwithstanding, MUSCL exhibited the minor relative error with less numerical iterations required for convergence probably due to the high-order spatial accuracy and its foundation in *total variation diminishing* (TVD) scheme (Harten, 1983). TVD schemes are well-known in providing high accuracy numerical solutions to partial differential equations which involve most likely the existence of shocks or discontinuities or even large gradients as characterized by the multiphase flow nature in trickle-bed reactors. It is worth noting that current MUSCL scheme implemented in the CFD solver is a third-order convection scheme conceived from the original MUSCL (Van Leer, 1979) by blending a central-differencing scheme and second-order upwind scheme. Therefore, compared to the second-order upwind scheme, the third-order MUSCL revealed a fair potential to improve spatial accuracy of multiphase flow with the finest mesh (10^6 of tetrahedral cells) by reducing numerical diffusion, most significantly for complex three-dimensional flows in trickle-beds. In Fig. VI.9, frictional pressure drop predictions are plotted as a function of liquid flow rate with the same investigated differencing schemes for the liquid holdup. Once more, FOU simulations gave the worst agreement with pressure drop experimental data, and both SOU and *Power-Law* schemes gave approximately the same relative error. As a matter of fact, MUSCL predictions showed again the highest numerical accuracy followed by QUICK simulations. The relative errors obtained at L=15 kg/m^{2}s were 34.7, 18.5, 15.5, 8.5 and 1.0 % for FOU, SOU, PL, QUICK and MUSCL schemes, respectively.

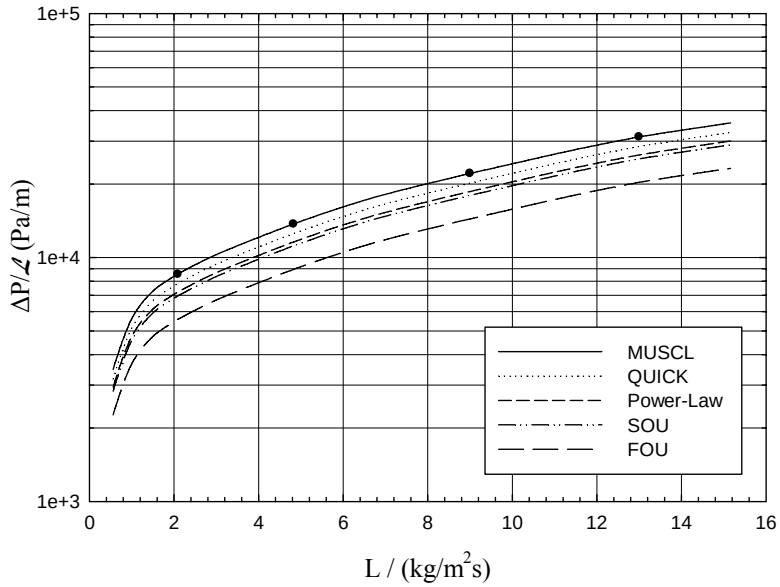

Figure VI.9. Effect of discretization scheme of volume fraction equation (MUSCL, QUICK, Power-Law, SOU and FOU) on two-phase pressure drop predictions as a function of liquid flow rate (time step = 10^{-5} s, 10^6 of tetrahedral cells, G=0.5 kg/m^{2}s, P=30 bar, d=2 mm and experimental data represented by dots from Nemec and Levec, 2005)

VI.6.3. Evaluation of RANS turbulence models

The parametric investigation of mesh size, time step, convergence criteria and momentum equation differencing scheme ascertained CFD independent results with one million tetrahedral cells, 10^{-5} s for the time step, scaled residuals of 10^{-5} with the MUSCL scheme. With this case setting, several Reynolds averaged Navier-Stokes turbulence models were tested in order to investigate the effect of turbulence model on hydrodynamic parameters. In the context of the *k-ε* models (standard (SKE), realizable (RKE) and renormalization group theory (RNG) based models), three multiphase different options were further examined: the mixture turbulence model, the dispersed turbulence model and a per-phase turbulence model. In what concerns the Reynolds stress model (RSM), two options were evaluated including the mixture turbulence and dispersed turbulence models.

In Fig. VI.10 it is shown the liquid holdup predictions as a function of liquid flow rate at P=30 bar and G=0.1 kg/m^{2}s for the SKE, RKE, RNG and RSM dispersed turbulence models. As it can be seen, the better concordance was obtained with SKE and RSM models. At the highest simulated liquid flow rate (L=15 kg/m^{2}s), the following increasing order for the relative error was RSM < SKE < RNG < RKE. In spite of the lower relative error attained with RSM simulations, RSM required the highest computing time with around 50,000 of numerical iterations. This fact is probably due to its inherent hypothesis of anisotropic eddy-viscosity as the RSM closes the RANS equations by solving transport equations for the Reynolds stresses, together with an equation for the dissipation.

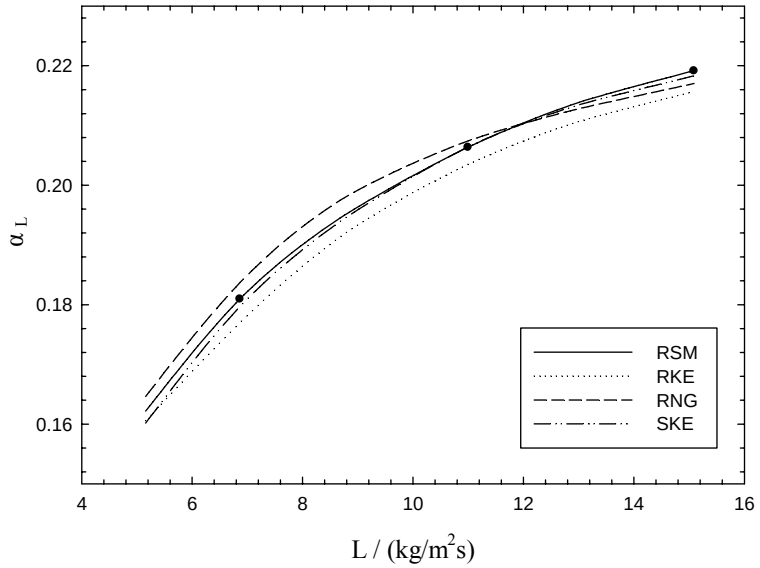

Figure VI.10. Influence of RANS turbulence model on liquid holdup predictions as a function of liquid flow rate (MUSCL, time step = 10^{-5} s, 10^6 of tetrahedral cells, G=0.1 kg/m^{2}s, P=30 bar, d=2 mm and experimental data represented by dots from Nemec and Levec, 2005)

Moreover, the better numerical accuracy can be also attributed since the RSM accounts for the effects of streamline curvature, swirl, rotation, and rapid changes in strain rate in a more rigorous manner than two-equation turbulence models (as standard *k*-*ε* models). Bearing in mind that multiphase flow in a packed bed poses a great problem to account properly for the boundary layer, it should be pointed out that the reliability of RSM predictions with the finest mesh (10^6 of tetrahedral cells) is still limited by the closure assumptions employed in the exact transport equations for the Reynolds stresses in trickle-beds. Although published works have already indicated that the mesh have to be dense enough in order to capture boundary layer phenomena over the walls (catalyst surface), the Reynolds number dependence of the mesh was found to have no significant effect during all RANS computations, but it should become significant with the increase of Reynolds number (Spalart, 2000).

During the RSM simulations, it was found that pressure-strain and dissipation-rate modelling were responsible for the expensive computations without giving a much different relative error for the liquid holdup (Fig. VI.10) in comparison with *k*-*ε* dispersed turbulence model. Alternatively, the CFD calculations with RKE and RNG did not show any improvement comparing with SKE. The major differences in the *k*-*ε* models are related with the method of calculating the turbulent viscosity, the turbulent Prandtl numbers of *k* and *ε* and the mathematical formulation of generation and destruction terms in the turbulent energy dissipation. Although RKE accounts for the transport of the mean-square vorticity fluctuation in the turbulent energy dissipation (*ε*) equation and RNG

theory provides an analytical formula for turbulent Prandtl numbers, after all SKE dispersed turbulence model demonstrated the better compromise between numerical accuracy and computational cost for both liquid holdup and pressure drop predictions. Two-phase pressure drop calculations were plotted in Fig. VI.11 as a function of liquid flow rate. Once more, RSM agreed better with experimental data followed by SKE, RKE and RNG dispersed turbulence models. The relative errors for the frictional pressure drop were 0.8, 1.0, 6.3 and 9.5% for RSM, SKE, RKE and RNG, respectively.

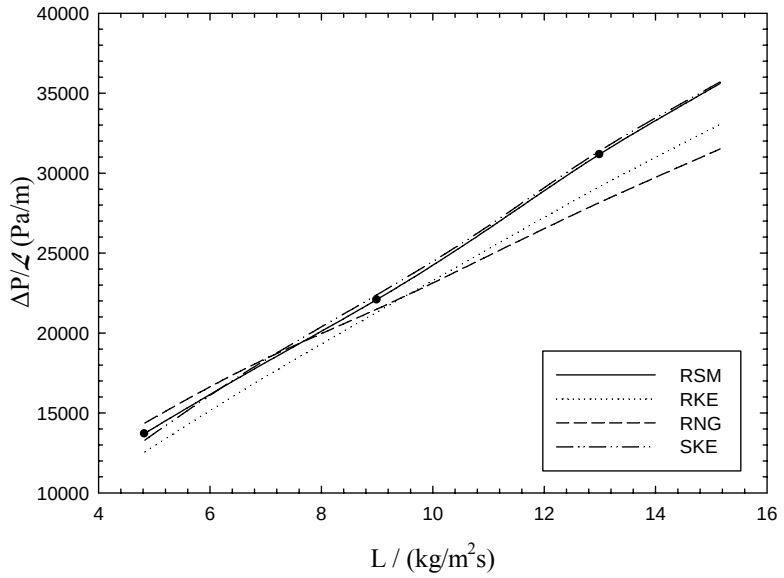

Figure VI.11. Influence of RANS turbulence model on two-phase pressure drop predictions as a function of liquid flow rate (MUSCL, time step = 10^{-5} s, 10^6 of tetrahedral cells, G=0.5 kg/m^{2}s, P=30 bar, d=2 mm and experimental data represented by dots from Nemec and Levec, 2005)

VI.6.4. Liquid and gas velocity profiles

As trickle-bed reactors are often operated at high temperatures either in petrochemical hydrotreatments or in the catalytic wet oxidations of high strength wastewaters (Bhargava *et al.*, 2006), the effect of temperature on TBR hydrodynamics was evaluated plotting the liquid and gas axial velocities at ambient temperature and at 200ºC. This higher temperature was selected since it is a common value in the organic content decontamination of phenolic wastewaters by means of catalytic wet air oxidation. In Fig. VI.12a it is shown the axial profile along the dimensionless coordinate, $z^*=z/\mathcal{L}$ of time averaged liquid velocity magnitude at T=25ºC, P=30bar, G=0.7 kg/m^{2}s and L=1 kg/m^{2}s.

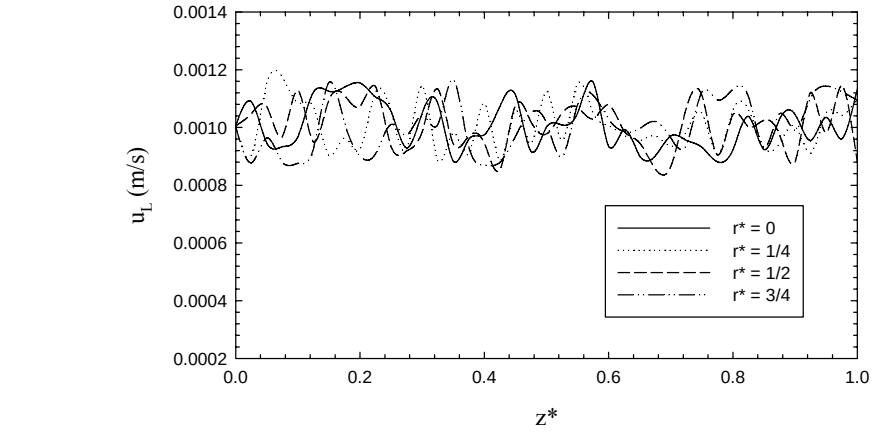

a)

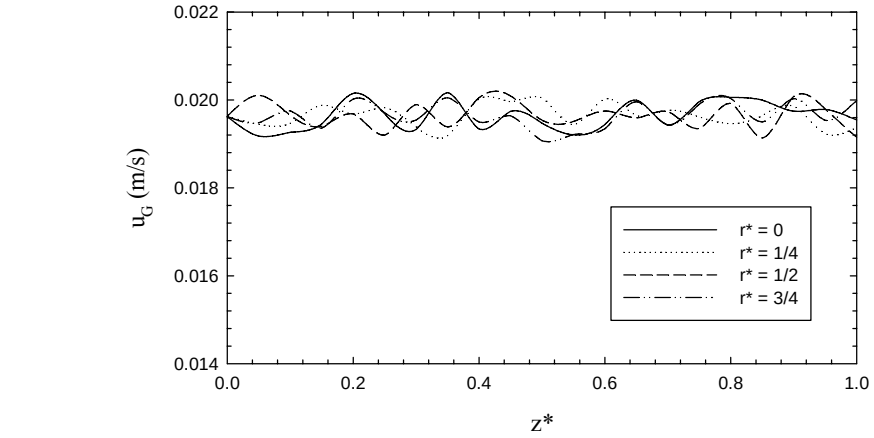

b)

Figure VI.12. Axial profile of time-averaged velocity along the packed bed for the **a)** liquid and **b)** gas phase at L=1 kg/m^{2}s and T=25ºC (MUSCL, time step = 10^{-5} s, 10^6 of tetrahedral cells, G=0.7 kg/m^{2}s, P=30 bar, d=2 mm)

This time averaging procedure consists in the selection of nominal operating times such as 10, 30, 60 and 360 s so that the axial liquid velocity is time-averaged for a single radial coordinate. Four dimensionless radial coordinates (r*=r/R, being R the radius of the trickle-bed reactor) were selected: r*=0, ¼, ½ and ¾. At the lowest liquid flow rate (L=1 kg/m^{2}s), according to Fig. VI.12 it was found an oscillatory behaviour for the axial liquid velocity around the mean value of u_L=0.1 cm/s. The intensity of these oscillations produced by the catalytic bed configuration was quantified with maxima of 15.2% and minima of -12.3% at the trickle-bed reactor centre (r*=0) and it may be attributed to the existence of different mixing levels at the catalyst scale being almost identical for all radial positions. The axial profile of gas velocity at the same operating conditions is shown in Fig. VI.12b. With a mean axial velocity value of about u_G=1.96 cm/s, the maxima and minima values were 2.8 and -2.3%, respectively. These values were substantially lower than those attained for the axial liquid velocity which indicated an improved homogeneity for the gas velocity spatial distribution. The spatial distribution of axial liquid and gas velocity can be seen in the snapshots of the velocity vector profiles inside the catalytic bed at two orthogonal axial planes as shown in Fig. VI.13a and b, respectively.

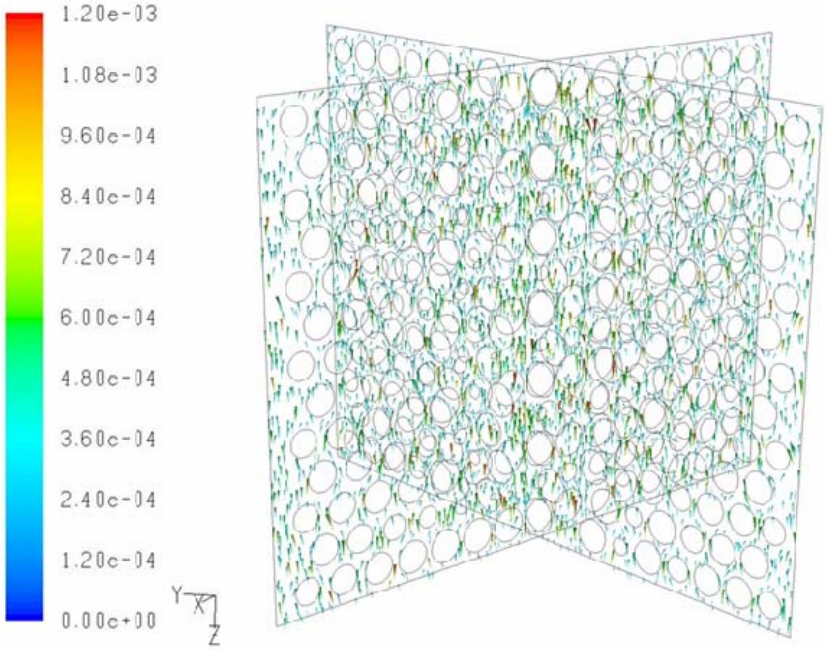

a)

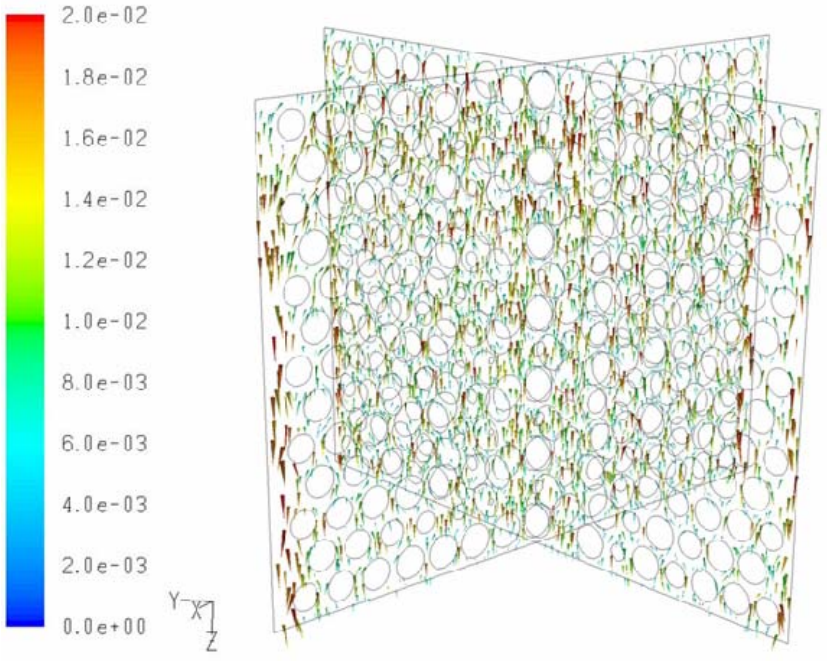

b)

Figure VI.13. Velocity vector distribution (*m/s*) along the packed bed at two orthogonal axial planes for the **a)** liquid and **b)** gas phase at L=1 kg/m^{2}s and T=25ºC (MUSCL, time step = 10^{-5} s, 10^6 of tetrahedral cells, G=0.7 kg/m^{2}s, P=30 bar, d=2 mm)

According to Fig. VI.13a, at T=25ºC, P=30bar, G=0.7 kg/m^{2}s and L=1 kg/m^{2}s the maxima values were about the same magnitude as observed in Fig. VI.12a. However, the minima values accomplished in Fig. VI.13a were lesser than 0.08 cm/s for any radial coordinate. The maxima and minima values for the time-averaged axial gas velocity observed in Fig. VI.12b can also be identified in Fig. VI.13b. Moreover, the liquid velocity profile attained with the lowest liquid flow

rate (L=1 kg/m^{2}s) in Fig. VI.13a illustrated the existence of flow channelling effects near the catalyst particles. This fact is often regarded as the result of improper liquid distribution at the top of the trickle-bed reactor. For this reason, during all CFD simulations it was mimicked an ideal gas-liquid distributor which prevents or at least limits the extension of liquid maldistribution in trickle-beds, thus channelling phenomena are here due to geometric and hydrodynamic bed characteristics.

Fig. VI.14a shows the axial liquid velocity profile increasing the operating temperature up to 200ºC maintaining the other operating variables constant (P=30 bar, G=0.7 kg/m^{2}s and L=1 kg/m^{2}s). As one can observe, the intensity of the maxima and minima values decreased considerably for both phases whatever the radial coordinated. The maxima and minima values for the time-averaged axial liquid velocity were 4.3 and -3.7% whereas for the axial gas velocity those values decreased down to 1.5 and -1.1%. Therefore, the increase of temperature has a flattening effect on the axial velocity profiles.

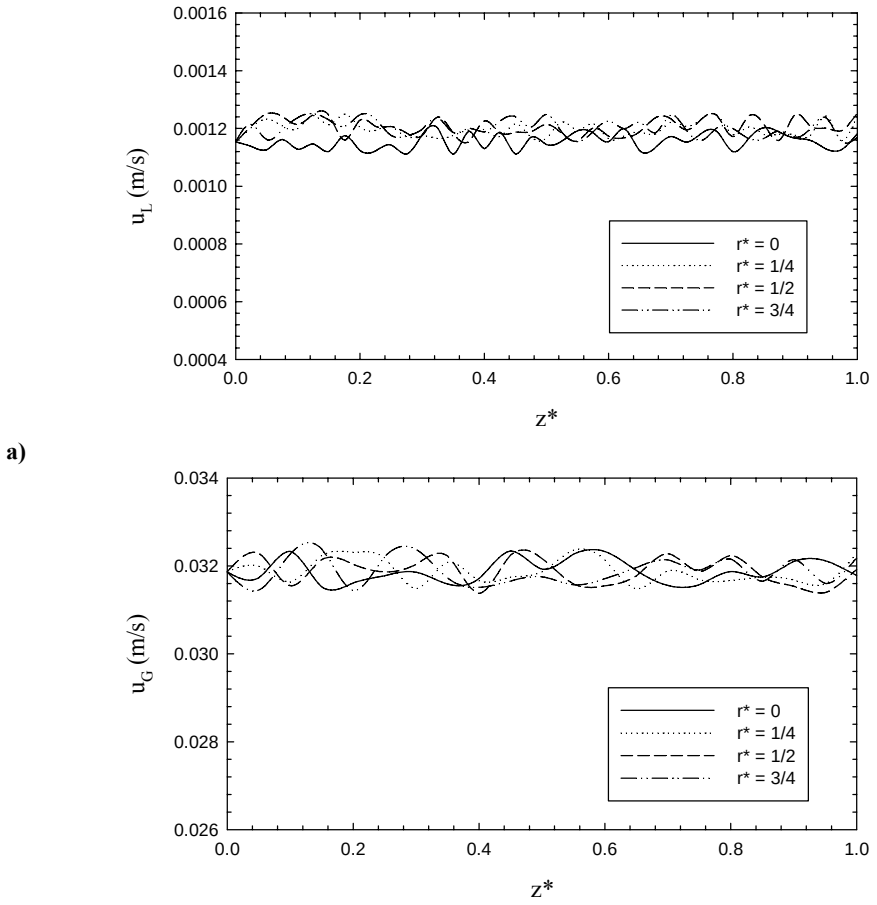

Figure VI.14. Axial profile of time-averaged velocity along the packed bed for the **a)** liquid and **b)** gas phase at L=1 kg/m^{2}s and T=200ºC (MUSCL, time step = 10^{-5} s, 10^6 of tetrahedral cells, G=0.7 kg/m^{2}s, P=30 bar, d=2 mm)

As the aforementioned simulations were carried out with the lowest liquid flow rate (L=1 kg/m^{2}s), four additional sets were performed at L=15 kg/m^{2}s, G=0.7 kg/m^{2}s, P=30bar. Fig. VI.15a and b display the axial liquid and gas velocity profiles at different dimensionless radial coordinates at T=25ºC. At r*=0, the maxima and minima for the liquid velocity were 3.3 and -6.5% whereas for the gas velocity those values were 3.5 and -5.9%, respectively. Comparing these values with those obtained in Fig. VI.12a and b, the phase velocity profiles were smoothed as long as the liquid flow rate increases from L=1 to 15 kg/m^{2}s. This fact can be explained due to the better and improved liquid distribution on the catalyst packing with higher liquid flow rates.

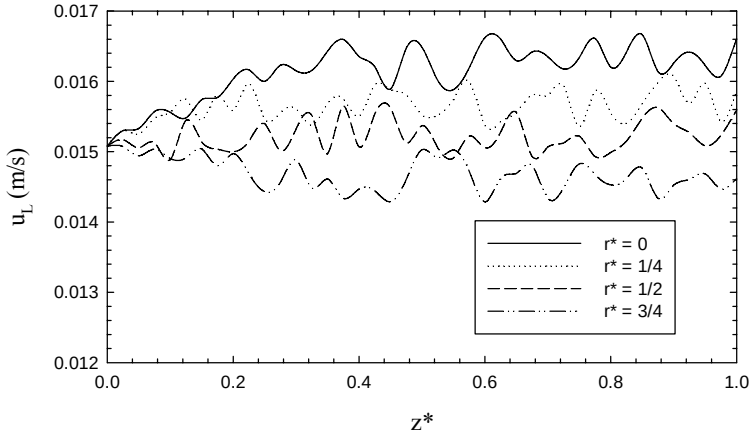

a)

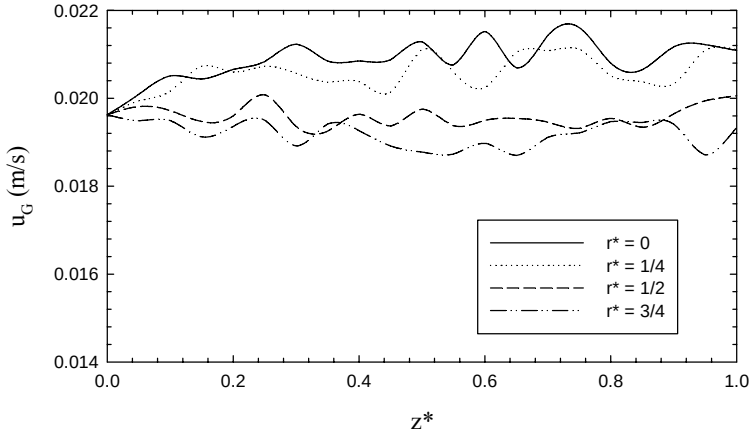

b)

Figure VI.15. Axial profile of time-averaged velocity along the packed bed for the **a)** liquid and **b)** gas phase at L=15 kg/m^{2}s and T=25ºC (MUSCL, time step = 10^{-5} s, 10^6 of tetrahedral cells, G=0.7 kg/m^{2}s, P=30 bar, d=2 mm)

In general and in concordance with the hydrodynamic predictions of liquid holdup already discussed, the higher liquid flow rate goes the higher liquid holdup is achieved for the TBR which had a positive effect on the liquid spreading over the particle surface. Furthermore, according to Figs. VI.15a and b it can now be observed that different time-averaged axial liquid profiles are obtained for different radial coordinates. Accordingly, the axial liquid velocity profiles begin to diverge as soon as the liquid phase is compelled to flow through the catalytic bed. The higher

liquid velocities were attained at the reactor centre and decreased as one moves towards the reactor wall. In order to evaluate also the influence of temperature at the highest simulated liquid flow rate (L=15 kg/m^{2}s), Fig. VI.16a and b plot the axial liquid and gas velocity profiles along the catalytic bed at T=200ºC, G=0.7 kg/m^{2}s, P=30bar, respectively. As expected, the maxima and minima became slightly lesser to 1.2, -3.3 and 3.3, -5.9 for the liquid and gas velocities, respectively. Once again, the divergence behaviour identified early at T=25ºC was now smoothened by the temperature increase to 200ºC.

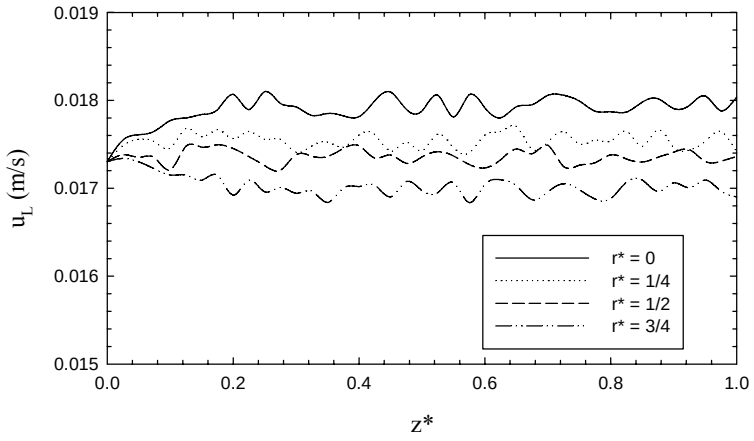

a)

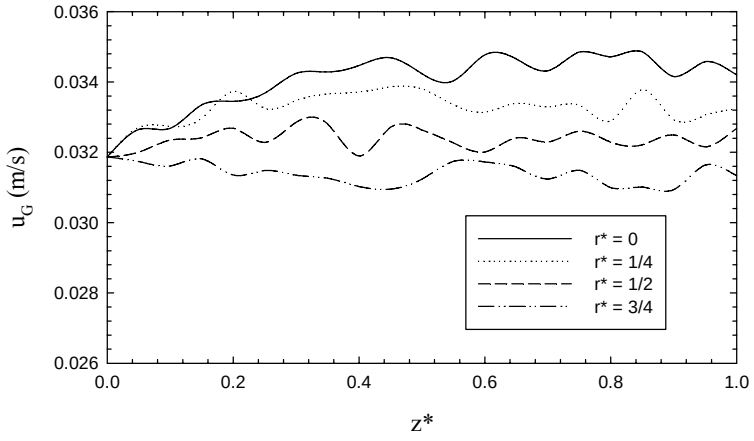

b)

Figure VI.16. Axial profile of time-averaged velocity along the packed bed for the **a)** liquid and **b)** gas phase at L=15 kg/m^{2}s and T=200ºC (MUSCL, time step = 10^{-5} s, 10^6 of tetrahedral cells, G=0.7 kg/m^{2}s, P=30 bar, d=2 mm)

VI.6.5. Liquid and gas turbulent kinetic energy profiles

At T=25ºC, P=30bar, G=0.7 kg/m^{2}s and L=15 kg/m^{2}s, the time-averaged axial profile for the liquid turbulent kinetic energy is shown in Fig. VI.17a for different dimensionless radial coordinates whereas the gas turbulent kinetic energy profile is depicted in Fig. VI.17b. At the highest simulated liquid flow rate, it was also identified a considerable degree of heterogeneity in the axial turbulent transport properties. As it can be seen, the maxima and minima values were 1.1, -2.0% and 4.1, -7.1% for the liquid and gas phases, respectively.

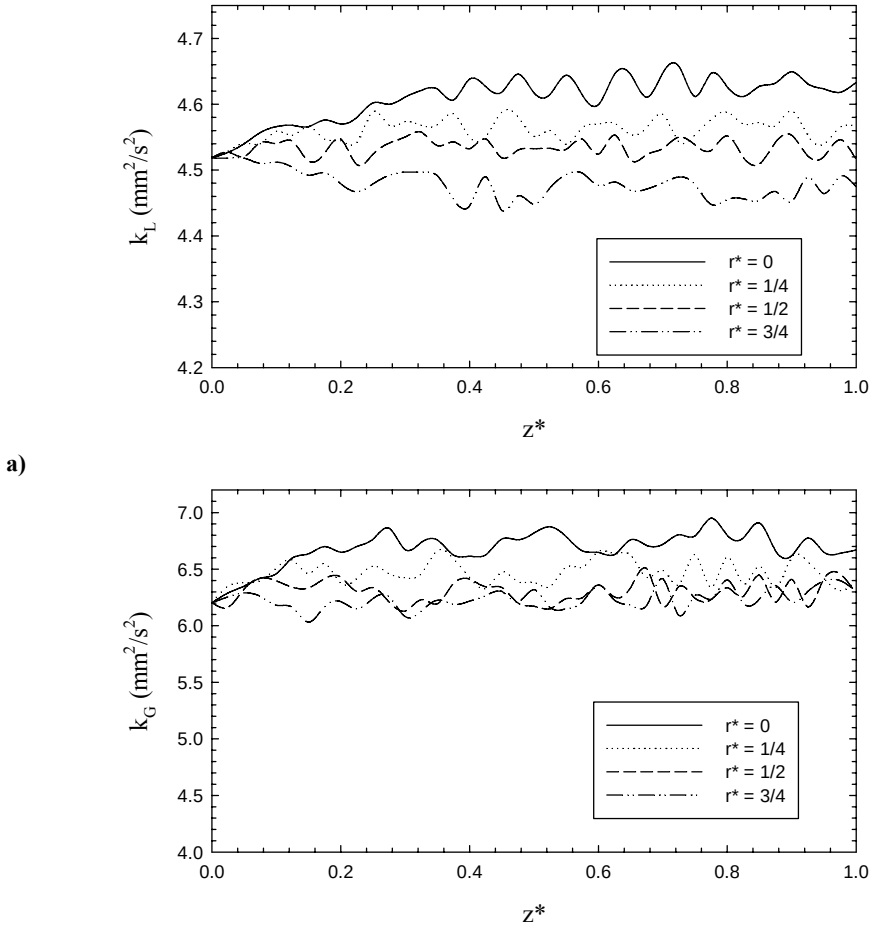

Figure VI.17. Time-averaged axial profile of turbulent kinetic energy (mm^2/s^2) along the packed bed for the **a)** liquid and **b)** gas phase at L=15 kg/m^{2}s and T=25ºC (MUSCL, time step = 10^{-5} s, 10^6 of tetrahedral cells, G=0.7 kg/m^{2}s, P=30 bar, d=2 mm)

Increasing the temperature up T=200ºC, Fig. VI.18a and b show the axial profile of the liquid and gas turbulent kinetic energy profiles. Accordingly, the new maxima and minima values were 0.7, -2.1% and 0.5, -1.0%, respectively. Once again, whatever the operating temperature the time-averaged turbulent kinetic energy property was deviating from the mean value established at the reactor inlet for either liquid or gas phases. This fact is a direct consequence of the divergence identified early in the time-averaged axial velocity profiles for both phases since the turbulent kinetic energy depends primarily on the phase velocity.

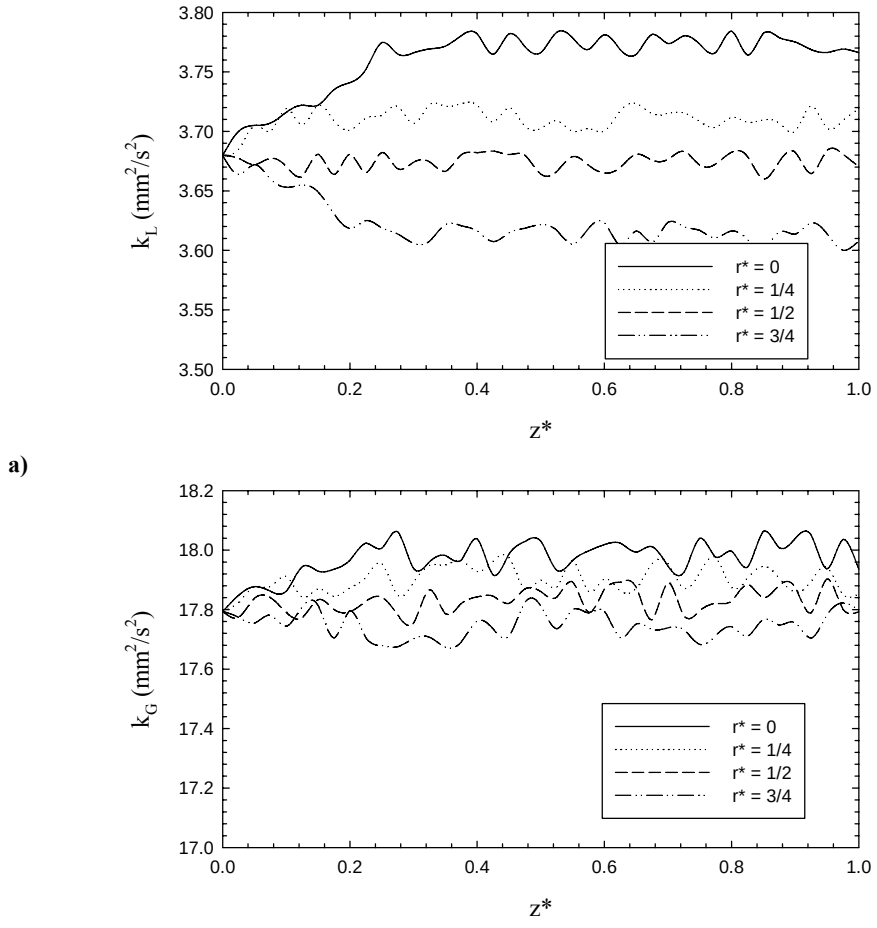

Figure VI.18. Time-averaged axial profile of turbulent kinetic energy (mm^2/s^2) along the packed bed for the **a)** liquid and **b)** gas phase at L=15 kg/m^{2}s and T=200ºC (MUSCL, time step = 10^{-5} s, 10^6 of tetrahedral cells, G=0.7 kg/m^{2}s, P=30 bar, d=2 mm)

At the lower temperature (T=25ºC), it was taken an instantaneous snapshot of a liquid holdup isosurface ($\alpha_L \approx 0.215$) coloured by the turbulent kinetic energy for the liquid phase as depicted in Fig. VI.19a whereas in Fig. VI.19b it is shown the gas holdup isosurface ($\alpha_G \approx 0.185$) coloured by the gas turbulent kinetic energy. As one can observe, the liquid and gas distribution is not uniform at the catalyst scale which identified computationally the so-called flow maldistribution of trickle-beds. These strong axial and radial heterogeneities were observed experimentally by Suekane *et al.* (2003) by means of a magnetic resonance imaging technique to directly measure the flow in a pore space of a packed bed. Comparing Fig. VI.17 and VI.18, in both plots it was detected that the turbulent kinetic energy profiles had a major magnitude variation for the liquid phase in opposition with the velocity profiles computed at the same operating conditions. Moreover, the increase of the temperature led to a slight decrease in the mean value of the liquid turbulent kinetic energy and an increase of gas turbulent kinetic energy.

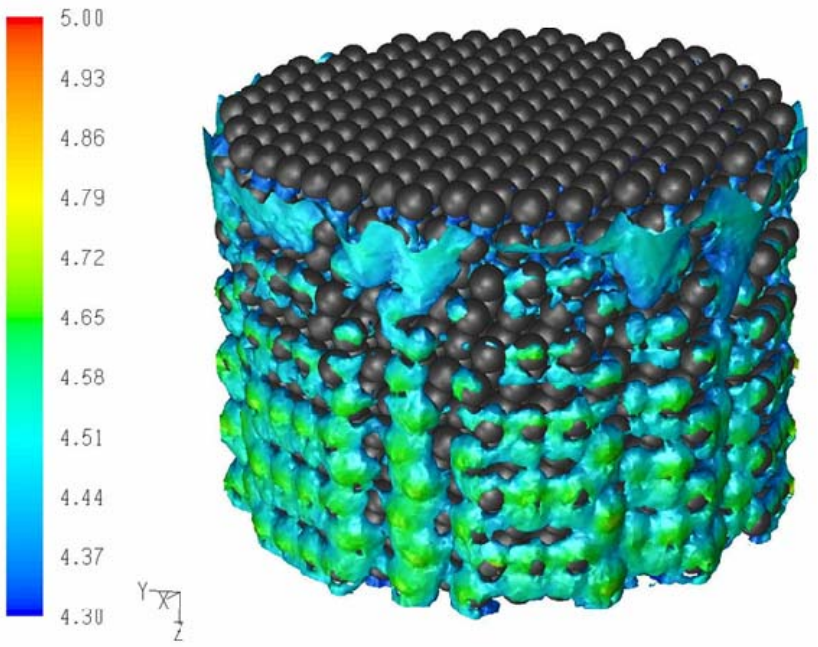

a)

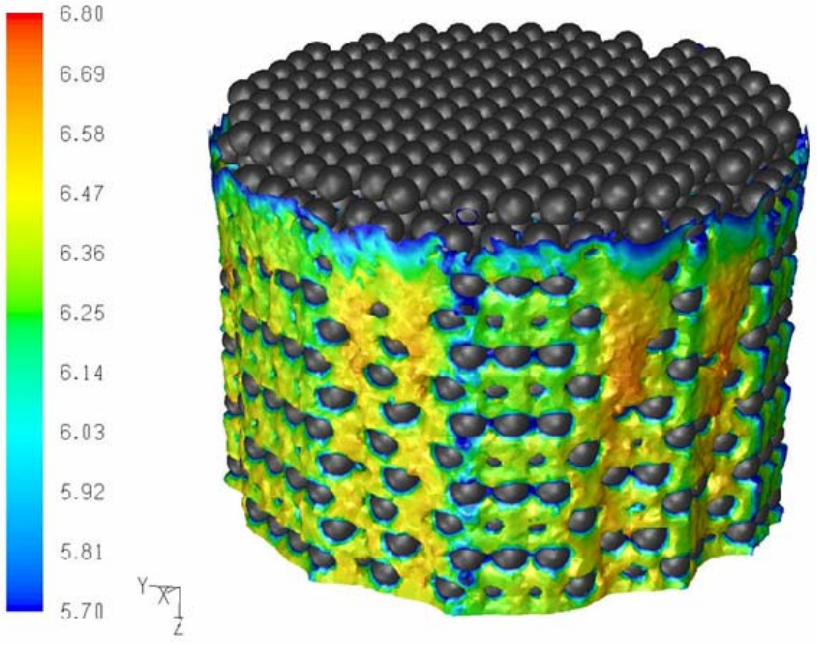

b)

Figure VI.19. CFD snapshot of liquid holdup isosurface (α_L = 0.215) coloured by turbulent kinetic energy (mm^2/s^2) for the **a)** liquid and **b)** gas phase at L=15 kg/m^{2}s and T=25ºC (MUSCL, time step = 10^{-5} s, 10^6 of tetrahedral cells, G=0.7 kg/m^{2}s, P=30 bar, d=2 mm)

VI.7. Conclusions

Aiming to understand the effect of turbulence models in multiphase flow, a Euler-Euler model was developed and coupled with different RANS turbulence based modes including standard, realizable and RNG k-ε models as well as RSM for the hydrodynamics simulation of high-pressure trickle-bed reactor.

First, several computational runs were performed for the parametric investigation of numerical solution parameters. As the accuracy of the simulation is mostly dependent on mesh density, different mesh sizes, time steps, convergence criteria and discretization schemes were compared for the hydrodynamic validation of the multiphase flow model. It was found that CFD predictions with the MUSCL scheme agreed better with the experimental data due to the fact that it is based on TVD algorithm which overcomes the numerical dispersion that arose in the multiphase flow simulations.

Second, the optimum values were used for the evaluation purpose of different RANS turbulence models. The standard k-ε dispersed turbulence was then used to evaluate the influence of flow temperature on axial velocity and turbulent kinetic energy profiles. The increase of temperature was found to be responsible in the smoothness of liquid maldistribution along the packed bed.

VI.8. Nomenclature

$C_{\mu}, C_{1\varepsilon}, C_{2\varepsilon}$	k-ε model parameters: 0.09, 1.44, 1.92
C_V	Added-mass coefficient: 0.5
d	Catalyst particle nominal diameter, m
D_q	Diffusivity of q^{th} phase, m^2/s
E_1, E_2	Ergun's constants: 150, 1.75
$\vec{g}$	Gravitational acceleration, $9.81 m/s^2$
G	Gas mass flux, kg/m^2s
G_k	Generation rate of turbulent kinetic energy
k	k-ε model kinetic energy
$\tilde{k}_{dc}$	Covariance of continuous-dispersed phase velocity
K_{dc}	Drag coefficient
k_{eff}	Effective thermal conductivity
k_{lp}	Covariance of the velocities of the continuous phase q and the dispersed phase l

L	Liquid mass flux, kg/m^{2}s
$L_{t,q}$	Length scale of the turbulent eddies
$\mathcal{L}$	Reactor length, m
p	Pressure, bar
r	Reactor radius coordinate, m
R	Reactor radius, m
Re_i	Reynolds number based on interstitial velocity [Re/ε]
R_{ij}	Reynolds stresses
S_q	Source mass for phase q
t	Time, s
T	Temperature, K
$\vec{u}$	Superficial vector velocity, m/s
$\vec{U}_q$	Phase-weighted velocity, m/s
$\vec{u}_{pq}$	Relative velocity
$\vec{u}_{dr}$	Drift velocity
z	Reactor axial coordinate, m

Greek letters

α_q	Volume fraction of q^{th} phase
ε	k-ε model dissipation energy
η_K	Kolmogorov length scale, m
ρ_q	Density of q^{th} phase, kg/m^3
ρ_m	Density of mixture, kg/m^3
Δp	Total pressure drop, bar
$\Pi_{kq}, \Pi_{\varepsilon q}$	Influence of the dispersed phases k and ε on the continuous phase
σ	Surface tension, N.m
$\sigma_k, \sigma_\varepsilon$	k-ε model parameters: 1.2, 1.0
τ	Residence time, s
τ_K	Kolmogorov time scale, s
$\overline{\overline{\tau}}_q$	Shear stress tensor of q^{th} phase, bar
$\tau_{F,pq}$	Characteristic phase relation time connected with inertial effect
$\tau_{t,pq}$	Lagrangian integral time scale calculated along particle trajectories

$\tau_{t,q}$	Characteristic time of the energetic turbulent eddies
μ_q	Viscosity of q^{th} phase, Pa.s

Subscripts

c	Continuous phase
G	Gas phase
l	Dispersed phase
L	Liquid phase
m	*k-ε* mixture turbulence model properties
q	q^{th} phase
S	Solid phase

VI.9. References

Al-Dahhan, M. H., Larachi, F., Dudukovic, M. P., Laurent, A. (1997). High pressure trickle-bed reactors: A Review. *Industrial and Engineering Chemistry Research* **36** (8), 3292-3314.

Anderson, D.H., Sapre, A.V. (1991). Trickle-bed reactors flow simulation. *A.I.Ch.E. Journal* **37**, 377-382.

Atta, A, Roy, Shantanu, Nigam, K.D.P. (2007). Prediction of pressure drop and liquid holdup in trickle bed reactor using relative permeability concept in CFD. *Chemical Engineering Science* **62**, 21, 5870-5879.

Attou, A., Ferschneider, G.A. (1999). Two-fluid model for flow regime transition in gas-liquid trickle-bed reactors. *Chemical Engineering Science* **54** (21), 5031-5037.

Calis, H. P. A., Nijenhuis, J., Paikert, B. C., Dautzenberg, F. M., van den Bleek, C. M. (2001). CFD Modelling and Experimental Validation of Pressure Drop and Flow Profile in a Novel Structured Catalytic Reactor Packing. *Chemical Engineering Science* **56**, 1713-1720.

Bhargava, S. K., Tardio, J., Prasad, J., Foger, K., Akolekar, D. B. and Grocott, S. C. (2006). Wet Oxidation and Catalytic Wet Oxidation. *Industrial and Engineering Chemistry Research* **45** (4), 1221-1258.

Dhole, S. D., Chhabra, R. P., Eswaran, V. (2004). Power Law Fluid through Beds of Spheres at Intermediate Reynolds Numbers: Pressure Drop in Fixed and Distended Beds. *Chemical Engineering Research and Design* **82** (A6), 1.

Dybbs, A., Edwards, R.V. (1984). Fundamentals of Transport Phenomena in Porous Media, *J. Bear and M. Corapcioglu Eds.*, Martins Nijhoff, Dordrecht.

FLUENT 6.1. (2005). User's Manual to FLUENT 6.1. Fluent Inc. Centrera Resource Park, 10 Cavendish Court, Lebanon, USA.

Freund, H., Zeiser, T., Huber, F., Klemm, E., Brenner, G., Durst, F., Emig, G. (2003). Numerical Simulations of Single Phase Reacting Flows in Randomly Packed/Fixed-Bed Reactors and Experimental Validation. *Chemical Engineering Science* **58**, 903-910.

GAMBIT 2. (2005). User's Manual to GAMBIT 2. Fluent Inc. Centrera Resource Park, 10 Cavendish Court, Lebanon, USA.

Guardo, A. Coussirat, M., Larrayoz, M.A., Recasens, F., Egusquiza, E. (2005). Influence of the turbulence model in CFD modelling of wall-to-fluid heat transfer in packed beds. *Chemical Engineering Science* **60**, 1733-1742.

Gunjal, Prashant R., Kashid, Madhavanand N., Ranade, Vivek V., Chaudhari, Raghunath V. (2005). Hydrodynamics of Trickle-Bed Reactors: Experiments and CFD Modeling. *Industrial and Engineering Chemistry Research* **44**, 6278-6294.

Gunjal, P.R., Ranade, V.V., Chaudhari, R.V. (2005). Computational study of a single-phase flow in packed beds of spheres. *A.I.Ch.E. Journal* **51** (2), 365-378.

Harten, A. (1983). High resolution schemes for hyperbolic conservation laws. *Journal of Computational Physics* **49**, 357-393.

Hill, R. J., Koch, D. L., Ladd, A. J. C. (2001a). Moderate-Reynolds-Number Flows in Ordered and Random Arrays of Spheres. *Journal of Fluid Mechanics* **448**, 243-278.

Hill, R. J., Koch, D. L., Ladd, A. J. C. (2001b). The First Effects of Fluid Inertia on Flows in Ordered and Random Arrays of Spheres. *Journal of Fluid Mechanics* **448**, 213-241.

Holub, R.A., Dudukovic, M.P., Ramachandran, P.A. (1992). A phenomenological model for pressure-drop, liquid holdup, and flow regime transition in gas–liquid trickle flow. *Chemical Engineering Science* **47**, 2343-2348.

Iliuta, I., Ortiz-Arroya, A., Larachi, F., Grandjean, B.P.A. and Wild, G. (1999). Hydrodynamics and mass transfer in trickle-bed reactors: An overview. *Chemical Engineering Science* **54**, 5329-5337.

Iliuta, I., Larachi, F., Al-Dahhan, M.H. (2000). Double-slit model for partially wetted trickle flow hydrodynamics. *A.I.Ch.E. Journal* **46**, 597-609.

Jiang, Y., Khadilkar, M.R., Al-Dahhan, M.H., Dudukovic, M.P. (2002). CFD modeling of multiphase in packed bed reactors: results and applications. *A.I.Ch.E. Journal* **48**, 716-730.

Jolls, K. R., Hanratty, T. J. (1966). Transition to turbulence for flow through a dumped bed of spheres. *Chemical Engineering Science* **21**, 1185-1190.

Latifi, M. A., Midoux, N., Storck, A., Gence, J. N. (1989). The use of micro-electrodes in the study of the flow regimes in a packed bed reactor with single phase liquid flow. *Chemical Engineering Science* **44**, 2501-2508.

Logtenberg, S.A., Nijemeisland, M., Dixon, A.G. (1999). Computational fluid dynamics simulations of fluid flow and heat transfer at the wall particle contact points in a fixed bed reactor. *Chemical Engineering Science* **54**, 2433-2439.

Lopes, R.J.G., Quinta-Ferreira, R.M. (2007). Trickle-Bed CFD Studies in the Catalytic Wet Oxidation of Phenolic Acids. *Chemical Engineering Science* **62** (24) 7045-7052.

Lopes, R.J.G., Quinta-Ferreira, R.M. (2008). Three-Dimensional Numerical Simulation of Pressure Drop and Liquid Holdup for High-Pressure Trickle-Bed Reactor. *Chemical Engineering Journal* **145** (1), 112-120.

Lopes, R.J.G., Quinta-Ferreira, R.M. (2009). Turbulence modelling of high-pressure trickle-bed reactor. *Chemical Engineering Science* **64** (8), 1806-1819.

Magnico, P. (2003). Hydrodynamic and transport properties of packed beds in small tube-to-sphere diameter ratio: pore scale simulation using an Eulerian and a Lagrangian approach. *Chemical Engineering Science* **58**, 5005-5024.

Martin, J. J., McCabe, W. L., Monrad, C. C. (1951). Pressure Drop through Stacked Spheres. *Chemical Engineering Progress* **47** (2), 91-94.

Merrikh, A.A., Lage, J.L. (2005). Natural convection in an enclosure with disconnected and conducting solid blocks. *International Journal of Heat and Mass Transfer* **48**, 1361-1372.

Mickley, H. S., Smith, K. A., Korchak, E. I. (1965). Fluid flow in packed beds. *Chemical Engineering Science* **20**, 237-246.

Nemec, D.; Levec, J. (2005). Flow through packed bed reactors: 2. Two phase concurrent downflow. *Chemical Engineering Science* **60** (24), 6958-6970.

Patankar, S. V. (1980). Numerical Heat Transfer and Fluid Flow. Hemisphere, Washington, DC

Rode, S., Midoux, N., Latifi, M. A., Storck, A., Saatdjian, E. (1994). Hydrodynamics of liquid flow in packed beds: an experimental study using electrochemical shear rate sensors. *Chemical Engineering Science* **49**, 889-900.

Romkes, S.J.P., Dautzenberg, F.M., Van Den Bleek, C.M., Calis, H.P.A. (2003). CFD modelling and experimental validation of particle-to-fluid mass and heat transfer in a packed bed at very low channel to particle diameter ratio. *Chemical Engineering Journal* **96**, 3-13.

Sáez, A.E., Carbonell, R.G. (1985). Hydrodynamic parameters for gas liquid cocurrent flow in packed beds. *A.I.Ch.E. Journal* **31** (1), 52-62.

Saroha, A.K. and Nigam, K.D.P. (1996). Trickle bed reactors. *Reviews in Chemical Engineering* **12** (3-4), 207-347.

Seguin, D., Montillet, A., Comiti, J. (1998a). Experimental characterisation of flow regimes in various porous media – I: Limit of laminar flow regime. *Chemical Engineering Science* **53**, 3751-3761.

Seguin, D., Montillet, A., Comiti, J., Huet, F. (1998b). Experimental characterization of flow regimes in various porous media – I: Transition to turbulent regime. *Chemical Engineering Science* **53**, 3897-3909.

Sørensen, J. P., Stewart, W. E. (1974). Computation of Forced Convection in Slow Flow through Ducts and Packed Beds—III. Heat and Mass Transfer in a Simple Cubic Array of Spheres. *Chemical Engineering Science*, **29**, 827-832.

Souadnia, A., Latifi, M.A. (2001). Analysis of two-phase flow distribution in trickle-bed reactors. *Chemical Engineering Science* **56**, 5977-5985.

Spalart, P.R. (2000). Strategies for turbulence modelling and simulations. *International Journal of Heat and Fluid Flow* **21** (3), 252-263.

Stanek, V., Szekely, J. (1974). Three-dimensional flow of fluids through non-uniform packed beds. *A.I.Ch.E. Journal* **20**, 974-980.

Van der Merwe, D. F., Gauvin, W. H. (1971). Velocity and turbulence measurements of air flow through a packed bed. *A.I.Ch.E. Journal* **17**, 519-528.

Stevenson, P. (2003). Comment on "Physical insight into the Ergun and Wen & Yu equations for fluid flow in packed and fluidised beds", by R.K. Niven [*Chemical Engineering Science* **57**, 527-534], *Chemical Engineering Science* **58** (23), 5379-5379.

Suekane, T., Yokouchi, Y., Hirai, S. (2003). Inertial flow structures in a simple-packed bed of spheres. *A.I.Ch.E. Journal* **49**, 10-17.

Tobis, J. (2000). Influence of Bed Geometry in Its Frictional Resistance under Turbulent Flow Conditions. *Chemical Engineering Science* **55** (22), 5359-5366.

Van Leer, B. (1979). Toward the Ultimate Conservative Difference Scheme. IV. A second Order Sequel to Godunov's Method. *Journal of Computational Physics* **32**, 101-136.

Vasquez, S. A., Ivanov, V. A. (2000). A Phase Coupled Method for Solving Multiphase Problems on Unstructured Meshes. *In Proceedings of ASME FEDSM'00: ASME 2000 Fluids Engineering Division Summer Meeting*, Boston, June.

Wegner, T. H., Karabelas, A. J., Hanratty, T. J. (1971). Visual studies of flow in a regular array of spheres. *Chemical Engineering Science* **26**, 59-63.

Zeiser, T., Steven, M., Freund, H., Lammers, P., Brenner, G., Durst, F., Bernsdorf, J. (2002). Analysis of the Flow Field and Pressure Drop in Fixed-Bed Reactors with the Help of Lattice Boltzmann Simulations. *Philosophical Transactions of Royal Society A*, **360** (1792), 507-520.

This page intentionally left blank

VII. CFD Modelling of Multiphase Flow Distribution In Trickle-Bed Reactors[1]

Multiphase flow in trickle-bed reactors (TBR) is known to be extremely complex and depends on a multitude of effects including the physico-chemical properties of both gas, liquid and solid phases, the ratio of column diameter to particle diameter and most importantly the gas and liquid superficial velocities. Despite several works devoted to the experimental investigation of liquid distribution, there is yet no universal agreement on the influence of interstitial phenomena on overall TBR hydrodynamics. Consequently, a Eulerian multiphase model was developed to predict the liquid holdup and pressure drop in the trickling flow regime with a 3D computational grid. The multiphase model was optimized in terms of mesh density and time step for the successful hydrodynamic validation activities. The model predictions correctly handled the effect of different numerical solution parameters.

Afterwards, particular attention is paid to the consequences on flow development and hydrodynamic parameters of imposing liquid maldistribution at the bed top with three types of liquid distributors. Several computational runs were carried out querying the effect of gas and liquid flow rate on overall hydrodynamics. CFD predictions demonstrated that liquid flow rate had a prominent effect on radial pressure drop profiles at the higher values whereas the gas flow rates had their major outcome at lower regimes. Regarding the liquid holdup predictions, several time averaged for radial and axial profiles illustrated that a 5 times increase on liquid flow rate can not be matched by an equivalent change on gas flow rate. The increase in both flow rates was found to smooth the oscillatory behaviour of local phenomena, but the gas flow rate had an outstanding consequence on both hydrodynamic parameters. Finally, CFD simulations at atmospheric conditions were compared with the pressurized ones. Liquid holdup fluctuations of about 25% between the liquid-rich and the gas-rich zone can be smoothened as long as the operating pressure is increased until 30 bar.

VII.1. Introduction

A trickle-bed reactor is a packed bed in which gas and liquid flow co-currently downwards. Several aspects of hydrodynamics including flow patterns, pressure drop, gas and liquid holdup, wetting efficiency, heat and mass transfer, etc. were extensively studied and reviewed by several authors (Satterfield, 1975; Gianetto *et al.*, 1978; Herskowitz and Smith, 1983; Al-Dahhan *et al.*,

[1] *This Chapter is based upon the publication Lopes and Quinta-Ferreira (2009)*

1997; Dudukovic *et al.*, 2002; Larachi *et al.*, 2003). TBRs have been commonly used in the petroleum industry for many years and are now gaining widespread use in several other fields from bio and electrochemical industries to the remediation of surface and underground water resources, being also recognized for their applications in advanced wastewaters treatments (Bhargava *et al.*, 2006).

For a concurrent downflow trickle-bed reactor, four different flow patterns exist: the gas-continuous or trickle flow at low liquid and gas rates, pulse flow at intermediate liquid and gas rates, liquid continuous or dispersed bubble flow at higher liquid rates. The main characteristic in trickling flow is that at a sufficiently low liquid flow, the catalyst particles will only be partially wetted (partial wetting regime). If the liquid flow rate is increased, the partial wetting regime will gradually change to a complete wetting regime (Ng and Chu, 1987). According to this flow map regime, the TBR selection choice is mainly motivated by hydrodynamic considerations in where one or more liquid-solid catalytic reactions occur. Liquid phase maldistribution is then an important factor in the design and scale-up of trickle bed reactors so that one of the major challenges in its operation is the prevention of liquid flow maldistribution which causes portions of the bed to be incompletely wetted by the flowing liquid. Hence, the catalyst bed is underutilized and reactor performance and productivity is reduced, particularly for liquid limited reactions at low liquid mass velocities.

The research on liquid flow maldistribution is often dedicated in the experimental liquid distribution studies carried out in laboratory scale units using a collector at the outlet of the bed. Recently, several groups had emphasized the use of tomographic and video imaging techniques, which provides the flow distribution information more quantitatively (Reinecke and Mewes, 1996; Sederman and Gladden, 2001; Harter *et al.*, 2001; Boyer and Fanget, 2002). The flow pattern and liquid maldistribution have been found to be dependent not only on the physicochemical properties of the liquid (density, viscosity, surface tension), liquid and gas flow rates (Onda *et al.*, 1973; Saroha *et al.*, 1998) but also on the ratio of reactor diameter to catalyst particle diameter (Herskowitz and Smith, 1983; Saroha *et al.*, 1998; Al-Dahhan and Dudukovic, 1994), wettability (Schwartz *et al.*, 1976), and shape and orientation of catalyst particles (Ng and Chu, 1987; Kundu *et al.*, 2001). And ineffective liquid inlet distributor may also lead to poor liquid distribution due to large non-wetted regions of the packed bed.

Consequently, the assumption of uniform wetting efficiency throughout the reactor made in conventional reactor models are found to overpredict the reaction rate (Funk *et al.*, 1990). The solution to this problem requires a deep understanding of interstitial flow in trickle beds. A number of models of the liquid distribution have been developed in the past two decades based on different

concepts or governing principles (Herskowitz and Smith, 1979; Crine *et al.*, 1979; Stanek *et al.*, 1981; Zimmerman and Ng, 1986; Fox, 1987; Melli and Scriven, 1991). Sáez and Carbonell (1985) developed a model based on concept of relative permeability whereas slit models proposed by Holub *et al.* (1992) and Iliuta *et al*. (2000) are based on phenomenological principles (Holub *et al.*, 1992; Iliuta *et al.*, 2000). In these models the local flow of liquid and gas around the particles is modelled by assuming flow in rectangular inclined slits of width related to void fraction of the medium. The interfacial force model presented by Attou and Ferschneider (1999) takes into account the drag force on each phase with the contribution from the particle–fluid interaction as well as from the fluid-fluid interaction. Recently, and with the increasing computational power and development of efficient Computational Fluid Dynamics (CFD) algorithms multiphase flow in TBR has been modelled in a fashionable manner accounting for a new methodology for liquid flow distribution studies by means of numerical simulations. In this category, Souadnia and Latifi (2001) and Atta *et al.* (2007) have used the porous media model and Jiang *et al.* (2002) and Gunjal *et al.* (2003) investigated the TBR hydrodynamics through the *k*-fluid model.

In the present work, the Eulerian framework is applied here to describe the multiphase flow in a three-dimensional geometry which allows the capture of interstitial flow in the packed bed. The Euler model is based on a set of continuity and momentum equations of each fluid phase with appropriate closures for the interaction forces. The individual drag forces are related with the flow velocities and volume fractions of each phase and to the physical properties of the gas, liquid and solid phases obtained from the fluid-fluid interfacial force model (Attou and Ferschneider, 1999). First, several computational runs were performed for the purpose of hydrodynamic model validation either in terms of liquid holdup or two-phase pressure drop. Afterwards, the quantitative understanding of flow maldistribution at the catalyst scale in the trickle bed is accomplished through the evaluation of time averaged axial and radial profiles for both hydrodynamic parameters. The influences of liquid distributor geometry as well as the effect of gas and liquid flow rates are investigated in the trickling flow regime.

VII.2. CFD Modelling

Multiphase flow in the trickle-bed reactor was modelled using a multifluid CFD Euler-Euler two-fluid model implemented in commercial software FLUENT (FLUENT 6.1, 2005). The Eulerian framework, including the description of the continuity and momentum equations, and the closure equations of the drag force formulation was developed using the model of Attou and Ferschneider (1999) as shown in Equations (V.1), (V.2) and (V.4)-(V.7) in Chapter V, respectively.

Accordingly, the *k-ε* dispersed turbulence model (Equations (V.9) and (V.10)) was used for the multiphase flow distribution studies.

VII.3. Numerical simulation

VII.3.1. Computational grid

The grid of the catalytic bed was created using the integrated solid modelling and meshing commercial program GAMBIT (GAMBIT 2, 2005) as described in Chapter V. The first and the last catalyst layers as well as two representative axial planes are shown in Fig. VII.1.

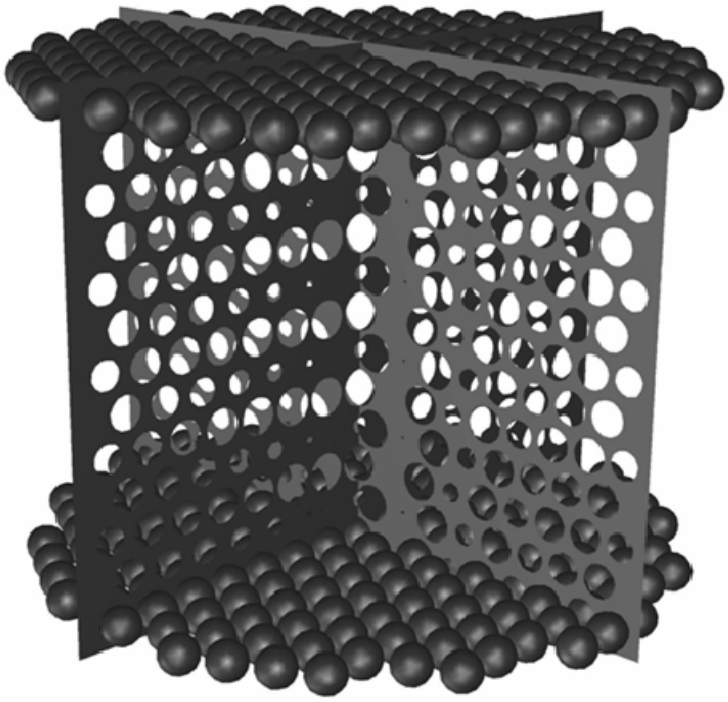

Figure VII.1. Representative axial planes and catalytic packing geometry for the trickle-bed reactor

Different mesh densities and discretization parameters were applied in the evaluation of probable geometrical errors arising from the mesh aperture. Consecutively, the number of cells necessary to produce grid independent results for the hydrodynamic parameters was increased from 2×10^5 to 3×10^6, with other numerical solution parameters including operating conditions given by Table VII.1, where discretization methods are referred: MUSCL for the momentum balance, according to the previous analysis, and QUICK for the other conservation equations, since lower iteration numbers to achieve final solution were needed contrarily to the FOU used in the studies along Chapter VI. Table VII.2 summarizes the gas and liquid thermophysical properties used in the Eulerian CFD simulations.

Table VII.1 – Numerical solution parameters used in the CFD simulation

Grid	1000 mm (axial) × 50 mm (radial)
Cell size	0.01 - 0.20 mm (tetrahedral and hexahedral)
Particle diameter	2 mm (spheres)
Time step	10^{-5} – 10^{-2} s
Convergence criteria	10^{-5} – 10^{-2}
Discretization	
Momentum	*MUSCL*
Volume fraction	*QUICK*
Turbulent kinetic energy	*QUICK*
Turbulent energy dissipation	*QUICK*
Iterations	≈ 50,000
Under-relaxation parameters	Pressure: 0.2-0.6
	Velocity: 0.4-0.8
	Turbulent kinetic energy: 0.8
	Turbulent energy dissipation: 0.8
Drag formulation	Attou and Ferschneider (1999)
Turbulence model	Dispersed phase standard k-ε

Table VII.2 – Relevant thermophysical properties of gas and liquid phases

Properties	Value (T=25ºC)	Units
Gas phase		
Density	1.170 (1 bar) 35.67 (30 bar)	kg/m^3
Viscosity	1.845×10^{-5}	Pa.s
Liquid phase		
Viscosity	8.925×10^{-4}	Pa.s
Density	998.4	kg/m^3
Surface tension	7.284×10^{-2}	N.m

VII.3.2. Operating and boundary conditions

High-pressure operation was simulated at 30 bar total operating pressure with inflow gas (G = 0.1–0.7 kg/m^{2}s) and liquid (L = 1–15 kg/m^{2}s) being distributed through one of three designed distributors: D1 corresponds to a single-point entry distributor with an 0.2 mm inlet diameter, D2 corresponds to a 60-hole distributor and D3 replicates a uniform distributor at the top of trickle-bed reactor. The boundary conditions were specified based on FLUENT documentation (FLUENT 6.1., 2005). Turbulent kinetic energy (k) was estimated from turbulence intensity and turbulent energy dissipation (ε) was estimated from the turbulent viscosity ratio as expressed in Equations (VI.1)-(VI.3) in Chapter VI. At 25º C and two different operating pressures 1 and 30 bar, the inlet turbulent kinetic energy and inlet turbulent energy dissipation for the gas and liquid phases are given in Table VII.3. Computations are time dependent and were carried out until steady state conditions were reached. During the simulations of turbulent multiphase flow, it was employed standard wall functions available in the commercial CFD solver. The calculations have been carried out on a Linux cluster based on AMD64 Dual-Core 2.2 GHz processor workstation.

Table VII.3 – Inlet boundary conditions for the gas and liquid phases: turbulent kinetic energy (k_q) and turbulent energy dissipation (ε_q) at T=25ºC

G (kg/m^{2}s)	L (kg/m^{2}s)	P (bar)	k_G (mm^2/s^2)	k_L (mm^2/s^2)	ε_G (mm^2/s^3)	ε_L (mm^2/s^3)
0.3	2	1	1.310×10^{3}	1.329×10^{-1}	4.895×10^{3}	8.640×10^{-4}
0.3	10	1	1.310×10^{3}	2.222	4.895×10^{3}	0.2415
0.1	5	1	1.915×10^{2}	0.6607	1.047×10^{2}	2.135×10^{-2}
0.7	5	1	5.770×10^{3}	0.6607	9.498×10^{4}	2.135×10^{-2}
0.3	2	30	1.408	0.1329	0.1726	8.640×10^{-4}
0.3	10	30	1.408	2.222	0.1726	0.2415
0.1	5	30	0.2059	0.6607	3.690×10^{-3}	2.135×10^{-2}
0.7	5	30	6.204	0.6607	3.349	2.135×10^{-2}

VII.4. Results and discussion

VII.4.1. Hydrodynamic validation: mesh sensitivity and time step

In this section, the numerical methodology is validated in terms of well-known hydrodynamic parameters by checking the mesh sensitivity and time step and by comparing the numerical results against the experimental data available in the open literature (Nemec and Levec, 2005). The previous studies involving a mesh size range of $2\times10^5 - 10^6$ are now extended to 3 million cells in order to reinforce the mesh independence so that the refinement is performed in seven levels: three levels for the coarser meshes with 2,4,6 $\times10^5$ of tetrahedral cells and four levels for the finer meshes with 8×10^5 and $1,2,3\times10^6$ of tetrahedral cells. Fig. VII.2 displays the influence of number of tetrahedral cells on the liquid holdup predictions with four simulation sets at constant liquid flow rate: L=1, 5, 10 and 15 kg/m^{2}s at G=0.1 kg/m^{2}s and P=30 bar.

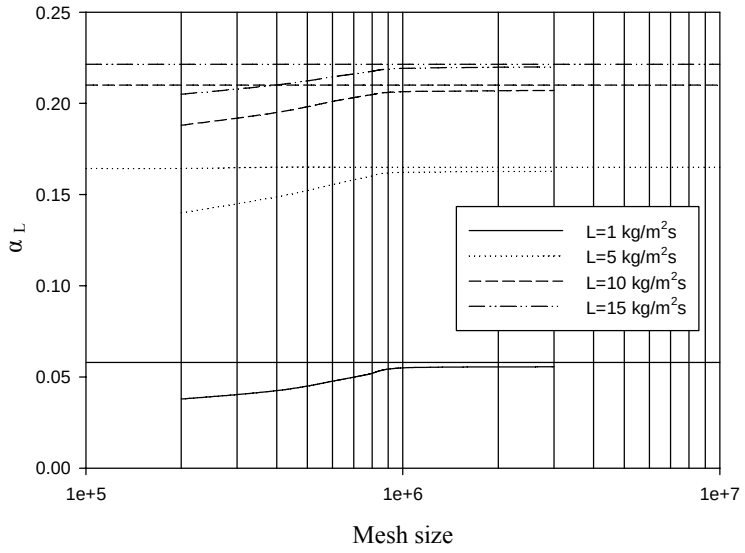

Figure VII.2. Comparison of liquid holdup predictions at different liquid flow rates for different mesh resolutions (G=0.1 kg/m^{2}s, P=30 bar, d=2 mm and experimental data from Nemec and Levec, 2005)

As it can be seen, the increase of mesh density led to an asymptotic solution as one increases the number of cells of one million onwards. The horizontal lines in the semi-log plot of Fig. VII.2 correspond to the experimental liquid holdup value (Nemec and Levec, 2005). According to Fig. VII.2, the relative error obtained with 2×10^5 of cells between the CFD liquid holdup predictions and experimental data was 23.8, 12.4, 6.2 and 4.1% for L=1, 5, 10 and 15 kg/m^{2}s, respectively. Let the true liquid holdup be the experimental value, $\alpha_{L,EXP}$, and the computed liquid holdup value, $\alpha_{L,CFD}$, then the relative error was defined by: Relative Error (%) = $(\alpha_{L,EXP} - \alpha_{L,CFD})/ \alpha_{L,EXP}$. At the same gas flow rate and operating pressure, the relative error shifted to 1.5, 1.3, 1.2 and 1.0% for the equivalent liquid flow rates with one million of cells. The CFD calculations performed with a further increase of mesh density with either 2 or 3×10^6 of tetrahedral cells did not show any improvement as the relative error became invariable with a value of 1.0% for the liquid holdup. In what concerns two-phase pressure drop, Fig. VII.3 shows a semi-log plot for the frictional pressure drop along the packed bed at G=0.1 kg/m^{2}s and P=30 bar with the same set of liquid flow rates. The horizontal lines in the semi-log plot of Fig. VII.3 correspond to the experimental value of two-phase pressure drop (Nemec and Levec, 2005). The CFD calculations performed with the coarsest mesh (2×10^5 of tetrahedral cells) exhibited a relative error of 32.7, 24.8, 18.3 and 14.3 while the computed results corresponding to 10^6 of cells gave a relative error of 1.6, 1.5, 1.2 and 1.0 for L=1, 5, 10 and 15 kg/m^{2}s, respectively. Hence, the Eulerian model with a TBR mesh comprising 10^6 of tetrahedral cells for both hydrodynamic parameters was likely to perform better at the highest liquid flow rates since at L=15 kg/m^{2}s it were found the lower relative error percentages between predictions and experimental data (Nemec and Levec, 2005).

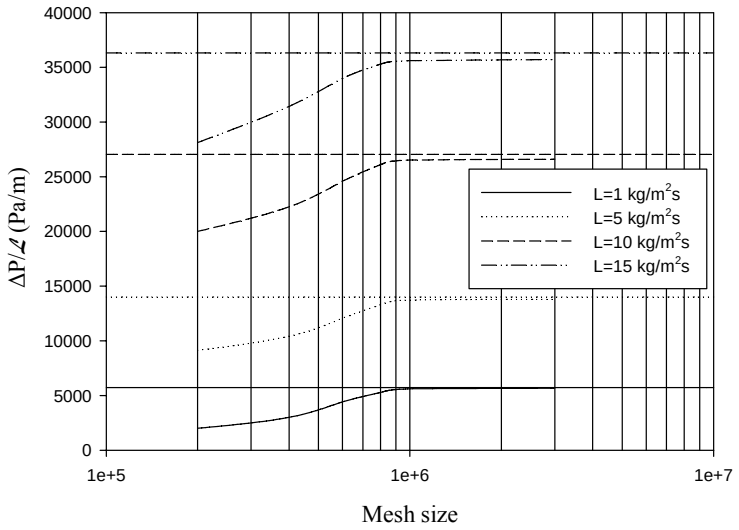

Figure VII.3. Comparison of two-phase pressure drop predictions at different liquid flow rates for different mesh resolutions (G=0.5 kg/m^{2}s, P=30 bar, d=2 mm and experimental data from Nemec and Levec, 2005)

The optimization of time step with respect to liquid holdup predictions, referred in the previous chapter, is shown here in Fig. VII.4 at G=0.1 kg/m^{2}s and P=30 bar in a log-log representation, allowing a clearer analysis of the effect of this numerical parameter in the Euler model validation. As expected, a time step too large led to the worst concordance between the numerical predictions and experimental results. The relative error obtained with time step of 10^{-2} s was 34.3, 26.1, 21.8 and 17.4 for L=1, 5, 10 and 15 kg/m^{2}s, respectively.

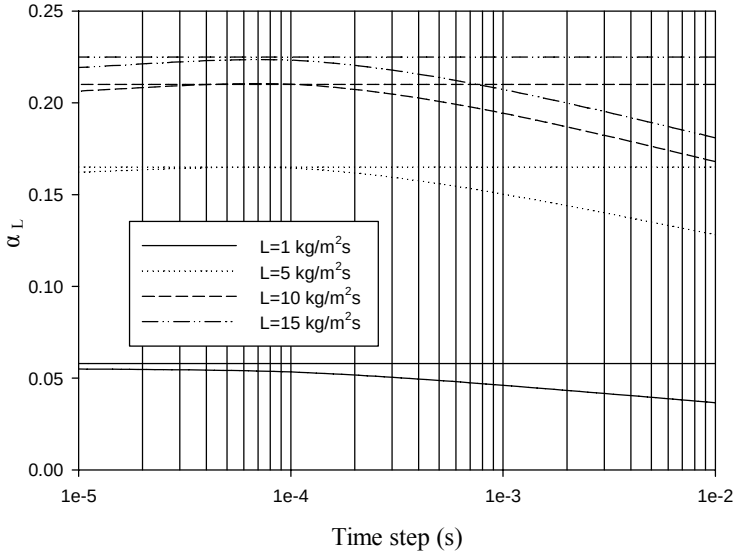

Figure VII.4. Effect of time step on liquid holdup predictions at different liquid flow rates (10^6 of tetrahedral cells, G=0.1 kg/m^{2}s, P=30 bar, d=2 mm and experimental data from Nemec and Levec, 2005)

A significant decrease down to 10^{-5} s led to the better agreement with 10^6 of tetrahedral cells. In this case, the relative error became 1.5, 1.3, 1.2 and 1.0% when increasing the liquid flow rate from 1 to 15 kg/m^{2}s. In terms of frictional pressure drop as depicted in Fig. VII.5, the CFD predictions gave a relative error of 37.1, 29.3, 23.4, 20.0% and 1.6, 1.3, 1.1 and 1.0% for time steps of 10^{-2} and 10^{-5} s, respectively. It is worth noting that a further decrease in the time step may be responsible for some degree of numerical instability or likely disturbed behaviour without giving relevant and feasible calculations for either liquid holdup or pressure drop. Therefore, after the comparison between the influence of time step on the liquid holdup and pressure drop calculations, a value of 10^{-5} s gave time step independent results when using a finer mesh (10^6 of tetrahedral cells).

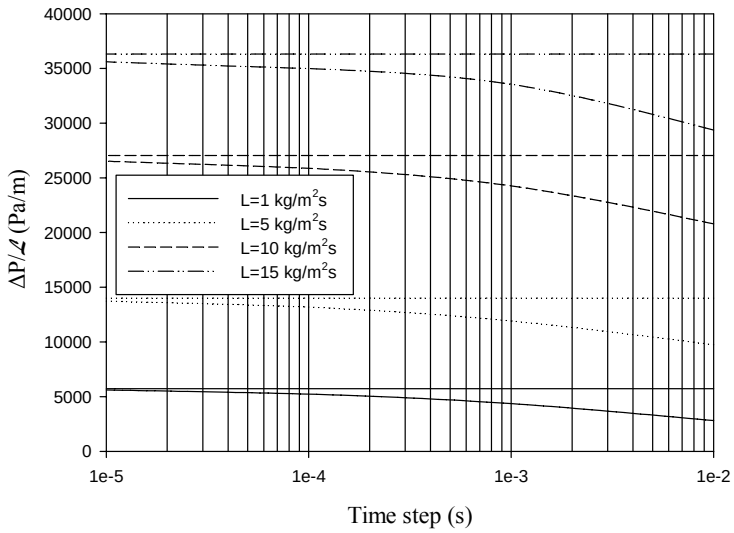

Figure VII.5. Effect of time step on two-phase pressure drop predictions at different liquid flow rates (10^6 of tetrahedral cells, G=0.5 kg/m^{2}s, P=30 bar, d=2 mm and experimental data from Nemec and Levec, 2005)

VII.4.2. Influence of distributor geometry

In most CFD simulations of trickle-beds reported in the open literature, the fluid distribution at the inlet was treated as perfectly uniform in the radial direction so that all fluid enters at a given superficial velocity either in the wall or at the column centre. However, real distributors have discrete orifices where liquid and gas enter the trickle-bed reactor, interspersed with closed areas where no fluid enters. Three liquid distributors are employed in the computational runs. First, a single-point entry is simulated (distributor D1) and it is located at the column axis in the top of the bed with 0.2 mm diameter. Second, a distributor was designed with 60 capillary tubes (0.12 mm internal diameter: distributor D2) which is used to replicate the distributor in our pilot plant. A similar configuration with 42 capillary tubes was previously used by Pintar *et al.* (1997) who found this configuration to be appropriate for maintaining the flux of both phases approximately uniform over the cross-sectional area. Finally, a perfectly uniform distributor (D3) was used to simulate the ideal case in where the fluids were allowed to enter the column at constant velocity using the total available entrance area.

In Fig. VII.6, the time averaged CFD liquid holdup predictions were plotted at different relative axial positions ($z^*=z/\mathcal{L}$) for the single-point, 60-hole and uniform distributor at G=0.3 kg/m^{2}s and P=30 bar. The CFD simulations performed with the lowest liquid flow rate (L=2 kg/m^{2}s) showed the prominent effect of the distributor geometry in multiphase flow distribution as depicted at $z^*=1/4$ with D1 distributor. It can be seen that the liquid phase tended to agglomerate predominantly at one side of the wall and then decreased significantly to the opposite side. With respect to the mean value of liquid holdup the maxima and minima values were (4.1, -2.6), (2.6, -

4.5), (3.7, -3.0), (5.5, -8.4)% for z*= ¼, ½, ¾ and 1 with the single-point distributor (D1), respectively.

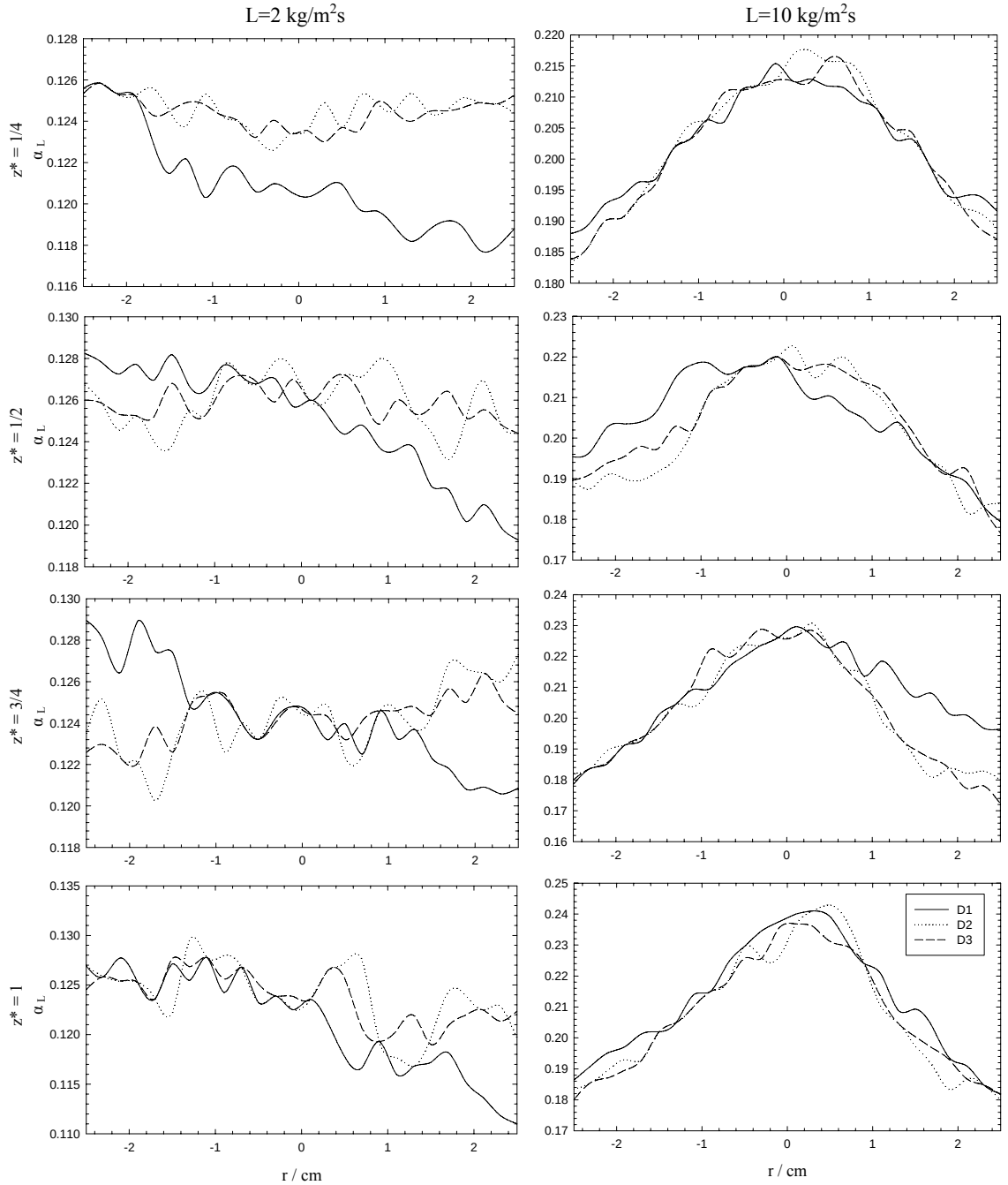

Figure VII.6. Time averaged liquid holdup profiles with different liquid distributors at different bed coordinates (time step = 10^{-5} s, 10^6 of tetrahedral cells, G=0.3 kg/m^{2}s, P=30 bar, d=2 mm)

The absolute values (maxima, minima) for the liquid holdup predictions at L=2 kg/m^{2}s with {D1, D2, D3} distributors were {(0.126, 0.118), (0.126, 0.123), (0.127, 0.123)} at z*= ¼. At z*=½: {(0.128, 0.119), (0.128, 0.123), (0.127, 0.124)}; at z*=¾: {(0.129, 0.121), (0.127, 0.120), (0.126, 0.122)}; and at z*=1: {(0.128, 0.111), (0.129, 0.117), (0.128, 0.119)}. As one can conclude, the

liquid flow distribution degrades as one moves along the packed bed being this fact supported by the increasing difference between maxima and minima liquid holdup values. The oscillatory behaviour may be attributed to the local effects near the catalyst particle surface which produces likely the wall effect phenomena or channelling as observed experimentally using high-resolution gamma ray tomography (Schubert *et al*., 2008). Gamma ray computed tomography is known to be better suited when high radiation energy is needed in comparison with magnetic resonance imaging, e.g. in the case of large reactor diameters, dense packing and in the case of steel walls and steel facilities for pressurized operation. Schubert *et al.* (2008) identified the above fact and claimed that the dynamic liquid saturation distribution indicates the development of liquid channels and regions which are completely separated from the flowing liquid with a glass packing. Moreover, the number and the dimension of the liquid channels increase with increasing liquid flow rate. The influence of distributor geometry on the maldistribution of the dynamic liquid holdup was analyzed for a spray nozzle producing a uniform initial distribution and a point source distributor producing a central liquid stream in both glass bead bed and porous catalyst bed. The experimental observations were similar to those advanced theoretically with the Eulerian predictions shown in Fig. VII.6.

Fig. VII.7 shows an instantaneous snapshot of liquid holdup taken at the two axial planes depicted in Fig. VII.1.

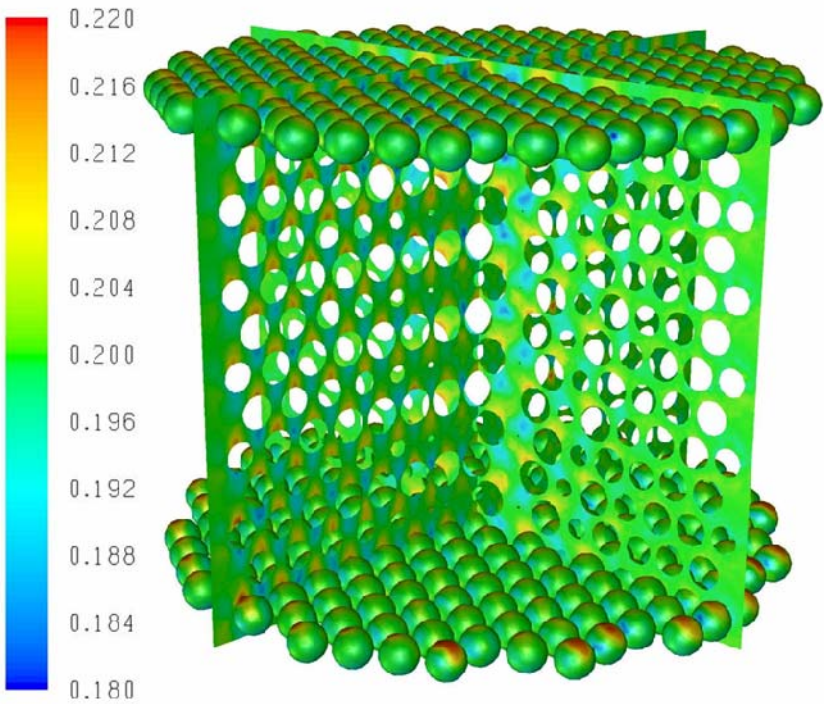

Figure VII.7. Instantaneous snapshot of liquid holdup taken at two axial planes (Fig. VII.1) and two catalyst layers(time step = 10^{-5} s, 10^6 of tetrahedral cells, L=2 kg/m^{2}s, G=0.3 kg/m^{2}s, P=30 bar, d=2 mm, D2 distributor)

According to Fig. VII.7 it was possible to identify qualitatively the 3D distribution of liquid phase in the packed bed. At L=2 kg/m^{2}s and P=30 bar, one can observe that the higher liquid holdup values were monitored on the catalyst surface, as expected. Indeed, it was also confirmed the difference between the maxima and minima values attained at the lowest liquid flow rate in the range 0.18-0.22. Concerning the 60-hole distributor (D2), these values were (1.0, -1.6), (2.6, -4.5), (3.7, -3.0), (5.5, -8.2)% while with D3 distributor were (1.1, -1.1), (1.7, -2.2), (2.5, -3.2), (4.5, -5.8)% for z*= ¼, ½, ¾ and 1, respectively. From these time averaged values, it can be pointed out that an ideal distributor (D3) did not differ too much from the 60-hole distributor (D2) whereas the CFD simulations performed with the single-point distributor (D1) showed strongly radial profiles in terms of liquid holdup.

Increasing the liquid flow rate up to L=10 kg/m^{2}s, Fig. VII.6 also displays the radial profiles of liquid holdup obtained with different distributors at G=0.3 kg/m^{2}s and P=30 bar. According to this time averaged liquid holdup values, it is clear a preferential and persistent behaviour of liquid flow through the trickle-bed reactor. The higher values were observed at the reactor centre which demonstrates likely the Poiseuille flow. It seems that an increase of liquid flow rate up to 10 kg/m^{2}s plays a dominant role over the distributor geometry even for D1 distributor. Moreover, this behaviour remains at different axial positions. It should be also stressed that we are on the boundary of trickling flow regime so that a further increase on either gas or liquid flow rates may shift the hydrodynamic regime towards the pulsing flow. As we are concerned about the effect of gas-liquid flow rates on the trickling flow, the remaining of the discussion is only applicable in those operating conditions. The maxima and minima values for the radial liquid holdup values were (6.5, -7.0), (7.6, -12.3), (10.5, -14.1), (13.9, -14.0) for z*= ¼, ½, ¾ and 1 with the single-point distributor (D1). These values were very similar to those obtained with the ideal distributor (D3): (7.0, -8.9), (5.2, -13.2), (13.1, -14.8), (14.2, -13.2). Therefore, it seems that the distributor geometry plays a major effect on hydrodynamics at lower interaction regimes (L=2 kg/m^{2}s) while the liquid flow rate control the multiphase flow radial distribution at higher interaction regimes (L=10 kg/m^{2}s). The absolute values (maxima, minima) for the liquid holdup predictions at L=10 kg/m^{2}s with {D1, D2, D3} distributors were {(0.215, 0.188), (0.218, 0.183), (0.216, 0.184)} at z*= ¼. At z*=½: {(0.220, 0.179), (0.222, 0.182), (0.220, 0.177)}; at z*=¾: {(0.230, 0.179), (0.231, 0.180), (0.229, 0.172)}; and at z*=1: {(0.241, 0.182), (0.243, 0.180), (0.237, 0.180)}.

At L=2 kg/m^{2}s, the time averaged liquid holdup predictions were plotted in Fig. VII.8 while the CFD calculations performed at L=10 kg/m^{2}s are shown in Fig. VII.9 both at G=0.3 kg/m^{2}s and P=30 bar.

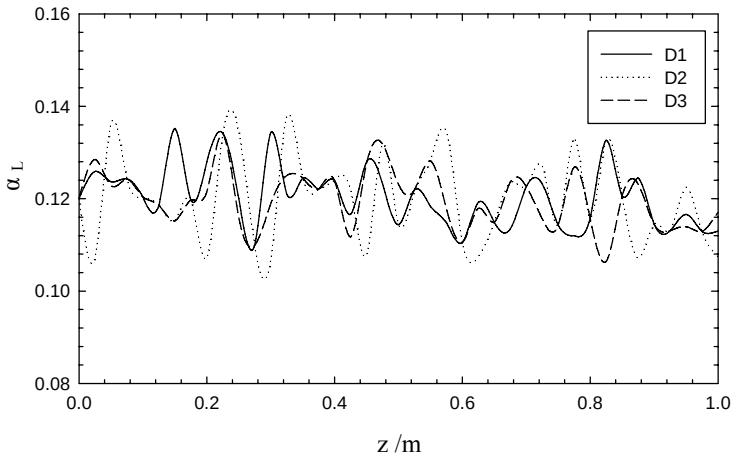

Figure VII.8. Time averaged liquid holdup profiles at L=2 kg/m^{2}s with different liquid distributors (time step = 10^{-5} s, 10^6 of tetrahedral cells, G=0.3 kg/m^{2}s, P=30 bar, d=2 mm)

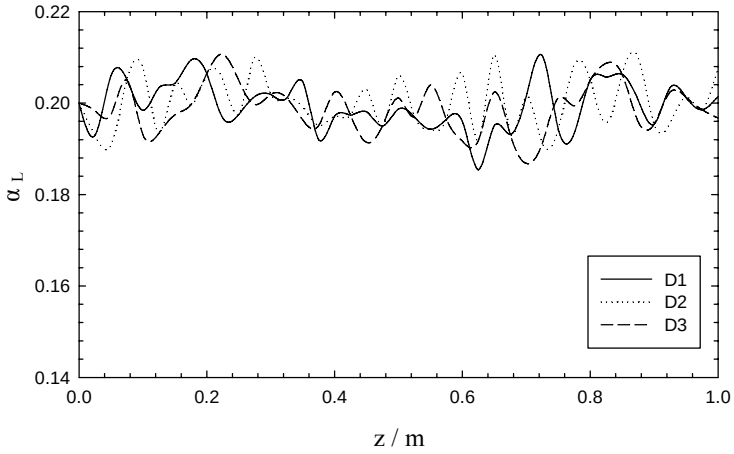

Figure VII.9. Time averaged liquid holdup profiles at L=10 kg/m^{2}s with different liquid distributors (time step = 10^{-5} s, 10^6 of tetrahedral cells, G=0.3 kg/m^{2}s, P=30 bar, d=2 mm)

As it can be seen, there is no significant qualitative difference between these two axial liquid holdup profiles with different distributors at different liquid flow rates. The main difference detected was in the magnitude of maxima and minima values attained with the quantitative comparison of liquid holdup. In fact, the maxima and minima values obtained at L=2 kg/m^{2}s were ±15% while at L=10 kg/m^{2}s were ±7%. Once more, the distributor geometry seems to have no effect on the axial liquid flow distribution but only the liquid flow rate can affect considerably the intensity of liquid holdup spots at P=30 bar.

VII.4.3. Effect of liquid flow rate

At a constant gas flow rate (G=0.3 kg/m^{2}s), Fig. VII.10 shows the time averaged radial profiles for the liquid holdup predictions at different axial positions and at different liquid flow rates with the

60-hole distributor. At the lowest liquid flow rate (L=2 kg/m^{2}s), it can be seen that the radial liquid distribution began with approximately a flat profile and suffered some degree of perturbation as one moves along the packed bed. One should also compare the level of the higher and lower liquid holdup traces.

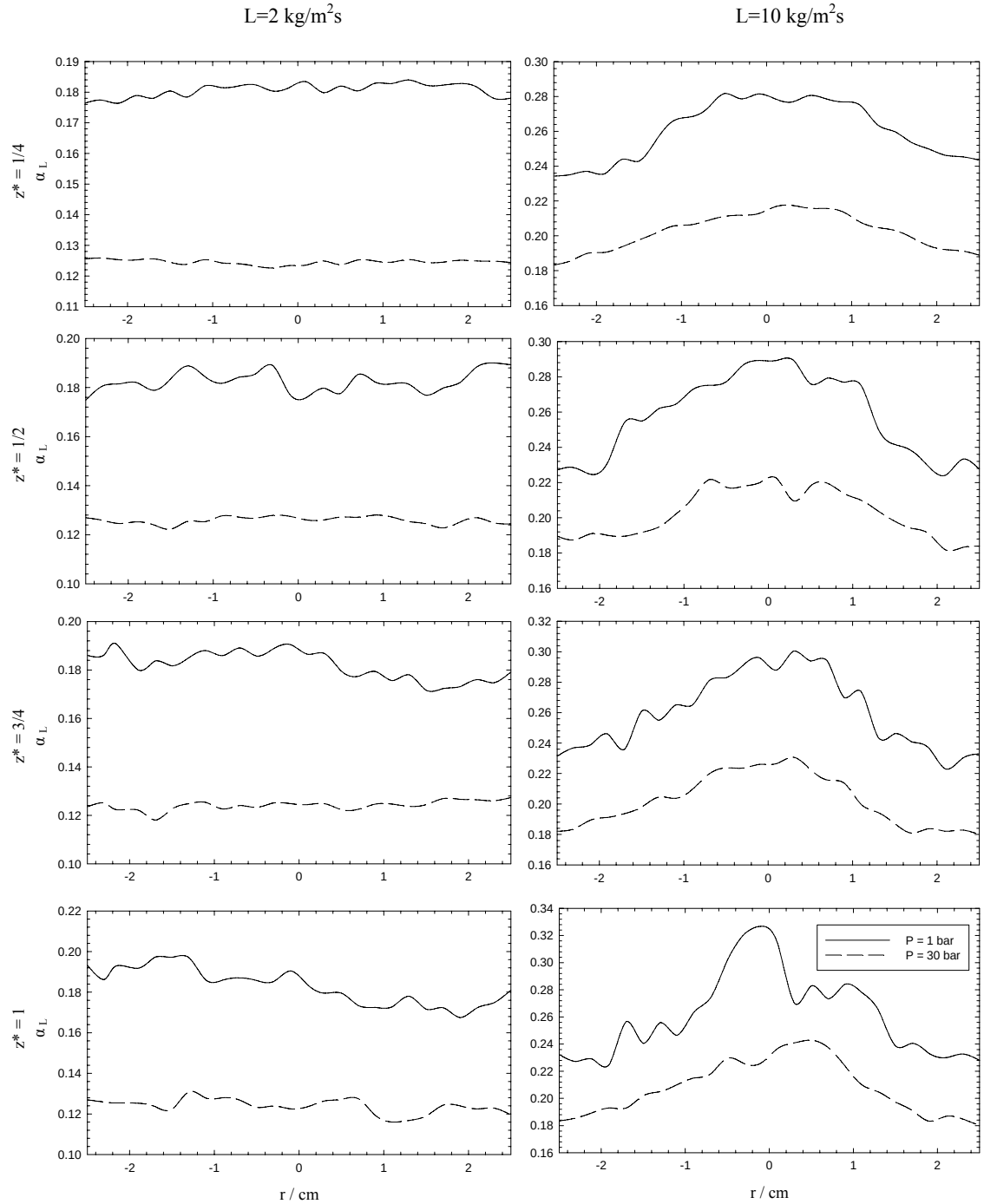

Figure VII.10. Time averaged liquid holdup profiles as a function of liquid flow rate at different bed coordinates and operating pressures (time step = 10^{-5} s, 10^6 of tetrahedral cells, G=0.3 kg/m^{2}s, d=2 mm, D2 distributor)

For a uniform distribution, the liquid holdup from the left-hand side and the right-hand side of radial coordinate should be at the same level. However, the maxima and minima liquid holdup

values attained with the lowest liquid flow rate were (1.0, -1.6), (1.7, -2.9), (2.5, -5.0), (5.7, -6.4)% for z*= ¼, ½, ¾ and 1 at P=30 bar. These values were even higher with the highest liquid flow rate: (7.5, -9.4), (10.1, -10.0), (14.3, -10.8), (17.1, -13.3)% for the equivalent axial positions. The absolute values (maxima, minima) for the liquid holdup predictions at L=2 kg/m^{2}s and P={1, 30}bar were {(0.184, 0.176), (0.126, 0.123)} at z*= ¼. At z*=½: {(0.190, 0.175), (0.128, 0.122)}; at z*=¾: {(0.191, 0.172), (0.127, 0.118)}; and at z*=1: {(0.197, 0.167), (0.131, 0.116)}. Again, it was confirmed that the higher liquid holdup values were found in the column centre. Therefore, the liquid flow rate has a propensity effect on the hydrodynamics at higher values but it can also be stated that is not sufficient to improve the liquid distribution by itself. Regarding the time averaged profiles, Fig. VII.11 displays the axial liquid holdup profiles with different liquid flow rates with D2 distributor at G=0.3 kg/m^{2}s and P=30 bar.

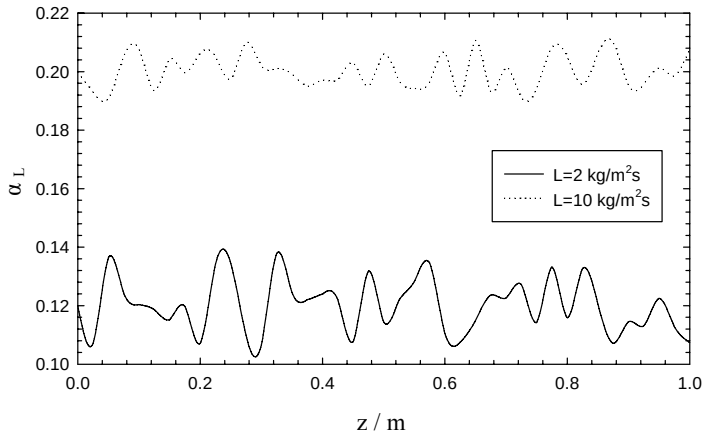

Figure VII.11. Time averaged liquid holdup profiles at different liquid flow rates (time step = 10^{-5} s, 10^6 of tetrahedral cells, G=0.3 kg/m^{2}s, P=30 bar, d=2 mm, D2 distributor)

As already advanced for the explanation of the influence of liquid distributor, the axial liquid distribution did not show a tendentious behaviour across the packed bed. Indeed, the only distinction detected was related to the smooth liquid holdup profile exhibited at the highest liquid flow rate (Kundu *et al*., 2001). The absolute values (maxima, minima) for the liquid holdup predictions at L=2 kg/m^{2}s and P={1, 30}bar were {(0.282, 0.234), (0.218, 0.183)} at z*= ¼. At z*=½: {(0.289, 0.224), (0.222, 0.182)}; at z*=¾: {(0.300, 0.223), (0.231, 0.180)}; and at z*=1: {(0.327, 0.225), (0.243, 0.180)}. The increase of liquid flow rate decreased the maxima/minima liquid holdup values from (14.7, -11.2)% with L=2 kg/m^{2}s to (5.2, -4.7)% with L=10 kg/m^{2}s.

Time averaged profiles for two-phase pressure predictions are shown in Fig. VII.12 at G=0.3 kg/m^{2}s and P=30 bar. According to these radial profiles, it was found that pressure drop was higher at the TBR centre mainly with the highest simulated liquid flow rate (L=10 kg/m^{2}s). While the frictional pressure drop maxima/minima were about 2-3% at L=2 kg/m^{2}s, these values were shifted up to 11% at L=10 kg/m^{2}s. In fact, the computed results were (9.0, -3.6), (10.3, -4.8), (11.1,

-5.5)% for z*= ¼, ½, ¾, respectively. Therefore, the effect of liquid flow rate on radial pressure drop profiles was more pronounced if the reactor is operated under higher interaction liquid flow regimes. In what concerns the axial pressure field, Fig. VII.13 shows a contour map of relative pressure values in two axial planes. As one can observe, with 13 catalyst layers the pressure decreased from 19000 to 11000 Pa at L=10 kg/m^{2}s, G=0.3 kg/m^{2}s and P=30 bar, as validated accordingly in Fig. VII.3.

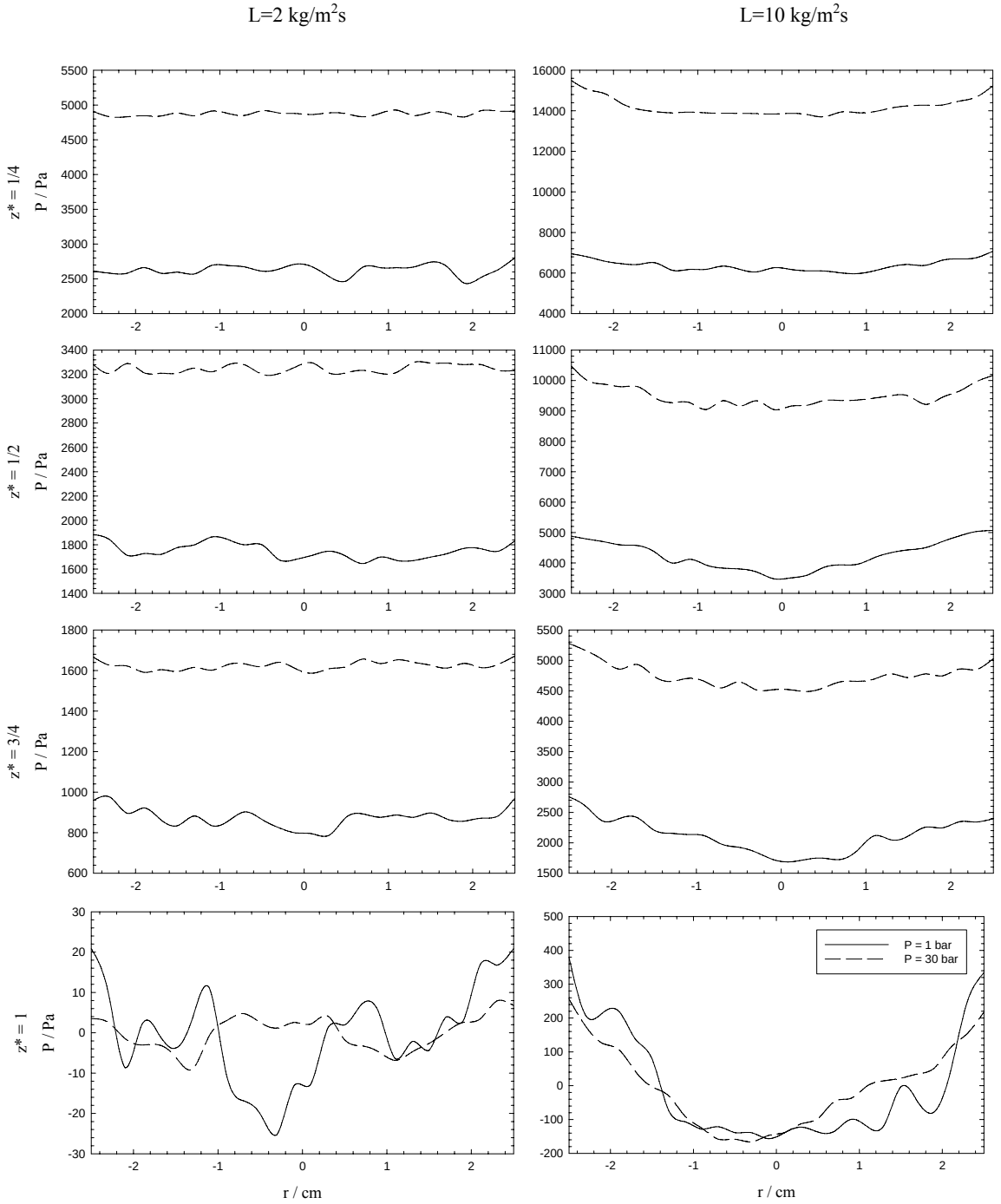

Figure VII.12. Time averaged two-phase pressure profiles as a function of liquid flow rate at different bed coordinates and operating pressures (time step = 10^{-5} s, 10^6 of tetrahedral cells, G=0.3 kg/m^{2}s, d=2 mm, D2 distributor)

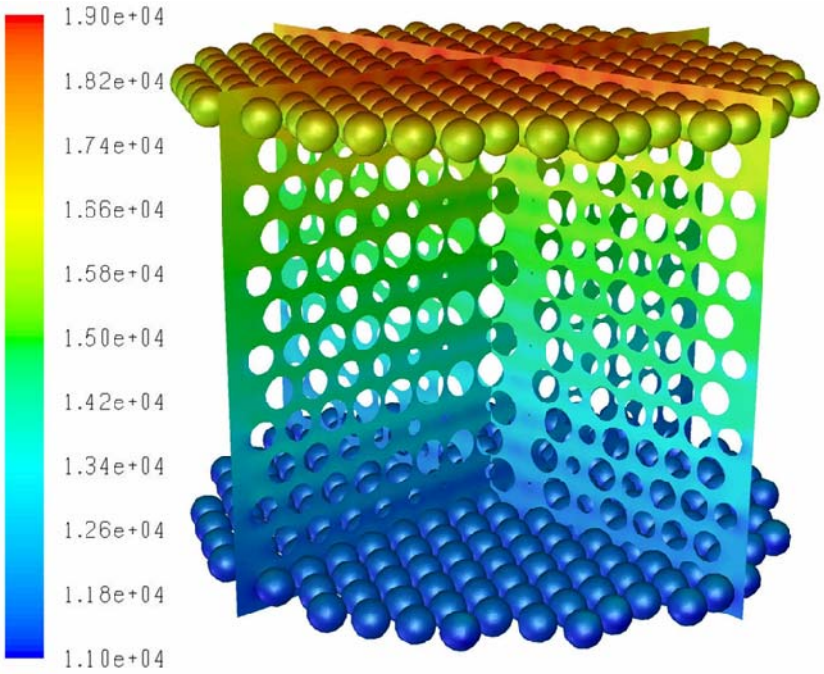

Figure VII.13. Instantaneous snapshot of pressure field taken at two axial planes (Fig. VII.1) and two catalyst layers(time step = 10^{-5} s, 10^6 of tetrahedral cells, L=10 kg/m^{2}s, G=0.3 kg/m^{2}s, P=30 bar, d=2 mm, D2 distributor)

VII.4.4. Effect of gas flow rate

In Fig. VII.14 it was plotted the time averaged liquid holdup predictions at a constant liquid flow rate (L=5 kg/m^{2}s) with D2 distributor at different axial positions. At the lowest gas flow rate (G=0.1 kg/m^{2}s) and P=30 bar, the maxima/minima liquid holdup values were (3.3, -3.4), (5.0, -3.4), (8.5, -9.5), (12.2, -11.1)% for z*= ¼, ½, ¾ and 1, respectively. The absolute values (maxima, minima) for the liquid holdup predictions at G=0.1 kg/m^{2}s and P={1, 30}bar were {(0.248, 0.228), (0.171, 0.160)} at z*= ¼. At z*=½: {(0.255, 0.228), (0.174, 0.160)}; at z*=¾: {(0.262, 0.215), (0.180, 0.150)}; and at z*=1: {(0.272, 0.206), (0.186, 0.147)}. As one can conclude, these values are increasing along the packed which degrade considerably the liquid distribution. Moreover, the computed profile attained for z*=3/4 and 1 illustrated a remarkable degree of inhomogeneity of radial liquid distribution. Increasing the gas flow rate up to 0.7 kg/m^{2}s, the CFD simulations of radial liquid holdup profiles are shown equally in Fig. VII.14. The increase of gas flow rate was found to be responsible for the enlargement of maxima/minima liquid holdup values with respect to the mean value. In fact, at G=0.7 kg/m^{2}s and P=30 bar, these values were (9.2, -13.5), (10.4, -13.6), (13.7, -13.6), (13.8, -13.7) for z*= ¼, ½, ¾ and 1, respectively. The absolute values (maxima, minima) for the liquid holdup predictions at G=0.7 kg/m^{2}s and P={1, 30}bar were {(0.162, 0.135), (0.120, 0.095)} at z*= ¼. At z*=½: {(0.163, 0.135), (0.121, 0.095)}; at z*=¾: {(0.162, 0.132), (0.125, 0.096)}; and at z*=1: {(0.165, 0.132), (0.125, 0.096)}.

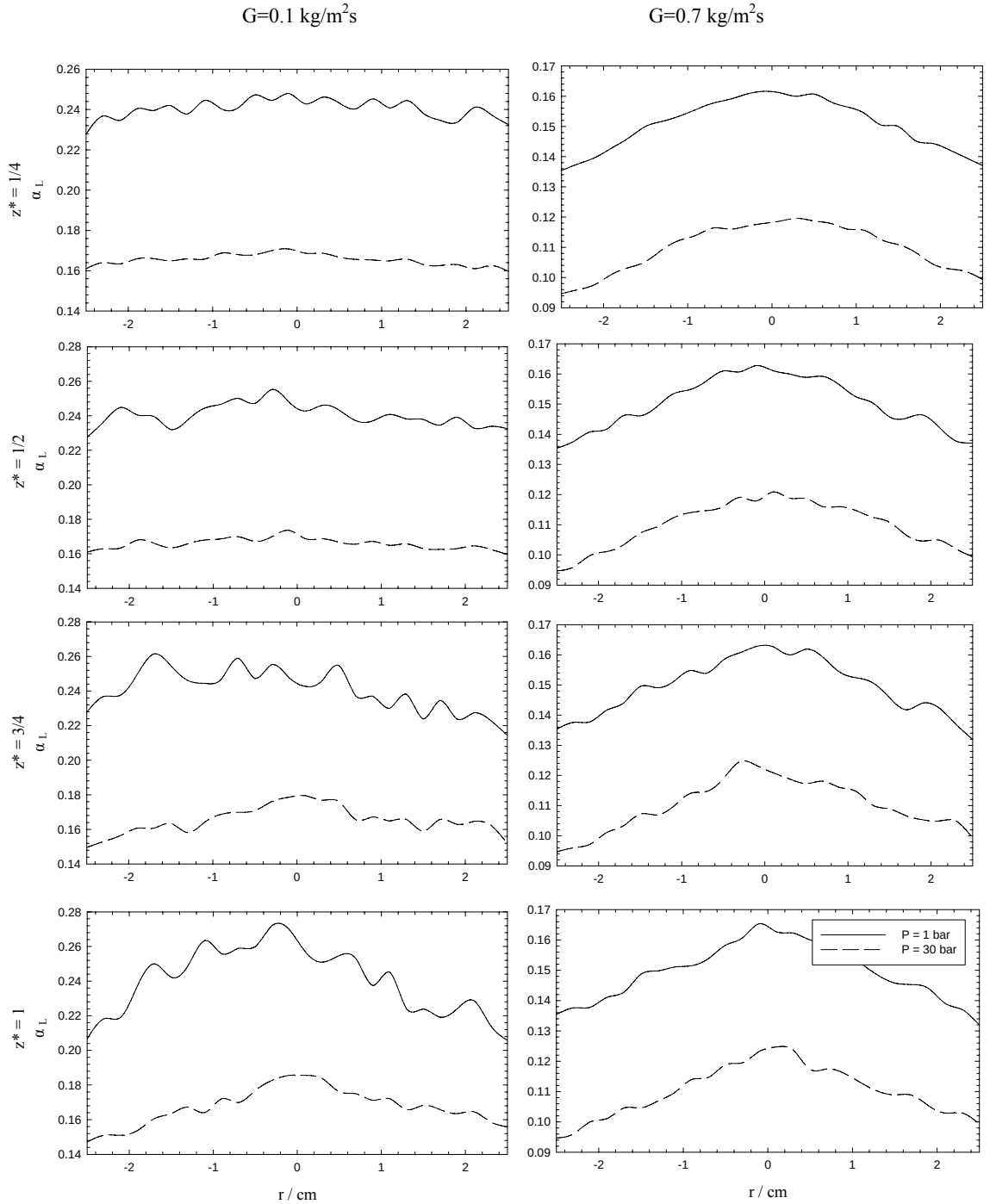

Figure VII.14. Time averaged liquid holdup profiles as a function of gas flow rate at different bed coordinates and operating pressures (time step = 10^{-5} s, 10^6 of tetrahedral cells, L=5 kg/m^{2}s, d=2 mm, D2 distributor)

Time averaged liquid holdup profiles are shown in Fig. VII.15 at L=15 kg/m^{2}s and P=30 bar with D2 distributor. As one can observe, the increase of gas flow rate was also found to smooth the axial liquid distribution as the liquid flow rate did. However, the increase of 5 times of liquid flow rate from L=2 to 10 kg/m^{2}s did not have the extensive and sizeable effect as the increase of 7 times on the gas flow rate from G=0.1 to 0.7 kg/m^{2}s.

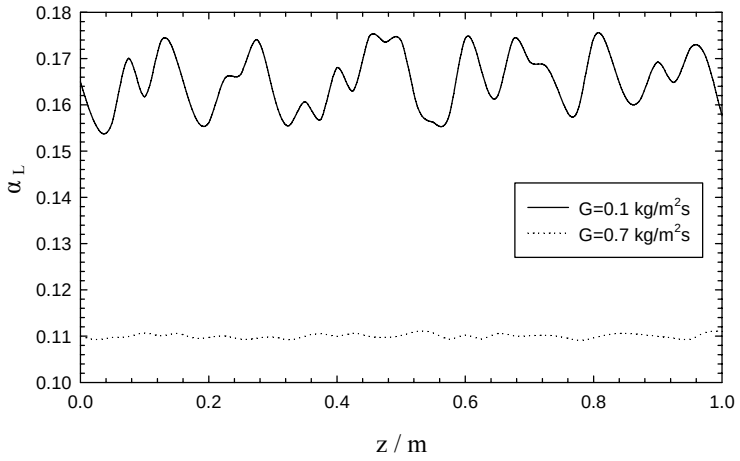

Figure VII.15. Time averaged liquid holdup profiles at different gas flow rates (time step = 10^{-5} s, 10^6 of tetrahedral cells, L=5 kg/m^{2}s, P=30 bar, d=2 mm, D2 distributor)

As the liquid and gas phase tend to flow an uneven route across the packed bed, the intensification of gas flow into the liquid-solid system smoothens the liquid distribution. An increase in gas flow rate is well-known to decrease the wall flow so that an increase in liquid flow and/or gas throughputs leading also to the increase of two-phase pressure drop may improve substantially to better liquid distribution. In fact, the maxima/minima values for the axial liquid holdup values were (5.7, -5.9) and (0.9, -0.8)% for G=0.1 and 0.7 kg/m^{2}s, respectively. Notwithstanding a better radial liquid distribution can be achieved with higher gas flow rates, the instantaneous snapshot of velocity field for the gas phase is still exhibiting a heterogeneous behaviour. This local effect is the result of interstitial phenomena as depicted in the velocity vector plot in Fig. VII.16 at G=0.7 kg/m^{2}s and P=30 bar.

Concomitantly, Fig. VII.17 also supported this fact with the illustration of gas streamlines coloured by the respective Reynolds number at the same operating conditions. As it can be seen, the velocity spots are observed predominantly near the catalyst particles and at the wall. The map of Reynolds number shown in Fig. VII.17 demonstrated that one can feature values up to 2500 so that the *k-ε* dispersed turbulence model can be regarded as a rational choice to capture the turbulence at the higher interaction regimes.

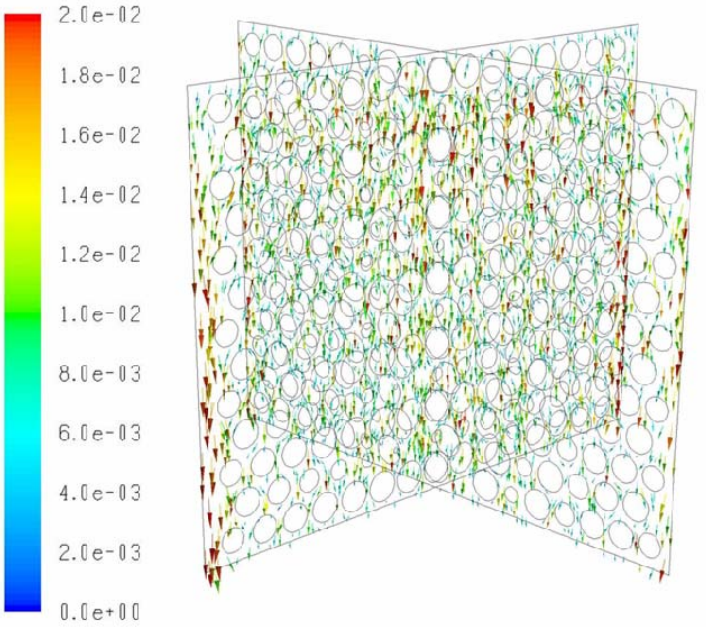

Figure VII.16. Gas velocity vector plot taken at two axial planes shown in Fig. VII.1 (time step = 10^{-5} s, 10^{6} of tetrahedral cells, L=5 kg/m^{2}s, G=0.7 kg/m^{2}s, P=30 bar, d=2 mm, D2 distributor)

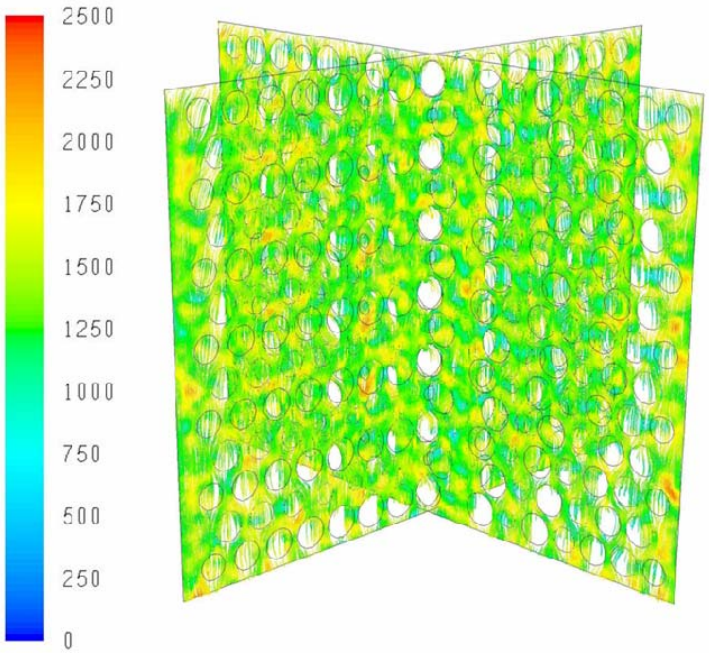

Figure VII.17. Instantaneous gas streamlines coloured by Reynolds number taken at two axial planes shown in Fig. VII.1 (time step = 10^{-5} s, 10^{6} of tetrahedral cells, L=5 kg/m^{2}s, G=0.7 kg/m^{2}s, P=30 bar, d=2 mm, D2 distributor)

Time averaged frictional pressure profiles attained with different gas flow rates are shown in Fig. VII.18 at L=5 kg/m^{2}s and P=30 bar. As it can be seen, the gas flow rate was found to have a greater impact on the liquid distribution with the lowest gas flow rate (G=0.1 kg/m^{2}s). The maxima/minima values computed for the two-phase pressure drop at the lowest gas flow rate were

(8.1, -6.5), (10.5, -8.2), (13.8, -7.3) for z*= ¼, ½ and ¾ , respectively. For the highest simulated gas flow rate (G=0.7 kg/m^{2}s), these values were significantly lower: (1.2, -0.8), (1.6, -1.2), (2.0, -1.1)% as one moves across the packed bed. Therefore, whereas the liquid flow rate seems to have a predominant effect on radial pressure drop profiles at the higher values, the gas flow rates have it major outcome at lower regimes.

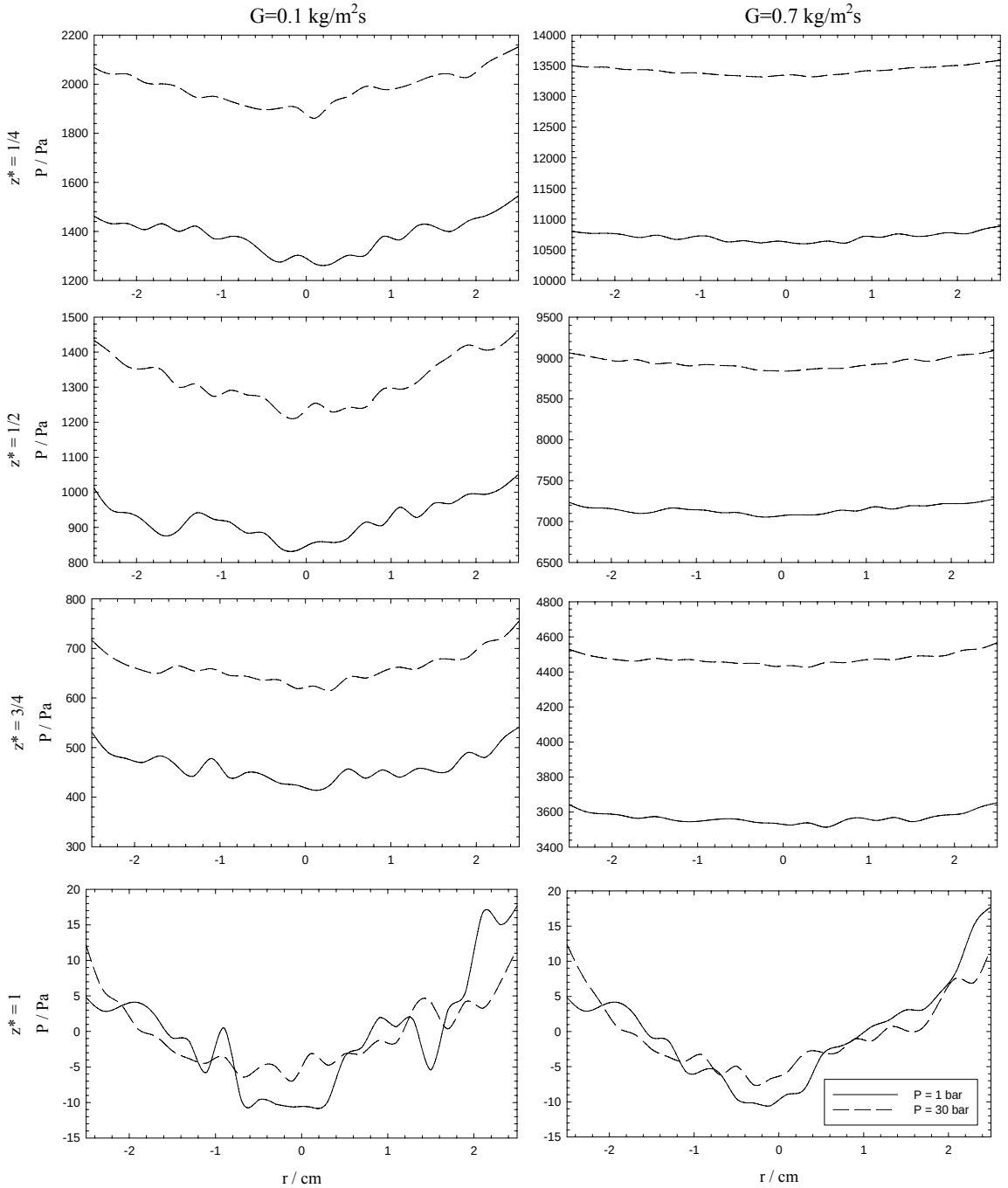

Figure VII.18. Time averaged two-phase pressure profiles as a function of gas flow rate at different bed coordinates and operating pressures (time step = 10^{-5} s, 10^6 of tetrahedral cells, L=5 kg/m^{2}s, d=2 mm, D2 distributor)

VII.4.5. Effect of operating pressure

As the packed bed flow not only depends on liquid and gas superficial velocities as well as on the physico-chemical properties and on the ratio of column diameter to particle diameter, one should also pay attention whether the TBR is pressurized or not. Hence, Fig. VII.10 and VII.12 plot also the effect of operating pressure on both radial liquid holdup and two-pressure profiles at G=0.3 kg/m^{2}s for two different liquid flow rates and operating pressures. When the operation is simulated at atmospheric conditions (P=1 bar), the liquid holdup values were found to be substantially higher than those obtained with a pressurized trickle-bed reactor (P=30 bar). At the lowest liquid flow rate (L=2 kg/m^{2}s), the maxima/minima values for liquid holdup predictions increased from (1.0, -1.6), (1.7, -2.9), (2.5, -5.0), (5.7, -6.4)% at P=30 bar to (1.9, -2.3), (4.2, -4.2), (4.8, -5.7), (7.9, -8.4)% at P=1 bar for z*= ¼, ½, ¾ and 1, respectively. At L=10 kg/m^{2}s, the shift was from (7.5, -9.4), (10.1, -10.0), (14.3, -10.8), (17.1, -13.3)% at P=30 bar to (8.3, -9.9), (12.6, -12.7), (15.5, -14.2), (25.5, -13.5)% at P=1 bar. Generally, the higher operating pressure the smoother radial liquid holdup profile. Moreover, at a constant gas and liquid flow rate the increase of operating pressure seems to give a better performance with respect to the radial liquid distribution. For this reason, the irregularities verified at lower interaction regimes can be further eliminated or at least dissipated with the respective increase of operating pressure.

Time averaged liquid holdup and two-phase pressure profiles plotted in Fig. VII.14 and VII.18 also demonstrated the effect of operating pressure for both hydrodynamic parameters. At the lowest gas flow rate (G=0.1 kg/m^{2}s), the maxima/minima liquid holdup values shifted from (3.3, -3.4), (5.0, -3.4), (8.5, -9.5), (12.2, -11.1)% at P=30 bar to (3.3, -5.2), (6.3, -5.2), (8.9, -10.7), (13.3, -14.3)% for z*= ¼, ½, ¾ and 1, respectively. Therefore, the radial liquid distribution is smoothened as long as the operating pressure is increased. This fact can be also supported at either higher gas flow rates (G=0.7 kg/m^{2}s) or even in terms of radial two-phase pressure drop profiles computed across the trickle-bed reactor.

VII.5. Conclusions

The improper liquid distribution has been found as one of the major reasons for non-optimal use of the catalyst, rapid deactivation and thermal instability in trickle-bed reactors. Despite the work carried out so far, many questions still remain unresolved, particularly concerning the evaluation of local phenomena at the catalyst scale that may be responsible for the integral behaviour of an entire industrial TBR unit. Bearing in mind that the reliable design of TBR is still concerned with trustworthy experimental data on the factors promoting uniform liquid distribution, a TBR was modelled by means of an Eulerian multiphase model at high-pressure.

First, the CFD model was validated under trickling flow regime and its predictions were compared against the experimental liquid holdup and two-phase pressure drop data. The model was optimized in terms of mesh size and time step giving reasonable predictions for both hydrodynamic parameters. Afterwards, the influence of liquid distributor at the top of the bed was evaluated through the comparison between a single-point entry, 60-hole and perfectly uniform distributors. The 60-hole distributor was found to be a good compromise if one is concerned on reactor performance since it allowed a better liquid distribution.

Second, several computational runs were performed to investigate time averaged axial and radial profiles of liquid holdup and two-phase pressure drop. The liquid flow rate had more prominent effect on radial pressure drop at higher values. Alternatively, the gas flow rate had a pronounced influence at lower interaction regimes. The increase of operating pressure on multiphase flow distribution was found to smooth the radial profiles for both hydrodynamic parameters.

VII.6. Nomenclature

d	Particle nominal diameter, m
G	Gas mass flux, kg/m^{2}s
k	k-ε model kinetic energy
L	Liquid mass flux, kg/m^{2}s
$\mathcal{L}$	Reactor length, m
p	Pressure, bar
r	Reactor radius, m
R	Reactor radius, m
$\vec{u}$	Superficial vector velocity, m/s
z	Reactor axial coordinate, m

Greek symbols

α_q	volume fraction of q^{th} phase
ε	k-ε model dissipation energy
μ_q	viscosity of q^{th} phase, Pa.s
ρ_q	density of q^{th} phase, kg/m^3
Δp	total pressure drop, bar
σ_k , σ_ε	k-ε model parameters: 1.2, 1.0
$\overline{\overline{\tau}}_q$	Shear stress tensor of q^{th} phase, bar

Subscripts

G	gas phase
L	liquid phase
q	q^{th} phase
S	solid phase

VII.7. References

Al-Dahhan, M. H., Larachi, F., Dudukovic, M. P., Laurent, A. (1997). High pressure trickle-bed reactors: A Review. *Industrial and Engineering Chemistry Research* **36** (8), 3292-3314.

Al-Dahhan, M.H., Dudukovic, M.P. (1994). Pressure drop and liquid holdup in high pressure trickle-bed reactors. *Chemical Engineering Science* **49**, 5681-5698.

Atta, A., Roy, S., Nigam, K.D.P. (2007). Prediction of pressure drop and liquid holdup in trickle-bed reactor using relative permeability concept in CFD. *Chemical Engineering Science* **62**, 21, 5870-5879.

Attou, A., Ferschneider, G.A. (1999). Two-fluid model for flow regime transition in gas-liquid trickle-bed reactors. *Chemical Engineering Science* **54** (21), 5031-5037.

Bhargava, S. K., Tardio, J., Prasad, J., Foger, K., Akolekar, D. B. and Grocott, S. C. (2006). Wet Oxidation and Catalytic Wet Oxidation. *Industrial and Engineering Chemistry Research* **45** (4), 1221-1258.

Boyer, C., Fanget, B. (2002). Measurement of liquid flow distribution in trickle bed reactor of large diameter with a new gamma-ray tomographic system. *Chemical Engineering Science* **57**, 1079-1089.

Crine, M., Marchot, P., L'Homme, G.A. (1979). Mathematical modeling of the liquid trickling flow through a packed bed using the percolation theory. *Computers and Chemical Engineering* **3**, 515-518.

Dudukovic, M.P., Larachi, F., Mills, P.L. (2002). Multiphase catalytic reactors: A perspective on current knowledge and future trends. *Catalysis Reviews. Science and Engineering* **44** (1), 123-246.

Dybbs, A., Edwards, R.V. (1984). Fundamentals of Transport Phenomena in Porous Media, *J. Bear and M. Corapcioglu Eds.*, Martins Nijhoff, Dordrecht.

FLUENT 6.1. (2005). User's Manual to FLUENT 6.1. Fluent Inc. Centrera Resource Park, 10 Cavendish Court, Lebanon, USA.

Fox, R.O. (1987). On the liquid flow distribution in trickle-bed reactors. *Industrial and Engineering Chemistry Research* **26** (12), 2413-2419.

Funk, G.A., Harold, M.P., Ng, K.M. (1990). A Novel model for reaction in trickle beds with flow maldistribution. *Industrial and Engineering Chemistry Research* **29** (5), 738-748.

GAMBIT 2 (2005). User's Manual to GAMBIT 2. Fluent Inc. Centrera Resource Park, 10 Cavendish Court, Lebanon, USA.

Gianetto, A., Specchia, B.V., Sicardi, S. (1978). Hydrodynamics and solid–liquid contacting effectiveness in trickle-bed reactors. *A.I.Ch.E. Journal* **24**, 1087-1104.

Gunjal, P.R., Kashid, M.N., Ranade, V.V., Chaudhari, R.V. (2005). Hydrodynamics of Trickle-Bed Reactors: Experiments and CFD Modeling. *Industrial and Engineering Chemistry Research* **44**, 6278-6294.

Gunjal, P.R., Ranade, V.V., Chaudhari, R.V. (2005). Computational study of a single-phase flow in packed beds of spheres. *A.I.Ch.E. Journal* **51** (2), 365-378.

Harter, I., Boyer, C., Raynal, L., Ferschneider, G., Gauthier, T. (2001). Flow Distribution Studies Applied to Deep Hydro-Desulfurization. *Industrial and Engineering Chemistry Research* **40**, 5262-5267.

Herskowitz, M., Smith, J.M. (1983). Trickle-bed reactors: a review. *A.I.Ch.E. Journal* **29**, 1-18.

Herskowitz, M., Smith, J.M. (1979). Liquid distribution in trickle-bed reactors. *A.I.Ch.E. Journal* **24**, 439-454.

Holub, R.A., Dudukovic, M.P., Ramachandran, P.A. (1992). A phenomenological model for pressure-drop, liquid holdup, and flow regime transition in gas-liquid trickle flow. *Chemical Engineering Science* **47**, 2343-2348.

Iliuta, I., Larachi, F., Al-Dahhan, M.H. (2000). Double-slit model for partially wetted trickle flow hydrodynamics, *A.I.Ch.E. Journal* **46**, 597-609.

Jiang, Y., Khadilkar, M.R., Al-Dahhan, M.H., Dudukovic, M.P. (2002). CFD modeling of multiphase in packed bed reactors: results and applications. *A.I.Ch.E. Journal* **48**, 716-730.

Kundu, A., Saroha, A.K., Nigam, K.D.P. (2001). Liquid distribution studies in trickle bed reactors. *Chemical Engineering Science* **56**, 5963-5967.

Larachi, F., Lamia, B., Ion, I., Bernard, P.A.G. (2003). Heat and mass transfer in co-current gas-liquid packed beds: analysis, recommendations and new correlations. *Industrial and Engineering Chemistry Research* **42**, 222-242.

Logtenberg, S.A, Nijemeisland, M., Dixon, A.G. (1999). Computational fluid dynamics simulations of fluid flow and heat transfer at the wall particle contact points in a fixed bed reactor. *Chemical Engineering Science* **54**, 2433-2439.

Lopes, R.J.G., Quinta-Ferreira, R.M. (2007). Trickle-Bed CFD Studies in the Catalytic Wet Oxidation of Phenolic Acids. *Chemical Engineering Science* **62** (24), 7045-7052.

Lopes, R.J.G., Quinta-Ferreira, R.M. (2008). Three-Dimensional Numerical Simulation of Pressure Drop and Liquid Holdup for High-Pressure Trickle-Bed Reactor. *Chemical Engineering Journal* **145** (1), 112-120.

Lopes, R.J.G., Quinta-Ferreira, R.M. (2009). CFD modelling of multiphase flow distribution in trickle beds. *Chemical Engineering Journal* **147** (2-3), 342-355.

Melli, T.R., Scriven, L.E. (1991). Theory of two-phase cocurrent downflow in networks of passages. *Industrial and Engineering Chemistry Research* **30** (5), 951-969.

Nemec, D., Levec, J. (2005). Flow through packed bed reactors: 2. Two phase concurrent downflow. *Chemical Engineering Science* **60** (24), 6958-6970.

Ng, K.M., Chu, C.P. (1987). Trickle bed reactors. *Chemical Engineering Progress* **83**, 55-63.

Onda, K., Takeuchi, H., Maeda, Y., Takeuchi, N. (1973). Liquid distribution in packed column. *Chemical Engineering Science* **28**, 1677-1783.

Patankar, S.V. (1980). Numerical Heat Transfer and Fluid Flow. *Hemisphere* Washington DC.

Pintar, A., Berčič, G., Levec, J. (1997). Catalytic liquid-phase oxidation of aqueous phenol solutions in a trickle-bed reactor. *Chemical Engineering Science* **52**, 4143-4153.

Sáez, A.E., Carbonell, R.G. (1985). Hydrodynamic parameters for gas liquid cocurrent flow in packed beds. *A.I.Ch.E. Journal* **31** (1), 52-62.

Satterfield, C.N. (1975). Trickle-bed reactors. *A.I.Ch.E. Journal* **21**, 209-228.

Saroha, A.K., Nigam, K.D.P., Saxena, A.K., Kapoor, V.K. (1998). Liquid distribution in trickle-bed reactors. *A.I.Ch.E. Journal* **44**, 2044-2052.

Schubert, M., Hessel, G., Zippe, C., Lange, R., Hampel, U. (2008). Liquid flow texture analysis in trickle bed reactors using high-resolution gamma ray tomography. *Chemical Engineering Journal* **140**, 332-340.

Schwartz, J.G., Weger, E., Dudukovic, M.P. (1976). A new tracer method for the determination of liquid-solid contacting efficiency in trickle-bed reactors. *A.I.Ch.E. Journal* **22**, 894-904.

Sederman, A.J., Gladden, L.F. (2001). Magnetic resonance imaging as a quantitative probe of gas-liquid distribution and wetting efficiency in trickle-bed reactors. *Chemical Engineering Science* **56**, 2615-2628.

Souadnia, A., Latifi, M.A. (2001). Analysis of two-phase flow distribution in trickle-bed reactors. *Chemical Engineering Science* **56**, 5977-5985.

Stanek, V., Hanika, J., Hlavacek, V., Tranka, O. (1981). The effect of liquid flow distribution on the behavior of a trickle bed reactor, *Chemical Engineering Science* **36** (6), 1045-1067.

Reinecke, N., Mewes, D. (1996). Tomographic imaging of trickle-bed reactors. *Chemical Engineering Science* **51**, 2131-2138.

Vasquez, S.A., Ivanov V.A. (2000). A Phase Coupled Method for Solving Multiphase Problems on Unstructured Meshes. *In Proceedings of ASME FEDSM'00: ASME 2000 Fluids Engineering Division Summer Meeting*, Boston, June.

Zimmerman, S.P., Ng, K.M. (1986). Liquid distribution in trickling flow trickle bed reactors. *Chemical Engineering Science* **41** (4), 861-866.

VIII. VOF Based Model for Multiphase Flow in High-Pressure TBR: Optimization of Numerical Parameters[1]

Aiming to understand the effect of various parameters such as liquid velocity, surface tension, and wetting phenomena, a Volume-of-Fluid (VOF) model was developed to simulate the multiphase flow in a high-pressure trickle-bed reactor (TBR). As the accuracy of the simulation is largely dependent on mesh density, different mesh sizes were compared for the hydrodynamic validation of this multiphase flow model. Several model solution parameters comprising different time steps, convergence criteria and discretization schemes were examined to establish model parametric independency results similarly to the previous analysis carried out within the Eulerian approach. High-order differencing schemes were found to agree better with the experimental data from the literature given that their formulation includes inherently the minimization of artificial numerical dissipation. The optimum values for the numerical solution parameters were then used to evaluate the hydrodynamic predictions at high-pressure demonstrating the significant influence of the gas flow rate mainly on liquid holdup rather than on two-phase pressure drop and exhibiting hysteresis in both hydrodynamic parameters. Afterwards, the VOF model was applied to evaluate successive radial planes of liquid volume fraction at different packed bed cross-sections.

VIII.1. Introduction

Trickle-bed reactors are catalytic fixed-bed tubular devices in which a gas-liquid stream flows vertically downwards. Industrial applications arise traditionally in petrochemical and chemical industries, in biochemical and electrochemical processing and more recently in waste gas and wastewater treatment. Well-known hydrodynamic issues are often related with partial particle-scale external wetting also referred as wetting efficiency that can cause inefficient catalyst utilization and poor heat and mass transfer rates. This hydrodynamic parameter is calculated from the percentage of external wetted surface area divided by the total solid particles surface area, and it is critical in setting the proper reactor operating specifications in order to maximize and promote higher conversion rates (Al-Dahhan *et al*., 1997; Dudukovic *et al*., 2002). In case of exothermic reactions, partial wetting can indeed lead to poor catalyst wetting effectiveness factors and poor heat withdrawal. In order to ensure full coverage with a continuous liquid film of all pellets in the bed, it is necessary to guarantee a sufficient gas and liquid feeding.

[1] *This Chapter is based upon the publication Lopes and Quinta-Ferreira (2009)*

The scaleup/down and design of laboratorial and commercial trickle-bed reactors depends heavily on the precise knowledge of two-phase pressure drop, liquid holdup and the catalyst wetting efficiency as a function of operating conditions and the mathematical formulation derived is frequently system specific and it is feasible only in a particular range of operation in which the correlation was obtained. Recently, computational fluid dynamics (CFD) appeared as a promising tool to understand the complex hydrodynamics in more detail requiring closure laws for the interphase coupling forces in the momentum balance equation based on the Eulerian–Eulerian approach (Jiang *et al*., 2002; Gunjal *et al*., 2005). However, this mathematical treatment is incapable to capture the wetting features as well as the so-called hysteresis in the operation of trickle beds reviewed by Nigam and Larachi (2005) and Saroha and Indraneel (2008).

The simulation of gas-liquid-solid interfaces of a multiphase flow is still under investigation presenting a computational challenge in CFD despite the advancements already achieved. Known issues are related with the exact location of the interface, calculation of surface tension and the high dissimilarity of fluid properties. For a water/air system the variation can be three orders of magnitude and the numerical method should be capable of maintaining a sharp interface without stretched it over a couple of cells due to numerical diffusion.

Therefore, it is of paramount importance to formulate detailed CFD model that can capture the microscale interaction processes between both surfaces. Our attempt is to supply a deep understanding of fluid hydrodynamics parameters through the development of a Volume of Fluid based computational fluid model for simulating the gas-liquid surface. There are two different classes of methods to deal with the surface modelling techniques: tracking and capturing methods. Front tracking, boundary integral, moving mesh and particle schemes are tracking methods because they are of Lagrangian type, in where the interface position is identified by a particle or a polygon called a Lagrangian marker. Alternatively, level set, continuum advection, volume tracking and phase field method schemes are capturing type methods (Kothe, 1998).

Several literature studies on wetting dynamics considered high velocities in the range 1-6 m/s (Crooks *et al*., 2001; Scheller and Bousfield, 1995; Ted *et al*., 1997), however in trickle bed reactors, the liquid phase interacts with catalyst solid surface with substantially lower velocities. In the theoretical field, recent works were published on the numerical simulation of gas-liquid flows by means of VOF model. Yuan *et al.* (2008) applied a VOF method based on piecewise linear interface construction (PLIC) to track liquid-vapor interface in the simulation of natural convection film boiling and forced convection film boiling on a sphere at saturated conditions. Glatzel *et al.* (2008) evaluated the performance of commercial CFD codes based on VOF method when applied as engineering tool for microfluidic applications. It was studied surface tension

effects and flow patterning of two fluids in terms of computational speed and comparison with experimental data. Gopala and van Wachem (2008) analyzed a number of numerical methods to track interfaces in multiphase flows including the level-set method, the marker particle method and the front tracking method. The authors concluded that VOF method has an advantage of being conceptually simple, reasonably accurate and phenomena such as interface breakup and coalescence are inherently included. Morel (2007) presented alternative modelling approaches for strongly non-homogeneous two-phase flows in where the flow domain is divided into a bubbly region and a droplet region separated by a free surface. The closure problem is discussed for each model and the three models are compared according to several criteria. Heggemann *et al.* (2007) modelled the fluid flow in liquid distributors and the validation was accomplished in the uniform distribution of liquid above structured packings for its performance prediction.

None of the VOF models published in the literature were used to simulate the trickling flow or even the spraying and pulsing hydrodynamic regimes in TBRs. Taking into account the large number of studies that were carried out for measurement of pressure drop and liquid holdup in trickle beds (Al-Dahhan *et al*., 1997; Sáez and Carbonell, 1985; Herskowitz and Smith, 1983) a limited number can only be found which addressed the effect of prewetted and non-prewetted bed conditions on two-phase pressure drop and liquid holdup including the respective hysteresis. Kan and Greenfield explained the hysteresis phenomenon based on the formation of liquid bridges and surface tension (Kan and Greenfield, 1978; Kan and Greenfield, 1979). Christensen *et al.* (1986), Levec *et al.* (1986) and Levec *et al.* (1988) observed that the radial distribution of the liquid in the bed changes depending on whether the liquid flow rate increases or decreases and stated it as a cause for hysteresis. Rode *et al.* (1994) have also reported multiple hydrodynamics states in various flow regimes of trickle-bed reactors. Ravindra *et al.* (1997) presented experimental data on hysteresis while Melli and Scriven (1991) studied hysteresis theoretically in a two-dimensional bed. Recently, Gunjal *et al.* (2005) modelled the hysteresis in pressure drop and liquid holdup by means of an Eulerian framework.

The present VOF model was undertaken to simulate the wetting phenomena in high-pressure (30 *bar*) trickle-bed reactors providing a better understanding of their liquid distribution and hysteresis. The hydrodynamic validation is accomplished in terms of pressure drop and liquid holdup experimental data taken from the open literature and afterwards, computational predictions for the wetting efficiency will be investigated at different liquid flow rates.

VIII.2. CFD Modelling

VIII.2.1. Volume Fraction Equation

The VOF method was used to compute phase volume fractions as well as velocity field maps. The multiphase flow is assumed to be vertical downward and incompressible, with the mathematical description for the flow of a viscous fluid through a three dimensional catalytic bed based on a single set of momentum equations and tracking the volume fraction of each of the fluids throughout the domain. Taking into account that packed bed flow is often described in transient mode, so did the present VOF formulation was used to compute a time-dependent solution. The volume fraction of the phase q in the computational cell is specified for each one of the phases as α_q. In each control volume, the volume fractions of all phases sum to unity and the fields for all variables and properties are shared by the phases and represent volume-averaged values, as long as the volume fraction of each of the phases is known at each location. Thus the variables and properties in any given cell are either purely representative of one of the phases, or representative of a mixture of the phases, depending upon the volume fraction values: if the q^{th} fluid's volume fraction in the cell is denoted as α_q, then the following three conditions are possible: $\alpha_q = 0$: the cell is empty of the q^{th} fluid; $\alpha_q = 1$: the cell is full of the q^{th} fluid; $0 < \alpha_q < 1$: the cell contains the interface between the both fluid phases. Based on the local value of α_q, the appropriate properties and variables will be assigned to each control volume within the domain (see Appendix A, section A.1).

The tracking of the interface between the phases is accomplished by the solution of a continuity equation for the volume fraction of one (or more) of the phases. For the q^{th} phase, this equation has the following form of Equation (VIII.1).

$$\frac{\partial}{\partial t}(\alpha_q \rho_q) + \nabla \cdot (\alpha_q \rho_q \vec{u}_q) = \sum_{p=1}^{n} (\dot{m}_{pq} - \dot{m}_{qp}) + S_q \qquad \text{(VIII.1)}$$

where $\dot{m}_{pq}$ is the mass transfer from phase q to phase p and $\dot{m}_{qp}$ is the mass transfer from phase p to phase q. The source term on the right-hand side of Equation (VIII.1), S_q, is used to compute the mass source for each phase. The primary-phase volume fraction was computed based on the following constraint:

$$\sum_{q=1}^{n} \alpha_q = 1 \qquad \text{(VIII.2)}$$

VIII.2.2. Momentum Equation

A single momentum equation is solved throughout the computational domain, and the resulting velocity field is shared among the phases. The momentum equation, shown below in Equation (VIII.3), is dependent on the volume fractions of all phases through the mixture properties ρ_m and μ_m.

$$\frac{\partial}{\partial t}\left(\rho_{\mathrm{m}}\vec{u}\right)+\nabla\cdot\left(\rho_{\mathrm{m}}\vec{u}\vec{u}\right)=-\nabla p+\nabla\cdot\left[\mu_{\mathrm{m}}\left(\nabla\vec{u}+\nabla\vec{u}^{T}\right)\right]+\rho_{\mathrm{m}}\vec{g}+\vec{F}_{vol} \qquad \text{(VIII.3)}$$

One limitation of the shared-fields approximation is that in cases where large velocity differences exist between the phases, the accuracy of the velocities computed near the interface can be adversely affected. A viscosity ratio more than 10^3 may also lead to convergence difficulties so that the compressive interface capturing scheme for arbitrary meshes was evaluated throughout the TBR modelling.

VIII.2.3. Surface Tension

The VOF model includes the effects of surface tension along the interface between each pair of phases and the additional specification of the contact angles between the phases and the walls (Gunjal *et al*., 2005). Surface tension arises because of attractive forces between molecules in a fluid. At the surface between air and water, the net force is radially inward, and the combined effect of the radial components of force across the entire surface is to make the surface contract, thereby increasing the pressure on the concave side of the surface. The surface tension is a force, acting only at the surface that is required to maintain equilibrium in such instances. It acts to balance the radially inward inter-molecular attractive force with the radially outward pressure gradient force across the surface. In regions where two fluids are separated, the surface tension acts to minimize free energy by decreasing the area of the interface. The surface tension is modelled by means of the continuum surface force (CSF) model proposed by Brackbill *et al.* (1992). With this model, the addition of surface tension to the VOF calculation results in a source term in the momentum equation, $\vec{F}_{vol}$. In case of surface tension is constant along the surface and considering only the forces normal to the interface, the pressure drop across the surface depends upon the surface tension coefficient, σ, and the surface curvature as measured by two radii in orthogonal directions, R_1 and R_2, as expressed in Equation (VIII.4).

$$p_2 - p_1 = \sigma\left(\frac{1}{R_1}+\frac{1}{R_2}\right) \qquad \text{(VIII.4)}$$

where p_1 and p_2 are the pressures in the two fluids on either side of the interface. In the formulation of the CSF model, the surface curvature is computed from local gradients in the surface normal at

the interface. Let n be the surface normal, defined in Equation (VIII.5) as the gradient of α_q, the volume fraction of the q^{th} phase.

$$n = \nabla \alpha_q \tag{VIII.5}$$

The curvature, κ , is defined in Equation (VIII.6) in terms of the divergence of the unit normal (Brackbill *et al*., 1992), $\hat{n}$:

$$\kappa = \nabla \cdot \hat{n} \tag{VIII.6}$$

where

$$\hat{n} = \frac{n}{|n|} \tag{VIII.7}$$

The surface tension is expressed in terms of the pressure jump across the surface. The force at the surface can be expressed as a volume force using the divergence theorem. It is this volume force that is the source term, which is added to the momentum equation and has the following form:

$$\vec{F}_{vol} = \sum_{pairs\ pq} \sigma_{pq} \frac{\alpha_p \rho_p \kappa_q \nabla \alpha_q + \alpha_q \rho_q \kappa_p \nabla \alpha_p}{\frac{1}{2}\left(\rho_q + \rho_p\right)} \tag{VIII.8}$$

Equation (VIII.8) allows for a smooth superposition of forces near cells where more than two phases are present. If only two phases are present in a cell, then κ_q = -κ_p and $\nabla \alpha_q = -\nabla \alpha_p$, this equation simplifies to Equation (VIII.9).

$$\vec{F}_{vol} = \sigma_{pq} \frac{\rho \kappa_p \nabla \alpha_p}{\frac{1}{2}\left(\rho_p + \rho_q\right)} \tag{VIII.9}$$

where ρ is the volume-averaged density computed using equation: $\rho = \sum \alpha_q \rho_q$. The importance of surface tension effects is determined based on the value of two dimensionless quantities: the Reynolds number, *Re*, and the capillary number, *Ca*; or the Reynolds number, *Re*, and the Weber number, *We*. Surface tension effects can be neglected if *Ca >> 1* or *We >> 1*. For *Re << 1*, the quantity of interest is the capillary number given by Equation (VIII.10).

$$Ca = \frac{\mu u}{\sigma} \tag{VIII.10}$$

and for *Re >> 1*, the quantity of interest is the Weber number as shown in Equation (VIII.11).

$$We = \frac{\rho L u^2}{\sigma} \tag{VIII.11}$$

VIII.2.4. Wall adhesion

In order to specify the wall adhesion angle in conjunction with the surface tension model, VOF model taken from work done by Brackbill *et al.* (1992) was also investigated. Rather than impose this boundary condition at the wall itself, the contact angle that the fluid is assumed to make with the wall is used to adjust the surface normal in cells near the wall. If θ_w is the contact angle at the wall, then the surface normal at the cell next to the wall is given by Equation (VIII.12).

$$\hat{n} = \hat{n}_w \cos\theta_w + \hat{t}_w \sin\theta_w \qquad \text{(VIII.12)}$$

where $\hat{n}_w$ and $\hat{t}_w$ are the unit vectors normal and tangential to the wall, respectively. The combination of this contact angle with the usually calculated surface normal one cell away from the wall determines the local curvature of the surface, and this curvature is used to adjust the body force term in the surface tension calculation.

VIII.2.5. Turbulence modelling

Trickle-beds are mostly operated at low interaction regimes so that the flow is often assumed laminar either at the reactor level or at the catalyst particle scale. However, several studies have looked at the transition to turbulence, the level of turbulence intensity in the void space, and the description of flow regimes in fixed bed flow being unfeasible to establish which Reynolds number values detach the laminar and turbulent flows as already described in Chapter VI, section VI.2. Therefore, since the Reynolds numbers range for the gas phase is wide (min: 10, max: 2500), *k*-ε model was applied for turbulence modelling (Elghobashi *et al*., 1984; FLUENT 6.1, 2005). The turbulence kinetic energy, k, and the turbulent energy dissipation, ε, are computed from Equations (VIII.13)-(VIII.14) in terms of mixture properties, ρ_m and μ_m, e.g., $\rho_m = \alpha_p \rho_p + (1-\alpha_p)\rho_q$.

$$\frac{\partial}{\partial t}(\rho_m k) + \nabla\cdot(\rho_m \vec{u}_m k) = \nabla\cdot\left(\frac{\mu_{t,m}}{\sigma_k}\nabla k\right) + G_{k,m} - \rho_m \varepsilon \qquad \text{(VIII.13)}$$

$$\frac{\partial}{\partial t}(\rho_m \varepsilon) + \nabla\cdot(\rho_m \vec{u}_m \varepsilon) = \nabla\cdot\left(\frac{\mu_{t,m}}{\sigma_\varepsilon}\nabla \varepsilon\right) + \frac{\varepsilon}{k}\times(C_{1\varepsilon}G_{k,m} - C_{2\varepsilon}\rho_m \varepsilon) \qquad \text{(VIII.14)}$$

and the production of turbulence kinetic energy, $G_{k,m}$, is computed from Equation (VIII.15).

$$G_{k,m} = \mu_{t,m}\left(\nabla\vec{u}_m + (\nabla\vec{u}_m)^T\right):\nabla\vec{u}_m \qquad \text{(VIII.15)}$$

$C_{1\varepsilon}$ and $C_{2\varepsilon}$ are the constants of standard *k*-ε model whereas σ_k and σ_ε are the turbulent Prandtl numbers for k and ε, respectively.

VIII.3. Numerical simulation

Trickle-bed geometry, fluid properties, operating and boundary conditions

The numerical methodologies including the integration, discretization, linearization and algorithm followed by the CFD solver are described in Appendix A. The present case study encompasses a trickle-bed reactor that was designed using regular shape catalyst particles for multifluid Eulerian simulations as shown by the computational mesh of the catalytic bed in Fig. VI.1 (Chapter VI). The numerical solution parameters including operating conditions are given by Table VIII.1 as well as the discretization methods offered by FLUENT for VOF methodology, i. e., *QUICK (Quadratic Upwind Interpolation for Convective Kinematics)*, GR (*Geometric Reconstruction), CICSAM (Compressive Interface Capturing Scheme for Arbitrary Meshes*) and HRIC (*High Resolution Interface Capturing)* described in Appendix A, section A.4.

Table VIII.1 – Numerical solution parameters used in the CFD simulation

Grid	1000 mm (axial) × 50 mm (radial)
Cell size	0.01 - 0.20 mm (tetrahedral and hexahedral)
Particle diameter	2 mm (spheres)
Time step	10^{-7} – 10^{-2} s
Convergence criteria	10^{-6} – 10^{-3}
Discretization method	*QUICK*, *Geo-Reconstruct*, *CICSAM* and *HRIC*
Iterations	≈ 50,000
Under-relaxation parameters	VOF: 0.4 (pressure), 0.6 (velocity)
Drag formulation	Brackbill *et al*. (1992)
Turbulence model	*k-ε* model (Elghobashi *et al*., 1983)

Gas and liquid thermophysical properties used in the simulation are summarized in Table VIII.2. High-pressure operation was simulated at 30 *bar* total operating pressure with inflow gas (G = 0.1 – 0.7 kg/m^{2}s) and liquid (L = 1 – 15 kg/m^{2}s) being distributed uniformly with given superficial velocity replicating a uniform distributor at the top of trickle-bed reactor. The boundary conditions were specified based on FLUENT documentation (FLUENT 6.1, 2005). Inlet turbulent kinetic energy (k) was estimated from turbulence intensity as expressed in Equation (VIII.16).

$$k = \frac{3}{2}(uI)^2 \tag{VIII.16}$$

where I is the turbulence intensity being given by Equation (VIII.17).

$$I = 0.16\left(\mathrm{Re}_{d_H}\right)^{-1/8} \tag{VIII.17}$$

Inlet turbulent energy dissipation (ε) was estimated from the turbulent viscosity ratio as expressed by Equation (VIII.18).

$$\varepsilon = \rho C_\mu \frac{k^2}{\mu}\left(\frac{\mu_t}{\mu}\right)^{-1} \tag{VIII.18}$$

where C_μ is an empirical constant specified in the turbulence model (0.09).

Table VIII.2 – Relevant thermophysical properties of gas and liquid phases

Properties	Value (P = 30bar) T_1 = 25ºC	T_1 = 200ºC	Units
Liquid phase			
Viscosity	8.925×10^{-4}	1.340×10^{-4}	Pa.s
Density	998.4	866.9	kg/m^3
Surface tension	7.284×10^{-2}	3.770×10^{-2}	N.m
Gas phase			
Viscosity	1.845×10^{-5}	2.584×10^{-5}	Pa.s
Density	35.67	21.97	kg/m^3

At 30 *bar* and 25 *ºC*, the inlet turbulent kinetic energy and inlet turbulent energy dissipation for the gas and liquid phases are given in Table VIII.3 and VIII.4.

Table VIII.3 – Inlet boundary conditions for the gas phase: turbulent kinetic energy (k_q) and turbulent energy dissipation (ε_q) at P=30 bar

G (kg/m^{2}s)	***k_G (mm^2/s^2)***	***ε_G (mm^2/s^3)***
0.1	0.2059	3.690×10^{-3}
0.4	2.330	0.4723
0.7	6.204	3.349

Table VIII.4 – Inlet boundary conditions for the liquid phase: turbulent kinetic energy (k_q) and turbulent energy dissipation (ε_q) at P=30 bar

L (kg/m^{2}s)	***k_L (mm^2/s^2)***	***ε_L (mm^2/s^3)***
1	3.952×10^{-2}	7.637×10^{-5}
8	1.504	0.1106
15	4.518	0.9982

Table VIII.5 systematizes the initial and boundary conditions used during the VOF simulations.

Table VIII.5 – Initial and boundary conditions for the gas and liquid phases

	t = 0	*z = 0*
α_G	0.25	0.25
α_L	0.15	0.15
G / (kg/m^{2}s)	0.1-0.7	0.1-0.7
L / (kg/m^{2}s)	1-15	1-15
P / bar	10-40	10-40
k / (m^2/s^2)	*see Tables VIII.3-4*	
ε / (m^2/s^3)		

Computations are time dependent and were carried out until steady state conditions were reached. The time discretization methods are also described in section A.4 of Appendix A. Standard wall functions available in the commercial CFD solver were employed in the numerical simulations and

the reactor wall and catalyst surfaces are treated as no slip boundaries. Although FLUENT documentation recommends a range of 30-50 for the cell thickness (y^+), in packed-bed flow it is almost impossible to meet the y^+ criterion everywhere on the sphere surface so that this value computed by the CFD solver was always below 200. The calculations have been carried out on a Linux cluster based on AMD64 Dual-Core 2.2 GHz processor workstation.

VIII.4. Results and Discussion

VIII.4.1. Mesh size optimization

The liquid holdup and pressure drop predicted by the CFD simulations are quantitatively compared with the literature experimental results (Nemec and Levec, 2005) for different mesh densities. In Fig. VIII.1 it is plotted the liquid holdup predictions as a function of liquid flow rate at P=30 bar and G=0.1 kg/m^{2}s with different mesh resolutions. This criterion was based on the number of tetrahedral cells needed to achieve a grid independent solution. The routine procedure was as follows: at a given liquid flow rate, the flow domain was initialized for a fixed number of cells and after reaching the steady-state solution, the liquid holdup value was used to build the hydrodynamic profiles shown in Fig. VIII.1.

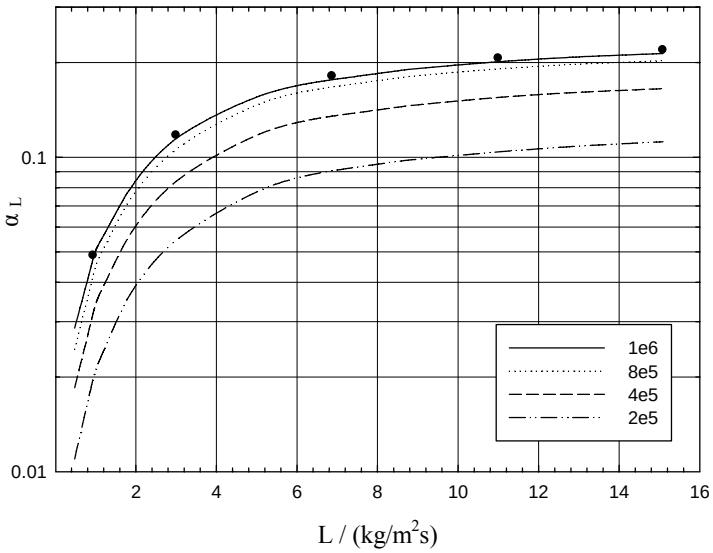

Figure VIII.1. Comparison of liquid holdup predictions as a function of liquid flow rate for different number of cells (G=0.1 kg/m^{2}s, P=30 bar, d=2 mm and experimental data from Nemec and Levec, 2005)

This procedure was replicated increasing the number of tetrahedral cells until the asymptotic value for liquid holdup was found. This iterative method is accomplished for different liquid flow rates in the range 0.5-15 kg/m^{2}s. The coarsest mesh corresponds to about 2×10^5 of tetrahedral cells and the finest mesh had about one million of tetrahedral cells. The average cell size is in the range

0.01-0.2 mm that gives a spatial resolution less than d/20, for the finer meshes. It is worth noting that this cell size was determined after the gap imposition between the catalyst particles of 2 mm that is needed to prevent the loss of numerical accuracy but simultaneously it must not produce unexpected numerical diffusion errors arising in the grid generation. Furthermore, the wall functions available in the CFD solver were evaluated during grid optimization being selected standard wall functions throughout the TBR simulation at high-pressure.

Several authors have simulated heat transfer phenomena in gas-solid packed beds. Nijemeisland and Dixon (2001) modelled the contact points between catalyst particles with common nodes on the surfaces so that the computational cells around these contact points used two nodes on either wall to define their volume. In our TBR mesh, this procedure created noteworthy skewed cells, which means that surfaces were much larger than others within the one tetrahedron. While in laminar flow simulations this fact did not distress convergence, for turbulent flow simulation the Reynolds stresses calculations were affected because the flow velocities in the contact points are significant higher. Therefore, the small gap corresponding to 2-3% of catalyst diameter had to be imposed in order to prevent numerical convergence issues with skewed tetrahedral cells. According to Fig. VIII.1, the numerical simulations performed at L=15 kg/m^{2}s with the coarser meshes (2×10^5, 4×10^5) gave a relative error of 48.9 and 24.6%, while the finer meshes (8×10^5, 10^6) gave 7.4 and 2.7% of relative error, respectively. At L=1 kg/m^{2}s, the relative errors for the computed liquid holdup results were 59.4, 34.4, 13.4 and 6.9%. Therefore, an optimum number of about 10^6 cells gave mesh-independent results with respect to liquid holdup. In Fig. VIII.2 it is shown the frictional pressure drop predictions as a function of liquid flow rate at high-pressure operation.

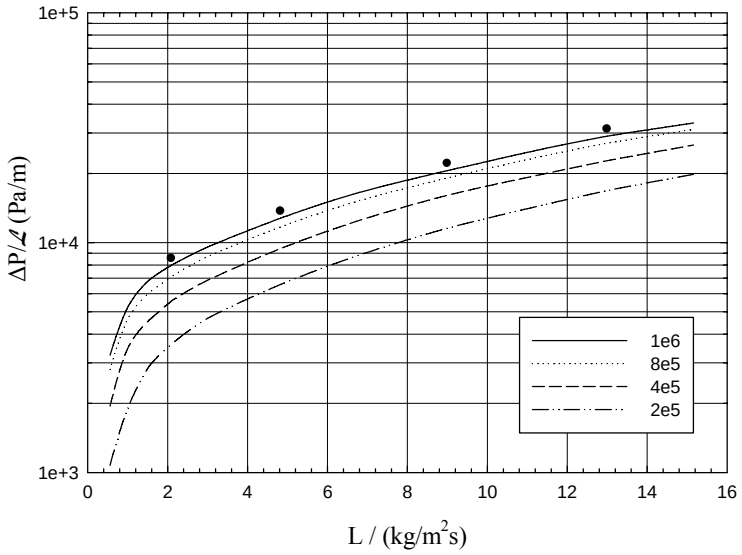

Figure VIII.2. Comparison of two-phase pressure drop predictions as a function of liquid flow rate for different number of cells (G=0.1 kg/m^{2}s, P=30 bar, d=2 mm and experimental data from Nemec and Levec, 2005)

At P=30 bar and L=15 kg/m^{2}s, the relative errors obtained for the two-phase pressure drop were 45.9, 27.1, 13.1 and 7.7% from the coarse to the fine meshes, respectively. If the operation is simulated at the lowest liquid flow rate (L=1 kg/m^{2}s), the relative errors became 57.5, 34.6, 16.4 and 8.4% for 2×10^5, 4×10^5, 8×10^5 and 10^6 of tetrahedral cells, respectively. As one can conclude, both hydrodynamic parameters are underpredicted if one uses coarse meshes and the same value for the number of tetrahedral cells were achieved for mesh-independent results with respect to both liquid holdup and pressure drop so that the finest mesh was used as the base case setting for subsequent parametric investigation of other VOF modelling parameters, as for the Euler-Euler model.

VIII.4.2. Time step and convergence criterion

Since the finest grid with about one million of tetrahedral cells gave mesh-independent results, this mesh was used for time step studies. A nominal time step in the range 0.01-0.001 s has often been used for gas-liquid flow in the Eulerian simulations for packed-bed flows (Jiang *et al*., 2002; Gunjal *et al*., 2005; Lopes and Quinta-Ferreira, 2007). However, with the VOF model during the grid optimization several fixed time step sizes were investigated. For the coarse grid, whatever time step was being used, the numerical accuracy was not always satisfactory. Alternatively, with the fine grid, times steps of 0.001 and 0.005 s gave very similar steady state results but neither 0.005 s nor 0.001 s time steps produce the best accurate computed results close to the experimental values. Additionally, a time step of 0.001 s led to a slightly different transient behaviour being the multiphase flow profiles for either pressure drop or liquid holdup more stable in time with shorter time steps rather than with higher time steps. Following the earlier time step screening activities, its value was decreased from 10^{-3} s to 10^{-4} s and further to 10^{-5} s. In Fig. VIII.3 it was plotted the liquid holdup from the numerical simulations as a function of liquid flow rate for several time steps investigated with VOF multiphase model whereas the pressure drop simulations at P=30 bar are given in Fig. VIII.4 for the same tested time steps. Indeed, as long as the time step is decreased to 10^{-5} s, the hydrodynamic predictions were found to be in good agreement with experimental data. At G=0.1 kg/m^{2}s and for the highest liquid flow rate simulated (L=15 kg/m^{2}s), the relative errors obtained with time steps of 10^{-2}, 10^{-3}, 10^{-4} and 10^{-5} s were 60.9, 36.5, 10.0 and 2.7% for the liquid holdup computations (Fig. VIII.3), respectively. For the case of pressure drop calculations (Fig. VIII.4), the relative errors obtained between the computed and experimental results were larger than those attained with liquid holdup remaining at 61.4, 40.7, 15.1 and 7.7% for the corresponding time steps. The time step was also decreased to 10^{-6} and 10^{-7} s, but seemingly, this operation led to different dynamic behaviour being unbearable the achievement of numerical convergence and stable solution. In fact, a time step of about 10^{-7} s can be only useful in the first iterations to promote the numerical stabilization and depending regularly on the viscosity and

density ratios between the two fluid phases. Therefore, a time step of 10^{-5} s led to affordable hydrodynamic predictions for both liquid holdup and two-phase pressure drop at high-pressure being selected to generate time-step independent CFD results as already concluded within the Euler model analysis.

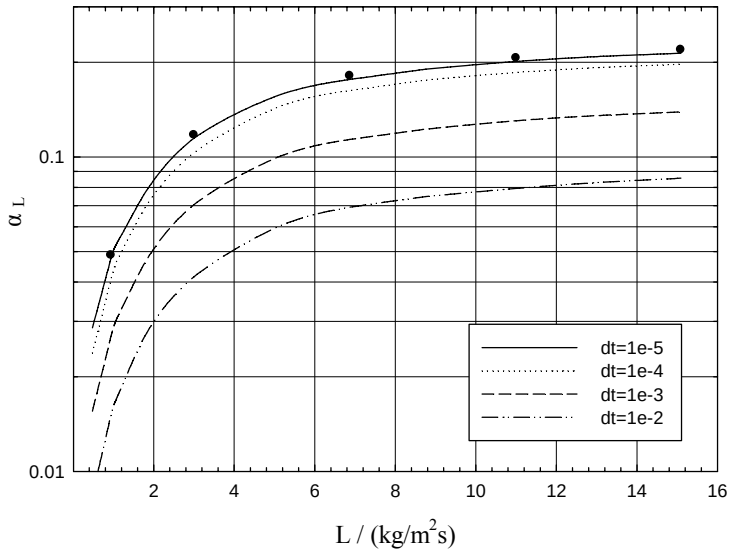

Figure VIII.3. Effect of time step (*dt*) on liquid holdup predictions as a function of liquid flow rate with the finest mesh (10^6 of tetrahedral cells, G=0.1 kg/m^{2}s, P=30 bar, d=2 mm and experimental data from Nemec and Levec, 2005)

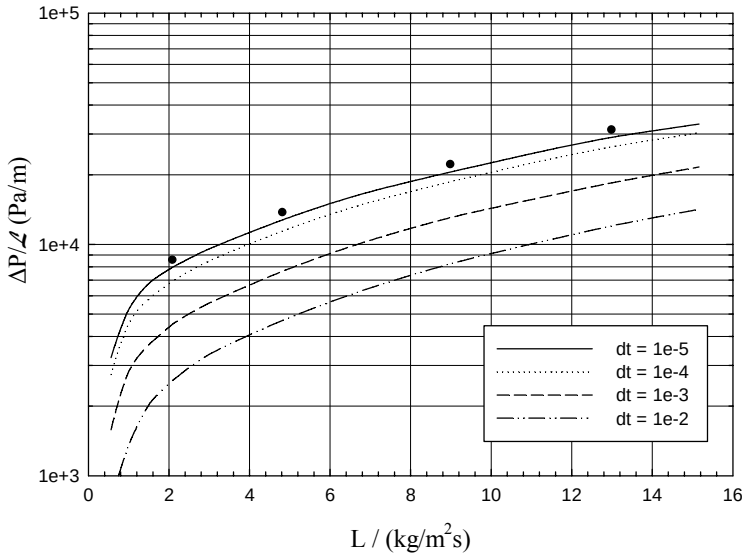

Figure VIII.4. Effect of time step (*dt*) on two-phase pressure drop predictions as a function of liquid flow rate with the finest mesh (10^6 of tetrahedral cells, G=0.1 kg/m^{2}s, P=30 bar, d=2 mm and experimental data from Nemec and Levec, 2005)

One should bear in mind that the mesh size, time step and convergence criteria are deeply inter-related. The present case that is concerned with the multiphase flow simulation in a packed bed is heavily characterized by the unsteady-state behaviour expressed directly in the computation of hydrodynamic parameters. Therefore, as the current VOF formulation was performed in transient

mode, the CFD model predicted cell properties one step at a time and converges them by an iterative procedure until a specified convergence criterion is satisfied. As long as the time step becomes smaller, the predicted change of liquid holdup (or pressure drop) in a specific cell between two consecutive temporal iterations may become smaller. The selection of time step too small as 10^{-7} s or even less had a negative impact on the simulation accuracy and the relative error became higher. However, if the time step is too large as 10^{-2} s, it gave at all less accurate hydrodynamic results. The calculation of a cell property between two temporal iterations also depends on the tetrahedral cell sizes as observed in Figs. VIII.1 and VIII.2. For the TBR time-dependent VOF calculations, the time step used for the volume fraction calculation may not be the same as the time step used for the rest of the transport equations so that a maximum Courant number (N_c) of 0.25 was used in the VOF simulations. The dimensionless Courant number compares the time step in a calculation to the characteristic time of transit of a fluid element across a control volume as expressed in Equation (VIII.19). In this case, based on the Courant-Friedrichs-Lewy condition (CFL) the time step was chosen to be at most one-fourth the minimum transit time for any cell near the interface.

$$N_c = \frac{\Delta t}{\Delta x_{cell} / u_{fluid}} \tag{VIII.19}$$

In Fig. VIII.5 is was plotted the liquid holdup predictions as a function of liquid flow rate with different convergence criteria for the scaled residual component of mass, velocity, etc. variables at P=30 bar.

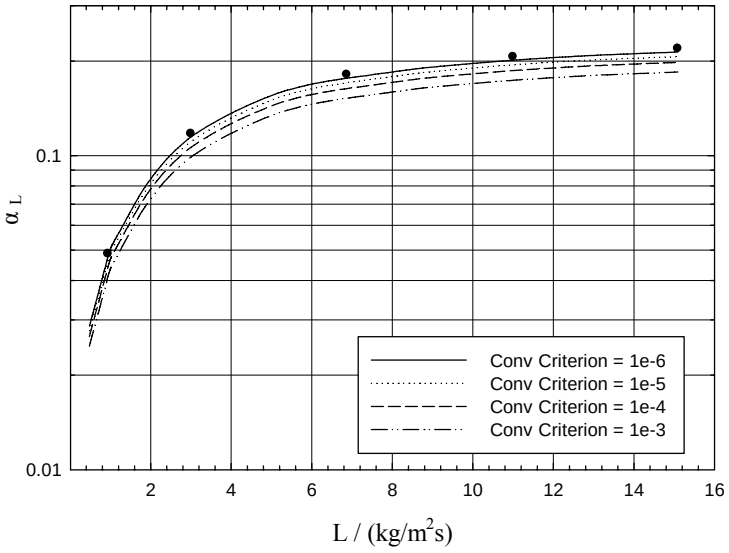

Figure VIII.5. Effect of convergence criteria on liquid holdup predictions as a function of liquid flow rate (time step = 10^{-5} s, 10^6 of tetrahedral cells, G=0.1 kg/m^{2}s, P=30 bar, d=2 mm and experimental data from Nemec and Levec, 2005)

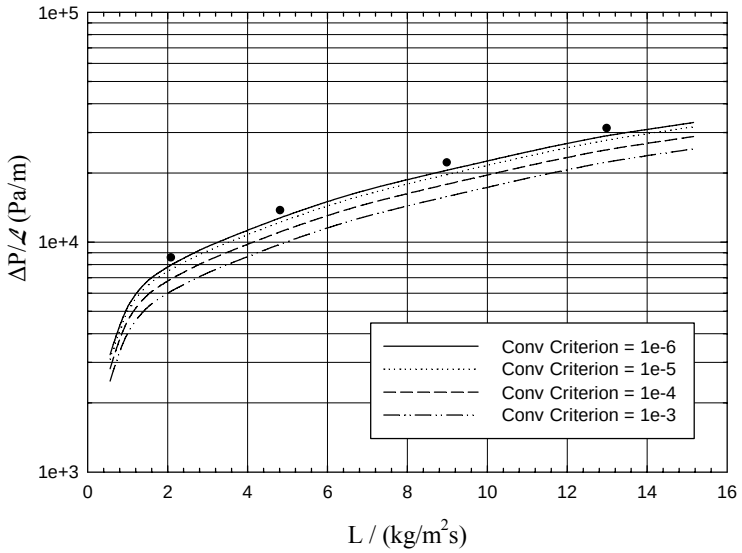

Figure VIII.6. Effect of convergence criteria on two-phase pressure drop predictions as a function of liquid flow rate (time step = 10^{-5} s, 10^6 of tetrahedral cells, G=0.1 kg/m^{2}s, P=30 bar, d=2 mm and experimental data from Nemec and Levec, 2005)

This numerical solution parameter was not found to have the same influence than the effect of time step or mesh size. At L=15 kg/m^{2}s, the convergence criteria of 10^{-3} which corresponds to the default value in the CFD solver gave a relative error of 15.8% for the liquid holdup computation whereas with convergence criteria of 10^{-6}, 10^{-5} and 10^{-4} the relative errors were 2.7, 5.7 and 9.6%, respectively. As expected, a stricter convergence criterion that implied a more accurate calculation gave a better concordance with the experimental data (Nemec and Levec, 2005). This fact was also identified for the two-phase pressure drop simulations (Fig. VIII.6) with the following decreasing order of relative error achieved at L=15 kg/m^{2}s: 7.7, 10.7, 18.9 and 28.3 for the 10^{-6}, 10^{-5}, 10^{-4} and 10^{-3} convergence criteria.

VIII.4.3. VOF differencing scheme

After the establishment of base case settings to produce either mesh-independent or time step-independent CFD results with respect to liquid holdup and two-phase pressure drop, the finest mesh of about one million of cells and a time step of 10^{-5} s were used to perform additional studies on the discretization scheme of volume fraction equation. As long as high order discretization schemes are generally able to capture more realistic physical behaviour, several discretization methods were investigated including the QUICK, GR, CICSAM and HRIC schemes described in Appendix A, section A.4. In Fig. VIII.7 the predicted liquid holdup was plotted as a function of liquid flow rate with the above differencing schemes at G=0.1 kg/m^{2}s and P=30 bar. According to Fig. VIII.7, the calculated relative errors between the computed and experimental liquid holdup results at L=15 kg/m^{2}s were 38.4, 13.2, 10.9 and 2.7% for the *QUICK*, *GR*, *CICSAM* and *HRIC*

schemes, respectively. Therefore, *QUICK* discretization scheme was found to gave the worst concordance between CFD predictions and experimental data whilst the high-order differencing schemes (*CICSAM*, *HRIC*) were found to produce reasonably accurate results and thus solving the problem of poor convergence verified with *QUICK* scheme.

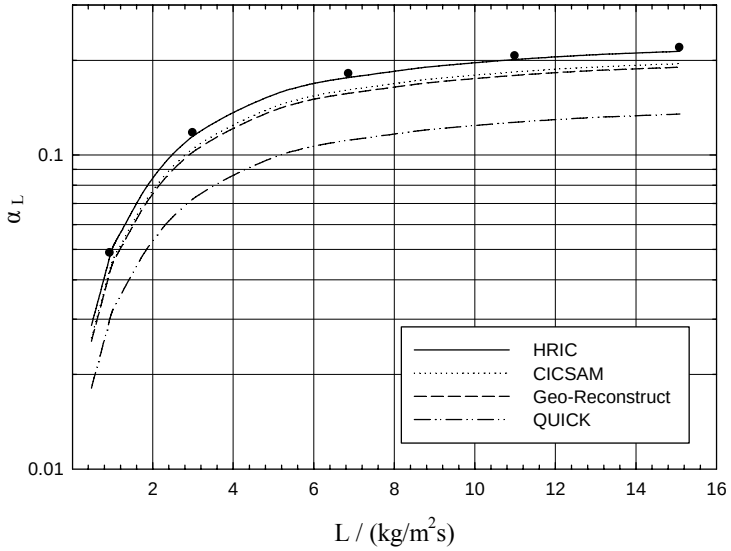

Figure VIII.7. Effect of discretization scheme of volume fraction equation (*QUICK*, *GR*, *CICSAM* and *HRIC*) on liquid holdup predictions as a function of liquid flow rate (time step = 10^{-5} s, 10^6 of tetrahedral cells, G=0.1 kg/m^{2}s, P=30 bar, d=2 mm and experimental data from Nemec and Levec, 2005)

These schemes were used to discretize the convective term in the scalar equation for the transport of the volume fraction through the computational domain and the main reason advanced for the better quantitative agreement is definitely related to their high resolution algorithms in order to minimize the influence of artificial numerical dissipation and to keep the shape of the step interface profile. As long as upwind and central differencing schemes are known to introduce artificial diffusion or dispersion respectively to their order of accuracy, high-order schemes (mainly *CICSAM* and *HRIC*) were found to avoid these artificial numerical effects and concurrently assuring a compressive character or sharpening of the step interface profile (Ubbink and Issa, 1999; Muzaferija *et al*., 1998).

Two-phase frictional pressure drop predictions were plotted in Fig. VIII.8 as a function of liquid flow rate with the same discretization schemes at G=0.1 kg/m^{2}s and P=30 bar. According to Fig. VIII.8, it was found that *GR* scheme almost gave the same pressure drop results that *CICSAM* and *HRIC*. Once more, the high-order differencing schemes gave a better concordance with experimental pressure drop data and minimal relative errors. In fact, at the highest simulated liquid flow rate the relative errors were 29.8, 9.2, 8.5 and 7.7% for the *QUICK*, *GR*, *CICSAM* and *HRIC*

schemes, respectively. Hence, as the normalized variable diagram provides the mathematical foundation for both *CICSAM* and *HRIC* schemes (Muzaferija *et al*., 1998) and while *CICSAM* is based on the convective boundedness criterion, the *HRIC* explicit independence on the CFL condition showed to give the best VOF multiphase predictions either for liquid holdup or pressure drop as observed in both Figs. VIII.8 and VIII.9.

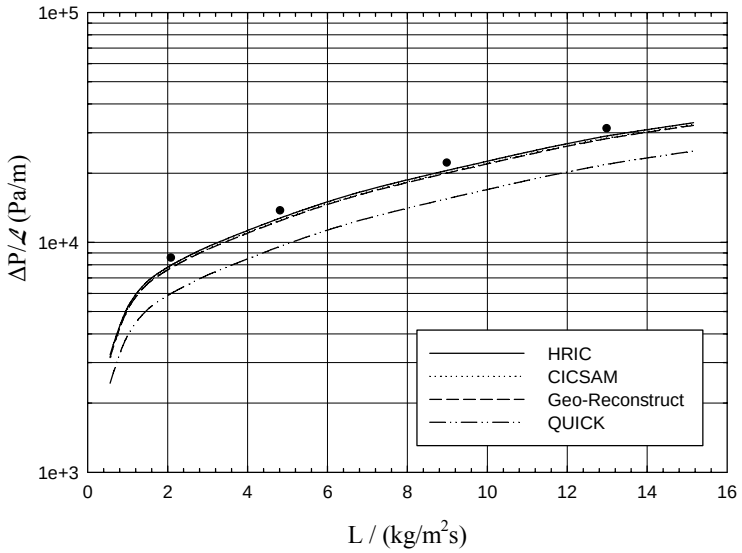

Figure VIII.8. Effect of discretization scheme of volume fraction equation (*QUICK*, *GR*, *CICSAM* and *HRIC*) on two-phase pressure drop predictions as a function of liquid flow rate (time step = 10^{-5} s, 10^6 of tetrahedral cells, G=0.1 kg/m^{2}s, P=30 bar, d=2 mm and experimental data from Nemec and Levec, 2005)

VIII.4.4. Hydrodynamics predictions

For the purpose of additional and sustainable VOF corroboration studies, several CFD simulations were carried out to evaluate the effect of gas flow rate on the TBR hydrodynamics. In Fig. VIII.9 it was plotted the computed liquid holdup results as a function of liquid flow rate at P=30 bar and charging the gas flow rate in the range 0.1-0.7 kg/m^{2}s. As it can be seen, two branches were obtained for a single gas flow rate. Increasing the liquid flow rate from 2 to 15 kg/m^{2}s, the computed liquid holdup corresponds to the lower profile of a non-prewetted bed while the upper profile was obtained decreasing the liquid flow rate in a prewetted catalytic bed. It is worth noting that at G=0.7 kg/m^{2}s and L=15 kg/m^{2}s, the prevailing hydrodynamic regime is still trickling flow according to several published flow map regimes (Al-Dahhan *et al*., 1997).

Fig. VIII.10 shows two-phase pressure drop predictions following the same procedure as mentioned above at different gas flow rates. The capillary pressure acting on the solid-liquid interface is dominant for a dry catalytic bed which restricts the spreading within the bed and the liquid flows through the confined region of the bed. As expected, a larger gas-liquid interfacial

interaction can be attained and the frictional pressure drop profile showed hysteresis when the liquid flow rate was decreased from 15 to 2 kg/m^{2}s.

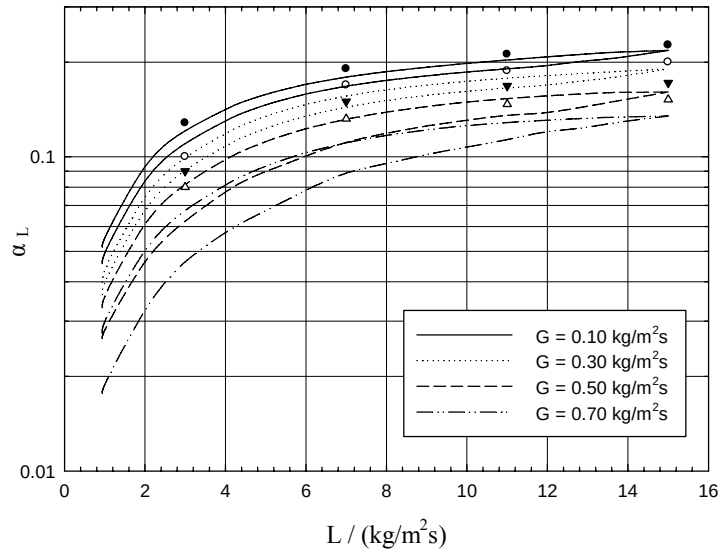

Figure VIII.9. Effect of gas flow rate on liquid holdup predictions as a function of liquid flow rate (*HRIC*, time step = 10^{-5} s, 10^6 of tetrahedral cells, P=30 bar, d=2 mm and experimental data from Nemec and Levec, 2005)

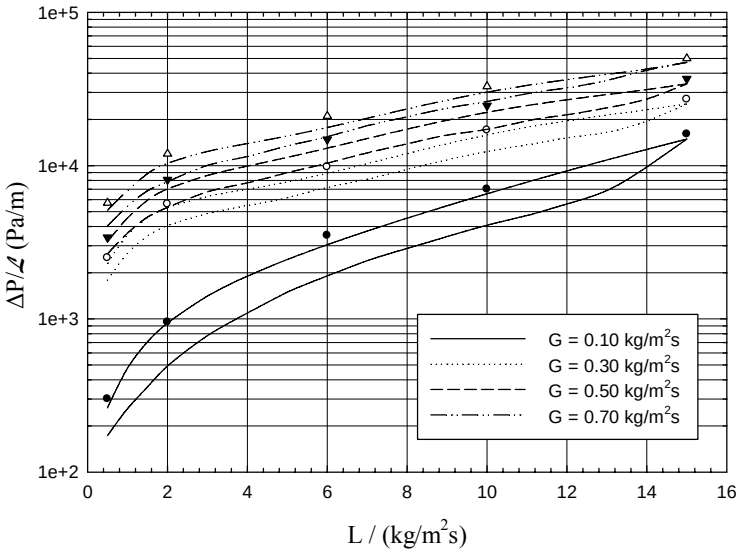

Figure VIII.10. Effect of gas flow rate on two-phase pressure drop predictions as a function of liquid flow rate (*HRIC*, time step = 10^{-5} s, 10^6 of tetrahedral cells, P=30 bar, d=2 mm and experimental data from Nemec and Levec, 2005)

The hysteresis behaviour may also depend on initial flow distribution in the catalytic bed so that it was mimicked an ideal gas-liquid distributor at the top of TBR. The VOF computations for liquid holdup showed similar trends of hysteresis as those found for pressure drop which may be explained based on the formation of liquid bridges and surface tension effect. According to Fig. VIII.9, it was found that VOF underpredicted the liquid holdup in the whole range of gas and liquid simulated flow rates. In fact, at the lowest liquid flow rate (L=1 kg/m^{2}s) and varying the gas flow rate from 0.1 to 0.7 kg/m^{2}s the relative error for the computed upper liquid holdup profile

were increased from 6.9 to 19.4% demonstrating that the current VOF formulation did not account the influence of gas flow rate accurately. It seems that as long as the reactor is operated under higher interaction regimes (G=0.7 kg/m^{2}s), so did the relative errors became larger. The pressure drop predictions were plotted in Fig. VIII.10 as a function of liquid flow rate and modifying also the gas flow rate from 0.1 to 0.7 kg/m^{2}s at P=30 bar. The calculated relative error between the computed and experimental two-phase pressure drop (Nemec and Levec, 2005) was found to be smaller than those obtained with the liquid holdup simulations at G=0.7 kg/m^{2}s. At the lowest liquid flow rate, the pressure drop relative error moved from 8.4 to 16.2% as the gas flow rate increased from 0.1 to 0.7 kg/m^{2}s. Moreover, in the opposite extreme (high liquid flow rate L=15 kg/m^{2}s) the pressure drop relative error became 7.7% at G=0.1 kg/m^{2}s. Therefore, while the increase of liquid flow rate shortened the relative errors for either liquid holdup (Fig. VIII.9) or two-phase pressure drop (Fig. VIII.10), the relative errors were found to be directly proportional to the increase of gas flow rate.

Fig. VIII.11 shows the liquid holdup predictions as a function of liquid flow rate at different operating pressures. As one can observe, the higher the liquid flow rate was, the larger deviation between the liquid holdup experimental data and computed results was found. The liquid holdup profiles at different pressures were qualitatively similar as those obtained in the evaluation of gas flow rate in Fig. VIII.10. The effect of operating pressure on two-phase pressure drop as a function of liquid flow rate is shown in Fig. VIII.12. A higher pressure drop was obtained when increasing the operating pressure up to 40 bar. Indeed, the VOF model exhibited consistent behaviour for the whole range of simulated liquid flow rate demonstrating that the lower relative errors were obtained at lower interaction regimes.

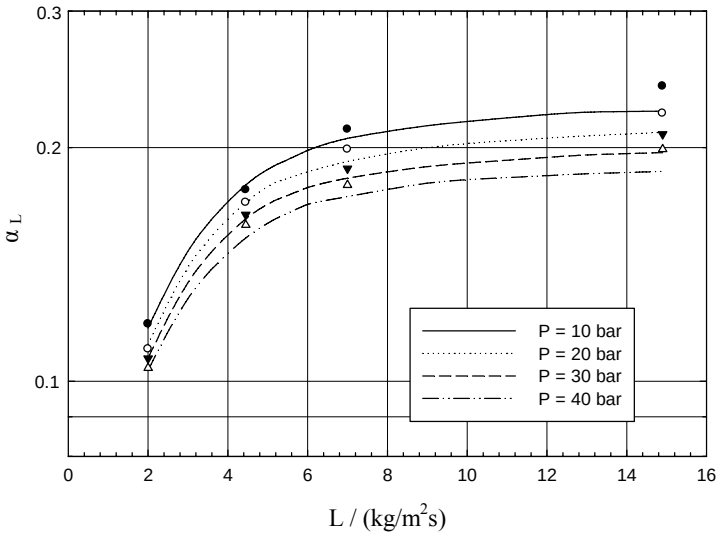

Figure VIII.11. Effect of operating pressure on liquid holdup predictions as a function of liquid flow rate (*HRIC*, time step = 10^{-5} s, 10^6 of tetrahedral cells, G=0.1 kg/m^{2}s, P=30 bar, d=2 mm and experimental data from Nemec and Levec, 2005)

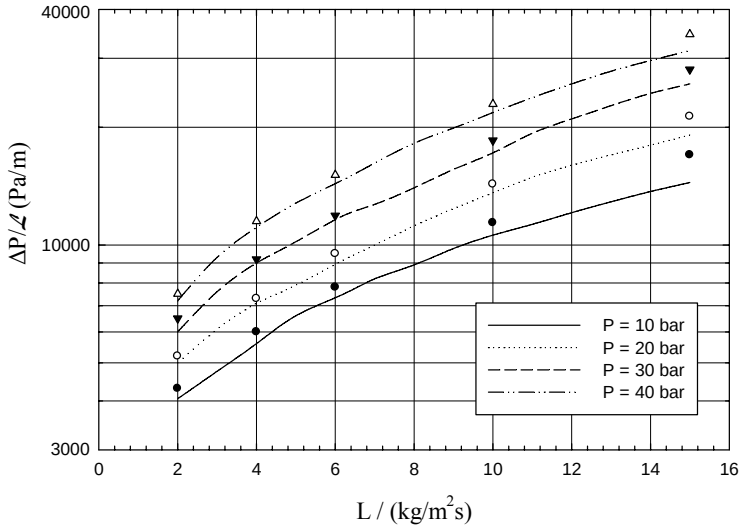

Figure VIII.12. Effect of operating pressure on two-phase pressure drop predictions as a function of liquid flow rate (*HRIC*, time step = 10^{-5} s, 10^6 of tetrahedral cells, G=0.1 kg/m^{2}s, P=30 bar, d=2 mm and experimental data from Nemec and Levec, 2005)

VIII.4.5. Catalyst wetting

As pilot and bench-scale trickle-bed reactors are generally operated at the same liquid hourly space velocities as the commercial-scale reactors, inefficient catalyst wetting has been reported at relatively low liquid superficial velocities. The VOF model was then used to evaluate this hydrodynamic performance parameter that is often related with the low utilization degree of the catalyst packing preventing optimum reactant conversions and product selectivities. Since the *HRIC* scheme gave discretization scheme-independent CFD results for both liquid holdup and two-phase pressure, it was used to compute the average and local catalyst wetting efficiency in the trickle-bed reactor with the finest mesh and with a time step of 10^{-5} s.

Fig. VIII.13a shows a semi-cylindrical slice made inside the catalytic bed at L=1 kg/m^{2}s, G=0.1 kg/m^{2}s, P=30 bar. The orientation is given by the orthogonal axes shown adjacent to the 3D slice. This 3D visualization of trickle flow shows two distinct regions of liquid holdup: liquid rivulets characterized by their relatively large cross-sectional area and surface liquid seen as thin layers on the solid surfaces. The rivulet formation has been identified experimentally by means of magnetic resonance imaging. In order to gain insight how the individual rivulets develop, Fig. VIII.13b shows the same semi-cylindrical slice increasing the liquid flow rate up to 15 kg/m^{2}s at G=0.1 kg/m^{2}s, P=30 bar. As one can observe, the catalytic bed became more flooded with liquid and the overall wetting efficiency was enhanced due to the better axial and radial liquid distribution. This procedure was then used to determine the catalyst surface area that was filled with liquid as a function of liquid flow rate and how the wetting efficiency of individual catalyst particles was influenced by the local structure of the TBR packing.

In Fig. VIII.14a-f), successive radial planes were presented at L=1 kg/m^{2}s, G=0.1 kg/m^{2}s, P=30 bar for the liquid phase along the catalytic bed at the second, forth, sixth, eighth, ninth and tenth axial catalytic layers.

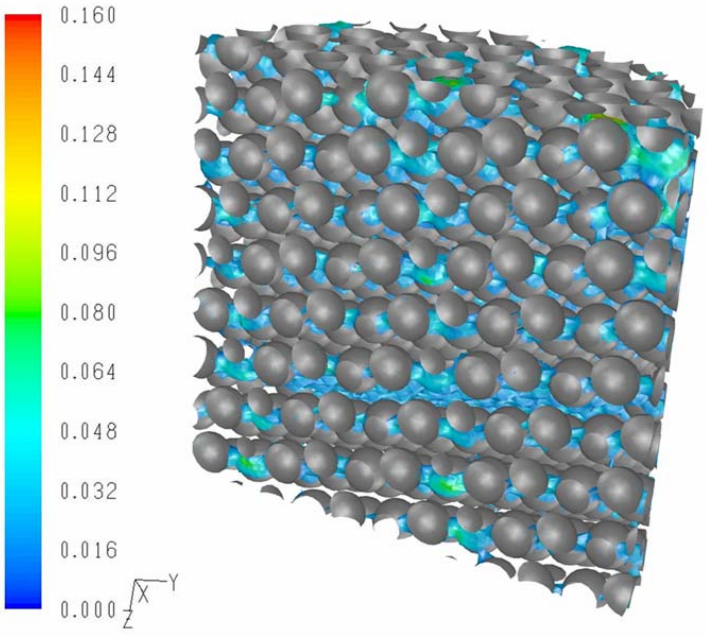

a)

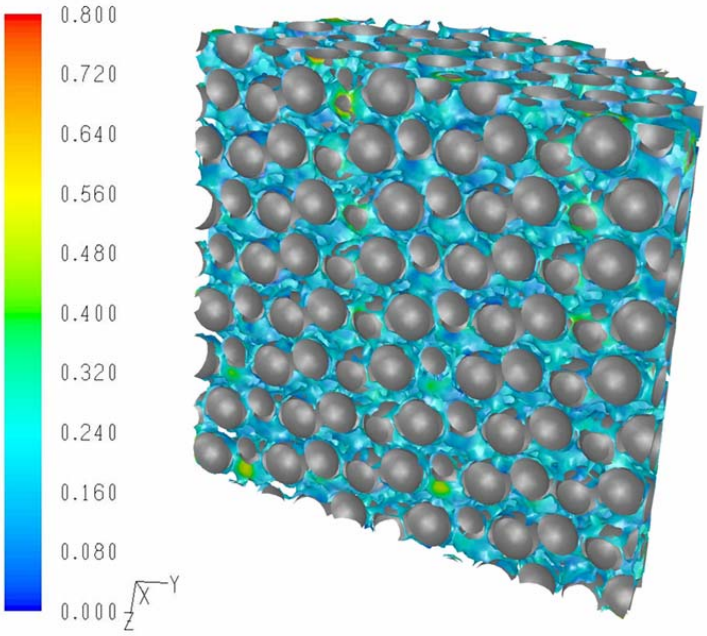

b)

Figure VIII.13. Semi-cylindrical slice made inside the catalytic bed at **a)** L=1 kg/m^{2}s and **b)** L=15 kg/m^{2}s, G=0.1 kg/m^{2}s, P=30 bar.

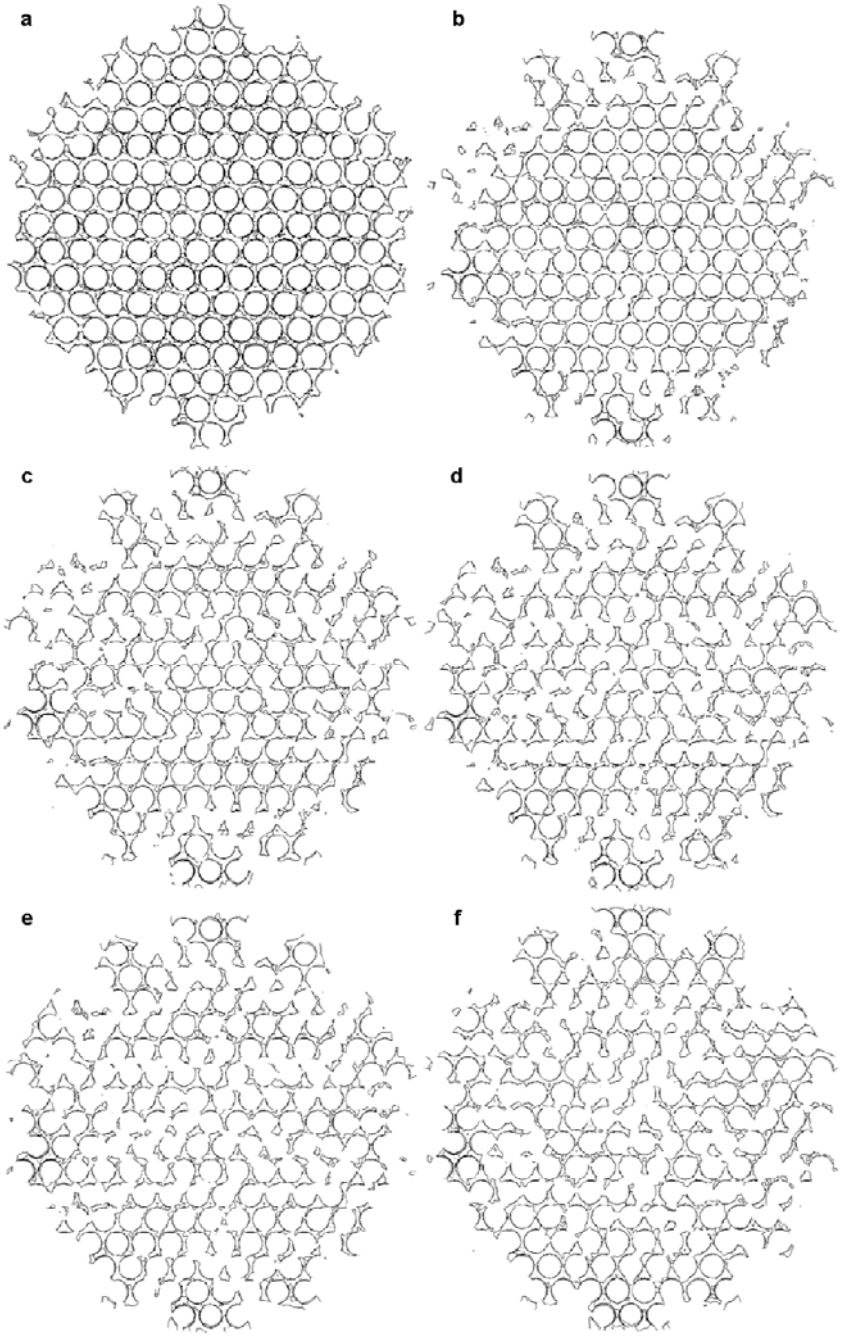

Figure VIII.14a-f). Radial planes of the liquid volume fraction at different cross-sections for the 2nd, 4th, 6th, 8th, 9th and 10th axial catalytic layers (*HRIC*, time step = 10^{-5} s, 10^6 of tetrahedral cells, L=1 kg/m^{2}s, G=0.1 kg/m^{2}s, P=30 bar, d=2 mm)

This axial evolution of wetting efficiency at different cross-sections demonstrates that as long the liquid flows throughout the catalytic bed the liquid phase is spreading out of films on the catalyst particle by surface tension effect. It should be stressed out that the calculation of surface tension effects on triangular and tetrahedral meshes is not as accurate as on quadrilateral and hexahedral meshes according to FLUENT documentation (FLUENT 6.1, 2005). However, the hydrodynamic

validation accomplished in Figs. VIII.1 and VIII.2 did not revealed any significant impact of the tetrahedral mesh choice for mesh-independent results. According to Fig. VIII.14a), it is clear that at the second layer the catalyst particle does not adsorb the liquid phase as Fig. VIII.14b) shows at forth layer. As one moves along the catalytic bed, the liquid phase is better adsorbed by the catalyst particle and further enhancing the wetting efficiency. At the tenth catalytic layer, Fig. VIII.14f) shows that the liquid phase filled the void space between the catalyst particles with a higher extension when comparing with earlier radial planes for the liquid volume fraction (i.e. Fig. VIII.14a) and consequently the gas phase flows around the existent gap left after the adsorption of liquid phase on the spherical particle. The average wetting efficiency computed with the VOF model at the final cross-section (tenth catalytic layer) was about 82%. It should be pointed out that in the CFD simulations, the boundary conditions at the TBR inlet specified a homogeneous distribution of the liquid flow which guarantees at least a better liquid distribution in the reactor and reduces possible radial heterogeneities of wetting efficiency even at lower superficial liquid velocities (L=1 kg/m^{2}s).

At L=1 kg/m^{2}s, G=0.1 kg/m^{2}s, P=30 bar, in Fig. VIII.15a) it was taken an instantaneous snapshot of a liquid holdup isosurface (α_L = 0.06) colored by velocity magnitude values whereas in Fig. VIII.15b) the same instantaneous liquid holdup snapshot was colored by the value of Courant number defined in Equation (VIII.19). The Courant number distribution map ($N_c \approx 0.05$) in Fig. VIII.15b) showed that the CFL condition was always met during the VOF calculations. This computational domain is located in the TBR centre so that it can be assumed that inlet flow effects can be neglected throughout the entire VOF hydrodynamic simulation. According to Fig. VIII.15a), with an average value of about 0.003 *cm/s*, the axial evolution of wetting efficiency addressed in Fig. VIII.14-f) was found to confirm the qualitative radial profiles for the liquid distribution around the catalyst particle and its relationship with the superficial liquid velocities. At high-pressure operation, the liquid holdup isosurface revealed spatially the existence of relevant dry zones formed in the packed bed and confirmed the channeling phenomena typically encountered in lower interaction regimes that is often identified as the main cause of poor hydrodynamic and reaction performance of trickle-bed reactors.

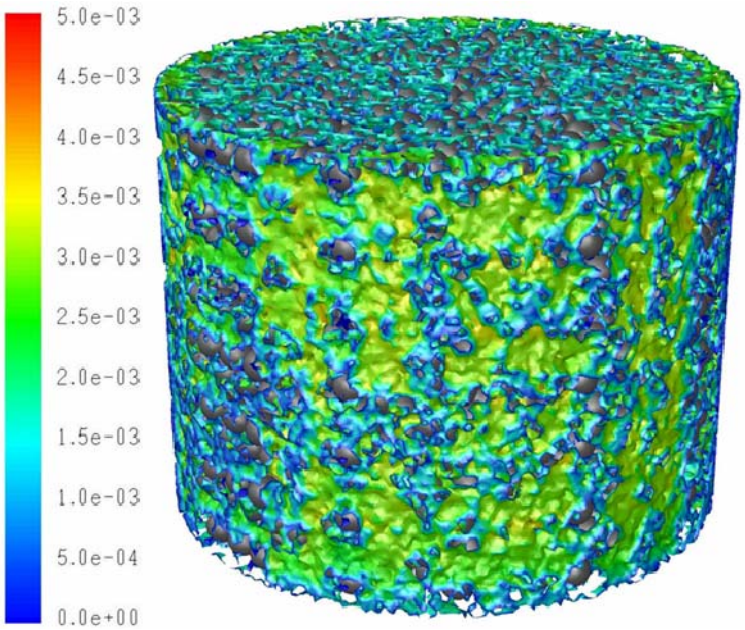

a)

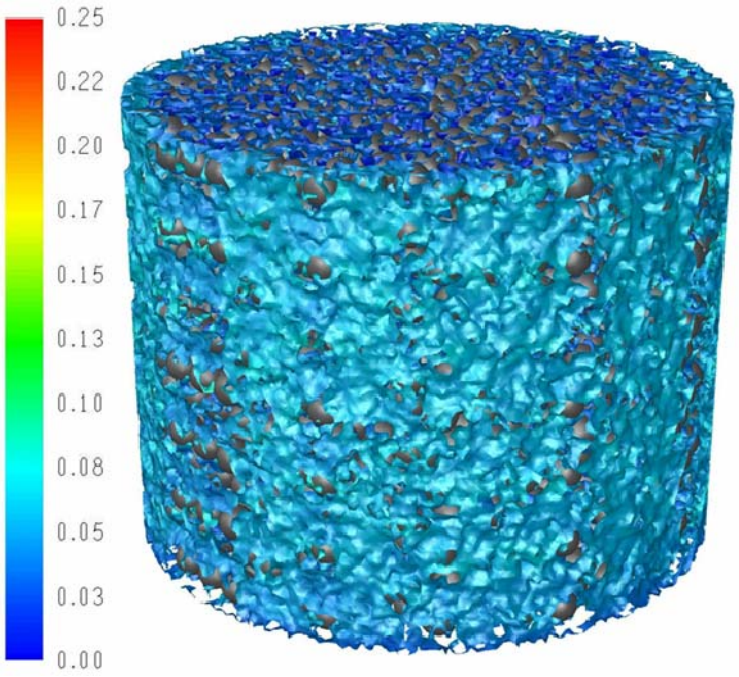

b)

Figure VIII.15. Instantaneous snapshot of liquid holdup isosurface (α_L = 0.06) coloured by **a)** liquid velocity magnitude and **b)** coloured by the computed dimensionless Courant number (*HRIC*, time step = 10^{-5} s, 10^6 of tetrahedral cells, L=1 kg/m^{2}s, G=0.1 kg/m^{2}s, P=30 bar, d=2 mm)

VIII.5. Conclusions

A high-pressure trickle-bed reactor was modelled by means of a Volume-of-Fluid CFD model. The numerical simulations were evaluated quantitatively by experimental data from the literature. During grid optimization and validation, the effects of mesh size, time step and convergence criteria were evaluated plotting the hydrodynamic predictions as a function of liquid flow rate. Several discretization methods for the volume fraction equation were investigated including *Quadratic Upwind Interpolation for Convective Kinematics*, *Geometric Reconstruction*, *Compressive Interface Capturing Scheme for Arbitrary Meshes* and *High Resolution Interface Capturing* schemes. It was found that high-order differencing schemes gave better computed results for either liquid holdup or two-phase pressure drop.

After ascertain mesh size, time step and differencing scheme independent CFD results, the VOF model was used to evaluate the effect of gas flow rate on hydrodynamics demonstrating its considerable influence on the liquid holdup in the range G=0.1-0.7 kg/m^{2}s. Finally, the multiphase model was used to compute radial planes of liquid volume fraction at different axial locations for the packed bed. It was found that wetting efficiency can be captured by VOF model and as long as the fluid phases move through the catalytic bed, so do the catalyst wetting is improved considerably. During the VOF simulations, it was also verified that the dimensionless Courant number was always below than 0.25 according to the Courant-Friedrichs-Lewy condition.

VIII.6. Nomenclature

$C_{\mu}, C_{1\varepsilon}, C_{2\varepsilon}$	k-ε model parameters: 0.09, 1.44, 1.92
d	Catalyst particle nominal diameter, m
$\vec{F}_{vol}$	Source term in the momentum equation
$\vec{g}$	Gravitational acceleration, 9.81m/s^2
G	Gas mass flux, kg/m^{2}s
G_k	Generation rate of turbulent kinetic energy
k	k-ε model kinetic energy
k_{eff}	Effective thermal conductivity
L	Liquid mass flux, kg/m^{2}s
$\mathcal{L}$	Reactor length, m
p	*P*ressure, bar
Re_i	Reynolds number based on intersticial velocity [Re/ε]

S_q	Source mass for phase q
t	Time, s
$\vec{u}$	Superficial vector velocity, m/s
z	Reactor axial coordinate, m

Greek letters

α_q	Volume fraction of q^{th} phase
ε	k-ε model dissipation energy
κ	Gas-liquid interface curvature
ρ_q	Density of q^{th} phase, kg/m^3
Δp	Total pressure drop, Pa
σ	Surface tension, N.m
σ_k , σ_ε	k-ε model parameters: 1.2, 1.0
τ	Residence time, s
$\overline{\overline{\tau}}_q$	Shear stress tensor of q^{th} phase, bar
μ_q	Viscosity of q^{th} phase, Pa.s

Subscripts

G	Gas phase
L	Liquid phase
q	q^{th} phase
S	Solid phase

VIII.7. References

Al-Dahhan, M. H., Larachi, F., Dudukovic, M. P., Laurent, A. (1997). High pressure trickle-bed reactors: A Review. *Industrial and Engineering Chemistry Research* **36** (8), 3292-3314.

Brackbill, J., Kothe, D., Zemach, C. (1992). A continuum method for modelling surface tension. *Journal of Computational Physics* **100**, 335-354.

Christensen, G., Sundaresan, S., McGovern, S. J. (1986). Cocurrent downflow of air and water in a two-dimensional packed column. *A.I.Ch.E. Journal* **32** (10), 1677-1689.

Crooks, R., Whitez, J.C., Boger, D.V. (2001). The role of dynamics surface tension and elasticity on the dynamics of drop impact. *Chemical Engineering Science* **56**, 5575-5592.

Dudukovic, M.P., Larachi, F., Mills, P.L. (2002). Multiphase catalytic reactors: A perspective on current knowledge and future trends. *Catalysis Reviews. Science and Engineering* **44**, 123-246.

Dybbs, A., Edwards, R.V. (1984). Fundamentals of Transport Phenomena in Porous Media, *J. Bear and M. Corapcioglu Eds.*, Martins Nijhoff, Dordrecht.

Elghobashi, S., Abou-Arab, T., Rizk, M., Mostafa, A. (1984). Prediction of the particle-laden jet with a two-equation turbulence model. *International Journal of Multiphase Flow* **10** (6), 697-710.

FLUENT 6.1. (2005). User's Manual to FLUENT 6.1. Fluent Inc. Centrera Resource Park, 10 Cavendish Court, Lebanon, USA.

GAMBIT 2 (2005). User's Manual to GAMBIT 2. Fluent Inc. Centrera Resource Park, 10 Cavendish Court, Lebanon, USA.

Glatzel, T., Litterst, C., Cupelli, C., Lindemann, T., Moosmann, C., Niekrawietz, R., Streule, W., Zengerle, R., Koltay, P. (2008). Computational fluid dynamics (CFD) software tools for microfluidic applications – A case study. *Computers and Fluids* **37**, 218-235.

Gopala, V.R., van Wachem, B.G.M. (2008). Volume of fluid methods for immiscible-fluid and free-surface flows. *Chemical Engineering Journal* **141**, 204-221.

Gunjal, P.R., Kashid, M.N., Ranade, V.V., Chaudhari, R.V. (2005). Hydrodynamics of Trickle-Bed Reactors: Experiments and CFD Modelling. *Industrial and Engineering Chemistry Research* **44**, 6278-6294.

Gunjal, P.R., Ranade, V.V., Chaudhari, R.V. (2005). Computational study of a single-phase flow in packed beds of spheres. *A.I.Ch.E. Journal* **51**, 365-378.

Heggemann, M., Hirschberg, S., Spiegel, L., Bachmann, C. (2007). CFD Simulation and Experimental Validation of Fluid Flow in Liquid Distributors. *Chemical Engineering Research and Design* **85**, 59-64.

Herskowitz, M, Smith, J.M. (1983).Trickle Bed Reactors: A Review. *A.I.Ch.E. Journal* **29**, 1-18.

Hirt, C.W., Nichols, B.D. (1981). Volume of Fluid (VOF) Method for the Dynamics of Free Boundaries. *Journal of Computational Physics* **39**, 201-225.

Jiang, Y., Khadilkar, M.R., Al-Dahhan, M.H., Dudukovic, M.P. (2002). CFD modelling of multiphase in packed bed reactors: results and applications. *A.I.Ch.E. Journal* **48**, 716-730.

Kan, K.M., Greenfield, P.F. (1978). Multiple hydrodynamic states in cocurrent two phase down flow through packed beds. *Industrial and Engineering Chemistry Process Design and Development* **17** (4), 482-485.

Kan, K.M., Greenfield, P.F. (1979). Pressure drop and hold up in two phase cocurrent trickle flows through beds of small packings. *Industrial and Engineering Chemistry Process Design and Development* **18** (4), 740-745.

Kothe, D.B. (1998). Perspective on Eulerian finite volume methods for incompressible interfacial flows. *Free Surface Flows, Springer-Verlag*, 267-331.

Leonard, B.P. (1991). The ULTIMATE conservative difference scheme applied to unsteady one-dimensional advection. *Computational Methods in Applied Mechanical Engineering* **88**, 17-74.

Levec, J., Grosser, K., Carbonell, R.G. (1988). The hysteretic behaviour of pressure drop and liquid hold up in trickle beds. *A.I.Ch.E. Journal* **34** (6), 1027-1030.

Levec, J., Grosser, K., Carbonell, R.G. (1986). The hydrodynamics of trickling flow in packed beds, Part II: Experimental observations. *A.I.Ch.E. Journal* **32**, 369-380.

Lopes, R.J.G., Quinta-Ferreira, R.M. (2007). Trickle-Bed CFD Studies in the Catalytic Wet Oxidation of Phenolic Acids. *Chemical Engineering Science* **62** (24), 7045-7052.

Lopes, R.J.G., Quinta-Ferreira, R.M. (2009). VOF based Model for Multiphase Flow in High-Pressure Trickle-Bed Reactor: Optimization of Numerical Parameters. *A.I.Ch.E. Journal.* DOI: 10.1002/aic.11862.

Melli, T.R., Scriven, L.E. (1991). Theory of two phase cocurrent downflow in networks of passages. *Industrial and Engineering Chemistry Research* **30** (5), 951-969.

Morel, C. (2007). Modelling approaches for strongly non-homogeneous two-phase flows. *Nuclear Engineering and Design* **237**:1107-1127.

Muzaferija, S., Peric, M., Sames, P., Schelin, T. (1998). A two-fluid Navier-Stokes solver to simulate water entry, In *Proceedings of 22nd Twenty-Second Symposium on Naval Hydrodynamics*, Washington, DC, 277-289.

Nemec, D., Levec, J. (2005). Flow through packed bed reactors: 2. Two phase concurrent downflow. *Chemical Engineering Science* **60** (24), 6958-6970.

Nigam, K.D.P., Larachi, F. (2005). Process intensification in trickle-bed reactors. *Chemical Engineering Science* **60**, 5880-5894.

Nijemeisland, M., Dixon, A.G. (2001). Comparison of CFD simulations to experiment for convective heat transfer in a gas-solid fixed bed. *Chemical Engineering Science* **82**, 231-246.

Ravindra, P.V., Rao, D.P., Rao, M.S. (1997). Liquid flow texture in trickle bed reactors: an experimental study. *Industrial and Engineering Chemistry Research* **36** (12), 5133-5145.

Rode, S., Midoux, N., Latifi, M.A., Storck, A. (1994). Multiple hydrodynamic states in trickle beds operating in high interaction regimes: liquid saturation and flow regime transitions. *Chemical Engineering Science* **49** (15), 2535-2540.

Sáez, A.E., Carbonell, R.G. (1985). Hydrodynamic parameters for gas liquid cocurrent flow in packed beds. *A.I.Ch.E. Journal* **31**, 52-62.

Saroha, A.K., Indraneel, N. (2008). Pressure drop hysteresis in trickle bed reactors. *Chemical Engineering Science* **63** (12), 3114-3119.

Scheller, B.L., Bousfield, D.W. (1995). Newtonian drop impact with solid surface. *A.I.Ch.E. Journal* **41**, 1357-1367.

Ted, M., Kuhn, D.C.S., Tran, H. (1997). Spread and rebound of liquid droplets upon impact on flat surfaces. *A.I.Ch.E. Journal* **43**, 2169-2179.

Ubbink, O., Issa, R.I. (1999). Method for Capturing Sharp Fluid Interfaces on Arbitrary Meshes, *Journal of Computational Physics* **153**, 26-50.

Yuan, M.H., Yang, Y.H., Li, T.S., Hu, Z.H. (2008). Numerical simulation of film boiling on a sphere with a volume of fluid interface tracking method. *International Journal of Heat and Mass Transfer* **51**, 1646-1657.

IX. Numerical Simulation of TBR Hydrodynamics with RANS-Based Models Using a VOF Technique[1]

A trickle-bed reactor (TBR) was modeled by means of the Volume of Fluid (VOF) model to provide a hydrodynamic behavior analysis in trickling flow conditions. Fluid dynamics of the TBR is characterized by poor liquid distribution and inefficient catalyst utilization and conventional modeling techniques are unable to address these key design issues. Therefore, the VOF code was used to investigate the major hydrodynamic parameters in a three-dimensional packed bed providing a more rigorous physical description of the underlying flow process. Several numerical solution parameters including different mesh densities, time steps and convergence criteria were optimized in order to provide computational independent results.

During the parametric optimization it was found that VOF model is more sensible to mesh density and time step than with respect to convergence criteria. The computational fluid dynamic model was thoroughly validated by comparing the model predictions with the published experimental data for liquid holdup and two-phase pressure drop. After the VOF optimization, selected values for the numerical solutions parameters were used to perform the assessment of different turbulent flow models at two nominal gas flow rates. Afterwards, several computational runs were performed in the evaluation of the influence of either gas or liquid flow rate on TBR hydrodynamics.

IX.1. Introduction

Trickle-bed reactors are extensively employed in several industrial operations, ranging from chemical and biochemical plants to wastewater treatment and agricultural manufacturing processes. These gas-liquid-solid systems have some distinct advantages over other methods of three-phase reactors (slurry reactors, fluidized bed reactors and bubble fixed-bed reactors), such as low-pressure drop, low liquid hold-up, high catalyst loading and high conversion as both gas and liquid flow regimes approach plug flow. Known disadvantages are often related with partial catalyst wetting, poor liquid-phase distribution, high intraparticle resistance, low mass transfer coefficient, poor radial mixing and temperature control can be difficult (Al-Dahhan *et al*., 1997).

Over the last decades, a noteworthy amount of literature has been published on the determination of the so-called hydrodynamic parameters – liquid holdup and pressure drop – in both laboratory

[1] *This Chapter is based upon the publication Lopes and Quinta-Ferreira (2009)*

and pilot scale TBRs. The design of commercial-scale TBRs traditionally depends on expensive pilot-scale experiments and the mathematical formulation based on dimensional analysis (or even applying the neural networks concept) is mainly focused on improving the simulation of the steady-state operation by developing more suitable empirical correlations. Nevertheless, due to the fact that the majority of correlations for the estimation of liquid holdup, two-phase pressure drop, gas-liquid mass transfer and interfacial area, and catalyst wetting efficiency (Al-Dahhan *et al.*, 1997), have been developed under steady-state conditions and are intended to describe only steady-state reactor operation, most of the correlations are inappropriate for the description of the reactor performance under transient conditions. Recent advances in the improvement of multiphase reactor models indicated that computational fluid dynamics (CFD) is a valuable tool to address the complete multidimensional flow equations coupled with chemical species transport and reaction kinetics instead of traditional TBR models reported in the literature considering isothermal operation in either pseudo-homogeneous or heterogeneous models with plug-flow for gas and liquid phases (Al-Dahhan *et al.*, 1997). Two approaches for CFD modeling of gas-liquid-solid flows have been implemented for the hydrodynamics predictions: the Lagrangian-Eulerian model in particulate flows simulation (Deen *et al*., 2004) and the Eulerian-Eulerian model in trickle-bed reactors (Dudukovic *et al*., 1999; Jiang *et al*., 2001; Gunjal *et al*., 2005a). Using the Lagrangian-Eulerian model, particle trajectories of the discrete phase are tracked by solving individual equations of motion, whereas the continuum phase is modeled using an Eulerian framework. Consequently, the Lagrangian-Eulerian model requires large computational resources for large systems of particles. With the Eulerian-Eulerian model, the base assumption is that gas and liquid phases are interpenetrating continua. Therefore, the Eulerian-Eulerian model for gas-liquid-solid flows is the more commonly used CFD model to predict the dynamic behavior of trickle-bed reactors (Iliuta and Larachi, 2005). However, the Eulerian-Eulerian approach does not accomplish interface tracking by the solution of a continuity equation for the volume fraction of one (or more) phases, and for this reason is unable to capture the wetting characteristics at the gas-liquid interface in the operation of trickle beds. The contacting efficiency is directly related to the spreading of a liquid on either wet or dry catalyst solid surfaces. It is of paramount importance to address the wetting phenomenon to understand its impact on other hydrodynamic and reaction parameters. The interface between both phases is important in evaluating the performance of the reactor and therefore free surface modeling is necessary. Volume of fluid (VOF) and level set approaches belong to the two best possible implicit free surface reconstruction methods. VOF model was extensively used for many applications (Chen and Li, 1998; Cerne *et al*., 2001; Karim *et al*., 2009). The velocity field and bubble profile in a vertical gas–liquid slug flow inside the capillaries has been modeled with a VOF technique and it was found to be in good agreement with published experimental measurements (Taha and Cui, 2004).

In order to gain insight about the pertinent parameters that may affect the liquid-solid interface, several works have been published on the simulation of liquid drop impact with the solid surface (Gunjal *et al*., 2005b; Rioboo *et al*., 2002; Crooks *et al*., 2001). The experimental and simulation data for different contact angles (Mao *et al*., 1997) and velocities (Rioboo *et al*., 2002) indicated that few experimental and simulation studies were conducted at lower velocities that are characteristic of trickling flow regime. Therefore, additional simulation activities on the gas-liquid-solid interface at different flow regimes are needed for the meaningful knowledge of interaction between TBR hydrodynamics and reaction parameters. This work is devoted to the Volume of Fluid model for TBR modeling comprising the numerical validation in terms of well-known hydrodynamic parameters. Liquid holdup and two-phase pressure drop were selected for the parametric optimization of several models parameters including mesh aperture, time step and different convergence criteria. The multiphase flow regime will be presented with several RANS turbulent flow models as well as the laminar one. The effect of gas and liquid flow rate on either frictional pressure drop or liquid holdup will be also examined under trickling flow conditions with three-dimensional packed bed geometry.

IX.2. Modelling Approach and Mathematical Models

IX.2.1. Governing Equations for Multiphase Flow

Understanding the behavior of the fluid flow through the packed particle bed is important to enhance the performance of trickle-bed reactors from design and operating considerations. The solution of the hydrodynamic problem for multiphase reactors using a phenomenological approach should take into account several phenomena including the porous media flow and the interfacial effects, as well as the process parameters such as the bed package, the particles shape and porosity (Maiti *et al*., 2005).

In general, trickle-bed reactors use regular shape catalyst particles, moderate to high gas and liquid flow rates and pressures, and can operate from trickling to pulsing flow regime. These characteristics have a strong influence on hydrodynamic parameters so that a reliable scale-up analysis is often performed with specific data for these processes. In the present study, the detailed information of momentum transport is investigated in a fixed bed by means of CFD codes with different turbulent flow models. A trickle-bed reactor of non-overlapping spherical particles in cylindrical geometry was modeled with a specified void fraction and a set of fluid physical properties; the Navier-Stokes equations are solved for the velocity and pressure fields in the fluid phase of the void space. The computational geometry was designed so that the catalyst particles do not touch each other. The distance between two particles is within 3% of the sphere diameter to

facilitate the grid generation avoiding numerical difficulties that arise in the calculation of convective terms with the representative arrangement of catalyst particles shown in Fig. IX.1.

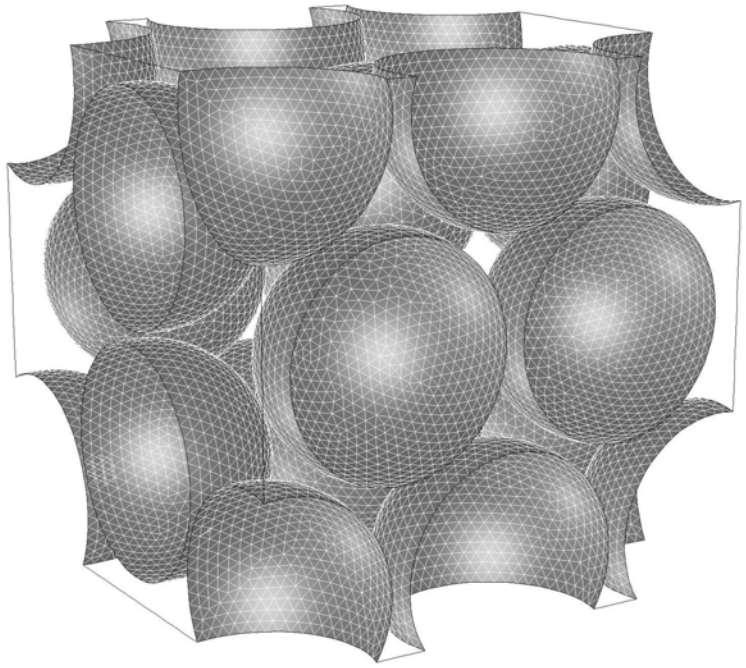

Figure IX.1. Configuration of catalyst particle arrangement for the trickle-bed used in VOF simulations

The purpose of this work is to develop a computational model to analyze the fluid flow through the cylindrical bed including the evaluation of liquid holdup and two-phase pressure drop predictions. In particular, the liquid-gas flow through a catalytic bed was considered comprised of monosized, spherical, solid particles arranged in a cylindrical container of a pilot TBR unit (50 mm_{ID}×1.0 m_{Length}). The VOF method was used to compute velocity field as well as liquid volume fraction distributions. The multiphase flow is assumed vertical downward and incompressible, with the mathematical description for the flow of a viscous fluid through a three-dimensional catalytic bed based on the Navier–Stokes equations for momentum and mass conservation.

The VOF model enables the computation of multiphase flows in which gas-liquid-solid interfaces are clearly identified. It is thus well adapted for calculating the breakup of liquid jets or films sheared by a gas flow (Ryan, 2006) or bubble dynamics (Zheng *et al*., 2007; Liovic and Lakehal, 2007). In the VOF model, the variable fields for all variables (pressure, velocity, etc) are shared by the both phases and correspond to volume-averaged values. It is thus necessary to know the volume fraction, α_q, of each phase, q, in the entire computational domain. The VOF continuity and momentum equations, the free surface model including the surface tension and wall adhesion were described in Equations (VIII.1)-(VIII.9) in Chapter VIII. Different turbulent flow Reynolds

Averaged Navier-Stokes models were investigated during the VOF computations including the multiphase standard and realizable k-ε approach as well as the multiphase Renormalization Group Theory based model (Yakhot and Orszag, 1986) and multiphase Reynolds Stress Model. The mathematical equations for the multiphase standard and realizable k-ε model and the Reynolds Stress Model were presented in Tables VI.1- VI.4 in Chapter VI.

IX.2.2. Numerical simulation

Computational mesh representing the solid catalyst of the trickle-bed reactor was created using the integrated solid modeling and meshing program GAMBIT (GAMBIT 2, 2005). In order to obtain grid-independent results under different operation conditions, the cell number was varied in the range $2\times10^5 - 3\times10^6$. For spherical particles of 2 mm diameter, the cell size in the bulk is less than d/20 and the average cell sizes are in the range 0.01–0.20 mm depending mainly in the geometric conditions tested (Lopes and Quinta-Ferreira, 2008). These dimensions were established after the mesh optimization and for the proper application of wall functions available in the CFD solver. The grid consists of a combination of structured and unstructured meshes, the region close to the wall being meshed with cells of about 0.01 mm in height containing approximately one million of computational cells.

As the accuracy of the simulation is largely dependent on mesh aperture, several different mesh sizes were compared for the hydrodynamic validation issues in multiphase flow operation. The numerical methodology used for the numerical simulation of incompressible transient two-phase flows needs to solve the Navier-Stokes equations together with the interfacial interaction parameters. The fact that the material parameters of the fluid at time t and position (x, y, z) depend on which phase is present at (x, y, z, t) must be accounted for. The VOF method simulates free-surface flow by means of a fluid fraction function, which has a value between unity and zero. The discretization of the governing equations is done by the finite-volume method. The grid independency was established after the evaluation of different mesh apertures in order to isolate mesh related discretization errors. All transport equations were discretized to be at least second order accurate in space.

A segregated implicit solver available in commercial CFD package FLUENT (FLUENT 6.1, 2005) was employed to evaluate the resulting linear system of equations. The conditions required for grid convergent results are based on a 1% relative error criterion and the simulations accuracy has been assessed by comparisons to experimental data available in the literature. At the interface, the additional interaction conditions depend on interfacial velocity and gradient of the surface tension. Three dimensional simulations have been carried out for the catalytic bed. The inlet

turbulence quantities such as turbulent kinetic energy and turbulent energy dissipation were specified based on FLUENT documentation (FLUENT 6.1, 2005). Turbulent kinetic energy (k) was estimated from turbulence intensity and turbulent energy dissipation (ε) was estimated from the turbulent viscosity ratio as expressed in Chapter VIII. At 30 *bar* and 25*ºC*, the inlet turbulent kinetic energy for the liquid (u_L = 0.001 m/s) and gas phase (u_G = 0.003 m/s) was 3.952×10^{-2} and 0.2059 mm^2/s^2, respectively, whereas the turbulent energy dissipation was 7.637×10^{-5} and 3.690×10^{-3} mm^2/s^3. For u_G = 0.02 m/s and u_L = 0.015 m/s, the turbulent kinetic energy are 6.204 and 4.518 mm^2/s^2, and the turbulent energy dissipation are 3.349 and 0.9982 mm^2/s^3, respectively. Additional k and ε values for the gas and liquid phases are given in Table IX.1 at 30 *bar* and 25*ºC*.

Table IX.1 – Inlet boundary conditions for the gas and liquid phases: turbulent kinetic energy (k_q) and turbulent energy dissipation (ε_q) at T=25ºC and P=30 bar

G (kg/m^2s)	L (kg/m^2s)	k_G (mm^2/s^2)	k_L (mm^2/s^2)	ε_G (mm^2/s^3)	ε_L (mm^2/s^3)
0.1	1	0.2059	3.952×10^{-2}	3.690×10^{-3}	7.637×10^{-5}
0.4	1	2.330	3.952×10^{-2}	0.4723	7.637×10^{-5}
0.7	1	6.204	3.952×10^{-2}	3.349	7.637×10^{-5}
0.1	15	0.2059	4.518	3.690×10^{-3}	0.9982
0.4	15	2.330	4.518	0.4723	0.9982
0.7	15	6.204	4.518	3.349	0.9982

IX.3. Results and Discussion

IX.3.1. Hydrodynamic validation and model optimization

The VOF multiphase model was validated in terms of major and well-known hydrodynamic parameters for trickle-bed reactors. For that purpose, several numerical solution parameters were optimized to obtain optimum results such as different tetrahedral mesh sizes and time steps reinforcing and following the route the previous analysis under these topics within the Eulerian studies.

In Fig. IX.2 it was plotted the liquid holdup predictions as a function of tetrahedral mesh density at constant liquid flow rates and P=30 bar.

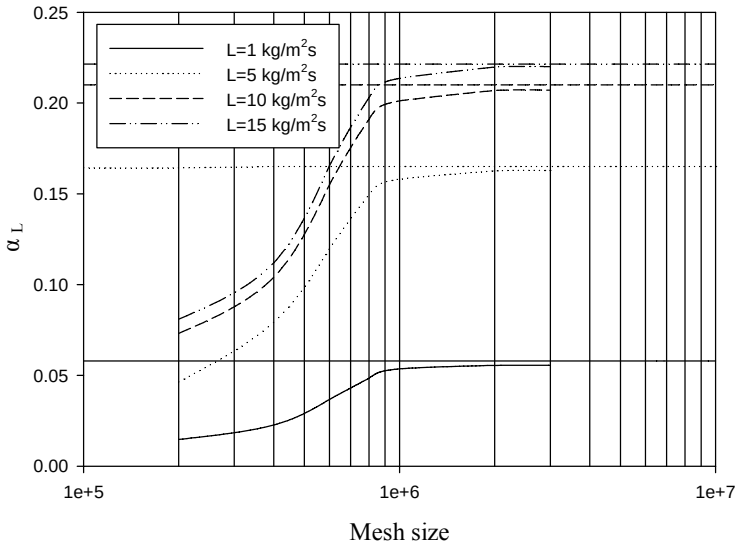

Figure IX.2. Comparison of liquid holdup predictions as a function of mesh density for different liquid flow rates (G=0.1 kg/m^{2}s, P=30 bar, d=2 mm and experimental data from Nemec and Levec, 2005)

As one can observe, the liquid holdup is increasing with mesh density until it reaches an asymptotic solution. This increase was higher and sharper with the highest simulated liquid flow rate (L=15 kg/m^{2}s). In fact, at L=1 kg/m^{2}s the relative errors between the numerical predictions and experimental data were 60.9, 36.6, 16.4, 7.6 % for 4×10^5, 6×10^5, 8×10^5, 10^6 of cells, respectively. The experimental data used for the parametric optimization were available from the work developed by Nemec and Levec (2005) in where it was described in detail the experimental setup. In that work, liquid holdup was measured by a gravimetric method that consists in weighting the column in two different ways to have good reproducibility. After the bed was extensively prewetted, the reactor with dimensions similar to the ones described previously was operated first in a high interaction regime and then reduced to the desired level at which the pressure drop and liquid holdup were measured. The horizontal lines in Fig. IX.2 correspond to the experimental value for the liquid holdup. For the highest simulated liquid flow rate (L=15 kg/m^{2}s), the relative errors became 49.4, 25.3, 8.4 and 3.5. Therefore, the VOF model exhibited a considerable dependence with respect to mesh density for higher liquid flow rates. However, the optimum number of tetrahedral cells was almost the same in the whole range of liquid flow rate. It was also carried out CFD calculations with higher mesh densities corresponding to 2 and 3×10^5 tetrahedral cells but this mesh apertures did not agreed reasonably with experimental data in comparison with the simulations performed with 10^6 tetrahedral cells.

The dependence of two-phase pressure drop predictions as a function of mesh density is shown in Fig. IX.3 at constant liquid flow rate at P=30 bar. The overall behavior of frictional pressure drop is generally the same as observed for the liquid holdup predictions. The two-phase pressure drop

increases with the mesh density and then became approximately independent from one million of tetrahedral cells onwards. The relative errors between the VOF predictions and experimental data were 66.9, 39.7, 18.9, 8.8% for 4×10^5, 6×10^5, 8×10^5, 10^6 of cells at L=1 kg/m^{2}s while it were 45.4, 26.9, 14.3, 8.7%, respectively for the highest liquid flow rate (L=15 kg/m^{2}s).

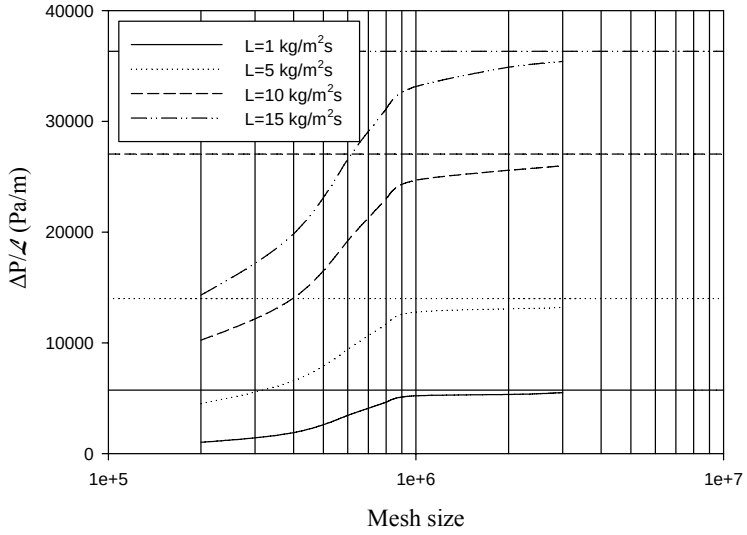

Figure IX.3. Comparison of two-phase pressure drop predictions as a function of mesh density for different liquid flow rates (G=0.1 kg/m^{2}s, P=30 bar, d=2 mm and experimental data from Nemec and Levec, 2005)

The optimization of time step in the liquid holdup is shown in Fig. IX.4 at constant liquid flow rate and P=30 bar.

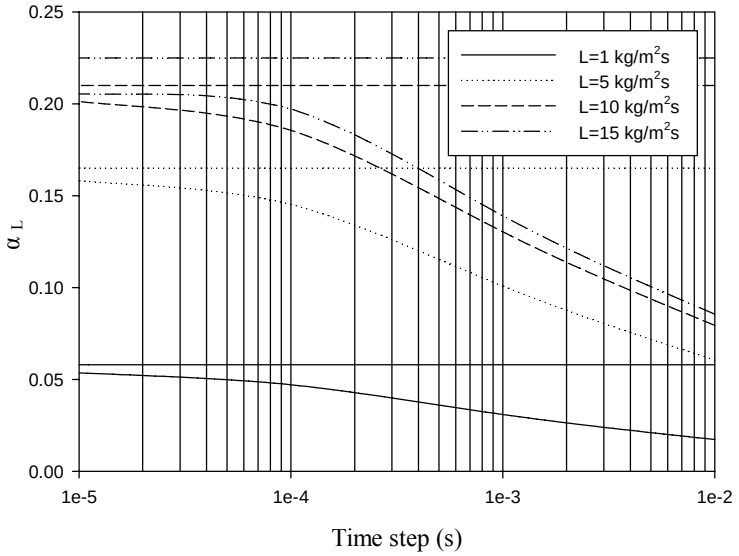

Figure IX.4. Effect of time step on liquid holdup predictions for different liquid flow rates (10^6 of tetrahedral cells, G=0.1 kg/m^{2}s, P=30 bar, d=2 mm and experimental data from Nemec and Levec, 2005)

The time step was decreased from 10^{-2} to 10^{-5} s in order to evaluate its effect on liquid holdup and according to Fig. IX.4, the higher the time step was, the higher deviation between the computed and experimental value of liquid holdup was for both the lower and higher values of liquid flow rate. Indeed, at the lowest liquid flow rate (L=1 kg/m^{2}s) the relative errors between the VOF calculation and experimental values were 70.1, 46.7, 18.7, 7.6 % for 10^{-2}, 10^{-3}, 10^{-4}, 10^{-5} s, respectively. These values became smaller once again at the highest liquid flow rate (L=15 kg/m^{2}s): 61.4, 37.2, 10.9, 3.5%. It should be pointed out that during the VOF simulations with the higher values for the time step, it was necessary to adjust systematically the under-relaxation parameters for the pressure-velocity coupling given that convergence issues arose in the momentum equation.

In Fig. IX.5, it is shown the influence of time step on the VOF predictions of two-phase pressure drop at constant liquid flow rate and P=30 bar. Globally, the smaller the time step was the better concordance between the numerical predictions and experimental values of frictional pressure drop. The semi-log plot shown in Fig. IX.5 demonstrated again that a time step of 10^{-5} s is necessary to achieve CFD independent results with respect to time step with a mesh comprising one million of tetrahedral cells. At L=1 kg/m^{2}s, the relative errors between the VOF calculations and experimental pressure drop data were 76.4, 51.0, 20.8, 8.8% for 10^{-2}, 10^{-3}, 10^{-4}, 10^{-5} s, respectively. These values were smaller for the VOF simulations performed at L=15 kg/m^{2}s: 60.1, 40.5, 16.4 and 8.7%. Consequently, the optimum time step of 10^{-5} s was selected to perform additional validation and corroboration activities in order to develop and establish a flow solver that can be used in trickle-bed reactor scale-up.

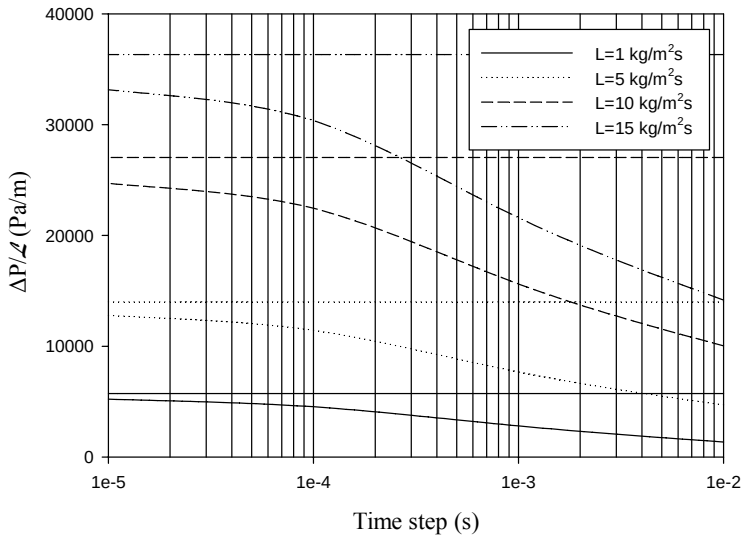

Figure IX.5. Effect of time step on two-phase pressure drop predictions for different liquid flow rates (10^6 of tetrahedral cells, G=0.1 kg/m^{2}s, P=30 bar, d=2 mm and experimental data from Nemec and Levec, 2005)

IX.3.2. Multiphase flow regime

Commercial trickle-bed reactors are often operated under trickling flow conditions which correspond to the lowest interaction regime between gas and liquid phases. However, one should bear in mind that multiphase flow maps presented in the literature (Al-Dahhan *et al*., 1997; Dudukovic *et al*., 1999) indicated that the boundary between trickling, spray, pulsing and foaming hydrodynamic regimes is not well defined and spans considerably if one uses Newtonian or pseudoplastic fuids or even if the packing methodology is accomplished randomly or if it is applied the random close packing technique to name a few parameters that can affect the definition of hydrodynamic boundary regimes encountered in trickle-beds. For that purpose, two different gas flow rates (G=0.1 and 0.7 kg/m^{2}s) were simulated with different multiphase turbulent models in order to investigate the numerical accuracy produced by assuming simple laminar flow (LAM) or employing standard (SKE) and realizable (RKE) multiphase *k-ε* models. The renormalization group based model (RNG) and the Reynolds Stress Model (RSM) were also examined for the two different gas flow regimes with the optimum values for the numerical solution parameters previously discussed.

In Fig. IX.6 the liquid holdup predictions are shown as a function of liquid velocity with different multiphase turbulent models at G=0.1 kg/m^{2}s and P=30 bar. The VOF simulations performed with the laminar flow model gave relatively the same liquid holdup predictions as the VOF calculations under the turbulent flow models: multiphase standard and realizable *k-ε* (SKE and RKE), RNG and RSM.

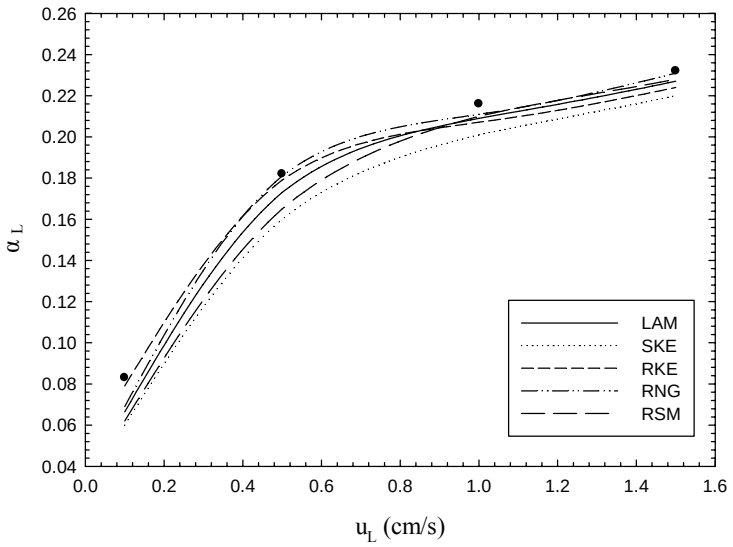

Figure IX.6. Influence of RANS turbulence model on liquid holdup predictions as a function of liquid flow rate at G=0.1 kg/m^{2}s (time step = 10^{-5} s, 10^6 of tetrahedral cells, P=30 bar, d=2 mm and experimental data from Nemec and Levec, 2005)

The same conclusion can be made according to Fig. IX.7 in where it is shown the VOF predictions of two-phase pressure drop as a function of liquid flow rate at P=30 bar. According to both plots for liquid holdup and frictional pressure drop one can observe that there is no significant difference whatever the turbulent flow model was being used. Nevertheless, at G=0.1 kg/m^{2}s the VOF laminar simulations were the ones that required less computational iterations until the convergence is reached. It should be also emphasized that the Reynolds stress model is often employed for highly swirling or anisotropic flows and involves the calculation of the individual Reynolds stresses using differential transport equations. The individual Reynolds stresses are then used to obtain closure of the Reynolds-averaged momentum equation and this fact brought a major computational expense expressed directly in the higher CPU calculation time.

At the highest gas flow rate (G=0.7 kg/m^{2}s), Fig. IX.8 shows the liquid holdup predictions as a function of liquid superficial velocity. As it can be seen, the VOF simulations with the laminar flow model thoroughly underpredicted the liquid holdup in the whole range of liquid superficial velocity. Conversely, the multiphase SKE, RKE, RNG and RSM turbulent models gave almost the same liquid holdup predictions.

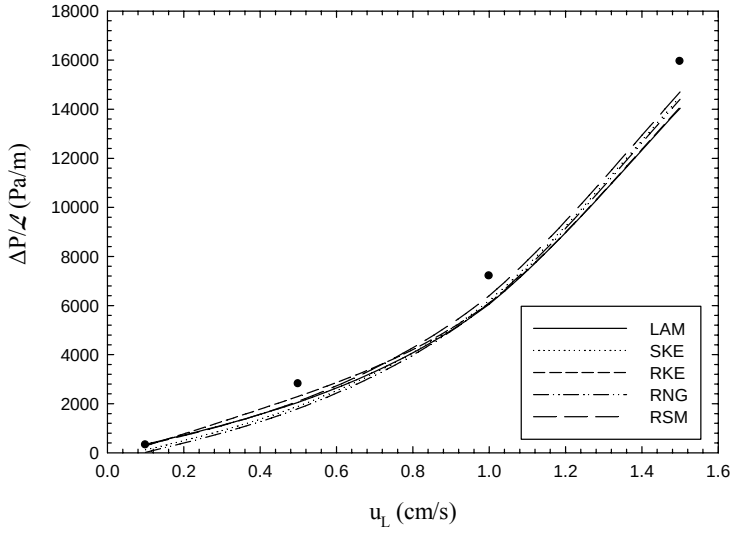

Figure IX.7. Influence of RANS turbulence model on two-phase pressure drop predictions as a function of liquid flow rate at G=0.1 kg/m^{2}s (time step = 10^{-5} s, 10^6 of tetrahedral cells, P=30 bar, d=2 mm and experimental data from Nemec and Levec, 2005)

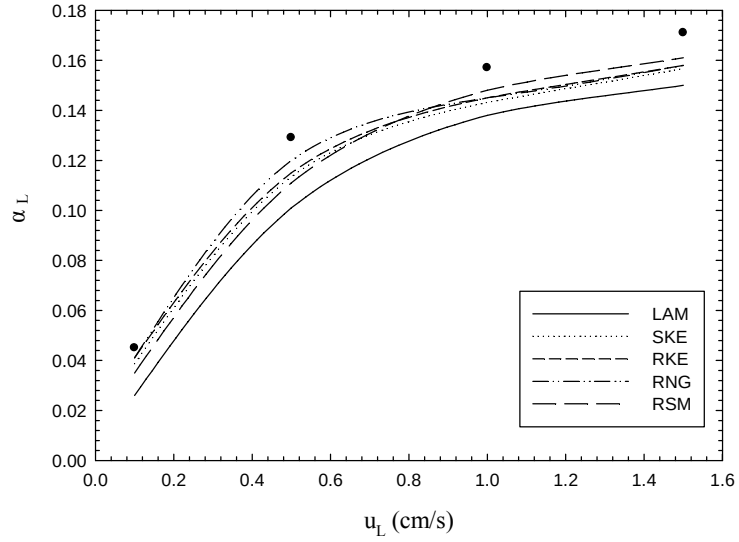

Figure IX.8. Influence of RANS turbulence model on liquid holdup predictions as a function of liquid flow rate at G=0.7 kg/m^{2}s (time step = 10^{-5} s, 10^6 of tetrahedral cells, P=30 bar, d=2 mm and experimental data from Nemec and Levec, 2005)

In Fig. IX.9 it is shown the VOF predictions of two-phase pressure drop with the same turbulent flow models at the highest gas flow rate (G=0.7 kg/m^{2}s). Once more, the VOF laminar flow model underpredicted the frictional pressure drop and the deviation is sharper for higher liquid flow rates. This fact illustrated that the multiphase regime attained with G=0.7 kg/m^{2}s should encompass not only a higher interaction regime between the gas and liquid phases, but it should be also the meaning of the relative closeness towards the hydrodynamic boundary of trickling flow regime.

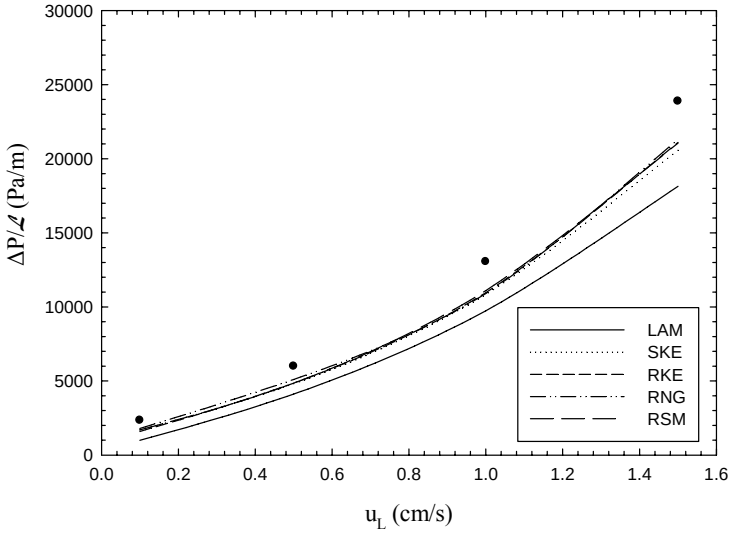

Figure IX.9. Influence of RANS turbulence model on two-phase pressure drop predictions as a function of liquid flow rate at G=0.7 kg/m^{2}s (time step = 10^{-5} s, 10^6 of tetrahedral cells, P=30 bar, d=2 mm and experimental data from Nemec and Levec, 2005)

In the VOF simulations performed with the SKE model at G=0.7 kg/m^{2}s, L=5 kg/m^{2}s and P=30 bar, Fig. IX.10 shows an instantaneous snapshot of liquid holdup isosurface (α_L = 0.15) colored by liquid velocity magnitude while Fig. IX.11 shows an instantaneous snapshot of gas holdup isosurface (α_G = 0.25) colored by gas velocity magnitude at the same operating conditions.

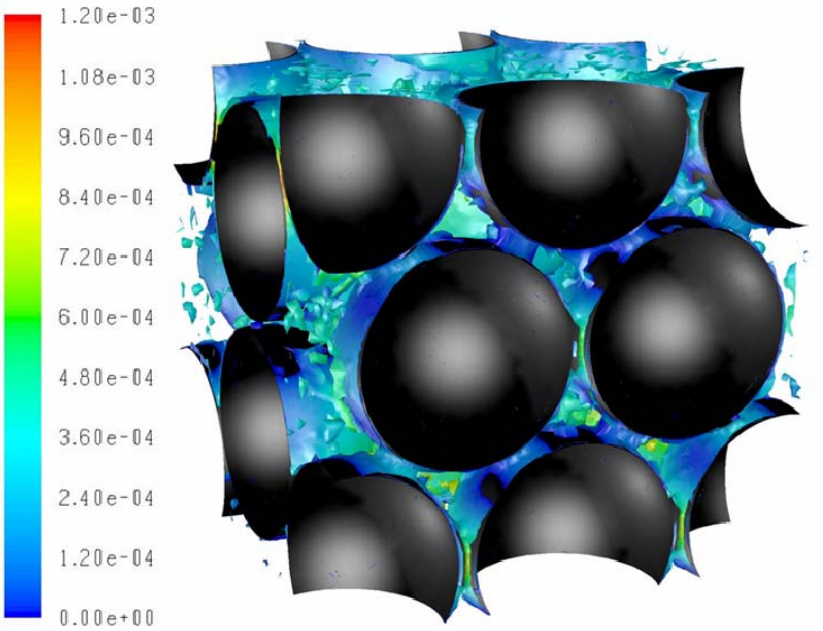

Figure IX.10. Instantaneous snapshot of liquid holdup isosurface (α_L = 0.15) colored by liquid velocity magnitude (*m/s*) (time step = 10^{-5} s, 10^6 of tetrahedral cells, L=5 kg/m^{2}s, G=0.7 kg/m^{2}s, P=30 bar, d=2 mm)

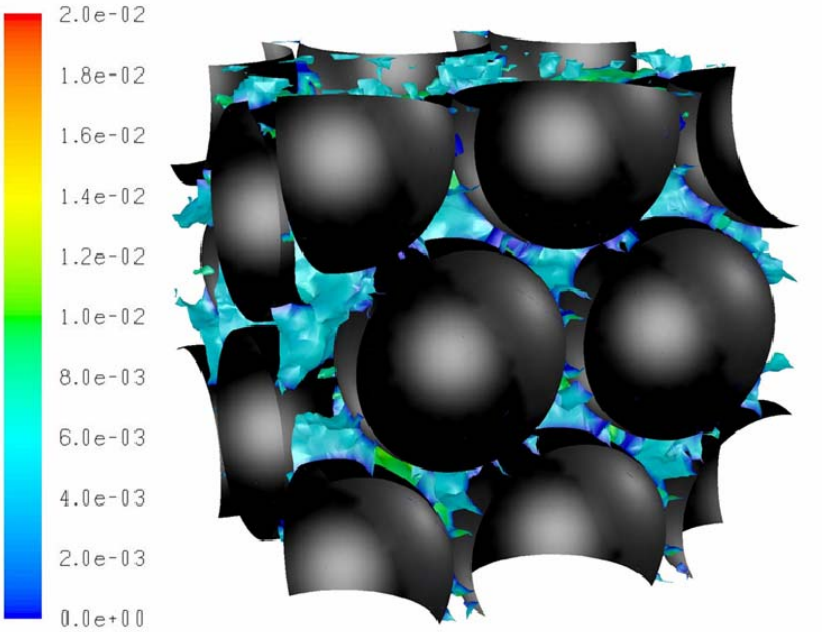

Figure IX.11. Instantaneous snapshot of gas holdup isosurface (α_G = 0.25) colored by gas velocity magnitude (*m/s*) (time step = 10^{-5} s, 10^6 of tetrahedral cells, L=5 kg/m^{2}s, G=0.7 kg/m^{2}s, P=30 bar, d=2 mm)

According to Figs IX.10 and IX.11, it is possible to identify the liquid flow consisting of rivulets and films, the former exhibiting poor liquid–solid contacting regions and the latter being good liquid–solid contacting. This computational behavior was experimentally observed by several authors who have systematized the rivulet/film classification in liquid distribution studies using computer-assisted tomography (Lutran *et al*., 1991; Ravindra *et al*., 1997; Wang *et al*., 1995). More recently, van der Merwe and Nicol (2005) measured the fraction of particle contact points that are exposed to flow for different flow conditions and pre-wetting procedures, which can be further compared against the VOF computations in the evaluation of bed utilization coefficient.

IX.3.3. Evaluation of VOF predictions: liquid holdup and pressure drop

The trickle-bed reactor performance is affected mainly by the liquid holdup and the two-phase pressure drop. Mass and heat transfer, conversion and selectivity, as well as power consumption are strongly influenced by those parameters, which thus represent a crucial starting point for reactor design, scale-up, scale-down and performance prediction. Our mathematical formulation is an alternative to empirical correlations that consists in the VOF continuum hydrodynamic model based on the equations of motion providing a more rigorous physical description of the underlying flow process. For the purpose of code validation as well as the investigation of gas and liquid flow rate on hydrodynamics in the present work, the computational results are compared with the liquid holdup and two-phase pressure drop experimental data available in the literature (Nemec and Levec, 2005). Fig. IX.12 shows the influence of gas velocity on the liquid holdup at different liquid velocities.

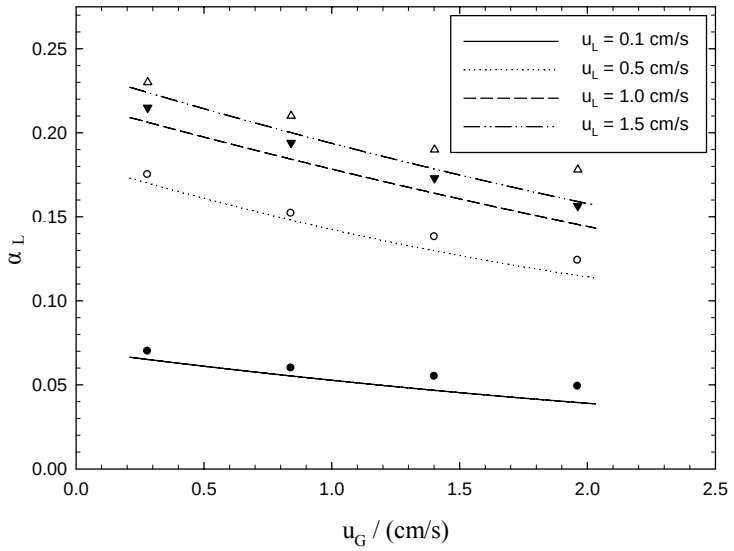

Figure IX.12. VOF predictions for the liquid holdup as a function of gas velocity for different liquid velocities (P=30 bar) and experimental data from Nemec and Levec (2005)

In Table IX.2, it was calculated the relative error between the VOF predictions for liquid holdup and pressure drop. According to Fig. IX.12, for gas velocities lower than 1.0 cm/s, these computational predictions are in reasonable agreement with experimental values, which enables the validation of our CFD model for this range of operation.

Table IX.2 – Relative error (%) of VOF predictions for liquid holdup (α_L) and pressure drop ($\Delta P/\mathcal{L}$) at different operating conditions

	G (kg/m^{2}s)	Relative Error %			
L (kg/m^{2}s)		1	5	10	15
α_L	0.1	6.85	2.84	4.10	2.65
	0.3	7.70	2.60	5.04	4.76
	0.5	15.01	6.00	5.23	6.07
	0.7	19.41	7.19	7.11	10.67
$\Delta P/L$ (Pa/m)	0.1	8.35	8.04	7.98	7.66
	0.3	7.62	9.64	2.58	8.47
	0.5	13.77	7.42	8.12	7.98
	0.7	16.23	8.73	9.03	6.17

However, for higher gas velocities the concordance level between the computed results and experimental data is not the same as observed for the lower interaction regime. Indeed, Table IX.2 indicates that at a given constant liquid flow rate, i.e., at L = 1 kg/m^{2}s, the relative error is increasing with the gas flow rate. At the lowest value of liquid flow rate, when the gas flow rate increased from 0.1 to 0.7 kg/m^{2}s, the relative error became almost 20% for the liquid holdup prediction. However, the same did not happen keeping the gas flow rate constant. At G = 0.1 kg/m^{2}s, if we increase the liquid flow rate from 1 to 15 kg/m^{2}s, the relative error decreases from 19.4 to 10.7 % demonstrating the opposite behavior already identified. This fact cannot be explained by any geometric considerations; for example, the simulated fixed-bed had a tube to particle diameter ratio of 25 so that the hydrodynamic flow regime should not be distressed by the reactor cylindrical wall. The liquid holdup prediction seems to be affected when the reactor is operated under higher interaction regimes favored by higher gas flow rates; in fact, when the liquid velocities increases, the liquid holdup also increases and the model predictions do not account in an appropriate mode for the effect of the gas flow. The influence of the gas flow at different isobaric conditions also revealed the previous fact for higher gas velocities in the evaluation of gas-liquid interfacial mass transfer in trickle-bed reactors at elevated pressures (Larachi *et al.*, 1998). However, the influence of the gas flow determined by a different operating pressure on the liquid holdup is less pronounced than in the case of different liquid velocities plotted in Fig. IX.12. The increase of operating pressure promotes a high driving force becoming that led to the large differences for the liquid holdup so that the effect of the superficial gas velocity on the liquid

holdup is often related with the pressure gradient over the reactor affecting the drag force at the gas-liquid interface (Al-Dahhan *et al*., 1997).

In Fig. IX.13 it is shown the computed pressure drop profiles at the same liquid flow rates simulated for the calculation of liquid holdup.

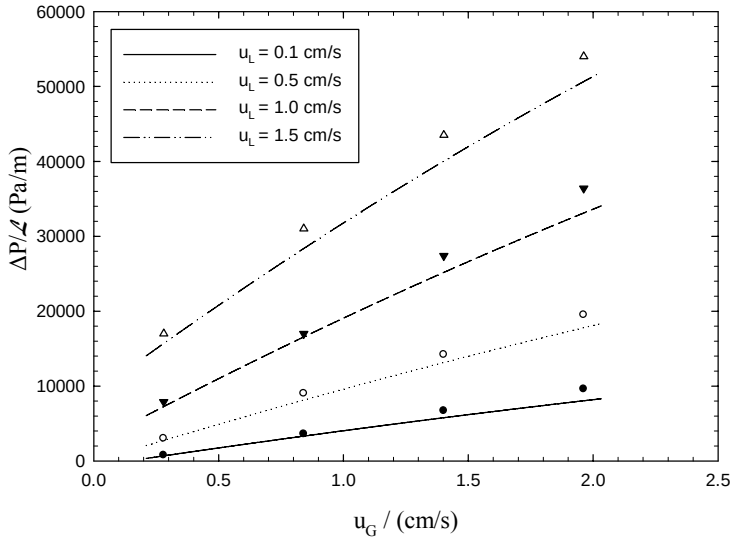

Figure IX.13. VOF predictions for the pressure drop as a function of gas velocity for different liquid velocities (P=30 bar) and experimental data from Nemec and Levec (2005)

Once more, VOF underpredicted the frictional pressure drop in the whole range of gas and liquid flow rates. The discrepancy between predicted results and experimental data became obvious for the highest gas flow rates. According to Table IX.2, at L = 1 kg/m^{2}s, the relative error for the computed pressure drop was 8.4 and 16.2 % for G = 0.1 and 0.7 kg/m^{2}s, respectively, revealing that gas velocity had a major effect on the TBR hydrodynamics. Therefore, for lower gas velocities the reasonable agreement of the numerical results are related with the strength of VOF model and its foundation based on the surface tension gradients in the interface for every computational cell but as soon as the gas velocity increases, the surface tension calculations are no more feasible in this regime. Nevertheless, TBRs are regularly operated under trickling flow that enables the lower interaction regime in which the VOF model can be successfully applied. The current VOF formulation can be an interesting option to capture the gas-liquid interaction in trickling flow regime and the effects of flow rates on three-phase packed-bed reactors. These computational results allow us to obtain a better understanding of the fundamental physics governing the efficiency of multiphase reactors for either TBR petrochemical applications or advanced wastewater treatment facilities so that CWAO technology deployment can be accelerated in the commercial-scale TBR.

IX.4. Conclusions

A multiphase VOF model was developed to provide a deeper understanding of the hydrodynamic behavior of a pilot trickle-bed reactor. The gas-liquid flow through a catalytic bed of spherical particles was used to compute velocity field and liquid volume fraction distributions considering interfacial phenomena as well as surface tension effects. Firstly, the VOF numerical solutions parameters such as mesh density, time step and convergence criteria were optimized with the concomitant evaluation of liquid holdup and two-phase pressure drop. Secondly, the optimum values were then used to examine the multiphase flow regime and the effect of gas flow rate on the numerical accuracy produced by either laminar or several turbulent flow models. At lower gas flow rates, the VOF predictions performed with the laminar flow model were found to produce qualitative and quantitatively the same computed results as turbulent flow models for both liquid holdup and frictional pressure drop, while for higher flow rates the turbulent flow models performed better indicating the considerable degree of turbulence induced by the gas phase. Finally, the VOF model was then used to understand the influence of gas and liquid flow rate on TBR hydrodynamics pointing out that during validation activities, a better agreement with published experimental measurements was achieved for lower gas flow rates.

IX.5. Nomenclature

d	Catalyst particle nominal diameter, m
G	Gas mass flux, kg/m^{2}s
k	Turbulent kinetic energy, m^2/s^2
L	Liquid mass flux, kg/m^{2}s
$\mathcal{L}$	Reactor length, m
$\hat{n}_w$	Unit vector normal to the wall
p	*P*ressure, bar
Re_i	Reynolds number based on intersticial velocity [Re/ε]
t	Time, s
$\hat{t}_w$	Unit vector tangential to the wall
$\vec{u}$	Superficial vector velocity, m/s

Greek letters

α_q	Volume fraction of q^{th} phase
ε	Turbulent dissipation energy

κ	Gas-liquid interface curvature
ρ_q	Density of q^{th} phase, kg/m^3
Δp	Total pressure drop, bar
σ	Surface tension, N.m
σ_k , σ_ε	k-ε model parameters: 1.2, 1.0
$\overline{\overline{\tau}}_q$	Shear stress tensor of q^{th} phase, bar
θ_w	Contact angle at the wall
μ_q	Viscosity of q^{th} phase, Pa.s

Subscripts

G	Gas phase
L	Liquid phase
q	q^{th} phase
S	Solid phase

IX.6. References

Al-Dahhan, M. H., Larachi, F., Dudukovic, M. P., Laurent, A. (1997). High pressure trickle-bed reactors: A Review. *Industrial and Engineering Chemistry Research* **36** (8), 3292-3314.

Brackbill, J.U., Kothe, D.B., Zemach, C. (1992). A Continuum Method for Modeling Surface Tension. *Journal of Computational Physics* **100** (2), 335-354.

Cerne, G., Petelin, S., Tiselj, I. (2001). Coupling of the interface tracking and the two-fluid models for the simulations of incompressible two phase-flow. *Journal of Computational Physics* **171** (2), 776-804.

Chen, L., Li, Y. (1998). A numerical method for two-phase flows with an interface. *Environmental Modelling and Software* **13** (3), 247-255.

Crooks, R., Whitez, J.C., Boger, D.V. (2001). The Role of Dynamics Surface Tension and Elasticity on the Dynamics of Drop Impact. *Chemical Engineering Science* **56** (19), 5575-5592.

Deen, N.G., van Sint Annaland, M., Kuipers, J.A.M. (2004). Multi-scale modeling of dispersed gas-liquid two-phase flow. *Chemical Engineering Science* **59** (8-9), 1853-1861.

Dudukovic, M.P., Larachi, F., Mills, P.L. (1999). Multiphase reactors – revisited. *Chemical Engineering Science* **54** (13-14), 1975-1995.

Elghobashi, S., Abou-Arab, T., Rizk, M., Mostafa, A. (1984). Prediction of the particle-laden jet with a two-equation turbulence model. *International Journal of Multiphase Flow* **10** (6), 697-710.

FLUENT 6.1. (2005). User's Manual to FLUENT 6.1. Fluent Inc. Centrera Resource Park, 10 Cavendish Court, Lebanon, USA.

GAMBIT 2 (2005). User's Manual to GAMBIT 2. Fluent Inc. Centrera Resource Park, 10 Cavendish Court, Lebanon, USA.

Gunjal, P.R., Kashid, M.N., Ranade, V.V., Chaudhari, R.V. (2005a). Hydrodynamics of Trickle-Bed Reactors: Experiments and CFD Modeling. *Industrial and Engineering Chemistry Research* **44** (16), 6278-6294.

Gunjal, P.R., Ranade, V.V., Chaudhari, R.V. (2005b). Dynamics of Drop Impact on Solid Surface: Experiments and VOF Simulations. *A.I.Ch.E. Journal* **51** (1), 59-78

Iliuta, I., Larachi, F. (2005). Modelling the Hydrodynamics of Gas-Liquid Packed Beds via Slit Models: A Review. *International Journal of Chemical Reactor Engineering* **3** R4.

Jiang, Y., Khadilkar, M.R., Al-Dahhan, M.H., Dudukovic, M.P. (2001). CFD modeling of multiphase flow distribution in catalytic packed bed reactors: scale down issues.*Catalysis Today* **66** (2-4), 209-218.

Karim, M.F., Tanimoto, K., Hieu, P.D. (2009). Modelling and simulation of wave transformation in porous structures using VOF based two-phase flow model. *Applied Mathematical Modelling* **33** (1), 343-360.

Larachi, F., Cassanello, M., Laurent, A. (1998). Gas-Liquid Interfacial Mass Transfer in Trickle-Bed Reactors at Elevated Pressures. *Industrial and Engineering Chemistry Research* **37** (3), 718-733.

Liovic, P., Lakehal, D. (2007). Interface-turbulence interactions in large-scale bubbling processes. *International Journal of Heat and Fluid Flow* **28** (1), 127-144.

Lopes, R.J.G., Quinta-Ferreira, R.M. (2007). Trickle-Bed CFD Studies in the Catalytic Wet Oxidation of Phenolic Acids. *Chemical Engineering Science* **62** (24), 7045-7052.

Lopes, R.J.G., Quinta-Ferreira, R.M. (2008). Three-Dimensional Numerical Simulation of Pressure Drop and Liquid Holdup for High-Pressure Trickle-Bed Reactor. *Chemical Engineering Journal* **145** (1), 112-120.

Lopes, R.J.G., Quinta-Ferreira, R. M. (2009). Numerical Simulation of Trickle-Bed Reactor Hydrodynamics with RANS-Based Models Using a Volume of Fluid Technique. *Industrial and Engineering Chemistry Research* **48** (4), 1740-1748.

Lutran, P.G., Ng, K.M., Delikat, E.P. (1991). Liquid distribution in trickle-beds. An experimental study using computer-assisted tomography. *Industrial and Engineering Chemistry Research* **30** (6), 1270-1280.

Maiti, R.N., Arora, R., Khanna, R., Nigam, K.D.P. (2005). The liquid spreading on porous solids: Dual action of pores. *Chemical Engineering Science* **60** (22), 6235-6239.

Mao, T., Kuhn, D.S.C., Tran, H. (1997). Spread and rebound of liquid droplets upon impact on flat surfaces. *A.I.Ch.E. Journal* **43** (9), 2169-2179.

Nemec, D., Levec, J. (2005). Flow through packed bed reactors: 2. Two phase concurrent downflow. *Chemical Engineering Science* **60** (24), 6958-6970.

Ravindra, P.V., Rao, D.P., Rao, M.S. (1997). Liquid flow texture in trickle-bed reactors: an experimental study. *Industrial and Engineering Chemistry Research* **36** (12), 5133-5145.

Rioboo, R., Marengo, M., Tropea, C. (2002). Time Evaluation of Liquid Drop Impact onto Solid Dry Surfaces. *Experiments in Fluids* **33** (1), 112-124.

Ryan, M. (2006). CFD prediction of the trajectory of a liquid jet in a non-uniform air crossflow. *Computers and Fluids* **35** (5), 463-475.

Taha, T., Cui, Z.F. (2004). Hydrodynamics of slug flow inside capillaries. *Chemical Engineering Science* **59** (6), 1181-1190.

van der Merwe, W., Nicol, W. (2005). Characterization of multiple flow morphologies within trickle flow regime. *Industrial and Engineering Chemistry Research* **44** (25), 9446-9450.

Wang, R., Mao, Z., Chen, J. (1995). Experimental and theoretical studies of pressure drop hysteresis in trickle bed reactors. *Chemical Engineering Science* **50** (14), 2321-2328.

Yakhot, V., Orszag, S.A. (1986). Renormalization group analysis of turbulence. I. Basic theory. *Journal of Scientific Computing* **1** (1), 3-51.

Zheng, D., He, X., Che, D. (2007). CFD simulations of hydrodynamic characteristics in a gas–liquid vertical upward slug flow. *International Journal of Heat and Mass Transfer* **50** (21-22), 4151-4165.

This page intentionally left blank

PART D. TBR REACTION OPERATION: CFD AND EXPERIMENTAL STUDIES

In this part of the work, kinetics of the catalytic wet oxidation is integrated on Euler-Euler and Volume-of-Fluid models to investigate the reaction behaviour of a pilot trickle-bed reactor unit considering the reaction aspects as well as the transport mechanisms involved in the treatment process of simulated phenolic wastewaters. The computational domains and modelling approach are firstly described and the hydrodynamics simulations are summoned up with single and two phase flow data reported in open literature. The trickle-bed reaction studies begin with the catalytic wet oxidation of an individual phenolic acid that is accomplished for the Total Organic Carbon degradation under transient mode. Subsequently, the catalytic wet oxidation of a phenolic acids mixture is simulated in the trickle-bed reactor with the Euler-Euler framework at different temperatures and pressures as well as different gas and liquid flow rates. Afterwards, both multiphase CFD models are used to gain insight and quantitative information on the evaluation of axial and radial profiles for the Total Organic Carbon depletion and temperature along the packed bed. The CFD theoretical calculations are compared against experimental data taken from the trickle-bed reactor pilot plant.

X. Kinetic Modelling and TBR CFD Studies in the Catalytic Wet Oxidation of Vanillic Acid[1]

Aiming to examine the catalytic wet air oxidation process in three phase reactors, a slurry reactor for kinetic studies and a pilot unit trickle-bed reactor were investigated considering reaction aspects as well as the transport mechanisms involved in the treatment of an aqueous vanillic acid solution, which is a compound typically found in olive mill wastewater. Kinetic studies were performed to bring up the lumped kinetic parameters in terms of total organic carbon (TOC) over a Mn-Ce-O laboratory-made catalyst. A hydrodynamic model for the prediction of pressure drop and liquid holdup for a trickle-bed reactor has been developed by means of CFD according to data taken from the open literature. Firstly, single-phase flow pressure drop was studied in a region of flow rates that is of particular interest to trickle bed reactors ($10<Re_G<400$) and it was demonstrated that the Eulerian model is able to predict reasonably the pressure drop of single-phase flow over spherical particles when Ergun equation adjusts pressure drop measurements within 10% on average. Two-phase flow operating regime is then investigated and CFD Eulerian model predicts very well liquid holdup in the range of gas flows studied ($G = 0.1 – 0.7$ kg/m^{2}s). Finally, CFD runs were performed in unsteady state for the catalytic wet air oxidation of the aqueous vanillic acid solution. TOC profiles indicated that complete reduction of organic matter was achieved at 30 *bar* and 200 ºC. Moreover, CFD demonstrated the considerable effect of temperature, whereas the air partial pressure only has minor influence.

X.1. Introduction

Nowadays, the increasing environmental concerns and restrictive legislation strongly require the development of suitable technologies for treatment of polluted wastewaters. Particularly, during the production of olive oil significant amounts of liquid effluents are generated from the water and olive juice added to the process, containing unrecoverable oil. High volumes of olive oil mill wastewater (OOMW) are produced each year ($10\text{-}30\times10^6$ m^3/year) with chemical oxygen demand (COD) charges between 45000 and 170000 mg/l being the large charge of phenolic compounds contained in these wastewaters one of the major obstacles to achieve the detoxification (Niaounakis and Halvadakis, 2004).

[1] *This Chapter is based upon the publication Lopes et al. (2007a)*

Technologies for OOMW treatment have been reviewed elsewhere including several physicochemical, biological and combined processes resulting in considerable organic load and toxicity abatement (Paraskeva and Diamadopoulos, 2006; Mantzavinos and Kalogerakis, 2005). Biological processes, aerobic and anaerobic, including anaerobic co-digestion with other effluents and composting, are predominant in the treatment of OOMW and it is ideally suited for low pollutant concentrations, with maximum concentrations up to 50 ppm (Paraskeva and Diamadopoulos, 2006; Mantzavinos and Kalogerakis, 2005; Imamura, 1999). Biodegradation and incineration are two typical examples of reactive destruction technologies. However, both these methodologies have their limitations and are not always the optimal solution. Incineration is ideal for highly concentrated liquid streams, typically around 350,000 ppm or higher COD content when the energy requirements become self sustaining (Mantzavinos and Kalogerakis, 2005). Neither process is optimal when the toxic organic compounds concentration falls between the extremes. Alternative destruction technologies have also been studied in the field, including non-catalytic and catalytic wet air oxidation (CWAO). The catalyst allows milder operating conditions than WAO while yielding similar if not superior kinetic performance. CWAO research has been conducted on a variety of organic compounds using numerous catalysts with different results and it is known to have a great potential in advanced wastewater treatment facilities (Bhargava *et al*., 2006; Paraskeva and Diamadopoulos, 2006; Mantzavinos and Kalogerakis, 2005; Imamura, 1999).

Trickle-bed reactors (TBR) are widely used for heterogeneous catalyzed reactions between gas and liquid reactants, such as hydrogenation, oxidation or partial oxidation and detoxification of liquid effluents; such systems are frequently used in petrochemical and chemical processes, wastewater treatment, biochemical and electrochemical processing (Saroha and Nigam, 1996). In these reactors, gas and liquid phase flow co-currently downward through a fixed bed of catalyst particles. Generally, three phase fixed bed reactors can operate in hydrodynamically different regimes whose boundaries depend on gas and liquid superficial velocities, catalyst bed and fluid properties. TBRs are characterized by high catalyst loading per unit volume of the liquid and the low energy dissipation make them preferable to slurry reactors due to the higher calorific capacity. Under continuous gas flow and low liquid flow rate conditions the trickle flow regime exists in which the liquid phase moves in drops or in small rivulets through the catalyst bed. With increasing gas and liquid loading through the bed so-called *spray*, *pulsing* and *foaming* hydrodynamic regimes are encountered (Dudukovic *et al*., 2002; Al-Dahhan *et al*., 1997; Saroha and Nigam, 1996). Trickle and pulse flow regimes are of particular industrial interest due to the higher catalyst surface utilization. The following studies in the paper are focused on the trickling regime under unsteady-state operation conditions in order to investigate the start-up behaviour of the TBR unit and to evaluate its influence in hydrodynamic parameters.

Heterogeneous catalysts used in TBR reveal important advantages for the wet oxidation technology, since in homogeneous operation a posterior metal recovery step is needed. Several important aspects with respect to the influence of external and intraparticle mass transfer limitations and partial wetting of catalyst particles have been studied in the literature and works about mass transfer effects have been reviewed (Al-Dahhan *et al*., 1997; Saroha and Nigam, 1996). Meanwhile, relatively few investigations have been published concerning catalytic liquid-phase oxidation of organic compounds in large-scale TBR for wastewater treatment where hydrodynamic parameters prevail. Therefore, experimental data, descriptions of mass-transfer processes and reaction courses, as well as reactor simulation activities, which are required for successful commercial exploitation have to be more explored at high pressure operation. In order to evaluate catalyst effectiveness in cocurrent downflow reactor, TBR was modelled to bring up hydrodynamic and reactions studies by means of Computational Fluid Dynamics (CFD) codes. The kinetic information was taken from a batch stirred tank reactor. With this methodology, it is possible to investigate the efficiency of different hydrodynamic regimes such as low and high interaction regimes involved in continuous operation of TBR.

A large number of studies have been reported in the literature on the various hydrodynamic aspects of TBRs. Though most of the research studies before 1990 have been performed at atmospheric pressure (Ellman *et al*., 1990; Sai and Varma, 1987), a considerable number of investigations were carried out in pressurised trickle-bed reactors after that period (Nemec and Levec, 2005; 2005 *et al*., 2005; Lakota *et al*., 2002; Jiang *et al*., 2000; Al-Dahhan *et al*., 1998; Larachi *et al*., 1991; Wammes and Westerterp, 1990). Numerous attempts are being made to model the hydrodynamics of trickle-bed reactors. It ranges from merely empirical correlations (Sie and Krishna, 1998; Iliuta *et al*., 1998; Larachi *et al*., 1991; Ellman *et al*., 1990) to physically sound models (Nemec and Levec, 2005; Attou *et al*., 1999; Larachi *et al*., 1999; Al-Dahhan *et al*., 1998).

The present paper aims to investigate the behaviour of a pilot TBR unit through CFD techniques considering the reaction aspects as well as the transport mechanisms involved in the treatment process of wastewaters from olive oil mills industries. The computational domains and modelling approach are firstly described and the hydrodynamics simulations are validated with single and two phase flow data reported in literature for experiments in TBR without chemical reaction. For the simulation of the oxidation process in TBR, a slurry reactor was previously used for experimental studies in order to achieve the reaction rate for the TOC degradation of vanillic acid, a phenolic compound typically found in OOMW, which is difficult to biodegrade at high-concentration levels.

X.2. Computational Model and Boundary Conditions

The performance of multiphase reactors can be predicted by solving the conservation equations for mass, momentum and thermal energy in combination with the constitutive equations for species transport, chemical reaction, and phase transition. However, because of the incomplete understanding of the physics plus the highly coupled and nonlinear nature of the equations, the complete solution is difficult to obtain unless one has reliable physical models, advanced numerical algorithms and sufficient computational power. Hence, in the past several decades, approaches based on residence-time distribution (RTD) (Gianetto and Specchia, 1992), together with the macromixing and micromixing models, have been the primary tool in reactor modelling used to characterize the non-ideal flow pattern and mixing in reactors without solving the complete velocity field. The disadvantage of such approaches is that they cannot be adopted well to serve as a diagnostic tool for operating units, which normally need to be operated under conditions not amenable to the preceding simplified analysis. To improve the capability of multiphase reactor models, one has to solve the complete multidimensional flow equations coupled with chemical species transport, reaction kinetics, and kinetics of phase change. Fortunately, CFD has made great progress during the last few years, and has been applied to several chemical processes (Gunjal *et al*., 2005; van der Merwe and Nicol, 2005; Joshi and Ranade, 2003; Burghardt *et al*., 1999).

Several efforts are being made to develop CFD models for TBRs. Attou *et al*. (1999) have developed a 1D flow model for prediction of global hydrodynamic parameters. For example, in order to consider the interactions between the fluid and particles, a global flow model in packed beds, an Eulerian k-fluid model, resulting from the volume averaging of the continuity and momentum equations, has been developed and solved for a 1D representation of the bed at steady state, and at isothermal non-reaction conditions (Attou *et al*., 1999). This model provided reasonable predictions for global hydrodynamic quantities such as liquid holdup and pressure drop. A similar *k*-fluid model, based on the relative permeability concept, was used to compute the 2D flow without considering porosity variation and without solving for the solid phase. It seems that the Eulerian *k*-fluid model is a rational choice for flow simulation in packed beds, if good closures for fluid/fluid and fluid/particle interactions can be found and used. Moreover, the geometrical complexity of packed beds can in a certain sense be avoided in a *k*-fluid model, since there is no need to deal with the exact boundaries of the particles and the solid phase is treated as a penetrated continuum.

The Eulerian multiphase model allows for modelling of multiple separate, yet interacting phases. The phases can be liquids, gases, or solids in nearly any combination. An Eulerian treatment is

used for each phase, in contrast to the Eulerian-Lagrangian treatment that is used for the discrete phase model. With the Eulerian multiphase model, the number of secondary phases is limited only by computer memory requirements and convergence behaviour. In fact any number of secondary phases can be modelled, provided that sufficient memory is available. For complex multiphase flows, however, solution is limited by convergence behaviour. In this context, the Eulerian-Eulerian approach with the 2D multifluid models appears to be most suitable for reactor engineering applications (Gunjal *et al*., 2005; Jiang *et al*., 2000) and was selected for the present work. The description of multiphase flow as interpenetrating continua incorporates the concept of phasic volume fractions, denoted here by α_q. Volume fractions represent the space occupied by each phase, and the laws of conservation of mass and momentum are satisfied by each phase individually. The derivation of the conservation equations is done by ensemble averaging the local instantaneous balance for each of the phases. The continuity and momentum equations have been described in Equations (V.1) and (V.2) in Chapter V in where the turbulence modelling approach was also presented in Equations (V.9) and (V.10). The species continuity equation is expressed in Equation (X.1):

$$\frac{\partial \alpha_q \rho_q C_{q,i}}{\partial t} + \nabla \cdot \left(\alpha_q \rho_q u_q C_{q,i}\right) = \nabla \cdot \left(\alpha_q \rho_q D_{q,i} \nabla C_{q,i}\right) + \alpha_q \rho_q S_{q,i} \qquad \text{(X.1)}$$

where, $C_{q,i}$ is the concentration of specie i in the q^{th} phase (gas or liquid), $D_{q,i}$ is the diffusivity of specie i in the q^{th} phase estimated using the Siddiqi–Lucas (1986) method, ρ_q and α_q is the density and volume fraction of the q^{th} phase. $S_{q,i}$ is the source for species i in phase q.The conservation of energy in Eulerian multiphase applications is described by a separate enthalpy equation for each phase:

$$\frac{\partial}{\partial t}\left(\alpha_q \rho_q h_q\right) + \nabla \cdot \left(\alpha_q \rho_q \vec{u}_q h_q\right) = -\alpha_q \frac{\partial p}{\partial t} + \overline{\overline{\tau}}_q : \nabla \vec{u}_q - \nabla \cdot \left(k_{eff} \nabla T\right)_q + \sum_{p=1}^{n} \left(\dot{m}_{pq} h_{pq} - \dot{m}_{qp} h_{qp}\right) + S_{h,q} \qquad \text{(X.2)}$$

where h_q is the specific enthalpy of the q^{th} phase, $\vec{q}_q$ is the heat flux, $S_{h,q}$ is a source term that includes sources of enthalpy due to chemical reaction of phenolic compounds: -3000 kJ/mol (Reid *et al*. (1987)). Water properties, dissolved oxygen, phenolic compound diffusion coefficients, water and gas heat capacities, water heat of evaporation, heats of reaction, water vapour pressure and water density have been obtained from data or methods included in Reid *et al.* (1987). Henry constants for oxygen solubility in water are taken from Himmelblau (1960). Phenolic compound and oxygen molecular diffusion coefficients have been also estimated by the method of Wilke and Chang (1955). Effective diffusion coefficient of pollutant in water and gaseous oxygen – solid mass transfer coefficient have been estimated from Piché *et al*. (2002) who used a turtuosity factor of 3. Phenolic compound liquid – solid mass transfer coefficient has been calculated from Goto

and Smith (1975) and gaseous oxygen – liquid volumetric mass transfer coefficient has been derived from Iliuta *et al*. (1999).

X.3. Kinetic studies

X.3.1. Experimental procedure

The kinetic CWAO experiments were performed in a high-pressure 1 *L* autoclave of 316-SS (4531M Parr model) described in Chapter III (Lopes *et al*., 2007b). Vanillic acid was obtained from Sigma-Aldrich and Mn–Ce–O was prepared by co-precipitation, by mixing aqueous solutions of the respective metal salts using the corresponding metal nitrates as precursors (Riedel-de-Häen and Labsolve). The solution of vanillic acid (200 ppm) was introduced in the system with the powder catalyst (6 $g.L^{-1}$), preheated up to the operating temperature (160–220 *ºC*) and pressurized with air (99.999%) up to the operating pressure (30 *bar* total pressure) and the starting TOC value was around 115 ppm. Liquid samples were immediately filtered and then analyzed for total organic carbon (TOC) with a Shimadzu 5000 TOC Analyser.

X.3.2.Kinetic law

After a catalyst screening to several commercial catalysts and laboratory-made manganese and silver cerium based catalysts (Lopes *et al*., 2007b), manganese cerium oxide (Mn-Ce-O) was selected for further studies in the trickle-bed reactor since it showed significantly more activity in respect to the abatement of TOC, revealing complete degradation of vanillic acid as observed in Fig. X.1 for different temperatures. With these results the kinetic parameters were calculated by using the Generalized Kinetic Model (GKM) (Zhang and Chuang, 1999; Matatov-Meytal and Sheintuch, 1998; Pintar and Levec, 1994; Li *et al*., 1991), which takes into account the degradation of vanillic acid (represented by *A*) either directly through a 1^{st} step (k'_1) to carbon dioxide and water (designed as C) or via a 2^{nd} step (k'_2) with the formation of intermediate compounds (*B*), namely phenol and acetic acid (Lopes *et al*., 2007b) subsequently degraded through the 3^{rd} step (k'_3) to the final end products (*C*). The reaction rates in terms of the TOC concentration of the lumped species *A, B* and *C* are then represented by Equation (X.3):

$$-r_{TOC_A} = -\frac{d\,C_{TOC_A}}{dt} = (k_1' + k_2')\,C_{TOC_A}$$
$$-r_{TOC_B} = -\frac{d\,C_{TOC_B}}{dt} = k_3' C_{TOC_B} - k_2' C_{TOC_A} \qquad \text{(X.3)}$$

where first order reactions were assumed for each step *j* (m_j = 1; *j* = 1-3). After integrating these equations a mathematical expression for TOC evolution is obtained in Equation (X.4):

$$\frac{C_{TOC}}{C_{TOC_0}} = \frac{k_2'}{k_1'+k_2'-k_3'} e^{-k_3' t} + \frac{k_1'-k_3'}{k_1'+k_2'-k_3'} e^{-(k_1'+k_2')t} \qquad \text{(X.4)}$$

whose adjustment to the experimental data of Fig. X.1 led to the kinetic constant values, k'_1, k'_2, k'_3 for each temperature; in particular the k_i' values for 200 and 220 ºC are:

$T = 200\ ºC$: $k'_1 = 1.003\times10^{-1}\ min^{-1}$; $k'_2 = 1.200\times10^{-3}\ min^{-1}$; $k'_3 = 1.520\times10^{-2}\ min^{-1}$ (X.5)

$T = 220\ ºC$: $k'_1 = 1.504\times10^{-1}\ min^{-1}$; $k'_2 = 5\times10^{-4}\ min^{-1}$; $k'_3 = 1.470\times10^{-2}\ min^{-1}$ (X.6)

The activation energies Ea_1, Ea_2, Ea_3 and the pre-exponential factors A_1, A_2, A_3, were calculated by using the Arrhenius plot:

$Ea_1 = 18.33\ kJ/mol$; $Ea_2 = 24.18\ kJ/mol$; $Ea_3 = 67.94\ kJ/mol$

$A_1 = 0.68\times10^{2}\ min^{-1}$; $A_2 = 3.17\times10^{1}\ min^{-1}$; $A_3 = 5.85\times10^{6}\ min^{-1}$ (X.7)

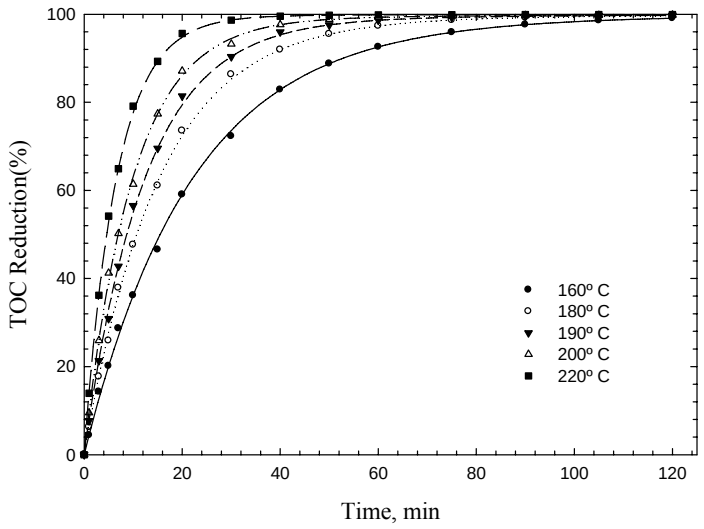

Figure X.1. GKM for TOC reduction of vanillic acid solution with 6 $g.L^{-1}$ Mn-Ce-O catalyst

These values were used in the corresponding expressions of the reaction rate constants k'_1, k'_2, k'_3 as a function of temperature, according to Arrhenius law as described in Equation (X.8).

$$\begin{aligned} k_1' &= 680 \cdot \exp\left(-\frac{2.205\times10^3}{T}\right)\ \text{min}^{-1}; \\ k_2' &= 31.7 \cdot \exp\left(-\frac{2.908\times10^3}{T}\right)\ \text{min}^{-1}; \\ k_3' &= 5.85\times10^6 \cdot \exp\left(-\frac{8.171\times10^3}{T}\right)\ \text{min}^{-1} \end{aligned} \qquad \text{(X.8)}$$

In order to investigate the reactor behaviour by means of CFD codes these kinetic expressions were then integrated in the TBR model in section X.5.

X.4. Analysis of the TBR hydrodynamics by CFD

X.4.1. TBR geometry

CFD studies were performed by taking into account the geometry of a TBR pilot plant unit installation at our laboratory. The cylindrical reactor was made of stainless steel (SS-316) with 50 mm of internal diameter and 1.0 m length according to the reactor unit used by Levec and coworkers (Nemec and Levec, 2005; Lakota *et al*., 2002). Two main features characterize the reactor: a distributor on the top and a gas-liquid separator in the bottom. The boundary conditions of the mesh were designed in a CAD commercial program (GAMBIT 2, 2005) where the liquid pollutant and gas phase are introduced downwards into the reactor through the distributor. Air can be supplied up to a total maximum pressure of 70 *bar*. Operating conditions simulated are 10-30 bar of reactor pressure and temperature range was from 200 to 220 ºC. Gas and liquid mass flow rate are in the range 0.10 – 0.70 and 0.05 – 15 kg/m^{2}s, respectively.

X.4.2. TBR modelling and hydrodynamic validation

In this section, the numerical methodology is validated against experimental data available from literature related to the hydrodynamic information for TBR operation at trickle flow regime at low and high pressure. To validate CFD models, the actual strategy is to compare CFD results in terms of well known parameters such as liquid holdup and pressure drop that are the two most employed characteristics in TBR development study (Carbonell, 2000). The experimental conditions and the parameters commonly measured in high pressure TBRs are evaluated extensively in topics such as: pressure effect on physicochemical properties, phenomenological analysis of two-phase flow, flow regime transition, single-phase pressure drop, two-phase pressure drop, liquid holdup, gas-liquid interfacial area and mass transfer, catalyst wetting efficiency as well as catalyst dilution with inert fines in laboratory scale TBRs. In this context, the mesh was validated by checking the mesh sensitivity and by comparing the numerical results against the single-phase and two-phase experimental data.

The mesh adopted in the TBR reactor is tetrahedral around and over the catalyst particles and hexahedral elsewhere being the cell number around one million. The mesh entrance has the gas-liquid distributor D2 which have 60 holes as described in Chapter VII. The momentum equations are solved with the coupling SIMPLE algorithm and the monotonic upwind discretization scheme. The pressure is computed by means of the PRESTO scheme. Runs were performed in unsteady state mode to investigate the unit start-up and to evaluate the TBR performance until steady state was reached. First, single-phase pressure drop simulations with only the gas phase flowing

downward the bed were performed and are presented in Figs X.2 and X.3. CFD results for single-phase flow were validated with experimental data obtained after extensively prewetting the bed being the reactor operated initially at pulse regime at high liquid and gas mass velocities, which were then reduced to the desired level at which the pressure drop and liquid holdup were measured (Nemec and Levec, 2005). This procedure minimizes the liquid maldistribution and prevents hysteresis effect in these parameters (Carbonell, 2000). Reynolds numbers for gas phase up to 400 were modelled by means of CFD codes as shown in Fig. X.2 where pressure drop measurements provided by Nemec and Levec (2005) and Ergun equation are plotted.

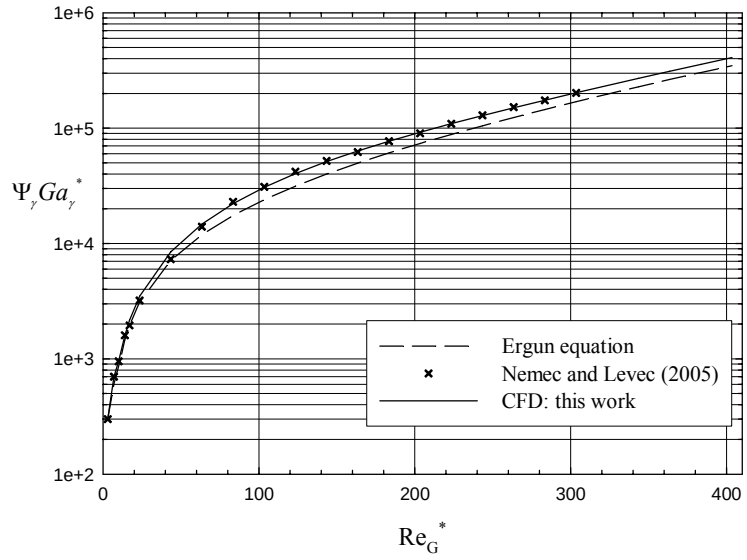

Figure X.2. Pressure drop for single-phase flow as function of Re^*_G

The effect of gas flow measured by Reynolds number on pressure drop for the packed bed made of spheres with diameter equal to 1 mm was observed by plotting dimensionless form in terms of modified Reynolds and Galileo numbers. The resulting pressure drop is given by the addition of laminar flow local losses with frictional losses. At very low velocities, exclusively laminar or viscous contributions to pressure drop are observed but at higher velocities the laminar term from *Blake-Kozeny-Carman* equation and the inertial term from *Burke-Plummer* equation are additive. This mutual contribution stands for Ψ_γ which represents the ratio between the static pressure and the hydrostatic pressure whose behaviour is shown in Fig. X.2. The operational region of flow rates ($10<Re_G<400$) was that of particular interest to trickle-bed reactors (Nemec and Levec, 2005; Lakota *et al*., 2002) where the viscous and inertial terms of the Ergun equation have more or less even or at least comparable contributions to the overall pressure drop. Ergun equation can describe the flow through packed beds made up of differently shaped particles with universal constants. However, if we brake up the problem down to smaller parts that involve groups of

particles of similar geometry some general principles regarding Ergun constants may be found. Particle shapes studied involve those most often encountered in packed bed reactors that are spheres.

As it can be concluded from Fig. X.2, the original Ergun equation with values of viscous and inertial constants of 150 and 1.75, respectively, fits the pressure drop data for beds of spheres quite well. This is in agreement with CFD results obtained for single-phase flow and with a number of works found in the open literature (Burghardt *et al*., 1999; MacDonald *et al*., 1991), which claim that the original Ergun constants are able to predict the pressure drop in beds composed of spherical particles to within acceptable limits of 10%. However, it should be pointed out that porosity values charge between 0.35 to 0.40 where Ergun equation agrees with such conclusions (MacDonald *et al*., 1991), whereas for other bed assemblies with higher porosities the original Ergun constants would over predict the pressure drop. In the present case, the CFD results obtained for single-phase flow are compared against the results predicted by applying the model of Attou and Ferschneider (1999) for the pressure drop in a parity plot illustrated in Fig. X.3. As it can be seen, the data scatter slightly more 10 % than in the case when the Ergun equation was implemented by the permeability concept. It should be also emphasized that the fixed-bed modelled in this work had the tube to particle diameter ratio higher than 10 so the available geometry and Ergun constants taken from literature should not be affected by the reactor column wall.

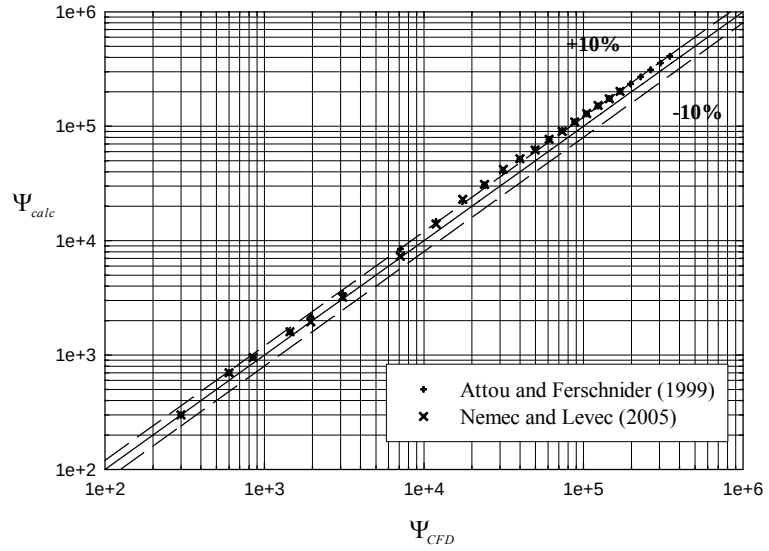

Figure X.3. Parity plot for pressure drop (P=30 bar, d=1 mm)

In Figs X.4 and X.5, liquid holdup and pressure drop are presented for different gas flow fluxes, respectively. In accordance with Fig. X.4, when ranging from low gas flows, G = 0.10 kg/m^{2}s, to

higher values, G = 0.70 kg/m^{2}s, liquid holdup decreases as observed by several researchers (Attou *et al*., 1999; Al-Dahhan *et al*., 1998; Gianetto and Specchia, 1992; Ellman *et al*., 1990).

For two-phase flow CFD simulations, practically in the whole range of the liquid holdup the predictions fit relatively well being underestimated in some values and overestimated in other values for liquid flows, in the range of pressure drop these differences were not so higher as shown in Fig. X.5. In first instance, this fact can be justified by the wall effects but according to the ratio between tube and sphere diameter modelled it seems more likely that this could be a characteristic of the model. Furthermore, the main reason could be directly related to the fact that model recommends general Ergun type constants.

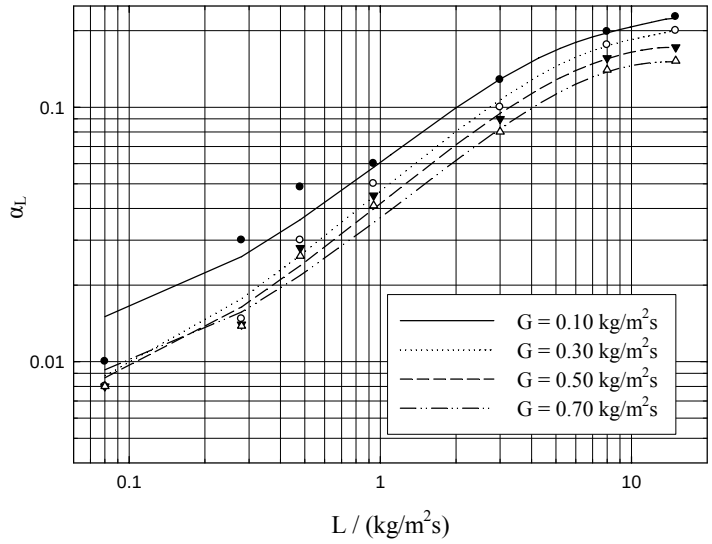

Figure X.4. Liquid holdup as a function of liquid mass flux at constant gas mass fluxes; P=30 bar, d=1 mm; experimental data from Nemec and Levec (2005)

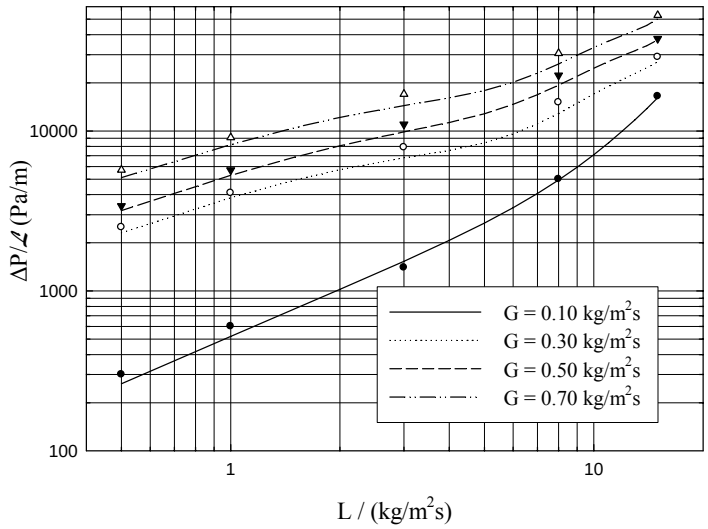

Figure X.5. Pressure drop as a function of liquid mass flux at constant gas mass fluxes; P=30 bar, d=1 mm; experimental data from Nemec and Levec (2005)

It should be stressed at this point that about the same discrepancy would be obtained for the same constants if they were applied for other particle shapes. Spheres were used by virtue of their unique shape and are incapable of influencing the structure of the bed by their orientation. Some additional differences between the porosities of beds, despite the same packing procedures, were due to wall effect, which as mentioned before did not affect the overall pressure drop. One can then conclude that the hydrodynamic behaviour in terms of liquid holdup and pressure drop seems to be well described by the Eulerian model, reflected by the fact that all the data lay on an expected performance for the packed bed. This is in agreement with a number of works for the viscous regime reviewed by Endo *et al*. (2002). With regards to the porosity dependence within the inertial regime and in agreement with the results obtained by Hill *et al*. (2001), it should be reported in the basis of theoretical simulations of flow through random arrays of spheres, that the porosity function is also well taken into account as long as the porosity is around 0.4 as is indeed the case for packed bed reactors when made up of spheres. The values of porosity distribution function for the present CFD Eulerian model were applied in the range from 0.38 to 0.40. As one can see, the experimental results for single-phase pressure drop presented in Figs X2 and X.3 are well predicted for spherical particles by CFD model in two-phase flow interaction regime.

X.5. Oxidation process in TBR by CFD simulations

By using the kinetic laws previously obtained in Equation (X.8), the evolution of vanillic acid TOC conversion at the reactor outlet against time (represented as total operation time minus reactor residence time) is plotted in Fig. X.6 at two different wall temperatures (200, 220ºC) and pressures (20, 30 bar), when the feed stream entered the reactor at ambient temperature, 25ºC.

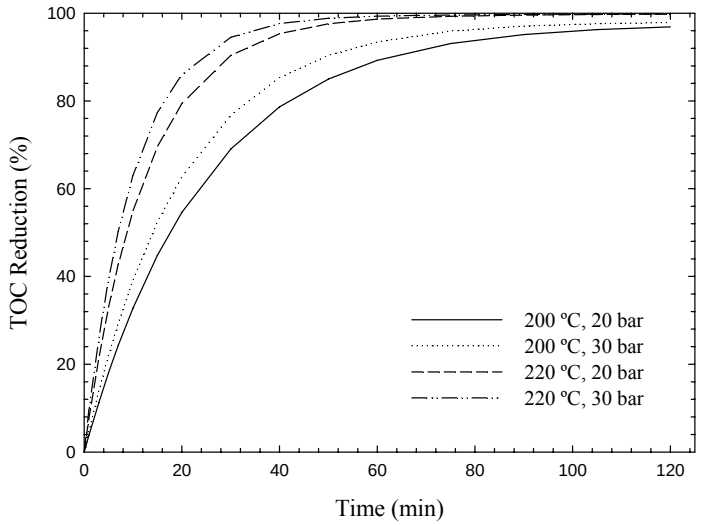

Figure X.6. CFD TOC profile as a function of time (L=0.25 kg/m^{2}s, G=0.1 kg/m^{2}s, d=1 mm)

These results show the transient values for TOC conversions at the TBR exit, along which temperature increases from the initial 25ºC until the wall temperature, being the steady-state operation achieved beyond 3h. In this case, with L=0.25 Kg/m^{2}s , the liquid residence time is 65.3 min, which enables to compare the final steady value of the TOC conversion, 88%, with the one experimentally observed in the batch reactor for the same reaction time and operating conditions, 99% (Fig. X.1, 200ºC and 30 bar), pointing out a deviation around to 8-10%. This seems to reveal a good interaction between the studies carried out with both reactional systems: the batch reactor for the kinetic studies and the TBR continuous operation analysed through the CFD simulations based on those rate laws. As expected temperature has a strong influence in the oxidation process as shown in Fig. X.6 and Fig. X.7 in which it was represented a snapshot after 15 min of the last one-third axial plane of total reactor column height with a TOC conversion of about 30%. In accordance to Fig. X.7, the lower TOC characteristic zones correspond to the surface of catalyst particles. According to Fig. X.6, air pressure seems only to have a slight effect when different runs were performed at 20 bar and 30 bar. Therefore, TOC reduction was higher (99.6%) at the highest temperature (220 ºC) and air pressure (30 bar) after 1 h. In the CFD model it was assumed that chemical reaction occurs namely on the catalyst surface. This assumption is expected to be mostly reasonable because of the hydrodynamic interaction regime achieved at trickling flow conditions. It should be also referred that the high reactor diameter to particle diameter ratio, averaged 10, exceeds the recommended value to prevent flow distribution problems (van der Merwe and Nicol, 2005). The CFD model has also taken into account external mass transfer limitations so that the kinetics is not only governed by the chemical reaction and their competition is the most suitable when operating at large scale pilot plant units as systematized by Al-Dahhan *et al*. (1997).

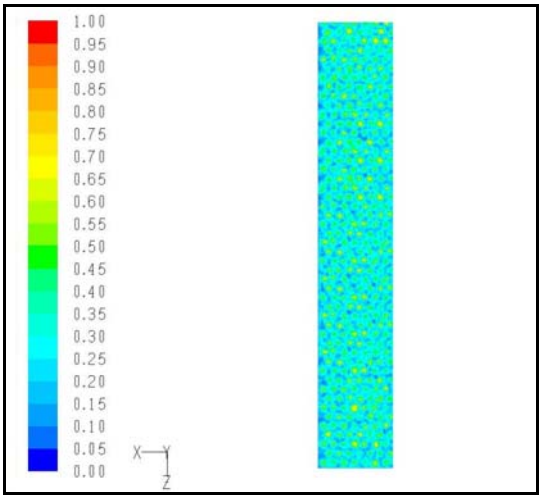

Figure X.7. Colour map of total organic carbon conversion at *t = 15 min* (L=0.25 kg/m^{2}s, G=0.1 kg/m^{2}s, P=30 bar, d=1 mm)

According to Figs. X.8 and X.9, temperature colour maps were taken for the first one-third of the TBR at 3600 s and 7200 s, respectively, and after evaluating successive temporal temperature colour maps it is possible to conclude that steady state of TBR unit is achieved practically in one hour and half.

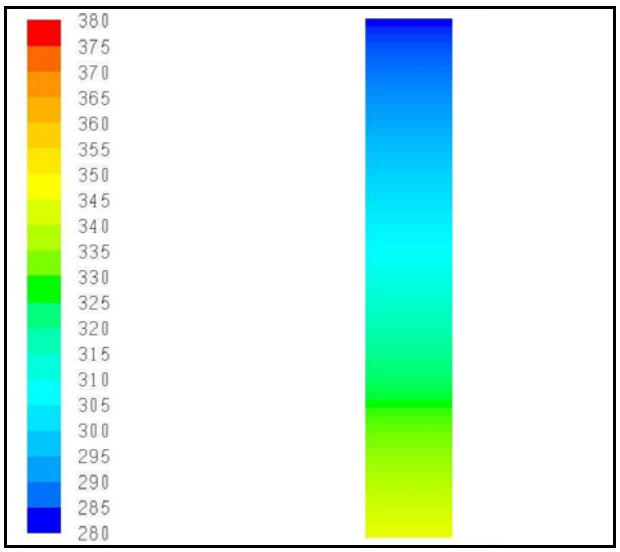

Figure X.8. Temperature colour map at *t = 1 h* (L=0.25 kg/m^{2}s, G=0.1 kg/m^{2}s, P=30 bar, d=1 mm)

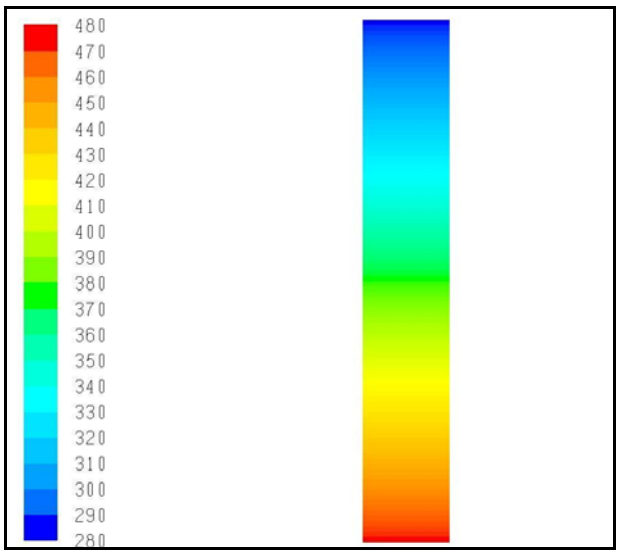

Figure X.9. Temperature colour map at *t = 2 h* (L=0.25 kg/m^{2}s, G=0.1 kg/m^{2}s, P=30 bar, d=1 mm)

In the first hour, temperature profiles indicated that the reactor is heating and it should be noted that was reached 380 K in some turbulence zones. Owing to a motionless catalyst bed, nearly plug flow is achieved in TBRs and they are superior to other three-phase reactors where the catalyst is either slurried or fluidized. This can be reached for a continuous wastewater treatment if catalyst life cycle analysis plays into the game. The TBRs are advantageous in comparison with fluidized reactors given that they are characterized by a higher catalyst loading per unit volume of the liquid

and therefore they have a lower energy dissipation. One should also bear in mind that catalyst wetting is a performance rating parameter in the degree of packed bed utilization and if the temperature increases, the locus of the maximum is found at lower residence time. Additionally, liquid holdup is a primordial parameter in TBR hydrodynamics described by the present CFD model either in single-phase or in two-phase flow where the interaction regime is also studied in terms of pressure drop. These results allocate an appropriate place for wastewater treatment where it is possible to find highly or slightly exothermic reactions and the knowledge of holdup is essential for avoiding hot spots and for preventing reactor runaway. Hence, liquid holdup is also related to the catalyst wetting efficiency affecting the reaction yield that depends on whether the reaction occurs on the wetted or dry catalyst areas. In accordance to Fig. X.10 where it is shown a snapshot of the catalyst surface temperature captured inside the trickle-bed reactor in the last one-third zone, our results make possible to identify this fact in terms of catalyst surface temperature ranging from 460 K to 480 K which can be related to the driving force to provide the TOC reduction. Therefore, external catalyst wetting efficiency is an essential parameter for design and scale-up issues in what regards the knowledge of catalyst utilization level in trickle-bed reactors where the internal contacting is normally assumed to be equal to one due capillary effects. In this context, CFD models are quite useful requiring however higher computational power to report that parameter along the packed bed. It should be stated that kinetics and thermodynamics of reactions conducted in TBRs require high temperatures, specifically in wastewater treatment, which in return increase the solubility of gaseous reactant into the liquid. In fact, to improve the gas solubility as well as the transport phenomena coefficients, it is also necessary higher operating pressures.

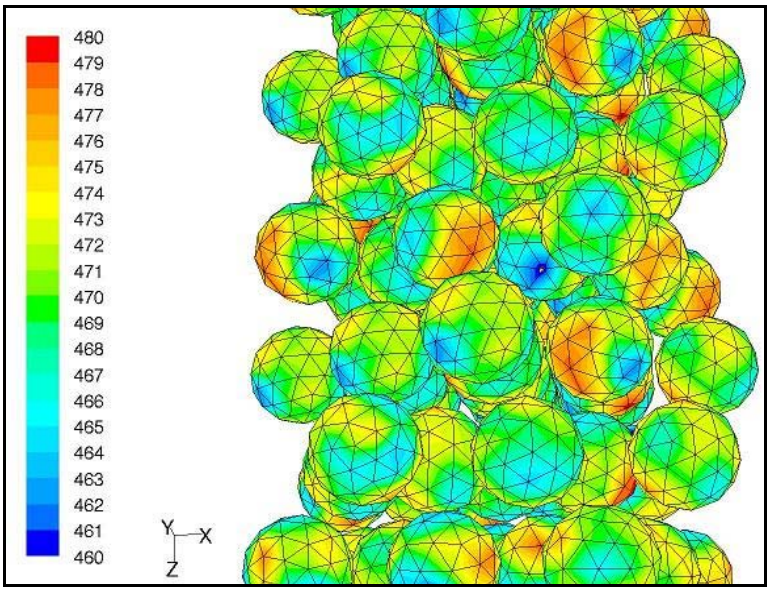

Figure X.10. Catalyst surface temperature gradient map at *t = 2 h* (L=0.25 kg/m^{2}s, G=0.1 kg/m^{2}s, P=30 bar, d=1 mm)

Due to complexities associated with transport/kinetics coupling in TBRs, general scale-up and scale-down rules have not been achieved for the quantitative description of transport phenomena in TBRs working under reaction conditions. This fact brings up in a phenomenological analysis which was developed to relate the wetting efficiency with operating conditions such as reactor pressure and gas and liquid flow rate which resulted in the five limiting cases reported in literature by Al-Dahhan *et al*. (1997). For a fixed liquid mass velocity, at high pressure and high gas flow rates, wetting efficiency improves noticeably whereas pressure drop increases significantly and liquid holdup decreases considerably. As liquid flow rate increases, contacting efficiency improves further due to an increase in both pressure drop and liquid holdup. The effect of gas flow rate on the wetting efficiency, pressure drop, and liquid holdup is more pronounced at elevated pressures as observed in Figs X.4 and X.5. The improvement in wetting efficiency with increased gas flow rate is due to the improved spreading of the liquid holdup over the external packing area. On the other hand, in TBR operation known controllability issues are directly related to liquid maldistribution that could be responsible by reactor underutilization. In order to achieve feasibility and to exploit TBR advantages in the presence of relatively slow catalyst deactivation, catalyst stability should be also investigated. This can dictate the success of continuous catalytic wet air oxidation technology in wastewater treatment. Moreover, any advance in TBR technology will represent substantial savings, which stimulates the continued research efforts aimed at improving TBR operation and performance.

X.6. Conclusions

The behaviour of a trickle-bed reactor for the catalytic wet air oxidation of an aqueous solution containing vanillic acid has been studied by using CFD techniques after performing slurry experiments with a Mn-Ce-O laboratory-made catalyst that revealed high activity for TOC degradation. The kinetic parameters were obtained taking into account the generalized kinetic model and this information was further integrated into a hydrodynamic model developed by means of CFD were the reaction aspects as well as the transport mechanisms were accounted for. CFD Eulerian model has been deployed for the prediction of pressure drop and liquid holdup in a trickle-bed reactor according to data taken from the open literature. Hydrodynamic parameters fit well for the high-pressure TBR modelled indicating that the effect of pressure on the design parameters, such as pressure drop and liquid holdup, is in accordance to experimental published data. Single-phase flow pressure drop studied in a region of flow rates related to a wide interaction regime where Re_G charged between 10 and 400, demonstrated that the Eulerian model is able to reasonably predict the pressure drop of single-phase flow over spherical particles. The CFD model

also showed that in two-phase flow runs, liquid holdup is decreased if gas flow rate increases. Moreover, the Eulerian model is able to give good predictions of liquid holdup in the range of gas flows investigated. After all, runs performed in unsteady state for the catalytic wet air oxidation of vanillic acid solution indicated that complete reduction of organic matter was achieved. Furthermore, CFD exhibited a considerable effect of temperature whereas the air partial pressure only had minor influence.

X.7. Nomenclature

C_{TOC}	Total organic carbon concentration, *(mg/L)*
d	Particle nominal diameter (*m*)
$\vec{g}$	Gravitational acceleration, 9.81m/s^2
G	Gas mass flux, kg/m^{2}s
Ga^*_q	Modified Galileo number, $[(\rho_q/\mu_q)^2 g(d\varepsilon/(1-\varepsilon))^3]$, dimensionless
GKM	Generalized Kinetic Model
h_q	specific enthalpy of the q^{th} phase, J/kg
k	Reaction rate constant, $(L/mg)^{m-1} \times (L/mol)^n \times (1/min)$
k'	Apparent reaction rate constant, $(L/mg)^{m-1} \times (1/min)$
k_{eff}	Effective thermal conductivity, *W/(m·K)*
L	Liquid mass flux, kg/m^{2}s
$\mathcal{L}$	Reactor length, m
p	Pressure, bar
$-r$	Oxidation rate $(mg/L) \times (1/min)$
Re^*_q	Modified Reynolds number,$[(\rho_q u_q d/\mu_q (1-\varepsilon)]$, dimensionless
S_q	Source mass for phase *q*
t	Time, s
T	Temperature, *ºC*
$\vec{u}$	Superficial vector velocity, m/s
z	Length of bed (*m*)

Subscripts

i	Lumped compound specie *(i=A, B, C or D)*
G	Gas phase
L	Liquid phase
S	Solid phase
q	q^{th} continuous phase
w	Wall
0	Initial time reaction

Greek letters

α_q	Volume fraction of q^{th} phase
Δp	Total pressure drop, bar
ρ_q	Density of q^{th} phase, kg/m^3
σ	Surface tension, N.m
$\bar{\bar{\tau}}_q$	Shear stress tensor of q^{th} phase, bar
ψ	Dimensionless pressure drop [$(\Delta P/\mathcal{L})/\rho g$]
μ_q	Viscosity of q^{th} phase, Pa.s

X.8. References

Al-Dahhan, M. H., Larachi, F., Dudukovic, M. P., Laurent, A. (1997). High pressure trickle-bed reactors: A Review. *Industrial and Engineering Chemistry Research* **36** (8), 3292-3314.

Al-Dahhan, M.H., Khadilkar, M.R., Wu, Y., Dudukovic, M.P. (1998). Prediction of pressure drop and liquid holdup in high pressure trickle bed reactors. *Industrial and Engineering Chemistry Research* **37** (3), 793-798.

Attou, A., Boyer, C., Ferschnider, G. (1999). Modelling of the hydrodynamics of the cocurrent gas-liquid trickle flow through a trickle-bed reactor. *Chemical Engineering Science* **54** (6), 785-802.

Bhargava, S. K., Tardio, J., Prasad, J., Foger, K., Akolekar, D. B. and Grocott, S. C. (2006). Wet Oxidation and Catalytic Wet Oxidation. *Industrial and Engineering Chemistry Research* **45** (4), 1221-1258.

Burghardt, A., Bartelmus, G., Gancarczyk, A. (1999). Hydrodynamics of pulsing flow in three-phase chemical reactors. *Chemical Engineering and Processing* **38** (4-6), 411-426.

Carbonell, R.G. (2000). Multiphase flow models in packed beds. *Oil & Gas Science and Technology* – Revue de l'IFP **55** (4), 417-425.

Dudukovic, M.P., Larachi, F., Mills, P.L. (2002). Multiphase catalytic reactors: A perspective on current knowledge and future trends. *Catalysis Reviews. Science and Engineering* **44** (1), 123-246.

Ellman, M.J., Midoux, N., Wild, G., Laurent, A., Charpentier, J.C. (1990). A new improved liquid holdup correlation for trickle bed reactors. *Chemical Engineering Science* **45** (7), 1677-1684.

Endo, Y., Chen, D-R., Pui, D.Y.H. (2002). Theoretical consideration of permeation resistance of fluid through a particle packed layer. *Powder Technology* **124** (1-2), 119-126.

FLUENT 6.1. (2005). User's Manual to FLUENT 6.1. Fluent Inc. Centrera Resource Park, 10 Cavendish Court, Lebanon, USA.

GAMBIT 2 (2005). User's Manual to GAMBIT 2. Fluent Inc. Centrera Resource Park, 10 Cavendish Court, Lebanon, USA.

Gianetto, A., Specchia, V. (1992). Trickle-bed reactors: State of the art and perspectives. *Chemical Engineering Science* **47** (13-14), 3197-3213.

Gunjal, P.R., Kashid, M.N., Ranade, V.V., Chaudhari, R.V. (2005). Hydrodynamics of Trickle-Bed Reactors: Experiments and CFD Modeling. *Industrial and Engineering Chemistry Research* **44**, 6278-6294.

Hill, R.J., Koch, D.L., Ladd, A.J.C. (2001). Moderate-Reynolds-number flows in ordered and random arrays of spheres. *Journal of Fluid Mechanics* **448** (1), 243-278.

Himmelblau, D.M. (1960). Solubilities of Inert Gases in Water. 0°C to Near the Critical Point of Water. *J. Chem. Eng. Data* **5**, 10-15.

Iliuta, I., Larachi, F., Grandjean, P.A. (1998). Pressure drop and liquid holdup in trickle-flow reactors: improved Ergun constants and slip correlations for the slit model. *Chemical Engineering Science* **37** (12), 4542-4550.

Iliuta, I., F. Larachi, B.P.A. Grandjean, Wild, G. (1999) Gas–Liquid Interfacial Mass Transfer in Trickle-bed Reactors: State-of-the-art Correlations. *Chem. Eng. Sci.* **54**, 5633-5645.

Imamura, S. (1999). Catalytic and Noncatalytic Wet Oxidation. *Industrial and Engineering Chemistry Research* **38** (5), 1743-1753.

Jiang, Y., Khadilkar, M.R., Al-Dahhan, M.H., Dudukovic, M.P. (2000). Single phase flow modeling in packed beds: discrete cell approach revisited. *Chemical Engineering Science* **55** (10), 1829-1844.

Joshi, J.B., Ranade, V.V. (2003). Computational Fluid Dynamics for Designing Process Equipment: Expectations, Current Status, and Path Forward. *Industrial and Engineering Chemistry Research* **42** (6), 1115-1128.

Lakota, A., Levec, J., Carbonell, R.G. (2002). Hydrodynamics of trickling flow in packed beds: relative permeability concept. *A.I.Ch.E. Journal* **48** (4), 731-738.

Larachi, F., Iliuta, I., Chen, M., Grandjean, B.P.A. (1999). Onset of pulsing in trickle beds: Evaluation of current tools and state-of-the-art correlation. *Canadian Journal of Chemical Engineering* **77** (4), 751-758.

Larachi, F., Laurent, A., Midoux, N., Wild, G. (1991). Experimental study of a trickle bed reactor operating at high pressure: two-phase pressure drop and liquid saturation. *Chemical Engineering Science* **46** (5-6), 1233-1246.

Li, L., Chen, P., Gloyna, E.F. (1991). Generalized Kinetic Model for Wet Oxidation of Organic Compounds. *A.I.Ch.E. Journal* **37** (11), 1687-1697.

Lopes, R.J.G., Silva, A.M.T., Quinta-Ferreira, R.M. (2007a). Kinetic Modelling and Trickle-Bed CFD Studies in the Catalytic Wet Oxidation of Vanillic Acid. *Industrial and Engineering Chemistry Research* **46** (25), 8380-8387.

Lopes, R.J.G., Silva, A.M.T., Quinta-Ferreira, R.M. (2007b). Screening of catalysts and effect of temperature for kinetic degradation studies of aromatic compounds during wet oxidation. *Applied Catalysis B: Environmental* **73** (1-2), 193-202.

MacDonald, M.J., Chu, C-F., Guilloit, P.P., Ng, K.M. (1991). A generalized Blake-Kozeny equation for multisized spherical particles. *A.I.Ch.E. Journal* **37** (10), 1583-1588.

Maiti, R.N., Arora, R., Khanna, R., Nigam, K.D.P. (2005). The liquid spreading on porous solids: Dual action of pores. *Chemical Engineering Science* **60** (22), 6235-6239.

Mantzavinos, D., Kalogerakis, N. (2005). Treatment of olive mill effluents Part I. Organic matter degradation by chemical and biological processes – an overview. *Environment International* **31** (2), 289-295.

Matatov-Meytal, Y., Sheintuch, M. (1998). Catalytic Abatement of Water Pollutants. *Industrial and Engineering Chemistry Research* **37** (2), 309-326.

Nemec, D., Levec, J. (2005). Flow through packed bed reactors: 2. Two phase concurrent downflow. *Chemical Engineering Science* **60** (24), 6958-6970.

Niaounakis, M., Halvadakis, C.P. (2004). Olive mill waste management. Literature review and patent survey. *Typothito-George Dardanos Publications*, Athens, Greece.

Paraskeva, P., Diamadopoulos, E. (2006). Technologies for olive mill wastewater (OMW) treatment: a review. *Journal of Chemical Technology and Biotechnology* **81** (9), 1475- 1485.

Piché, S., F. Larachi, I. Iliuta, Grandjean, B.P.A. (2002) Improving the Prediction of Liquid Back-mixing in Trickle-bed Reactors Using a Neural Network Approach. *J. Chem. Technol. Biotechnol.* **77**, 989-998.

Pintar, A., Levec, J. (1994). Catalytic Liquid-phase Oxidation of Phenol Aqueous Solutions. A Kinetic Investigation. *Industrial and Engineering Chemistry Research* **33** (12), 3070-3077.

Reid, R.C., J.M. Prausnitz, Poling, B.E. (1987) The Properties of Gases and Liquids. Mc-Graw-Hill, New York, NY.

Sai, P.S.T., Varma, Y.B.G. (1987). Pressure drop in gas-liquid downward flow through packed beds. *A.I.Ch.E. Journal* **33** (12), 2027-2036.

Saroha, A.K., Nigam, K.D.P. (1996). Trickle Bed Reactors. *Reviews in Chemical Engineering* **12** (3-4), 207-347.

Siddiqi, M.A., Lucas, K. (1986). Correlations for prediction of diffusion in liquid. *Canadian Journal of Chemical Engineering* **64**, 839.

Sie, S. T., Krishna, R. (1998). Process development and scale-up, III: Scaleup and scale down of trickle bed processes. *Reviews in Chemical Engineering* **14** (3), 203-252.

Silveston, P. (1990). New Applications of Periodic Operations. *Unsteady State Processes in Catalysis. Proceedings of the International Conference June 5-8*, 217-232.

van der Merwe, W., Nicol, W. (2005). Characterization of multiple flow morphologies within trickle flow regime. *Industrial and Engineering Chemistry Research* **44** (25), 9446-9450.

Wammes, W.J.A., Westerterp, K.R. (1990). The influence of reactor pressure on the hydrodynamics in a cocurrent gas-liquid trickle-bed reactor. *Chemical Engineering Science* **45** (8), 2247-2254.

Wilke, C.R., Chang, P. (1955). Correlation of diffusion coefficients in dilute solutions, *AIChE J.* **1** (2), 264-270.

Zhang, Q., Chuang, K.T. (1999). Lumped Kinetic Model for Catalytic Wet Oxidation of Organic Compounds in Industrial Wastewater. *A.I.Ch.E. Journal* **45** (1), 145-150.

This page intentionally left blank

XI. Trickle-bed CFD Studies in The Catalytic Wet Oxidation Of Phenolic Acids[1]

An Euler-Euler computational fluid model was developed successfully for the hydrodynamic prediction of a trickle-bed reactor designed for advanced wastewater treatment facilities. Catalytic wet air oxidation of phenolic acids was simulated in a trickle-bed reactor by means of CFD in the temperature range 170-200 ºC and pressures 10-30 bar. The hydrodynamic model validation was accomplished through the comparison of simulated pressure drop and liquid holdup with experimental data from the literature. In a broad range of gas and liquid flows studied (G = 0.10-0.70 and L = 0.5-5 kg/m^{2}s) at different operation conditions, CFD demonstrated the considerable effect of operating pressure in pressure drop, whereas a minor influence was detected for the liquid holdup. CFD runs were then performed for the catalytic wet air oxidation of aqueous phenolic acids solution. The reactor behaviour was analysed by means of total organic carbon profiles which reflected the influence of temperature, pressure, gas-liquid flows and initial pollutant concentration.

XI.1. Introduction

The growing public awareness and the increased demand for industrials to meet human requirements have created global problems involving overexploitation of available natural resources leading to pollution of the land, air and water environments. As a consequence, the stringent regulations established by the various governmental authorities are forcing industry to treat effluents to the required compliance level before discharge into the surroundings. Phenols and phenolic acids commonly appear in aqueous final streams arriving from different sources such as food and agroindustry as well as pharmaceutical, petrochemical and chemical companies. Unless the concentration is low enough, phenolic wastewaters are poorly biodegradable because of their bactericidal properties (Paraskeva and Diamadopoulos, 2006). Therefore, phenolic compounds must be specifically destroyed before discarding the effluent for subsequent treatment in conventional sewage plants. Among the advanced oxidation processes, catalytic wet air oxidation (CWAO) has been shown to be an effective technique for eliminating organic compounds, such as phenolic and other aromatic products (Bhargava *et al.*, 2006). In this ambit, catalyst screening studies have been performed successfully in our group with a model solution of several phenolic acids including syringic, vanillic, *3,4,5*-trimethoxybenzoic, veratric, protocatechuic and *4*-

[1] *This Chapter is based upon the publication Lopes and Quinta-Ferreira (2007a)*

hidroxybenzoic acids in which total organic carbon (TOC) was oxidised in batchwise slurry reactor (Lopes *et al.*, 2007b). In particular, the the Mn-Ce-O catalyst revealed good stability in terms of leaching and carbon adsorption leading to the complete TOC removal so that catalyst deactivation phenomena were not addressed in the present study.

However, at industrial level, three-phase reactors are required for the continuous wastewater treatment operating in trickle flow regime at trickle-bed reactors (TBR). In order to achieve industrial feasibility, four main aspects of CWO in continuous mode have to be considered, namely chemistry of CWO, reactor geometry, catalyst stability and scale-up (Sie and Krishna, 1998). If the first parameters have been reviewed in the literature, scheduling and scale-up studies leading to their applicability to industrial processes on CWO reaction engineering have not been fulfilled. Therefore, the present paper intends to examine the behaviour of a TBR by means of computational fluid dynamic (CFD) codes.

The use of TBRs is common in industrial multiphase catalytic processes and spans a broad range of applications from the manufacture of value-added products to the conversion of undesired chemicals into harmless and bio-compatible species. Despite nearly 50 years of worldwide research efforts, a satisfactory approach to trickle-bed reactors is still out of grasp. Even though fluid dynamics continue to be among the most intensely studied areas, TBR state-of-the-art is far from being complete and yet no universal approach has emerged as a panacea to predict conclusively TBR key fluid dynamic parameters (Carbonell, 2000; Al-Dahhan *et al.*, 1997; Gianetto and Specchia, 1992; Sáez and Carbonell, 1985; Goto and Smith, 1975). This is partly ascribable to the diverse entangling gas-liquid patterns met in a TBR which make such parameters depend in a complex manner on the fluid properties and throughputs, interfacial interactions and bed geometry. In these reactors, gas and liquid phase flow co-currently downward through a fixed bed of catalyst particles. Generally, three phase fixed bed reactors can operate in hydrodynamically different regimes whose boundaries depend on gas and liquid superficial velocities, catalyst bed and fluid properties (van der Merwe and Nicol, 2005; Attou and Ferschneider, 1999; Al-Dahhan *et al.*, 1997; Holub *et al.*, 1993).

In practice, many of the chemical reactors used in industry are truly multiphase and must be described in the context of CFD by multiple momentum equations (Jiang *et al.*, 2002). Direct numerical simulation of the transport equations for all phases with fully resolved interfaces between phases is only possible for multiphase systems characterized by lower Reynolds numbers. Such a detailed model could not be used to predict a large chemical reactor such as a trickle-bed reactor and other multiphase reacting flows (Gunjal *et al.*, 2005). As a middle-term approach, we evaluated in a previous work the TBR behaviour for the catalytic wet oxidation of a vanillic acid

solution by using the available methods in commercial CFD codes where the fluid is modelled by the volume fractions for each phase (Lopes *et al.*, 2007c) much in the same way used to describe micromixing in single-phase flows.

XI.2. Numerical model and governing flow equations

In this work, TBR is modelled by means of a multifluid CFD Euler-Euler two-fluid model implemented in commercial software FLUENT (FLUENT 6.1, 2005). In a first step, the hydrodynamic behaviour for the gas-liquid concurrent downflow is analysed in order to validate with results taken from the open literature. Afterwards, the influence of operation conditions on the catalytic wet oxidation in continuous mode is evaluated. At the subgrid scale, the two phases (G/L) are described by the corresponding volume fractions. The multifluid CFD model at its most basic level consists of mass and momentum balances for each phase. In the case of multiphase and incompressible flow, the pressure constrains the velocity field to ensure that the sum of the phase volume fractions equals unity. To reduce the computational requirements and numerical efforts, the mesh domain was previously optimized in terms of cell number. The mass and momentum conservation equations have been described in Equations (V.1) and (V.2) in Chapter V.

Mainly due to the intrinsic nature of multiphase reactors, the incomplete understanding of the physics plus the highly coupled and nonlinear nature of the equations, the complete solution is largely dependent in the mechanistic principles and advanced numerical analysis as well as satisfactory computational resources. Therefore, closures equations for fluid/fluid and fluid/particle interactions integrated in the overall momentum balance equation is often an approximation based in theoretical assumptions. The force balance equation includes the rate of change of momentum for the q^{th} phase, pressure forces, gravitational acceleration, average shear stresses and interphase momentum exchange. The pressure drop in the packed bed is usually correlated using the Ergun equation or its variants (Al-Dahhan *et al.*, 1997, Holub *et al.*, 1993; Sáez and Carbonell, 1985). Interphase coupling terms may therefore be formulated based on similar equations. The presence of liquid flow, however, leads to additional interphase exchanges, which need to be formulated correctly. We have used the model of Attou and Ferschneider (1999), which includes gas-liquid interaction forces and it was developed for the regime in which liquid flows in the form of film. The interphase coupling terms are expressed in terms of interstitial velocities and phase volume fractions for gas-liquid, gas-solid and liquid-solid momentum exchange forms as shown in Equations (V.4)-(V.7) in Chapter V in where it was also described the turbulence modelling approach in Equations (V.9) and (V.10). The species continuity balance was expressed in Equation (X.1) in Chapter X where it was also presented the conservation of energy

in Eulerian multiphase applications that is expressed by a separate enthalpy equation for each phase as shown in Equation (X.2) along with the description of the calculation procedure for the physical properties and mass transfer parameters in section X.2.

XI.3. Results and discussion

XI.3.1 TBR specifications and numerical techniques

The solution domain for the experimental system investigated in this work is shown in Fig. XI.1. It consists of a cylindrical vessel with 5 cm internal diameter and 1 m bed height packed with catalyst spherical particles 2 mm diameter.

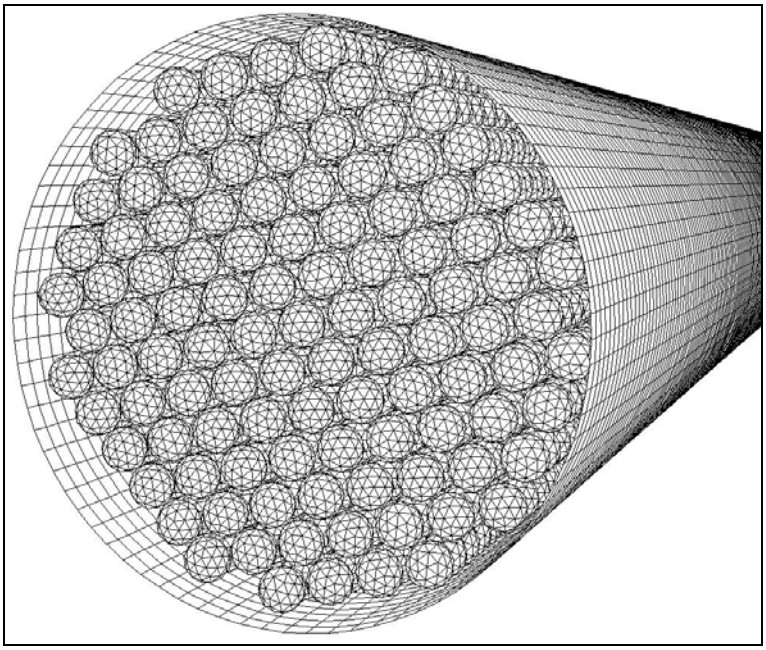

Figure XI.1. Computational mesh domain of TBR at the entrance

Numerical simulations are compared to experimental data in order to validate the predicted hydrodynamic parameters pressure drop and liquid holdup. The simulated operating conditions were 10-30 bar pressure and temperatures from 290 to 500 K. Gas and liquid mass flow rates were in the range 0.10 – 0.70 and 0.05 – 15 kg/m^{2}s, respectively.

The FLUENT preprocessor GAMBIT 2 (GAMBIT 2, 2005) was used as a geometry and mesh generator. The mesh of the packing bed was designed excluding surface roughness. The multigrid computational domain adopted in the TBR is characterized by tetrahedral cells around and over the catalyst particles and hexahedral elsewhere because this strategy takes advantage of the hierarchical nature of the grids, incorporating an efficient technique to generate the coarser grids in the mesh preprocessor GAMBIT 2. Aiming to achieve higher numerical precision, the compromise

is between the application of coarse meshes that are best designed in regions where temporal and spatial gradients of key quantities are relatively small and the preliminary numerical results that were carried out to identify the number of computational cells appropriate to obtain qualitative and quantitatively grid independent results.

Fig. XI.1 shows the essential features of one million tetrahedral cells per catalyst layer representing the catalytic bed. The system domain is discretized by an unstructured finite volume method, obtained using the solver FLUENT (FLUENT 6.1, 2005) in order to convert the governing equations like continuity and momentum equations to algebraic equations that can be solved numerically. The reactor wall and catalyst surfaces are treated as no slip boundaries with standard wall functions. The gas flow rate at the distributor is defined via inlet-velocity-type boundary condition with gas volume fraction charging according to the specifications made in the simulations. The computational domain mimics the D2 gas-liquid distributor with 60 holes uniformly arranged across the radial direction as described in Chapter VII. The use of under-relaxation factors represents a good compromise between physical accuracy and reasonable computational effort. The flow model is based on solving Navier-Stokes equations for the Eulerian-Eulerian multiphase model along with multiphase k-ε turbulent model. The governing differential equations are solved using iterative solution to the discrete form of the mathematical model using a SIMPLE algorithm for pressure-velocity coupling with high-order integration schemes. The gas and liquid are described as interpenetrating continua and equations for conservation of mass and momentum are solved for each phase. To avoid numerical difficulties, the transient calculations were made for two-phase flow starting with different time steps. The converged solution is assumed when the scaled residuals of all variables were smaller than 10^{-5}. Preliminary numerical simulations were carried out to identify the computational cells that are adequate to obtain grid independent results so that these numerical simulations showed that the predicted values of overall pressure drop and liquid holdup become insensitive to further grid refinement either when increasing the number of grid cells or using higher order discretization scheme that caused less than 5% change in pressure drop and less than 1% change in liquid volume fraction.

XI.3.2 Hydrodynamic studies

As the performance of the trickle bed reactor is affected by the fluid dynamic parameters, the hydrodynamic studies are discussed in terms of liquid holdup and pressure drop at different operating pressures in the range 10 to 30 bar. In order to validate the computational model, the runs were carried out for the vectorial field of liquid and gas velocity and for liquid hold up and pressure drop using spherical catalysts with 2 mm diameter. The CFD flow maps indicate that for

gas (Fig. XI.2) and liquid (Fig. XI.3), the velocity is higher at points where the flow is processed downward in axial direction. In accordance to these results, the maximum gas velocity is about 0.5 cm/s (Fig. XI.2) while the liquid velocity is about 0.005 cm/s (Fig. XI.3) which is in the range of well accepted trickle flow maps reviewed elsewhere (Al-Dahhan *et al.*, 1997; Wammes and Westerterp, 1990).

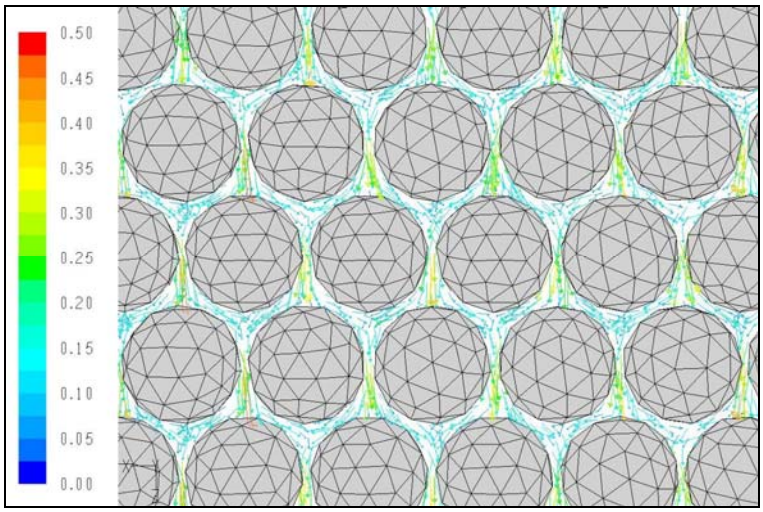

Figure XI.2. Gas velocity *(cm/s)* axial map

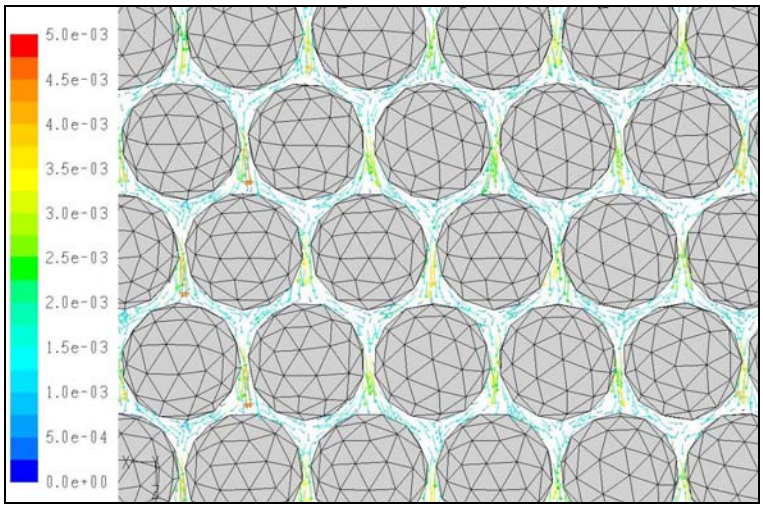

Figure XI.3. Liquid velocity *(cm/s)* axial map

Simulated CFD liquid holdup and pressure drop are represented in Figs 4 and 5 by lines as a function of liquid mass flux water when the reactor operates with air as the gas phase at different pressure values. The experimental data plotted in Figures 4 and 5 were available from the work developed by Nemec and Levec (2005) in where it was described in detail the experimental setup. In that work, liquid holdup was measured by a gravimetric method that consists in weighting the column in two different ways to have good reproducibility. After the bed was extensively prewetted, the reactor with dimensions similar to the ones described previously was operated first

in a high interaction regime and then reduced to the desired level at which the pressure drop and liquid holdup were measured.

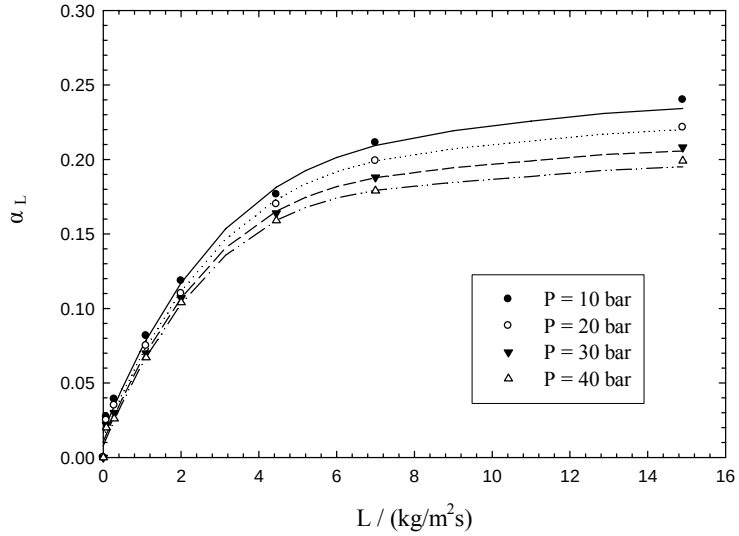

Figure XI.4. Liquid holdup as a function of liquid mass flux at constant pressure values (G = 0.5 kg/m^{2}s)

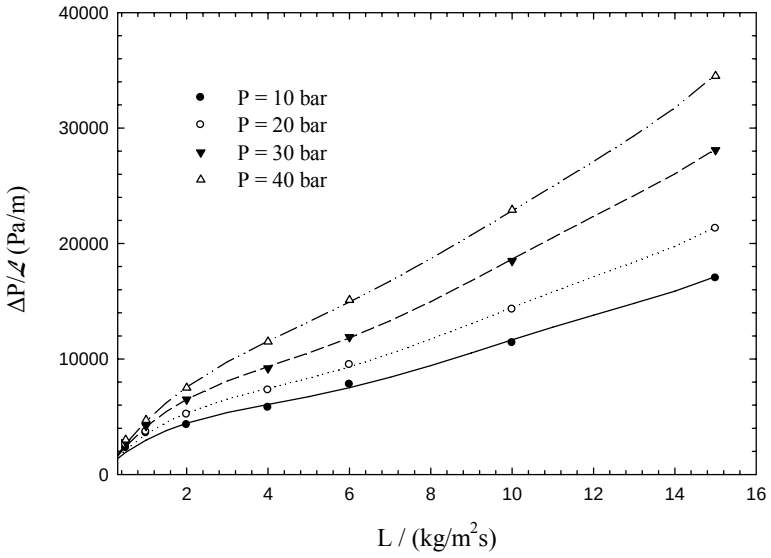

Figure XI.5. Pressure drop as a function of liquid mass flux at constant pressure values (G = 0.5 kg/m^{2}s)

These predictions are in good agreement with experimental values which enables the validation of our CFD model. In fact, the computational fluid dynamic model validation was carried out first in single-phase pressure drop simulations with only the gas phase flowing downward the bed; afterwards, two-phase flow is simulated to perform the final comparison between predicted hydrodynamic parameters and experimental data. In the whole range of Reynolds numbers for gas phase, pressure drop predictions are within 10% of error when comparing with the measurements provided by Nemec and Levec (2005). It should be pointed out that the operational region of flow

rates ($10<Re_G<400$) is that of particular interest to TBR and in this ambit Eulerian model fits the pressure drop data as well as liquid holdup quite well within acceptable limits of 10%. Moreover, our validation results are successfully compared against the results of Attou and Ferschneider (1999) for the pressure drop in a parity plot illustrated in Chapter X (Lopes *et al.*, 2007c). It should be also emphasized that the fixed-bed modelled in this work had the tube to particle diameter ratio higher than 10 so the available geometry and data taken from literature should not be affected by the reactor column wall. In accordance to Fig. XI.4, when the liquid mass flux increases, the liquid holdup also increases for L higher than 8 kg/m^{2}s being the growth rate smaller for the same total pressure value whereas an increase of the total pressure results in a considerable decrease of liquid holdup. The influence of the gas flow determined by a different operating pressure on the liquid holdup is less pronounced at low values of liquid mass fluxes. For example, in case the reactor operates at 40 bar, the liquid holdup is substantially lower compared when it operates at 10 bar. For gas-liquid flows, the total driving force increases partially due to the pressure gradient; nevertheless, as the liquid mass flux increases up to 8 kg/m^{2}s, the liquid holdup remains practically constant at 0.2 as observed by the threshold observed in Fig. XI.4 and only increases slightly. Comparing Fig. XI.4 and Fig. XI.5, where the pressure gradient per unit reactor length has been plotted as a function of liquid mass flux, we see that for very low values of pressure drop the liquid holdup are equally small. With the increase of pressure drop due to higher reactor pressures, the total driving force enlarges noticeably and, hence, the liquid holdup growth rate reduces when the liquid mass flux increases (Wammes and Westerterp, 1990). Moreover, the comparison between the hydrodynamic parameters determined at 10 and 40 bar shows that the effect of the reactor pressure has greater influence on the pressure drop than it has on the liquid holdup as expected.

XI.3.3 Effect of operating conditions on TOC conversion

Some TBR models reported in the literature considered isothermal operation and used either a pseudo-homogeneous or a heterogeneous model with plug-flow for gas and liquid phase while other models accounted for liquid flow non-uniformity by using an axial dispersion model or even a residence time distribution based model. In the present work, our CFD Euler-Euler two-fluid model incorporates the three fundamental balances, continuity, momentum and energy computed by means of phase-weighted averaging for turbulent multiphase flow. The TBR oxidation behaviour in terms of total organic carbon conversion is developed taking into account the kinetic expressions obtained in Chapter III (Lopes *et al.*, 2007b) dealing with the catalytic wet air oxidation of several phenolic acids (1200 ppm) over the Mn-Ce-O 70/30 catalyst prepared in our laboratory. The kinetic parameters of catalytic wet air oxidation for the phenolic mixture were calculated by means of the Generalized Kinetic Model (GKM), a lumped kinetic model widely used to describe the total organic carbon profiles in CWO reactions. GKM considers three types of

compounds: easier degraded reactants (***A***); intermediates with difficult degradation (***B***) and desired end products, namely carbon dioxide and water (***C***). In the oxidation process of the phenolic solutions with Mn-Ce-O 70/30, phenol and acetic acid were formed as intermediate compounds, being totally degraded during the treatment and the overall TOC practically reduced to zero. The activation energy and the pre-exponential factor were calculated by using the Arrhenius plot and the reaction rate constants as a function of temperature were then integrated in the TBR model as well as the individual reactions enthalpy computed from the difference between the enthalpy of formation of end products (CO_2 and H_2O) and initial reagents, considering total organic carbon conversion of the six phenolic acids. In the computational model, the liquid reactants were assumed to be non-volatile and the gas phase is pure at constant partial pressure of the reacting oxygen. The results of our simulations have assumed a uniform flow at the reactor entrance and that the catalyst diameter (2 mm) has a minor influence in terms of wall flow. In fact, according to the literature recommendations the catalyst geometry has significant effect on the wall flow treatment in FLUENT at catalyst spherical diameters higher than 5 mm. The effectiveness of the trickle-bed reactor for phenolic content conversion was investigated in terms of different reactor heating temperatures, total pressures, gas and liquid mass fluxes and initial concentrations of the pollutant.

The effect of temperature on TOC conversion at the reactor outlet is shown at steady-state in Fig. XI.6 for different liquid mass fluxes when the inlet is equal to the wall temperature. Negligible conversion was obtained for low temperatures and as the temperature increases, a considerable influence in total organic carbon abatement is observed leading to reduction values higher than 95% for lower liquid flow rates, i.e. for higher residence times.

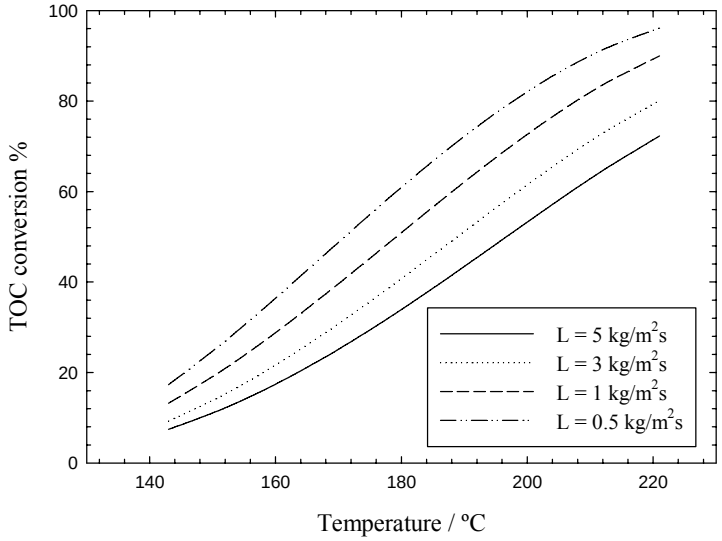

Figure XI.6. TOC conversion as a function of mean bed temperature for different liquid mass fluxes (G = 0.5 kg/m^{2}s; P = 30 bar)

Fig. XI.7 shows that the effect of reactor pressure on conversion is significantly lower than the one observed for the temperature and it can be seen that increasing pressure from 10 to 30 bar leads to higher TOC conversions. Therefore, for higher pressures, the gas density and its solubility also increases in the liquid phase. Additionally, an increase in gas pressure provides a high interaction force for the reactants to cover as much surface area as possible.

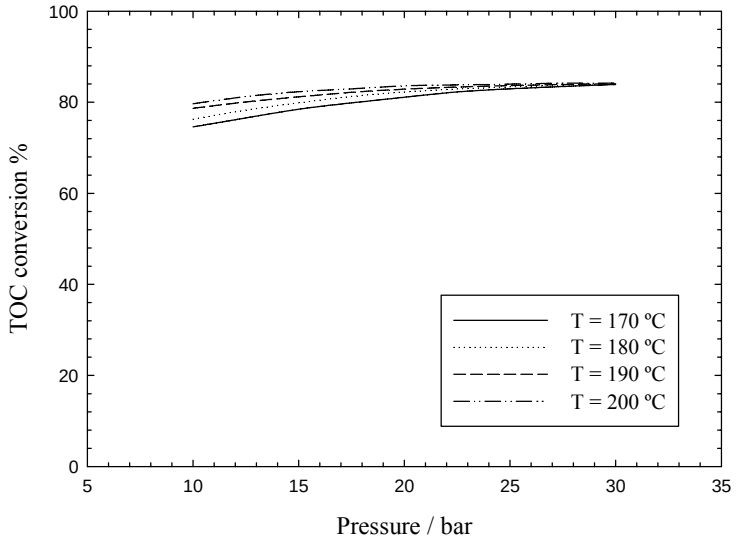

Figure XI.7. TOC conversion as a function of operating pressure for different temperatures (L = 0.5 kg/m^{2}s)

The effect of liquid mass flux on conversion is shown in Fig. XI.8 at different pressures while the result of gas mass flux on TOC degradation is represented in Fig. XI.9.

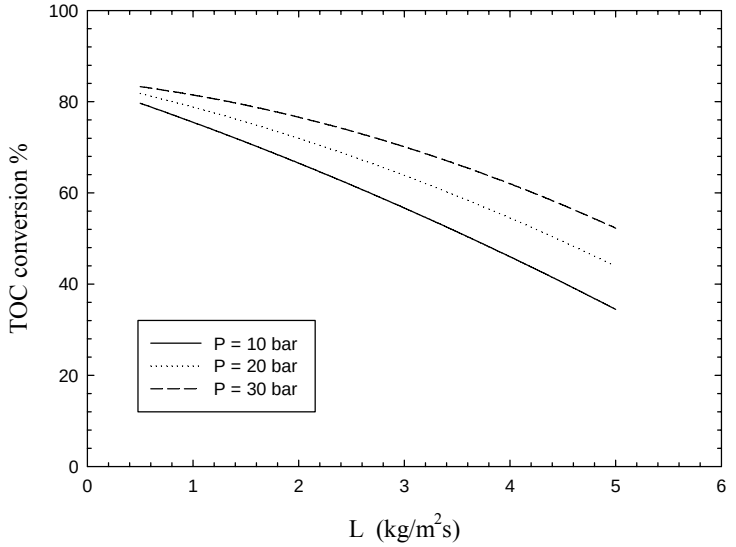

Figure XI.8. TOC conversion as a function of liquid mass flux for different pressures (G = 0.5 kg/m^{2}s)

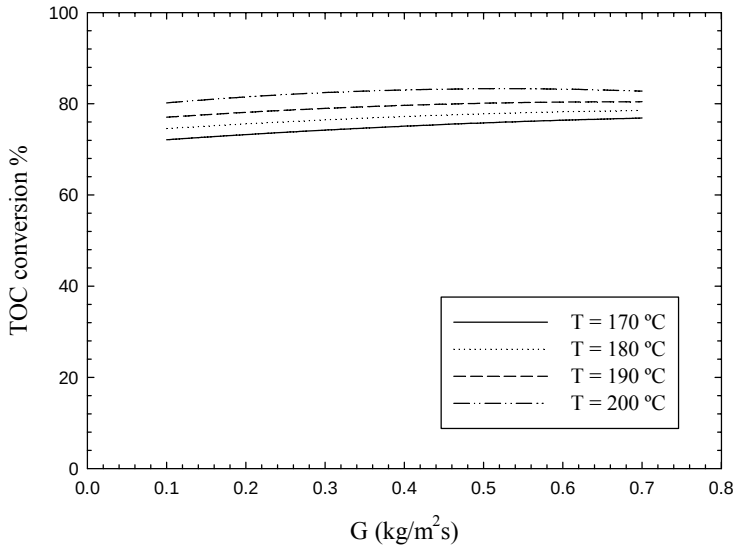

Figure XI.9. TOC conversion as a function of gas mass flux for different temperatures (L = 0.5 kg/m^{2}s; P = 30 bar)

TOC conversion gradually decreased with increasing liquid mass flux since the corresponding lower residence times of the reactant reduce the reaction time of pollutant. It has also been observed that the gas flow rate has not the same effect in TOC conversion. Fig. XI.9 shows a plot for conversion against gas mass flux revealing that for higher temperatures the degradation may reach a maximum value, increasing initially with gas flow rate and decreasing afterwards. This fact could be interpreted by the improvement achieved for higher temperatures in the distribution of liquid film over catalyst and hence wetting increases as observed by several authors.

The effect of inlet TOC concentration on CWO is shown in the Fig. XI.10 from 200 to 1200 mg/L improving TOC degradation. As the solution is highly diluted, the augment in initial total organic carbon content leads to higher oxidation rates and hence better conversions.

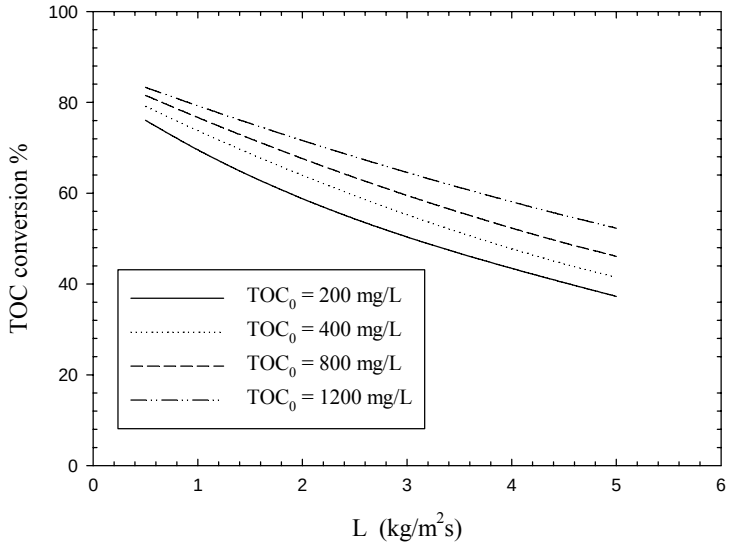

Figure XI.10. TOC conversion as a function of liquid mass flux for different initial TOC values (TOC_0) (G = 0.5 kg/m^{2}s; P = 30 bar)

XI.4. Conclusions

A trickle-bed reactor designed for the catalytic wet air oxidation of phenolic acids was modelled by means of computational fluid dynamics. The model consists in a Euler-Euler treatment for the fluid phases coupled with the energy equation. The numerical simulations are compared against experimental data to validate the predicted hydrodynamic parameters pressure drop and liquid holdup. Operating conditions were simulated with 10-30 bar of reactor pressure while gas and liquid mass flow rate were in the range 0.10 – 0.70 and 0.05 – 15 kg/m^{2}s, respectively.

The hydrodynamic studies pointed out that the liquid holdup increases as the liquid mass flux increases and decreases for higher operating pressure values. At low values of pressure drop the liquid holdup is small but with an increase value of pressure drop due to an increase of the reactor pressure, the liquid holdup growth rate reduces when the liquid mass flux increases. The influence of operating pressure on liquid holdup is less pronounced than it has on pressure drop.

Afterwards, the effect of operation conditions on TOC conversion is discriminated in terms of temperature, pressure, gas-liquid flow rate and initial pollutant concentration. TOC conversion depends heavily on the temperature bed while the operating pressure has minor influence in final conversion. When the liquid flow rate is decreased, the residence time increases and the conversion is higher but increasing the gas flow rate it was achieved an optimum value where the TOC conversion is maximum. Moreover, higher values of inlet pollutant concentration led also to higher conversions.

XI.5. Nomenclature

G	Gas mass flux, kg/m^{2}s
L	Liquid mass flux, kg/m^{2}s
$\mathcal{L}$	Reactor length, m
p	Pressure, bar
t	Time, s
T	Temperature, ºC
$\vec{u}$	Superficial vector velocity, m/s

Greek letters

α_q	Volume fraction of q^{th} phase
Δp	Total pressure drop, bar

Subscripts

G	Gas phase
L	Liquid phase
q	q^{th} continuous phase
S	Solid phase
0	Initial time reaction

XI.6. References

Al-Dahhan, M. H., Larachi, F., Dudukovic, M. P., Laurent, A. (1997). High pressure trickle-bed reactors: A Review. *Industrial and Engineering Chemistry Research* **36** (8), 3292-3314.

Attou, A., Ferschneider, G.A. (1999). Two-fluid model for flow regime transition in gas-liquid trickle-bed reactors. *Chemical Engineering Science* **54** (21), 5031-5037.

Bhargava, S. K., Tardio, J., Prasad, J., Foger, K., Akolekar, D. B. and Grocott, S. C. (2006). Wet Oxidation and Catalytic Wet Oxidation. *Industrial and Engineering Chemistry Research* **45** (4), 1221-1258.

Carbonell, R.G. (2000). Multiphase flow models in packed beds. *Oil & Gas Science and Technology* – Revue de l'IFP **55** (4), 417-425.

FLUENT 6.1. (2005). User's Manual to FLUENT 6.1. Fluent Inc. Centrera Resource Park, 10 Cavendish Court, Lebanon, USA.

GAMBIT 2 (2005). User's Manual to GAMBIT 2. Fluent Inc. Centrera Resource Park, 10 Cavendish Court, Lebanon, USA.

Gianetto, A., Specchia, V. (1992). Trickle-bed reactors: State of the art and perspectives. *Chemical Engineering Science* **47** (13-14), 3197-3213.

Goto, S., Smith, J.M. (1975). Trickle bed reactors performance: I hold-up and mass transfer effects. *A.I.Ch.E. Journal* **21** (4), 706-713.

Gunjal, P.R., Ranade, V.V., Chaudhari, R.V. (2005). Computational study of a single-phase flow in packed beds of spheres. *A.I.Ch.E. Journal* **51** (2), 365-378.

Holub, R.A., Dudukovic, M.P., Ramachandran, P.A. (1993). Pressure drop, liquid hold-up and flow regime transition in trickle flow. *A.I.Ch.E. Journal* **39** (2), 302-321.

Jiang, Y., Khadilkar, M.R., Al-Dahhan, M.H., Dudukovic, M.P. (2002). CFD modelling of multiphase in packed bed reactors: results and applications. *A.I.Ch.E. Journal* **48**, 716-730.

Lopes, R.J.G., Quinta-Ferreira, R.M. (2007a). Trickle-Bed CFD Studies in the Catalytic Wet Oxidation of Phenolic Acids. *Chemical Engineering Science* **62** (24), 7045-7052.

Lopes, R.J.G., Silva, A.M.T., Quinta-Ferreira, R.M. (2007b). Screening of catalysts and effect of temperature for kinetic degradation studies of aromatic compounds during wet oxidation. *Applied Catalysis B: Environmental* **73** (1), 193-202.

Lopes, R.J.G., Silva, A.M.T., Quinta-Ferreira, R.M. (2007c). Kinetic Modelling and Trickle-Bed CFD Studies in the Catalytic Wet Oxidation of Vanillic Acid. *Industrial and Engineering Chemistry Research* **46** (25), 8380-8387.

Nemec, D.; Levec, J. (2005). Flow through packed bed reactors: 2. Two phase concurrent downflow. *Chemical Engineering Science* **60** (24), 6958-6970.

Paraskeva, P., Diamadopoulos, E. (2006). Technologies for olive mill wastewater (OMW) treatment: a review. *Journal of Chemical Technology and Biotechnology* **81** (9), 1475-1485.

Sáez, A.E., Carbonell, R.G. (1985). Hydrodynamic parameters for gas liquid cocurrent flow in packed beds. *A.I.Ch.E. Journal* **31** (1), 52-62.

Sie, S.T., Krishna, R. (1998). Process development and scale up: III. Scale-up and scale-down of trickle bed processes. *Reviews in Chemical Engineering* **14** (3), 203-252.

Taylor, R., Krishna, R. 1993. Multicomponent Mass Transfer. *John Wiley and Sons Inc.*, New York.

van der Merwe, W., Nicol, W. (2005). Characterization of multiple flow morphologies within trickle flow regime. *Industrial and Engineering Chemistry Research* **44** (25), 9446-9450.

Wammes, W.J.A., Westerterp, K.R. (1990). The influence of reactor pressure on the hydrodynamics in a cocurrent gas–liquid trickle-bed reactor. *Chemical Engineering Science* **45** (8), 2247-2254.

XII. Assessment of CFD Euler-Euler Method for CWO Modelling in Trickle-bed Reactor[1]

Trickle-bed reactors are envisaged as a breakthrough technology in industrial wastewater treatment plants. According to the literature, the generous research in environmental reaction engineering has indicated that scale-up of TBR is erroneous if one considers isothermal operation and uses either a pseudo-homogeneous or a heterogeneous model with plug flow for gas and liquid phases. Even though axial dispersion model may account for liquid distribution non-uniformity, the reaction parameters are strongly dependent on the reactor fluid dynamics.

In our case-study, we developed an Eulerian CFD framework based on empirical interphase coupling parameters in the momentum balance equation. After the hydrodynamic validation, the catalytic wet oxidation of phenolic wastewaters was taken as an example to evaluate axial and radial profiles for the total organic carbon depletion and temperature along the packed bed. The theoretical calculations were compared against experimental data taken from a trickle-bed reactor pilot plant. The Eulerian computations have shown promising results on how fluid dynamics can be correlated with chemical reaction, namely on the prediction of total organic carbon conversions attained at different temperatures.

XII.1. Introduction

Bisphenols, alkylphenols, trihydroxybenzenes, hydroxybiphenyls, catechols and phenol ethers belong to a class of toxic organic compounds listed by the EPA (Environmental Protection Agency) as priority pollutants. These compounds often contaminate the natural water bodies and are produced in the petrochemical, pharmaceutical, pesticide, dye and agro-industries. Phenol derivatives are characterized by their toxicity, difficulty and persistency at the time of water decontamination. Consequently, highly efficient techniques such as photocatalytic and sonochemical degradation, Fenton oxidation, ozonation, microwave irradiation, supercritical water oxidation and wet air oxidation (WAO) are advanced oxidation techniques, which mineralize organics to harmless final products using appropriate catalysts (Collin *et al.*, 2009; Rivas *et al*., 2008; Zhou *et al.*, 2007; Cañizares *et al.*, 2007; Mandal *et al.*, 2004; Pera-Titus *et al*., 2004; Esplugas *et al.*, 2002).

[1] *This Chapter is based upon the publication Lopes and Quinta-Ferreira (2009a)*

Among these alternative destruction technologies, catalytic wet air oxidation (CWAO) has been used in the treatment of wastewaters containing either moderately concentrated non-toxic or bio-toxic organic pollutants. The biological refractory pollutants are oxidised by dissolved molecular oxygen which can be further accelerated with a homogeneous or heterogeneous catalysts. However, the industrial application of CWAO has been controlled by the scarce development of catalysts that are stable at high operating values of temperature and pressure (Bhargava *et al.*, 2006). The recent development of economical and stable catalysts is an encouraging factor concerning the catalyst deactivation and the formation of carbonaceous deposits that hampers the access to the catalyst sites. The selection of a suitable reactor in another key criterion that can affect the industrial implementation of advanced wastewater treatment facilities. While most laboratory studies have been carried out in slurry and/or fixed-bed reactors, recent comparisons between those operating configurations have shown that fixed-bed reactors are advantageous either in terms of process selectivity or stability. While agitated reactors (slurry or spinning basket) exhibiting high liquid-to-catalyst ratio can promote negatively parallel homogeneous polymerisation reactions, fixed-bed reactors in CWAO have emerged as the best choice for systems with high potential for polymerisation reactions (Pintar and Levec, 1994; Stüber *et al.*, 2001). According to several experimental studies on activated carbon, the increasing catalyst activity loss and lower selectivity towards complete mineralisation strongly affects the organic carbon decontamination rates when one operates with batch stirred vessels (Stüber *et al.*, 2001). Nevertheless, Maugans and Akgerman (2003) among have shown that Total Organic Carbon (TOC) depletion rates on a co-current fixed-bed reactor can be successfully predicted with kinetic expressions obtained from batch reaction studies.

Experimental studies on CWAO indicated that trickle-bed reactors have often been implemented in contrast with other operation modes for gas-liquid-solid reactions (Pintar *et al.*, 2001; Tukac *et al.*, 2001; Stüber *et al.*, 2001; Fortuny *et al.*, 1999; Goto and Smith, 1975). In this ambit, three important hydrodynamic parameters, two-phase pressure drop, total liquid holdup and axial dispersion have been selected as the major benchmarking parameters in the comparison of trickle-bed reactor operation modes. Two-phase pressure drop and total liquid holdup are higher for the upflow mode of operation at lower gas and liquid velocities, but with increasing flow rates, the two parameters were comparable for upflow and downflow modes as stated by Chander *et al*. (2001). Saroha and Khera (2006) demonstrated that the values of Peclet number were higher in downflow mode of operation for the entire range of flow rates studied indicating the presence of lower backmixing in the downflow mode of operation and a comparison of the experimental observation with the correlations available in literature is presented.

One should also bear in mind that the design rules of multiphase reactors are still weak and, for this reason, sophisticated scale-up procedures based on modern Computational Fluid Dynamic (CFD) codes have received much more attention during the last decade (Dudukovic *et al*., 2002). Given that traditional scale-up procedures are prone to more uncertainty and it is not possible in general to relate via simple scale-up rules the performance of laboratory size units to large-scale reactors, further investigation of CWAO kinetics in another reactor types coupled with CFD models of the large units are usually becoming the preferred route in process development. CFD show promising results in understanding fluid dynamics and its interactions with chemical reactions. Gunjal and Ranade (2007) have developed a CFD model for simulating flow and reactions in the laboratory scale and commercial scale hydro-processing trickle-bed reactors. The CFD models were first evaluated by comparing the model predictions with the published experimental data. The models were then used to understand the influence of porosity distribution, particle characteristics and reactor scale on overall performance and validated model was used to predict the performance of the commercial scale reactor.

Eulerian based CFD models are being constantly developed in order to gain a deep understanding how the hydrodynamic parameters affect the performance of trickle-bed reactors. Lopes and Quinta-Ferreira (2008) presented an Euler-Euler model and solved for a three-dimensional representation of the catalytic bed. The Eulerian mutiphase model was successfully used in the computation of pressure drop and liquid holdup and over a wide range for the calculated flow regime as a function of gas and liquid flow rates, the CFD theoretical predictions were in good agreement for both hydrodynamic parameters. Later, Lopes and Quinta-Ferreira (2009b) studied the interstitial phenomena and several computations on multiphase flow distribution have been accomplished querying the effect of gas and liquid flow rate on overall hydrodynamics. Lopes and Quinta-Ferreira (2009c) also investigated turbulence phenomena with four RANS multiphase turbulence models. The authors have found that standard k-ε dispersed turbulence models gave the better compromise between computer expense and numerical accuracy in comparison with both realizable, renormalization group and Reynolds stress based models. Several computational runs were performed at different temperatures for the evaluation of either axial velocity and turbulent kinetic energy profiles for gas and liquid phases. Flow disequilibrium and strong heterogeneities detected along the packed bed demonstrated liquid distribution issues with slighter impact at high temperatures.

It is well known that various critical issues arise in TBR scale-up if one is only concerned with hydrodynamics. CFD models have also to be validated at reacting flow conditions, which can improve the global understanding of further industrial application of CWAO. From the above survey and to the best of our knowledge, none experimental study on CWAO have been correlated

with CFD at reaction conditions. The Eulerian simulations carried out so far have only been addressed the hydrodynamics and, with the present contribution, an Euler-Euler model results and experimental data are presented here for the sake and completeness of CFD validation. This task will be useful for understanding the complex hydrodynamics, its interaction with chemical reactions and influence of different reactor scales on performance of the TBRs.

XII.2. CFD Model

XII.2.1. Euler-Euler conservation equations

The Eulerian framework, including the description of the continuity and momentum equations, and the closure equations of the drag force formulation was developed using the model of Attou and Ferschneider (1999) as shown in Equations (V.1), (V.2) and (V.4)-(V.7) in Chapter V, respectively. According to this Chapter, the *k-ε* dispersed turbulence model (Equations (V.9) and (V.10)) was used for the reaction studies. The species continuity balance was expressed in Equation (X.1) in Chapter X where it was also presented the conservation of energy in Eulerian multiphase applications that is described by a separate enthalpy equation for each phase as shown in Equation (X.2). Volume averaged properties of fluids were used for calculating the flux across the control cell. Two-film theory was used for accounting mass transfer. The resistance in gas-liquid film was considered as the rate limiting resistance (Bhaskar *et al*., 2004). Mass transfer coefficient was computed according to Satterfield *et al*. (1978) correlation and heat transfer coefficient was calculated according to the correlation developed by Boelhouwer *et al*. (2001) as expressed by Equations (XII.1) and (XII.2), respectively.

$$Sh = 0.815\, Re^{0.822}\, Sc^{1/3} \qquad \text{(XII.1)}$$

$$Nu = 0.111\, Re^{0.8}\, Pr^{1/3} \qquad \text{(XII.2)}$$

XII.2.2. Simulation setup

The discretization of the governing equations is done by the finite-volume method as described in Chapter V and X. A segregated implicit solver available in commercial CFD package FLUENT (FLUENT 6.1, 2005) was employed to evaluate the resulting linear system of equations. The conditions required for grid convergent results are based on a 1% relative error criterion and the simulations accuracy has been assessed by comparisons to experimental data. The computational mesh representing the solid catalyst of the trickle-bed reactor was created using the integrated solid modelling and meshing program GAMBIT (GAMBIT 2, 2005). All the calculations were carried out on a workstation farm characterized by AMD64 Dual-Core technology. The description of the calculation procedure for the physical properties and mass transfer parameters are given in section X.2.

XII.3. Experimental

XII.3.1. Materials

Low- to moderate-molecular weight phenolic compounds are known to be the major contributors to the toxicity and the antibacterial activity of olive oil wastewater. Hence, six phenolic-like compounds were obtained from Sigma-Aldrich to mimic the bactericide behaviour of olive oil processing wastwaters, namely: syringic, vanillic, *3,4,5*-trimethoxybenzoic, veratric, protocatechuic and *trans*-cinnamic acid. The simulated effluent was prepared through an aqueous solution with 200 ppm for each phenolic acid. Following the screening studies performed in batch mode, a commercial catalyst CuO-MnO_x (N-140: CuO-22%; MnO_x - 50%) available from the Süd-Chemie Group, Munich was employed throughout the trickle-bed reactor studies. N-140 catalyst was provided as cylindrical pellets with regular dimensions 4.8×4.8 mm and density 0.9 kg/L. The commercial catalyst has a specific surface area 161 m^2/g. For CFD studies spherical particles were used with an equivalent diameter of 4.8 mm based on the equal ratio area/volume of both cylindrical and spherical geometries. The ratio [catalyst surface area]/[catalyst particle volume] is 1250 m^2/m^3; the bulk porosity is 0.44 and the bulk density is 0.504 kg/L.

XII.3.2. Equipment

The trickle-bed reactor studies have been carried out in a pilot plant comprising a cylindrical reactor in stainless steel (SS-316) with 50 mm of internal diameter and 1.0 m length as illustrated in Fig. XII.1. A gas-liquid distributor is attached at the top of the vertical column to promote a better multiphase flow distribution at the reactor inlet. In order to maintain the flux of both phases approximately uniform over the cross-sectional area, the liquid distributor was designed with 60 capillary tubes (0.12 mm internal diameter). The capillaries are held between two plates 1 cm apart. The bottom plate has circular holes around the capillaries: the holes are slightly larger in diameter than the outer diameter of the capillary tubes. The gas phase was introduced into the chamber formed between the plates, and it exited the distributor through these holes. The top of the packing was 0.5 cm below the distributor, while the packing itself was kept in place by a stainless steel mesh placed at the bottom of the column. A gas-liquid separator is connected to the bottom of the trickle-bed reactor.

An upstream electronic mass flow controller and a downstream electronic backpressure controller (*Brooks* 5866 series with maximum pressure operation of 100 bar) were used to obtain and maintain the desired flow of gas and operating pressure. The pressure drop across the packed bed was monitored with a high-pressure differential transducer, which was connected to the top and the

bottom of the reactor bed. The liquid phase was delivered to the reactor by a high-pressure *Dosapro Milton Roy* (model XB140K5A100 – SS 316) and can work up to 100 bar and 114 L/h, while the gas phase was delivered to the reactor from high-pressure gas cylinders. The liquid feed was preheated by an external oven from *Carbolite Peak Series* PN120 1500 W equipped with a PID controller for temperature stability ± 0.5K and 7 electrical heating jackets (800W) were attached to the trickle-bed reactor wall.

Total organic carbon was measured with a *Shimadzu 5000 TOC Analyser*, which operates based on the combustion/nondispersive infrared gas analysis method. The parameter uncertainty in TOC measurement, quoted as the deviation of three separate measurements, was never larger than 2% for the range of the TOC concentrations.

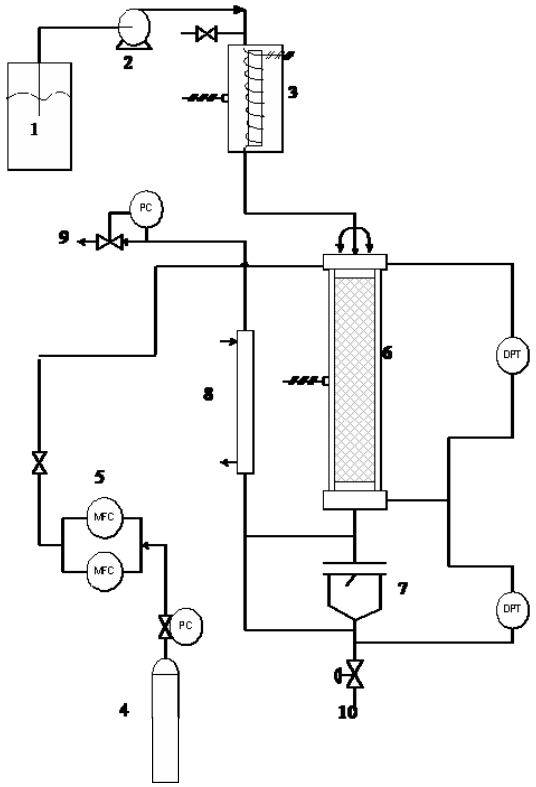

1 – Effluent feed tank
2 – High-pressure pump
3 – Oven preheater
4 – Air feed cylinder
5 – Mass flow controller
6 – Trickle-bed reactor
7 – Gas-liquid separator
8 – Gas-liquid condenser
9 – Back-pressure controller
10 – Liquid sewer

Figure XII.1. Schematic diagram of trickle-bed reactor experimental set-up

XII.3.3. Experimental procedure

The liquid feed was preheated at the temperature set-point (160, 200ºC) and pure air (99.999 %) was used as the oxygen source and flowed from the rack of gas cylinders through the mass flow controller into the top of the reactor where it was *mixed* with the phenolic acids solution feed at the gas-liquid distributor before entering the reactor. The trickle-bed reactor configuration was such that the feed passed over a short bed (length: 5 cm) of inert glass beads before entering the catalyst zone. After exiting the reactor the effluent was cooled and depressurized.

The reactor was loaded with 990 g of N-140 catalyst and run continuously until the completion of the flow reactor studies. Liquid flow rate was maintained constant in the range 1-15 kg/m^{2}s and the air inlet flow rate was maintained in the range 0.1-0.7 kg/m^{2}s which allows one to operate in the trickling flow conditions (Al-Dahhan *et al*., 1997). The flow rates were kept constant throughout the trickle bed studies in order to maintain consistent hydrodynamics (liquid holdup and two-phase pressure drop) in the reactor to eliminate side effects such as natural pulsing flow that would exist at the upper values for the gas and liquid flow rates. Pressure was maintained at approximately 30 bar while the temperature range studied was from 160ºC to 200ºC. The temperature along the different axial points of the reactor is monitored by means of six *Omega* thermocouples (*K-type*) inserted in one single rod in the radial centre of the reactor. The trickle-bed reactor has five equidistant sample points disposed axially.

XII.4. Results and Discussion

XII.4.1. Eulerian hydrodynamic validation

The Eulerian framework has been proposed to model trickle-bed reactors at elevated pressures in the prediction of the hydrodynamic parameters pressure drop and liquid holdup. At non-reacting flow conditions, the accuracy of three-dimensional simulations was studied following the successive refinement of tetrahedral meshes. Lopes and Quinta-Ferreira (2008) ascribed the effect of packing size on the pressure drop and liquid holdup by different specific surface areas of the packing material for the trickle-bed reactor as presented in Chapter V. It was found that the packing characteristics affect the gas and liquid velocity with the effect of gas velocity being prominent at high superficial gas mass velocities. In this ambit, the theoretical calculations pointed out how the interphase phenomena affected the integral hydrodynamic parameters revealing again the major effect of the gas phase in trickling flow conditions.

The application of different turbulence models including standard, realizable and RNG k-ε models as well as RSM for the hydrodynamics simulation of high-pressure trickle-bed reactor was evaluated thoroughly with the Eulerian multiphase model in Chapter VI. On the parametric optimization of several numerical solution parameters, the CFD calculations were examined in terms of tetrahedral mesh size, time step, convergence criteria and discretization schemes. Lopes and Quinta-Ferreira (2009c) found that coupling a *monotonic upwind scheme for conservation laws* (MUSCL) with a standard k-ε dispersed turbulence can reduce the numerical dispersion that arose in the multiphase flow simulations and, concomitantly, giving the better compromise between numerical accuracy and computational expenditure.

Aiming to investigate the multiphase flow distribution phenomena at high-pressure operation, Lopes and Quinta-Ferreira (2009b) performed several Eulerian computations with different gas-liquid distributors (Chapter VII). The interstitial phenomena were investigated through time averaged axial and radial profiles of liquid holdup and two-phase pressure drop and it was found that liquid flow rate had more prominent effect on radial pressure drop at higher values. Additionally, the gas flow rate had a pronounced influence at lower interaction regimes and the increase of operating pressure on multiphase flow distribution was found to smooth the radial profiles for both hydrodynamic parameters.

After performing the Eulerian hydrodynamic validation at non-reacting flow conditions, those optimum numerical solution parameters were integrated into the multiphase flow model aiming to evaluate the axial and radial mapping of reaction parameters (temperature and total organic carbon concentration) in the catalytic wet air oxidation of phenolic wastewaters.

XII.4.2. Reaction studies

Gas-liquid flow inside the TBR was simulated using the Eulerian CFD model and the predicted flow field (velocities and volume fractions of different phases) was further used for solving species transport equations for simulating the pollution abatement in the trickle-bed reactor. Aiming to evaluate the dynamic behaviour of the trickle-bed reactor under reacting flow conditions, several Eulerian CFD computations were performed on the catalytic wet air oxidation of phenolic wastewaters. Each simulation is characterized by the axial and radial total organic carbon concentration and temperature profiles obtained for the trickle-bed reactor startup until the steady-state was reached. In this ambit, an initial perturbation on the inlet total organic carbon concentration was accomplished and the dynamic response of the trickle-bed reactor predicted by the CFD model is compared against the experimental data on bulk temperature and TOC conversions. In order to replicate computationally the TBR oxidation startup, the reactor was firstly heated at the wall temperature (T_w = 160 and 200 ºC) and at the time $t^* (t/\tau)$ = 0, the feed stream previously heated up at the bed temperature entered the reactor representing a step change in the inlet total organic carbon concentration. High order discretization scheme (MUSCL) for the Eulerian momentum balance equation has been employed so as to avoid the numerical diffusion that arose during the CFD simulations.

Axial Total Organic Carbon profiles

Figures XII.2 and XII.3 show the transient axial profiles predicted by Eulerian CFD model of the mean radial values of the bulk-phase total organic carbon concentration for $T_0 = T_w$ = 160 and 200 *ºC*, respectively. As expected, the increase of temperature led to higher TOC decontamination

rates since the catalytic wet air oxidation follows the Arrhenius law. At $T_0 = T_w = 160$ ºC, the outlet TOC conversions were 75.5, 76.8, 77.8, 78.7, 79.3 and 82.0% for t^* (t/τ) = 1, 2, 4, 6, 8, 10 as shown in Fig. XII.2. If one increases the wall/inlet temperature up to $T_0 = T_w = 200$ ºC, the TOC conversions are increased to 82.3, 82.8, 83.2, 83.6, 83.8 and 84.8% for t^* = 1, 2, 4, 6, 8, 10, respectively. Therefore, the steady-state was reached around t^* = 10 for both operating temperatures, specifically 82.0% and 84.8% for $T_0 = T_w = 160$ and 200 ºC, respectively. According to these axial concentration profiles, the Eulerian model agreed better with the experimental data for the highest simulated wall/inlet temperatures at steady-state.

As it can be seen through the comparison of the axial total organic carbon concentration profiles shown in Figs. XII.2 and XII.3, there is no reasonable difference between the axial TOC profiles obtained at t^* = 1 and t^* = 10 (steady-state) for the highest simulated temperature ($T_0 = T_w = 200$ ºC). In fact, the experimental data lie over the CFD profiles when the wall/inlet temperature was 200ºC; notwithstanding a higher difference was detected when the catalytic wet air oxidation was simulated with a wall/inlet temperature 160ºC. Although the qualitative behaviour of TBR was almost the same with both simulated temperatures, it should be pointed that the backmixing degree was higher at $T_0 = T_w = 200$ºC and the relative errors between computed TOC conversions and experimental data were higher for the lowest simulated temperature ($T_0 = T_w = 160$ºC).

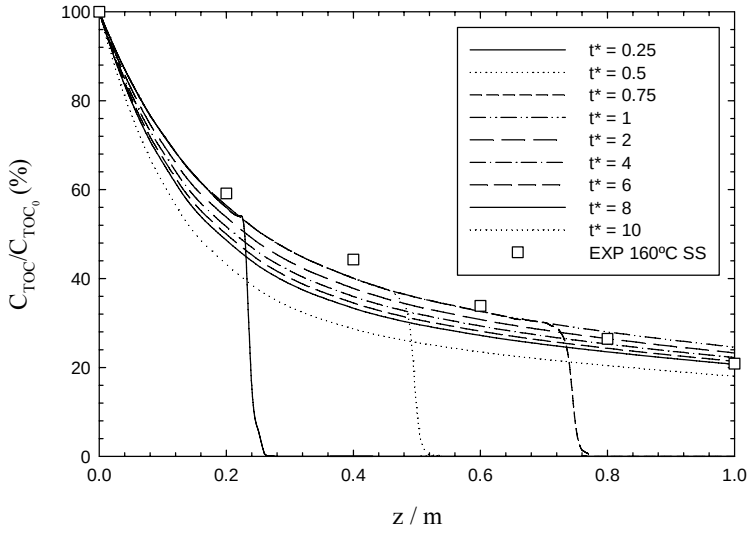

Figure XII.2. Mean radial bulk total organic carbon profiles for axial coordinate at transient conditions for different operating dimensionless times, , t^* ($T_0 = T_w = 160$ ºC, L = 5 kg/m^{2}s, G = 0.5 kg/m^{2}s, P = 30 bar)

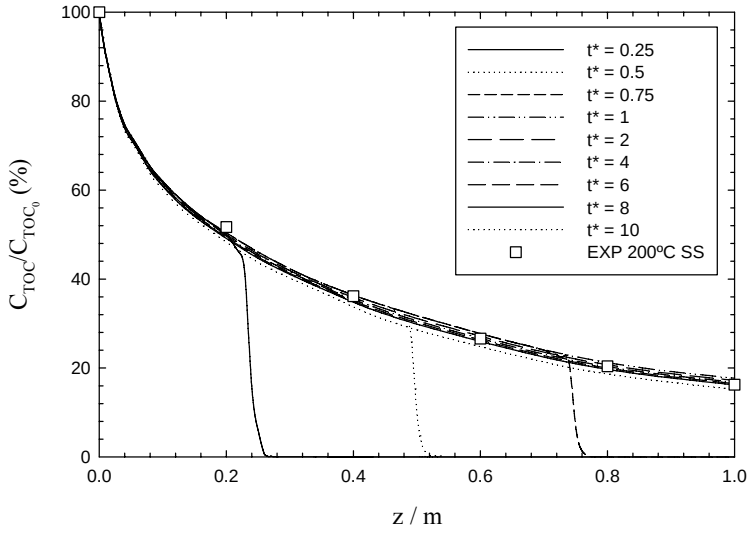

Figure XII.3. Mean radial bulk total organic carbon profiles for axial coordinate at transient conditions for different operating dimensionless times, t^* ($T_0 = T_w = 200$ ºC, L = 5 kg/m^{2}s, G = 0.5 kg/m^{2}s, P = 30 bar)

Axial Temperature profiles

Figures XII.4 and XII.5 show the influence of the operating temperature on the computed thermal profiles and experimental data attained for the catalytic wet air oxidation of phenolic wastewater. If one compares the axial temperature and total organic carbon concentration profiles previously shown in Figures XII.2 and XII.3, it can be concluded that the operation time required for the thermal wave and for the TOC wave to achieve the steady-state is roughly the same, $t^* = 10$. Conversely, the Eulerian CFD model underpredicted the temperature elevation in comparison with the experimental data obtained for both operating temperatures.

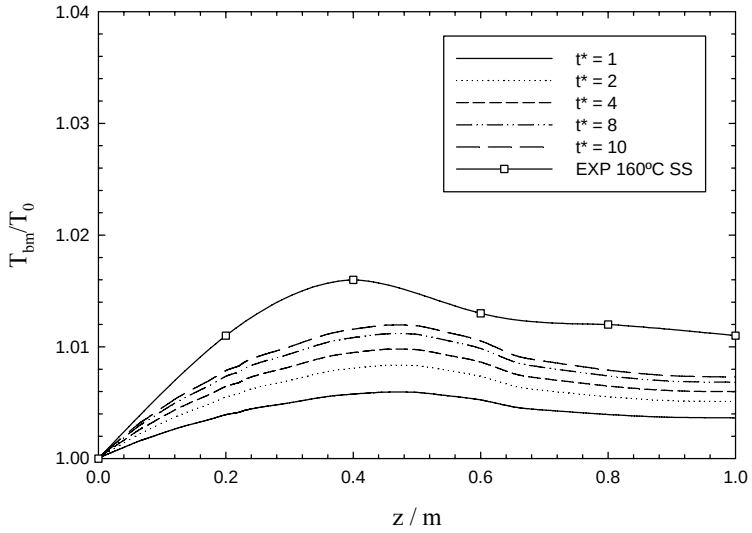

Figure XII.4. Mean radial bulk temperature profiles for axial coordinate at transient conditions for different operating dimensionless times, t^* ($T_0 = T_w = 160$ ºC, L = 5 kg/m^{2}s, G = 0.5 kg/m^{2}s, P = 30 bar)

At the lowest temperature ($T_0 = T_w$ = 160ºC), the axial temperature profiles computed by the Eulerian CFD model indicated that the hotspot is located nearly the axial centre of the trickle-bed reactor (z = 0.45 m) whereas the CFD simulation performed at the highest temperature revealed that the hotspot was achieved earlier (z = 0.36 m). None of the simulated operating temperatures in the catalytic wet air oxidation have shown a superior quantitative prediction on the TBR axial temperature being almost the same the relative errors between the computed and the experimental data.

Additionally, the major difference between the Eulerian axial temperature profiles shown in Figs. XII.4 and XII.5 can be depicted from the intensity of the maximum mean radial bulk temperature. When the CFD simulation was carried out at $T_0 = T_w$ = 160 ºC the maximum temperature was 161.9 ºC and it was increased up to 203.2 ºC when at $T_0 = T_w$ = 200 ºC. This fact is directly related with the positive effect of wall/inlet temperature on the catalytic wet air oxidation so that the TOC oxidation rate was promoted by the temperature increase from 160 to 200 ºC. One should also bear in mind that the saturated oxygen concentration raises significantly with both increased temperature and oxygen partial pressure in the operating range typical for wet air oxidation. Taking into account that the present CFD simulations were performed at isobaric conditions, a temperature increase from 160 to 200 ºC increased oxygen solubility in water at these conditions providing a strong driving force for mass transfer and caused a sharper elevation for the bulk temperature also supported by the experimental data in Fig. XII.5.

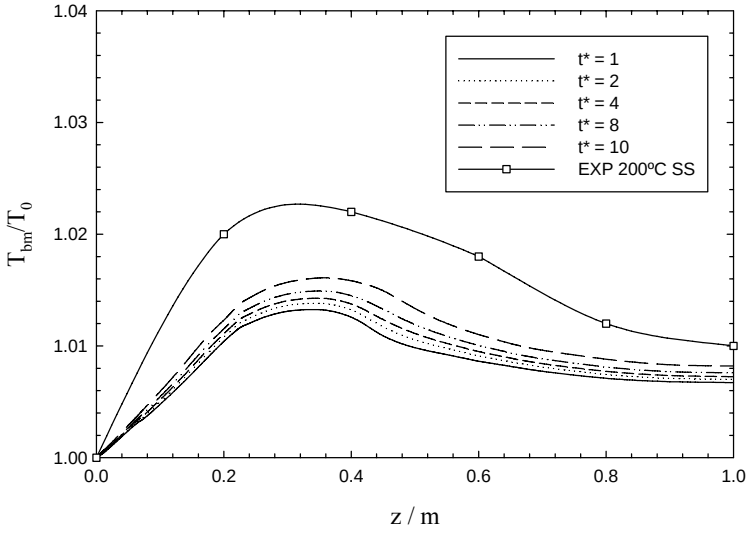

Figure XII.5. Mean radial bulk temperature profiles for axial coordinate at transient conditions for different operating dimensionless times, t^* ($T_0 = T_w$ = 200 ºC, L = 5 kg/m^{2}s, G = 0.5 kg/m^{2}s, P = 30 bar)

Radial Total Organic Carbon profiles

Figure 5 shows the transient radial profiles of total organic carbon concentration predicted by the Eulerian CFD model at $T_0 = T_w = 160$ ºC and $z = 0.45$ m, while Fig. XII.7 shows the radial total organic carbon concentration profiles obtained at $T_0 = T_w = 200$ ºC and z = 0.36 m. According to Fig. XII.6, the radial concentration profiles exhibited 5.0% of difference between the TBR centre and the wall at the steady-state and $T_0 = T_w = 160$ ºC. In fact, if one increases the wall/inlet temperature up to 200ºC the difference of total organic carbon conversions between these radial coordinates became 7.6% which reinforce the poor radial mixing effects attained at the hotspot zone.

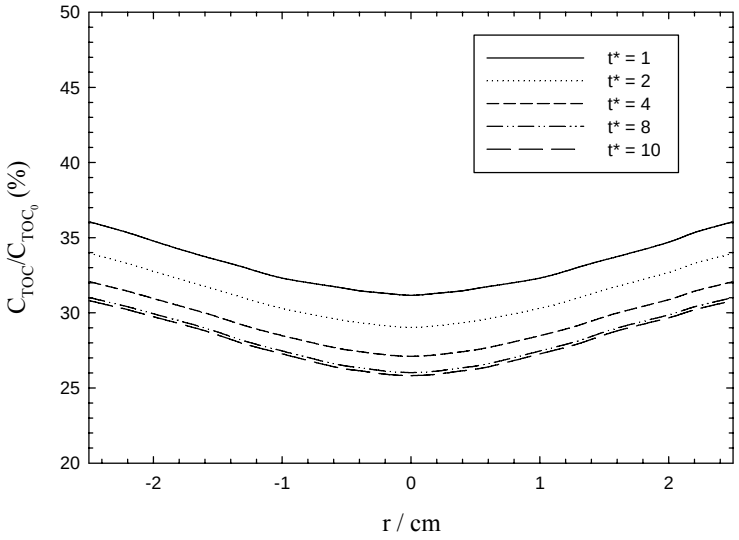

Figure XII.6. Radial total organic carbon profiles at the hot spot for different operating dimensionless times , t^* ($T_0 = T_w$ = 160 ºC, L = 5 kg/m^{2}s, G = 0.5 kg/m^{2}s, P = 30 bar)

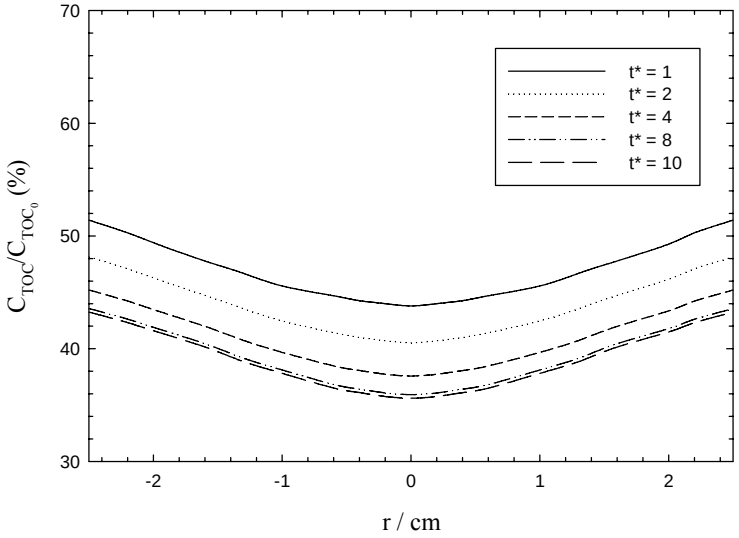

Figure XII.7. Radial total organic carbon profiles at the hot spot for different operating dimensionless times, t^* ($T_0 = T_w$ = 200 ºC, L = 5 kg/m^{2}s, G = 0.5 kg/m^{2}s, P = 30 bar)

The behaviour shown by the radial TOC profiles obtained by the CFD model at different temperatures is a consequence of the higher temperature that endorses higher TOC removal efficiencies. The higher TOC conversions achieved at the trickle-bed reactor centre can be also sustained by the gas-liquid interaction forces that enable and improve a better multiphase flow distribution previously analysed in Chapter VII.

Radial Temperature profiles

Figures XII.8 and XII.9 represent the transient radial temperature profiles computed for the hot spot at z = 0.45 and 0.36 m for $T_0 = T_w$ = 160 and 200 *ºC*, respectively. As already advanced in the discussion of radial TOC profiles, the radial temperature distribution was identical for both simulated wall/inlet temperatures. According to Fig. XII.8, the maximum temperature obtained at $T_0 = T_w$ = 160 *ºC* was 162.2 ºC which is comparable to the value already obtained for the axial temperature profile at the same operating temperature. It should be stressed out that although the literature-recommended ratio between the trickle-bed reactor length and diameter obey to the ratio $L/d \leq 20$, an equivalent temperature elevation was computed by the Eulerian CFD model for the axial and radial temperature profiles. The increase of wall/inlet temperature up to 200ºC generated a maximum temperature difference of 3.7 ºC between the TBR centre and wall at the hotspot which was also similar to the difference attained along the axial coordinate. After the comparison between the radial total organic carbon concentration and temperature profiles plotted in Figs. XII.6-XII.9, it can be observed that TOC concentration is decreasing from the wall to the centre whereas the bulk temperature is increasing from the reactor wall to the centre.

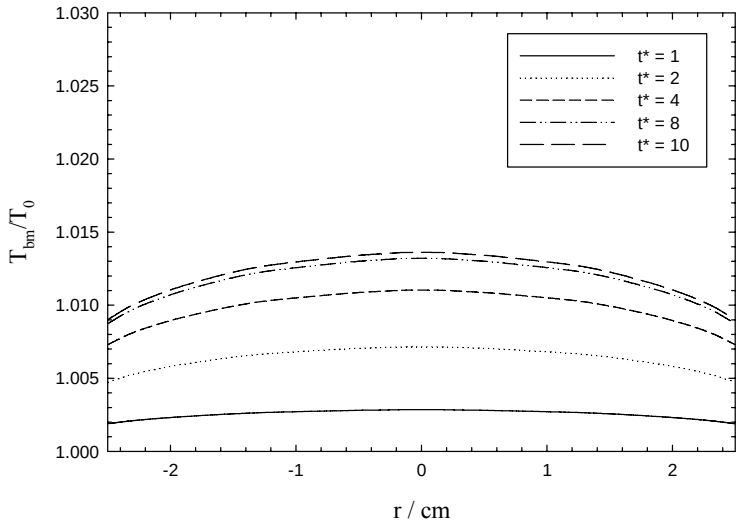

Figure XII.8. Radial temperature profiles at the hot spot for different operating dimensionless times, t^* ($T_0 = T_w$ = 160 ºC, L = 5 kg/m^{2}s, G = 0.5 kg/m^{2}s, P = 30 bar).

This fact can be explained by the chemical reaction thermodynamics which promotes higher TOC decontamination rates at elevated temperatures. Notwithstanding, the Eulerian CFD simulations performed at $T_0 = T_w = 160$ and 200 ºC indicated that steady-state was reached roughly at $t^* = 10$.

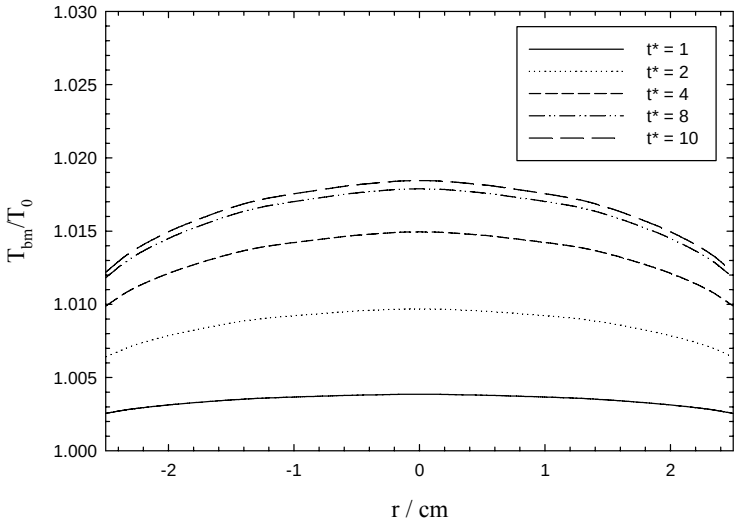

Figure XII.9. Radial temperature profiles at the hot spot for different operating dimensionless times, t^* ($T_0 = T_w = 200$ ºC, L = 5 kg/m^{2}s, G = 0.5 kg/m^{2}s, P = 30 bar).

XII.5. Conclusions

Aiming to investigate the dynamic behaviour of a pilot trickle-bed reactor, an Eulerian CFD model was developed to simulate the gas-liquid flow through a catalytic bed of spherical particles. Following the hydrodynamic corroboration, the Eulerian CFD model was validated with experimental data taken from a trickle-bed reactor pilot plant specifically designed for the catalytic wet oxidation of low- to moderate strength wastewaters. Several computational runs were carried out under unsteady-state operation to evaluate the dynamic performance addressing the total organic carbon concentration and temperature profiles. The effect of operating temperature was examined in terms of axial/radial TOC and temperature profiles. During the CFD model validation at the higher operating temperature, it was found that the Eulerian model predicted better the TOC removal efficiency than for the lower operating temperature. However, the axial bulk temperature profiles have not shown the same confidence level of temperature prediction as demonstrated in the axial TOC conversion profiles. Nevertheless, the Eulerian CFD framework is envisaged as a valuable tool to accelerate the industrial implementation of trickle-bed reactors in advanced wastewater treatment plants.

XII.6. Nomenclature

G	Gas mass flux, kg/m^{2}s
L	Liquid mass flux, kg/m^{2}s
Nu	Nusselt number
p	*P*ressure, bar
Pr	Prandtl number
r	Reactor radius, m
Sh	Sherwood number
t	Time, s
t^*	Dimensionless time, (t/τ)
T	Temperature, K
TOC	Total organic carbon, ppm

Greek letters

α_q	Volume fraction of q^{th} phase
Δp	Total pressure drop, Pa
τ	Residence time, s

Subscripts

G	Gas phase
L	Liquid phase
w	Wall
0	Initial time reaction

XII.7. References

Al-Dahhan, M. H., Larachi, F., Dudukovic, M. P., Laurent, A. (1997). High pressure trickle-bed reactors: A Review. *Industrial and Engineering Chemistry Research* **36** (8), 3292-3314.

Attou, A., Ferschneider, G.A. (1999). Two-fluid model for flow regime transition in gas-liquid trickle-bed reactors. Chemical Engineering Science **54** (21), 5031-5037.

Bhargava, S. K., Tardio, J., Prasad, J., Foger, K., Akolekar, D. B. and Grocott, S. C. (2006). Wet Oxidation and Catalytic Wet Oxidation. *Industrial and Engineering Chemistry Research* **45** (4), 1221-1258

Bhaskar, M., Valavarasu, G., Sairam, B., Balaraman, K.S., Balu, K. (2004). Three-phase reactor model to simulate the performance of pilot-plant and industrial trickle-bed reactors sustaining hydrotreating reactions. *Industrial and Engineering Chemistry Research* **43**, 6654-6669.

Boelhouwer, J. G., Piepers, H. W., Drinkenburg, A. A. H. (2001). Particle-liquid heat transfer in trickle-bed reactors. *Chemical Engineering Science* **56**, (3), 1181-1187.

Cañizares, P., Lobato, J., Paz, R., Rodrigo, M.A., Sáez, C. (2007). Advanced oxidation processes for the treatment of olive-oil mills wastewater. *Chemosphere* **67** (4), 832-838.

Chander, A., Kundu, A., Bej, S. K., Dalai, A. K., Vohra, D. K. (2001). Hydrodynamic characteristics of cocurrent upflow and downflow of gas and liquid in a fixed bed reactor. *Fuel* **80** (8), 1043-1053.

Collin, J.G., Puma, G.L., Bono, A., Krishnaiah, D. (2009). Sonophotocatalysis in advanced oxidation process: a short review. *Ultrasonics Sonochemistry*, DOI: 10.1016/j.ultsonch.2009.02.002

Dudukovic, M.P., Larachi, F., Mills, P.L. (2002). Multiphase catalytic reactors: A perspective on current knowledge and future trends. *Catalysis Reviews. Science and Engineering* **44**, 123-246.

Elghobashi, S., Abou-Arab, T., Rizk, M., Mostafa, A. (1984). Prediction of the particle-laden jet with a two-equation turbulence model. *International Journal of Multiphase Flow* **10** (6), 697-710.

Esplugas, S., Giménez, J., Contreras, S., Pascual, E., Rodríguez, M. (2002). Comparison of different advanced oxidation processes for phenol degradation. *Water Research* **36**, (4), 1034-1042.

Fortuny, A., Bengoa, C., Font, J., Castells, F., Fabregat, A. (1999). Water Pollution Abatement by Catalytic Wet Air Oxidation in a Trickle Bed Reactor. *Catalysis Today* **53**, 107-114

FLUENT 6.1. (2005). User's Manual to FLUENT 6.1. Fluent Inc. Centrera Resource Park, 10 Cavendish Court, Lebanon, USA.

GAMBIT 2 (2005). User's Manual to GAMBIT 2. Fluent Inc. Centrera Resource Park, 10 Cavendish Court, Lebanon, USA.

Goto, S., Smith, J.M. (1975).Trickle-bed Reactor Performance Part II. Reaction Studies, AIChE J. **21**, 714-720.

Gunjal, P.R., Ranade, V.V. (2007). Modelling of laboratory and commercial scale hydro-processing reactors using CFD. *Chemical Engineering Science* **62** (18-20), 5512-5526.

Mandal, A., De, A.K., Bhattacharjee, S. (2004). Removal of catechol from aqueous solution by advanced photo-oxidation process. *Chemical Engineering Journal* **102** (2), 203-208.

Maugans, C.B., Akgerman, A. (2003). Catalytic wet oxidation of phenol in a trickle bed reactor over a Pt/TiO_2 catalyst. *Water Research* **37** (2), 319-328.

Larachi, F., Cassanello, M., Laurent, A. (1998). Gas-Liquid Interfacial Mass Transfer in Trickle-Bed Reactors at Elevated Pressures. *Industrial and Engineering Chemistry Research* **37** (3)*,* 718-733.

Lopes, R.J.G., Quinta-Ferreira, R.M. (2008). Three-Dimensional Numerical Simulation of Pressure Drop and Liquid Holdup for High-Pressure Trickle-Bed Reactor. *Chemical Engineering Journal* **145** (1), 112-120.

Lopes, R.J.G., Quinta-Ferreira, R.M. (2009a). Assessment of CFD Euler-Euler Method for CWO Modelling in Trickle-bed Reactor. *Chemical Engineering Journal* (*submitted*).

Lopes, R.J.G., Quinta-Ferreira, R.M. (2009b). CFD modelling of multiphase flow distribution in trickle beds. *Chemical Engineering Journal* **147** (2-3), 342-355.

Lopes, R.J.G., Quinta-Ferreira, R.M. (2009c). Turbulence modelling of high-pressure trickle-bed reactor. *Chemical Engineering Science* **64** (8), 1806-1819.

Pera-Titus, M., García-Molina, V., Baños, M.A., Giménez, J., Esplugas, S. (2004). Degradation of chlorophenols by means of advanced oxidation processes: a general review. *Applied Catalysis B: Environmental* **47** (4), 20 219-256.

Pintar, A., Levec, J. (1994). Catalytic Liquid-phase Oxidation of Phenol Aqueous Solutions. A Kinetic Investigation. *Ind. Eng. Chem. Res.* **33**, 3070-3077.

Pintar, A., Besson, M., Gallezot, P. (2001). Catalytic Wet Air Oxidation of Kraft Bleach Plant Effluents in a Trickle Bed Reactor Over a Ru/TiO2 Catalyst. *Appl. Cat. B: Environ.* **31**, 275-290.

Rivas, F.J., Carbajo, M., Beltrán, F., Gimeno, O., Frades, J. (2008). Comparison of different advanced oxidation processes (AOPs) in the presence of perovskites. *Journal of Hazardous Materials* **155** (3), 407-414.

Saroha, A.K., Khera, R. 2006). Hydrodynamic study of fixed beds with cocurrent upflow and downflow. *Chemical Engineering and Processing* **45** (6), 455-460.

Satterfield, C. N., van Eek, M.W., Bliss, G. S. (1978). Liquid-solid mass transfer in packed beds with downward concurrent gas-liquid flow. *A.I.Ch.E. Journal* **24** (4), 709-717.

Stüber, F., Polaert, I., Delmas, H., Font, J., Fortuny, A., Fabregat, A. (2001). Catalytic Wet Air Oxidation of Phenol Using Active Carbon: Performance of Discontinuous and Continuous Reactors. *J. Chem. Technol. Biotechnol.* **76**, 743-751.

Tukac, V., Vokál, J., Hanika, J. (2001). Mass Transfer Limited Wet Oxidation of Phenol. *J. Chem. Techn. Biotechnol.* **76**, 506-510.

Zhou, M., He, J. (2007). Degradation of azo dye by three clean advanced oxidation processes: Wet oxidation, electrochemical oxidation and wet electrochemical oxidation – A comparative study. *Electrochimica Acta* **53** (4), 1902-1910.

This page intentionally left blank

XIII. Assessment of CFD VOF Method for CWO Modelling in TBR[1]

A trickle-bed reactor (TBR) was modelled by means of the Volume of Fluid (VOF) model to provide a reaction behavior analysis in transient conditions. Since conventional modelling techniques are unable to address multiphase flow distribution and local temperature variation, the VOF model was used to investigate the dynamic performance under reaction conditions providing a more rigorous physical description of the underlying flow process. The catalytic wet air oxidation was taken as example to evaluate axial and radial profiles for the total organic carbon depletion and temperature along the packed bed.

Computational runs are compared against experimental data from a pilot plant and the VOF model was then used to understand the influence of operating temperature in the total organic carbon distribution and to describe its interaction with chemical oxidation reaction. The computational runs exhibited backmixing effects more pronounced for lower operating temperatures. The mean radial temperature profiles revealed the existence of hot spots in the simulated flow regime. Furthermore, poor radial mixing was remarked mainly at the hot spot locations addressed in mass and thermal profiles.

XIII.1. Introduction

During the last decades, global reforms, regulations and planetary environmental policies imposed the intensification of the technological development to become self sustainable in respect to the severe exploitation of natural resources. In this ambit, water has been sheltered by the enforcement of efficient treatments of contaminated industrial and domestic water effluents. A vast majority of industries generate large quantities of aqueous wastes containing toxic and organic substances. The integrated treatment of polluted water streams typically includes a combination of physical, chemical, and biological methods. While biological processes are important for the removal of organic pollutants, but often not suitable for waste streams originating from the chemical industry since they may contain toxic, non-biodegradable and hazardous pollutants, chemical oxidations on the liquid phase is widely recognized by an alternative and feasible solution. Examples of toxic compounds are phenol derivatives as well as a large variety of chlorine based organic compounds. In fact, the maximum concentration of phenol that can be treated biologically has been reported to lie in the range 50-200 mg/dm^3, which is typically, exceeded in common industries (Bhargava *et*

[1] *This Chapter is based upon the publication Lopes and Quinta-Ferreira (2009a)*

al., 2006). Moreover, biodegradation technologies are inherently slow and result in considerable large installations for the successful treatment of wastewaters. Sludge is then often produced in large quantities that must be disposed off either landfilling or by burning which increases the final economical cost.

It is worthwhile to mention that wastewater streams having an organic pollutant load in the range of few hundred to few thousand *ppms* are too dilute to incinerate but yet too toxic and concentrated for a biological treatment (Paraskeva and Diamadopoulos, 2006). Within this range of concentrations and toxicity, sub-critical solid-catalyzed wet air oxidation (CWAO) technique is among the most suitable disposal routes. CWAO technology is based on the catalytic oxidative breakdown of oxidizable contaminants in water and carbon dioxide at elevated oxygen pressures and high temperatures. Solid catalysts offer a practical and technological alternative to the conventional non-catalytic or homogeneously catalyzed routes because the treatment can be carried out under much milder conditions, at notably shorter residence times within more compact installations, besides the catalyst may in principle be easily recovered, regenerated and reused (Pintar and Levec, 2007; Matatov-Meytal and Sheintuch, 1998). Excellent reviews on the use of carbon materials as catalytic support or direct catalyst in catalytic wet air oxidation of organic pollutants have been reviewed by Stüber *et al*. (2005) with detailed information on relevant engineering aspects including the characterization, activity and stability of carbon.

The liquid-phase catalyzed oxidation processes fall into the category of gas-liquid-solid reactions and are still not at a mature stage of development and technological implementation (Mills and Chaudhari, 1999). At the time of proper and reliable industrial design, the chemical reactor engineer must overcome the complex nature on the inter-phase and intra-particle heat and mass transport, chemical kinetics, thermodynamics, flow patterns and hydrodynamics. Several laboratory studies that are being released in the academic and patent literature are merely intended to the development of stable and economical catalysts for the wastewaters remediation (Singh *et al*., 2004; Maugans and Akgerman, 2003). Only a few number of studies on computer-aided tools has been reported in the open literature for the design of catalytic wet oxidation in trickle-bed reactors (Lopes *et al*., 2007a; Lopes and Quinta-Ferreira, 2007b) and bubble column reactors (Debellefontaine *et al*., 1999; Schlüter *et al*., 1992).

Nowadays, following the progress of computing technology and computational fluid dynamics (CFD), several numerical models based on numerical simulation of Navier-Stokes equations have been developed for multiphase flows. Numerous studies have been devoted to the transport of non-reacting bubble and droplet sprays in order to fully understand their dynamic nature but it clearly appears that specific approaches must be carried out for the concomitant description of interface

behavior in gas-liquid-solid systems. Computing interface motion in multiphase flows is a wide field of research and several approaches can be used. Front tracking methods (Unverdi and Tryggvason, 1992), Volume of fluid methods (Gueyffier *et al*., 1999) and level set methods (Sussman *et al*., 1994) are the most common numerical strategies used to predict interface motion. Front tracking methods are based on the Lagrangian tracking of marker particles that are attached to the interface motion, but appear numerically limited for 3D geometries, especially for the distribution of the marker particles when irregularities occur on the interface. VOF methods are based on the description of the volumetric fraction of each phase in grid cells. The main difficulty of the method is that while 2D interface reconstruction is workable, 3D reconstruction is numerically expensive. A consequence can be some uncertainties on the interface curvature and thus on the surface tension forces. The basis of the Level Set methods has been referred elsewhere (Osher and Sethian, 1988) in which the interface is described with the zero level curve of a continuous function defined by the signed distance to the interface. To ensure that the function remains the signed distance to the interface, a predestining algorithm is applied, but it is well known that its numerical computation can generate mass loss in under-resolved regions, which is the main drawback of level set methods. To describe the interface discontinuities, two approaches can be used, namely the continuous force formulation ("delta" formulation), which assumes that the interface is 2 or 3 grid meshes thick, and the ghost fluid method, which has been derived to capture jump conditions on the interface (Fedkiw *et al*., 1999).

As wetting characteristics play a dominant role in the hydrodynamic operation of trickle beds at reacting flow conditions, the VOF model was used to compute the axial/radial concentration and temperature profiles accounting at the same time for the liquid spreading on catalyst solid surfaces in high-pressure TBR. The hydrodynamic and reaction parameters are correlated on how they can be affected by the wetting phenomenon through the simulation of the catalytic wet oxidation on the TBR.As trustworthy designing and scale-up of reactors as well as process optimization requires detailed knowledge and information from the perspective of multiphase reactor engineering to gas-liquid-solid catalytic wet oxidation, this work is devoted to the VOF model for TBR modelling with applications in environmental pollution abatement. Liquid effluents arising in chemical and agro-alimentary plants are contaminated with a high content of toxic and hazardous organic compounds revealing chemical oxygen demands in the range 10-100 $g.L^{-1}$. Among advanced oxidation technologies, catalytic wet air oxidation has demonstrated in the recent literature the necessary suitability for the treatment of liquid effluents, in which direct biological purification is unfeasible, by offering lower energy requirements and higher oxidation efficiencies rather than with the non-catalytic wet air oxidation. Specifically, olive oil mill wastewater is characterized by a high total organic carbon fraction (TOC) so that three-phase reactors are

required for the continuous wastewater treatment operating in trickle flow regime at trickle-bed reactors. VOF model is used to gain insight and quantitative information about the concentration and temperature profiles when a phenolic model solution is employed to simulate the CWAO in the multiphase reactor.

XIII.2. Mathematical Model

XIII.2.1. Governing Flow Equations

A trickle-bed reactor of non-overlapping spherical particles in cylindrical geometry was modelled with a specified void fraction and a set of fluid physical properties. The computational geometry shown in Fig XIII.1 was designed so that a distance gap of about 3% of the sphere diameter facilitate the grid generation avoiding numerical difficulties that arise in the calculation of convective terms as described in Chapter V (Lopes and Quinta-Ferreira, 2008a; Nijemeisland and Dixon, 2001).

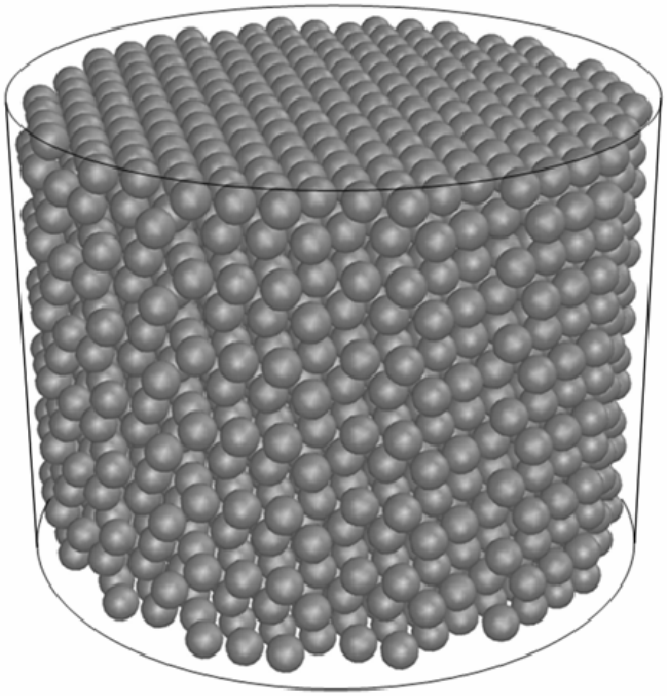

Figure XIII.1. Configuration of catalyst particle arrangement for the trickle-bed used in VOF simulations

The purpose of this work is to develop a computational model to analyze the fluid flow through the cylindrical bed including the evaluation of axial and radial profiles for TOC concentration and temperature variables. In particular, the liquid-gas flow through a catalytic bed was considered comprised of monosized, spherical, solid particles arranged in a cylindrical container of a pilot TBR unit (50 mm_{ID}×1.0 m_{Length}). The VOF method was used to compute velocity field as well as liquid volume fraction distributions. The multiphase flow is assumed vertical downward and

incompressible, with the mathematical description for the flow of a viscous fluid through a three-dimensional catalytic bed based on the Navier-Stokes equations for mass and momentum conservation. The VOF continuity and momentum equations, the free surface model including the surface tension and wall adhesion were described in Equations (VIII.1)-(VIII.9) in Chapter VIII. The turbulence kinetic energy, k, and the turbulent energy dissipation, ε, are computed from Equations (VIII.13)-(VIII.14) presented in Chapter VIII.

XIII.2.2. Species Continuity and Energy Equations

The predicted flow field including velocities and volume fractions of both phases was further used for solving species transport equations for simulating the catalytic wet air oxidation of a model phenolic solution in the TBR reactor. These equations are expressed in the mass balance equation for any species, i:

$$\frac{\partial \alpha_q \rho_q C_{q,i}}{\partial t} + \nabla \cdot \left(\alpha_q \rho_q u_q C_{q,i}\right) = \nabla \cdot \left(\alpha_q \rho_q D_{q,i} \nabla C_{q,i}\right) + \alpha_q \rho_q S_{q,i} \qquad \text{(XIII.1)}$$

where, $C_{q,i}$ is the concentration of species i in the q^{th} phase (gas or liquid), $D_{q,i}$ is the diffusivity of specie i in the q^{th} phase estimated using the Siddiqi–Lucas (1986) method, ρ_q and α_q is the density and volume fraction of the q^{th} phase. $S_{q,i}$ is the source for species i in phase q. Volume averaged properties of fluids were used for calculating the flux across the control cell. Two-film theory was used for accounting mass transfer. The resistance in gas-liquid film was considered as the rate limiting resistance (Bhaskar *et al*., 2004). Mass transfer coefficient was computed according to Satterfield *et al*. (1978) correlation and heat transfer coefficient was calculated according to the correlation developed by Boelhouwer *et al*. (2001) as expressed by Equations (XIII.2) and (XIII.3), respectively.

$$Sh = 0.815\, Re^{0.822}\, Sc^{1/3} \qquad \text{(XIII.2)}$$

$$Nu = 0.111\, Re^{0.8}\, Pr^{1/3} \qquad \text{(XIII.3)}$$

The VOF model treats energy, E, and temperature, T, as mass-averaged variables. The energy equation, also shared among the phases, is shown in Equations (XIII.4) and (XIII.5):

$$\frac{\partial}{\partial t}\left(\rho E\right) + \nabla \cdot \left(\vec{u}\left(\rho E + p\right)\right) = \nabla \cdot \left(k_{eff} \nabla T\right) + S_h \qquad \text{(XIII.4)}$$

$$E = \frac{\sum_{q=1}^{n} \alpha_q \rho_q E_q}{\sum_{q=1}^{n} \alpha_q \rho_q} \qquad \text{(XIII.5)}$$

where E_q for each phase is based on the specific heat of that phase and the shared temperature. The properties ρ and k_{eff} (effective thermal conductivity) are shared by the phases. The source term, S_h contains contributions from volumetric reaction heat sources.

XIII.2.3. Numerical simulation

Tetrahedral mesh representing the interstitial space of the trickle-bed reactor was created using the integrated solid modelling and meshing program GAMBIT (GAMBIT 2, 2005). Numerical details of cell sizes and the boundary layer treatment have been described in Chapter IX (Lopes and Quinta-Ferreira, 2009b). The VOF method simulates free-surface flow by means of a fluid fraction function, which has a value between unity and zero. The discretization of the governing equations is done by the finite-volume method. The grid independency was established after the evaluation of different mesh natures and apertures in order to isolate mesh related discretization errors. A segregated implicit solver available in commercial CFD package FLUENT (FLUENT 6.1, 2005) was employed to evaluate the resulting linear system of equations. The conditions required for grid convergent results are based on a 1% relative error criterion and the simulations accuracy has been assessed by comparisons to experimental data available in the literature. At the interface, the additional interaction conditions depend on interfacial velocity and gradient of the surface tension. The CWAO kinetic parameters were derived from the work developed by Lopes *et al*. (2007c). Our case study is based in the kinetic studies performed with commercial and laboratory-made catalyst carried out in batch mode operation. Several authors including the recent work developed by Manole *et al.* (2007) who reported that data in continuous trickle-bed reactor in downflow or upflow flooded-bed reactor indicate oxidation behavior similar to that observed in batch mode, despite very different liquid-solid ratios for the catalytic wet air oxidation of *4*-hydroxybenzoic acid.

Turbulent kinetic energy (k) was estimated from turbulence intensity and turbulent energy dissipation (ε) was estimated from the turbulent viscosity ratio as expressed in Chapter VIII. Computations are time dependent and were carried out until steady state conditions were reached. Standard wall functions were employed for turbulent flow conditions. Until liquid reaches the outlet, the time step is very low (about 10^{-7} s). The time step is increased awhile from 10^{-7} s to a final value of 10^{-4} s or 10^{-3} s, the latter value depending mostly on the density ratio between the two fluids. The time-stepping strategy depends on the number of iterations by time step needed to ensure very low residuals values (all less than 10^{-5}). The time step value is increased by a factor of four, if one obtains 10 consecutive time calculations with less than four iterations by time step. In the representative case of multiphase reactor, the time step was increased up to 5×10^{-4} s, and the calculation was stopped after 1000 iterations with this time step without any significant change in the outlet concentration, temperature and mass flux value. CFD calculations have been carried out on Linux cluster based on AMD64 Dual-Core 2.2 GHz processor.

XIII.3. Results and Discussion

XIII.3.1. Non-reacting flow validation

To gain insight on the effect of various parameters such as liquid velocity, surface tension, and wetting phenomena, the current VOF model was studied in non-reacting flow conditions to simulate the multiphase flow in the high-pressure trickle-bed reactor. The accuracy of simulations was evaluated in terms of tetrahedral mesh size and several model solution parameters were optimized including time step and convergence criteria. On the discretization of volume fraction equation, high-order differencing schemes (HRIC and CICSAM) were found to give the better computed results for both liquid holdup and two-phase frictional pressure drop as described in Chapter IX (Lopes and Quinta-Ferreira, 2009b). According to the numerical simulations carried out so far, the VOF model was used to evaluate the effect of gas flow rate in the range G=0.1-0.7 kg/m^2s on hydrodynamics demonstrating its considerable influence on the liquid holdup in comparison with the effect of liquid flow rate. The optimum values for the numerical solution parameters were further used in the VOF model to evaluate the hysteresis on both hydrodynamic parameters at high-pressure. During the VOF simulations, Lopes and Quinta-Ferreira (2009c) found that wetting efficiency can be captured through the evaluation of successive radial planes of liquid volume fraction at different packed bed cross-sections as discussed previously in Chapter VIII. Additionally, the effect of gas flow rate on the numerical accuracy produced by either laminar or several turbulent flow models was investigated for both hydrodynamic parameters. At lower gas flow rates, the VOF predictions performed with the laminar flow model were found to produce qualitative and quantitatively the same computed results as turbulent flow models for both liquid holdup and frictional pressure drop, while for higher flow rates the turbulent flow models performed better indicating the considerable degree of turbulence induced by the gas phase as shown in Chapter IX (Lopes and Quinta-Ferreira, 2009b). Following the VOF hydrodynamic validation, those optimum numerical solution parameters were integrated into the multiphase flow model aiming to evaluate the axial and radial mapping of reaction parameters (temperature and total organic carbon concentration) in the catalytic wet air oxidation of phenolic wastewaters.

XIII.3.2. Reaction studies

After the VOF model hydrodynamic validation, several test cases were performed with initial perturbation on the inflow total organic carbon concentration. The dynamic behavior of the trickle-bed reactor was studied evaluating the concentration and temperature profiles for the startup of the process until the steady-state was reached. This unsteady-state operating strategy leads to a further increase in the complexity of the physical and chemical processes determining the overall TBR behavior and therefore necessitates a more refined modelling approach, with special attention

being given to the axial and radial profiles under the dynamic operating conditions. The VOF multiphase model was employed to model the surface flow including surface tension effects mainly due to the increased importance of reaction, convection and diffusion for mixing phenomena. The reactor was initially heated at the wall temperature (T_w = 160 and 200 ºC) and at the time t^* = 0, the feed stream entered the reactor representing a step change in the inlet total organic carbon concentration. This fact led to the use of *High Resolution Interface Capturing* scheme in order to suppress the so-called "numerical diffusion" which is mainly related with the numerical errors being accumulated by the algorithm and introduced by step perturbation. The experimental procedure with a description of materials and equipment used for the oxidation experiments in the trickle-bed reactor installation was described in Chapter XII, section XII.3.

Axial Total Organic Carbon profiles

Figures XIII.2 and XIII.3 show the transient axial profiles predicted by VOF model of the mean radial values of the bulk-phase concentration for $T_0 = T_w$ = 160 and 200 *ºC*, respectively. According to these concentration profiles, the total organic carbon conversion is higher when the catalytic wet air oxidation is simulated at higher temperatures because the oxidation reaction is exothermic and follows Arrhenius dependence, therefore, the reaction rate increases with increasing temperature. For example, when $T_0 = T_w$ = 160 *ºC* and t^* = 0.6, the TOC conversion is about 78% but it is 92% when $T_0 = T_w$ = 200 *ºC*, indicating the positive effect in the pollutant degradation. The steady-state was reached around t^* = 10 for both operating temperatures, specifically 88% and 94% TOC reduction for $T_0 = T_w$ = 160 and 200 *ºC*, respectively.

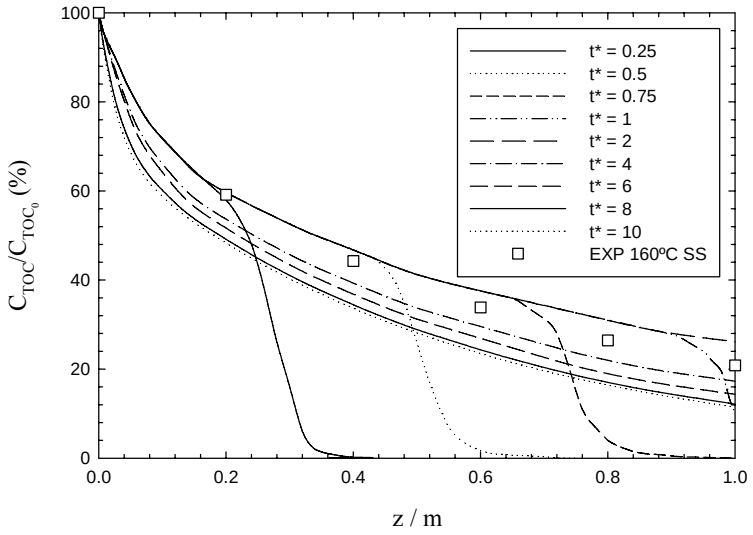

Figure XIII.2. Mean radial bulk total organic carbon profiles for axial coordinate at transient conditions for different operating dimensionless times, , t^* ($T_0 = T_w$ = 160 ºC, L = 5 kg/m^{2}s, G = 0.5 kg/m^{2}s, P = 30 bar)

As it can be seen, the VOF model overpredicted the experimental data on TOC removal and their differences are increasing with axial coordinate at the steady-state for both operating temperatures.

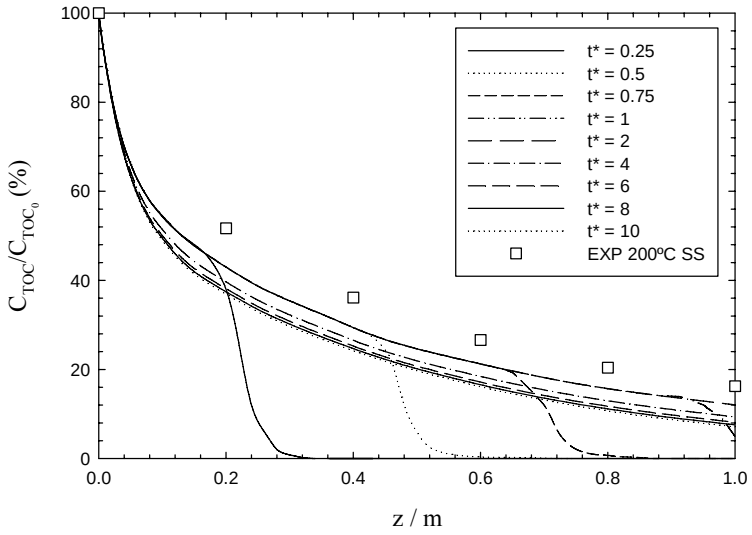

Figure XIII.3. Mean radial bulk total organic carbon profiles for axial coordinate at transient conditions for different operating dimensionless times, t^* ($T_0 = T_w$ = 200 ºC, L = 5 kg/m^{2}s, G = 0.5 kg/m^{2}s, P = 30 bar)

The axial dispersion observed for the total organic carbon concentration when $t^* < 1$ indicates some degree of backmixing in the trickle-bed reactor operating in downflow mode. In fact, the backmixing effect when the system operates at $T_0 = T_w = 200$ *ºC* is slightly lower than when it operates at $T_0 = T_w = 160$ *ºC*. At this temperature and when $t^* = 0.25$, the concentration profiles spans in the axial coordinate between 0.18 and 0.4 *m*, while for $T_0 = T_w = 200$ *ºC* and at the same operation time, the concentration spans between 0.18 and 0.26 *m*. It indicates that the backmixing decreases with an increase in the wall/inlet temperature for downflow operation mode.

Axial Temperature profiles

The influence of the operating temperature on the thermal profiles was plotted in Figs XIII.4 and XIII.5. After the comparison between these temperature axial profiles and the TOC profiles already plotted in Figs XIII.2 and XIII.3 for the same operating conditions, it can be seen that the operation time required for the thermal wave and for the TOC wave to achieve the steady-state is almost the same, $t^* = 10$. Once again, the VOF overpredicted the temperature elevation in comparison with the experimental data measured at the two different operating conditions. As it can be seen from Fig. XIII.4, the qualitative behavior between the temperature predicted by the VOF model and experimental data was reasonably similar at $T_0 = T_w = 160$ *ºC*. However, increasing the operating temperature up to $T_0 = T_w = 200$ *ºC*, a considerable difference was found

between the VOF predictions and experimental data for the bulk temperature obtained at steady-state.

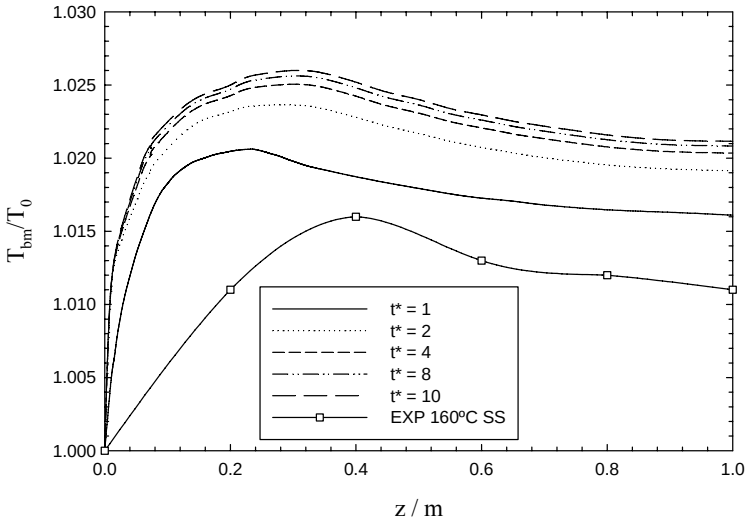

Figure XIII.4. Mean radial bulk temperature profiles for axial coordinate at transient conditions for different operating dimensionless times, t^* ($T_0 = T_w$ = 160 ºC, L = 5 kg/m^{2}s, G = 0.5 kg/m^{2}s, P = 30 bar)

The main intrinsic difference between both VOF axial profiles is related with the intensity of the maximum mean radial bulk temperature when the catalytic wet air oxidation is modelled at $T_0 = T_w$ = 160 and 200 *ºC*. In fact, we can observe that the hot spot was achieved earlier when the operating temperature is higher ($T_0 = T_w$ = 200 *ºC*: z = 0.2 m) than when the reactor was operated at lower temperature ($T_0 = T_w$ = 160 *ºC*: z = 0.25 m). This fact can be supported by the chemical reaction thermodynamics, so that higher temperatures favor the oxidation rates and then the heat delivery from this exothermic reaction will be higher.

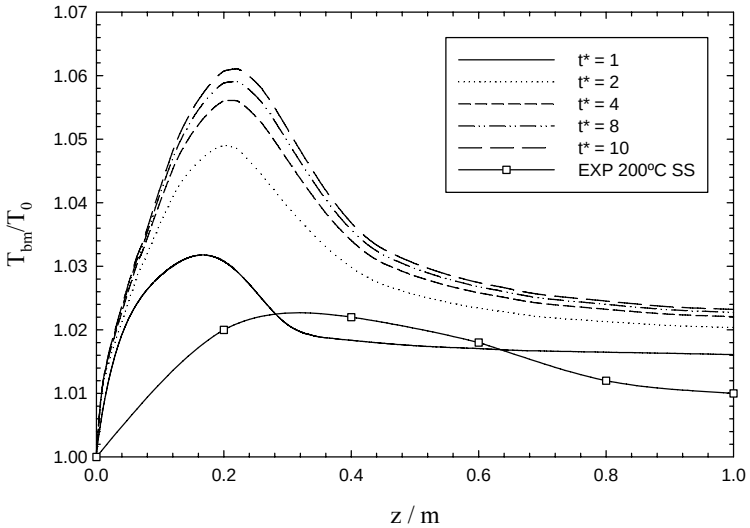

Figure XIII.5. Mean radial bulk temperature profiles for axial coordinate at transient conditions for different operating dimensionless times, t^* ($T_0 = T_w$ = 200 ºC, L = 5 kg/m^{2}s, G = 0.5 kg/m^{2}s, P = 30 bar)

For $T_0 = T_w = 160$ ºC, in the hot spot, a maximum temperature of about 164.5 ºC was achieved that corresponds to a difference of 4.5 ºC in respect to the wall/inlet temperature, but when the same chemical reaction is processed at $T_0 = T_w = 200$ ºC, the maximum temperature for the hot spot was 212 ºC which corresponds to 6 % more than the wall operating temperature. For both cases, the steady-state is accomplished at the same operating time, $t^* = 10$. Therefore, one can conclude that for higher inlet and wall temperatures, the magnitudes of the hot spots and the final reactant conversion are also higher, demonstrated by the mean radial bulk temperature and concentration profiles along the catalytic bed. One should also bear in mind that an increase in temperature also increases the equilibrium water vapor pressure so that an increase in operating temperature requires an increase in total operating pressure in order to maintain the oxygen partial pressure. Since the catalytic wet air oxidation of phenolic acids is exothermic it releases energy which raises the temperature of the liquid and gas streams leading to further water evaporation. This fact can be advantageous because water will act as a heat sink, preventing the reaction from running away.

Radial Total Organic Carbon profiles

For $T_0 = T_w = 160$ ºC and $z = 0.25$ m, which corresponds to the hot spot zone, Fig. XIII.6 represents the transient radial simulated profiles of total organic carbon variable for different times, while Fig. XIII.7 plots the same radial TOC profiles for the corresponding hot spot achieved when $T_0 = T_w = 200$ ºC.

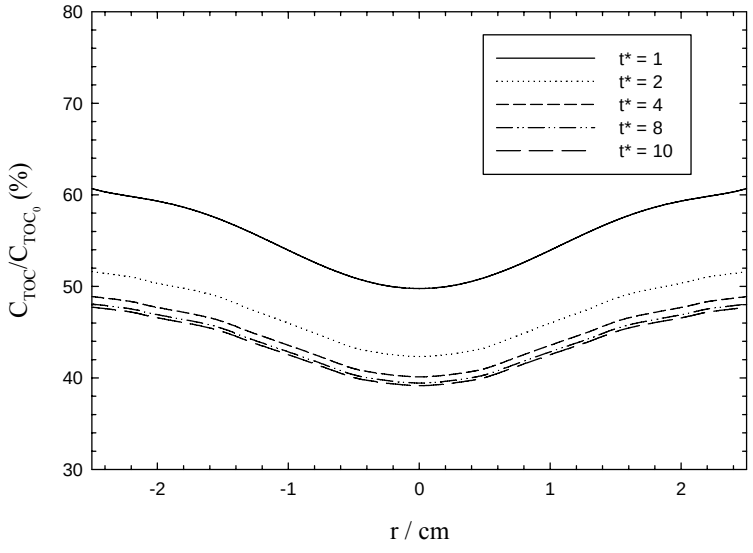

Figure XIII.6 Radial total organic carbon profiles at the hot spot for different operating dimensionless times , t^* ($T_0 = T_w = 160$ ºC, L = 5 kg/m^{2}s, G = 0.5 kg/m^{2}s, P = 30 bar)

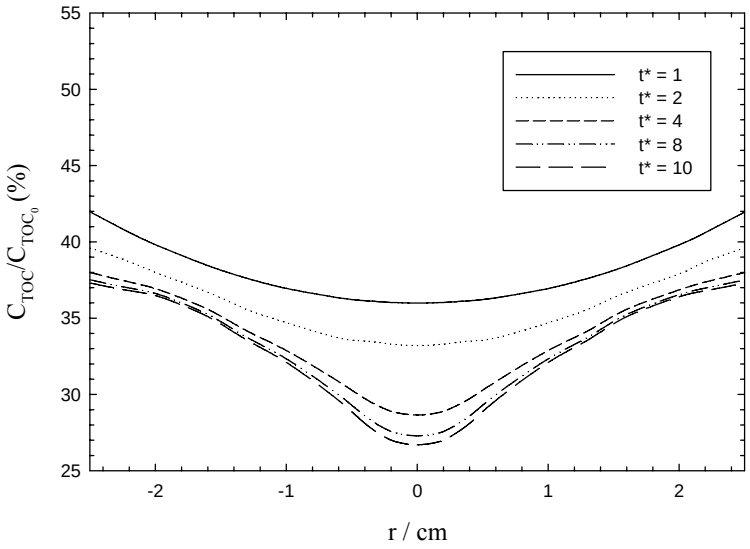

Figure XIII.7 Radial total organic carbon profiles at the hot spot for different operating dimensionless times, t^* ($T_0 = T_w$ = 200 ºC, L = 5 kg/m^{2}s, G = 0.5 kg/m^{2}s, P = 30 bar)

These concentration profiles indicated that the radial gradients attained for $T_0 = T_w$ = 160 *ºC* are about 10% of difference between the centerline and the wall values which demonstrates a considerable degree of poor radial mixing namely at the hot spot as a result of the exothermicity of the reaction system leading to higher temperatures in the reactor centre. Furthermore, as the multiphase flow is driven by pressure, the hydrodynamic parameters are the result of frictional forces building up where the gas and liquid phases are in contact with solid surfaces which result in drops of velocity in the fluid phases at these interfaces. The TOC profile obtained for $T_0 = T_w$ = 200 *ºC* plotted in Fig. XIII.7 indicated a maximum difference of 6 % for the total organic carbon degradation. For $t^* > 2$, the maximum concentration difference is achieved at the steady-state (t^* = 10) which can be explained by the higher temperature observed in the centre that leads to higher TOC oxidation rates and therefore, large variations for the TOC radial values.

Radial Temperature profiles

Figures XIII.8 and XIII.9 represent the transient radial temperature profiles computed for the hot spot at z = 0.2 and 0.25 m for $T_0 = T_w$ = 160 and 200 *ºC*, respectively. In this case, the thermal distribution is not very different whether the TBR is operated at 160 or 200 *ºC*. For $T_0 = T_w$ = 160 *ºC*, it can be observed in Fig. XIII.8 that the maximum temperature difference obtained radially is 4 *ºC* which is similar to the value already obtained for the axial temperature profile at the same operating temperature. This confirmation points out that the trickle-bed reactor also underwent some degree of radial mixing effects.

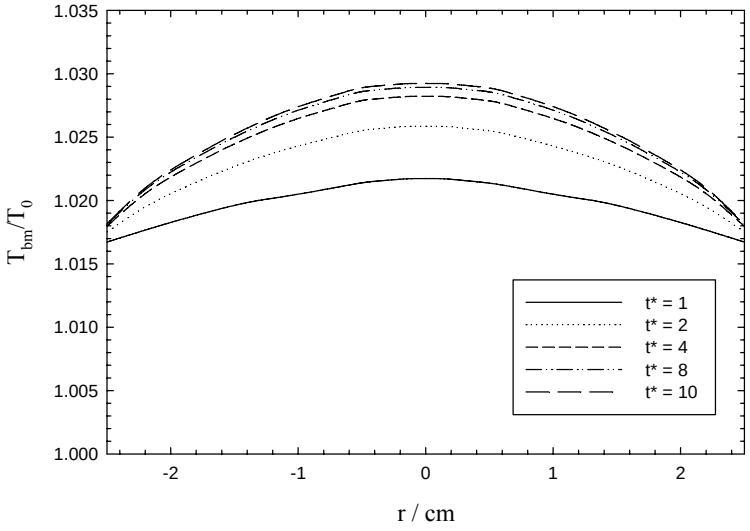

Figure XIII.8 Radial temperature profiles at the hot spot for different operating dimensionless times, t^* ($T_0 = T_w = 160$ ºC, L = 5 kg/m^{2}s, G = 0.5 kg/m^{2}s, P = 30 bar).

Fig. XIII.9 illustrates this fact prominently for $T_0 = T_w = 200$ *ºC*, in which the maximum radial temperature difference was 12.8 *ºC* and, once more, a value slightly higher than the difference attained for the axial coordinate. Comparing Figs. XIII.6- XIII.9, in which TOC concentration and temperature radial profiles were plotted, one can observe opposite behaviours already advanced for the explanation of these radial distributions.

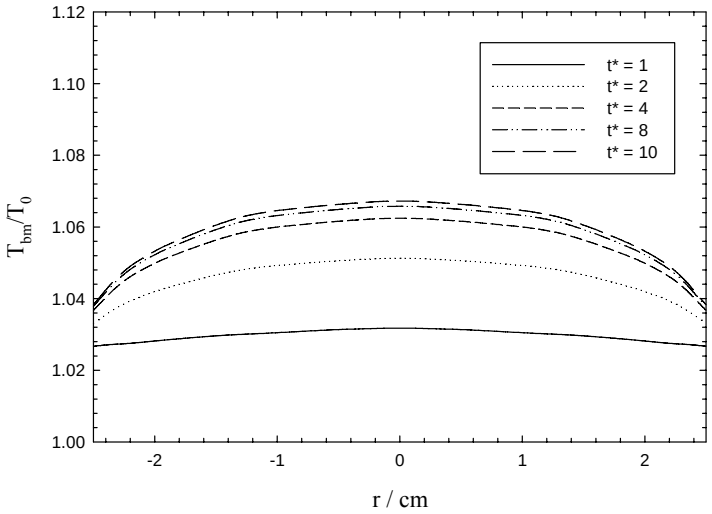

Figure XIII.9 Radial temperature profiles at the hot spot for different operating dimensionless times, t^* ($T_0 = T_w = 200$ ºC, L = 5 kg/m^{2}s, G = 0.5 kg/m^{2}s, P = 30 bar).

In fact, while the concentration profiles are diminishing from the wall to the centre, the thermal ones are augmenting from the wall to the centre since oxidation reactions are exothermic reaching the maximum at $r = 0$. As the chemical reaction is favoured by the higher operating temperatures,

it is expected also the higher conversions in those cases so that the TOC degradation reaction rates are higher as well. In all cases, the steady-state is reached at $t^* = 10$. These computational results show that the radial gradients are higher at the hot spot as observed in the temperature colour maps presented in Figs XIII.10a) and b) for different operating times, $t^* = 2$ and 10, respectively, in where the difference between the centreline and wall temperatures corresponds about 6 % of the wall and inlet temperature.

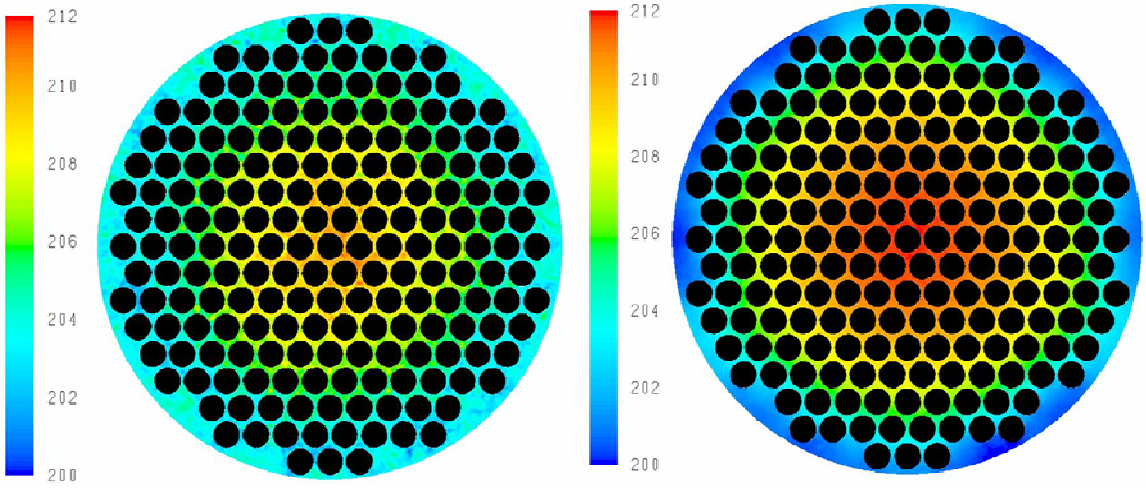

a) **b)**

Figure XIII.10 a) Radial temperature color map at the hot spot for $t^* = 2$ and **b)** $t^* = 10$ (steady-state)

Therefore, hotspot formation phenomenon may be attributed to the predicted radial dispersion being its relationship with underlying fluid dynamics illustrated by Figs. XIII.11a) and b). However according to Fig. XIII.11, the gas and liquid holdup radial distribution at the hot spot for $t^* = 10$ did not show the same behaviour as the thermal profile (Fig. XIII.10) already exhibited.

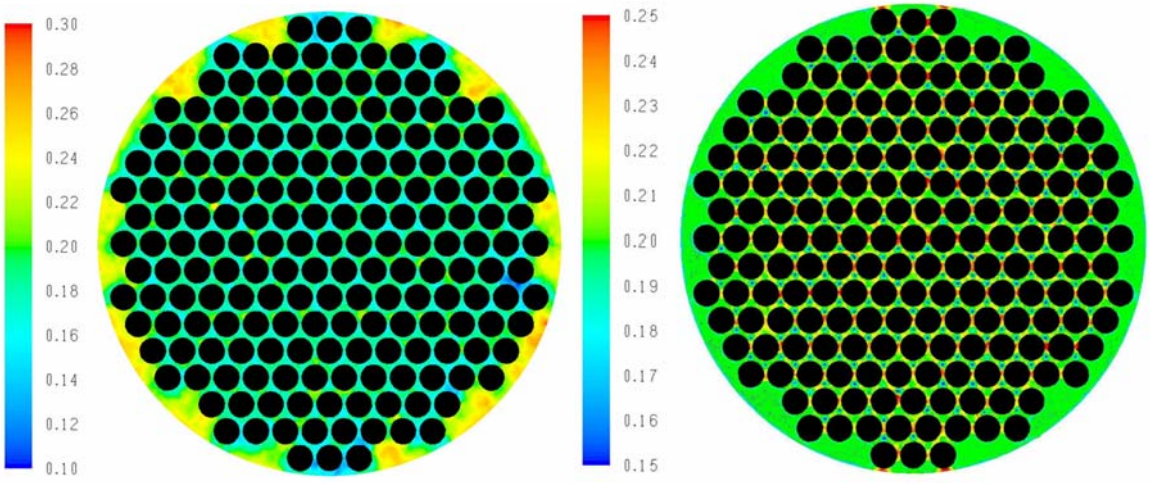

a) **b)**

Figure XIII.11 a) VOF snapshots for the gas and **b)** liquid holdup at the hot spot for $t^* = 10$ ($T_0 = T_w = 200$ ºC, L = 5 kg/m^{2}s, G = 0.5 kg/m^{2}s, P = 30 bar)

Phase holdup seems not having direct cause-effect with temperature non-uniformity and hotspot formation, which is caused by the reaction exothermicity. Moreover, the VOF snapshots for the gas (Fig. XIII.12a) and liquid velocity (Fig. XIII.12b) at the hot spot (t^* = 10, $T_0 = T_w$ = 200 ºC, L = 5 kg/m^{2}s, G = 0.5 kg/m^{2}s, P = 30 bar) also demonstrated that the local variation of gas-liquid velocities are practically independent of the temperature profile.

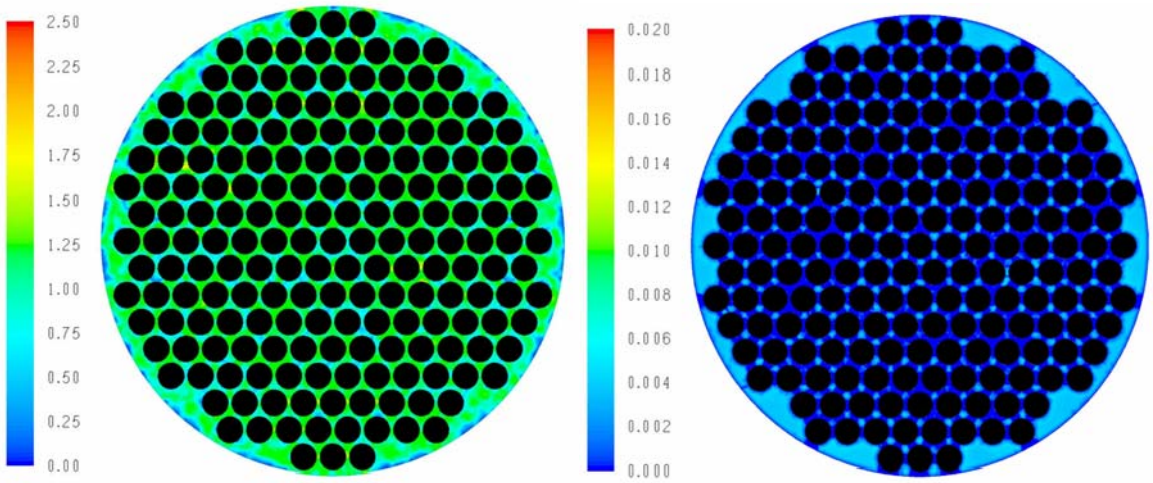

Figure XIII.12 a) VOF snapshots for the gas (cm/s) and **b)** liquid velocity (cm/s) at the hot spot for t^* = 10 ($T_0 = T_w$ = 200 ºC, L = 5 kg/m^{2}s, G = 0.5 kg/m^{2}s, P = 30 bar)

In fact, the VOF snapshot for the Total Organic Carbon concentration at the hot spot (Fig. XIII.13) showed a similar behavior that was observed for the radial distribution of bulk phase temperature. According to Fig. XIII.13, the radial profile TOC showed that the lower pollutant concentrations were achieved in the TBR centre being the maximum values attained at the wall.

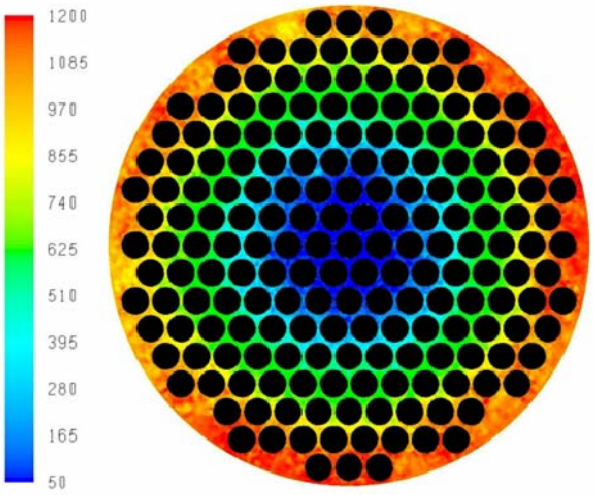

Figure XIII.13 VOF snapshot for the Total Organic Carbon concentration (ppm) at the hot spot for t^* = 10 ($T_0 = T_w$ = 200 ºC, L = 5 kg/m^{2}s, G = 0.5 kg/m^{2}s, P = 30 bar)

It should be stressed out that these hot spots might initiate undesired side reactions (polymerization of phenolic compounds) and damage the catalyst, leading in extreme cases to reactor runaway. Our computational runs confirmed that non-isothermal effects in trickle-bed reactor operation have to be accounted in CFD modelling. VOF model allows for the computation of local mass and heat transfer and recent simulation activities indicated that one can evaluate external wetting of the catalyst pellets (Lopes and Quinta-Ferreira, 2009b; Gunjal *et al*., 2005) and minimize the poor liquid distribution. In fact, during the computational runs it was possible to computed in Chapter VIII the mean value of wetting efficiency being almost 82% at L = 5 kg/m^{2}s, G = 0.5 kg/m^{2}s, P = 30 bar.

XIII.4. Conclusions

A multiphase VOF model was developed to provide a deeper understanding of the transient behavior of a pilot trickle-bed reactor. The gas-liquid flow through a catalytic bed of spherical particles was used to compute velocity field and liquid volume fraction distributions considering interfacial phenomena as well as surface tension effects. The computational model was used to simulate the catalytic wet air oxidation of a phenolic model solution in the multiphase reactor. Several runs were carried out under unsteady-state operation to evaluate the dynamic performance addressing the total organic carbon concentration and temperature profiles. Axial concentration profiles were then correlated with the radial ones for the simulated flow regime and the influence of the operating temperature in the thermal profiles illustrated the existence of such hot spots located in the first one forth of the axial coordinate with an intensity of about 6% higher than the inlet and wall temperatures. The transient radial temperature profiles corresponding to the hot spot showed the same intensity that was pointed out for the axial thermal profiles indicating the existence of considerable radial gradients that sustained the poor radial mixing in downflow operation mode.

The VOF methodology is then able to assist the multiphase reactor design and performance prediction for the early identification of hot spots that can lead to reactor runaway providing a useful guide for the successful scale-up of industrial trickle-bed reactor in wastewater treatment plants.

XIII.5. Nomenclature

C	Specie concentration, ppm
E	Thermal energy, J
$\vec{g}$	Gravitational acceleration, 9.81m/s^2
G	Gas mass flux, kg/m^{2}s
k_{eff}	Effective thermal conductivity, W/(m·K)
L	Liquid mass flux, kg/m^{2}s
$\hat{n}_w$	Unit vector normal to the wall
Nu	Nusselt number
p	*P*ressure, bar
Pr	Prandtl number
r	Reactor radius, m
S_q	Source mass for phase q
Sh	Sherwood number
t	Time, s
t^*	Dimensionless time, (t/τ)
T	Temperature, K
TOC	Total organic carbon, ppm
$\vec{u}$	Superficial vector velocity, m/s

Greek letters

α_q	Volume fraction of q^{th} phase
ρ_q	Density of q^{th} phase, kg/m^3
Δp	Total pressure drop, Pa
τ	Residence time, s

Subscripts

G	Gas phase
L	Liquid phase
q	q^{th} continuous phase
S	Solid phase
w	Wall
0	Initial time reaction

XIII.6. References

Bhargava, S. K., Tardio, J., Prasad, J., Foger, K., Akolekar, D. B. and Grocott, S. C. (2006). Wet Oxidation and Catalytic Wet Oxidation. *Industrial and Engineering Chemistry Research* **45** (4), 1221-1258.

Bhaskar, M., Valavarasu, G., Sairam, B., Balaraman, K.S., Balu, K. (2004). Three-phase reactor model to simulate the performance of pilot-plant and industrial trickle-bed reactors sustaining hydrotreating reactions. *Industrial and Engineering Chemistry Research* **43**, 6654-6669.

Boelhouwer, J. G., Piepers, H. W., Drinkenburg, A. A. H. (2001). Particle-liquid heat transfer in trickle-bed reactors. *Chemical Engineering Science* **56**, (3), 1181-1187.

Brackbill, J., Kothe, D., Zemach, C. (1992). A continuum method for modelling surface tension.*Journal of Computational Physics* **100**, 335-354.

Debellefontaine, H., Crispel, S., Reilhac, P., Périé, F., Foussard, J.N. (1999). Wet air oxidation (WAO) for the treatment of industrial wastewater and domestic sludge: design of bubble column reactors. *Chemical Engineering Science* **54**, 4953-4959.

Elghobashi, S., Abou-Arab, T., Rizk, M., Mostafa, A. (1984). Prediction of the particle-laden jet with a two-equation turbulence model. *International Journal of Multiphase Flow* **10** (6), 697-710.

Fedkiw, R., Aslam, T., Merriman, B., Osher, S. (1999). A non-oscillatory Eulerian approach to interfaces in multimaterial flows (the ghost fluid method). *Journal of Computational Physics* **152**, 457-492.

FLUENT 6.1. (2005). User's Manual to FLUENT 6.1. Fluent Inc. Centrera Resource Park, 10 Cavendish Court, Lebanon, USA.

GAMBIT 2 (2005). User's Manual to GAMBIT 2. Fluent Inc. Centrera Resource Park, 10 Cavendish Court, Lebanon, USA.

Gueyffier, D., Li, J., Nadim, A., Scardovelli, S., Zaleski, S. (1999). Volume of Fluid interface tracking with smoothed surface stress methods for three-dimensional flows. *Journal of Computational Physics* **152***,* 423-456.

Gunjal, P. R., Ranade, V.V., Chaudhari, R. V. (2005). Computational study of a single-phase flow in packed beds of spheres. *A.I.Ch.E. Journal* **51**, *2*, 365-378.

Lopes, R.J.G., Silva, A.M.T., Quinta-Ferreira, R.M. (2007a). Kinetic Modelling and Trickle-Bed CFD Studies in the Catalytic Wet Oxidation of Vanillic Acid. *Industrial and Engineering Chemistry Research* **46** (25), 8380-8387.

Lopes, R.J.G., Quinta-Ferreira, R.M. (2007b). Trickle-Bed CFD Studies in the Catalytic Wet Oxidation of Phenolic Acids. *Chemical Engineering Science* **62** (24), 7045-7052.

Lopes, R.J.G., Quinta-Ferreira, R.M. (2008a). Three-Dimensional Numerical Simulation of Pressure Drop and Liquid Holdup for High-Pressure Trickle-Bed Reactor. *Chemical Engineering Journal* **145**, (1), 112-120.

Lopes, R.J.G., Quinta-Ferreira, R.M. (2009a). Assessment of CFD Volume-of-Fluid Method for CWO Modelling in Trickle-bed Reactor. *Industrial and Engineering Chemistry Research*, DOI: 10.1021/ie9001348.

Lopes, R.J.G., Quinta-Ferreira, R. M. (2009b). Numerical Simulation of Trickle-Bed Reactor Hydrodynamics with RANS-Based Models Using a Volume of Fluid Technique. *Industrial and Engineering Chemistry Research* **48** (4), 1740-1748.

Lopes, R.J.G., Silva, A.M.T., Quinta-Ferreira, R.M. (2007c). Screening of catalysts and effect of temperature for kinetic degradation studies of aromatic compounds during wet oxidation. *Applied Catalysis B: Environmental* **73** (1-2), 193-202.

Lopes, R..J.G., Quinta-Ferreira, R.M. (2008b). Manganese and Copper Catalysts for the Phenolic Wastewaters Remediation by Catalytic Wet Air Oxidation. *International Journal of Chemical Reactor Engineering* **6**, A116.

Lopes, R.J.G., Quinta-Ferreira, R.M. (2009c). VOF based Model for Multiphase Flow in High-Pressure Trickle-Bed Reactor: Optimization of Numerical Parameters. *A.I.Ch.E. Journal*, DOI: 10.1002/aic.11862

Manole, C. C., Julcour-Lebigue, C., Wilhelm, A.M., Delmas, H. (2007). Catalytic Oxidation of 4-Hydroxybenzoic Acid on Activated Carbon in Batch Autoclave and Fixed-Bed Reactors. *Industrial and Engineering Chemistry Research* **46**, 8388-8396.

Matatov-Meytal, Y.I., Sheintuch, M. (1998). Catalytic Abatement of Water Pollutants. *Industrial and Engineering Chemistry Research* **37** (2), 309-326.

Maugans, C. B., Akgerman, A. (2003). Catalytic wet oxidation of phenol in a trickle bed reactor over a Pt/TiO_2 catalyst. *Water Research*, **37**, 319-328.

Mills, P.L., Chaudhari, R.V. (1999). Reaction engineering of emerging oxidation processes. *Catalysis Today* **48**, 17-29.

Mulinacci, N., Galardi, C., Pinelli, P., Vincieri, F.F. (2001). Polyphenolic Content in Olive Oil Waste Waters and Related Olive Samples. *Journal of Agricultural and Food Chemistry* **49** (8), 3509-3514.

Nijemeisland, M., Dixon, A.G. (2001). Comparison of CFD simulations to experiment for convective heat transfer in a gas-solid fixed bed. *Chemical Engineering Science* **82**, 231-246.

Osher, S., Sethian, J.A. (1988). Fronts propagating with curvature-dependent speed: algorithms based on Hamilton-Jacobi formulations. *Journal of Computational Physics* **79**, 12-49.

Paraskeva, P., Diamadopoulos, E. (2006). Technologies for olive mill wastewater (OMW) treatment: a review. *Journal of Chemical Technology and Biotechnology* **81** (9), 1475-1485.

Pintar, A., Levec, J. (2007). Catalytic wet-air oxidation processes: A review. *Catalysis Today* **124** (3-4), 172-184.

Saroha, A.K., Khera, R. (2006). Hydrodynamic study of fixed beds with cocurrent upflow and downflow. *Chemical Engineering and Processing* **45**, (6), 455-460.

Satterfield, C. N., van Eek, M.W., Bliss, G. S. (1978). Liquid-solid mass transfer in packed beds with downward concurrent gas-liquid flow. *A.I.Ch.E. Journal* **24** (4), 709-717.

Schlüter, S., Steiff, A., Weinspach, P.M. (1992). Modelling and simulation of bubble column reactors. *Chemical Engineering Processing* **31**, 97-117.

Siddiqi, M.A., Lucas, K. (1986). Correlations for prediction of diffusion in liquid. *Canadian Journal of Chemical Engineering* **64**, 839.

Singh, A., Pant, K.K., Nigam, K.D.P. (2004). Catalytic wet oxidation of phenol in a trickle bed reactor. *Chemical Engineering Journal* **103**, 51-57

Stüber, F., Fonta, J., Fortuny, A., Bengoa, C., Eftaxias, A., Fabregat, A. (2005). Carbon materials and catalytic wet air oxidation of organic pollutants in wastewater. *Topics in Catalysis*, **33** (1-4), 3-50.

Sussman, M., Smereka, P., Osher, S. (1994). A level set approach for computing solutions to incompressible two-phase flow. *Journal of Computational Physics* **114**, 146-159.

Unverdi, S.O., Tryggvason, G. (1992). A front-tracking method for viscous, incompressible multi-fluid flows. *Journal of Computational Physics* **100**, 25-37.

This page intentionally left blank

XIV. Evaluation of Multiphase CFD Models in TBR for Pollution Abatement[1]

The present work encompasses an assessment of multiphase fluid modelling techniques to allow the prediction of reaction parameters in trickle-bed reactors (TBR). After the development of Volume-of-Fluid (VOF) and an Euler-Euler model, the catalytic wet air oxidation of phenolic acids was simulated under unsteady state evaluating axial and radial profiles for total organic carbon concentration (TOC) and temperature for the bulk phase.

For the purpose of code validation, theoretical results were compared with experimental data obtained at pressures up to 40 bar in terms of major hydrodynamic parameters, pressure drop and liquid holdup. The Euler-Euler model gave better predictions in comparison with VOF model since it used empirically-based interphase coupling parameters in the momentum balance equation.

After the hydrodynamic validation, both multiphase models were used to investigate the dynamic performance under reaction conditions for the pollutant decontamination of phenolic wastewaters. VOF exhibited the highest TOC conversion as well as the highest temperatures whereas the Euler-Euler model predictions agreed better with experimental data for both simulated temperatures.

XIV.1. Introduction

Water quality is an actual and critical problem of human welfare in the twentieth-one century. The tremendous growth in the manufacture and use of synthetic chemicals in petrochemical, electrochemical and biochemical industry contributes heavily to the contamination of groundwater and surface waters. Therefore, an emerging area in lifecycle environmental applications that involves multiphase flows in advanced processes for wastewater treatment represents a great challenge for aquatic flora and fauna preservation. Bioremediation technologies have known limitations and alternative destruction methods such as catalytic wet air oxidation (CWAO) have been conducted on a variety of organic compounds using numerous catalysts with a great potential in advanced wastewater treatment facilities (Bhargava *et al.,* 2006).

TBR are catalytic randomly packed-bed tubular devices in which gas-liquid flow is processed vertical and concurrently downwards and form an essential part of multiphase reactors that are widely used for hydroprocessing industries and, more recently, for wastewater treatment

[1] *This Chapter is based upon the publication Lopes and Quinta-Ferreira (2009a)*

(Dudukovic *et al.,* 1999; Al-Dahhan *et al.,* 1997; Holub *et al*., 1993, Gianetto and Specchia, 1992; Sáez and Carbonell, 1985; Goto and Smith, 1975). The downflow operating mode offers a wide operating window for high gas-liquid interaction, including gas-liquid mass and heat transfer rates, as well as low pressure drops. Non-uniform liquid distribution issues are often a consequence of external bed porosity variations, improper gas-liquid distributors, wall effects and partial catalyst wetting. In fact, partial particle-scale external wetting is a key parameter for the proper and desired reactor operating specifications in order to avoid scarce utilization of the catalyst. This fact has been regarded as the cause of poor catalyst utilization, early catalyst deactivation, decreasing conversion, selectivity and production rates and development of axial and radial temperature profiles and hazardous hotspots.

XIV.2. Previous work

Exhaustive TBR reviews reported experimental data on pressure drop and liquid holdup as the main hydrodynamic parameters to describe the fluid flow within two categories (Al-Dahhan *et al.,* 1997; Saroha and Nigam, 1996). An empirical approach is based on the development of system specific correlations that arise from the numerical fitting of dimensionless numbers (Sie and Krishna, 1998; Ellman *et al*., 1990; Larachi *et al*., 1991). An alternative and more sophisticated methodology is rooted in the phenomenological principles of conservation laws. Recently, simulation studies have been reported in the prediction of the main hydrodynamic parameters with modern Computational Fluid Dynamics (CFD) codes. In fact, the increasing computational power has allowed a new methodology to investigate the complex hydrodynamics of TBR (Atta *et al*., 2007, Lopes and Quinta-Ferreira, 2007a; Gunjal *et al.*, 2005a; Jiang *et al.*, 2002; Carbonell, 2000) which provides a better understanding of liquid distribution and wetting phenomena in multiphase reaction engineering. Euler-Euler and Euler-Lagrange are the two main approaches that have been adopted to simulate gas-liquid flows. Whereas the Lagrangian mathematical treatment is computationally intensive providing a physical interpretation of the particle-fluid interaction in dispersed flows, the Eulerian model has been employed successfully in 2D and 3D exhibiting a good agreement between the theoretical predictions and experimental data.

CFD studies dealing with packed bed flow using a three-phase Eulerian model often make use of closure laws so that the drag-exchange coefficients are treated using the relative permeability concept or computed by a mathematical formulation based on Ergun equation for a bi- and tridimensional computational domain (Gunjal *et al.*, 2005a; Jiang *et al.*, 2002) However, CFD models based on the Eulerian-Eulerian approach are unable to capture the gas-liquid interface and its effect on wetting efficiency without the expense of interface tracking methods as VOF does.

Several works have been published on the simulation of liquid drop impact with the solid surface (Gunjal *et al.*, 2005b; Rioboo *et al.*, 2002; Richard *et al.*, 2002; Crooks *et al*., 2001; Bergeron *et al.*, 2000) The experimental and simulation data for different contact angles (Mao *et al*., 1997) and velocities (Richard *et al.,* 2002) indicated that few experimental and simulation studies were conducted at lower velocities that are characteristic of trickling flow regime. Therefore, additional simulation activities are needed for the meaningful knowledge of interaction between TBR hydrodynamics and reaction parameters.

Despite of the large number of studies reported in the literature on the various hydrodynamic aspects of TBR, a lot of work remains to be done in environmental reaction engineering. In fact, relatively few investigations have been published concerning catalytic liquid-phase oxidation of organic compounds in large-scale TBR for wastewater treatment where hydrodynamic parameters prevail. This study aims to evaluate most recent multiphase models in order to investigate the reaction behaviour of a trickle-bed reactor designed for wastewater treatment in terms of total organic carbon (TOC) profiles by means of CFD codes. Given that CWAO has demonstrated over the last decade the compulsory suitability and feasibility for the liquid effluents treatment, a trickle-bed reactor is simulated firstly in non-reaction conditions for the hydrodynamic validation and, afterwards, the CFD models are used to investigate the axial and radial temperature and TOC conversion profiles. Taking into account transport phenomena such as mass and heat transfer, an Eulerian *k*-fluid model was compared with VOF model resulting from the volume averaging of the continuity and momentum equations and solved for a 3D representation of the packed bed at unsteady state.

XIV.2. Computational Flow Domain

XIV.2.1. Volume-of-Fluid Model

VOF multiphase model was used to compute velocity field as well as liquid volume fraction distributions assuming that gas-liquid flow is processed vertically downwards through a three dimensional mesh representing the catalytic bed. Mass and momentum conservation equations are phase weighted averaged and the computation of gas-liquid-solid interfaces are carried through HRIC schemes (*High Resolution Interface Capturing*). VOF model assumed that the variable fields for all variables (pressure, velocity, etc) are shared by all phases and correspond to volume-averaged values. The VOF continuity and momentum equations, the free surface model including the surface tension and wall adhesion were described in in Equations (VIII.1)-(VIII.9) in Chapter VIII. The conservation of energy in VOF model was described in Equations (XIII.4) and (XIII.5) in Chapter XIII.

XIV.2.2. Euler-Euler Model

The continuity and momentum equations have been described in Equations (V.1) and (V.2) in Chapter V in where the turbulence modelling approach was also presented in Equations (V.9) and (V.10). The species continuity balance was expressed in Equation (X.1) in Chapter X where it was also described the conservation of energy in Eulerian multiphase applications that is described by a separate enthalpy equation for each phase as shown in Equation (X.2).

XIV.2.3. Numerical simulation

Finite-volume method has been used to discretize the governing equations as described in Chapter XII and XIII. A segregated implicit solver available in commercial CFD package FLUENT (FLUENT 6.1, 2005) was employed to evaluate the resulting linear system of equations. All the calculations were carried out on a workstation farm characterized by AMD64 Dual-Core technology. The description of the calculation procedure for the physical properties and mass transfer parameters were given in Chapter X, section X.2.

XIV.3. Results and Discussion

XIV.3.1. Hydrodynamic validation

The hydrodynamic validation of Euler-Euler and VOF models are accomplished in terms of pressure drop and liquid holdup at two different isobaric operating conditions, 10 and 40 bar. The computed pressure drop along the packed bed for both CFD models is plotted in Fig. XIV.1 while the liquid holdup is shown in Fig. XIV.2 as well as the experimental data available from the literature (Nemec and Levec, 2005).

According to Fig. XIV.1 the Eulerian model showed the better agreement with experimental data for 10 and 40 bar. At the highest operating pressure (40 bar), the VOF model underestimates pressure drop in the whole range of liquid flow rates simulated from 2 to 15 kg/m^{2}s, whilst the simulated pressure drop for 10 bar is only underestimated from 6 kg/m^{2}s onwards. Until this liquid flow rate, pressure drop is slightly underestimated for a lower interaction regime. For the purpose of CFD validation in terms of liquid holdup, the effect of operating pressure in the liquid holdup is plotted in Fig. XIV.2. Once more, the Eulerian model gave the better theoretical predictions for the liquid holdup at both isobaric operating conditions. This fact can be explained by the formulation of momentum balance equation given that it included the interphase momentum exchange terms that had an empirical basis so that the hydrodynamic validation is accomplished with improved agreement between the CFD predictions and experimental data.

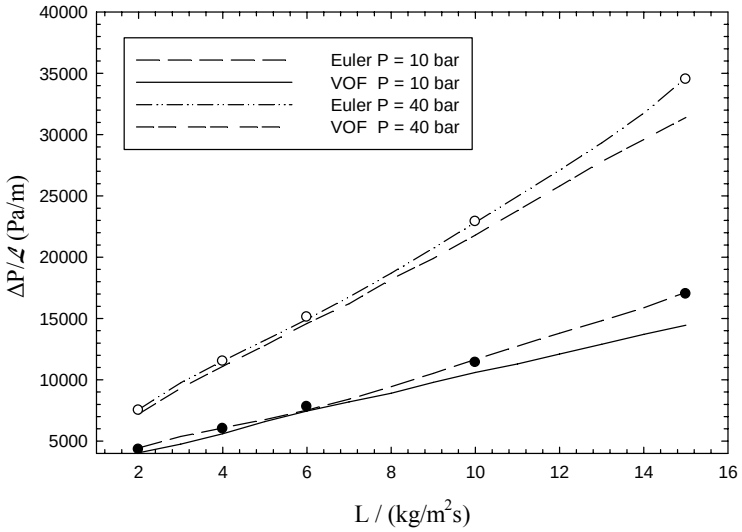

Figure XIV.1 Effect of liquid velocity on pressure drop at isobaric operation (experimental data from Nemec and Levec, 2005)

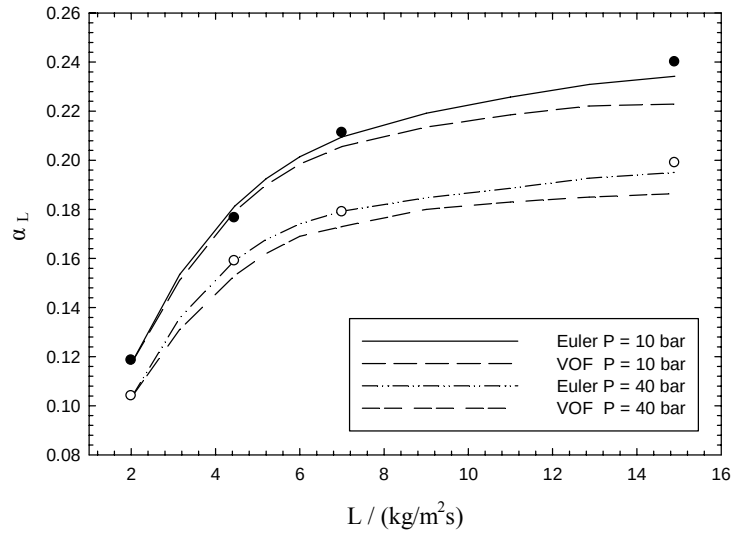

Figure XIV.2 Effect of liquid velocity on liquid holdup at isobaric operation (experimental data from Nemec and Levec, 2005)

The VOF model calculations of the liquid holdup also exhibited better concordance for lower liquid flow rates as well as for the calculation of pressure drop. The increase of liquid flow rate led to the higher liquid holdup values and then the higher absolute errors between the CFD results and experimental data were established at L = 15 kg/m^{2}s. This fact was also observed by Lopes and Quinta-Ferreira (2009b) so that for higher gas velocities, the concordance between the simulation results and experimental data was no longer observed demonstrating that liquid holdup is poorly accounted when the reactor is operated under higher interaction regimes. In fact, in the whole simulated range of liquid flow rates, the VOF model underestimates the effect of operating pressure in the liquid holdup. Therefore, the mechanistic formulation of the momentum balance

for the Eulerian model seems to be more effective for the calculation of either pressure drop or liquid holdup. Indeed, the development and inclusion of gas-liquid, gas-solid and liquid-solid interaction forces, expressed in terms of interstitial velocities and phase volume fractions, resulted in better theoretical predictions towards the hydrodynamic validation of Euler-Euler multiphase model. Comparing Figs. XIV.1and XIV.2 the influence of the operating pressure on the liquid holdup is less pronounced than in the case of pressure drop. This fact can be explained by the increase of the reactor pressure that leads to the larger values of pressure drop up to 35 kPa/m, proportionally. These higher proportional differences at higher liquid flow rates result from the fact that a further increase of the reactor pressure at a constant gas velocity corresponds to a higher driving force.

XIV.3.2.TOC and temperature profiles

The oxidation behaviour of the trickle-bed reactor in terms of total organic carbon conversion is developed taking into account the kinetic studies performed in Chapter III (Lopes *et al.*, 2007b) dealing with the catalytic wet air oxidation of several phenolic acids. The axial profile for total organic carbon removal and temperature as well as the radial ones are used to investigate the efficiency of the trickle-bed reactor for phenolic pollutant conversion. The methodology is based on the step perturbation of total organic carbon until a new steady-state is established. The dynamic behaviour of chemical reaction, convection and diffusion phenomena are coupled in both Euler-Euler and VOF models, so that high order discretisation schemes were used in order to suppress the so-called "numerical diffusion". The experimental data for the TOC oxidation in the trickle bed reactor have been collected according to the pilot installation described in Chapter XII, section XII.3.

Fig. XIV.3 shows transient axial profiles of the mean radial values of the bulk-phase TOC concentration for $T_0 = T_w$ = 160 and 200 ^oC. At the highest temperature, for both multiphase models, the TOC removal efficiency was higher at steady-state (t^* = 10) being 92.9 and 84.4 % of organic carbon oxidized with VOF and Euler-Euler models, respectively. At t^* = 1, TOC conversions were slightly lower for VOF and Euler-Euler models 88.0 and 82.3 % at $T_0 = T_w$ = 200 ^oC, respectively. Comparing both multiphase models, VOF predictions for the total organic carbon removal was always higher than with the Eulerian model. According to these axial concentration profiles, the Eulerian model agreed better with the steady-state experimental data in comparison with the VOF model. As one can see from the axial TOC profiles at steady-state, the Eulerian model overpredicted slightly the experimental data on TOC removal.

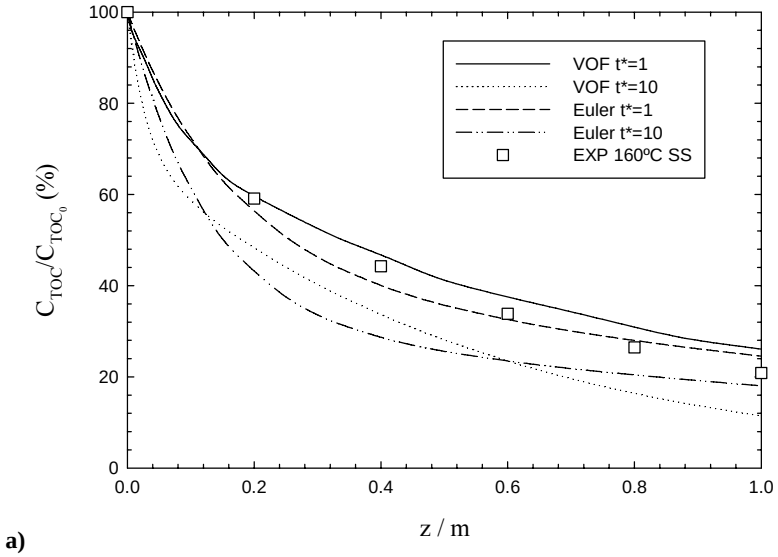

a)

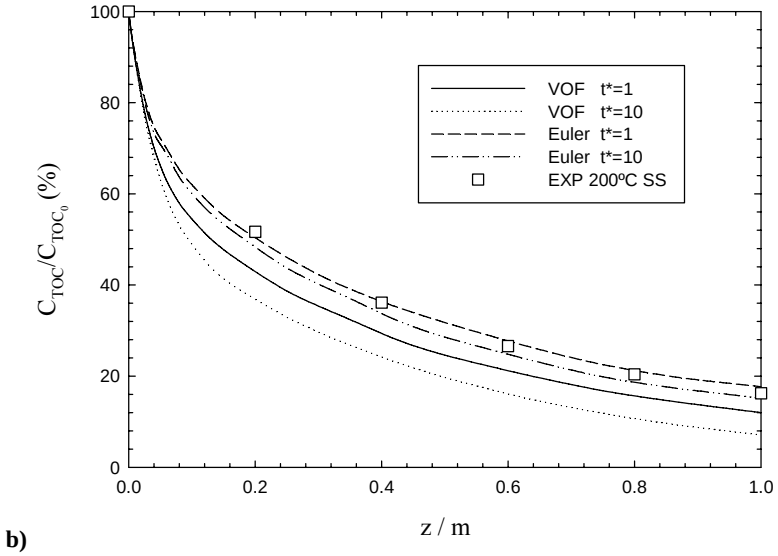

b)

Figure XIV.3. Mean radial bulk total organic carbon profiles for axial coordinate at transient conditions for different operating dimensionless times, t^* at **a)** $T_0 = T_w = 160$ ºC and **b)** $T_0 = T_w = 200$ ºC (L = 5 kg/m^{2}s, G = 0.5 kg/m^{2}s, P = 30 bar)

At the lowest temperature, $T_0 = T_w = 160$ ºC, once again both CFD models overpredicted the TOC conversion at steady-state. The relative errors between computer results and experimental data on TOC removal along the axial coordinate are given in Table XIV.1. From the tabulated data, it can be seen that whereas the relative errors are decreasing gradually from the reactor inlet to the outlet for the Eulerian model at $T_0 = T_w = 160$ ºC, those values decreased with some oscillations for the highest temperature ($T_0 = T_w = 200$ ºC). Conversely, the VOF computations exhibited the larger relative errors for both simulated temperatures. Moreover, the magnitude of these errors was higher at the highest temperature 56.2% with the VOF model whereas for the Eulerian model it was only 6.7% at the reactor outlet. This fact can be explained by the formulation of enthalpy balance meaning that a separate enthalpy equation for each phase in the Eulerian model is more efficient on the prediction of temperature, which is used to compute the species concentration,

against the shared formulation for enthalpy and temperature variables accounted by the VOF model.

Table XIV.1. Relative errors for TOC axial conversion at different temperatures for the Euler-Euler (EE) and VOF models

		z^*				
	$T_0=T_w$ ºC	0.2	0.4	0.6	0.8	1
EE	160	36.6	36.7	32.0	20.3	13.5
	200	15.4	9.6	10.3	2.7	6.7
VOF	160	25.5	26.3	33.7	32.3	45.2
	200	36.3	35.3	42.6	41.9	56.2

Fig. XIV.4 shows the axial thermal profile for the catalytic wet air oxidation simulated at $T_0 = T_w =$ 200 *ºC*.

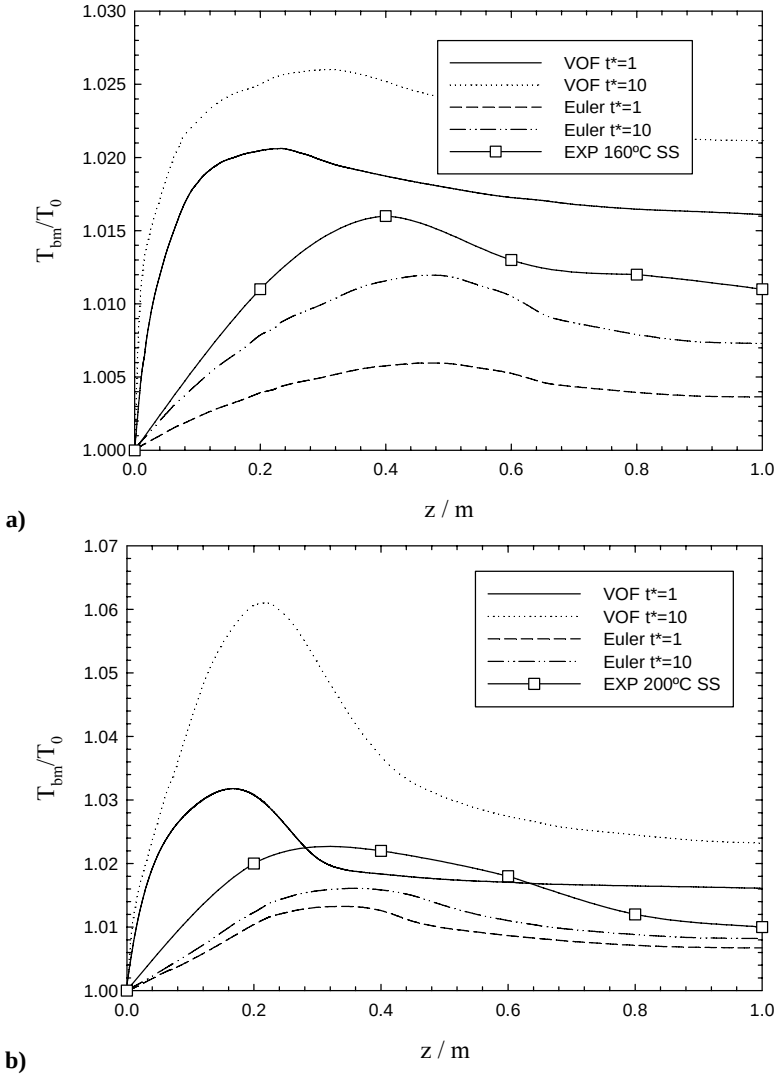

Figure XIV.4. Mean radial bulk temperature profiles for axial coordinate at transient conditions for different operating dimensionless times, t^* at **a)** $T_0 = T_w = 160$ *ºC* and **b)** $T_0 = T_w = 200$ *ºC* (L = 5 kg/m^{2}s, G = 0.5 kg/m^{2}s, P = 30 bar)

Comparing Figs XIV.3 and XIV.4, it can be pointed out that the thermal propagation is considerable different between the VOF and Eulerian models. In fact, the thermal profile computed by VOF model is much more steep in comparison with the Eulerian model for both simulated temperatures. The steady-state for both multiphase models was reached at the same operating time corresponding to about 10 times of residence time ($t^* = 10$). The main inherent difference among VOF and Euler-Euler models is related with the intensity of the maximum mean radial bulk phase temperature when the hotspot zone is attained in the first half of trickle-bed reactor. Indeed, at $T_0 = T_w = 200\ ^oC$ with VOF model the hotspot zone under steady-state is located at $z = 0.20$ m with a maximum temperature of about 212 ^oC which corresponds to 6 % of temperature increase in reference with the reactor wall or inlet temperature of feed stream. If one compares the axial temperature profiles attained at steady-state, one can observe that whereas the Eulerian model underpredicted reasonably the experimental data, the VOF model overpredicted unrealistically the experimental thermal profile at 200 ºC. At this temperature for $t^* = 10$, the magnitude of the hotspot achieved with Euler-Euler model was 1.6 % which gives the maximum temperature of 203 ^oC. Moreover, the hotspot is now pushed towards $z = 0.36$ m.

In Table XIV.2, the relative errors between the computed temperatures for both CFD models are presented for different temperatures at the hotspot zone. At it can be seen from the tabulated data, the magnitude of the relative errors attained by the CFD models were sufficiently lower when compared to the relative errors for the TOC conversion in Table XIV.1. The relative errors for the VOF model were higher than the Eulerian model ones. While these positive values for the Euler-Euler model indicate the undeprediction of experimental data 0.4 and 0.7% for $T_0 = T_w = 160$ and 200^oC, respectively, the relative errors for the VOF model were negative values which reflect the overprediction of reactor temperature -1.2 and -3.6% for $T_0 = T_w = 160$ and 200^oC, respectively. Additionally, the "relative errors" between both CFD models defined as (EE-VOF)/EE were calculated for both simulated temperatures revealing once again the lower magnitude of temperature errors. If one compares the amplitude of relative errors achieved for the axial TOC profile with the Euler-Euler model, ≈37-3%, and the VOF model, ≈26-56%, against the computed errors obtained for the axial temperature profile, Euler-Euler ≈0.4-0.7% and VOF ≈1.2-3.6%, the Eulerian model is envisaged as a rational choice for the prediction of reaction properties in the trickle-bed reactor. According to the hydrodynamics studies carried out in Chapters V-VII for the Euler-Euler model and Chapters VIII-IX for the VOF model, one has also concluded that the Eulerian CFD framework predicted with more confidence the liquid holdup and two-phase pressure drop. This fact was explained by the empirically based development of interphase coupling parameters in the momentum balance equation, which gave the better agreement against experimental data on hydrodynamics. Presently at reacting flow conditions, the lower amplitudes

of relative errors for the axial TOC and temperature variables were obtained with the Euler-Euler model that enables once more a more accurate formulation of both momentum and enthalpy balances by the Eulerian CFD model. Thus, within the Eulerian predictions it is possible to conclude that TOC deviations below 15% (7-14%) at the TBR exit, where conversions are more meaningful for the global treatment, and errors lower than 1% (0.4 and 0.7%) for the maximum temperatures, the ones that may induce more concern in reactor operation, may ensure a safe validation of this CFD tool to be used in the analysis of such complex multiphase systems. Finally, a positive judgment regarding the effectiveness of the wastewater treatment by the catalytic wet oxidation technology can be strongly emphasized.

Table XIV.2. Relative errors for temperature at the hotspot zones for different temperatures for the Euler-Euler (EE) and VOF models

						Relative errors (%)	
	$T_0=T_w$ / ºC	z^*	T_{max}	ΔT	$\%\Delta T$	(EE-VOF)/EE	(EXP-CFD)/EXP
EE	160	0.45	161.9	1.9	1.2	-1.6	0.4
	200	0.36	203.2	3.2	1.6	-4.3	0.7
VOF	160	0.25	164.5	4.5	2.8		-1.2
	200	0.2	212	12	6		-3.6
EXP	160	0.39	162.6	2.6	1.6		
	200	0.32	204.6	4.6	2.3		

Fig. XIV.5 shows the transient radial profiles of total organic carbon variable at $t^* = 1$ and 10 at $T_0 = T_w = 200$ ºC for the VOF and Eulerian models, at $z = 0.20$ and 0.36 m, which corresponds to the hotspot zones, respectively.

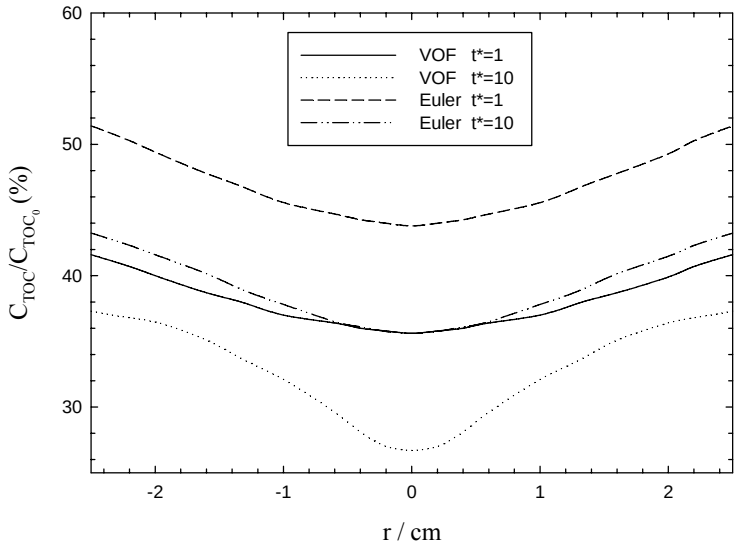

Figure XIV.5. Radial total organic carbon profiles at the hotspot for different operating dimensionless times, t^* ($T_0 = T_w = 200$ ºC, L = 5 kg/m^{2}s, G = 0.5 kg/m^{2}s, P = 30 bar)

The concentration profile indicates a radial gradient with about 16.8 and 39.7 % of TOC conversion difference at $t^* = 1$ and 10, respectively, between the reactor wall and centre with VOF model, whereas with the Euler-Euler model gave a TOC conversions of 17.3 and 21.4%. Therefore, the VOF model exhibited a considerable poor radial mixing at the hotspot mainly at the steady-state much more emphasized than with the Euler-Euler model for the same operating wall/inlet temperature. Figures XIV.6a) and b) show a snapshot of an axial plane for the liquid holdup simulated by VOF and Eulerian models, respectively, for the axial segment between z = 0.15 and 0.40 comprehending the hotspot zone.

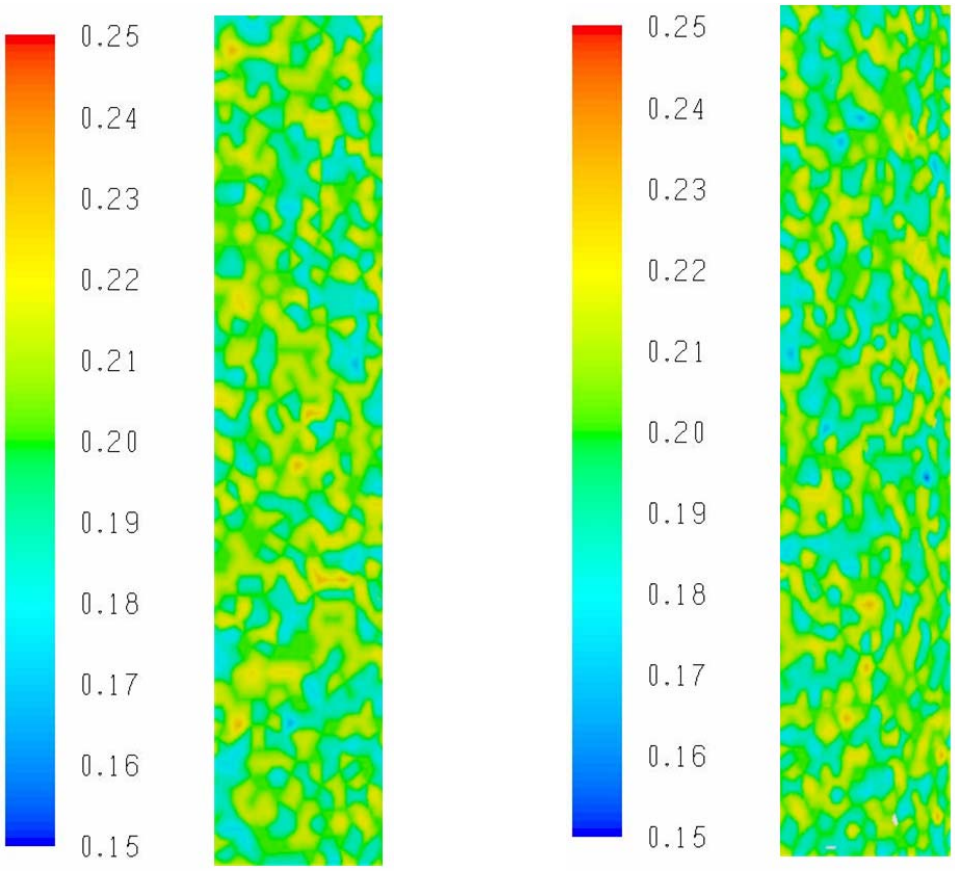

Figure XIV.6. Liquid holdup snapshot taken between z = 0.15 and 0.40 m for: **a)** VOF and **b)** Euler-Euler models

The liquid holdup shown in that plane was the time-averaged result of the liquid volume fraction since we were using a Reynolds Averaged Navier-Stokes turbulence framework. As one can conclude, the liquid holdup was not the cause for poor radial mixing so that it remains in the range of 0.19-0.21 in the whole radial coordinate. In fact, the TOC and thermal radial distribution observed at the hotspot can be related with the reaction exothermicity coupled with inefficient wetting characteristics predicted by both multiphase CFD models. This fact is mainly due to the

radial thermal gradients so that with an exothermic reaction the temperature was higher at the reactor centre. The radial distribution for the reactant concentration has been regarded in the literature as the main disadvantage of multiphase reactors operating in downflow mode in which the coupling between hydrodynamic and reaction parameters are the result of frictional forces that may cause liquid-gas mixture maldistribution and incomplete external wetting of catalyst particles. The transient radial temperature profiles computed for the hotspot at z = 0.20 (VOF) and 0.36 m (Euler-Euler) for $T_0 = T_w = 200$ *ºC* are plotted in Fig. XIV.7.

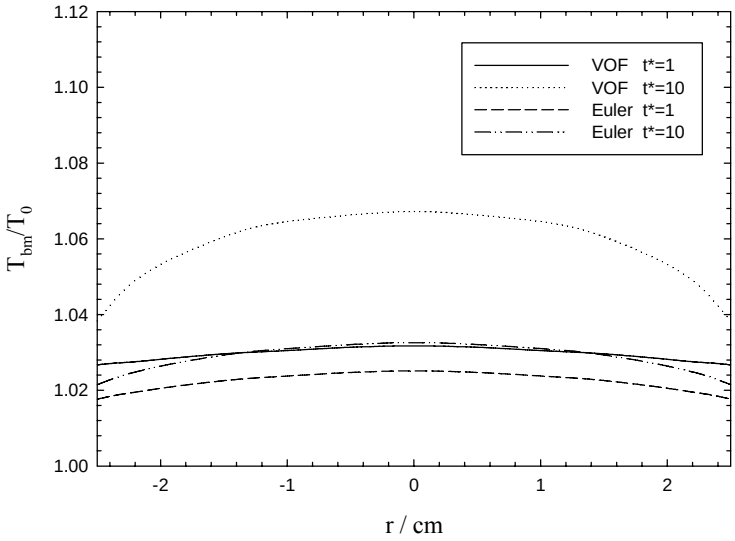

Figure XIV.7. Radial temperature profiles at the hotspot for different operating dimensionless times ($T_0 = T_w$ = 200 ºC, L = 5 kg/m^{2}s, G = 0.5 kg/m^{2}s, P = 30 bar).

As the TOC conversion radial profile showed, VOF predictions give the larger temperatures attained for the hotspot. In fact, with VOF model the maximum temperatures were 206.3 and 212 *ºC* at t^* = 1 and 10, respectively, which corresponds to a temperature increase of 6 % in reference with wall/inlet temperature at steady-state. Conversely, the Eulerian model gave a maximum percentage of 1.6 % for the bulk phase temperature, which is lower than the maximum obtained with the VOF model. The thermal profile shown in Fig. XIV.7 confirmed the poor radial mixing for the multiphase system pointing out the possible occurrence of local maximum temperatures inside the catalytic bed.

XIV.5. Conclusions

The catalytic wet air oxidation in a TBR was modelled by means of VOF and Eulerian CFD codes. Regarding the hydrodynamic validation, the Eulerian calculations showed a better concordance between computer results and experimental data since the formulation of momentum balance equation is accomplished with the interphase momentum exchange terms integrating both viscous and inertial forces. Afterwards, several runs were carried out under transient operation to evaluate the dynamic performance addressing the total organic carbon concentration and temperature profiles in the multiphase system involving the pollutant removal by CWAO. The Euler-Euler model agreed better with the experimental data on TOC removal performed at different temperatures. At the reactor outlet, whereas the relative error for the axial concentration profile obtained with the Eulerian model was 6.7%, the VOF model overpredicted 56.2% the TOC conversion at the highest temperature. This fact was attributed to the formulation of enthalpy conservation equation that has a shared structure in the VOF model. Regarding the axial temperature profiles, the Eulerian model underpredicted the reactor temperature with a slight deviation of 0.7% whilst the VOF model overpredicted up to 3.6%. Notwithstanding, the magnitude of relative errors obtained for the temperature profile was significantly lower than the TOC conversion for both simulated temperatures, 160 and 200ºC. The radial TOC conversion profiles for both multiphase models indicated a considerable degree of poor radial mixing at the hotspot caused by the reaction exothermicity, being this phenomenon reached sooner with VOF than with Euler-Euler model. In conclusion, the lower amplitudes of relative errors for the axial TOC and temperature variables obtained by the Euler-Euler model enable a more accurate development of constitutive balances in the mineralization of phenolic wastewaters through catalytic wet oxidation. This way, the ultimate goal of our work endorsing the validation of a CFD methodology to analyze the complex behaviour of multiphase reactors under trickle flow regime for such remediation technology was successfully achieved.

XIV.6. Nomenclature

G	Gas mass flux, kg/m^{2}s
L	Liquid mass flux, kg/m^{2}s
$\mathcal{L}$	Reactor length, m
p	*P*ressure, bar
t	Time, s
t^*	Dimensionless time, (t/τ)
T	Temperature, K

TOC	Total organic carbon, ppm

Greek letters

α_q	Volume fraction of q^{th} phase
Δp	Total pressure drop, Pa
τ	Residence time, s

Subscripts

G	Gas phase
L	Liquid phase
S	Solid phase
w	Wall
0	Initial time reaction

XIV.7. References

Al-Dahhan, M. H., Larachi, F., Dudukovic, M. P., Laurent, A. (1997). High pressure trickle-bed reactors: A Review. *Industrial and Engineering Chemistry Research* **36** (8), 3292-3314.

Atta, A., Roy, S., Nigam, K.D.P. (2007). Prediction of pressure drop and liquid holdup in trickle bed reactor using relative permeability concept in CFD. *Chemical Engineering Science* **62** (21), 5870-5879.

Attou, A., Ferschneider, G.A. (1999). Two-fluid model for flow regime transition in gas-liquid trickle-bed reactors. Chemical Engineering Science **54** (21), 5031-5037.

Bergeron, V., Bonn, D., Martin, J.Y., Vovelle, L. (2000). Controlling Droplet Deposition with Polymer Additives. *Nature* **405** (6788), 772-775.

Bhargava, S. K., Tardio, J., Prasad, J., Foger, K., Akolekar, D. B. and Grocott, S. C. (2006). Wet Oxidation and Catalytic Wet Oxidation. *Industrial and Engineering Chemistry Research* **45** (4), 1221-1258.

Brackbill, J.U., Kothe, D.B., Zemach, C. (1992). A Continuum Method for Modeling Surface Tension. *Journal of Computational Physics* **100** (2), 335-354.

Carbonell, R.G. (2000). Multiphase flow models in packed beds. *Oil & Gas Science and Technology* – Revue de l'IFP **55** (4), 417-425.

Crooks, R., Whitez, J.C., Boger, D.V. (2001). The Role of Dynamics Surface Tension and Elasticity on the Dynamics of Drop Impact. *Chemical Engineering Science* **56** (19), 5575-5592.

Dudukovic, M.P., Larachi, F., Mills, P.L. (1999). Multiphase reactors – revisited. *Chemical Engineering Science* **54** (13-14), 1975-1995.

Ellman, M.J., Midoux, N., Wild, G., Laurent, A., Charpentier, J.C. (1990). A new improved liquid holdup correlation for trickle bed reactors. *Chemical Engineering Science* **45** (7), 1677-1684.

FLUENT 6.1. (2005). User's Manual to FLUENT 6.1. Fluent Inc. Centrera Resource Park, 10 Cavendish Court, Lebanon, USA.

GAMBIT 2 (2005). User's Manual to GAMBIT 2. Fluent Inc. Centrera Resource Park, 10 Cavendish Court, Lebanon, USA.

Gianetto, A., Specchia, V. (1992). Trickle-bed reactors: State of the art and perspectives. *Chemical Engineering Science* **47** (13-14), 3197-3213.

Goto, S., Smith, J.M. (1975). Trickle bed reactors performance: I hold-up and mass transfer effects. *A.I.Ch.E. Journal* **21** (4), 706-713.

Gunjal, P.R., Ranade, V.V., Chaudhari, R.V. (2005a). Computational study of a single-phase flow in packed beds of spheres. *A.I.Ch.E. Journal* **51** (2), 365-378.

Gunjal, P.R., Ranade, V.V., Chaudhari, R.V. (2005b). Dynamics of Drop Impact on Solid Surface: Experiments and VOF Simulations. *A.I.Ch.E. Journal* **51** (1), 59-78.

Holub, R.A., Dudukovic, M.P., Ramachandran, P.A. (1993). Pressure drop, liquid hold-up and flow regime transition in trickle flow. *A.I.Ch.E. Journal* **39** (2), 302-321.

Jiang, Y., Khadilkar, M.R., Al-Dahhan, M.H., Dudukovic, M.P. (2002). CFD modeling of multiphase in packed bed reactors: results and applications. *A.I.Ch.E. Journal* **48**, 716-730.

Khadilkar, M. R., Wu, Y. X., Al-Dahhan, M. H., Dudukovic, M. P., Colakyan, M. (1996). Comparison of Trickle-Bed and Upflow Reactor Performance at High Pressure: Model Predictions and Experimental Observations. *Chemical Engineering Science* **51**, 2139-2148.

Larachi, F., Laurent, A., Midoux, N., Wild, G. (1991). Experimental study of a trickle bed reactor operating at high pressure: two-phase pressure drop and liquid saturation. *Chemical Engineering Science* **46** (5-6), 1233-1246.

Larachi, F., Cassanello, M., Laurent, A. (1998). Gas-Liquid Interfacial Mass Transfer in Trickle-Bed Reactors at Elevated Pressures. *Industrial and Engineering Chemistry Research* **37** (3), 718-733.

Lopes, R.J.G., Quinta-Ferreira, R.M. (2007a). Trickle-Bed CFD Studies in the Catalytic Wet Oxidation of Phenolic Acids. *Chemical Engineering Science* **62** (24), 7045-7052.

Lopes, R.J.G., Silva, A.M.T., Quinta-Ferreira, R.M. (2007b). Screening of catalysts and effect of temperature for kinetic degradation studies of aromatic compounds during wet oxidation. *Applied Catalysis B: Environmental* **73** (1), 193-202.

Lopes, R.J.G., Quinta-Ferreira, R.M. (2009a). Evaluation of Multiphase CFD Models in TBR for Pollution Abatement. *Chemical Engineering Science*, DOI: 10.1016/j.ces.2009.06.039

Lopes, R.J.G., Quinta-Ferreira, R.M. (2009b). Assessment of CFD Volume of Fluid Method for Trickle-bed Reactor Modelling, *Industrial and Engineering Chemistry Research*, DOI: 10.1021/ie9001348.

Mao, T., Kuhn, D.S.C., Tran, H. (1997). Spread and rebound of liquid droplets upon impact on flat surfaces. *A.I.Ch.E. Journal* **43** (9), 2169-2179.

Nemec, D., Levec, J. (2005). Flow through packed bed reactors: 2. Two phase concurrent downflow. *Chemical Engineering Science* **60** (24), 6958-6970.

Richard, D., Clanet, C., Quéré, D. (2002). Surface phenomena: Contact Time of a Bouncing Drop. *Nature* **417** (6891), 811.

Rioboo, R., Marengo, M., Tropea, C. (2002). Time Evaluation of Liquid Drop Impact onto Solid Dry Surfaces. *Experiments in Fluids* **33** (1), 112-124.

Sáez, A.E., Carbonell, R.G. (1985). Hydrodynamic parameters for gas liquid cocurrent flow in packed beds. *A.I.Ch.E. Journal* **31** (1), 52-62.

Saroha, A.K., Nigam, K.D.P. (1996). Trickle Bed Reactors. *Reviews in Chemical Engineering* **12** (3-4), 207-347.

Sie, S.T., Krishna, R. (1998). Process development and scale up: III. Scale-up and scale-down of trickle bed processes. *Reviews in Chemical Engineering* **14** (3), 203-252.

Wu, Y., Khadilkar, M.R., Al-Dahhan, M.H., Dudukovic, M.P. (1996). Comparison of Upflow and Downflow Two-Phase Flow Packed-Bed Reactors with and without Fines: Experimental Observations. *Industrial and Engineering Chemistry Research* **35** (2), 397-405.

This page intentionally left blank

PART E. CONCLUSIONS AND FORTHCOMING WORK

In this part of the thesis, a general overview of the main results is presented, along with the most relevant conclusions. Finally, suggestions for future work are recommended.

XV.1. General Overview and Concluding Remarks

Given that a countless number of wastewater streams originated in chemical, petrochemical, pharmaceutical and agro-alimentary plants are contaminated with toxic and hazardous organic compounds, the removal of pollutants from industrial process waters and wastewaters is a challenging and imperative research area. As long as the water availability in the world continue to decline due to either an increasing demand or lengthy drought stages, rigorous environmental regulations motivated by political and economical interests have been introduced worldwide to realize ecological stipulations on industrial processes. During the last decade, phenol derivatives in several petrochemical, chemical and pharmaceutical and agricultural industries have obtained an increasing awareness mainly due to their toxicity, health and environmental non-benign properties.

Several technologies have been investigated for wastewater remediation including biological, thermal and chemical treatments. Conventional biological methods are environmentally friendly with reasonable costs but require long residence times for micro-organisms to degrade the liquid pollutants. The intrinsic drawback of thermal treatments relies on the significant emissions of other hazardous compounds. Among chemical treatments, advanced oxidation processes based on the high reactivity of hydroxyl radicals exhibited interesting mineralization properties. In this ambit, catalytic wet oxidation has been envisaged as a plausible technology to decontaminate chemical and agro-food wastewaters streams. Specifically, olive oil mill wastewater is characterized by high content of organic matter, which imposes serious issues at the time of proper management and secure disposal. The heterogeneous nature of catalytic wet oxidation technology intends to be assigned in multiphase reactors at different levels: research on catalyst screening, activity and stability, establishment of kinetic rate laws (Part B), computational flow modelling of catalytic reactors and validation at non- (Part C) and reacting flow conditions (Part D). Parts A and E are respectively devoted to the generic introduction and final conclusions of the overall work.

In this context, Part B of this thesis was dedicated to six major pollutants typically found in olive oil mill wastewaters to mimic the polyphenolic content. Knowing that non-catalytic wet oxidation is not able to promote more than 50% of TOC conversion, several commercial ($CuO\text{-}MnO_x/Al_2O_3$, $CuO\text{-}ZnO/Al_2O_3$, $Fe_2O_3\text{-}MnO_x$ and $CuO\text{-}MnO_x$) and laboratory-made catalysts (Mn-Ce-O, Ag-Ce-O, MnCu, Mn-O and Ag-O) were used to evaluate the catalytic activity in terms of TOC removal efficiencies. Laboratory-made catalysts Mn-Ce-O and Ag-Ce-O showed the higher activity in TOC reduction for total oxidation of polyphenols and complete abatement of the intermediate compounds formed in the reaction. The crescent order for the difficulty of degradation of the phenolic acids was syringic, vanillic, *3,4,5*-trimethoxybenzoic, veratric, protocatechuic and *trans*-

cinnamic acid. The TOC content in the solution was successfully removed by catalytic wet air oxidation at 200 ºC and 30 bar total pressure with Mn-Ce-O catalyst. The higher molar quantity of manganese in both co-precipitated and wetness impregnated catalyst led to the best TOC degradation results. Kinetic parameters were obtained by means of a lumped kinetic model highlighting a quite interesting phenomenon coming from the concurrent treatment of various pollutants. The co-oxidation process was identified in the simultaneous treatment of a phenolic acids mixture clearly showing the enhancement of carbon content depletion in comparison with the individual degradation of the same compounds. Slight leaching of manganese was identified and the carbon content in the solution was removed by oxidation and not by adsorption on the solid catalyst. The catalytic stability was also addressed in terms of catalyst poisoning due to deposition of carbonaceous materials. Both manganese and copper catalysts exhibited low levels of carbon and hydrogen adsorption. Therefore, given the most active and stable behaviour, manganese/cerium catalyst was identified as an interesting formulation for further industrial implementation in CWAO of olive oil mill wastewaters.

A high-pressure trickle-bed reactor has been modelled along Part C of the present work by a three-dimensional CFD framework aiming to evaluate the hydrodynamic predictions in terms of pressure drop and liquid holdup. The Euler-Euler model takes into account the interphase coupling terms in the momentum transfer between the gas, liquid and solid phases. CFD calculations with different mesh sizes were checked against experiments and a good agreement was achieved. Different mesh apertures were evaluated to establish grid independence using a relative error measure of hydrodynamic parameters magnitude between the coarse and fine solutions. The effect of packing size on the pressure drop and liquid holdup was ascribed by different surface area of the packing material for the trickle-bed reactor. The theoretical predictions from the model correctly account for the strong influence of the gas flow on the hydrodynamic behaviour of the trickle-bed reactors. These gas interactions on the liquid phase appear noticeably significant at high superficial gas mass velocities. Several Reynolds Averaged Navier-Stokes turbulence models were investigated within the Eulerian framework, namely, standard, realizable and Renormalization Group Theory k-ε models as well as Reynolds Stress Model for the hydrodynamics simulation of high-pressure trickle-bed reactor. In a first stage, the parametric optimization of different numerical solution parameters was accomplished at cold flow conditions for the validation of the multiphase flow model. High-order discretization schemes agreed better with the experimental data as long as they are based on Total Variation Diminishing algorithm that overcomes the numerical dispersion. Standard k-ε dispersed turbulence was then used to evaluate the influence of flow temperature on axial velocity and turbulent kinetic energy profiles and it was found to be responsible for the smoothness of liquid maldistribution along the packed bed. Multiphase flow

distribution has been examined at trickling flow conditions querying the effect of different liquid distributors at the top of the trickle-bed reactor. Additionally, time averaged axial and radial profiles of liquid holdup and two-phase pressure drop were computed to evaluate the effect of gas and liquid flow rates and pressure. The increase of pressure on multiphase flow distribution was found to smooth the radial profiles for both hydrodynamic parameters whereas the liquid flow rate had more prominent effect on radial pressure drop at higher values in relative comparison to an equivalent change in gas flow rate.

The trickle-bed was also modelled by means of a VOF model. During grid optimization and validation, the effects of mesh size, time step and convergence criteria were evaluated plotting the hydrodynamic predictions as a function of liquid flow rate. High-order differencing schemes were investigated for the discretization of the volume fraction equation. VOF was also used to examine the multiphase flow regime and the effect of gas flow rate on the numerical accuracy produced by either laminar or several turbulent flow models. At lower gas flow rates, the VOF predictions performed with the laminar flow model were found to produce qualitative and quantitatively the same computed results as turbulent flow models for both liquid holdup and frictional pressure drop, while for higher flow rates the turbulent flow models performed better, indicating the considerable degree of turbulence induced by the gas phase. The effect of gas flow rate on hydrodynamics revealed a significant influence on the liquid holdup in the range G=0.1 – 0.7 kg/m^2s. Catalyst wetting efficiency can be captured by VOF model according to the radial mapping of liquid volume fractions of the packed bed.

In Part D of the thesis, at reacting flow conditions the behaviour of a trickle-bed reactor for the catalytic wet air oxidation of an aqueous solution containing vanillic acid has been studied by the Eulerian CFD model. The Eulerian framework was deployed accounting for the transport mechanisms as well as the CWAO reaction kinetics. The CFD simulation has been accomplished in transient mode and exhibited a considerable effect of temperature whereas the air partial pressure only had minor influence. Afterwards, the catalytic wet oxidation of a six phenolic acids mixture was carried out at different operating conditions as follows: 10 – 30 bar of reactor pressure while gas and liquid mass flow rates were in the range 0.10 – 0.70 and 0.05 – 15 kg/m^2s, respectively. TOC depletion rates were systematized in terms of temperature, pressure, gas-liquid flow rate and initial pollutant concentration. TOC conversion depends heavily on the temperature bed while the operating pressure has minor influence in final performance. When the liquid flow rate is decreased, the residence time increases and the conversion is higher, but increasing the gas flow rate it was achieved an optimum value where the TOC conversion is maximum. Moreover, higher values of inlet pollutant concentration led also to higher conversions.

Following the hydrodynamic corroboration, the Eulerian CFD model was validated with experimental data taken from a trickle-bed reactor pilot plant specifically designed for the catalytic wet oxidation of low- to moderate strength wastewaters. Various computational runs were carried out under unsteady-state operation to evaluate the dynamic performance addressing the total organic carbon concentration and temperature profiles. The effect of operating temperature was examined in terms of axial/radial TOC and temperature profiles. During the CFD model validation at the higher operating temperature, it was found that the Eulerian model overpredicted the TOC removal efficiency whereas the axial bulk temperature profiles were undepredicted for both simulated temperatures. Axial concentration profiles were then correlated with the radial ones revealing a poor radial mixing for the simulated flow regime namely at the hotspots caused by the reaction exothermicity. Concomitantly, several runs were carried out under unsteady-state operation to evaluate the dynamic performance addressing the total organic carbon concentration and temperature profiles by means of VOF multiphase model. The highest TOC conversion and temperature at the hotspot as well as the poorest radial mixing were obtained with the VOF model. The influence of the operating temperature in the thermal profiles illustrated the existence of local hotspots located in the first half of the reactor with an intensity of about 6% higher than the inlet and wall temperatures (160, 200ºC). From the comparison between both multiphase models, the better agreement of the Eulerian model with the experimental data on TOC removal at the reactor outlet has been attributed to the formulation of enthalpy conservation equation that has a shared structure in the VOF model. In what concerns the axial temperature profiles, the Eulerian model underpredicted the reactor temperature whereas the VOF model overpredicted up to 4%. Nevertheless, according to the multiphase CFD simulations the magnitude of relative errors obtained for the temperature profile was significantly lower than the TOC conversion for both simulated temperatures. In a nutshell, the lower amplitudes of relative errors for the axial TOC and temperature variables exhibited by the Euler-Euler model empowered a secure estimation of reaction properties in the catalytic abatement of phenolic wastewaters by wet oxidation in a trickle-bed reactor. The validation of CFD methodology was then accomplished at trickling flow conditions addressing both hydrodynamic and reaction parameters.

Being aware that trickle-bed reactor operation may have controllability issues related to liquid maldistribution that could be responsible for reactor runaway, CFD results stated that local hotspots were observed and liquid distribution assumed a major role in order to achieve feasibility and to improve the catalyst wetting efficiency. The current CFD formulations are interesting options to capture the wetting phenomena and the effects of flow regimes on three-phase packed-bed reactors. Specifically, Euler-Euler can be used to probe the hydrodynamic behaviour of a TBR in terms of pressure drop, liquid holdup and catalyst wetting efficiency in detail as never before.

These computational results allow us to obtain a better understanding of the fundamental physics governing the efficiency of multiphase reactors for advanced wastewater treatment facilities and the CWAO technology deployment in the commercial-scale TBR. In comparison to the VOF model, the Eulerian CFD framework is envisaged as a valuable tool to accelerate the industrial implementation of trickle-bed reactors in advanced wastewater treatment plants. Furthermore, the commercial catalyst N140 has exhibited promising results in continuous operation for the TOC removal of high-strength phenolic wastewaters.

XV.2. Suggestions for Forthcoming Work

The results of the present work showed that CFD tools are able to predict reasonably well the hydrodynamic and reaction variables of multiphase reactors operating in trickling flow regime. Both experimental research and numerical predictions should continue in order to contribute to an improved understanding and numerical predictability of trickle-bed reactors hydrodynamic and reaction parameters over a wide range of operating flow regimes that characterize the trickle-bed reactor operation including the trickle flow, spray flow, pulse and bubbly flow.

Steady and unsteady state modelling should be then accomplished for different hydrodynamic regimes. Most of the research currently taking place in the field of multiphase reactors concerns the study of turbulent flows. The present work showed that different turbulence frameworks should be taken into account even for lower values of Reynolds number defined in terms of interstitial velocity. If one operates at $Re_l > 300$, the flow is highly unsteady, chaotic and qualitatively resembling turbulent flow. The three major types of turbulence methodologies to be tested for different hydrodynamic regimes are Direct Numerical Simulation and Large Eddy Simulation apart from Reynolds Averaged Navier-Stokes modelling. Whereas under certain conditions this method can be very accurate, it is not always suitable for transient pulsing and bubbling flows because the averaging process attempts to model the turbulence by performing time or space averaging. Direct Numerical Simulation, on the other hand, attempts to solve all time and spatial scales. Unfortunately, Direct Numerical Simulation is unrealistic for the majority of multiphase systems mainly because it is computationally unrealistic. Therefore, the numerical study should begin with the compromise offered between these two methods that is Large Eddy Simulation. The resulting methodology is a hybrid framework between these those methods, which involves the filtering of the Navier-Stokes equations to separate those scales to be modelled from those which will be solved as in the Direct Numerical Simulation.

The CFD models, Euler-Euler and Volume-of-Fluid, have to be verified and validated for different flow regimes encompassing a wide range of operating Reynolds numbers. Why should one verify and validate those multiphase frameworks. Mainly because validation has to do with whether or not the correct equations have been chosen for the task at hand. Thus, the Eulerian and other multiphase models should be tested with the momentum exchange forms presented in this thesis for other hydrodynamic conditions. Verification, on the other hand, has to do with whether or not the chosen equations are being solved correctly. Verification procedures address whether the grid resolution is sufficient, whether a solution is converging, and whether the algorithm has been coded correctly. After all, modern and sophisticated techniques including Laser Dopler Anemometry and Particle Image Velocimetry should be regarded for the CFD validation.

The interaction of hydrodynamics of the trickle-bed reactor with chemical reaction can be further investigated by using the Probability Density Function methods for different flow regimes. Further research on Mn-Ce-O catalytic stability and activity in trickle-bed reactors are suggested in the near future to move forward the industrial implementation and, mainly, to improve the environmental performance of catalytic wet oxidation. This can dictate the success of continuous CWAO technology in wastewater treatment. Finally, any advance in TBR technology will represent substantial savings, which stimulates the continued research efforts aimed at improving TBR operation and performance.

This page intentionally left blank

APPENDIX A. FLUENT SOLVER

This Appendix describes the FLUENT solver methodologies. Details about the solver algorithms used by FLUENT are provided after a brief overview of flow solvers for the solution of the general scalar transport equation. Afterwards, pressure-velocity coupling and time-advancement algorithm are presented for the numerical solution of the general scalar transport equation. Finally, discretization schemes for spatial and temporal derivatives are described along the evaluation methods of gradients and derivatives.

A.1 Approaches to Multiphase Modelling

Advances in computational fluid dynamics have provided the basis for further insight into the dynamics of multiphase flows. Currently there are three approaches for the numerical calculation of multiphase flows: the Euler-Euler, the Euler-Lagrange and the VOF models.

Euler-Euler Model

In the Euler-Euler approach, the different phases are treated mathematically as interpenetrating continua. Since the volume of a phase cannot be occupied by the other phases, the concept of phasic volume fraction is introduced. These volume fractions are assumed to be continuous functions of space and time and their sum is equal to one. Conservation equations for each phase are derived to obtain a set of equations, which have similar structure for all phases. These equations are closed by providing constitutive relations that are obtained from empirical information, or, in the case of granular flows, by application of kinetic theory.

In the Eulerian model a set of n momentum and continuity equations is derived by ensemble averaging the local instantaneous balance for each phase. Coupling is achieved through the pressure and interphase exchange coefficients. The manner in which this coupling is handled depends upon the type of phases involved; granular (fluid-solid) flows are handled differently than nongranular (fluid-fluid) flows. Momentum exchange between the phases is also dependent upon the type of mixture being modelled. FLUENT's user-defined functions are used for the momentum exchange calculations.

Euler-Lagrange Model

In this approach, the fluid phase is treated as a continuum by solving the time averaged Navier-Stokes equations in the same manner as for a single-phase system, while the dispersed phase is solved by tracking a large number of particles, bubbles or droplets through the calculated flow field using Newtonian equation of motion.

VOF Model

The VOF model is a surface-tracking technique applied to a fixed Eulerian mesh. It is designed for two or more immiscible fluids where the position of the interface between the fluids is of interest. In the VOF model, a single set of momentum equations is shared by the fluids, and the volume fraction of each of the fluids in each computational cell is tracked throughout the domain. Applications of the VOF model include stratified flows, free-surface flows, filling, sloshing, the

motion of large bubbles in a liquid, the motion of liquid after a dam break, the prediction of jet breakup (surface tension), and the steady or transient tracking of any liquid-gas interface.

A.2 Overview of Flow Solvers[1]

FLUENT allows one of the two numerical methods: pressure- and density-based solver. Whereas the pressure-based approach was developed for low-speed incompressible flows, the density-based approach was mainly used for high-speed compressible flows. However, recently both methods have been extended and reformulated to solve and operate for a wide range of flow conditions beyond their traditional or original intent.

For both methods the velocity field is obtained from the momentum equations. In the density-based approach, the continuity equation is used to obtain the density field while the pressure field is determined from the equation of state. On the other hand, in the pressure-based approach, the pressure field is extracted by solving a pressure or pressure correction equation which is obtained by manipulating continuity and momentum equations. Using either method, FLUENT solves the governing integral equations for the conservation of mass and momentum, and (when appropriate) for energy and other scalars such as turbulence and chemical species. In both cases a control-volume-based technique is used that consists of:

- Division of the domain into discrete control volumes using a computational grid.
- Integration of the governing equations on the individual control volumes to construct algebraic equations for the discrete dependent variables such as velocities, pressure, temperature, and conserved scalars.
- Linearization of the discretized equations and solution of the resultant linear equation system to yield updated values of the dependent variables.

Taking into account that both numerical methods employ a similar discretization process (finite-volume), the mathematical approach used to linearize and solve the discretized equations is only given for the pressure-based solver.

The pressure-based solver employs an algorithm which belongs to a general class of methods called the projection method. In the projection method, the constraint of mass and momentum conservation is achieved by solving a pressure (or pressure correction) equation. The pressure equation is derived from the continuity and the momentum equations in such a way that the velocity field, corrected by the pressure, satisfies the continuity. Since the governing equations are

[1] *Adapted from FLUENT 6 User's Manual, Fluent Inc. Centrera Resource Park, 10 Cavendish Court, Lebanon, USA*

nonlinear and coupled to one another, the solution process involves iterations wherein the entire set of governing equations is solved repeatedly until the solution converges. Two pressure-based solver algorithms are available in FLUENT: a segregated algorithm, and a coupled algorithm. These two approaches are discussed in the sections below.

The Pressure-Based Segregated Algorithm

According this methodoly, the pressure-based solver uses a solution algorithm where the governing equations are solved sequentially (i.e., segregated from one another). Because the governing equations are non-linear and coupled, the solution loop must be carried out iteratively in order to obtain a converged numerical solution.

In the segregated algorithm, the individual governing equations for the solution variables (e.g., *u, p, T, k, ε*) are solved one after another. Each governing equation, while being solved, is "decoupled" or "segregated" from other equations, hence its name. The segregated algorithm is memory-efficient, since the discretized equations need only to be stored in the memory one at a time. However, the solution convergence is relatively slow, inasmuch as the equations are solved in a decoupled manner. With the segregated algorithm, each iteration consists of the steps illustrated in Figure A.1, where the coupled algorithm is also represented, and outlined below:

1. Update fluid properties (e,g, density, viscosity, specific heat) including turbulent viscosity (diffusivity) based on the current solution.
2. Solve the momentum equations, one after another, using the recently updated values of pressure and face mass fluxes.
3. Solve the pressure correction equation using the recently obtained velocity field and the mass-flux.
4. Correct face mass fluxes, pressure, and the velocity field using the pressure correction obtained from Step 3.
5. Solve the equations for additional scalars, if any, such as turbulent quantities, energy and chemical species concentration using the current values of the solution variables.
6. Update the source terms arising from the interactions among different phases (e.g., source term for the carrier phase due to discrete phase).
7. Check for the convergence of the equations.

These steps are continued until the convergence criteria are met.

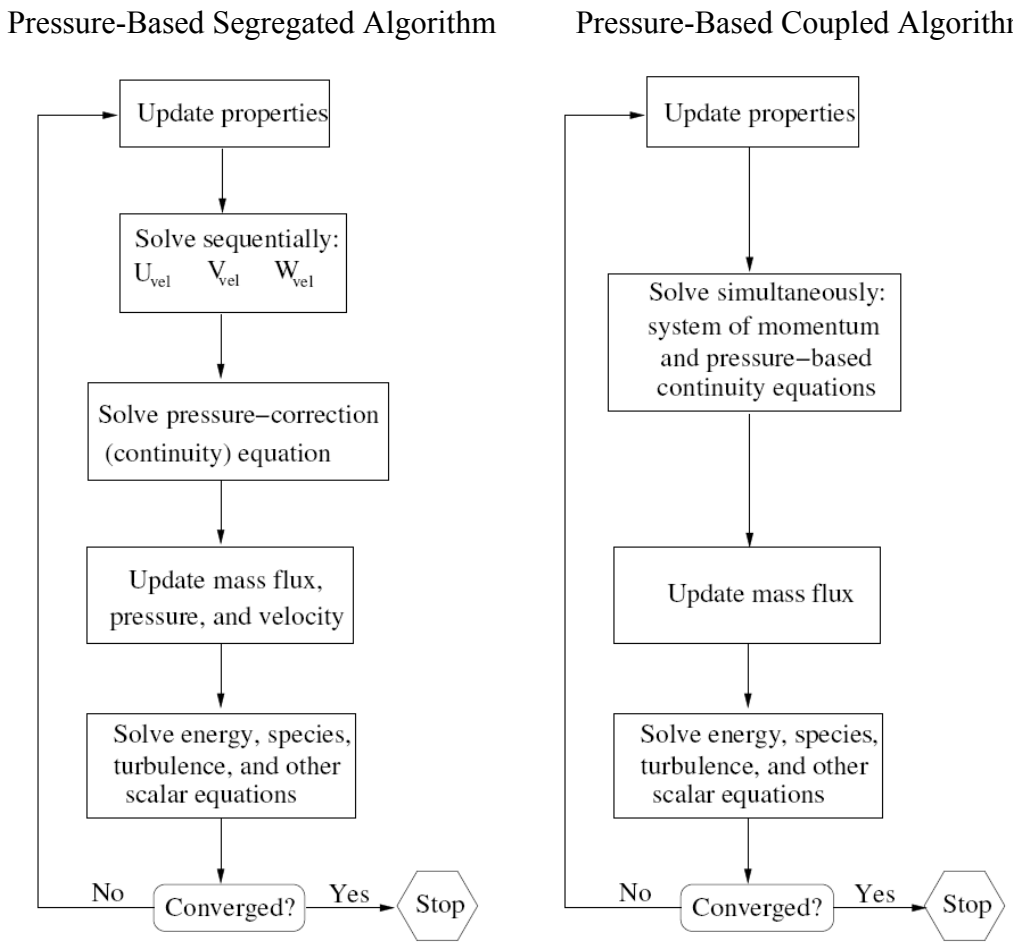

Figure A.1 Overview of the Pressure-based solution methods

The Pressure-Based Coupled Algorithm

Unlike the segregated algorithm described above, the pressure-based coupled algorithm solves a coupled system of equations comprising the momentum equations and the pressure-based continuity equation. Thus, in the coupled algorithm, Steps 2 and 3 in the segregated solution algorithm are replaced by a single step in which the coupled system of equations are solved. The remaining equations are solved in a decoupled fashion as in the segregated algorithm.

Since the momentum and continuity equations are solved in a closely coupled manner, the rate of solution convergence significantly improves when compared to the segregated algorithm. However, the memory requirement increases by 1.5 - 2 times that of the segregated algorithm since the discrete system of all momentum and pressure-based continuity equations need to be stored in the memory when solving for the velocity and pressure fields (rather than just a single equation, as is the case with the segregated algorithm).

A.3 General Scalar Transport Equation: Discretization and Solution[2]

FLUENT uses a control-volume-based technique to convert a general scalar transport equation to an algebraic equation that can be solved numerically. This control volume technique consists of integrating the transport equation about each control volume, yielding a discrete equation that expresses the conservation law on a control-volume basis. Discretization of the governing equations can be illustrated most easily by considering the unsteady conservation equation for transport of a scalar quantity ϕ. This is demonstrated by the following equation written in integral form for an arbitrary control volume V as follows:

$$\int_V \frac{\partial \rho \phi}{\partial t} dV + \oint \rho \phi \vec{u} \cdot d\vec{A} = \oint \Gamma_\phi \nabla \phi \cdot d\vec{A} + \int_V S_\phi dV \qquad \text{(A.1)}$$

where ρ is density, $\vec{u}$ is the velocity vector, $\vec{A}$ is the surface area vector, Γ_ϕ is the diffusion coefficient for ϕ, $\nabla\phi$ is the gradient of ϕ and S_ϕ is the source of ϕ per unit volume. Equation (A.1) is applied to each control volume, or cell, in the computational domain. The two-dimensional, triangular cell shown in Figure A.2 is an example of such a control volume. Discretization of Equation (A.1) on a given cell yields:

$$\frac{\partial \rho \phi}{\partial t} V + \sum_f^{N\ faces} \rho_f \vec{u}_f \phi_f \cdot \vec{A}_f = \sum_f^{N\ faces} \Gamma_\phi \nabla \phi_f \cdot \vec{A}_f + S_\phi V \qquad \text{(A.2)}$$

where N_{faces} is the number of faces enclosing cell, ϕ_f is the value of ϕ convected through face f, $\vec{A}_f$ is the area of face f, $\nabla\phi_f$ is the gradient of ϕ at face f and V is the cell volume. The equations solved by FLUENT take the same general form as the one given above and apply readily to multi-dimensional, unstructured meshes composed of arbitrary polyhedra.

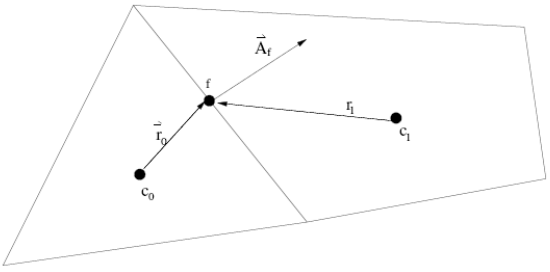

Figure A.2 Control volume used to illustrate discretization of a scalar transport equation

[2] *Adapted from FLUENT 6 User's Manual, Fluent Inc. Centrera Resource Park, 10 Cavendish Court, Lebanon, USA*

A.3.1 Solving the Linear System

The discretized scalar transport Equation (Equation (A.2)) contains the unknown scalar variable ϕ at the cell center as well as the unknown values in surrounding neighbor cells. This equation will, in general, be non-linear with respect to these variables. A linearized form of Equation (A.2) can be written as:

$$a_P \phi = \sum_{nb} a_{nb} \phi_{nb} + b \tag{A.3}$$

where the subscript *nb* refers to neighbor cells, and a_P and a_{nb} are the linearized coefficients for ϕ and ϕ_{nb}. The number of neighbors for each cell depends on the grid topology, but will typically equal the number of faces enclosing the cell. Similar equations can be written for each cell in the grid. This results in a set of algebraic equations with a sparse coefficient matrix. For scalar equations, FLUENT solves this linear system using a point implicit (Gauss-Seidel) linear equation solver in conjunction with an algebraic multigrid method.

A.3.2 Discretization of the Momentum Equation

In this section, special practices related to the discretization of the momentum and continuity equations and their solution by means of the pressure-based solver are addressed. These practices are most easily described by considering the steady-state continuity and momentum equations in integral form:

$$\oint \rho \vec{u} \cdot d\vec{A} = 0 \tag{A.4}$$

$$\oint \rho \vec{u} \vec{u} \cdot d\vec{A} = -\oint pI \cdot d\vec{A} + \oint \bar{\bar{\tau}} \cdot d\vec{A} + \int_V \vec{F} dV \tag{A.5}$$

where I is the identity matrix, $\bar{\bar{\tau}}$ is the stress tensor, and $\vec{F}$ is the force vector. The discretization scheme for a scalar transport equation is also used to discretize the momentum equations. For example, the x-momentum equation can be obtained by setting $\phi = u$:

$$a_P u = \sum_{nb} a_{nb} u_{nb} + \sum p_f A \cdot \hat{i} + S \tag{A.6}$$

If the pressure field and face mass fluxes are known, Equation (A.6) can be solved directly and a velocity field obtained. However, the pressure field and face mass fluxes are not known a priori and must be obtained as a part of the solution. There are important issues with respect to the storage of pressure and the discretization of the pressure gradient term; these are addressed next. FLUENT uses a co-located scheme, whereby pressure and velocity are both stored at cell centers.

However, Equation (A.6) requires the value of the pressure at the face between cells c_0 and c_1, shown in Figure A.2. Therefore, an interpolation scheme is required to compute the face values of pressure from the cell values.

Pressure Interpolation Schemes

The default scheme in FLUENT interpolates the pressure values at the faces using momentum equation coefficients:

$$P_f = \frac{\frac{P_{c0}}{a_{p,c0}} + \frac{P_{c1}}{a_{p,c1}}}{\frac{1}{a_{p,c0}} + \frac{1}{a_{p,c1}}} \tag{A.7}$$

This procedure works well as long as the pressure variation between cell centers is smooth. When there are jumps or large gradients in the momentum source terms between control volumes, the pressure profile has a high gradient at the cell face, and cannot be interpolated using this scheme. If this scheme is used, the discrepancy shows up in overshoots/undershoots of cell velocity.

Several alternate methods are available for cases in which the standard pressure interpolation scheme is not valid:

- The linear scheme computes the face pressure as the average of the pressure values in the adjacent cells.
- The second-order scheme reconstructs the face pressure in the manner used for second-order accurate convection terms. This scheme may provide some improvement over the standard and linear schemes, but it may have some trouble if it is used at the start of a calculation and/or with a bad mesh. The second-order scheme is not applicable for flows with discontinuous pressure gradients imposed by the presence of a porous medium in the domain or the use of the VOF or mixture model for multiphase flow.
- The body-force-weighted scheme computes the face pressure by assuming that the normal gradient of the difference between pressure and body forces is constant. This works well if the body forces are known a priori in the momentum equations (e.g., buoyancy and axisymmetric swirl calculations).
- The PRESTO (PREssure STaggering Option) scheme uses the discrete continuity balance for a "staggered" control volume about the face to compute the "staggered" (i.e., face) pressure. This procedure is similar in spirit to the staggered-grid schemes used with structured meshes. Note that for triangular, tetrahedral, hybrid, and polyhedral meshes, comparable accuracy is obtained using a similar algorithm. The PRESTO scheme is available for all meshes.

A.3.3 Discretization of the Continuity Equation

Equation (A.4) may be integrated over the control volume in Figure A.2 to yield the following discrete equation:

$$\sum_{f}^{N\ faces} J_f A_f = 0 \tag{A.8}$$

where J_f is the mass flux through face f, ρu_n.

In order to proceed further, it is necessary to relate the face values of velocity, $\vec{u}_n$, to the stored values of velocity at the cell centers. Linear interpolation of cell-centered velocities to the face results in unphysical checker-boarding of pressure. The face value of velocity is not averaged linearly; instead, momentum-weighted averaging, using weighting factors based on the a_P coefficient from Equation (A.6), is performed. Using this procedure, the face flux, J_f, may be written as:

$$\begin{aligned} J_f &= \rho_f \frac{a_{p,c0}u_{n,c0} + a_{p,c1}u_{n,c1}}{a_{p,c0} + a_{p,c1}} + d_f\left(\left(p_{c0} + (\nabla p)_{c0} \cdot \vec{r}_0\right) - \left(p_{c1} + (\nabla p)_{c1} \cdot \vec{r}_1\right)\right) \\ &= \hat{J}_f + d_f\left(p_{c0} + p_{c1}\right) \end{aligned} \tag{A.9}$$

where p_{c0}, p_{c1} and $u_{n,c0}$, $u_{n,c1}$ are the pressures and normal velocities, respectively, within the two cells on either side of the face, and $\hat{J}_f$ contains the influence of velocities in these cells (see Figure A.2). The term d_f is a function of $\overline{a}_p$, the average of the momentum equation a_P coefficients for the cells on either side of face f.

For incompressible flows, FLUENT uses arithmetic averaging for density. For compressible flow calculations (i.e., calculations that use the ideal gas law for density), FLUENT applies upwind interpolation of density at cell faces. Several interpolation schemes are available for the density upwinding at cell faces: first-order upwind (default), second-order-upwind, QUICK, MUSCL, and when applicable, central differencing and bounded central differencing. The first-order upwind scheme sets the density at the cell face to be the upstream cell-center value. This scheme provides stability for the discretization of the pressure-correction equation, and gives good results for most classes of flows. The first-order scheme is the default scheme for compressible flows. Although this scheme provides the best stability for compressible flow calculations, it gives very diffusive representations of shocks. The second-order upwind scheme provides stability for supersonic

flows and captures shocks better than the first-order upwind scheme. The QUICK scheme for density is similar to the QUICK scheme used for other variables.

A.3.4 Pressure-Velocity Coupling

Pressure-velocity coupling is achieved by using Equation (A.9) to derive an additional condition for pressure by reformatting the continuity equation (Equation (A.8)). The pressure-based solver allows solving a flow problem in either a segregated or coupled manner. FLUENT provides the option to choose among five pressure-velocity coupling algorithms: SIMPLE, SIMPLEC, PISO and Coupled. All the aforementioned schemes, except the "coupled" scheme, are based on the predictor-corrector approach. Note that SIMPLE, SIMPLEC, PISO, and Fractional Step use the pressure-based segregated algorithm, while Coupled uses the pressure-based coupled solver.

Segregated Algorithms

SIMPLE

The SIMPLE algorithm uses a relationship between velocity and pressure corrections to enforce mass conservation and to obtain the pressure field. If the momentum equation is solved with a guessed pressure field p^*, the resulting face flux, J^*_f, computed from Equation (A.10):

$$J^*_f = \hat{J}^*_f + d_f\left(p^*_{c0} - p^*_{c1}\right) \tag{A.10}$$

does not satisfy the continuity equation. Consequently, a correction J'_f is added to the face flux J^*_f so that the corrected face flux, J_f:

$$J_f = J^*_f + J'_f \tag{A.11}$$

satisfies the continuity equation. The SIMPLE algorithm postulates that J'_f be written as

$$J'_f = d_f\left(p'_{c0} - p'_{c1}\right) \tag{A.12}$$

where p' is the cell pressure correction. The SIMPLE algorithm substitutes the flux correction equations (Equations (A.11) and (A.12)) into the discrete continuity equation (Equation (A.8)) to obtain a discrete equation for the pressure correction p' in the cell:

$$a_P p' = \sum a_{nb} p'_{nb} + b \tag{A.13}$$

where the source term b is the net flow rate into the cell:

$$b = \sum_{f}^{N\ faces} J^*_f A_f \tag{A.14}$$

The pressure-correction equation (Equation (A.13)) may be solved using the algebraic multigrid (AMG) method. Once a solution is obtained, the cell pressure and the face flux are corrected using:

$$p = p^* + \alpha_p p' \tag{A.15}$$

$$J_f = J^*_f + d_f\left(p'_{c0} - p'_{c1}\right) \tag{A.16}$$

Here α_p is the under-relaxation factor for pressure. The corrected face flux, J_f, satisfies the discrete continuity equation identically during each iteration.

SIMPLEC

A number of variants of the basic SIMPLE algorithm are available in the literature. In addition to SIMPLE, FLUENT offers the SIMPLEC (SIMPLE-Consistent) algorithm. SIMPLE is the default, but many problems will benefit from the use of SIMPLEC. The SIMPLEC procedure is similar to the SIMPLE procedure outlined above. The only difference lies in the expression used for the face flux correction, J'_f. As in SIMPLE, the correction equation may be written as shown in Equation (A.16):

$$J_f = J^*_f + d_f\left(p'_{c0} - p'_{c1}\right)$$

However, the coefficient d_f is redefined as a function of $\left(a_P - \sum_{nb} a_{nb}\right)$. The use of this modified correction equation has been shown to accelerate convergence in problems where pressure-velocity coupling is the main deterrent to obtaining a solution. For meshes with some degree of skewness, the approximate relationship between the correction of mass flux at the cell face and the difference of the pressure corrections at the adjacent cells is very rough. Since the components of the pressure-correction gradient along the cell faces are not known in advance, an iterative process similar to the PISO neighbor correction described below is desirable. After the initial solution of the pressure-correction equation, the pressure-correction gradient is recalculated and used to update the mass flux corrections. This process, which is referred to as "skewness correction", significantly reduces convergence difficulties associated with highly distorted meshes. The SIMPLEC skewness correction allows FLUENT to obtain a solution on a highly skewed mesh in approximately the same number of iterations as required for a more orthogonal mesh.

PISO

The Pressure-Implicit with Splitting of Operators (PISO) pressure-velocity coupling scheme, part of the SIMPLE family of algorithms, is based on the higher degree of the approximate relation between the corrections for pressure and velocity. One of the limitations of the SIMPLE and SIMPLEC algorithms is that new velocities and corresponding fluxes do not satisfy the momentum balance after the pressure-correction equation is solved. As a result, the calculation must be repeated until the balance is satisfied. To improve the efficiency of this calculation, the PISO algorithm performs two additional corrections: neighbor correction and skewness correction.

The main idea of the PISO algorithm is to move the repeated calculations required by SIMPLE and SIMPLEC inside the solution stage of the pressure-correction equation. After one or more additional PISO loops, the corrected velocities satisfy the continuity and momentum equations more closely. This iterative process is called a momentum correction or "neighbor correction". The PISO algorithm takes a little more CPU time per solver iteration, but it can dramatically decrease the number of iterations required for convergence, especially for transient problems.

For meshes with some degree of skewness, the approximate relationship between the correction of mass flux at the cell face and the difference of the pressure corrections at the adjacent cells is very rough. Since the components of the pressure-correction gradient along the cell faces are not known in advance, an iterative process similar to the PISO neighbor correction described above is desirable. After the initial solution of the pressure-correction equation, the pressure-correction gradient is recalculated and used to update the mass flux corrections. This process, which is referred to as "skewness correction", significantly reduces convergence difficulties associated with highly distorted meshes. The PISO skewness correction allows FLUENT to obtain a solution on a highly skewed mesh in approximately the same number of iterations as required for a more orthogonal mesh. For meshes with a high degree of skewness, the simultaneous coupling of the neighbor and skewness corrections at the same pressure correction equation source may cause divergence or a lack of robustness. An alternate, although more expensive, method for handling the neighbor and skewness corrections inside the PISO algorithm is to apply one or more iterations of skewness correction for each separate iteration of neighbor correction. For each individual iteration of the classical PISO algorithm form, this technique allows a more accurate adjustment of the face mass flux correction according to the normal pressure correction gradient.

Coupled Algorithm

As previously mentioned, the pressure-based solver computes the solution in either a segregated or coupled manner. Using the coupled approach offers some advantages over the non-coupled or segregated approach. The coupled scheme obtains a robust and efficient single phase implementation for steady-state flows, with superior performance compared to the segregated solution schemes. This pressure-based coupled algorithm offers an alternative to the density-based and pressure-based segregated algorithm with SIMPLE-type pressure-velocity coupling. For transient flows, using the coupled algorithm is necessary when the quality of the mesh is poor, or if large time steps are used.

The pressure-based segregated algorithm solves the momentum equation and pressure correction equations separately. This semi-implicit solution method results in slow convergence. The coupled

algorithm solves the momentum and pressure-based continuity equations together. The full implicit coupling is achieved through an implicit discretization of pressure gradient terms in the momentum equations, and an implicit discretization of the face mass flux.

In the momentum equations (A.6), the pressure gradient for component *k* is of the form:

$$\sum_f p_f A_k = -\sum_j a^{u_k p} p_j \tag{A.17}$$

Where $a^{u_k p}$ is the coefficient derived from the Gauss divergence theorem and coefficients of the pressure interpolation schemes (Equation (A.7)). Finally, for any i^{th} cell, the discretized form of the momentum equation for component u_k is defined as:

$$\sum_j a_{ij}^{\ u_k u_k} u_{kj} + \sum_j a_{ij}^{\ u_k p} p_j = b_i^{\ u_k} \tag{A.18}$$

In the continuity equation, Equation (A.8), the balance of fluxes is replaced using the flux expression in Equation (A.9), resulting in the discretized form:

$$\sum_k \sum_j a_{ij}^{\ p u_k} u_{kj} + \sum_j a_{ij}^{\ pp} p_j = b_i^{\ p} \tag{A.19}$$

As a result, the overall system of Equations (A.18) and (A.19), after being transformed to the δ-form, is presented as:

$$\sum_j \left[A\right]_{ij} \vec{X}_j = \vec{B}_i \tag{A.20}$$

where the influence of a cell *i* on a cell *j* has the form:

$$A_{ij} = \begin{bmatrix} a_{ij}^{pp} & a_{ij}^{pu} & a_{ij}^{pv} & a_{ij}^{pw} \\ a_{ij}^{up} & a_{ij}^{uu} & a_{ij}^{uv} & a_{ij}^{uw} \\ a_{ij}^{vp} & a_{ij}^{vu} & a_{ij}^{vv} & a_{ij}^{vw} \\ a_{ij}^{wp} & a_{ij}^{wu} & a_{ij}^{wv} & a_{ij}^{ww} \end{bmatrix} \tag{A.21}$$

and the unknown and residual vectors have the form:

$$\vec{X}_j = \begin{bmatrix} p'_i \\ u'_i \\ v'_i \\ w'_i \end{bmatrix};\ \vec{B}_i = \begin{bmatrix} -r_i^{\,p} \\ -r_i^{\,u} \\ -r_i^{\,v} \\ -r_i^{\,w} \end{bmatrix} \tag{A.22; A.23}$$

A.3.5 Solution Method in FLUENT for Multiphase Flows

For Eulerian multiphase calculations, FLUENT uses the phase coupled SIMPLE (PC-SIMPLE) algorithm for the pressure-velocity coupling. PC-SIMPLE is an extension of the SIMPLE algorithm to multiphase flows. The velocities are solved coupled by phases, but in a segregated

fashion. The block algebraic multigrid scheme is used to solve a vector equation formed by the velocity components of all phases simultaneously. Pressure and velocities are then corrected so as to satisfy the continuity constraint.

The Pressure-Correction Equation

For incompressible multiphase flow, the pressure-correction equation takes the form:

$$\sum_{q=1}^{n} \frac{1}{\rho_{rq}} \left\{ \frac{\partial}{\partial t} \alpha_q \rho_q + \nabla \cdot \alpha_q \rho_q \vec{u}_q^{'} + \nabla \cdot \alpha_q \rho_q \vec{u}_q^{*} - \left(\sum_{l=1}^{n} \left(\dot{m}_{lq} - \dot{m}_{ql} \right) \right) \right\} = 0 \tag{A.24}$$

where ρ_{rq} is the phase reference density for the q^{th} phase (defined as the total volume average density of phase q), $\vec{u}_q^{'}$ is the velocity correction for the q^{th} phase, and $\vec{u}_q^{*}$ is the value of $\vec{u}_q$ at the current iteration. The velocity corrections are themselves expressed as functions of the pressure corrections.

Volume Fractions

The volume fractions are obtained from the phase continuity equations. In discretized form, the q^{th} volume fraction is given by Equation (A.25).

$$a_{p,q} \alpha_q = \sum_{nb} \left(a_{nb,q} \alpha_{nb,q} \right) + b_q = R_q \tag{A.25}$$

These equations satisfy the condition that all volume fractions sum to one as expressed in Equation (A.26).

$$\sum_{q=1}^{n} \alpha_q = 1 \tag{A.26}$$

A.3.6 Steady-State Iterative Algorithm

If performing a steady-state calculation, the governing equations for the pressure-based solver do not contain time-dependent terms. For steady-state flows, the following section describes control-volume-based discretization of the steady-state transport equation.

Under-Relaxation of Variables

The under-relaxation of variables is used in all cases for some material properties and in the pressure-based coupled algorithm where this explicit under-relaxation is used for momentum and pressure. Because of the nonlinearity of the equation set being solved by FLUENT, it is necessary to control the change of ϕ. This is typically achieved by under-relaxation of variables (also

referred to as explicit relaxation), which reduces the change of ϕ produced during each iteration. In a simple form, the new value of the variable ϕ within a cell depends upon the old value, ϕ_{old}, the computed change in ϕ, $\Delta\phi$, and the under-relaxation factor, α, as follows:

$$\phi = \phi_{old} + \alpha\Delta\phi \tag{A.27}$$

Under-Relaxation of Equations

The under-relaxation of equations, also known as implicit relaxation, is used in the pressure-based solver to stabilize the convergence behavior of the outer nonlinear iterations by introducing selective amounts of ϕ in the system of discretized equations. This is equivalent to the location-specific time step.

$$\frac{a_P\phi}{\alpha} = \sum_{nb} a_{nb}\phi_{nb} + b + \frac{1-\alpha}{\alpha}a_P\phi_{old} \tag{A.28}$$

The Courant-Friedrichs-Lewy (CFL) number is a solution parameter in the pressure-based coupled algorithm and can be written in terms of α:

$$\frac{1-\alpha}{\alpha} = \frac{1}{CFL} \tag{A.29}$$

A.3.7 Time-Advancement Algorithm

The temporal discretization of the transient derivative in the Equation (A.2) is accomplished using first-order and second-order schemes in time. The pressure-based solver in FLUENT uses an implicit discretization of the transport equation. As a standard default approach, all convective, diffusive, and source terms are evaluated from the fields for time level *n+1*.

$$\int_V \frac{\partial\rho\phi}{\partial t}dV + \oint \rho^{n+1}\phi^{n+1}\vec{u}^{\,n+1}\cdot d\vec{A} = \oint \Gamma_\phi{}^{n+1}\nabla\phi^{n+1}\cdot d\vec{A} + \int_V S_\phi{}^{n+1}dV \tag{A.30}$$

In the pressure-based solver, the overall time-discretization error is determined by both the choice of temporal discretization (e.g., first-order, second-order) and the manner in which the solutions are advanced to the next time step (time-advancement scheme). Temporal discretization introduces the corresponding truncation error; $O(\Delta t)$, $O[(\Delta t)^2]$, for first-order and second-order, respectively. The segregated solution process by which the equations are solved one by one introduces splitting error. There are two approaches to the time-advancement scheme depending on how we want to control the splitting error.

Iterative Time-Advancement Scheme

In the iterative scheme, all the equations are solved iteratively, for a given time-step, until the convergence criteria are met. Thus, advancing the solutions by one time-step normally requires a number of outer iterations as shown in Figure A.3 and Figure A.4. With this iterative scheme, non-linearity of the individual equations and inter-equation couplings are fully accounted for, eliminating the splitting error. The iterative scheme is the default in FLUENT.

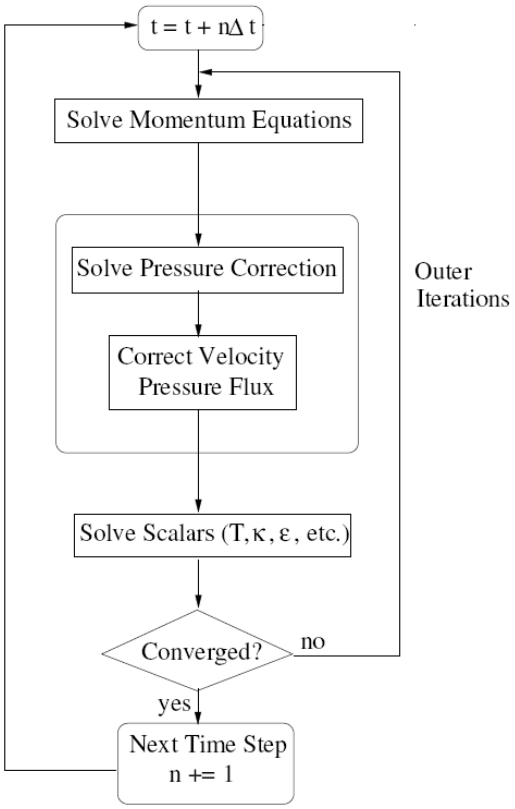

Figure A.3 Overview of the iterative time advancement solution method for the segregate solver

The standard fully-implicit discretization of the convective part of Equation (A.30) produces non-linear terms in the resulting equations. In addition, solving these equations generally requires numerous iterations per time step. As an alternative, FLUENT provides an optional way to discretize the convective part of Equation (A.2) using the mass flux at the cell faces from the previous time level *n*.

$$\oint \rho\phi\vec{u} \cdot d\vec{A} = \oint \rho^n \phi^{n+1} \vec{u}^n \cdot d\vec{A} \qquad \text{(A.31)}$$

The solution still has the same order of accuracy but the non-linear character of the discretized transport equation is essentially reduced and the convergence within each time step is improved.

Non-Iterative Time-Advancement Scheme

The iterative time-advancement scheme requires a considerable amount of computational effort due to a large number of outer iterations performed for each time-step. The idea underlying the non-iterative time-advancement (NITA) scheme is that, in order to preserve overall time accuracy, one does not really need to reduce the splitting error to zero, but only have to make it the same order as the truncation error. The NITA scheme, as seen in Figure A.4, thus does not need the outer iterations, performing only a single outer iteration per time-step, which significantly speeds up transient simulations. However, the NITA scheme still allows for an inner iteration to solve the individual set of equations.

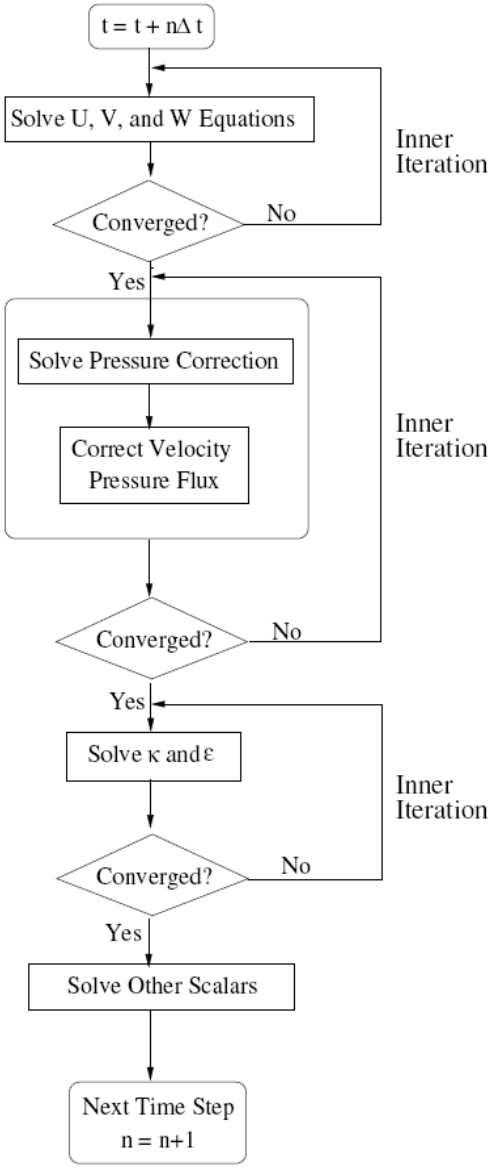

Figure A.4 Overview of the non-iterative time advancement solution method

A.4 Discretization[3]

A.4.1 Spatial Discretization

By default, FLUENT stores discrete values of the scalar ϕ at the cell centers. However, face values ϕ_f are required for the convection terms in Equation (A.2) and must be interpolated from the cell center values. This is accomplished using an upwind scheme.

Upwinding means that the face value ϕ_f is derived from quantities in the cell upstream, or "upwind," relative to the direction of the normal velocity u_n in Equation (A.2). FLUENT has several upwind schemes: first-order upwind, second-order upwind, power law, and QUICK. The diffusion terms in Equation (A.2) are central-differenced and are always second-order accurate.

First-Order Upwind Scheme

When first-order accuracy is desired, quantities at cell faces are determined by assuming that the cell-center values of any field variable represent a cell-average value and hold throughout the entire cell; the face quantities are identical to the cell quantities. Thus when first-order upwinding is selected, the face value ϕ_f is set equal to the cell-center value of ϕ in the upstream cell.

Power-Law Scheme

The power-law discretization scheme interpolates the face value of a variable, ϕ, using the exact solution to a one-dimensional convection-diffusion equation:

$$\frac{\partial}{\partial x}(\rho u \phi) = \frac{\partial}{\partial x}\Gamma\frac{\partial \phi}{\partial x} \tag{A.32}$$

where Γ and ρu are constant across the interval ∂x. Equation (A.32) can be integrated to yield the following solution describing how ϕ varies with x:

$$\frac{\phi(x)-\phi_0}{\phi_L-\phi_0} = \frac{\exp\left(Pe\frac{x}{L}\right)-1}{\exp(Pe)-1} \tag{A.33}$$

where

$\phi_0 = \phi|_{x=0}$

$\phi_L = \phi|_{x=L}$

and Pe is the Peclet number:

[3] *Adapted from FLUENT 6 User's Manual, Fluent Inc. Centrera Resource Park, 10 Cavendish Court, Lebanon, USA*

$$Pe = \frac{\rho u L}{\Gamma} \tag{A.34}$$

Second-Order Upwind Scheme

When second-order accuracy is desired, quantities at cell faces are computed using a multidimensional linear reconstruction approach. In this approach, higher-order accuracy is achieved at cell faces through a Taylor series expansion of the cell-centered solution about the cell centroid. Thus when second-order upwinding is selected, the face value ϕ_f is computed using the following expression:

$$\phi_{f,SOU} = \phi + \nabla\phi \cdot \vec{r} \tag{A.35}$$

where ϕ and $\nabla\phi$ are the cell-centered value and its gradient in the upstream cell, and $\vec{r}$ is the displacement vector from the upstream cell centroid to the face centroid. This formulation requires the determination of the gradient $\nabla\phi$ in each cell. Finally, the gradient $\nabla\phi$ is limited so that no new maxima or minima are introduced.

Central-Differencing Scheme

The second-order central-differencing scheme calculates the face value for a variable (ϕ_f) as follows:

$$\phi_{f,CD} = \frac{1}{2}(\phi_0 + \phi_1) + \frac{1}{2}(\nabla\phi_0 \cdot \vec{r}_0 + \nabla\phi_1 \cdot \vec{r}_1) \tag{A.36}$$

where the indices *0* and *1* refer to the cells that share face *f* and $\vec{r}$ is the vector directed from the cell centroid toward the face centroid. It is well known that central-differencing schemes can produce unbounded solutions and non-physical wiggles, which can lead to stability problems for the numerical procedure. These stability problems can often be avoided if a deferred approach is used for the central-differencing scheme. In this approach, the face value is calculated as follows:

$$\phi_f = \underbrace{\phi_{f,UP}}_{implicit\ part} + \underbrace{(\phi_{f,CD} - \phi_{f,UP})}_{explicit\ part}$$

where *UP* stands for upwind. As indicated, the upwind part is treated implicitly while the difference between the central-difference and upwind values is treated explicitly. Provided that the numerical solution converges, this approach leads to pure second-order differencing.

QUICK Scheme

FLUENT also provides the QUICK scheme for computing a higher-order value of the convected variable ϕ at a face. QUICK-type schemes are based on a weighted average of second-order-

upwind and central interpolations of the variable. For the face *e* in Figure A.5, if the flow is from left to right, such a value can be written as:

$$\phi_e = \theta\left[\frac{S_d}{S_d+S_c}\phi_P + \frac{S_c}{S_d+S_c}\phi_E\right] + (1-\theta)\left[\frac{S_u+2S_c}{S_u+S_c}\phi_P - \frac{S_c}{S_u+S_c}\phi_W\right] \tag{A.37}$$

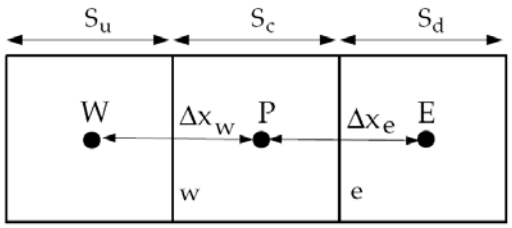

Figure A.5 One-dimensional control volume

θ=1 in the above equation results in a central second-order interpolation while θ=0 yields a second-order upwind value. The traditional QUICK scheme is obtained by setting θ=1/8. The implementation in FLUENT uses a variable, solution-dependent value of θ=1, chosen so as to avoid introducing new solution extrema.

Third-Order MUSCL Scheme

This third-order convection scheme was conceived from the original MUSCL (Monotone Upstream-Centered Schemes for Conservation Laws) by blending a central differencing scheme and second-order upwind scheme as:

$$\phi_f = \theta\phi_{f,CD} + (1-\theta)\phi_{f,SOU}$$

where $\phi_{f,CD}$ is defined in Equation (A.36), and $\phi_{f,SOU}$ is computed using the second-order upwind scheme as described above in Equation (A.35). Compared to the second-order upwind scheme, the third-order MUSCL has a potential to improve spatial accuracy for all types of meshes by reducing numerical diffusion, most significantly for complex three-dimensional flows, and it is available for all transport equations.

Modified HRIC Scheme

For simulations using the VOF multiphase model, upwind schemes are generally unsuitable for interface tracking because of their overly diffusive nature. Central differencing schemes, while generally able to retain the sharpness of the interface, are unbounded and often give unphysical results. In order to overcome these deficiencies, FLUENT uses a modified version of the High Resolution Interface Capturing (HRIC) scheme. The modified HRIC scheme is a composite

Normalised Variable Diagram (NVD) scheme that consists of a non-linear blend of upwind and downwind differencing.

First, the normalized cell value of volume fraction, $\tilde{\phi}_c$, is computed and is used to find the normalized face value, $\tilde{\phi}_f$, as follows:

$$\tilde{\phi}_c = \frac{\phi_D - \phi_U}{\phi_A - \phi_U} \tag{A.38}$$

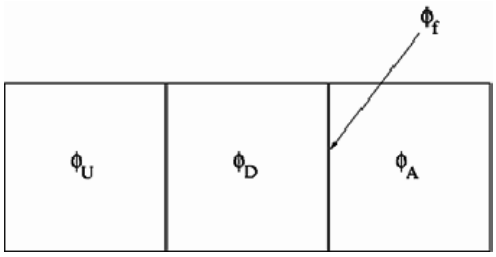

Figure A.6 Cell representation for modified HRIC scheme

where *A* is the acceptor cell, *D* is the donor cell, and *U* is the upwind cell, and

$$\tilde{\phi}_f = \begin{cases} \tilde{\phi}_c & \tilde{\phi}_c < 0 \text{ or } \tilde{\phi}_c > 1 \\ 2\tilde{\phi}_c & 0 \le \tilde{\phi}_c \le 0.5 \\ 1 & 0.5 \le \tilde{\phi}_c \le 1 \end{cases} \tag{A.39}$$

Here, if the upwind cell is not available, an extrapolated value is used for ϕ_U. Directly using this value of $\tilde{\phi}_f$ causes wrinkles in the interface, if the flow is parallel to the interface. So, FLUENT switches to ULTIMATE QUICKEST scheme (the one-dimensional bounded version of the QUICK scheme) based on the angle between the face normal and interface normal:

$$\phi_f^{\tilde{U}Q} = \begin{cases} \tilde{\phi}_c & \tilde{\phi}_c < 0 \text{ or } \tilde{\phi}_c > 1 \\ MIN\left(\tilde{\phi}_f, \frac{6\tilde{\phi}_c + 3}{8}\right) & 0.5 \le \tilde{\phi}_c \le 1 \end{cases} \tag{A.40}$$

This leads to a corrected version of the face volume fraction, $\tilde{\phi}_f^*$:

$$\tilde{\phi}_f^* = \tilde{\phi}_f \sqrt{\cos\theta} + \left(1 - \sqrt{\cos\theta}\right)\phi_f^{\tilde{U}Q} \tag{A.41}$$

where

$$\cos\theta = \frac{\nabla\phi \cdot \vec{d}}{|\nabla\phi|\,|\vec{d}|} \tag{A.42}$$

and $\vec{d}$ is a vector connecting cell centers adjacent to the face f.

The face volume fraction is now obtained from the normalized value computed above as expressed in Equation (A.43):

$$\tilde{\phi}_f = \tilde{\phi}_f^* \left(\phi_A - \phi_U\right) + \phi_U \tag{A.43}$$

Geometric Reconstruction Scheme

In the VOF geometric reconstruction approach, the standard interpolation schemes that are used in FLUENT are applied to obtain the face fluxes whenever a cell is completely filled with one phase or another. When the cell is near the interface between two phases, the geometric reconstruction scheme is used. The geometric reconstruction scheme represents the interface between fluids using a piecewise-linear approach. It assumes that the interface between two fluids has a linear slope within each cell, and uses this linear shape for calculation of the advection of fluid through the cell faces. The first step in this reconstruction scheme is calculating the position of the linear interface relative to the centre of each partially-filled cell, based on information about the volume fraction and its derivatives in the cell. The second step is calculating the advecting amount of fluid through each face using the computed linear interface representation and information about the normal and tangential velocity distribution on the face. The third step is calculating the volume fraction in each cell using the balance of fluxes calculated during the previous step.

Donor-Acceptor Scheme

In the donor-acceptor approach, the standard interpolation schemes that are used in FLUENT are used to obtain the face fluxes whenever a cell is completely filled with one phase or another. When the cell is near the interface between two phases, a "donor-acceptor" scheme is used to determine the amount of fluid advected through the face. This scheme identifies one cell as a donor of an amount of fluid from one phase and another (neighbour) cell as the acceptor of that same amount of fluid, and is used to prevent numerical diffusion at the interface. The amount of fluid from one phase that can be convected across a cell boundary is limited by the minimum of two values: the filled volume in the donor cell or the free volume in the acceptor cell. The orientation of the interface is also used in determining the face fluxes. The interface orientation is either horizontal or vertical, depending on the direction of the volume fraction gradient of the q^{th} phase within the cell, and that of the neighbour cell that shares the face in question. Depending on the interface's orientation as well as its motion, flux values are obtained by pure upwinding, pure downwinding, or some combination of the two.

Compressive Interface Capturing Scheme for Arbitrary Meshes Scheme

The compressive interface capturing scheme for arbitrary meshes (CICSAM), based on the Ubbink's work, is a high resolution differencing scheme. The CICSAM scheme is particularly suitable for flows with high ratios of viscosities between the phases. CICSAM is implemented in FLUENT as an explicit scheme and offers the advantage of producing an interface that is almost as sharp as the geometric reconstruction scheme.

A.4.2 Temporal Discretization

For transient simulations, the governing equations must be discretized in both space and time. The spatial discretization for the time-dependent equations is identical to the steady-state case. Temporal discretization involves the integration of every term in the differential equations over a time step Δt. The integration of the transient terms is straightforward, as shown below.

A generic expression for the time evolution of a variable ϕ is given by:

$$\frac{\partial \phi}{\partial t} = F(\phi) \tag{A.44}$$

where the function F incorporates any spatial discretization. If the time derivative is discretized using backward differences, the first-order accurate temporal discretization is given by:

$$\frac{\phi^{n+1} - \phi^{n}}{\Delta t} = F(\phi) \tag{A.45}$$

and the second-order discretization is given by:

$$\frac{3\phi^{n+1} - 4\phi^{n} + \phi^{n-1}}{2\Delta t} = F(\phi) \tag{A.46}$$

where ϕ is a scalar quantity, $n+1$ is the value at the next time level, $t+\Delta t$, n is the value at the current time level, t, and $n-1$ is the value at the previous time level, $t-\Delta t$.

Once the time derivative has been discretized, a choice remains for evaluating $F(\phi)$, in particular, which time level values of ϕ should be used in evaluating F: the implicit or explicit time integration method.

Implicit Time Integration

One method is to evaluate $F(\phi)$at the future time level:

$$\frac{\phi^{n+1} - \phi^{n}}{\Delta t} = F(\phi^{n+1}) \tag{A.47}$$

This is referred to as "implicit" integration since ϕ^{n+1} in a given cell is related to ϕ^{n+1} in neighbouring cells through $F\left(\phi^{n+1}\right)$:

$$\phi^{n+1} = \phi^n + \Delta t F\left(\phi^{n+1}\right) \tag{A.48}$$

This implicit equation can be solved iteratively at each time level before moving to the next time step. The advantage of the fully implicit scheme is that it is unconditionally stable with respect to time step size.

Explicit Time Integration

This method evaluates $F(\phi)$ at the current time level:

$$\frac{\phi^{n+1} - \phi^n}{\Delta t} = F\left(\phi^n\right) \tag{A.49}$$

and is referred to as "explicit" integration since ϕ^{n+1} can be expressed explicitly in terms of the existing solution values, ϕ^n:

$$\phi^{n+1} = \phi^n + \Delta t F\left(\phi^n\right) \tag{A.50}$$

Here, the time step Δt is restricted to the stability limit of the underlying solver (i.e., a time step is limited by the Courant-Friedrich-Lewy condition). In order to be time-accurate, all cells in the domain must use the same time step. For stability, this time step must be the minimum of all the local time steps in the domain.

Time Schemes in Multiphase Flow

In many multiphase applications, the process can vary spatially as well as temporally. In order to accurately model multiphase flow, both higher-order spatial and time discretization schemes are necessary. In addition to the first-order time scheme in FLUENT, the second-order time scheme is available in the Eulerian multiphase model and with the VOF Implicit Scheme.

In multiphase flow, a general transport equation (Equation (A.44) may be written as:

$$\frac{\partial(\alpha\rho\phi)}{\partial t} + \nabla \cdot \left(\alpha\rho\vec{u}\phi\right) = \nabla \cdot \overline{\overline{\tau}} + S_\phi \tag{A.51}$$

where ϕ is either a mixture or a phase variable, α is the phase volume fraction (unity for the mixture equation), ρ is the mixture phase density, $\vec{u}$ is the mixture or phase velocity (depending on the equations), $\overline{\overline{\tau}}$ is the diffusion term, and S_ϕ is the source term. As a fully implicit scheme, this second-order time-accurate scheme achieves its accuracy by using an Euler backward approximation in time (see Equation (A.46)). The general transport equation, Equation (A.51) is discretized as:

$$\frac{3\left(\alpha_p \rho_p \phi_p V\right)^{n+1} - 4\left(\alpha_p \rho_p \phi_p V\right)^{n} + \left(\alpha_p \rho_p \phi_p V\right)^{n-1}}{2\Delta t} = \sum\left[A_{nb}\left(\phi_{nb} - \phi_p\right)\right]^{n+1} + S_U^{n+1} - S_p^{n+1}\phi_p^{n+1} \tag{A.52}$$

Equation (A.52) can be written in simpler form:

$$A_p \phi_p = \sum A_n b \phi_n b + S_\phi \tag{A.53}$$

where:

$$A_p = \sum A_{nb}^{n+1} + S_p^{n+1} + \frac{1.5\left(\alpha_p \rho_p V\right)^{n+1}}{\Delta t}$$

$$S_\phi = S_U^{n+1} + \frac{2\left(\alpha_p \rho_p \phi_p V\right)^{n} - 0.5\left(\alpha_p \rho_p \phi_p V\right)^{n-1}}{\Delta t}$$

This scheme is unconditionally stable; however, the negative coefficient at the time level t_{n-1}, of the three-time level method, may produce oscillatory solutions if the time steps are large. This problem can be eliminated if a bounded second-order scheme is introduced. However, oscillating solutions are most likely seen in compressible liquid flows. Therefore, a bounded second-order time scheme has been implemented in FLUENT for compressible liquid flows only. For single phase and multiphase compressible liquid flows, the second-order time scheme is, by default, the bounded scheme.

Volume-of-Fluid Model Time Schemes

In the Volume-of-Fluid model, the volume fraction equation may be solved either through implicit or explicit time discretization.

When the implicit scheme is used for time discretization, FLUENT's standard finite-difference interpolation schemes, QUICK, Second Order Upwind and First Order Upwind, and the Modified HRIC schemes, are used to obtain the face fluxes for all cells, including those near the interface.

$$\frac{\alpha_q^{n+1}\rho_q^{n+1} - \alpha_q^{n}\rho_q^{n}}{\Delta t} V + \sum_f \left(\rho_q^{n+1} U_f^{n+1} \alpha_{q,f}^{n+1}\right) = \left[S_{\alpha_q} + \sum_{p=1}^{n}\left(\dot{m}_{pq} - \dot{m}_{qp}\right)\right] V \tag{A.54}$$

where $n+1$ and n represents the index for the new and previous time step, respectively. $\alpha_{q,f}$ is the face value of the q^{th} volume fraction, computed from the first- or second-order upwind, *Quadratic Upwind Interpolation for Convective Kinematics* (*QUICK*), *Compressive Interface Capturing Scheme for Arbitrary Meshes* (*CICSAM*) and *High Resolution Interface Capturing* (*HRIC*) schemes. V is the volume of cell and U_f is the volume flux through the face, based on normal velocity. The face fluxes were interpolated either using interface reconstruction or using a finite volume discretization scheme. The reconstruction based scheme investigated was *Geometric Reconstruction* (*GR*) method given by *Donor-Acceptor* scheme can be used only with quadrilateral

or hexahedral meshes. For the computations of interpolation near the interface, the control-volume formulation required that convection and diffusion fluxes through the control volume faces be computed and balanced with source terms within the control volume itself. In the geometric reconstruction and donor-acceptor schemes, it was applied an interpolation treatment to the cells that lie near the interface between two phases.

Since Equation (A.54) requires the volume fraction values at the current time step (rather than at the previous step, as for the explicit scheme), a standard scalar transport equation is solved iteratively for each of the secondary-phase volume fractions at each time step.

The implicit scheme can be used for both time-dependent and steady-state calculations. In the explicit approach, FLUENT's standard finite-difference interpolation schemes are applied to the volume fraction values that were computed at the previous time step.

$$\frac{\alpha_q^{n+1}\rho_q^{n+1} - \alpha_q^n \rho_q^n}{\Delta t} V + \sum_f \left(\rho_q U_f^n \alpha_{q,f}^n\right) = \left[S_{\alpha_q} + \sum_{p=1}^{n} \left(\dot{m}_{pq} - \dot{m}_{qp}\right)\right] V \tag{A.55}$$

This formulation does not require iterative solution of the transport equation during each time step, as is needed for the implicit scheme. When the explicit scheme is used for time discretization, the face fluxes can be interpolated either using interface reconstruction or using a finite volume discretization scheme. The reconstruction based schemes available in FLUENT are Geo-Reconstruct and Donor-Acceptor. The discretization schemes available with explicit scheme for VOF are First Order Upwind, Second Order Upwind, CICSAM, Modified HRIC, and QUICK.

A.4.3 Evaluation of Gradients and Derivatives

Gradients are needed not only for constructing values of a scalar at the cell faces, but also for computing secondary diffusion terms and velocity derivatives. The gradient $\nabla\phi$ of a given variable ϕ is used to discretize the convection and diffusion terms in the flow conservation equations. The gradients are computed in FLUENT according to the following methods: Green-Gauss Cell-, Green-Gauss Node- or Least Squares Cell-based methods.

Green-Gauss Theorem

When the Green-Gauss theorem is used to compute the gradient of the scalar ϕ at the cell center c_0, the following discrete form is written as:

$$\left(\nabla\phi\right)_{c0} = \frac{1}{\nu}\sum_f \bar{\phi}_f \vec{A}_f \tag{A.56}$$

where ϕ_f is the value of ϕ at the cell face centroid, computed as shown in the sections below. The summation is over all the faces enclosing the cell.

Green-Gauss Cell-Based Gradient Evaluation

By default, the face value, $\bar{\phi}_f$, in Equation (A.56) is taken from the arithmetic average of the values at the neighboring cell centers, i.e.,

$$\bar{\phi}_f = \frac{\phi_{c0} + \phi_{c1}}{2} \tag{A.57}$$

Green-Gauss Node-Based Gradient Evaluation

Alternatively, $\bar{\phi}_f$ can be computed by the arithmetic average of the nodal values on the face:

$$\bar{\phi}_f = \frac{1}{N_f} \sum_{n}^{Nf} \bar{\phi}_n \tag{A.58}$$

where N_f is the number of nodes on the face.

The nodal values, $\bar{\phi}_n$ in Equation (A.58), are constructed from the weighted average of the cell values surrounding the nodes. This scheme reconstructs exact values of a linear function at a node from surrounding cell-centered values on arbitrary unstructured meshes by solving a constrained minimization problem, preserving a second-order spatial accuracy. The node-based averaging scheme is known to be more accurate than the default cell-based scheme for unstructured meshes.

Least Squares Cell-Based Gradient Evaluation

In this method the solution is assumed to vary linearly. In Figure A.7, the change in cell values between cell c_0 and c_i along the vector δr_i from the centroid of cell c_0 to cell c_i, can be expressed as:

$$(\nabla\phi)_{c0} \cdot \Delta r_i = (\phi_{ci} - \phi_{c0}) \tag{A.59}$$

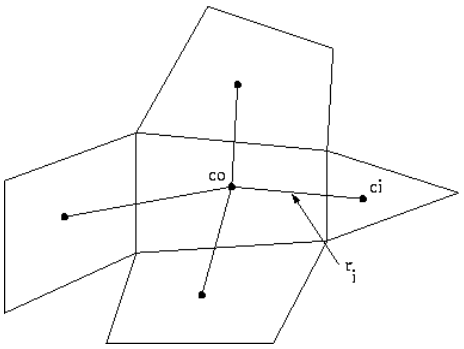

Figure A.7 Cell centroid evaluation

If we write similar equations for each cell surrounding the cell c_0, we obtain the following system written in compact form:

$$[J](\nabla\phi)_{c0} = \Delta\phi \tag{A.60}$$

where [*J*] is the coefficient matrix which is purely a function of geometry. The objective here is to determine the cell gradient, $\nabla\phi_0 = \phi_x\hat{i} + \phi_y\hat{j} + \phi_z\hat{k}$, by solving the minimization problem for the system of the non-square coefficient matrix in a least-squares sense. The above linear-system of equation is over-determined and can be solved by decomposing the coefficient matrix using the Gram-Schmidt process. This decomposition yields a matrix of weights for each cell. Thus for our cell-centered scheme this means that the three components of the weights (W^x_{i0}, W^y_{i0}, W^z_{i0}) are produced for each of the faces of cell c_0.

Therefore, the gradient at the cell center can then be computed by multiplying the weight factors by the difference vector $\Delta\phi = (\phi_{c1} - \phi_{c0})$:

$$(\phi_x)_{c0} = \sum_{i=1}^{n} W^x_{i0} \cdot (\phi_{ci} - \phi_{c0}) \tag{A.61}$$

$$(\phi_y)_{c0} = \sum_{i=1}^{n} W^y_{i0} \cdot (\phi_{ci} - \phi_{c0}) \tag{A.62}$$

$$(\phi_z)_{c0} = \sum_{i=1}^{n} W^z_{i0} \cdot (\phi_{ci} - \phi_{c0}) \tag{A.63}$$